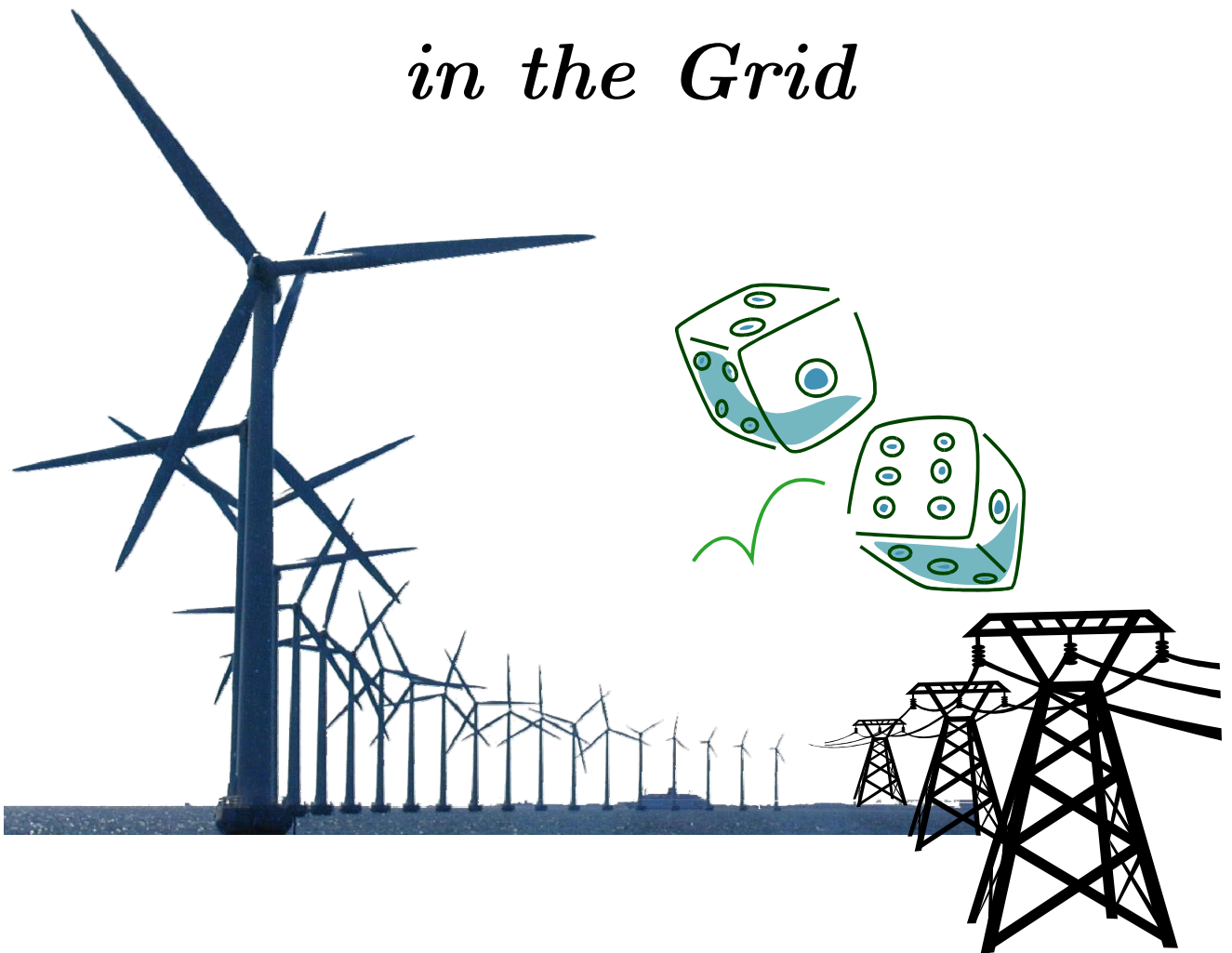




UNIVERSIDAD DE ZARAGOZA
Departamento de
Ingeniería Eléctrica



Wind Power Variability in the Grid



Joaquín Mur Amada

*Dissertation Thesis Supervised by
Dr. Ángel Antonio Bayod Rújula*

Zaragoza, November 2009

A Inma, por hacerme tan feliz.

A mi familia, a quienes debo cuanto soy.

Preface

Author's Declaration

I hereby declare that I am the sole author of this thesis.

I further authorize the University of Zaragoza to reproduce this thesis electronically, by photocopying or by other means, in total or in part, at the request of other institutions or individuals for the purpose of scholarly research.

Acknowledgements

I am specially thankful for the great freedom, support and confidence Dr. Ángel Bayod posed on me. I am specially grateful for his patience with my anarchic and individual way of working.

The enthusiasm from my collages at the Electrical Engineering Department of the University of Zaragoza and from my former students fuelled this long-lasting effort. I sincerely appreciate the empathy of the Department during my resign as lecturer in order to accomplish this work. Lecturing on Electricity and Magnetism has been an unforgettable experience.

I would like to express my gratitude to the GISEP group of CIRCE Foundation for sharing their extensive knowledge and experience. Their continuous good mood and humour has always been welcomed too!

The first prototypes of AIRE, a multifunctional datalogger, and my first nightmares during doctorate have been partially supported by Department of Education and Culture of Aragón through the B134/1998 grant.

I am specially grateful to Compañía Eólica Aragonesa S.A. (now NEO Energía), TAIM-NEG-MICON (now Vestas), Molinos de Aragón (Grupo SAMCA) and ACCIONA. Without their collaboration, this thesis would be incomplete.

Thanks to all those that have cheered me up along this arduous work. They are so many, from the nearest desk to the remote Antioquia, that any list would be inevitably short.

Finally, but most importantly, I am deep in debt with my family for their constant support and love all over these years.

Resumen en español de la tesis
Wind Power Variability In The Grid
(Variabilidad De La Potencia
Eólica En La Red Eléctrica)

La presente tesis ha analizado las principales características de la variabilidad de la energía eólica. Esta tesis se ha centrado en proporcionar un marco teórico para el análisis sistemático de la variabilidad de la energía eólica en el tiempo y en el espacio. El enfoque es principalmente empírico, basado en el procesamiento de datos y el concepto de viento equivalente. Junto con los modelos, se han realizado programas para el tratamiento de los datos registrados –véase, por ejemplo los gráficos en los anexos–. El núcleo de la tesis es el análisis de datos experimentales y su modelización, con especial énfasis en la variabilidad de la potencia eólica generada.

Algunos modelos de la estructura del viento en el espacio y el dominio de la frecuencia son extensiones de algunos modelos disponibles en la literatura. Las variaciones estocásticas han sido analizadas en el dominio de la frecuencia y en el dominio del tiempo.

La representación de la frecuencia de las fluctuaciones del viento facilita la estimación de la potencia de suavizado debido a la estructura de la turbulencia y las características cíclicas. Por una parte, la representación ortogonal de un proceso estocástico normal es su transformada de Fourier. Por otra parte, el enfoque de dominio del tiempo está más relacionado con la integridad estructural, el sistema de control, la evolución del tiempo, eventos excepcionales como rachas y el error de la predicción. Cuando ha sido posible, se ha combinado el análisis temporal y frecuencial utilizando espectrogramas.

El programa WINDFREEDOM ha sido desarrollado para comprobar el grado de aproximación de algunos modelos empíricos de la variación del viento a lo largo del tiempo y el espacio.

El programa EQWIGUST ha sido desarrollado para estudiar las variaciones extremas del viento equivalente. Puesto que las fluctuaciones del viento muestran un comportamiento de la multiplicación, se proporcionan dos transformaciones simples para compensar el comportamiento no Gaussiano del viento.

La variabilidad de la energía generada depende principalmente de la turbulencia y la evolución del clima. Además de la turbulencia y de las desconexiones, las vibraciones mecánicas y a las oscilaciones eléctricas producen fluctuaciones rápidas de potencia.

Estas peculiaridades han sido caracterizadas a partir de mediciones, pero los resultados son específicos para el modelo de la turbina y las condiciones atmosféricas momentáneas. Por lo tanto, el análisis puede ser sistematizado, pero las conclusiones de las mediciones son difíciles de generalizar.

La predicción del viento y la desconexión intempestiva de la turbina son fenómenos muy específicos, fuera del ámbito de la tesis. Sin embargo, la distribución del error de predicción y la probabilidad de una desconexión de la turbina son consideradas en el modelo propuesto de la variabilidad de la energía eólica, basado en cadenas de Markov.

La caracterización fundamental de la variabilidad del viento se presenta en el segundo capítulo. Las fluctuaciones del viento medidas con un anemómetro habitualmente se caracterizan por la variación en la densidad espectral del viento. La estructura espacial de las fluctuaciones del viento suele ser descrita por la coherencia de viento, que es el coeficiente de correlación en el dominio de la frecuencia espacial.

La estructura espacial de las turbulencias afecta al par aerodinámico de torsión experimentado por la turbina. Las oscilaciones del par de torsión debidas a la turbulencia pueden estimarse a partir de la estructura espacio-temporal del viento. Varios modelos de fluctuaciones se han obtenido y comparado con la literatura.

De hecho, la gran superficie barrida por las palas implica que las oscilaciones turbulentas muy localizadas afectan poco al par de la turbina, aunque pueden excitar modos de vibración de la máquina. En general, la dimensión espacial de las fluctuaciones del viento parece ser inversamente proporcional a su frecuencia. Por lo tanto, la relación entre las oscilaciones medidas con un anemómetro y las oscilaciones de torsión aerodinámica puede estimarse. Además, el viento equivalente se define como el que produce los mismos efectos que el campo vectorial de viento real. Las variaciones del par en función del viento se han calculado con la teoría de elementos de pala en el anexo C.

La velocidad equivalente del viento contiene: una componente estocástica debido a los efectos de la turbulencia y una componente rotacional, debida a que las palas barren un viento variable con la altura y con la perturbación provocada por la presencia de la torre de la turbina. Según la aplicación en la que se utilice la velocidad equivalente del viento, puede ser necesario incluir componentes adicionales debido a las vibraciones mecánicas y eléctricas presentes en la turbina.

La comparación entre las mediciones de la turbina y las simulaciones es complicada por la incertidumbre de la distribución del viento. Normalmente la velocidad del viento se mide en un solo lugar, por lo que no se puede comparar directamente las medidas y las simulaciones de la turbina. Sin embargo, las densidades espectrales de las varianzas del proceso medido y simulado sí se pueden comparar directamente porque son propiedades estacionarias del proceso.

El viento equivalente puede considerarse una versión filtrada del viento medido con un anemómetro. El par de torsión aerodinámico real no puede ser reconstruido a partir de una medida de un solo punto debido a la naturaleza estocástica del viento y a las complejas vibraciones de la torre. Sin embargo, las principales características estadísticas del par -o del viento equivalente- sí se pueden predecir.

El concepto de viento equivalente se puede extender a un parque eólico o incluso a un grupo de turbinas de viento. El filtrado equivalente del parque se puede definir a partir de las densidades espectrales de la varianza de la potencia del parque y de una turbina significativa. Este filtro estima el suavizado debido a la diversidad espacial de la

turbulencia a través de un parque eólico. El filtro equivalente de un conjunto de parques también se define de forma análoga al filtro de parque.

Un concepto interesante es el viento de suavizado en un área. Si existen varios parques eólicos distribuidos más o menos uniformemente en una zona, el nivel de suavizado puede estimarse a partir de las dimensiones de la región y los parámetros de la turbulencia.

Si bien las fluctuaciones lentas de la potencia generada por turbinas están fundamentalmente relacionadas con el viento, las fluctuaciones rápidas se deben en gran parte a las vibraciones de la turbina y del generador con su control electrónico.

Dado que las vibraciones de la turbina y del equipo eléctrico varían notablemente de un modelo a otro, el cuarto capítulo de esta tesis propone una metodología para caracterizar las oscilaciones observadas experimentalmente. Los fundamentos de la metodología se explican en el capítulo cuatro y se dan algunos ejemplos en el anexo B. También se presenta una revisión de la literatura sobre la densidad espectral de potencia (PSD) y los periodogramas de la potencia eólica.

Las fluctuaciones de potencia entre la frecuencia de la primera torre (por lo general algunas décimas de hercios) y la frecuencia de la red dependen de las características específicas de cada máquina. La predicción realista de estas fluctuaciones requiere un modelo muy completo de la turbina, que suele ser confidencial y privado. Incluso disponiendo de un modelo completo de la turbina, la validación de modelo con medidas experimentales no es trivial.

Una contribución de este capítulo es la caracterización experimental de las fluctuaciones de energía de tres turbinas comerciales. Las variaciones de potencia durante la operación continua de las turbinas son caracterizadas experimentalmente en intervalos de tiempo que abarcan desde el periodo de la red hasta minutos. Se presentan algunas mediciones experimentales en el dominio conjunto tiempo-frecuencia para comprobar el modelo estocástico.

La admitancia del parque eólico se define como el cociente de las oscilaciones de un parque eólico frente a las fluctuaciones de una sola turbina, suficientemente representativa del funcionamiento del resto del parque. Un modelo frecuencial vincula el comportamiento global de un gran número de turbinas a la operación de una sola turbina.

La naturaleza de la turbulencia y de las vibraciones son diferentes. La turbulencia es un proceso estocástico de amplio espectro sin frecuencias características. El equivalente de las fluctuaciones del viento, debido a la turbulencia son procesos estocásticos de banda ancha sin frecuencias características. Sin embargo, las vibraciones y oscilaciones eléctricas son procesos estocásticos casi cicloestacionarios, generalmente con varias frecuencias características de oscilación.

Las variaciones de potencia medida son el resultado de la turbulencia, las vibraciones mecánicas y las oscilaciones eléctricas, que son procesos estocásticos con propiedades diferentes.

Sin embargo, un parque eólico tiene normalmente más de cuatro turbinas y la suma de las potencia de más de cuatro turbinas converge aproximadamente en un proceso Gaussiano, a pesar de la naturaleza del proceso.

Una demostración visual del fenómeno de cancelación parcial de oscilaciones se ha desarrollado, basado en la rotación de las turbinas. Se suele asumir que la presencia de la torre produce un descenso de par aerodinámico cuando la pala está delante de la torre. Este fenómeno es complejo, ya que la perturbación de la torre interacciona con las vibraciones de la turbina. Por conveniencia, ese déficit momentáneo de potencia se representa en el quinto capítulo como un pulso periódico y determinista.

Dado que la velocidad de la turbina varía ligeramente de una a otra, las posiciones de las palas no se sincronizan. Como mucho, varias palas pueden pasar delante de su torre de forma casi simultánea de forma eventual. El paso de las palas delante de su torre se ha modelado como un proceso de Poisson. La probabilidad de las variaciones de potencias debidas a este fenómeno en un parque se deriva en el quinto capítulo.

De hecho, las vibraciones y las oscilaciones eléctricas tienen una naturaleza casi cicloestacionaria, relativamente deterministas y periódicas. No obstante, la potencia agregada converge a un proceso de Gauss en un amplio rango de frecuencias. En un parque eólico típico, la densidad espectral de varianza se agrega cuadráticamente en el rango de un centésimo de Hertz hasta la frecuencia de la red. Por lo tanto, la amplitud de las oscilaciones de la potencia, relativa a la potencia media del parque, es inversamente proporcional al número de turbinas en esas frecuencias.

En el rango de frecuencias muy bajas, las oscilaciones son dominadas por turbulencia relativamente coherente, que tiene un comportamiento fundamentalmente multiplicativo. Las variaciones de potencia de baja frecuencia en el parque tienen mayor amplitud porque estas oscilaciones presentan una menor variabilidad espacial. Además, las desviaciones lentas tienen una distribución aproximadamente laplaciana mientras que las variaciones de mayor frecuencia tienen una distribución más gaussiana. Este comportamiento laplaciano se representará mediante una transformación biyectiva de un proceso normal.

Un modelo flickermeter aproximado en el dominio de la frecuencia se presenta también en el quinto capítulo para demostrar la poca relevancia de la emisión de flicker a nivel del parque. En las mediciones del parque, el nivel de parpadeo es muy bajo debido a la cancelación parcial de las oscilaciones y a la fortaleza de la red en el punto de conexión.

La densidad espectral del viento determina el comportamiento estocástico del viento, siempre que se pueda considerar un proceso Gaussiano estacionario. En el sexto capítulo, esta densidad espectral se usará para analizar las características de las variaciones del viento en el dominio del tiempo y para sintetizar las muestras de viento equivalente.

Los mecanismos que generan la turbulencia son analizados pues están estrechamente relacionados con la forma de las rachas y la distribución de las variaciones de velocidad. Las diferencias de viento respecto de la media tienen, aproximadamente, una distribución de Laplace, que indica que hay un cierto efecto multiplicativo implicado en las desviaciones extremas.

La generación estocástica de ráfagas es una valiosa herramienta para obtener muestras aleatorias de viento con ciertas características. El fundamento de este método es la simulación estocástica condicionada de los procesos, que se basa en las distribuciones condicionales. Una transformación biyectiva se define para obtener la distribución experimental. Algunas transformaciones más sofisticadas pueden ser utilizadas para mejorar el ajuste de la forma y la probabilidad de ocurrencia de los datos experimentales. Por ejemplo, en algunos estudios se ha observado que la rampa frontal real de la ráfaga es, en promedio, mayor que la rampa de cola. Sin embargo, las ráfaga predichas son simétricas cuando se visualizan hacia delante y cámara atrás.

Las ráfagas tipo pico y tipo rampa se sintetizan en el dominio de la frecuencia utilizando la expansión de Karhunen-Loève y la teoría de la simulación condicional de los procesos normales. Un método aproximado se presenta para evitar dificultades numéricas que aparecen cuando se generan muestras de gran longitud.

El concepto de la ráfaga de viento equivalente se puede extender a un área geográfica y puede servir para calcular la máxima variabilidad de la potencia esperada en una región.

El programa EQWIGUST genera ráfagas de viento equivalente y estima su frecuencia de ocurrencia.

La variabilidad de la velocidad del viento puede ser modelada durante intervalos cortos con la teoría clásica de procesos normales estacionarios, que se ha presentado en los capítulos anteriores. Sin embargo, el viento es un proceso no estacionario y esto es necesario ser considerado para horizontes más de una hora.

Dado que las variaciones del viento muestran un comportamiento bastante multiplicativo, el método de Aproximación de Markov es adecuado para modelar el comportamiento estocástico no lineal del viento. Esta técnica es una poderosa herramienta para optimizar el control del sistema, especialmente si la distribución del error de las predicciones numéricas del tiempo están disponibles. En caso de que no se disponga de predicciones meteorológicas, las cadenas de Markov se pueden utilizar para generar predicciones probabilísticas basada en el comportamiento del sistema observado previamente.

Muchos dispositivos en la red son discretos y su control no puede ser linealizado porque su conmutación innecesaria puede producir su desgaste prematuro o perturbaciones evitables en la red. El diseño y el control óptimos se pueden alcanzar mediante la asignación de costos a la permanencia del sistema en el mismo estado y al salto a otros estados.

Un procedimiento para discretizar el sistema generando un número reducido de estados se presenta en el capítulo 7, basado en un sistema de agrupación y clasificación de las observaciones.

Una aplicación potencial de este método se encuentra en el cálculo probabilístico de flujo de cargas. Otra aplicación es el diseño óptimo y el control de un sistema aislado con generación renovable y almacenamiento.

Contribuciones originales de la tesis

Algunas de las contribuciones provienen de la experiencia adquirida en el diseño, construcción, instalación y análisis de un registrador de datos multipropósito que, a día de hoy, está disponible comercialmente. El trabajo realizado en el desarrollo de este registrador de datos se puede ver en algunos de los artículos citados en la sección de publicaciones al final de la tesis. El desarrollo de un analizador de redes basado en un PC en el año 1998, que además almacenaba de forma sincronizada datos meteorológicos y de la turbina o del parque eólico, fue un logro. Aunque hoy en día el registrador de datos es bastante diferente del original, la experiencia adquirida con los primeros prototipos, desarrollados durante los primeros años de esta tesis, ha sido fundamental para que el registrador multifuncional AIRE estuviera disponible comercialmente.

El tercer capítulo calcula el suavizado del viento equivalente a partir de las dimensiones del área considerada y de los parámetros de la turbulencia. El viento equivalente ha sido utilizado también en la simulación de modelos de conjuntos de parques eólicos. Sin embargo, la estimación del suavizado del viento equivalente de un parque eólico o de una zona geográfica a partir de la coherencia del viento es una contribución importante de esta tesis.

Una nueva metodología para la caracterización de las oscilaciones medidas en la potencia de una turbina de viento o de un parque eólico ha sido propuesta en el capítulo cuatro.

El quinto capítulo muestra la convergencia a un proceso gaussiano de las oscilaciones globales debido a las vibraciones, la turbulencia y las fluctuaciones eléctricas. Este modelo también muestra la poca relevancia de la emisión de flicker de los parques eólicos.

Las ráfagas de viento equivalente se calculan en el sexto capítulo, y pueden servir para calcular la máxima variabilidad de la potencia eólica esperada en una región.

El séptimo capítulo presenta la aplicación del método de Aproximación de Markov para optimizar el diseño del sistema y el control en dos casos.

El anexo A se muestra un modelo estadístico simplificado para representar a un parque eólico en un estudio de flujo de cargas, teniendo en cuenta la variabilidad de la potencia eólica.

El anexo B muestra algunos ejemplos de los análisis de los datos experimentales obtenidos con el registrador de datos multipropósito. Algunos efectos observados en los datos como la medición de las oscilaciones son bastante difíciles de predecir utilizando únicamente simulaciones.

El anexo C presenta un modelo aerodinámico para calcular la influencia de la componente determinista del viento (variación del viento con la altura y la perturbación de la torre) utilizando el coeficiente del par y las dimensiones de la turbina.

La representación de un parque eólico requiere conocer la distribución de las velocidades del viento y de las turbulencias a lo largo de un parque eólico. El modelo incluido en el anexo D permite, además, probar diferentes modelos de estelas.

Otra contribución de esta tesis es el programa que descarga, representa y analiza los datos de la red de estaciones meteorológicas que suelen utilizar los organismos meteorológicos para la predicción del tiempo.

El manual del usuario del programa WINDFREEDOM con el análisis de tres emplazamientos ha sido incluido para demostrar el uso potencial de este programa.

Otra contribución de esta tesis es el programa que genera ráfagas de viento equivalente con ciertas características y estima su probabilidad de ocurrencia.

En resumen, esta tesis ha intentado aportar una metodología para el estudio de las variaciones de potencia eólica, basándose en la distribución espacio-temporal del viento y en el análisis de medidas experimentales. Además, proporciona un marco para el diseño y control óptimo de sistemas afectados por la disponibilidad del viento.

Index

PREFACE	I
Author's Declaration.....	i
Acknowledgements.....	i
INDEX	I
LIST OF FIGURES	VII
LIST OF TABLES	XVII
CHAPTER 1: INTRODUCTION	1
1.1. Background	1
1.1.1. Relationship between wind power variability and its forecast	1
1.1.2. Influence of the wind variability on the grid.....	1
1.1.3. Geographic diversity on wind power.....	2
1.1.4. Demand response and wind variability	3
1.1.5. Estimated cost of wind power variability	3
1.2. Scope and Aims	4
1.3. Thesis Outline	5
CHAPTER 2: VARIABILITY OF WIND IN THE FREQUENCY DOMAIN	9
2.1. Introduction	9
2.2. Characterization of the turbulence	10
2.2.1. Energy cascade in eddies	10
2.2.2. Largest and shortest length scales	11
2.2.3. Taylor's Hypothesis of "frozen turbulence"	11
2.3. Wind spectra	12
2.3.1. Properties of spectra	12
2.3.2. Integral length scale.....	13
2.3.3. Classic description of turbulence in the frequency domain.....	13
2.3.4. Kaimal wind spectrum.....	15
2.3.5. Davenport wind spectrum.....	16
2.3.6. Harris wind spectrum	16
2.3.7. Von Karman wind spectrum.....	16
2.3.8. IEC 61400-1 spectrum	16
2.3.9. Slettringen spectrum recommended by the Norwegian Petroleum Directorate.....	16
2.3.10. Van der Hoven's wind spectra	16
2.3.11. Horns Rev wind spectra	17
2.3.12. Coherence models.....	17
2.4. Spectrum and coherence estimated from the weather station network	17
2.4.1. Coherence between Logroño and Zaragoza airports (Spain, 140,5 km apart).....	18
2.4.2. Coherence between Pamplona and Zaragoza airports (Spain, 133,6 km apart).....	22
2.4.3. Coherence between Pamplona and Logroño airports	23
Conclusions	23
CHAPTER 3: THE TURBINE TORQUE AND THE EQUIVALENT WIND	25
3.1. Wind turbine torque	25
3.2. Definition of the equivalent wind, equivalent turbulence and effective quadratic turbulence	25
3.2.1. Equivalent wind	25
3.2.2. Equivalent turbulence	26
3.2.3. Effective quadratic turbulence	26
3.2.4. Linearization of quadratic turbulence	27
3.3. Effect of transversal components of wind	27
3.4. Wind smoothing from turbine rotor and equivalent wind	27
3.4.1. Fundamentals of spatial filtering in rotor	27
3.4.2. Turbulence models for estimating smoothing of equivalent wind.....	28
3.4.3. Average rotor wind speed vs. wind speed at hub height	30
3.5. Calculation of aerodynamic filter based on 3D wind waves	32
3.5.1. Comparison of 3D wind waves with frozen turbulence	32
3.5.2. Model of 3D wind waves	32
3.5.3. Spatial turbulence averaged along the blades.....	33
3.5.4. Spatial turbulence averaged across the rotor disk area	33
3.6. Torque dependence on rotor position	34
3.6.1. Cascade rotational sampling filter from Petru and Thiringer	34
3.6.2. Proposed rotational sampling model	36
3.7. Small signal model of aerodynamic torque	38
3.7.1. Derivation of the small signal model.....	38
3.7.2. Classification of turbines according their controllable parameters.....	38
3.7.3. Analysis of fluctuations at characteristic operational points	39
3.7.4. Small signal approximation of effective quadratic turbulence $\Delta(U_{eq}^2)$ on equivalent turbulence ΔU_{eq}	40
3.7.5. Influence of turbine control.....	40
3.8. Equivalent wind of turbine clusters	40
3.8.1. Equivalent wind of a farm.....	40
3.8.2. Equivalent wind of turbines distributed along a geographical area	43

3.8.3. Equivalent wind smoothing due to turbine spatial layout.....	44	5.4.3. Estimation of total flicker during continuous operation(periodic and aperiodic).....	78
Conclusions	45	5.5. Spectrum of the eye output and the average instantaneous flicker	79
CHAPTER 4: VARIABILITY OF POWER IN THE FREQUENCY DOMAIN	47	5.6. Conclusions.....	80
4.1. Introduction.....	47	CHAPTER 6: CHARACTERIZATION OF WIND GUSTS IN THE TIME DOMAIN	81
4.2. Overview of wind power fluctuations	47	6.1. Introduction	81
4.2.1. Random and cyclic fluctuations.....	48	6.2. Statistical distribution of wind variations depending on turbulence mechanism.....	81
4.2.2. Major difficulties on the fluctuation characterization	48	6.2.1. Wind distributions in the literature	82
4.3. Mathematical framework.....	49	6.2.2. Simplistic models based on energy or momentum transfer.....	83
4.3.1. Definitions.....	49	6.2.3. Constant probability of acceleration direction change	85
4.3.2. Statistical properties of the sum of stochastic spectral phasor densities	50	6.2.4. Multiplicative processes in turbulence due to energy cascade	85
4.3.3. Spectral density of uncorrelated oscillations in a group of turbines.....	53	6.3. Conclusion on turbulence mechanisms.....	86
4.4. Sum of partially correlated phasor densities of power from several turbines.....	54	6.4. Memory-less transformation of the Gaussian process.....	87
4.4.1. Sum of fully correlated and fully uncorrelated spectral components.....	54	6.4.2. Maximum speed expected in a register of length T	89
4.4.2. Sum of partially linearly correlated spectral components	54	6.5. Unconditional generation of random samples	91
4.4.3. Estimation of wind farm power admittance.....	56	6.5.1. Notation of sampled stochastic processes	91
4.5. Parameterization of the power output spectrum	56	6.5.2. Foundations of the unconstrained generation of random samples.....	92
4.5.1. Estimation of power variance during a time interval	58	6.6. Peak type gusts	93
4.6. Estimation of parameters from measured data .	58	6.6.1. Gust concept	93
4.6.1. General features of measured data.....	58	6.6.2. Assessment of peak type gust.....	96
4.6.2. Procedure to estimate model parameters	59	6.6.3. Mean shape of a peak gust	96
4.7. Estimation of parameters from the literature ...	60	Conclusions.....	99
4.8. Conclusions	60	CHAPTER 7: VARIABILITY OF RENEWABLE GENERATION IN THE TIME DOMAIN	101
CHAPTER 5: ALMOST PERIODIC FLUCTUATIONS IN THE TIME DOMAIN	63	7.1. Introduction to Markov Decision Processes.....	101
5.1. Blade angle difference among turbines in a wind farm	63	7.2. Formulation.....	101
5.2. Tower shadow and wind shear effect in the wind farm power	63	7.2.1. Introduction to Markov chains.....	101
5.2.1. Distribution of the fluctuation	64	7.2.2. Markov chain approximation for continuous systems.....	102
5.2.2. Rate of tower shadow events	66	7.2.3. Time-Averaged vs Instantaneous Values.....	103
5.2.3. Modulation of the pulse density at the wind farm with randomly distributed pulses.....	69	7.2.4. Reconstruction of continuous signal from logged values	103
5.3. Contribution of periodic components to Flicker	73	7.2.5. Considerations on the state discretization	105
5.3.1. Voltage variations of induced by power fluctuations	73	7.2.6. Need for discretization of continuous random variables	106
5.3.2. Standard IEC 61400-21 approach to flicker emission from wind farms.....	74	7.3. Piecewise linear interpolation of system properties	106
5.4. Contribution of aperiodic components to Flicker	77	7.3.1. Triangular probability distribution of the sates from observations (i.e.)	106
5.4.1. Simplified PSD for flicker estimation	77	7.3.2. Distribution of observations from state probabilities	106
5.4.2. Flicker contribution from a parameterized PSD ...	78	7.3.3. Estimation of state centroids $\vec{\gamma}$	107

7.3.4. Expected observation from state probabilities....	107	7.10.9. Probabilistic discretized model of SOC	128
7.4. Systems with multiple observations at time k .108		7.10.10. Model of Water Reservoir Storage.....	129
7.4.1. Estimation of \mathbf{P} from conventional clustering. ..	108	Conclusions	129
7.4.2. Improving state estimation.....	108	CHAPTER 8: CONCLUSIONS AND FUTURE	WORK
7.4.3. Estimation of \mathbf{P} from fuzzy clustering.....	109		131
7.4.4. Generation of interpolated samples.....	109	8.1. Conclusions	131
7.5. Autocorrelation function of Markov Chains.....110		8.2. Original Contributions	133
7.5.1. Power Spectral Density of discrete Markov chains	110	8.3. Perspectives and future research.....	133
7.5.2. Further considerations on the PSD of continuous	110	8.4. Publications.....	134
MC	110	ANNEX A: SIMPLIFIED ELECTRICAL MODEL	OF THE WIND FARM
7.6. Addition of long-lasting memory feature.....110			137
7.6.1. Hourly, daily, weekly and seasonal dependence ..	111	A.1. Introduction	137
7.7. Interpolation among basic periodic states112		A.2. Simplified electrical model of the wind farm ..	138
7.7.1. Introduction.....	112	A.2.1. Turbine power curve	138
7.7.2. Periodic interpolation approach as a multivariate	112	A.2.2. Wind farm power curve.....	139
Markov chain.....	112	A.3. Wind farm model	141
7.7.3. Comparison of linear, cosine and Gaussian periodic	113	A.3.1. Final representation of the Farm	141
interpolation	113	A.3.2. Substation modeling.....	142
7.7.4. Periodic linear interpolation	113	A.4. Modeling of the underground MV network....	142
7.7.5. Benefits from discrete approximation of continuous	115	A.4.2. Modeling of the turbines	143
time and state Markov models	115	A.4.3. Uncertainty of the model	146
7.8. Application Example I: Characterization of wind		A.4.4. Model of the electrical grid of the farm.....	147
power variability with Markov Chains115		A.4.5. Model of nearby wind farms.....	148
7.8.1. Introduction.....	115	A.5. Reactive power control	148
7.8.2. Step changes in Power Output	115	A.5.1. Limits on reactive power	148
7.8.3. Statistical Approach to Variability.....	116	A.5.2. Reactive Power Policy.....	149
7.8.4. Characterization of Power Variability of Wind	117	A.5.3. Constant power factor regulation.....	149
Generation with Markov Chains.....	117	A.5.4. Automatic voltage control.....	149
7.8.5. State selection.....	117	A.5.5. Scheduled reactive control.....	150
7.8.6. Considerations on $\hat{\mathbf{P}}$	118	A.5.6. Reactive power under centralized control.....	150
7.9. Experimental Validation of Case Study I.....118		A.5.7. Effect on power losses	151
7.9.1. Markov Model Based on Wind Parameters	118	A.5.8. Uncertainty analysis.....	151
7.9.2. Improving Markov model with weather forecast. 118		Conclusions	152
7.9.3. Discerning switching events from continuous	118	Annex: Example Data.....	152
operation.....	118	ANNEX B: ANALYSIS OF WIND POWER	VARIABILITY FROM MEASURED DATA
7.9.4. Stochastic time interpolation	119		153
7.9.5. Input data.....	119	B.1. Fixed speed, stall regulated turbine of 750 kW 153
7.9.6. Estimation of the state sequence	119	B.1.1. Record of 20/10/00, 13:37-13:50 (low winds)	153
7.10. Stochastic power flows119		B.1.2. Analysis of real power output.....	153
7.10.1. Markov chains in stochastic power flow.....	119	B.1.3. Analysis of reactive power output	155
7.10.2. Simplified model of a wind farm to account active	121	B.1.4. Analysis of wind measured at the meteorological	155
and reactive losses	121	mast 40 m above surface level.....	155
7.10.3. Essence of the new approach to probabilistic power	122	B.1.5. Analysis of phase-to-phase voltage	156
flow.....	122	B.1.6. Bode magnitude plots.....	157
7.10.4. Description of the group of wind farms.....	122	B.2. Fixed speed, stall regulated turbine of 600 kW 158
7.10.5. Markov model obtained from conventional	123		
clustering	123		
7.10.6. System dynamics and equivalent stochastic	124		
differential equations	124		
7.10.7. Permanence time in a state.....	126		
Application example II: Isolated system with storage			
.....127			
7.10.8. Battery State of Charge.....	127		

B.2.1. Record of 28/7/00, 13:48 to 13:52 and 13:36 to 13:41 (medium winds).....	158	C.4.1. Relative flow angle variation $\Delta\phi(\varphi)$ on the blade near the tower	195
B.2.2. Analysis of real power output	159	C.4.2. Equivalent average squared inverse tip speed ratio $\langle\lambda_i^{-2}\rangle$	196
B.2.3. Analysis of reactive power output	160	C.4.3. Equivalent average squared inverse tip speed ratio $\langle\lambda_i^{-2}\rangle$ on the blades not affected by tower shadow	196
B.2.4. Analysis of wind measured at the meteorological mast 40 m above surface level.....	162	C.4.4. Equivalent average squared inverse tip speed ratio $\langle\lambda_i^{-2}\rangle$ on the lowest blade.....	196
B.2.5. Analysis of phase-to-phase voltage.....	162	C.4.5. Comparison of the accuracy of the approximate analytical formulas	197
B.2.6. Bode magnitude plots.....	163	C.4.6. Comparison of the aerodynamic torque accuracy from the approximate models.....	197
B.3. VRIG wind farm	164	C.5. Tower lateral and longitudinal bending oscillations.....	198
B.3.1. Record of 26/2/99, 13:52:53-14:07:30 (low winds)	164	C.5.1. Tower longitudinal bending.....	198
B.3.2. Analysis of real power output	164	C.5.2. Tower lateral bending.....	198
B.3.3. Analysis of reactive power output	165	C.6. Numerical integration of rotor torque	199
B.3.4. Analysis of wind measured at the meteorological mast 40 m above surface level.....	166	C.6.1. Turbine aligned with the wind	199
B.3.5. Analysis of phase-to-phase voltage.....	167	C.6.2. Turbine misaligned with respect average wind direction	199
B.3.6. Bode magnitude plots.....	167	Conclusions.....	200
B.4. DFIG wind turbines.....	168	ANNEX D: WAKE ESTIMATION IN AN OFFSHORE WIND FARM	201
B.4.1. Notes on the estimation of model parameters	168	D.1. Introduction	201
B.4.2. Wind turbine at medium winds, 12/3/99, 9:52 to 10:07 and 10:07 to 10:14	169	D.2. Momentum deficit in a wake.....	201
B.4.3. Analysis of real power output	170	D.2.1. Model fit to experimental measures.....	204
B.4.4. Analysis of reactive power output	171	D.2.2. Upstream/downstream ordering of turbines.....	204
B.4.5. Analysis of wind measured at the meteorological mast 30 m above surface level.....	171	D.2.3. Cascade estimation of the wind field	205
B.4.6. Analysis of line voltage	173	D.3. Added turbulence in a wake	205
B.4.7. Bode magnitude plots.....	173	D.3.1. Cascade estimation of the squared turbulence....	205
B.5. Wind farm at medium winds, 12/3/99, 9:48 to 10:01 and 10:09 to 10:19	174	D.3.2. Definition of the speed deficit and the turbulence excess in the source code	206
B.5.1. Analysis of real power output	175	D.4. Conclusions.....	206
B.5.2. Analysis of reactive power output	176	ANNEX E: MANUAL OF THE PROGRAM WINDFREDOM	209
B.5.3. Analysis of wind measured at the meteorological mast 30 m above surface level.....	177	E.1. Instalación del programa “Mathematica Player”	209
B.5.4. Analysis of phase-to-phase voltage.....	177	E.2. Apertura del fichero de cálculos	209
B.5.5. Bode magnitude plots.....	178	E.3. Datos disponibles de estaciones meteorológicas mundiales	210
B.6. Comparison of PSD of a wind farm with respect to one of its turbines, 12/3/99, 9:48 to 10:01 and 10:09 to 10:19.....	179	E.4. Solapas del programa.....	211
B.6.1. Real power	179	E.4.1. Mapa de las estaciones meteorológicas cercanas ..	211
B.6.2. Reactive power	180	E.4.2. Disponibilidad de las estaciones meteorológicas..	212
B.7. Spectrogram	181	E.4.3. Selección de la estación meteorológica de referencia	213
Conclusions	183	E.4.4. Selección de la estación meteorológica a comparar	220
ANNEX C: TORQUE ESTIMATION FROM BLADE ELEMENT THEORY	185	E.4.5. Periodograma y ratio entre espectrogramas.....	221
C.1. Blade element theory fundamentals	185	E.4.6. Coherencia entre dos series temporales.....	223
C.2. Alternative torque calculation by Sørensen....	190	E.4.7. Fase de la coherencia entre dos estaciones (desfase entre los espectros).....	223
C.3. Modulation of torque due to wind shear	190		
C.3.1. Two-bladed turbine.....	191		
C.3.2. Three-bladed turbine.....	192		
C.3.3. Effect of rotor tilt and coning in the equivalent tip speed ratio	192		
C.4. Tower shadow effect	193		

E.4.8. Módulo de la coherencia entre dos estaciones 225

E.5. Resumen de la comparación entre las estaciones
226

ANNEX F: MANUAL OF THE PROGRAM
EQWIGUST **229**

F.1. Espectro del viento equivalente229

F.2. Generación de serie aleatoria de viento
equivalente230

F.3. Forma promedio de racha tipo pico230

F.4. Generación de racha tipo pico aleatoria.....231

F.5. Generación de racha tipo rampa aleatoria.....231

ANNEX G: SYMBOLS AND NOMENCLATURE
233

G.1. Frequently Used Symbols and Abbreviations .233

G.1.1. General Acronyms 233

G.1.2. Aerodynamic variables and functions 233

G.1.3. Power output variables and functions 233

G.1.4. Model parameters 234

G.1.5. Markov Decision Processes 234

G.2. Nomenclature234

G.2.1. General conventions..... 234

G.2.2. Nomenclature in frequency domain..... 235

G.2.3. Convention for indicating the typical range of
 magnitudes 237

G.2.4. Nomenclature in Markov Decision Processes 237

G.2.5. Convention for indicating the typical range of
 magnitudes 237

REFERENCES **239**

List of Figures

<p>Fig. 1: Drawing of a turbulent flow by Leonardo da Vinci (1452–1519), who recognized that turbulence involves a multitude of eddies at various scales. Taken from Benoit Cushman-Roisin [55]..... 10</p> <p>Fig. 2: Eddy orbital velocity versus eddy length scale in homogeneous turbulence. The largest eddies spin the fastest. Taken from “Environmental Fluid Mechanics” of Benoit Cushman-Roisin [55] and modified from Simon Watson [56]. 10</p> <p>Fig. 3: Schematic of eddies as a function of height at atmospheric boundary layer. Taken from Simon Watson [56]. 10</p> <p>Fig. 4: The turbulent energy cascade. According to this theory, the energy fed by external forces excites the largest possible eddies and is gradually passed to ever smaller eddies, all the way to a minimum scale where this energy is ultimately dissipated by viscosity. Taken from Benoit Cushman-Roisin [55]. 10</p> <p>Fig. 5: Example of a idealized eddy of 100 m (represented by a cloud) passing through a meteorological mast according to Taylor’s Hypothesis of “frozen turbulence”... 12</p> <p>Fig. 6: Model spectra of the streamwise velocity component 50 m above ground level in flat terrain for neutral (L infinite), stable ($L = 30$ m) and unstable ($L = -30$ m) conditions, where L is the Monin-Obukhov length. The areas under the curves are proportional to the variances. Taken from “Wind Power Meteorology” by Risø National Laboratory [63]..... 14</p> <p>Fig. 7: Probability distribution of length scales from the Vindeby site at heights of 48 m. Length scales were derived by the “half variance” method. Taken from “Wind Power Meteorology” by Risø National Laboratory [63]. 15</p> <p>Fig. 8: Van der Hoven’s spectral model (from [78])..... 17</p> <p>Fig. 9: Definition of distance d and angle α between the points r and c. 17</p> <p>Fig. 10: Map from WINDFREDOM program [54] with the location of Zaragoza and Logroño in the Iberian Peninsula..... 18</p> <p>Fig. 11: Periodogram and spectrogram of Zaragoza airport (Spain) estimated with WINDFREDOM program [54]. 18</p> <p>Fig. 12: Periodogram and spectrogram of Logroño airport (Spain) estimated with WINDFREDOM program [54]. 18</p> <p>Fig. 13: Periodogram and spectrogram of Logroño airport divided by the ones of Zaragoza airport (estimated by WINDFREDOM program [54]). 19</p> <p>Fig. 14: Phase difference between the periodogram and spectrogram of Zaragoza airport respect the ones of</p>	<p>Logroño airport (estimated by WINDFREDOM program [54]). 19</p> <p>Fig. 15: Time lag of the oscillations of Zaragoza airport respect the ones of Logroño airport (estimated by WINDFREDOM program [54]). 20</p> <p>Fig. 16: Quantiles 5%, 25%, 50% and 95% of the estimated time delay (in days) between the fluctuations in Zaragoza airport respect the fluctuations of Logroño airport of the same frequency (estimated by WINDFREDOM program [54]). 20</p> <p>Fig. 17: Coherence of Zaragoza and Logroño airport winds (estimated by WINDFREDOM program [54])..... 21</p> <p>Fig. 18: Comparisons of several coherence models Time lag of oscillations of Zaragoza airport respect the ones of Logroño airport (estimated by WINDFREDOM program [54]). 21</p> <p>Fig. 19: Map from WINDFREDOM program [54] with the location of Zaragoza and Pamplona in the North of the Iberian Peninsula. 22</p> <p>Fig. 20: Periodogram and spectrogram of Logroño airport (Spain) estimated with WINDFREDOM program [54]..... 22</p> <p>Fig. 21: Periodogram and spectrogram of Pamplona airport divided by the periodogram and spectrogram of Zaragoza airport (estimated by WINDFREDOM program [54])..... 22</p> <p>Fig. 22: Quantiles 5%, 25%, 50% and 95% of the estimated time delay (in days) between the fluctuations in Zaragoza airport respect the fluctuations of Pamplona airport of the same frequency. 23</p> <p>Fig. 23: Time lag of the oscillations of Zaragoza airport respect the ones of Pamplona airport. 23</p> <p>Fig. 24: Comparison of several coherence models Time lag of oscillations of Zaragoza airport respect the ones of Pamplona airport..... 24</p> <p>Fig. 25: Coherence of Zaragoza and Pamplona airport winds. 24</p> <p>Fig. 26: Coherence of Logroño and Pamplona airport winds. 24</p> <p>Fig. 27: Effect of an uneven wind-speed distribution over the swept rotor area on the upwind velocity of the rotating rotor blades. The lagrangian motion coordinates are added assuming the turbine is aligned with the wind. Taken from “Dynamic wind turbine models in power system simulation tool DIGSILENT” by Risø National Laboratory [88]. 25</p> <p>Fig. 28: Rotor power coefficient $C_p(\lambda, \theta)$ for a variable-pitch turbine. 26</p> <p>Fig. 29: Rotor torque coefficient $C_q(\lambda, \theta)$ for a variable-pitch turbine. 26</p> <p>Fig. 30: Differential sector area to compute the average fluctuation along the rotor area. 29</p>
--	--

Fig. 31: Differential annular area assuming rotational symmetry.....	29	Fig. 51: Rectangular area divided in smaller transversal areas.....	44
Fig. 32: Comparison of aerodynamic filters (42) –dashed purple line–, (47) –solid blue line– and (48) –dot-dashed brownish line– for a rotor of radius $R = 50$ m, average wind speed $\langle U \rangle = 10$ m/s and integral turbulence length $\ell_{\text{int}} = 1000$ m ($f_{\text{int}} = 0,0245$ Hz approximately).....	30	Fig. 53: Normalized ratio $PSD_{\text{transversal}}(f) / PSD_{\text{longitudinal}}(f)$ for transversal (solid thick black line) and longitudinal areas (dashed dark gray line for $A_{\text{trans}} = 4$, long dashed light gray line for $A_{\text{long}} = 1,8$). Horizontal axis is expressed in either longitudinal and lateral adimensional frequency $a A_{\text{trans}} f / \langle U \rangle$ or $b A_{\text{long}} f / \langle U \rangle$	45
Fig. 33: Shear exponent α as a function of roughness length and elevation, relative to hub height from eq. (53).	31	Fig. 54: Model of the phasor diagram at frequency f of a park with four turbines with similar uncorrelated fluctuation level $P(f)$	51
Fig. 34: Differential area assuming dependence only with height.	31	Fig. 55: Sum of two phasor with same magnitude.	51
Fig. 35: Ratio $m = \langle U_{\text{wind}} \rangle_{\text{rotor}} / U_{\text{wind}}(H)$ with shear exponent $0 < \alpha < 1$ for different tower heights.....	31	Fig. 56: Sum of two phasor with different magnitude.	51
Fig. 36: Plot of the longitudinal wind component corresponding to a 3D wave which at an anemometer appears as a fluctuation of frequency $f = 5$ Hz and a turbine rotor of radius $R = 50$ m.	32	Fig. 57: Normalized $PDF_{\text{P}}(P)$ for wind farms with $N = 8, 16$ and 32 turbines.	52
Fig. 37: Flow curls due to the eddies and the corresponding modulation of the longitudinal wind component.....	33	Fig. 58: Basic procedure for estimating P' , r' , f' and f_{int}	59
Fig. 38: Averaged wind fluctuation along the blades of a rotor of radius $R = 50$ m, $v_{\text{max}} \approx v_{\text{min}}$ and the asymptotic approximation to a system of order $r = 1$	33	Fig. 59: Power output at a single turbine with blade rate 1 Hz, depth of tower shadow $\alpha = 0,06$ p.u. and average power loss $= \alpha \tau / T = 0,0075$ p.u. (the power dip shapes are rectangular, triangular and Gaussian).....	64
Fig. 39: Averaged wind fluctuation in the area of the rotor disk radius $R = 50$ m, $v_{\text{max}} \approx v_{\text{min}}$ and the asymptotic approximation to a system of order $r = 3/2$	34	Fig. 60: CDF of pulses at a wind farms of 1, 3, 5, 10, 20 and 50 turbines (starting from upper part at zero fluctuation). The parameters of the pulses correspond to Fig. 59 and rectangular shape ($p = \tau / T = 0,125$). The discrete CDF (210) has been evaluated at midpoints to account that real pulses are continuous and derivable.	65
Fig. 40: Block diagram of the cascade model in [43] for off-line equivalent wind time series generation (actual rotor angle φ and pitch angle θ are not considered).	34	Fig. 61: Probability of farm output exceeding the normalized deviation $y/N \alpha$ for farms with of 1, 3, 5, 10, 20 and 50 turbines as in the previous figure.	65
Fig. 41: Wind speed power spectral density before and after the application of aerodynamic filters and a system of fractional order $r = 1.6947$. (Other conditions: von Karman, $U = 10$ m/s, $L2 = 150/2,329$ m, $I = 0,10$, $f_{\text{int}} = 1,0$ Hz, $R = 50$ m, $gd = 2\pi f_{\text{int}} / 15$).....	35	Fig. 62: Discretization of a pulse dip into tree segments taking the mass center of each segment.	66
Fig. 42: Estimation of σ_{max} from the rotor aerodynamic torque.	35	Fig. 63: Discrete counterpart of the continuous pulse dip of Fig. 62. Notice that the energy power loss (area beneath the pulse) of both pulses are the same.	66
Fig. 44: Diagram of the generation in the time domain of the equivalent wind in a farm.....	37	Fig. 64: Power output of 5 turbines with blade position uniformly distributed. The parameters of the pulses correspond to Fig. 59 and Gaussian shape.	67
Fig. 45: Diagram of the proposed additive rotational sampling model for the off-line estimation of the equivalent wind in the frequency domain.	37	Fig. 65: Overall tower shadow effect at the wind farm output as the sum of individual turbine power of Fig. 64.	67
Fig. 46: Simplified block scheme for off-line equivalent wind time series generation (actual rotor angle φ and pitch angle θ are not considered).....	37	Fig. 66: Individual tower shadow pulses of Fig. 64 and their sum (notice the diminution of fluctuation due to the smoothness of Gaussian pulses).....	68
Fig. 47: Wind farm dimensions, angles and distances among wind farm points for the general case.	43	Fig. 67: Individual tower shadow pulses of Fig. 64 with triangular shape and their sum (notice that the fluctuation of the pulse sum increases with the sharpness of individual fluctuations shape).	68
Fig. 48: Wind farm parameters when wind has the x direction ($\beta = 0$).	43	Fig. 68: Individual tower shadow pulses of Fig. 64 with rectangular shape and their sum (notice that rectangular pulse shape is the contour that produces the most variable output at the wind farm).	68
Fig. 49: Wind farm with turbines aligned transversally to the wind.....	44	Fig. 69: Individual tower shadow pulses with Gaussian shape and random blade position corresponding to a wind	
Fig. 50: Wind farm with turbines aligned longitudinally to the wind.....	44		

farm with $N = 20$ turbines spinning at $\Omega = 20$ rpm (1 blade/s).....	69	Fig. 85: Measured and fitted probability density of instantaneous wind minus the instantaneous wind at $T =$ 10,2 s, 10 s, 20 s, 200 s and 2000 seconds (from top to bottom). For great clarity, the plots are displaced downwards. Reproduced from F. Böttcher, St. Barth, and J. Peinke [231].	83
Fig. 70: Small signal model of the farm.....	73	Fig. 86: Control volume laterally limited by stream lines upstream the turbine.	84
Fig. 71: Simplified block diagram of IEC Flickermeter according to IEC 61000-4-15	74	Fig. 87: PDF of a normal random variable X (solid blue line) and the distribution of $\pm X^\circ$ where X is normal (dashed purple line). Both distributions have unity variance and zero mean	85
Fig. 72: Flicker coefficient for a farm with Gaussian rotational effect.	76	Fig. 88: PDF of a normal random variable X (solid blue line) and the distribution of $\pm X$ where X is normal (dashed purple line). Both distributions have unity variance and zero mean.	85
Fig. 73: Flicker coefficient for a farm with rectangular rotational effect.	77	Fig. 89: Graph of the bijective transformation of the auxiliary Gaussian process $x(t)$ into the real process $y(t)$, with Laplacian distribution, compared to the identity transformation.	87
Fig. 74: Flicker coefficient for a farm with triangular rotational effect.	77	Fig. 90: Graph of the bijective transformation of the auxiliary Gaussian process $x(t)$ into the real process $y(t)$, with signed Chi-Squared distribution, compared to the identity transformation.....	87
Fig. 75: Flicker coefficient (332) for a farm with simple PSD.....	78	Fig. 91: PDF for different distributions (Normal: solid line; Laplacian: purple long dashed; X distribution where X is a zero mean normal: brownish dot-dashed line; X° distribution: green dotted line). All the distributions have been adjusted to unity variance and zero mean.	88
Fig. 76: PSD of squared voltage variations $f(t)$ and its integral g_0 ($\beta = 0.001$) for a SCIG (fixed speed, stall regulated) wind turbine.	79	Fig. 92: Normalized PDF of ΔU_{wind} in blue solid line, $\Delta(U_{eq}^2)$ in purple dashed line and $\Delta(U_{eq}^3)$ in brownish dot-dashed line. The distribution of ΔU_{eq} is assumed to be Laplacian (double exponential) and the three PDFs have been scaled to have unity variance.....	88
Fig. 77: PSD of squared voltage variations $f(t)$ and its integral g_0 ($\beta = 0.001$) for a VRIG (opti-slip) wind turbine.....	80	Fig. 93: Equivalent peak gust of $\Delta U_{eq} = 1$ m/s, generated from $PSD_{eq}(f)$	89
Fig. 78: PSD of squared voltage variations $f(t)$ and its integral g_0 ($\beta = 0.001$) for a DFIG (variable speed) wind turbine.	80	Fig. 94: PDF de la distribución normal.	90
Fig. 79: PSD of squared voltage variations $f(t)$ and its integral g_0 ($\beta = 0.001$) for Remolinos wind farm.	80	Fig. 95: Normalized PDF of the Laplacian distribution.	90
Fig. 80: Measured and fitted probability density of instantaneous wind minus the instantaneous wind at $T =$ 1,5 s, 4,5 s, 15 s, 48 s and 162 seconds before (from top to bottom). For great clarity, the plots are displaced downwards. Reproduced from M. Wächter et al. [225].....	82	Fig. 96: Normalized PDF of $U_{eq}''(t)$ (square-root-normal distribution).....	91
Fig. 81: Probability distribution of longitudinal wind variations (u) respect the average longitudinal velocity (U) in Oak Creek (California) at 80 m. The dark blue line corresponds to the actual probability density and the light pink line corresponds to the normal distribution fitted from data (the vertical axis is in logarithmic scale). Reproduced from G. C. Larsen, [221].	82	Fig. 100: Difficulties involved in the measurement of gusts. ...	96
Fig. 82: : Distribution of lateral wind variations (v) respect the average longitudinal velocity (U) in Oak Creek (California) at 80 m. The dark blue line corresponds to the measured probability density and the light pink line corresponds to the normal distribution fitted from data (the vertical axis is in logarithmic scale). Reproduced from G. C. Larsen, [221].	82	Fig. 103: Model of the data logger of the wind farm.....	103
Fig. 83: Changes in average generated output from wind farms, based on hourly averages. Reproduced from B. Fox et al. [228].....	82	Fig. 104: Plot of frequency response of the network analyzer with a zeroth order reconstruction filter.	103
Fig. 84: Comparison of the experimental probability distribution of ΔU_{eq} (circles), the Gaussian distribution (dashed red curve), the q-exponential distribution for $q=1.42$ (solid thick black curve) and the Laplacian distribution (a blue dot-dashed broken line) in the Florence Airport. Reproduced from S. Rizzo and A. Rapisarda [230].	83	Fig. 105: Rectangular, triangular, Gaussian (minimum ripple and triangular approximation), and cosine kernels corresponding to analytical signals to interpolate discrete- time Markov Chain at $(k - 1)\Delta t \leq t \leq (k + 1)\Delta t$	103
		Fig. 106: Estimated continuous signal $\hat{y}(t)$ from sequence $y[k]= \{1, 0.4, 0.2, 0.8, 1\}$ using a rectangular kernel. Rectangular analytical signal is equivalent to order zero interpolation. This model is not realistic since the signals are not continuous.	104

Fig. 107: Estimated continuous signal $\hat{y}(t)$ from sequence $y[k]=\{1, 0.4, 0.2, 0.8, 1\}$ using triangular kernel. Triangular analytical signal is equivalent to order one interpolation. 104

Fig. 108: Estimated continuous signal $\hat{y}(t)$ from sequence $y[k]=\{1, 0.4, 0.2, 0.8, 1\}$ using cosine kernel. The continuous signal is smooth but the interpolation is not suitable due to the flat slope at the sequence points. 104

Fig. 109: Estimated continuous signal $\hat{y}(t)$ from sequence $y[k]=\{1, 0.4, 0.2, 0.8, 1\}$ using Gaussian kernel and the same standard deviation as the triangle ($\sigma = \Delta t / \sqrt{6}$). The continuous signal shows an undesirable oscillation at $1 < t < 2$ 104

Fig. 110: Estimated continuous signal $\hat{y}(t)$ from sequence $y[k]=\{1, 0.4, 0.2, 0.8, 1\}$ using Gaussian kernel and the standard deviation of minimum ripple ($\sigma = \Delta t / \sqrt{2\sqrt{\pi}}$). This estimation is the smoothest among all analyzed and it does not show induced oscillations. 104

Fig. 111: Plot of frequency response of the network analyzer with a Gaussian reconstruction filter. 105

Fig. 112: Conditional probability for the Markov states given the observation y , $\Pr(\text{state} | y)$ 106

Fig. 113: $pdf(y)$ given the state probability, $\Pr(\text{state} | y)$ from (503). 107

Fig. 114: Deterministic transition diagram of hour state. The behaviour is purely periodic since transitions are deterministic (probability = 100%). 111

Fig. 115: Stochastic transition diagram of type of day (at the end of each day). Time transitions are stochastic (probability < 100%) except for the Saturday to Sunday/Bank Holyday transition. 111

Fig. 116: Deterministic transition diagram of the week day. 111

Fig. 117: Cyclic transition diagram of the year state. 111

Fig. 118: Stochastic transition diagram of the approximate seasonal model. Season transitions are stochastic (probability = 1/91 a day). 111

Fig. 119: Seasonal pattern Conditional probability given the day estimated using linear interpolation, $\Pr(\text{Seasonal Pattern} | \text{day})$ 113

Fig. 120: Seasonal pattern Conditional probability given the day estimated using the original normal interpolation, $\Pr(\text{Seasonal Pattern} | \text{day})$ 113

Fig. 121: Seasonal pattern Conditional probability given the day estimated using Gaussian interpolation, $\Pr(\text{Seasonal Pattern} | \text{day})$ 114

Fig. 122: Rate diagram and transition matrix of a periodic system with two states. 114

Fig. 123: Conditional probability of a two state periodic Markov chain computed using cosine formula (542). 114

Fig. 124: Conditional probability of a two state periodic Markov chain computed using Gaussian formula (538)... 114

Fig. 125: Seasonal pattern Conditional probability given the day estimated using cosine interpolation, $\Pr(\text{Seasonal Pattern} | \text{day})$ 115

Fig. 126: Van der Hoven’s spectral model (from [78]). 115

Fig. 127: Power output of a single turbine experiencing 24 repetitive stops due to over temperature in 20/07/1998 (24 h). 116

Fig. 128: Active power output of a wind farm with 26 turbines experiencing repetitive connection and disconnection of up to two turbines due to internal errors in 7/02/1999 (mean speed at meteorological mast was around 14 m/s). 116

Fig. 129: Active power output of a wind farm experiencing high variability in 9/02/1999 due to a sudden change in the weather at 17:30. 116

Fig. 130: Active power output (MW) of Spanish wind farms experiencing high increase in 18/01/2005 between 12:00 and 15:00. 116

Fig. 131: Active power output of a wind farm experiencing a disconnection in 3/02/1999 due to a trip of the homopolar protection relay between 21:05:24 and 21:10:55. Three minutes later, the output reached normal values. 116

Fig. 132: Discretization of power output of one wind farm into a number of states (four in this figure). Only transitions from states 1 and 2 are shown for clarity. 117

Fig. 133: Schematic relationship between measures (observations) and estimated states when they can not be derived straightforward from measures (adapted from []). 118

Fig. 134: Work flow for the proposed model. 120

Fig. 135: Original and concentrated model of a MV circuit in a wind farm. 121

Fig. 136: Model of the farm using a fourth pole realization. 121

Fig. 137: PQ relationship of a wind farm at 220 kV node during one year 121

Fig. 138: PSAT model for the tree wind farms, modelled as PQ nodes connected to the PCC. 123

Fig. 139: Scatterplots between active farm power P and their histogram (classes are shown in blue, green, magenta, red, black and dark blue). 123

Fig. 140: Color graph of centroids of P and Q powers of table I. 123

Fig. 141: Histogram of the states in data from a whole year operation. 124

Fig. 142: Color map representation of transition matrix $\hat{\mathbf{P}}$ 124

Fig. 143: Probability of permanence more than a given time in each state (complementary cumulative distribution function of permanency time) (x axis scaled to the characteristic time $\tau_i = 1/\ln(p)$). 125

Fig. 144: Probability mass distribution of permanency time in each state (x axis scaled to $1/\ln(p)$ and y axis scaled to $1/p-1$). 125

Fig. 145: Probability mass distribution of permanency time in each state (normalized scalfing time by state characteristic time).....	126	Fig. 171: Influence of voltage on real power.....	146
Fig. 146: Average permanency time in each state (in hours) from (555).	127	Fig. 172: Influence of voltage on reactive power.	146
Fig. 147: Rate diagram of an intermediate state	128	Fig. 173: Original and concentrated model of a MV circuit in a park.	147
Fig. 148: Rate diagram of the model with two states (lineal model)	129	Fig. 174: Model of the farm using its transmission matrix... ..	147
Fig. 149: Transition diagram of the model with two states (lineal model)	129	Fig. 175: Model of the farm using a fourth pole realization.	147
Fig. 150: Example of measured power curve (from [370])....	138	Fig. 176: Operational limits of turbine reactive power Q_{re} due to excessive voltage deviations and over current at the wind turbine.	149
Fig. 151: Simplified power curve from (587) for example dataof Annex I.	138	Fig. 177: Distribution of voltage deviations at PCC due to the wind farm of Annex I (data corresponding to P.F. at wind turbine 0,95 inductive in blue; 0,95 capacitive in yellow and unity in magenta).	150
Fig. 152: Plot of CDF $\sigma_{\text{Power Output}}$ for the wind turbine of the example of Annex I.	138	Fig. 178: Reactive power injected at PCC by the wind farm of Annex I.....	150
Fig. 153: Plot of average Power Output versus average wind speed at hub height of the wind farm for the example. ...	138	Fig. 179: Realizable reactive power at the wind turbine for the example of Annex I.....	151
Fig. 154: Plot of $\sigma_{\text{Power Output}}$ versus average wind speed at hub height of the wind farm for the example.	139	Fig. 180: Availability of reactive power injection (capacitive behaviour of the WT) by the wind farm of Annex I.....	151
Fig. 155: Plot of PDF $\sigma_{\text{Power Output}}$ for example of Annex I.	139	Fig. 181: Availability of reactive power absorption (inductive behaviour of the WT) by the wind farm of Annex I.....	151
Fig. 156: Power curve of the wind farm (solid) and the turbine (dashed) for the example of annex I.	140	Fig. 182: Operation of a SCIG 750 kW wind turbine for wind speeds around 6,5 m/s during 14 minutes. From top to bottom, time series of the real power P [kW] (in black), wind speed U_{m} [m/s] at 40 m in the met mast (in red, with a magnification factor x 10 respect the vertical axis) and reactive power Q [kVAr] (in dashed green).	153
Fig. 157: Plot of PDF $\sigma_{\text{Power Output}}$ for the wind farm power output of Annex I.	140	Fig. 183: Real power of a SCIG 750 kW wind turbine for wind speeds around 6,5 m/s during one minute.	153
Fig. 158: Power curve of the wind farm (dots) and the uncertainty of the power for the example of annex I.....	141	Fig. 184: Real power of a SCIG 750 kW wind turbine for wind speeds around 6,7 m/s during 20 s.....	154
Fig. 159: Model of the farm with fixed tap transformer using its transmission matrix.....	141	Fig. 185: Real power of a SCIG 750 kW wind turbine for wind speeds around 6,7 m/s during 10s.	154
Fig. 160: Model of the farm from the utility point of view..	142	Fig. 186: Power from a fixed speed stall-regulated wind turbine at 10 m/s (from [186])......	154
Fig. 161: Voltage uncoupled model for parks with load regulation transformer (model from the WT point of view).....	142	Fig. 187: $PSD_r(f)$ parameterization of real power of a SCIG 750 kW wind turbine for wind speeds around 6,7 m/s (average power 190 kW) computed from 13 minute data.	154
Fig. 162: Model of the substation of the farm.	142	Fig. 188: Contribution of each frequency to the variance of power corresponding to Fig. 187 (the area bellow $f \cdot PSD_r(f)$ is the variance of power).	154
Fig. 163: Concentrated model of a MV circuit in a park....	142	Fig. 189: Reactive power of a SCIG 750 kW wind turbine corresponding to Fig. 183.	155
Fig. 164: Model of the MV circuit and the turbines of a park.	142	Fig. 190: Reactive power Q [kVAr] of a SCIG 750 kW wind turbine corresponding to the real power of Fig. 184.	155
Fig. 165: Complete scheme of the medium voltage network, using the aggregated generator model.	143	Fig. 191: $PSD_r(f)$ of the reactive power corresponding to Fig. 187.....	155
Fig. 166: Simplified scheme of the medium voltage network of the park with added generator model.....	143	Fig. 192: $PSD_{\text{re}}(f)$ of the wind corresponding to Fig. 187 ($U_{\text{m}} = 6.71 \text{ m/s} \pm 1,86 \text{ m/s}$ at 40 m height). Beyond 0,67 Hz, some artifices appear due to measuring limitations. ...	156
Fig. 167: Joint model of the MV circuit and the turbines of a park.....	144		
Fig. 168: Compact model, compensated for the variability of the power injected by the turbines.....	145		
Fig. 169: Equivalent circuit of a turbine with a directly connected induction generator.....	145		
Fig. 170: Complete model of a park with directly-connected induction generators, valid when the number of capacitors and the auxiliary consumption can be estimated.....	145		

Fig. 193: $PSD_{\dots}(f)$ of the low voltage phase to phase corresponding to Fig. 187.	156	Fig. 212: $PSD_{\dots}(f)$ of the wind corresponding to series #1. Beyond 1 Hz, some artifices appear due to measuring limitations.	162
Fig. 194: Bode magnitude plot of real power P [W] respect wind U_{\dots} [m/s] (beyond 0,7 Hz, the transfer function is underestimated due to limitations in the wind measure).	157	Fig. 213: $PSD_{\dots}(f)$ of the wind corresponding to series #2. Beyond 1 Hz, some artifices appear due to measuring limitations.	162
Fig. 195: Bode magnitude plot of reactive power Q [VAr] respect wind U_{\dots} [m/s] (beyond 0,7 Hz, the transfer function is underestimated due to limitations in the wind measure).	157	Fig. 214: $PSD_{\dots}(f)$ of the low voltage phase R to phase S corresponding to series #1.	163
Fig. 196: Reactive power Q [VAr] versus real power P [W] in the 750 kW SCIG turbine (25 kVAr capacitor banks).	157	Fig. 215: Bode magnitude plot of real power P [W] respect wind U_{\dots} [m/s] for series #1 (beyond 1 Hz, the transfer function is underestimated due to limitations in the wind measure).	163
Fig. 197: Bode magnitude plot of reactive power Q [VAr] respect real power P [W].	158	Fig. 216: Bode magnitude plot of reactive power Q [VAr] respect wind U_{\dots} [m/s] for series #1 (beyond 15 Hz, the transfer function is underestimated due to limitations in the wind measure).	163
Fig. 198: Bode magnitude plot of line voltage V_{\dots} [V] respect real power P [W].	158	Fig. 217: Bode magnitude plot of reactive power Q [VAr] respect real power P [W] for series #1.	163
Fig. 199: Bode magnitude plot of line voltage V_{\dots} [V] respect reactive power Q [VAr].	158	Fig. 218: Bode magnitude plot of line voltage V_{\dots} [V] respect real power P [W] for series #1.	164
Fig. 200: Operation of a SCIG 600 kW wind turbine for wind speeds around 9,5 m/s during 5:30 minutes (series #1). From top to bottom, time series of the real power P [kW] (in black), wind speed U_{\dots} [m/s] at 40 m in the met mast (in red, with a magnification factor x 10 respect the vertical axis) and reactive power Q [kVAr] (in dashed green).	158	Fig. 219: Bode magnitude plot of line voltage V_{\dots} [V] respect reactive power Q [VAr] for series #1.	164
Fig. 201: Operation of a SCIG 600 kW wind turbine for wind speeds around 9,8 m/s during 3:30 minutes (series #2).	159	Fig. 220: Operation of VRIG wind farm with wind speeds around 7,6 \pm 2,0 m/s during 14,6 minutes. From top to bottom, time series of the real power P [MW] (in black), wind speed U_{\dots} [m/s] at 40 m in the met mast (in red) and reactive power Q [MVar] (in dashed green).	164
Fig. 202: Detail of real power of a SCIG 600 kW wind turbine for wind speeds around 9,5 m/s during 1 minute in series #1.	160	Fig. 221: Real power of a VRIG wind farm for wind speeds around 7,6 m/s during one minute.	165
Fig. 203: Detail of real power of a SCIG 600 kW wind turbine for wind speeds around 7 m/s during one minute in series #1.	160	Fig. 222: Real power of a VRIG wind farm for wind speeds around 6,7 m/s during 20 s.	165
Fig. 204: Detail of real power of a SCIG 600 kW wind turbine for wind speeds around 9,5 m/s during 20 seconds in series #2.	160	Fig. 223: $PSD_{\dots}(f)$ parameterization of real power of a VRIG wind farm for wind speeds around 7,6 m/s (average power 3,6 MW) computed from Fig. 220.	165
Fig. 205: $PSD_{\dots}(f)$ parameterization of real power of a SCIG 600 kW wind turbine for time series #1.	160	Fig. 224: Contribution of each frequency to the variance of power computed from Fig. 220 (the area bellow $f \cdot PSD_{\dots}(f)$ is the variance of power).	165
Fig. 206: $PSD_{\dots}(f)$ parameterization of real power of a SCIG 600 kW wind turbine for time series #2.	160	Fig. 225: Reactive power Q [MVar] of a VRIG wind farm corresponding to real power P shown in Fig. 221.	166
Fig. 207: Rective power Q [kVAr] (in solid black line) of a SCIG 600 kW wind turbine for series #1, corresponding to Fig. 200, and its linear estimation from real power ($\hat{Q} \approx 0,1702P - 14,524$).	161	Fig. 226: Reactive power Q [MVar] of a VRIG wind farm corresponding to the real power of Fig. 222.	166
Fig. 208: Detail corresponding to the reactive power of Fig. 204 (in solid black line) and its linear estimation from real power (red dots).	161	Fig. 227: Reactive power Q [VAr] versus real power P [W] computed from Fig. 220.	166
Fig. 209: Reactive vs. real power scatter plot of series #1 of a SCIG 600 kW wind turbine.	161	Fig. 228: $PSD_{\dots}(f)$ of the wind computed from Fig. 220.	166
Fig. 210: Reactive vs. real power scatter plot of series #2 of a SCIG 600 kW wind turbine.	161	Fig. 229: $PSD_{\dots}(f)$ of the wind computed from Fig. 220. Beyond 6 Hz, some artifices appear due to measuring limitations.	167
Fig. 211: $PSD_{\dots}(f)$ of the reactive power corresponding to Fig. 207.	161	Fig. 230: $PSD_{\dots}(f)$ of the low voltage phase to phase computed from Fig. 220.	167

Fig. 232: Bode magnitude plot of reactive power Q [VAr] respect wind $U_{\underline{}}$ [m/s] (beyond 6 Hz, the transfer function is underestimated due to limitations in the wind measure).....	168	Fig. 252: Bode magnitude plot of reactive power Q [VAr] respect wind $U_{\underline{}}$ [m/s] for series #1 (beyond 1 Hz, the transfer function is underestimated due to limitations in the wind measure).	174
Fig. 233: Bode magnitude plot of reactive power Q [VAr] respect real power P [W].	168	Fig. 253: Bode magnitude plot of reactive power Q [VAr] respect real power P [W] for series #1.....	174
Fig. 234: Bode magnitude plot of line voltage $V_{\underline{}}$ [V] respect real power P [W].	168	Fig. 254: Bode magnitude plot of line voltage $V_{\underline{}}$ [V] respect real power P [W] for series #1.....	174
Fig. 235: Bode magnitude plot of line voltage $V_{\underline{}}$ [V] respect reactive power Q [VAr].	168	Fig. 255: Bode magnitude plot of line voltage $V_{\underline{}}$ [V] respect reactive power Q [VAr] for series #1.....	174
Fig. 236: Operation of a DFIG 648 kW wind turbine for wind speeds around 8,75 m/s during 10:37 minutes (series #1). From top to bottom, time series of the real power P [kW] (in black), wind speed $U_{\underline{}}$ [m/s] at 30 m in the met mast (in red, with a magnification factor x 10 respect the vertical axis) and reactive power Q [kVAr] (in dashed green).	169	Fig. 256: Operation of a DFIG wind farm for wind speeds around 8,75 m/s during 12:51 minutes (series #1). From top to bottom, time series of the real power P [MW] (in black), wind speed $U_{\underline{}}$ [m/s] at 30 m in the met mast (in red, with a attenuation factor x0,1 respect the vertical axis) and reactive power Q [MVar] (in dashed green).....	175
Fig. 237: Operation of a DFIG 648 kW wind turbine for wind speeds around 8,7 m/s during 7:27 minutes (series #2).....	170	Fig. 257: Operation of a DFIG wind farm for wind speeds around 8,7 m/s during 10:27 minutes (series #2). From top to bottom, time series of the real power P [MW] (in black), wind speed $U_{\underline{}}$ [m/s] at 30 m in the met mast (in red, with a attenuation factor x0,1 respect the vertical axis) and reactive power Q [MVar] (in dashed green).....	175
Fig. 238: Detail of real power of a DFIG 648 kW wind turbine for wind speeds around 8,75 m/s during 1 minute in series #1.	170	Fig. 258: Detail of real power (in MW) of a DFIG wind farm during 1 minute in series #1.	176
Fig. 239: Detail of real power of a DFIG 648 kW wind turbine for wind speeds around 8,75 m/s during 20 seconds in series #1.....	170	Fig. 259: Detail of real power (in MW) of a DFIG wind farm during 20 seconds in series #2.	176
Fig. 240: $PSD_r(f)$ parameterization of real power of a DFIG 648 kW wind turbine for time series #1.....	170	Fig. 260: $PSD_r(f)$ parameterization of the real power of the DFIG wind farm during time series #1.	176
Fig. 241: $PSD_r(f)$ parameterization of real power of a DFIG 648 kW wind turbine for time series #2.....	170	Fig. 261: $PSD_r(f)$ parameterization of the real power of the DFIG wind farm during time series #2.	176
Fig. 242: Reactive vs. real powers of a DFIG 648 kW wind turbine for series #1, based on the original one grid cycle values.	171	Fig. 262: Reactive vs. real powers of the DFIG wind farm during time series #1, based o the original one grid cycle values.....	176
Fig. 243: Previous figure, but based on averaged one-second values instead of the original one grid cycle values.	171	Fig. 263: $PSD_r(f)$ of the reactive power in series #1.....	177
Fig. 244: $PSD_r(f)$ of the reactive power in series #1.	171	Fig. 264: $PSD_r(f)$ of the reactive power in series #2.....	177
Fig. 245: $PSD_r(f)$ of the reactive power in series #2.	171	Fig. 265: $PSD_{\underline{}}(f)$ of the phase R to phase S substation voltage corresponding to series #1.	177
Fig. 246: $PSD_{\underline{}}(f)$ of the wind corresponding to series #1. Beyond 15 Hz, some artifices appear due to measuring limitations.	172	Fig. 266: $PSD_{\underline{}}(f)$ of the phase R to phase S substation voltage corresponding to series #2.	178
Fig. 247: $PSD_{\underline{}}(f)$ of the wind corresponding to series #2. Beyond 15 Hz, some artifices appear due to measuring limitations.	172	Fig. 267: Bode magnitude plot of real power P [W] respect wind $U_{\underline{}}$ [m/s] for series #1.....	178
Fig. 248: $PSD_{\underline{}}(f)$ of the wind corresponding to the full record (28:44 minutes). Notice that spectrum show a slower droop at low frequency due to the longer record. .	172	Fig. 268: Bode magnitude plot of reactive power Q [VAr] respect wind $U_{\underline{}}$ [m/s] for series #1 (beyond 15 Hz, the transfer function is underestimated due to limitations in the wind measure).	178
Fig. 249: $PSD_{\underline{}}(f)$ of the low voltage phase R to phase S corresponding to series #1.	173	Fig. 269: Bode magnitude plot of reactive power Q [VAr] respect real power P [W] for series #1.....	179
Fig. 250: $PSD_{\underline{}}(f)$ of the low voltage phase R to phase S corresponding to series #2.	173	Fig. 270: Bode magnitude plot of line voltage $V_{\underline{}}$ [V] respect real power P [W] for series #1.....	179
Fig. 251: Bode magnitude plot of real power P [W] respect wind $U_{\underline{}}$ [m/s] for series #1.....	173	Fig. 271: Bode magnitude plot of line voltage $V_{\underline{}}$ [V] respect reactive power Q [VAr] for series #1.....	179

- Fig. 272: $PSD_r(f)$ of a wind farm (in solid black) and $PSD_r(f)$ of one of its DFIG 648 kW turbines times 18 (in dashed green), for time series #1. Both the farm $PSD_r(f)$ and the scaled turbine $PSD_r(f)$ agree notably..... 180
- Fig. 273: Power output of the wind farm (in solid black) and the power of the turbine times 14..... 180
- Fig. 274: Admittance of the real power (ratio of the farm PSD to the turbine PSD). 180
- Fig. 275: $PSD_r(f)$ of a wind farm (in solid black) and $PSD_r(f)$ of one of its DFIG 648 kW turbines times 9 (in dashed green), for time series #1. Eventhough both the farm $PSD_r(f)$ and the scaled turbine $PSD_r(f)$ agree in general terms for reactive power, the fit is significantly worse than for real power. 181
- Fig. 276: Admittance of the reactive power (ratio of the farm PSD to the turbine PSD). Notice that reactive power admittance deviates from the average more than the real power in Fig. 274..... 181
- Fig. 277: Spectrogram of total power at SCIG (Squirrel Cage Induction Generator) of 750 kW turbine start-up. . 182
- Fig. 278: Spectrogram of total power at SCIG of 750 kW turbine start-up. Detail of tower shadow frequencies..... 182
- Fig. 279: Spectrogram of output power at SCIG of 750 kW during normal operation operating at $\approx 9,5$ m/s?. 182
- Fig. 280: Spectrogram of total current at SCIG of 750 kW turbine start-up. 182
- Fig. 281: Spectrogram of real power of a SCIG 600 kW wind turbine for wind speeds around 9,5 m/s corresponding to Fig. 200..... 182
- Fig. 282: Spectrogram of real power of a SCIG 600 kW wind turbine for wind speeds around 9,5 m/s corresponding to Fig. 201..... 183
- Fig. 283: Spectrogram of a VRIG pitch regulated wind farm operating at low winds in a stop and re-start time series. 183
- Fig. 284: Spectrogram of a 750 kW induction generator, stall regulation WT operating at 6,5 m/s..... 183
- Fig. 285: Distribution of tangential and axial aerodynamic forces over the blade length. Modified from Hau [394]. ... 185
- Fig. 286: Tangential load distribution over the blade length of the experimental WKA-60 wind turbine. Modified from Hau [394]. 185
- Fig. 287: Schematic of blade elements: r , location of the element of Δr depth; R , rotor radius; Ω_r , angular velocity of rotor. 186
- Fig. 288: Detail of airfoil nomenclature. 186
- Fig. 289: Flow velocities and aerodynamic forces at the airfoil cross-section of a blade element..... 186
- Fig. 290: Sketch of the angles and forces along the blades used to compute the rotor torque..... 187
- Fig. 291: Geometric position of the blade element in the rotor disk. 187
- Fig. 292: Velocities at the rotor plane with upstream wind perpendicular to the rotor plane. 187
- Fig. 293: The pitch angle can be measured respect the element chord θ_e , or respect the blade tip chord θ 188
- Fig. 294: Detail of velocities at the rotor plane with wind oblique to the rotor plane. 188
- Fig. 295: Computation of equivalent tip speed ratio in blade element..... 191
- Fig. 296: Normalized average of λ^* , $\mu_{\underline{r}}$, in a two-bladed turbine. 192
- Fig. 297: Normalized modulation amplitude of λ^* , $A_{\underline{r}}$, in a two-bladed turbine. Negative amplitudes indicate that a torque minimum occurs instead of a maximum when the blade is aligned with the tower. 192
- Fig. 298: Normalized average of λ^* , $\mu_{\underline{r}}$, in a three-bladed turbine. 192
- Fig. 299: Normalized modulation amplitude of λ^* , $A_{\underline{r}}$, in a three-bladed turbine. Negative amplitudes indicate that a torque minimum occurs instead of a maximum when the blade is aligned with the tower. 192
- Fig. 300: Wind turbine geometry described by four coordinate systems. Reproduced from [396]. 193
- Fig. 301: Simplified turbine geometry to compute blade element distance to tower axis, ρ 193
- Fig. 302: Flow around a cylinder computed by potential flow (the streamlines, the lines of equal wind modulus and the cartesian coordinates are plotted). 194
- Fig. 303: Position of blade element near the tower. For details on relative wind speed composition, see Fig. 292.. 194
- Fig. 304: 3-D representation of the wind field section. 194
- Fig. 305: Average wind angle deviation $\phi_{\underline{r}}(\varphi)$ at the blade crossing the tower computed with exact expression (724) and approximation (725) in a turbine with $R/R = 0.2$, $R/R = 0.95$, $a/R = 2/50$, $d/R = 4/50$, $\gamma = -0.02$ radians. 195
- Fig. 306: Detail of velocities at the rotor plane with and without rotor shadow..... 195
- Fig. 307: Rotor-averaged relative flow angle variation $\Delta\phi(\varphi)$ in degrees computed from (729) for the operational conditions of Fig. 308..... 196
- Fig. 308: Inverse squared blade tip ratio $\lambda^*(\varphi)$ computed with exact expression (734) and its analytical approximations: (741) –completely superimposed in dotted pink– and (743) –in dashed blue–. In light blue is λ^* without considering tower shadow (700). Turbine with $U_{\underline{r}}(H) = 10$ m/s, $R = 50$ m, $H/R = 2$, $R/R = 0.2$, $R/R = 0.95$, $a/R = 2/50$, $d/R = 4/50$, $\gamma = -0.02$ rad, $N_{\underline{r}} = 3$, $\alpha_r = 0,2$, $\lambda_{\underline{r}} = 7$ 197
- Fig. 309: Aerodynamic torque in a 1500 kW wind turbine corresponding to the parameters of Fig. 308 (near rated wind speed: $U_{\underline{r}}(H) = 10$ m/s, $\lambda_{\underline{r}} = 7$ and pitch $\theta = 0^\circ$). The dashed line, $\lambda^*(\varphi)$ multiplied by a factor, has been added to show that fluctuations are mostly proportional bellow rated wind speed. 197

- Fig. 310: Aerodynamic torque in a 1500 kW wind turbine corresponding to the parameters of Fig. 308 but near cut-off speed: $U_{-}(H) = 20$ m/s, $\lambda_s = 3,58$ and pitch $\theta = 19,5^\circ$. The dashed line is $\lambda(\varphi)$ multiplied by a factor to show that torque fluctuations are not proportional to $\lambda(\varphi)$ at full load. 198
- Fig. 311: Aerodynamic torque in a 1500 kW wind turbine corresponding to the parameters of Fig. 308 computed near rated wind speed (solid line: $U_{-}(H) = 10$ m/s, $\lambda_s = 7$ and pitch $\theta = 0^\circ$ corresponding to Fig. 309) and at cut-off wind speed (dashed line: $U_{-}(H) = 20$ m/s, $\lambda_s = 3,58$ and pitch $\theta = 19,5^\circ$ corresponding to Fig. 310). 198
- Fig. 312: Exciting forces and degrees of vibrational freedom of a wind turbine. From F. Kießling [], page 24. 198
- Fig. 313: Sideways oscillation of the tower. Reproduced from Thiringer [186]. 199
- Fig. 314: Influence of tower shadow on the rotor torque at the example of the experimental MOD-0 two-bladed wind turbine. Taken from Hau [88] (originally from []). 199
- Fig. 316: Near field flow around a turbine rotor modelled as an actuator disk. 201
- Fig. 317: Thrust development of a 1.5 MW rotor depending on wind speed and pitch angle, rotational velocity 1.93 rad/s (blue), deterministic winds. Normal turbine operation is shown as red line. Taken from A. Knauer [408]. 202
- Fig. 318: Plot of a thrust force coefficient lookup table. Taken from Knauer [408]. 202
- Fig. 319: Simplified representation of the wind turbine wake. Taken from A. Jiménez [407]. 202
- Fig. 321: Wake cross section shape $\phi(x, y, z)$ for $\sigma_y = \sigma_z = 2,5 H$ 203
- Fig. 323: Downstream distance of turbine b respect turbine a in Lagrangian coordinates 204
- Fig. 324: Expansion of cascaded wakes due to the increased turbulence downstream, respect the more upstream turbines in the wind farm. Reproduced from Risø report 1615 [403]. 205
- Fig. 325: Portion of source code where the shape function and the increment of turbulence, $\Delta TurbInt(x)$ are defined. 206

List of tables

<p>Table I: Wind generation variability as a function of the number of generators and time interval (from “20% wind energy by 2030: Increasing Wind Energy” [4])..... 3</p> <p>Table II: Summary of statistical properties of UNCORRELATED sinusoidal fluctuations in a cluster of N turbines 55</p> <p>Table III: comparison of spectrum parameters of power output 61</p> <p>Table IV: Process of computing the distribution of fluctuations in a wind farm due to tower shadow..... 64</p> <p>Table V: approximated tower shadow effect on flicker..... 76</p> <p>Table VI: parameters of the PSD model of real power turbine output (321)..... 77</p> <p>Table VII: Typical short circuit values (from []). 79</p> <p>Table VIII: Centroids of P and Q values p.u. of Three Wind Farms 123</p> <p>Table IX: Initial Probability Transition Matrix $\hat{\mathbf{P}}$ 124</p> <p>Table X: Probability Transition Matrix $\hat{\mathbf{P}}$ (Adjusted joining similar infrequent transitions) 124</p> <p>Table XI: Average Permanence In States (in hours) 127</p> <p>Table XII: Parameters of the battery in the Ah model 127</p>	<p>Table XIII: Parameter equivalence of the pumped storage and Ah battery model..... 129</p> <p>Table XIV: parameters of the 750 kW SCIG turbine, series 20/10/00, 13:37-13:50 ($f_{\underline{m}} \approx 1,12$ Hz) 153</p> <p>Table XV: typical line parameters [386] 156</p> <p>Table XVI: parameters of the 600 kW SCIG turbine series #1, (date 28/7/00, from 13:36:10 to 13:41:40, $f_{\underline{m}} \approx 1,35$ Hz) 159</p> <p>Table XVII: parameters of the 600 kW SCIG turbine, series #2, (date 28/7/00, from 13:48:30 to 13:52:00, $f_{\underline{m}} \approx 1,35$ Hz) 159</p> <p>Table XVIII: parameters of the VRIG wind farm, series 26/2/99, 13:52:53-14:07:30 ($f_{\underline{m}} \approx 1,48$ Hz)..... 164</p> <p>Table XIX: parameters of the 648 kW DFIG turbine series #1, (date 12/3/99, from 9:52:00 to 10:02:37, $f_{\underline{m}} \approx 1,54$ Hz) 169</p> <p>Table XX: parameters of the 648 kW DFIG turbine, series #2, (date 12/3/99, from 13:48:30 to 13:52:00, $f_{\underline{m}} \approx 1,54$ Hz) 169</p> <p>Table XXI: parameters of a DFIG wind farm, series #1, (date 12/3/99, from 9:48:09 to 10:01:00, $f_{\underline{m}} \approx 1,54$ Hz)..... 175</p> <p>Table XXII: parameters of a DFIG wind farm, series #2, (date date 12/3/99, from 10:09:00 to 10:19:27, $f_{\underline{m}} \approx 1,54$ Hz)..... 175</p>
---	--

Chapter 1:

Introduction

1.1. Background

The installed capacity for wind power is increasing substantially in response to the worldwide interest in low-emissions power sources and a desire to decrease the dependence on petroleum.

The European Union directive 2009/28/EC [1] enforces the mandatory target of a 20 % share of energy from renewable sources in overall Community energy consumption by 2020 and a mandatory 10 % minimum target to be achieved by all Member States for the share of biofuels in transport petrol and diesel consumption by 2020. These targets may require between 30 and 40 % of the electricity in the European Union to come from renewable energy sources by 2020.

In the U.S., the world's top wind producer [2], wind currently makes up just one percent of the energy supply. Wind power generation share is expected to grow up to 20% in the USA by 2030 [3,4]. Moreover, many U.S. states have legislated similarly ambitious renewable energy portfolio standards.

These goals were set without regard for the fact that many in the scientific community have concluded a theoretical wind penetration limit of only 20% due to the degradation of system reliability [5]. The Department of Energy states that there is no fundamental technical reason why 20 percent of wind energy cannot be assimilated into the grid by 2030. To help make its point, the agency debunks the reliability myth in its fact sheet on Wind Energy Myths [6].

According to S. Feldman [7], the renewable output could leap to 40 percent of the Irish electricity share; in Denmark to 33 percent; in Portugal to 28 percent; and in Germany and Greece to 25 percent. After 2020, a higher proportion may be needed. A significant amount of this renewable electricity is likely to come from wind, and the variability of this power needs to be managed.

With this amount of wind generation, the future electricity markets could be very different to those of today: instead of thermal power stations dominating the system, the market could be dominated by large amounts of price-insensitive nuclear and wind power, combined with highly intermittent output from the wind farms [8].

The extent of uncertainty and variability in wind generation makes this resource different from the traditional, dispatchable generation resources, with the result that wind power generation cannot be readily integrated into standard system operating procedures [9]. At relatively low levels of installed capacity, wind turbines and the output from large wind farms can essentially be absorbed into traditional system operations without degrading system reliability. At the current higher projected levels of penetration, wind power requires more sophisticated mechanisms to maximize its

participation in the power system without penalizing it for the unavoidably intermittent nature of its resource [10].

In some real time markets, and at low levels of penetration, wind is treated as negative load [24]. But the perception of wind power is changing from being considered a negative load to a capacity resource. Wind power can be integrated into system and market operations as a generating resource that could provide not only energy but also capacity and ancillary services [11].

1.1.1. Relationship between wind power variability and its forecast

Wind varies in space and in time. The forecasts try to predict this variation from climate dynamics and from the systematic behaviour of the weather.

The inherent uncertainty and availability of the meteorological data decreases the accuracy of the next day's wind generation forecast [12]. The issue of uncertainty in wind generation can be addressed by improving the accuracy of forecasting the wind resource. In addition, advances in wind forecasting and turbine controls suggest that wind power can participate in ancillary service markets.

The simplest forecast of a stochastic process is the persistence principle: the expected value during next period $[t, t+\Delta t]$ is the average value of the previous period $[t-\Delta t, t]$. The mean square error of the persistence prediction is just the variance of the average process during the interval $[t-\Delta t, t]$.

Thus, the ratio of the forecast root squared error to the standard deviation of the variable predicted is just the performance of the forecast relative to the persistence model.

Usually, numerical weather prediction significantly outperforms persistence for horizons longer than 6 hours. For shorter horizons, statistical methods can be more adequate due to the lack of a dense network of weather sensors near the wind farms. In such cases, the characterization of wind power variability is essential.

1.1.2. Influence of the wind variability on the grid

Wind power presents the most economically viable renewable solution, apart from hydro power [5]. The utility system is designed to accommodate load fluctuations, which occur continuously. This feature also facilitates accommodation of wind plant output fluctuations when wind penetration is low.

In order to make the long-term growth of wind generation possible, the variability and the intermittency of wind power must be managed [13]. In Denmark, Northern Germany, and parts of Spain, wind supplies 20% to 40% of electric loads without sacrificing reliability.

Generally, wind power forecast are targeted to optimize the hourly power dispatch. However, the electric system has to cope with instantaneous variation of load, generation and equipment trips. Such variations are usually unpredictable and they are usually considered deviations from the expected power tendency.

The variability of wind power has several negative effects on the reliability and system operation of the electric grid as well as wind project economics [14]. The stability of the electric grid depends upon reliable and consistent power generation that is balanced to the load through unit commitment (interhour), economic dispatch (intrahour), and regulation (intraminute), and wind power is counterproductive towards that effort. Due to its stochastic nature, wind generation is not dispatchable and therefore cannot be called upon to serve load. As a result, the capacity credit of a wind farm is very small—even as low as 8% of nameplate capacity according to a probabilistic loss-of-load analysis [15].

Greater reliance on wind power requires more ancillary services, especially responsive reserves, to match the lost generation and ramp rate of wind turbines when the wind dies down. One study of a typical wind farm indicated ramp rates up to 4.4% of capacity per second [16], implying a large burden on ancillary services. In fact, an empirical analysis of increasing wind penetration in the Pacific Northwest U.S. demonstrated that reserve requirements increased with the square of installed wind capacity, and the need for total reserve capacity doubled after just 2500 MW of installed wind capacity [17].

In some applications, the estimation of wind power variability can be as important as its prediction. The forecasted values are usually the hourly wind or the hourly power generated by one turbine or a cluster of them. Most forecast models predict only the average hourly wind or wind power and they are intended for the requirements of the electricity markets. Only a few models characterize the uncertainty of the forecast and quantify the instantaneous fluctuations inside the time period.

The main applications which benefit from variability assessment are:

- The control of wind turbines and wind farms, where the short timescales involved makes forecasting unpractical.
- Automatic generation control, automatic voltage control or changes in automatic taps on transformers, more concerned with interhourly variations, that are quite difficult to predict.
- Improving the power quality, more related to voltage variations and hence, instantaneous power variations.
- Optimum sizing of storage devices or of running reserves in isolated or weak systems, where electricity must be supplied even in the worst case scenario.
- In risk assessment and the safe operation of the grid. The system must cope with unexpected outcomes when the forecast has big uncertainty.

1.1.3. Geographic diversity on wind power

Both the generated power and the forecast error decrease as more wind power producers are aggregated. Due to the geographic dispersion of wind generators, some power variations and prediction errors can be partially cancelled by other errors in other locations.

On the one hand, the forecast errors can be very low in wide geographic areas. The power balance can be met provided the electricity transmission networks are strong enough to carry the undispachable generated power from remote areas [18, 19].

On the other hand, many quality parameters of the grid must be met locally and the reinforcement of the electricity networks is costly and, sometimes, it is not feasible. In islands, the power balance cannot rely on geographical diversity and other measures are required to counteract the wind power variability.

The weather conditions may remain stable for relative long periods among shift weather changes. Quick local turbulent fluctuations are tougher to predict in time and place than some smooth weather evolution. In fact, a good parameter of the accuracy of the prediction is the error relative to the variance of the random variable to be predicted.

However, the wind power forecast accuracy is usually referred to the total installed wind power considered in the prediction. These figures must be considered with caution:

- A 15% prediction error of the hourly power one day ahead of a single wind farm can be an accurate forecast [20, 21].
- A 15% prediction error of the hourly power one day ahead in a big system is a poor forecast [22].

The variance of the wind power decreases when increasing the time period of the measure or the spatial diversity of the wind generators. Therefore, increasing the time or space horizon of the predictions lowers the absolute prediction error. The standard deviation to mean ratio, called coefficient of variation (CV) [16, 23], is also sensitive to the geographic, the time averaging and the prediction horizon, as can be seen in Table 1.

The table 1 compares output at the start and end of the indicated time period in terms of the percentage of total generation from each turbine group. Std. Dev. is the abbreviation for standard deviation. CV stands for coefficient of variation, the ratio of standard deviation respect the mean of wind power.

The power spectral density identifies which frequencies of variation are contributing to the variance [24]. The coherence indicates the degree of partial cancellation of the oscillation among the turbines at different frequencies [38]. These two magnitudes can explain the effect of the geographic and time averaging. In the spatial domain, high frequencies smooth out a wind farm's aggregate power output since the coherence of the turbines' outputs is low, while low spatial frequencies cause a coherent variation in the farm's turbines.

Table 1: Wind generation variability as a function of the number of generators and time interval (from “20% wind energy by 2030: Increasing Wind Energy” [4])

	14 Turbines (%)	61 Turbines (%)	138 Turbines (%)	250+ Turbines (%)
1-Second Interval				
Average CV	0.4	0.2	0.1	0.1
Std. Dev.	0.5	0.3	0.2	0.1
1-Minute Interval				
Average CV	1.2	0.8	0.5	0.3
Std. Dev.	2.1	1.3	0.8	0.6
10-Minute Interval				
Average CV	3.1	2.1	2.2	1.5
Std. Dev.	5.2	3.5	3.7	2.7
1-Hour Interval				
Average CV	7.0	4.7	6.4	5.3
Std. Dev.	10.7	7.5	9.7	7.9

1.1.4. Demand response and wind variability

To a large extent, load exhibits similar characteristics – uncertainty and variability– to wind power [24]. Load patterns though, have been more extensively studied for many years and so are better understood and more accurately forecasted than the wind resource. The purpose of this effort in load modelling is to understand load patterns well enough to operate the power system through the control of individual generation and transmission facilities, in order to serve load and maintain system reliability.

Thus, load is extensively modelled and *other* facilities are controlled to serve load, with relatively little effort made to control load itself. This trend is not absolute, as there are traditional utility mechanisms, such as interruptible contracts and direct load control, to reduce load at times when system reliability would otherwise be threatened. There is also persistent interest in developing mechanisms for more dynamic load response for both reliability and economic purposes.

Recent efforts to allow load to be more responsive to system conditions and a more active participant in electricity markets arise for multiple reasons [25]. In addition to giving customers incentives to decrease their demand in the short run to improve system reliability during times of system peak, demand response can be used in the long term to decrease required capacity expansion and lower total costs. Demand response is also an important and essentially absent element in electricity markets. If it were to be more widely implemented, market efficiency would be likely to improve. Many efforts are being made to demonstrate the feasibility and the convenience of smart grids.

1.1.5. Estimated cost of wind power variability

The estimated cost of the uncontrollability of the wind resource has been widely researched from governmental policy makers to Independent System Operators [26]. An

understanding of the impacts of the variable sources of renewable energy must take into account the wider issues associated with managing electricity systems [27].

Modern integrated networks are designed to cope with ‘shocks’ such as the sudden loss of large thermal power stations and with uncertainties in consumer demand, such as those caused by televised sports events. As the tools to deal with these are already available, the key question is the extent to which the introduction of large amounts of wind energy will increase the overall uncertainty in matching supply and demand. This extra uncertainty means that additional short-term reserves are needed to guarantee the security of the system [28].

The variability of wind power also adversely affects wind project economics. A stochastic power source like wind is inherently less valuable than a deterministic source. Net payments to wind generators are reduced by balancing-costs to compensate for unfulfilled obligations to generate power [29].

The study [30] determined that net payments in the USA to wind farms vary from \$32/MWh for very small wind farms to less than \$10/MWh for farms larger than 2000 MW.

The report [19] states that at wind penetrations of up to 20% of gross demand (energy), system operating cost increases arising from wind variability and uncertainty amounted to about 1~4 €/MWh. This is 10% or less of the wholesale value of the wind energy.

The cost of grid reinforcements due to wind power is very dependent on where the wind power plants are located relative to load and grid infrastructure. The grid reinforcement costs from studies vary from 50 €/kW to 160 €/kW in the report [19]. The costs are not continuous; there can be single very high cost reinforcements, and there can also be differences in how the costs are allocated to wind power.

According to D. Milborrow [31], the extra cost in the UK of these reserves –with wind providing 20% of electricity consumption– is unlikely to be more than £1.20/MWh on electricity bills (a little over 1% on domestic bills). With 40% of electricity provided by wind, the corresponding figure would be £2.80/MWh.

A second costs of wind variability is the backup cost for periods of very low wind resource along extensive geographical areas. Recharge reported in [32] that the calculations made by Oxford University Environmental Change Institute showed that between 1970-2003, low wind speeds all across the whole UK —those too slow to generate energy— occurred simultaneously in the country only one hour per year on average. In other words, the total wind power in the UK varies, but a 0% generation is quite unlikely event. According to D. Milborrow [31], wind energy does not require the introduction of special back-up provisions in the UK and its back-up costs are modest. Though the UK was the focus of the study, the results are relevant worldwide, as characteristics of wind are broadly similar everywhere.

All generating plants make use of a common pool of backup plant that is typically around 20% of the peak demand on the electricity network. When wind is introduced, system operators do not rely on the rated power of all the installed wind farms being available at the times of peak demand, but a

lower amount - roughly 30% of the rated capacity at low penetration levels, falling to about 15% at high penetration levels. This lower ‘capacity credit’ gives rise to a modest ‘backup cost’. ‘Constraint costs’ arise when the output from the wind turbines exceeds the demand on the electricity network. They are unlikely to arise until wind energy is contributing around 25% of electricity requirements.

Overall, it is concluded that the additional costs associated with variability – with wind power providing up to about 40% of all electricity, are quite small. For example, if wind provides 22% of electricity in the UK by 2020, variability costs would increase the domestic electricity price by about 2%, according to D. Milborrow [31]. Further increases in the level of wind penetration beyond that point are feasible and do not rely on the introduction of new technology.

There are numerous technical innovations at various stages of development that can mitigate the costs associated with variability. Improved methods of wind prediction are under development worldwide and could potentially reduce the costs of additional reserve by around 30%. Most other mitigation measures reduce the costs of managing the electricity network as a whole. ‘Smart grids’, for example, cover a range of technologies that may reduce the costs of short-term reserves; additional interconnections with continental Europe, including ‘Supergrids’ also deliver system-wide benefits and aid the assimilation of variable renewables.

Electric cars hold out the prospect of reduced emissions for the transport network as a whole and could act as a form of storage for the electricity network –for which the electricity generator would not have to pay.

With current technology, wind power plants can be designed to meet industry expectations such as riding through voltage dips, supplying reactive power to the system, controlling terminal voltage, and participating in system operation with output and ramp rate control.

Although some aspects of the management of wind variability can be controversial and costly, many utilities agree that there is no insuperable technical reason why high proportions of wind energy cannot be assimilated into the system [33]. There is a large body of literature on the topic [34] and the steady growth of wind power, worldwide, indicates that it is seen as a robust choice for reducing greenhouse gas emissions.

1.2. Scope and Aims

The aim of this thesis is to contribute with a framework for the systematic analysis of the wind power variability in time and in space. The time scope ranges from seconds to days and the geographic scope ranges from a wind farm to regions a hundred of kilometres away.

Numeric weather predictions are usually based on public models and they are usually run by governmental organizations. However, most studies on wind power variability are based on confidential or not publicly accessible data even for non-profit research [24]. Even if weather behaviour could be predicted very accurately, a model output statistics would be required to transform into generated wind power. The models are adjusted from experimental data and

many of them do not have a straightforward interpretation. Thus, it is difficult to generalize from these results.

One of the objectives of this thesis is to obtain a general variability model able to explain qualitatively the wind power variability. The model for large distances and hourly/daily variations is based on data available in the web from national meteorological institutions [54]. For short intervals and inside a wind farm, the model is based on the experience with a logger system designed and installed in four wind farms [35, 36], the wind coherence model of W. Schlez and D. Infield [37], and the general coherence function derived by Risø Institute in Horns Rev wind farm [38, 39].

The complexities inherent to this mathematical model are partially circumvented presenting some case studies with meaningful graphs and using the classical tools of signal processing and time series analysis when possible.

The application of the classical theory of stochastic processes is widespread in telecommunications, radar detection, audio and other fields, but it is less usual in wind power. The classical stochastic framework brings the research made in other fields of knowledge into wind power. Other benefit of the classic theory is the more straightforward interpretation of the obtained results.

The classical signal analysis of data from the meteorological weather stations in the time-frequency domain is a contribution of this thesis in the form of a freely available program. Special efforts have been done to design a user friendly interface, an intuitive operation and meaningful graphics.

To account the non-linear behaviour of the wind, the Markov Chain Approximation Method is employed as a tool to discretize the stochastic differential equations involved in the wind power dynamics. This framework makes possible the utilization of the dynamic optimization of wind power using Markov Decision Processes [40, 41]. These techniques have been customarily used in other fields, but they are quite novel in wind power.

One of the advantages of using Markov Chains is that the wind power dynamics can be characterized through a matrix and its stochastic interpretation is straightforward. The discretization of a stochastic system into Markov Chains is easy to interpret. Moreover, the Markov Chain Approximation can be used to optimize the system operation using deterministic tools when the uncertainty of the forecast can be estimated. Markov Chain Approximation and Monte Carlo Analysis of dynamic systems are closely related.

Considering the thesis scope, its aims have been achieved through the following items:

- Characterization of the variability in the time domain of the wind measured with an anemometer through its power spectral density (PSD).
- Estimation of the spatial variability in the swept area using the potential flow theory, wind shear and turbulence.
- Estimation of the aerodynamic torque of the turbine accounting the spatial diversity of the wind.
- Estimation of the equivalent wind defined as the wind that produces the same turbine or farm output

as the real wind field using the simplified formula of the torque or power coefficient.

- Creation of an interactive computer program to estimate the coherence of the wind measured at two weather stations as the experimental time and frequency variability of the wind. This program also classifies the system composed of two sites into states and computes the Markov transition matrix among the states.
- Creation of an interactive computer program to estimate gusts of equivalent wind for a turbine or for a cluster of turbines.
- Derivation of a simplified statistical model of the electric grid of a wind farm.
- Creation of an interactive computer program to estimate the wakes in an offshore wind farm.
- Characterization of the non-linear dynamics of wind power experimentally using the Markov Chain Approximation Method in a small demonstrative case.

1.3. Thesis Outline

This thesis is structured into eight chapters and six annexes. It is also accompanied by several interactive programs to demonstrate some applications of this thesis. Since some sections are indeed quite dense, the author recommends trying the accompanying programs (their manuals are at the end of this thesis) before revising the main body of this thesis.

Many programs have been developed during the realization of this thesis, some of them for developing a multipurpose datalogger and others for data processing. In fact, only the more versatile and illustrative programs have been included, those that can be run in a standard PC with freely available data and without requiring buying licenses.

The first chapter consists in this introduction. The fundamentals of the wind variability are introduced in the second chapter. The computation of the turbine torque and the concept of equivalent wind are derived in the third chapter. The characterization of the variability of the wind power in the frequency domain is presented in the fourth chapter. The fifth chapter deals about almost periodic fluctuations in the time domain. The sixth chapter is devoted to gust models. The seventh chapter characterizes the wind power variability in the time domain using the Markov Chain Approximation Method and it proposes the Markov Decision Processes for optimizing dynamically controllers and policies. The last chapter contains the closure with the main contributions of this thesis.

Chapter 2: Variability of Wind in the Frequency Domain

Chapter 2 introduces the basic concepts and features concerning the variation of the wind. The concept of spectrum of wind is presented, which is a common way to characterize the frequency content of the turbulence present in the wind. The spectra of wind more often used in wind power are compared.

The Taylor hypothesis of turbulence, a simple model that relates about spatial variations and temporal variations of the wind, is discussed. This hypothesis can be used to reconstruct

the approximate spatial structure of wind from measurements with an anemometer fixed at a point in space. A more advanced concept is the spatial and temporal coherence of the wind, which statistically quantifies the variations of wind in different points in space or in separate moments of time.

Chapter 3: The turbine torque and the equivalent wind

Chapter 3 introduces the simplified calculation of the aerodynamic torque coefficient based on the torque of the turbine, which assumes that the wind is uniform in the area swept by the turbine. From this formula, a simplified small signal model is derived to estimate the torque when the wind conditions in the swept area are not uniform.

Based on this approximation, the equivalent wind is defined as the one that produce the same effects that the non-uniform real wind field. This simplification implies that the effects of the wind field, which cannot be measured directly, can be estimated from an equivalent wind, usually estimated from the measurements of an anemometer.

Thus, the aerodynamic torque can be computed approximately with a simple formula from the torque coefficient and from the equivalent wind, derived from the measured wind.

The equivalent wind speed contains a stochastic component due to the effects of turbulence, a rotational component due to the wind shear and the tower shadow and the average value of the wind in the swept area, considered constant in short intervals. The fluctuations in the aerodynamic torque due to the real wind field along the swept rotor area are introduced in the equivalent wind modifying its spectra. This simplification works relatively well since the vibrational turbine dynamics randomize the real dependence of the generator torque with the rotor angle.

The combination of the small signal model and the wind coherence permits to derive the spatial averaging of random wind variations. A stochastic model that links the overall behaviour of a large number of turbines is derived from the behaviour of a single turbine.

The power spectral density of the equivalent wind of a cluster of turbines is estimated from parameters of an isolated turbine, lateral and longitudinal dimensions of the cluster region and the decay factor of the spatial coherence.

Although the proposed model is an oversimplification of the actual behaviour of a group of turbines scattered across the area, this model quantifies the influence of the spatial distribution of the turbines in the smoothing and in the frequency content of the aggregated power. This stochastic model is in agreement with the experimental observation that slow changes are highly correlated among a turbine cluster while fast changes are poorly correlated.

Chapter 4: Variability of power in the frequency domain

In the previous chapters, the wind has been analyzed to estimate the variations of aerodynamic torque. However, the aerodynamic torque interacts with the structural and drive-train vibrations. Consequently, the power injected in the grid has a stochastic nature even in total absence of turbulence.

There are many specific characteristics that impact notably in the power fluctuations between the first tower frequency (usually some tenths of Hertz) and the grid frequency. The realistic reproduction of power fluctuations needs a comprehensive model of each turbine, which is usually confidential and private.

One contribution of this chapter is the experimental characterization of the power fluctuations of three commercial turbines, whose data is shown in annex B. The variations of power during the continuous operation of turbines are measured and experimentally characterized for timescales in the range of minutes to the grid period. Some experimental measurements in the joint time-frequency domain are presented to test the mathematical model of the fluctuations.

The admittance of the wind farm is defined as the ratio of the oscillations from a wind farm compared to the fluctuations from a single turbine, representative of the operation of the turbines in the farm. The partial cancellation of power fluctuations in a wind farm are estimated from the ratio of the farm fluctuation relative to the fluctuation of one representative turbine. Some stochastic models are derived in the frequency domain to link the overall behaviour of a large number of wind turbines from the operation of a single turbine.

A literature review on Power Spectral Densities (PSD) and periodograms (averaged spectrum) of wind power are presented. The variability of PSD is also studied, a step ahead from the literature, in the joint time-frequency domain through spectrograms.

Chapter 5: Almost Periodic Fluctuations in the time domain

Chapter 5 analyzes from a phenomenological point of view the aggregation of unsynchronized almost periodic fluctuations from the turbines in the time domain, assuming a characteristic behaviour at each turbine. This almost determinist behaviour does not represent the real stochastic nature of the power injected by the turbines. However, this assumption illustrates that the output of a wind farm is stochastic even if each turbine power has non-synchronized periodic fluctuations.

In the first part of this chapter, the statistical distribution of turbine blade positions along a wind farm is derived in an unsynchronized wind farm. The blade crossing in front of its turbine tower is modelled as a Poisson Process. The variability of the wind farm power output due to tower shadow and the probability of extreme conditions (such as simultaneous tower shadow events at all turbines of a wind farm) are estimated in the time domain.

In the second part of this chapter, the flicker emission of a turbine cluster is derived from the output of a representative turbine of the cluster. Flicker emission of a wind farm during continuous operation has three main sources: wind turbulence, tower shadow and generator or power converter oscillations. Flicker emission of a wind farm during continuous operation is derived from the output of a single wind turbine since fast fluctuations are low correlated among turbines. A stochastic model of the power output PSD is parameterized and a simple formula is derived to estimate flicker level from PSD and network parameters. This simple

formula assesses the individual influence in flicker level of wind turbulence, tower shadow and generator/converter.

The flicker model has been tested with data from several wind farms. In wind farms with induction generators and squirrel cage or variable resistance rotor, wind turbulence was the main flicker source since the turbine coupling was soft enough to damper generator oscillations and torque variations related to rotor angle. In wind farms with doubly fed induction generators, the main flicker source was the induced noise at frequencies around maximum flicker sensitivity by the power converter. In the cases analyzed, the flicker level was very low due to the strength of the network at the point of common coupling.

Some experimental measurements are presented to test the mathematical model of the fluctuations.

Chapter 6: Characterization of wind gusts in the time domain

The previous chapters have introduced the wind spectral density as the feature that summarizes the stochastic behaviour of the wind. In this chapter we will use this spectral density to analyze the characteristics of wind variations in the time domain and to synthesize samples of equivalent wind with some features.

The mechanisms that generate turbulent wind changes are analyzed, since they are closely related to the shape of the bursts and the distribution of velocity variations. Experimental wind variations fit approximately a Laplacian distribution, indicating some unknown multiplicative effect involved in the extreme deviations. A bijective transformation is defined to obtain the target distribution.

The average shape of the peak gust and the ramp gust are defined and their probabilities are estimated from the theory of conditional generation of samples. The peak gust is characterized by the wind speed deviation ΔU_{wind} respect the average. The ramp gust is characterized by the variation of wind ΔU_{wind} between two instants separated by a time Δt (this parameterization specifies both the average gradient and the duration of the ramp). The properties of a normal process led to significant conclusions about the behaviour of the equivalent wind.

The peak and ramp gusts are synthesized in the frequency domain using the Karhunen-Loève expansion and the theory of conditional simulation of normal processes. An approximate method to avoid numerical difficulties that arise generating very long samples.

The concept of the equivalent wind gust can be extended to a geographic area and it can serve to compute the maximum variability of the power expected in a region.

Chapter 7: Variability of wind power in the time domain

The variability of wind speed can be modelled during short intervals with the classical theory of stationary normal processes, which has been presented in the previous chapters. However, the weather is a non-stationary process and this cannot be neglected for horizons longer than some hours. The evolution of wind power can be described in the time domain by stochastic differential equations. Numerical Weather Prediction (NWP) models the physics of meteorological dynam-

ics. Wind speed is customarily transformed into generated power with a power curve or with a model output statistics (MOS).

Since the wind variations show a fairly multiplicative behaviour, the Markov Approximation Method is suitable for modelling the non-linear stochastic behaviour of the wind. This technique is analogous to the finite difference approximation in deterministic differential equations and it is a powerful tool to optimally control the system, especially if numerical weather predictions are available.

Indeed, if numerical weather predictions are unattainable, the Markov chain can be used for generate basic probabilistic forecasts based on the system behaviour previously observed. The transmission matrix among the Markov states models the non-stationarity of wind, present in long time spans.

The optimal control of a Markov system is called a Markov decision process and they can be expressed as a policy, which gives the best action to take for a given wind farm state, regardless of the prior history. Once a Markov decision process is combined with a policy, this fixes the action of the control for each state and the resulting combination behaves indeed like a Markov chain.

The classic control theory of linear and time-invariant systems is well established. However, many devices in the grid are discrete and their control can not be linearized because their unnecessary switching can produce grid disturbances or excessive device wear.

Markov chains can model switching or jump events such the probability of wind farm trips and the connection or disconnection of devices such as reactors or capacitors. Some events such as extreme wind variations or generator disconnections due to severe grid conditions can eventually jeopardize the grid. Thus, the stochastic control is better suited to manage these events than the classical control of linear and time invariant systems. The optimum design and the optimum control can be achieved assigning costs to staying in the same system state or jumping to other states. Thus, the Markov decision processes can be used to optimize the design and control of many devices which should encompass the non-linear and time-dependent variability of the wind power.

Usually, Markov chains have been utilized as Monte Carlo random generators in stochastic power flows due to the high dimension of their state space. To reduce the state space, a discretization methodology is presented where the number of states is remarkably reduced through careful system modelling and clustering. This makes the optimal control tractable through Markov decision processes.

The classification of states can be based on power output, equivalent wind speed or wind speed prediction, depending on the available data and the aim of the wind farm model. The performance matrix in Standard IEC 61400-12-3 can be used as emission matrix to relate wind and power in a wind farm using a Hidden Markov Model. The wind farm model can be used also as time interpolation or to guess if there is an outlier in the state (a switching event).

One application example is a probabilistic power flow. A methodology to optimize the power flow based on Markov processes is presented. Load, generation and network topology is classified into a small set of cases represented by the centroids of the fuzzy clusters. Afterwards, regular determi-

nistic power flow is run for each pattern centroid and the statistics and the system stochastic dynamics are derived from the transition matrix of the embedded Markov Process. Finally, the optimal control of generation, network topology and discrete elements such as switches and transformer tap changers can be computed conveniently by Markov Decision Processes. This approach is advantageous for loads highly or barely interrelated and for non-controllable generators such as wind and solar. Other possible application is the design and control of reactors and capacitors in a wind farm to maximize the profit due to reactive power control. In that case, a simplified, quadratic model of the wind farm in the steady state can be used to estimate the maximum absorption and injection of reactive power at different points of the farm.

Other application is the optimal design and control of the load consumption of an isolate system with renewable generation and storage. The optimal design minimize the cost of the system infrastructure with the expected cost of maintenance, energy losses, load deferring and not supplying regular and critical loads. The control of the optimal design manages the loads for optimize the expected profit.

Chapter 8: Conclusions and Future work

In this chapter, the general conclusions of this thesis will be presented, emphasizing its scientific contributions. Future work lines will be also outlined.

Annex A: Simplified electrical model of the wind farm

This annex presents a simplified statistical model to represent a wind farm in a power flow study. This model has been developed taking into account the variability in the generated power from windmills and its normal operation. Its main advantages are its simplicity and the possibility of calculating the voltage in the park's network without having to run a power flow program. Another advantage of the proposed method is that it is based in the fourth-pole theory, widely used in electrical engineering. Finally, the uncertainty of the model is assessed.

One possible application is to study the influence of nearby wind farms. Other possible application of this model is to study the management of reactive power in wind farms. The reactive power strategies for wind turbines and wind farms are analyzed as an application example.

Previous Spanish regulation stated unity power factor (P.F.) as target. New regulation introduced in the Royal Decrees 436/2004 and 661/2007 rewarded up to 8% with P.F. $< 0,95$ inductive (on low-load hours) and P.F. $< 0,95$ capacitive (on peak hours).

A better utilization of the infrastructure can be attained considering the reactive power generation availability even in calm periods –depending on the reactive power compensation scheme implemented in the wind farm-. This can lead to a voltage support strategy in a nearby node, especially if the voltage at that node can be estimated despite tap changing transformers.

The effect of some control strategies in nearby nodes are quantified statistically regarding the stochastic nature of wind power.

Annex B: Analysis of wind power variability from measured data

The models developed in this thesis are based in the personal experience gained designing, installing and analyzing the records of a multipurpose data logger for wind turbines and wind farms. The first prototypes have been developed further and now it is commercially available under the name AIRE (Analizador Integral de Recursos Energéticos).

This annex shows some examples of data analysis. The contributions of these examples are the analysis methodology and the conclusions gained from the analysis of the measurements shown in the annex. In fact, some effects observed in the data such the measured oscillations are quite difficult to obtain from simulations.

The measurement system was installed in several wind farms between 1998 and 2000 owned by CEASA (now NEO Energía) and TAIM-NEG-MICON (now VESTAS).

Borja wind farm had 27 Vestas' turbines with variable pitch and wound rotor induction generators with a variable resistor connected to their rotor, VRIG (generator speed vary from 1500 to 1560 rpm).

Remolinos wind farm is in a cliff top and it has doubly fed induction generators (DFIG) from Gamesa, with generator speed ranging from 1220 to 1620 rpm. There are 15 x G42 wind turbines of 648 kW (42 m rotor diameter) and 3 turbines G47 of 660 kW (47 m rotor diameter), both of them with variable pitch.

It was also installed in Valdecuadros, a wind farm with two 600 kW wind turbines and one 750 kW turbine and with fixed pitch (stall control). The utilized generators are squirrel cage induction generators (SCIG), fixed speed, directly connected to the network. The 600 kW WT has a solo generator, with one fixed speed (1500 to 1514 rpm). The 750 kW wind turbine has a secondary 200 kW generator to increase production at low wind by reducing rotor speed (1000-1006 rpm versus 1500-1510 rpm).

Annex C: Torque estimation from blade element theory

This annex introduces an aerodynamic model to estimate the influence of deterministic wind component (wind shear and tower shadow) from the torque coefficient and the main properties geometry of the turbine. The model is derived using blade element theory, potential flow upstream the tower and uniform blade loading.

The aim of this model is to compute the aerodynamic torque at the low-speed shaft, simply enough to be included in the generator control or for simulating a cluster of turbines, and requiring only basic features such as the aerodynamic torque coefficient and the main constructive parameters of the turbine. This model can also be used to study the effect of mismatches in the blades (pitch errors in each blade) and errors in orientation of the turbine.

Besides its computational efficiency, another advantage of this method is that only requires the torque coefficient and the main dimensions of the turbine (it does not need to know the airfoil section along blades).

The model presented in this chapter is based on blade element theory with constant tangent force distribution, also known as uniform blade loading. The tangential force

distribution is approximately constant in the main body of the blade when the turbine operates at partial load (maximum turbine efficiency), but may introduce errors when the tip of the blades stalls. However, the starting of the blade stall is intricate and a more complex model is needed to take into account the hysteresis of the separation of the boundary layer in the blades. Since pitch controlled turbine is unusually operating with attached flux and the proposed method is valid for pitch controlled turbines.

Annex D: Wake estimation in an offshore wind farm

The distribution of wind speeds and turbulences along a wind farm is required to achieve a fair representation of a wind farm.

For simplicity, this model is targeted to offshore wind farms, where there is no influence of land topography. The wake is estimated in this annex using a kinematic model.

One of the contributions of this model is the simplicity of testing different wakes models.

Annex E: Manual of the program WINDFREEDOM

One contribution of this thesis is the program that downloads, represents and analyzes the data from the network of meteorological weather stations, typically used by meteorological organizations for weather prediction.

An user manual of the program WINDFREEDOM with three case studies has been included to show the potential use of this program.

Annex F: Manual of the program EQWIGUST

Another contribution of this thesis is the program that generates gust or random samples with certain features of equivalent wind.

This program estimates the average shape of gusts of the equivalent wind with some features from the characteristics of the wind and the turbine.

An user manual of the program EQWIGUST with two three random samples has been included to show the potential use of this program.

Chapter 2:

Variability of Wind

in the Frequency Domain

2.1. Introduction

Wind oscillations due to momentary wind speed variations can be classified according to their rate and their spatial extent. Slow fluctuations (in the range of tens of minutes and hours) are mainly due to meteorological dynamics and they are highly correlated among near wind farms.

Fast fluctuations have lower spatial correlation [42, 43] and wind gust and turbulence effects are smoothed in the output of the wind farm. A swift gust arriving simultaneously to all turbines dispersed in an area of kilometres is also very uncommon. The correlated component of wind is estimated in [44] from the Davenport type and Schlez and Infield's decay factors [45], showing that coherence for distances greater than 100 m is below 10^{-20} at tower shadow frequencies (between 0.5 Hz and 2 Hz). In fact, the coherence for the usual dimension of a wind farm is low for oscillations quicker than 0,001 Hz [46]. Thus, the fluctuations quicker than 10 minutes are low correlated among the turbines a wind farm.

Fluctuations of power output can be divided into cyclic and acyclic components. Cyclic components are due to tower shadow, wind shear, modal vibrations, etc. Acyclic components are due to turbulence, weather dynamics and events (turbine connection or disconnection, change in generator configuration, etc.). Oscillations from a few minutes up to a grid cycle are mainly linearly uncorrelated and their sum across a wind farm can be estimated using stochastic analysis commonly applied in other areas such as multipath fading in communication channels, clutter and target cross section in radars, interference in communication systems, etc. However, this approach is novel in wind energy.

In [47], a transfer function of the wind farm power output of N turbines respect the output of a single turbine is estimated with gain N at low frequencies ($f < 0.03$ Hz) and gain \sqrt{N} at high frequencies ($f > 0.09$ Hz). Micro-meteorological and dynamic fluid models can predict the correlated fluctuations which predominate at the very low frequencies. Fully correlated fluctuations scales proportional to the number of turbines N whereas linearly uncorrelated fluctuations cancel partially among turbines and they scale up typically in a factor \sqrt{N} , according to the central limit theorem.

The influence of blade position in a single turbine power output has been widely analyzed in the literature [48, 49, 50]. The aerodynamic coupling among the turbines in a wind farm is negligible due to the turbulent flow mixing. According to [51], a very weak electrical network and a very low turbulence is necessary for synchronization to happen driven by voltage drops. Since these conditions are not realistic, the rotor position has random angles and the crossing of a blade

in front of the turbine tower is a random event with constant probability rate.

Experimental measurements [52] have corroborated that the synchronization of blades is unusual. It has also been observed that the cuasi-periodic aerodynamic torque oscillations are transformed into stochastic oscillation of electric power due to the complex wind turbine dynamics. The power oscillations of frequency below 0,03 Hz are greatly reduced at the farm output and the main source of variability in the wind power injected in the grid is the meteorological dynamics.

To sum up, this chapter focuses on the spatial and temporal variability of the wind for short horizons. Fast fluctuations of wind power during continuous operation of wind turbine are not an issue for utilities. Only in isolated or in weak networks, or in the simultaneous tripping event of big amounts of wind power they are an issue.

These results can be extended to several wind farms since the uncorrelated components increases when the distances among turbines become bigger.

The models developed in this thesis are based in the personal experience gained designing, installing and analyzing the records of a custom data logger for wind turbines and wind farms [53]. The main system was composed by a PC computer, a DAQ (Digital Acquisition Board), signal conditioning modules and LabVIEW software for logging and analyzing the measurements. It could be placed in the low voltage side of a WT or connected to the measuring transformers of the wind farm substation.

The first prototypes have been developed further and now they are commercially available under the name AIRE (Analizador Integral de Recursos Energéticos).

The measurement system was installed in several wind farms between 1998 and 2000 owned by CEASA (now NEO Energía) and TAIM-NEG-MICON (now VESTAS).

Borja wind farm had at that time 27 Vestas' turbines with variable pitch and wound rotor induction generators with a variable resistor connected to their rotor, VRIG (generator speed vary from 1500 to 1560 rpm).

Remolinos wind farm is in a cliff top and it has doubly fed induction generators (DFIG) from Gamesa, with generator speed ranging from 1220 to 1620 rpm. There are 15 x G42 wind turbines of 648 kW (42 m rotor diameter) and 3 turbines G47 of 660 kW (47 m rotor diameter), both of them with variable pitch.

Valdecuadros is an experimental wind farm with two 600 kW wind turbines and one 750 kW turbine and with fixed

pitch (stall control). The utilized generators are squirrel cage induction generators (SCIG), fixed speed, directly connected to the network. The 600 kW WT has an unique generator, with one fixed speed (1500 to 1514 rpm). The 750 kW wind turbine has a secondary 200 kW generator to increase production at low wind by reducing rotor speed (1000-1006 rpm versus 1500-1510 rpm).

The model of geographic variation of wind has been tested with data from the World Meteorological Organization (WMO). Even though these stations are not so exposed to the wind, the measured wind speed can be scaled up to the typical levels in a wind farm and interesting conclusions can be drawn from the vast network of weather stations available.

A program called WINDFREDOM [54] has been developed for retrieving the weather data from the servers of Wolfram Research Inc. and computes the coherence from nearby weather stations. This program can be run freely with the *Mathematica* Player and it will be accessible in <http://www.windygrid.org/software> under the GNU General Program License after the public defence of this thesis. A brief manual of this program is included in the annexes of this thesis and a copy of the software is attached in the CDROM.

2.2. Characterization of the turbulence

At a very basic level, a turbulence flow can be interpreted as a population of many eddies (vortices), of different sizes and strengths, embedded in another and forever changing, giving a random appearance to the flow (Fig. 1). Two variables then play a fundamental role: d , the characteristic diameter of the eddies, and \hat{u} , their characteristic orbital velocity.

Since the turbulent flow consist in many eddies, of varying sizes and speeds, \hat{u} and d do not assume each of a single value but vary within a certain range. In stationary, homogeneous and isotropic turbulence, that is, a turbulent flow that statistically appears unchanging in time, uniform in space and without preferential direction, all eddies of a given size (same d) behave more or less in the same way and can be thought of sharing the same characteristic velocity \hat{u} . In other words, we make the assumption that \hat{u} is a function of d (Fig. 2) [55].



Fig. 1: Drawing of a turbulent flow by Leonardo da Vinci (1452–1519), who recognized that turbulence involves a multitude of eddies at various scales. Taken from Benoit Cushman-Roisin [55].

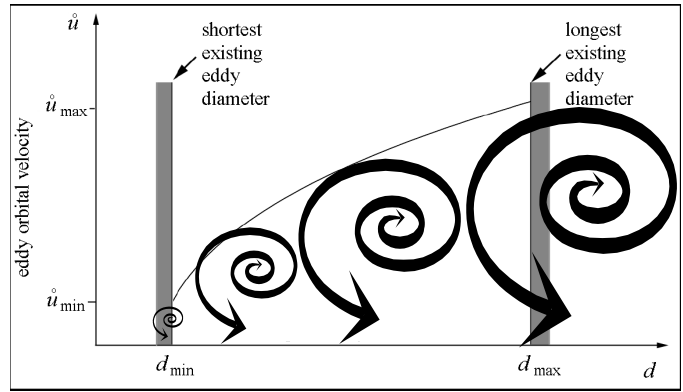


Fig. 2: Eddy orbital velocity versus eddy length scale in homogeneous turbulence. The largest eddies spin the fastest. Taken from “Environmental Fluid Mechanics” of Benoit Cushman-Roisin [55] and modified from Simon Watson [56].

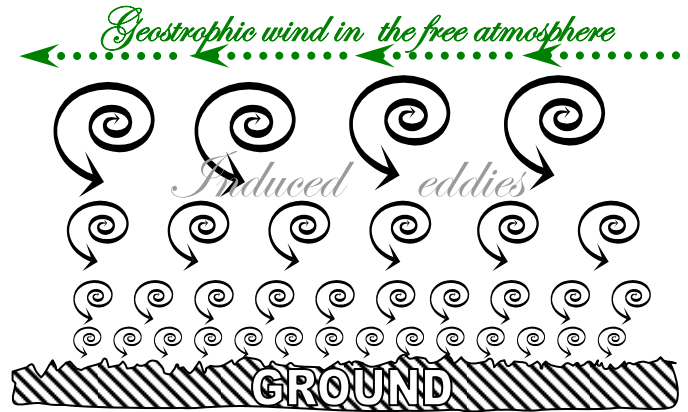


Fig. 3: Schematic of eddies as a function of height at atmospheric boundary layer. Taken from Simon Watson [56].

2.2.1. Energy cascade in eddies

In the view of Kolmogorov [57], turbulent motions span a wide range of scales ranging from a meteorological macroscale at which the energy is supplied, to a microscale at which energy is dissipated by viscosity. The interaction among the eddies of various scales passes energy sequentially from the larger eddies gradually to the smaller ones (Fig. 3). This process is known as the turbulent energy cascade (Fig. 4).

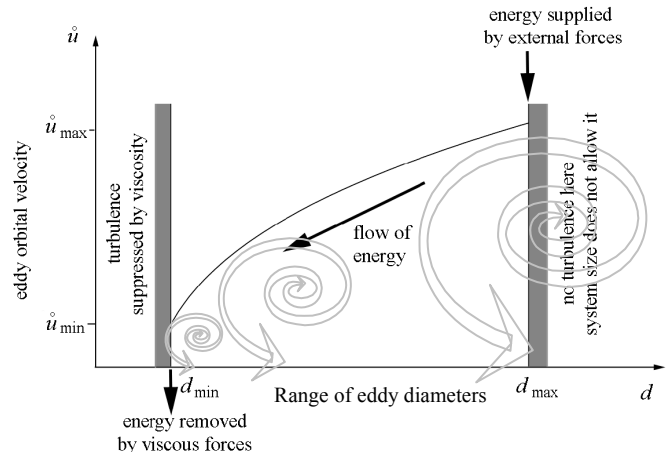


Fig. 4: The turbulent energy cascade. According to this theory, the energy fed by external forces excites the largest possible eddies and is gradually passed to ever smaller eddies, all the way to a minimum scale where this energy is ultimately dissipated by viscosity. Taken from Benoit Cushman-Roisin [55].

If the state of turbulence is statistically steady (statistically unchanging turbulence intensity), then the rate of energy transfer from one scale to the next must be the same for all scales, so that no group of eddies sharing the same scale sees its total energy level increase or decrease over time. It follows that the rate at which energy is supplied at the largest possible scale (d_{max}) is equal to that dissipated at the shortest scale (d_{min}). Let us denote by ε this rate of energy supply/dissipation, per unit mass of fluid:

ε = energy supplied to fluid per unit mass and time = power cascading from scale to scale, per unit mass = energy dissipated by viscosity, per unit mass and time.

With Kolmogorov, we further assume that the characteristics of the turbulent eddies of scale d depend solely on d itself and on the energy cascade rate ε . This is to mean that the eddies know how big they are, at which power density is supplied to them and at which rate they must supply it to the next smaller eddies in the cascade. Mathematically, \hat{u} depends only on d and ε . The dimensional analysis of the magnitudes, $[\hat{u}] = LT^{-1}$, $[d] = L$ and $[\varepsilon] = L^2T^{-3}$; the only dimensionally acceptable possibility is $\hat{u} = A(\varepsilon d)^{1/3}$, in which A is a dimensionless constant on the order of unity. This relation implies that the smaller d , the weaker \hat{u} . Thus, the larger ε , the larger \hat{u} . This makes sense, for a greater energy supply to the system generates stronger eddies. This could not have been anticipated and must be accepted as a result of the theory. The implication is that the smallest eddies have the lowest speeds, while the largest ones have the highest speeds and thus contain the bulk of the kinetic energy.

2.2.2. Largest and shortest length scales

Typically, the largest possible eddies in the turbulent flow are those that extend across the entire system, from boundary to opposite boundary, and therefore $d_{max} = L$, where L is the geometrical dimension of the system (such as the width of the domain or the cubic root of its volume). In the atmosphere, the height has a short vertical extent and a comparatively long horizontal extent (distance, length) of the system.

Therefore, the eddies that rotate in the vertical plane (about a horizontal axis, as shown in Fig. 3) have significant characteristics from those that rotate horizontally (about a vertical axis).

The shortest eddy scale is set by viscosity, because the shorter the eddy scale, the stronger the velocity shear and the more important the effect of viscosity. Consequently, the shortest eddy scale can be defined as the length scale at which viscosity becomes dominant. The ambient air kinematic viscosity is $\nu_{air} = 1,51 \times 10^{-5} \text{ m}^2/\text{s}$.

If we assume that d_{min} depends only on ε , the rate at which energy is supplied to that scale, and on ν_{air} , because those eddies sense viscosity, then the only dimensionally acceptable relation is $d_{min} \sim \nu_{air}^{3/4} \varepsilon^{-1/4}$. Therefore, d_{min} depends on the energy level of the turbulence. The stronger the turbulence (the bigger ε), the shorter the minimum length scale at which it is capable of stirring. The quantity $\nu_{air}^{3/4} \varepsilon^{-1/4}$, called the *Kolmogorov scale*, is typically on the order of a few millimetres or shorter.

The span of length scales in a turbulent flow is related to its Reynolds number. Indeed, in terms of the largest velocity scale, which is the orbital velocity of the largest eddies, $\hat{u}_{max} =$

$\hat{u}(d_{max}) = A(\varepsilon L)^{1/3}$, the energy supply/dissipation rate is $\varepsilon = (\hat{u}_{max}/A)^3 L^{-1} \sim \hat{u}_{max}^3/L$ and the length scale ratio can be expressed as $L/d_{min} \sim L/(\nu_{air}^{3/4} \varepsilon^{-1/4}) \sim Re^{3/4}$, where $Re = \hat{u}_{max}L/\nu_{air}$ is the Reynolds number of the flow. As we could have expected, a flow with a higher Reynolds number contains a broader range of eddies.

The atmospheric boundary layer spans up to a height of about 1000 m above the ground. Since wind speeds are in the range of 10 m/s, then the Reynolds number can be estimated as $Re = \hat{u}_{max}L/\nu_{air} = 10 \text{ m/s} \cdot 1000 \text{ m} / 1,51 \times 10^{-5} \text{ m}^2/\text{s} = 6,6 \times 10^8$, which yields $Re^{3/4} = 4,1 \times 10^6$ and $d_{min} \sim L/Re^{3/4} = 2,4 \times 10^{-4} \text{ m}$ or about 0,24 mm.

The power mass density supply/dissipation is estimated to be around $\varepsilon \sim \hat{u}_{max}^3/L = (10 \text{ m/s})^3/(1000 \text{ m}) = 1 \text{ m}^2/\text{s}^3$ or 1 Watt per kilogram of air.

2.2.3. Taylor's Hypothesis of "frozen turbulence"

Turbulent flow can be viewed as a collection of eddies that evolve in time and space as they float along in the mean flow (Reynolds decomposition). The structure, size and distribution of these eddies determine the mixing efficiency of turbulence and thus the importance of turbulent transport. The distribution of eddies is very irregular in space and in time and it is subject to ongoing change.

The question is: how then can we begin to measure the size and distribution of these eddies that define turbulence? It is impractical (or even impossible) to have such high instrument density that every eddy is covered all the time. Even spatial "snapshots" are difficult and expensive.

Under certain conditions (homogeneous and stationary process) an average over a time-series of observations in one place is an adequate representation of the ensemble average (incorporating all possible eddies).

However, a time series essentially samples only those eddies that happen to float past a given sensor. If we can determine the average of all eddies that way, can we also determine their size?

One difficulty is that such observations are not a pure time-series: Because the eddies evolve in time (change shape, fall apart etc.), we sample a mixture of a time series and a spatial transect through the flow.

A practical suggestion for an escape from this dilemma came 1938 from Geoffrey I. Taylor: *in certain circumstances, turbulence can be considered as "frozen", as it passes by a sensor*. This suggestion became known as Taylor's Hypothesis and assumes that the rate of change of an eddy is small compared to the velocity of the mean flow, so that it changes only negligibly over the time it takes to float by the sensor.

Fig. 5 shows an example of the Taylor's Hypothesis of the "frozen turbulence". An idealized eddy of 100 m horizontal dimension contains a wind difference of $\pm 1 \text{ m/s}$ from one end to the other. At this point, the sensor measures a speed of 9 m/s. The same eddy has now floated past the sensor with a mean wind velocity of 10 m/s. The sensor now measures 11 m/s, assuming the structure of the eddy has not changed.

Of course, turbulence always evolves and is in reality never frozen. However Taylor's Hypothesis assumes that the time it takes the eddy to float past ($\Delta t = 10 \text{ s}$ in this case) is too

small for the eddy to change noticeably. In other words: it appears to be frozen.

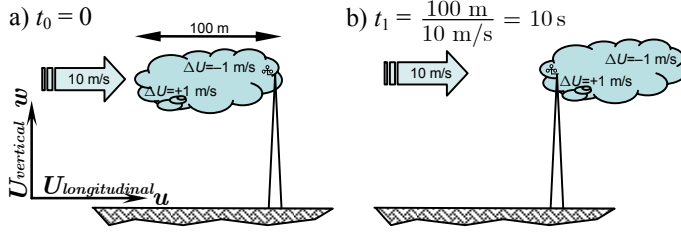


Fig. 5: Example of a idealized eddy of 100 m (represented by a cloud) passing through a meteorological mast according to Taylor's Hypothesis of "frozen turbulence".

2.3. Wind spectra

The fluctuations in the wind can be thought of as resulting from a composite of sinusoidally varying winds imposed on the mean steady wind. These sinusoidal variations will have a variety of frequencies and amplitudes. The term 'spectrum' is used to describe functions of frequency. Thus the function that characterizes turbulence as a function of frequency is known as a 'spectral density' function. Since the average value of any sinusoid is zero, the amplitudes are characterized in terms of their mean square values. This type of analysis originated in electric power applications, where the square of the voltage or current is proportional to the power. The complete name for the function describing the relation between frequency and amplitudes of sinusoidally varying waves making up the fluctuating wind speed is therefore 'power spectral density' or *PSD* for short.

There are three points of particular importance to note regarding *PSD*'s.

- The wind variance due to fluctuations within a frequency range may be found by integrating the $PSD_{U_{wind}}^+(f)$ in that range.
- The integral of $PSD_{U_{wind}}^+(f)$ over all frequencies is equal to the total wind variance.
- If two-sided $PSD(f)$ are used instead of $PSD^+(f)$, the variance is twice the $PSD(f)$ if only positive frequencies are used in the integration domain.

Therefore, *PSD* is the variance spectral density of a signal, irrespective of the signal nature (voltage, wind speed or the power from a wind farm). However, the term "Power Spectral Density" is in widespread use for referring to the spectral density of the variance of a signal. Thus, that usual convention will be used in this work.

The spectral density of the wind variance is often used in dynamic analyses. The variations of wind in the stream direction of the flow are usually characterized through the *PSD* of the longitudinal component of the instantaneous speed. A number of power spectral density functions are used as models in wind energy engineering when representative turbulence power spectral densities are unavailable for a given site. The mathematical forms for along-wind velocity spectra which are currently used in major current, or recent, wind codes and standards [58] are due to von Karman, Kaimal and Davenport.

2.3.1. Properties of spectra

The spectral representation theorem (Karhunen–Loève theorem) states that any real valued, covariance stationary process, such as the wind or the power from the wind farm turbines, can be represented as the weighted sum of orthogonal periodic components. The benefit of applying a spectral approach to the analysis is that it allows for the decomposition of these moments into constituent frequency components —providing a richer representation of dynamic interactions.

Specifically, the longitudinal component of wind can be expressed in frequency components using phasors. The stochastic spectral phasor density of the longitudinal wind in a time series of duration T are:

$$\vec{U}_{wind}(f) = U_{wind}(f) e^{j\varphi_{U_{wind}}(f)} = \frac{1}{\sqrt{T}} \int_0^T U_{wind}(t) e^{-j2\pi f t} dt \quad (1)$$

Alternatively, the stochastic spectral phasor density can be expressed from the cosine $a(f)$ and sine $b(f)$ Fourier coefficients of the time series considered as a period as $U_{wind}(f) = \frac{1}{2}\sqrt{T}[a(f) + j b(f)]$ for $f > 0$.

The longitudinal wind in the time domain can be retrieved from the spectral phasor density through the scaled inverse transform:

$$\begin{aligned} U_{wind}(t) &= \int_{-\infty}^{\infty} \frac{\vec{U}_{wind}(f)}{\sqrt{T}} e^{j2\pi f t} df \stackrel{\vec{U}_{wind}(f) = \vec{U}_{wind}^*(-f)}{=} \quad (2) \\ &= \frac{2}{\sqrt{T}} \operatorname{Re} \left[\int_0^{\infty} \vec{U}_{wind}(f) e^{j2\pi f t} df \right] \stackrel{\vec{U}_{wind}(f) = U_{wind}(f) e^{j\varphi_{U_{wind}}(f)}}{=} \\ &= \frac{2}{\sqrt{T}} \int_0^{\infty} U_{wind}(f) \cos[2\pi f t + \varphi_{U_{wind}}(f)] df \end{aligned}$$

where e is the base of the natural logarithm, j is the imaginary unit, Re states for the real part of a complex number and $*$ stands for complex conjugate.

The wind is usually assumed to be a stochastic process characterized by its two-sided power spectral density $PSD_{U_{wind}}(f)$, corresponding to the average squared modulus of the stochastic spectral phasor $\langle U_{wind}^2(f) \rangle$.

In the meteorological literature, it is more common to use the dimensionless unilateral power spectral density, $f PSD_{U_{wind}}^+(f) / \sigma_{U_{wind}}^2$ (excluding the DC term at $f=0$). It represents the frequency distribution of the turbulence when plotted in a semi logarithmic graph, see (10) for details.

The integral of $PSD_{U_{wind}}^+(f)$ for positive frequencies is the variance of the instantaneous wind, $\sigma_{U_{wind}}^2$ (Parseval's theorem).

$$\begin{aligned} \int_0^{\infty} PSD_{U_{wind}}^+(f) df &= \int_{-\infty}^{\infty} PSD_{U_{wind}}(f) df = \\ &= \left\langle \int_0^T \frac{U_{wind}^2(t)}{T} dt \right\rangle = \langle U_{wind}(t) \rangle^2 = \sigma_{U_{wind}}^2 \quad (3) \end{aligned}$$

The probability density function of the wind speed provides a measure of the likelihood of particular values of wind speed. It provides no information, however, about what the speed is likely to be, given what it has been. A measure of that tendency is provided by the autocorrelation function.

The autocorrelation function can be used to determine the integral time scale of turbulence. The normalized auto correlation function is:

$$ACF_{U_{wind}}(\tau) = \frac{\left\langle \left[U_{wind}(t+\tau) - \langle U_{wind} \rangle \right]^* \left[U_{wind}(t) - \langle U_{wind} \rangle \right] \right\rangle}{\sigma_{U_{wind}}^2} \quad (4)$$

where the asterisk $*$ denotes complex conjugation and it can be omitted since wind is a real value.

Alternatively, the normalized autocorrelation $ACF_{U_{wind}}(\tau)$ can be computed as the inverse Fourier Transform of $PSD_{U_{wind}}(f)$ divided by $\sigma_{U_{wind}}^2$ according to the Wiener–Khinchin theorem.

The $PSD_{U_{wind}}(f)$ at very low frequencies would represent the very slow weather dynamics but the wind is not stationary at very low frequencies since it shows intermittency between stable meteorological situations. Since frequency representation of wind is based on the theory of stationary signals, $PSD_{U_{wind}}(f)$ must be considered with prudence at low frequencies.

The low frequency asymptotic trend (5) can be derived from the Wiener–Khinchin theorem:

$$\lim_{f \rightarrow 0^+} PSD_{U_{wind}}^+(f) \simeq 4 \sigma_{U_{eq}}^2 \frac{\ell_{U_{wind}}}{\langle U_{wind} \rangle} \quad (5)$$

where $\ell_{U_{wind}}$ is the integral length scale to be defined later. However, (5) has relatively small relevance and, in fact, some popular models of wind spectra do not obey this relationship.

2.3.2. Integral length scale

The autocorrelation function $ACF_{U_{wind}}(\tau)$ will, if any trends are removed before starting the process, decay from a value of 1.0 at $\tau=0$ to the first zero crossing at the lag noted τ_{fzc} and then $ACF_{U_{wind}}(\tau)$ tends to take on small positive or negative values as the lag increases τ . A measure of the average time over which wind speed fluctuations are correlated with each other is found by integrating the autocorrelation (usually from zero lag to the first zero crossing, τ_{fzc} for better numerical stability). The single resulting value is known as the integral time scale of the turbulence, $T_{U_{wind}}$.

$$T_{U_{wind}} = \int_0^\infty ACF_{U_{wind}}(\tau) d\tau \approx \int_0^{\tau_{fzc}} ACF_{U_{wind}}(\tau) d\tau \quad (6)$$

One problem of the infinite integral is the influence of the subtraction of the estimated mean [59] or a trend correction [60]. Due to these difficulties, the integral time scale is estimated, as aforementioned, using the truncated autocorrelation function $ACF_{U_{wind}}(\tau)$ up to the first zero crossing τ_{fzc} or, equivalently, the windowed periodogram or smoothed Fast Fourier Transform (FFT) [61]. The smoothing is arbitrary and therefore estimation of $T_{U_{wind}}$ via FFT is subjective [62]. Alternatively, a spectral model can be adjusted and the time scale can be derived from its fit.

While typical values of $T_{U_{wind}}$ are less than 10 seconds, the integral time scale is a function of the site, atmospheric stability, and other factors and may be significantly greater than 10 seconds. Gusts are relatively coherent (well correlated) rises and falls in the wind, and have characteristic times on the same order as the integral time scale. Moreover,

the aerodynamic filter, which relates actual and equivalent wind speed, has characteristic times of the same order for multi-megawatt turbines.

Multiplying the integral time scale by the mean wind velocity gives the integral length scale. The integral length scale tends to be more constant over a range of wind speeds than is the integral time scale, and thus is somewhat more representative of a site.

The integral length scale of the turbulence, $\ell_{U_{wind}}$ is defined as the integral time scale $T_{U_{wind}}$ times the wind speed average, $\langle U_{wind} \rangle$.

$$\ell_{U_{wind}} = \langle U_{wind} \rangle T_{U_{wind}} \quad (7)$$

and the dimensionless frequency is $f_{dl} = f T_{U_{wind}} = f \frac{\ell_{U_{wind}}}{\langle U_{wind} \rangle}$.

The length scale is dependent on the surface roughness, z_0 , as well as the height above ground, z . Standards used for wind turbine loading calculations specify different turbulence spectra and/or different length scales to be used in different test conditions. The length scale dependence on the height above ground can be simplified until a constant as is done in the Danish standard DS472 or in the IEC standard 61400-1.

The turbulence intensity is the standard deviation normalized by the average wind speed (8):

$$I_{U_{wind}} = \sigma_{U_{wind}} / \langle U_{wind} \rangle \quad (8)$$

Other normalizations are possible, especially for wind turbine design calculations [90]. The standard deviation $\sigma_{U_{wind}}$ of the wind speed longitudinal component varies depending on the stability regime of the boundary layer. The standard IEC 61400-1 assumes an average value of the standard deviation $\langle \sigma_{U_{wind}} \rangle = I_{ref} (0,75 U_{wind} + 3,8)$ with a variance $Var(\sigma_{U_{wind}}) = (1,44 I_{ref})^2$ in S.I. units.

Experimental measurements in the inertial subrange and dimensional analysis have shown the following tendency at high frequencies, with $A = 0.10 \sim 0.15$:

$$\frac{f PSD_{U_{wind}}^+(f)}{\sigma_{U_{wind}}^2} \approx A \left(\frac{f \ell_{U_{wind}}}{\langle U_{wind} \rangle} \right)^{-2/3} \quad (9)$$

2.3.3. Classic description of turbulence in the frequency domain

The turbulent variations of the wind speed are typically expressed in terms of the standard deviation, $\sigma_{U_{wind}}$ of velocity fluctuations measured over 10 to 60 minutes, normalized by the friction velocity u_* or by the mean wind speed $\langle U_{wind} \rangle$. The variation in these ratios is caused by a large natural variability, but also to some extent because they are sensitive to the averaging time and the frequency response of the sensor used. In horizontally homogeneous terrain, the turbulence intensity, $I_{U_{wind}} = \sigma_{U_{wind}} / \langle U_{wind} \rangle$, is a function of height and roughness length in addition to stability, whereas $\sigma_{U_{wind}}$ divided by the friction speed u_* may be considered a function only of stability near the ground. A typical value for neutral conditions is $\sigma_{U_{wind}} / u_* = 2,5$ for homogeneous flat terrain, often larger for inhomogeneous terrain, but with very large local variations.

The turbulence intensity is a widely used measure, and for neutral conditions with a logarithmic wind profile over flat

terrain, we find $I_{U_{wind}} \approx 1/Ln(z - z_0)$. Typical values of $I_{U_{wind}}$ for neutral conditions in different terrains are [63]:

- Sea: 8%
- Flat open grassland: 13%
- Complex terrain: 20% or more

The variations with stability can also be considerable, especially at low to moderate wind speeds, with smaller resulting turbulent intensities in stable conditions and larger values in unstable conditions; values of 25% are not unusual in flat open grassland for moderately unstable conditions. The variances are quite sensitive to the averaging time because much of the turbulent kinetic energy appears at quite low frequencies, in both unstable and particularly in stable conditions. In the latter case, the variance can be completely dominated by large-scale slow variations in wind speed and direction overlaid with very little turbulence [64].

In wakes we see increased turbulence levels together with decreased mean wind speeds, leading to significantly larger turbulence intensities than for the free flow [102].

The turbulent velocity fluctuations can be described as a result of stochastic broadband processes. We see variations in velocity in a broad range of frequencies and scales, and numerous models have been used to describe the distribution of energy over different scales as a function of stability and height (see Fig. 6). These models can be subdivided into two ‘families’: the so-called Kaimal-spectra and their generalizations [70], providing good empirical descriptions of observed spectra in the atmosphere, and the von Kármán spectra, which may provide a good description of turbulence in tube-flows and wind tunnels [63]. The popularity of the latter can be attributed mainly to the fact that they feature simple analytical expressions for the correlations and follows the Wiener-Khinchine relation between autocorrelation and spectral density, $PSD_{U_{wind}}(f=0) = 4\sigma_{U_{wind}}^2 \ell_{U_{wind}} / \langle U_{wind} \rangle$, where $\ell_{U_{wind}}$ is the integral scale (i.e., the mean wind speed times the area under the normalized auto correlation function of the wind).

Usually, the PSD is represented in a way that the total area below the graph is the variance of velocity fluctuations, $\sigma_{U_{wind}}^2$ and the height of the curve indicates the relative content of the signal at such frequency. Since only positive frequencies are plotted, PSD^+ is one-sided (one-sided PSD^+ is the double of two-sided power spectral density PSD). To increase the dynamic range of the plot, the logarithmic scale is used for frequency in the horizontal axis. Using the Riemann–Stieltjes integral, it is straightforward that the vertical axis must be the wind spectra times the frequency in linear axis (see the Van der Hoven spectra in Fig. 8 or Fig. 6) for the underlying area being $\sigma_{U_{wind}}^2$.

$$\begin{aligned} \sigma_{U_{wind}}^2 &= \int_{f_{min}}^{f_{max}} PSD_{U_{wind}}^+(f) df = \left\{ \begin{array}{l} \text{Area below conventional graph} \\ \text{of } PSD_{U_{wind}}^+(f) \text{ with linear axis} \end{array} \right\} \\ &= \int_{Log(f_{min})}^{Log(f_{max})} \frac{PSD_{U_{wind}}^+(f)}{d[Log(f)]} d[Log(f)] = \\ &= \int_{Log(f_{min})}^{Log(f_{max})} f \cdot PSD_{U_{wind}}^+(f) d[Log(f)] = \left\{ \begin{array}{l} \text{Area below Log-Lin} \\ \text{graph of } f \cdot PSD_{U_{wind}}^+(f) \end{array} \right\} \end{aligned} \quad (10)$$

If the logarithmic scale is used both for frequency and for PSD , then the dynamic range of the spectra is increased, the

order of the system is easier determined and the peaks of semi-log and bi-logarithmic graphs coincide since the logarithmic mapping is a monotone increasing function. However the area below the bi-logarithmic graph of $f \cdot PSD^+(f)$ does neither represent the wind speed variance nor the height of the graph is proportional to the frequency content of the signal. Hence, if a bi-logarithmic scale is used, then it is recommended to plot $PSD^+(f)$ instead of $f \cdot PSD^+(f)$.

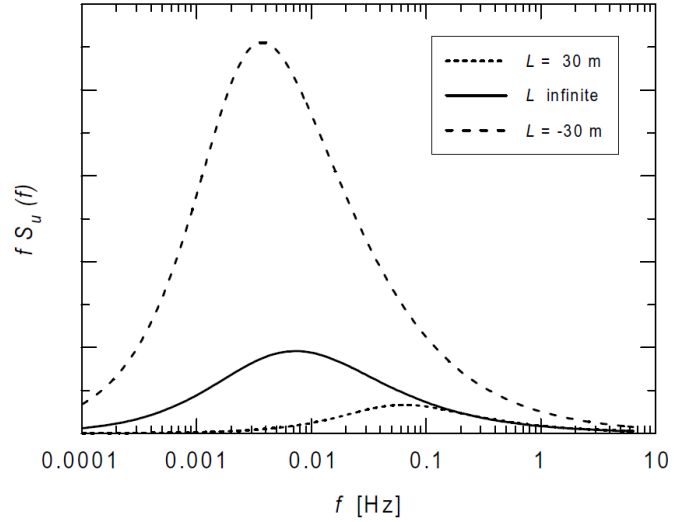


Fig. 6: Model spectra of the streamwise velocity component 50 m above ground level in flat terrain for neutral (L infinite), stable ($L = 30$ m) and unstable ($L = -30$ m) conditions, where L is the Monin-Obukhov length. The areas under the curves are proportional to the variances. Taken from ‘‘Wind Power Meteorology’’ by Risø National Laboratory [63].

Typical spectra, (at near neutral, and not too close to the ground) are dominated by broad maxima and falling towards high frequencies as $f^{5/3}$. Note the quite large differences in the variances for different stabilities in Fig. 6 (area below the plots). The large variances correspond to unstable boundary layer and much smaller variances happen with stable boundary layer. The peak of $f \cdot PSD^+(f)$ is lower in unstable atmosphere than in stable atmosphere. The characteristic period of the turbulent oscillations in unstable boundary layer is $\tau_{peak, unstable} = 1/f_{peak, unstable} \sim 1/0,004$ Hz = 250 s. In stable boundary layer, the characteristic period is much smaller, $\tau_{peak, stable} = 1/f_{peak, stable} \sim 1/0,07$ Hz = 14 s and the oscillations have smaller amplitude due to the reduced variance. The neutral atmosphere behaviour is between stable and unstable behaviour.

The very low frequency behaviour is typically characterized by a large amount of variation and statistical uncertainty. In fact, frequency analysis of stochastic signals is based on linear, time-invariant system behaviour (i.e., system characteristics do not vary significantly inside the time of study). The very low frequencies are related to long time spans, where the atmospheric characteristics do vary significantly. This is the reason why numeric weather models or Markov chains are more suitable than frequency models for analyzing very long time spans (very low frequencies).

The traditional way of relating length and time scales in turbulence is through the so-called Taylor ‘frozen turbulence’ approximation, i.e. the turbulence statistics can be regarded as a result of a frozen picture of turbulence advected past the observer by the mean wind, such that $\lambda = \langle U_{wind} \rangle / f$, where λ is a length scale and f the corresponding frequency observed in a fixed frame of reference. In the simple Kaimal formulation

for neutral conditions, approached from stable conditions, spectra close to the ground have a dominating length scale of about 22 times the height above the ground. This is a fair approximation at low heights and moderate wind speeds, but above 30–40 m and for high wind speeds [65] the length scale approaches a constant value, typically 500–1500 m. Therefore, significant power fluctuations are due to eddies with length scales of a bigger magnitude than the rotor radius R .

Terrain inhomogeneities may locally give rise to very large changes in the spectra. In flow over hills, the pressure field perturbations induced on the flow by the presence of the hill lead to an (almost) instantaneous redistribution of energy from the stream wise component of the wind to the vertical component by rapid distortion [66, 67]. In situations with changing roughness, the turbulence changes gradually downstream, first at small scales (high frequencies), and later also at larger scales. Because it can take considerable amounts of time (tens of minutes to hours) to change the large, energy-containing eddies, the turbulence of the flow “remembers” the upstream conditions far downstream [103]. The general effect of inhomogeneous terrain is to increase turbulence, typically at length scales comparable in size to the characteristic terrain features [41]. In this way, the shape of the spectrum approaches that of the unstable spectrum, where typical length scales of the energy-containing range are of the order of several kilometres.

Neutral conditions are very rare events, typically occurring only as transitions between stable and unstable conditions. However, near-neutral conditions occur also during overcast skies and moderate to high wind speeds. This variation in stability means that at a particular site, a wide range of dominating length scales are seen: from tens of meters to several kilometres, the distribution of which depends very much on the local stability climatology.

The probability distribution of length scales at a coastal site is shown in Fig. 7. Here, the length scale was defined instead of the length scale corresponding to the peak of the semi logarithmic plot of $f PSD_{wind}(f)$, as the scale for which half of the variance of the stream wise component is distributed on larger scales and the other half on smaller scales –i.e., the scale corresponding to the turbulence median in a semi logarithmic plot of $f PSD_{wind}(f)$. This length scale does not coincide exactly with the peak of the power spectrum –the difference being $< 10\%$ for a typical spectrum– but the length scale defined in this way is much easier to measure reliably.

In Fig. 7, the most common length scale is 500–600 m, but the distribution is skewed (almost symmetric in the logarithmic representation) and the average length scale is about 1000 m. Length scale distributions are presented also for other heights in [68]; from 15 m and above these are very similar (for the 7-m level the scales were found to be significantly smaller) with a slight tendency towards smaller scales closer to land. Also, it has been observed at the offshore location, 2 km from the coast, that the scales are smaller for offshore flow and larger for onshore flow.

Wind spectra from von Karman, Davenport, Kaimal, etc. can be thought as the squared transfer functions fed with white noise. Such filters can be applied to white noise to generate random wind with the same spectral properties as the real wind [42, 153, 176, 177]. The wind cut-off frequency depends on the turbulence length scale and the average

wind speed. If turbulence intensity is constant, then wind spectrum is proportional to the standard deviation of wind.

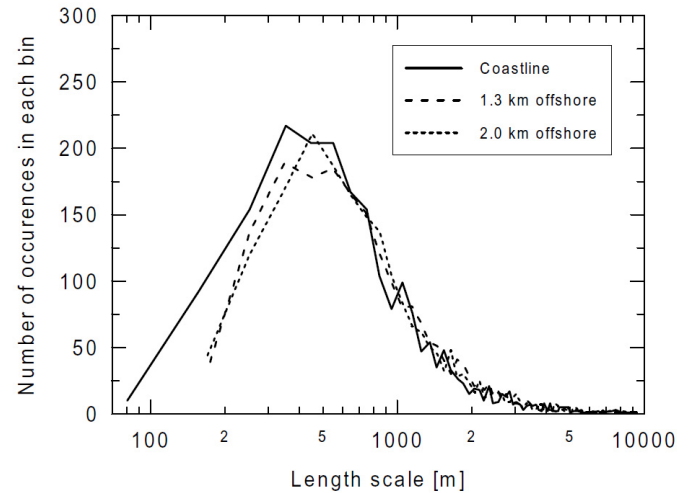


Fig. 7: Probability distribution of length scales from the Vindeby site at heights of 48 m. Length scales were derived by the “half variance” method. Taken from “Wind Power Meteorology” by Risø National Laboratory [63].

2.3.4. Kaimal wind spectrum

The Kaimal power spectra pattern was fitted based on several experimental data collected with neutral atmosphere over flat homogeneous terrain in Kansas as explained in [70]. This spectrum implies a relatively low terrain roughness. Furthermore, the model applies for neutral conditions only (strong winds), as convection is not accounted for. However, these conditions are met in a large number of applications like off-shore wind farms. Also, because of its simple expression, the Kaimal spectrum is widely used. The selection of this spectrum is discussed in [69].

The Kaimal spectrum model is, like other ones, usually presented under a PSD function. For the longitudinal wind speed component, the model defined by Kaimal relates frequency, length scale and average wind speed, [70]:

$$\frac{f PSD_{Kaimal}^+(f)}{\sigma_{U_{wind}}^2} = \frac{4a \left(f \ell_{U_{wind}} / \langle U_{wind} \rangle \right)}{\left[1 + 6a \left(f \ell_{U_{wind}} / \langle U_{wind} \rangle \right) \right]^{5/3}} \quad (11)$$

where $PSD_{Kaimal}^+(f)$ is the one-sided auto-spectral density function of the wind, f is the frequency in Hertz, σ is the standard deviation of wind, $\ell_{U_{wind}}$ is the integral length scale (proposed maximum 600 m) and $\langle U_{wind} \rangle$ is the average wind speed at the hub height, all in the upwind direction. The wind spectra at high and low frequencies is tuned with the parameter a : $a=1,7$ in the draft Eurocode ENV 1991-2-4 and thus, the inertial subrange constant in (9) is $A = 0.14$.

The Kaimal power spectra is similar to a low-pass filter of cut-off frequency $f_{cut-off} = \langle U_{wind} \rangle / (6a \ell_{U_{wind}})$ of order $r=5/6$. In other words, the Fourier transform of wind is approximately constant up to $f_{cut-off}$ and then decays in a factor $10^{5/6}$ each decade (the PSD decays with the squared factor). In a double logarithmic plot, the slope of the Fourier transform of wind is $20 \cdot (5/6)$ dB/decade or $10^{5/6}$ per decade if regular scale is used.

2.3.5. Davenport wind spectrum

This spectrum is based on the average of measurements obtained at various heights above the ground [71].

$$\frac{f PSD_{Davenport}^+(f)}{\sigma_{U_{wind}}^2} = \frac{\frac{4}{6} (f L_{Dav} / \langle U_{wind} \rangle)^2}{\left[1 + (f L_{Dav} / \langle U_{wind} \rangle)^2\right]^{4/3}} \quad (12)$$

where L_{Dav} is a turbulence length scale different from $\ell_{U_{wind}}$ and usually chosen as 1200 m. Assuming $L_{Dav} \sim 11,9 \ell_{U_{wind}}$, the inertial subrange constant in (9) is $A = 0.13$.

2.3.6. Harris wind spectrum

The Harris wind spectrum is nearly identical to the von Karman form if L_{Harris} is taken as $11,9 \ell_{U_{wind}}$.

$$\frac{f PSD_{Harris}^+(f)}{\sigma_{U_{wind}}^2} = \frac{0,6 (f L_{Harris} / \langle U_{wind} \rangle)}{\left[2 + (f L_{Harris} / \langle U_{wind} \rangle)^2\right]^{5/6}} \quad (13)$$

where L_{Harris} is a turbulence length scale different from $\ell_{U_{wind}}$, usually chosen as 1800 m. Equation (5) holds neither for Davenport nor for Harris spectrum.

2.3.7. Von Karman wind spectrum

Von Karman proposed a PSD for wind speeds in 1948 [72]. The von Karman spectrum is also suitable for the structure of the turbulence experienced by wind turbines, particularly in complex terrain, [73, 74]. Its power spectral density is:

$$\frac{f PSD_{Karman}^+(f)}{\sigma_{U_{wind}}^2} = \frac{4 \left(f \ell_{U_{wind}} / \langle U_{wind} \rangle \right)}{\left[1 + 70,8 \left(f \ell_{U_{wind}} / \langle U_{wind} \rangle \right)^2 \right]^{5/6}} \quad (14)$$

The inertial subrange constant in (9) is $A = 0.12$. Several experimental works demonstrated that the von Karman model and the Kaimal model have the following main differences:

- The Kaimal spectral expressions for the three spatial wind components describe adequately the experimental data as to the shape and peak frequencies but not as to the power levels;
- The von Karman model seems to fit the 3D experimental data better than the Kaimal with respect to the power levels. In the longitudinal component, a power deficit at low frequencies is observed.

2.3.8. IEC 61400-1 spectrum

The international standard IEC 61400-1 [97] for design requirements for wind turbines specifies a Kaimal type PSD function (11) with factor $a = 1/2$, which can be used in wind turbine design. The length scale is $\ell_{U_{wind}} = 5,67z$, where z is the height above ground, i.e. the hub height in our case. For heights above $z \geq 60$ m, the value of $\ell_{U_{wind}}$ takes the maximum length scale, 340,2 m.

Inside a wind farm, IEC 61400-1 recommends to apply the model proposed by Frandsen [75] to include the added turbulence generated by upwind turbines in the structural

design of wind turbines. Frandsen proposes to calculate the turbulence σ_{wf} according to:

$$\sigma_{wf} = \frac{1}{2} \left[\sigma_{wind} + \sqrt{\left(\frac{0,36 \langle U_{wind} \rangle}{1 + 0,2 \sqrt{s_1 s_2} / C_T} \right)^2 + \sigma_{wind}^2} \right] \quad (15)$$

where $\sigma_{U_{wind}}$ is the turbulence in the ambient flow. The separations between rows and columns in the farm, normalised by the wind turbine rotor diameter, are s_1 and s_2 respectively. C_T is the wind turbine thrust coefficient.

The wind turbines in the front with expected free inflow have a standard deviation of the longitudinal component of the wind equal to $\sigma = \sigma_{U_{wind}}$ and the remaining wind turbines inside the wind farm are assumed to have a standard deviation equal to $\sigma = \sigma_{wf}$.

2.3.9. Slettringen spectrum recommended by the Norwegian Petroleum Directorate

The Norwegian Petroleum Directorate (NPD) published in 1992 a different spectrum based on extensive wind measurements off the coast of mid-Norway and it is henceforth referred to as the ‘‘NPD spectrum’’ [76, 77]. Its power spectral density is:

$$PSD_{NPD}^+(f) = \frac{320 \left(\frac{z}{10} \right)^{0,45} \left(\frac{\langle U_{wind} \rangle}{10} \right)^2}{\left[1 + \left(172 f \left(\frac{z}{10} \right)^{2/3} \left(\frac{\langle U_{wind} \rangle}{10} \right)^{-3/4} \right)^n \right]^{5/3n}} \quad (16)$$

where $n = 0.468$ is a constant, z denotes the height above sea level in meters and $\langle U_{wind} \rangle$ is the 1 hr mean wind speed at a reference height 10 m above sea level.

The NDP spectrum is intended for describing gust and mean wind speeds above 10 m/s. The NDP spectrum deviates significantly from the other two in that it contains considerably more power at low frequencies. The reason for this is that the other spectra are based on observations of wind over land while the NDP spectrum is fitted to measurements of wind over sea, where the thermal structure is different.

The Højstrup spectra is sometimes used because it includes more power than the Kaimal spectrum at the low frequencies, and this has shown to agree better in a number of cases [153].

2.3.10. Van der Hoven’s wind spectra

The Van der Hoven’s wind spectrum [78] differs from the previous spectra that has a very wide dynamical range, from seconds to several days. It shows a gap between 3 minutes/cycle and 5 hours/cycle that separates fast fluctuations from slow fluctuations. Other works also reported a gap between mesoscale and microscale wind at the free atmosphere [79]. Nevertheless, this gap has been not found at some locations [80, 81, 82]. In [83], the 5 h gap were not found in the meteorological records measured at an experimental field site near Oak Ridge, Tennessee, USA during the years 1995 to 1998. Other measurements carried out in wind farms indicate that the presence of the gap is dependent on the location.

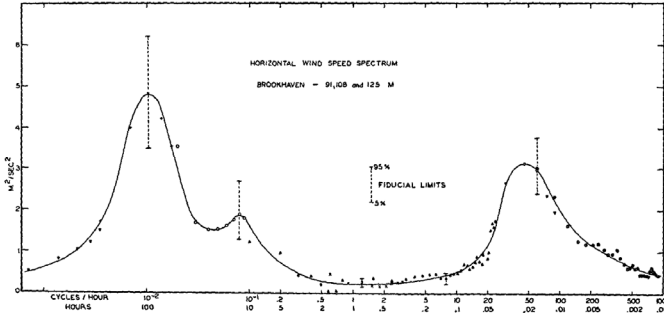


Fig. 8: Van der Hoven's spectral model (from [78]).

2.3.11. Horns Rev wind spectra

According to e.g. [84] there is a significant variability of the wind speed at lower frequencies, which is not included in the Kaimal spectrum. The Kaimal type PSD functions are valid only for shorter time scales, corresponding to what is normally considered in mechanical design of wind turbines, i.e. from 0.02 sec to 600 sec. For simulations of wind farm power fluctuations, the PSD functions are required on a longer time scale (up to several hours).

According to Sørensen et Al. [85], the Høvsøre measurements have been applied to fit the $PSD_{LF}(f)$ for low frequencies, and the fit is expressed as:

$$PSD_{LF}(f) = \frac{(\alpha_{LF} \langle U_{wind} \rangle + \beta_{LF})^2 \frac{z}{\langle U_{wind} \rangle}}{\left(\frac{z f}{\langle U_{wind} \rangle} \right)^{5/3} \left[1 + 100 \left(\frac{z f}{\langle U_{wind} \rangle} \right) \right]} \quad (17)$$

In Høvsøre, the coefficients estimated from measurements are $\alpha_{LF} = 0,0046$ and $\beta_{LF} = 0$. Thus, the total spectrum is composed of low and high frequency contributions:

$$PSD_{Høvsøre}(f) = PSD_{Kaimal}(f) + PSD_{LF}(f) \quad (18)$$

2.3.12. Coherence models

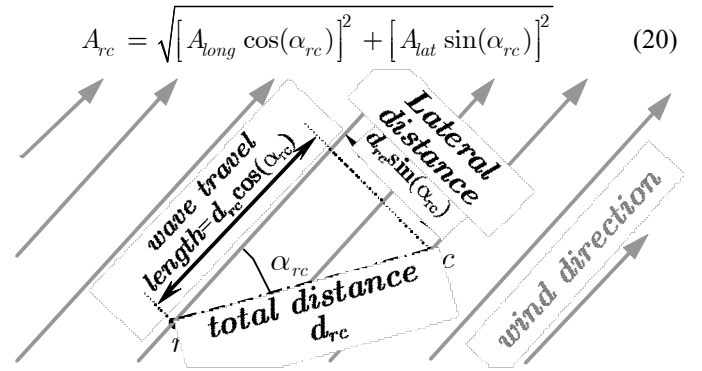
IEC 61400-1 [97] specifies the coherence function (in absolute value) $\gamma_{IEC}(f)$ for two points r and c separated a distance d_{rc} in the rotor plane according to:

$$\gamma_{IEC}(f) = \exp \left[-A \sqrt{\left(\frac{d_{rc} \cdot f}{\langle U_{wind} \rangle} \right)^2 + \left(0,12 \frac{d_{rc}}{\ell_{U_{wind}}} \right)^2} \right] \quad (19)$$

IEC 61400-1 recommends $A \approx 12$; Frandsen [86] recommends $A \approx 5$ and Saranyasoontorn [82] recommends $A \approx 9,7$. Note that this expression is intended for points in the area swept by the blades. Therefore, it is not intended for estimating the wind coherence at different turbines.

Schlez and Infield [45] derived an empirical model, based mainly on measurements with 18 m high masts with distances up to 102 m in the Rutherford Appleton Laboratory, UK. According to them, the coherence decreases exponentially at a site-specific rate respect wind travel time. The decay constants for lateral and longitudinal directions are, A_{long} and A_{lat} , respectively. A_{long} is the decay factor when the flow is longitudinal ($\alpha_{rc} = 0$). A_{lat} is the decay factor when the flow is lateral, i.e. when the wind direction is perpendicular to the line between points r and c ($\alpha_{rc} = \pi/2$ rad).

Thus, a compound decay constant A_{rc} can be estimated according to (20) for any arbitrary disposition of points r and c (see Fig. 9).

Fig. 9: Definition of distance d_{rc} and angle α_{rc} between the points r and c .

Schlez and Infield [45] recommended for the Rutherford Appleton Laboratory $A_{long} \approx (15 \pm 5) \sigma_{U_{wind}} / \langle U_{wind} \rangle$ and $A_{lat} \approx (17,5 \pm 5) (\text{m/s})^{-1} \sigma_{U_{wind}}$, where $\sigma_{U_{wind}}$ is the standard deviation of the wind speed in m/s.

Saranyasoontorn et Al. adjusted a coherence model from experimental data in LIST Test site at Bushland, Texas. The statistical properties of the estimation can be reviewed in [87] and a comparison of standard coherence models form inflow turbulence with estimates from field measurements is presented in [82].

Sørensen et Al. [85] fitted the lateral and longitudinal decay factors, $A_{long} = 4$ and $A_{lat} = \langle U_{wind} \rangle / (2 \text{ m/s})$, respectively, from measurements at 80 m height with up to 1.2 km distances in Høvsøre, Denmark. With these parameters, Sørensen et Al. used a complex rooth coherence $\vec{\gamma}_{rc}(f)$ (adding an average phase delay to the absolute squared coherence $|\vec{\gamma}_{rc}(f)|^2$ proposed by Schlez and Infield [45]). Since complex coherence is used, the phase of the coherence indicates the average delay between wind fluctuations at different points. Sørensen et Al. used the Taylor's "frozen turbulence" model in [191] to compute the average time delay τ_{rc} as the time difference between the arrival to the points r and c of a flat wind wave front travelling at average wind speed.

$$\tau_{rc} = \frac{d_{rc} \cos(\alpha_{rc})}{\langle U_{wind} \rangle} \quad (21)$$

where d_{rc} is the distance between points r and c (see Fig. 9).

Finally, the expression of the complex rooth coherence $\vec{\gamma}_{rc}(f)$ for Høvsøre is:

$$\vec{\gamma}_{rc}(f) = \exp \left[-f \left(A_{rc} \frac{d_{rc}}{\langle U_{wind} \rangle} + j2\pi\tau_{rc} \right) \right] \quad (22)$$

It can be derived that at low frequencies $\vec{\gamma}_{rc}(f)$ tends to unity with zero phase (fully positive correlated fluctuations) and at high frequencies $\vec{\gamma}_{rc}(f)$ tends to zero with random phase (uncorrelated fluctuations).

2.4. Spectrum and coherence estimated from the weather station network

The network of weather stations provides a wide coverage of slow variations of wind. Many stations provide hourly or half-hourly data. These data is used in the program WINDFREEDOM [54] to compute the wind spectra and the coherences between nearby locations.

Quick fluctuations of wind are more related to the turbine integrity, structural forces and control issues. But they are quite local, and they cancel partially among clusters of wind farm. The slower fluctuations are more cumbersome from the grid point of view, since they have bigger coherences with small phase delays.

2.4.1. Coherence between Logroño and Zaragoza airports (Spain, 140,5 km apart)

This example analyzes the coherence and the spectrum of wind speed oscillations up to 12 days, at the airports of the Spanish cities of Logroño and Zaragoza. Both cities are located in the Ebro River and share a similar wind regime. The weather stations are 140,5 km apart (see Fig. 10) and the analysis is based on one year data, from October 2008 to October 2009.

Map	Station availability	Station #1	Station #2	Spect. Ratio	Coherence phase	Coherence module	Fit of coherence models	About this program
-----	----------------------	------------	------------	--------------	-----------------	------------------	-------------------------	--------------------

You can change the geographic area dragging the locator out of the center of the map and using the zoom control at the bottom

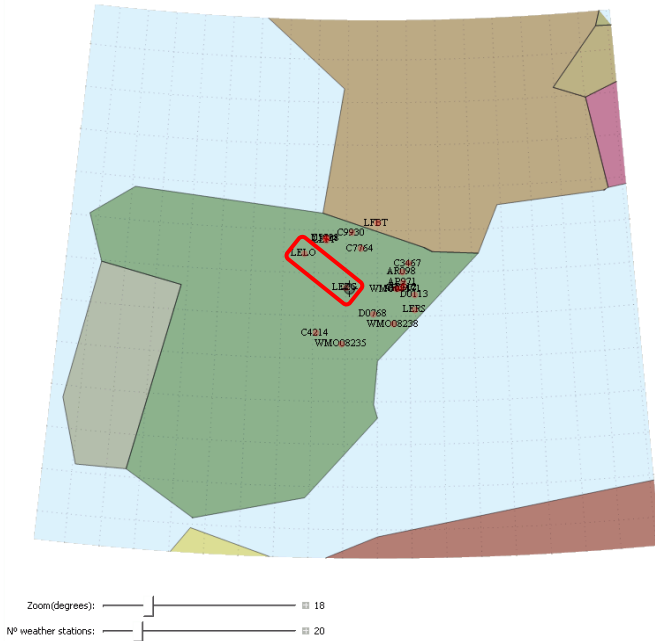


Fig. 10: Map from WINDFREEDOM program [54] with the location of Zaragoza and Logroño in the Iberian Peninsula.

The spectrograms in Fig. 11 and Fig. 12 show the evolution of the power spectrum of the signal, computed from consecutive signal portions of 12 days. The details of the estimation procedure can be found in the annexes of this thesis.

Wind spectra and coherence has been computed from the periodogram, and the spectrograms of the signals are also shown to inform of the variability of the frequency content. The quartiles and the 5% and 95% quantiles of the wind speed are also shown in the lower portions of in Fig. 11 and Fig. 12. The unavailable data have been interpolated between the nearest available points. Some measurements are outliers, as it can be noticed from the 5% quantiles in Fig. 11 and Fig. 12, but they have not been corrected due to the lack of further information.

The diurnal and semi-diurnal variation peaks can be recognized in clearly in the periodograms of Fig. 11 and Fig. 12 (gray graph on the left) or as dark-bluish horizontal lines in the spectrogram (color image on the right). The oscillation magnitude is not constant along one year because the horizontal lines get lighter or darker along the time.

Wind speed [km/h] in LEZG from Sun 5 Oct 2008 17:30:00. to Mon 5 Oct 2009 14:30:00

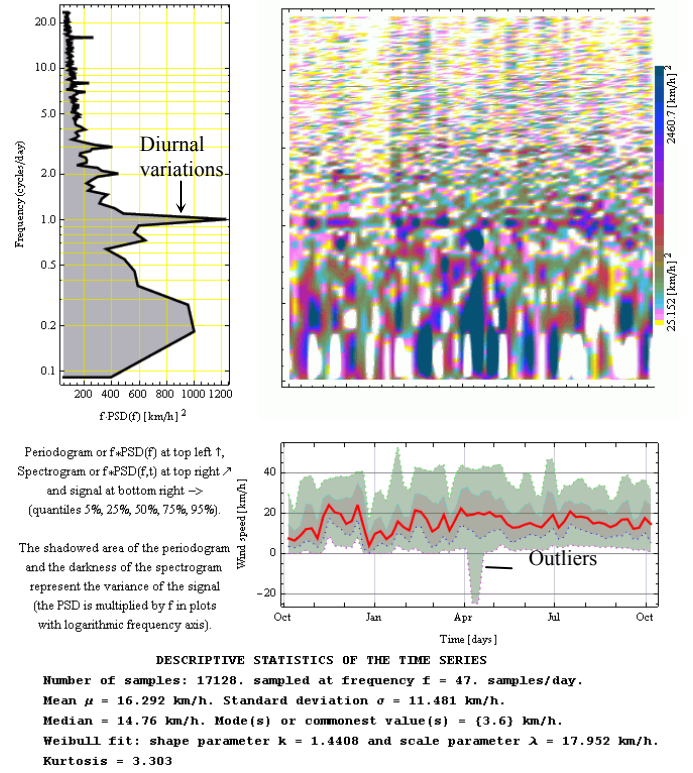


Fig. 11: Periodogram and spectrogram of Zaragoza airport (Spain) estimated with WINDFREEDOM program [54].

Wind speed [km/h] in LELO from Sun 5 Oct 2008 18:00:00. to Mon 5 Oct 2009 14:00:00

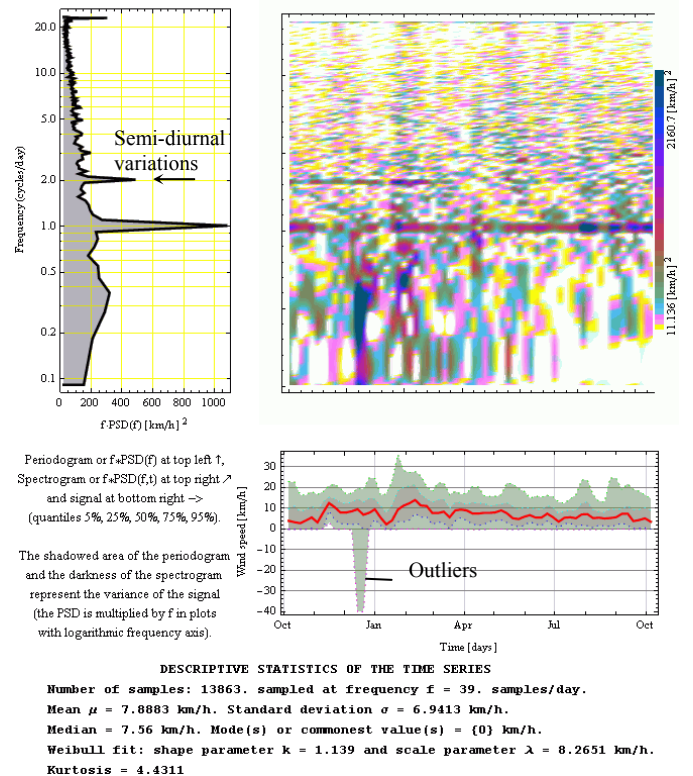


Fig. 12: Periodogram and spectrogram of Logroño airport (Spain) estimated with WINDFREEDOM program [54].

The ratio between the periodograms and spectrograms of Fig. 11 and Fig. 12 is shown in Fig. 13. The wind in Zaragoza airport meteorological station (LEZG for short) is the double in average than in the weather station of Logroño airport (LELO for sort). The average ratio is about 0,4~0,6, indicating that the ratio of oscillation amplitudes are around $\sqrt{0,4}\sim\sqrt{0,6}$. The coefficient of variation (standard deviation divided by the mean) is 87% in Logroño and 70% in Zaragoza.

The quartiles of the time series at Logroño and Zaragoza (lower graph in Fig. 13) show significant differences. The red shadow indicates the interquartile range of Zaragoza and the thick red line is its median (the blue colours correspond to Zaragoza). The wind in Logroño (in blue) is about half the wind in Zaragoza in average.

The wind variations in each station show different features eventually. Some variations are replicated on the other station but with some non-systematic delay and with different magnitude. These features are the reason of the relatively small coherence of the two stations.

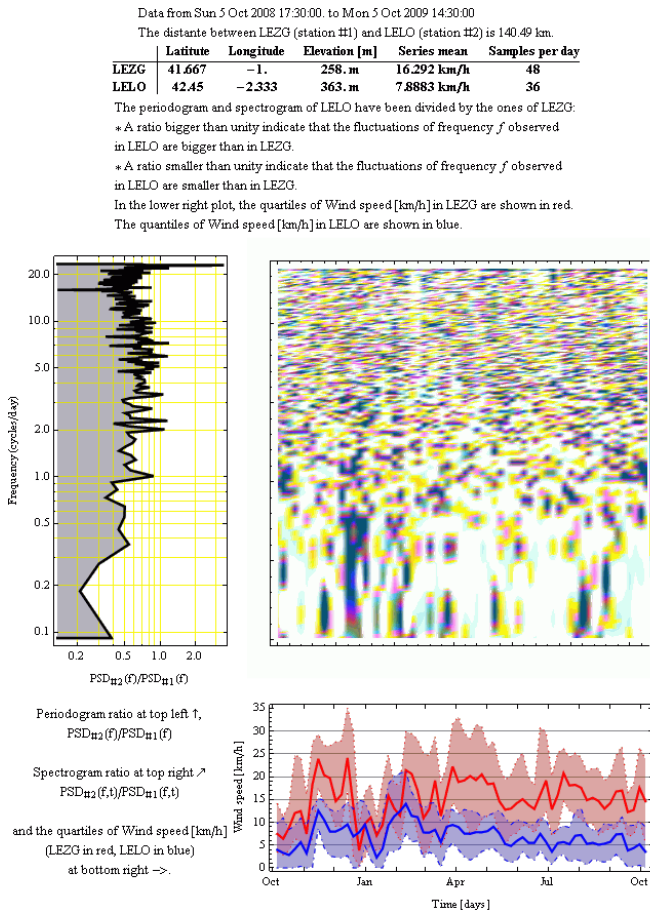


Fig. 13: Periodogram and spectrogram of Logroño airport divided by the ones of Zaragoza airport (estimated by WINDFREEDOM program [54]).

In practice, the oscillations observed in one station are seen, in some extent, in other station with some delay or in advance. The coherence $\vec{\gamma}_{\#1,\#2}$ is a complex magnitude with modulus between 0 and 1 and a phase, which represent the delay (positive angles) or the advance (negative angles) of the oscillations in the second weather station respect the first one (considered the reference). Since the spectrum of a signal is complex, the argument of the coherence $\vec{\gamma}_{rc}(f)$ is the average phase difference of the fluctuations.

The coherence $\vec{\gamma}_{rc}(f)$ indicates the correlation degree and the time pattern of the fluctuations. The modulus is analogous to the correlation coefficient of the spectrum lines from both locations. If the ratio among complex power spectrums shown in Fig. 13 is constant (in modulo and in phase), then the coherence is the unity and its argument is the average phase difference. If the complex ratio is random (in modulo or in phase), then the coherence is null.

However, the wind direction is not considered in this estimation, but it has a great impact on the coherence estimate. The time delay between oscillations τ depends greatly on the wind direction. Thus, the phase difference of the fluctuations, $\varphi = 2\pi f \tau$, can change notably and this would lead to very low coherences. If there are several preferential wind directions, the phase difference can experience great variability. In such cases, a more detailed model –maybe using Markov states indicating prevailing wind directions– is needed.

The red/purple colours in Fig. 13 indicate that phase difference is near 0 up to 0,5 cycles/day (small delay of fluctuations). However, the phase difference at frequencies above 2 cycles/day is quite big, indicating that the timing sequence of the fluctuations has varied along the study period (one year).

The phase difference between the spectrum of LEZG and LELO is computed to estimate the lag between the oscillations in both stations.

* A phase difference positive indicate that the fluctuations of f frequency are observed (in average) first in LEZG and then in LELO and viceversa.

* The average time lag can be computed as $\text{lag} = \text{phase} / (2\pi f)$ when the phase is expressed in radians.

=> In general, slow fluctuations show a phase proportional to frequency indicating that the slow fluctuations are observed with a constant time delay between stations.

* A random phase indicates that the fluctuations happen first indifferently in any station without a simple temporal link

=> In general, fast fluctuations show non-systematic phases indicating that they are local.

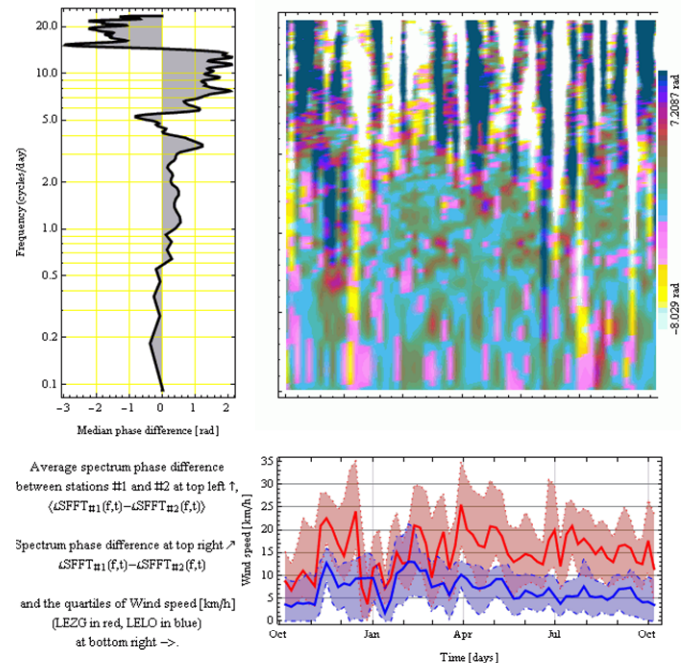


Fig. 14: Phase difference between the periodogram and spectrogram of Zaragoza airport respect the ones of Logroño airport (estimated by WINDFREEDOM program [54]).

Generally, the time delay between fluctuations of a given frequency, $\tau_{rc} = \varphi / (2\pi f)$ is more informative than the phase difference φ because the time delay of the arrival of events is constant under the Taylor hypothesis of frozen turbulence. According to it, the time lag is the travel time of the perturbation from one station to the other (see Fig. 5).

Thus, the time lag is the distance divided by the displacement speed of the perturbation, projected in the line joining the two weather stations. It can be computed through formula (21), where τ_{rc} is the observed time lag, d_{rc} is the distance between the weather stations and $\langle U_{wind} \rangle$ and α_{rc} must be interpreted as the perturbation travel speed and direction (see Fig. 9). For far away stations, this speed can differ notably from the wind speed and direction due to the differences between the boundary layer and the free atmosphere.

If time lags present characteristic values, this can be due to different wind directions at higher levels of the atmosphere. In the Fig. 15, the commonest lags are -4,4 days (white in the picture) and +3,0 days (indigo in the picture). This bimodal behaviour might match the wind regime in the Ebro River, dominated by the “Cierzo” and “Bochorno” winds, with contrary directions.

Since the distance between the stations is 140,5 km, the displacement speed of the perturbation, projected in the line joining the two weather stations, is -2,25 km/h to +2,0 km/h. This speed seems to be very small to correspond to the real displacement of the weather features and further research should be done to obtain conclusions.

The bigger variability of the time delay is observed at fluctuations quicker than four hours (upper part of the picture in Fig. 15, with yellow, pink and cyan colours) and at fluctuations of three to five days hours (lower part of the picture).

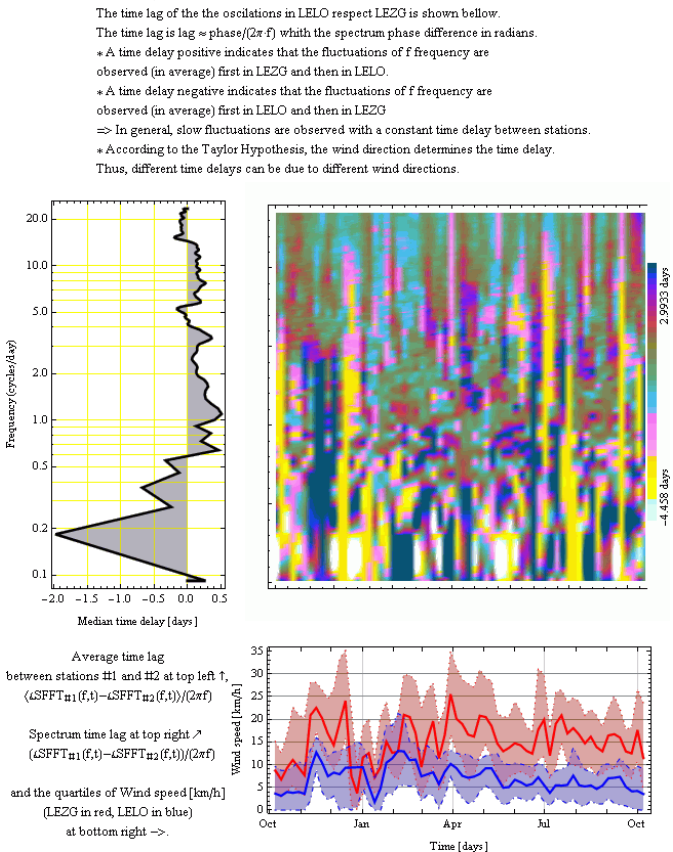


Fig. 15: Time lag of the oscillations of Zaragoza airport respect the ones of Logroño airport (estimated by WINDFREDOM program [54]).

The variability of time lag in fluctuations quicker than four hours can be a symptom that the weather perturbations evolve as they extent geographically (see Fig. 16). The high variability of the fluctuation delay of three to five days can be

due to different wind regimes (commonest wind storms occur each 5 days on average in Zaragoza).

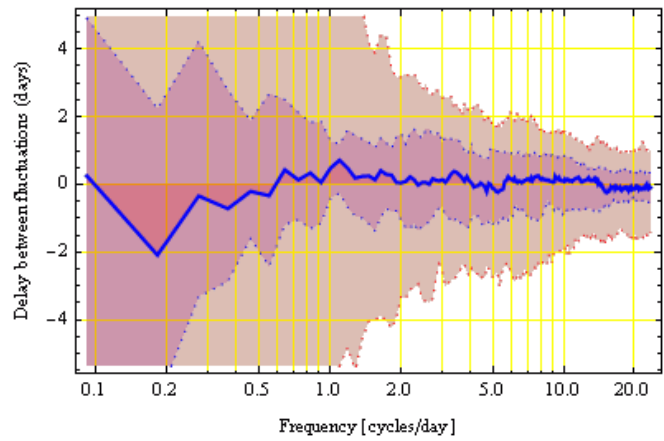


Fig. 16: Quantiles 5%, 25%, 50% and 95% of the estimated time delay (in days) between the fluctuations in Zaragoza airport respect the fluctuations of Logroño airport of the same frequency (estimated by WINDFREDOM program [54]).

It should be noted the phase unwrapping can have notorious influence on the time lag estimation. One reason that increases the variability of the time lags is the fact that there are different mechanisms involved in slow, daily and intra-day oscillations. Since the spectrum phase difference φ' is wrapped in $[-\pi, +\pi]$ radians, it is not easy to guess the actual time delay $\tau_{rc} = (\varphi' + 2\pi k) / (2\pi f)$.

The phase unwrapping applied in WINDFREDOM program [54] detects 2π radians jumps in the cross power spectrum density of the stochastic time series. Actual phase unwrapping considers that there is no phase wrap at lowest frequencies ($f_{lowest} = 1/12$ cycles/day for 48 samples a day and 512 samples in the Short Time Fourier Transform, STFT).

The time delay at lowest frequencies has a standard deviation of about 3 days (one forth of the period length considered in the STFT or $\pi/2$ radians). At high frequencies, the standard deviation reduces to about half day. The weather dynamics imposes a great variability on the time delay of slow oscillations.

In Fig. 16, the median delay is usually below half a day, but the variability is very big. The oscillations during 5 days happen, on median, two days first in Logroño than in Zaragoza. However, the great variability of the time delay indicates that the behaviour of slow weather oscillations behaviour is not systematic and weather dynamics must be taken into account to explain low frequency wind dynamics. This high variability of the time delay decreases the coherence module at low frequencies.

Diurnal and semi-diurnal variations ($f = 1$ and 2 cycles/day, respectively) present a much smaller dispersion, with an interquartile range of about 2 days in Fig. 16. Diurnal and semi-diurnal oscillations are related mainly to wind dynamics due to the sun heating, and thus, the time lag at such frequencies is primarily not related to travel time.

The coherence module of fluctuations lasting one day or more is about 30% ~ 50%, as can be seen in Fig. 17. It has aforementioned that this is due to the changing time delay of fluctuations.

The interquartile range shown in Fig. 16 tends to 1 day at intraday oscillations, with 2 days of 90% range. However, intraday oscillations last less than its interquartile range and the coherence module at such frequencies is decreases up to 5% in Fig. 17. Hence, intraday oscillations can be considered mainly statistically independent.

The image in Fig. 17 shows that the relative oscillation module is quite close to unity (indigo color) in general. But since the phase difference varies noticeably, the modulus of the average of the complex coherence is below unity (graph on the left).

The coherence between the spectrum of LEZG and LELO indicate the correlation between the oscillation magnitude at a given frequency in both stations.

* A coherence near unity indicate that the fluctuations are almost fully linearly correlated and a coherence near zero indicate that the fluctuations are not linearly correlated.

⇒ In general, slow fluctuations show a strong correlation (coherence near unity) with a constant time delay between stations.

*A random phase indicates that the fluctuations happen first indifferently in either station without a simple temporal link.

⇒ In general, fast fluctuations show a low correlation (coherence near zero) and small time delays indicating that fast fluctuations are local.

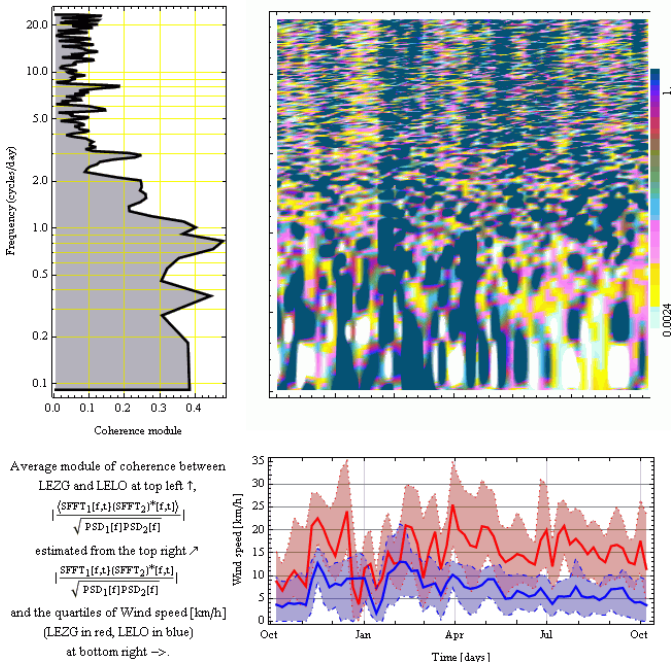


Fig. 17: Coherence of Zaragoza and Logroño airport winds (estimated by WINDFREEDOM program [54]).

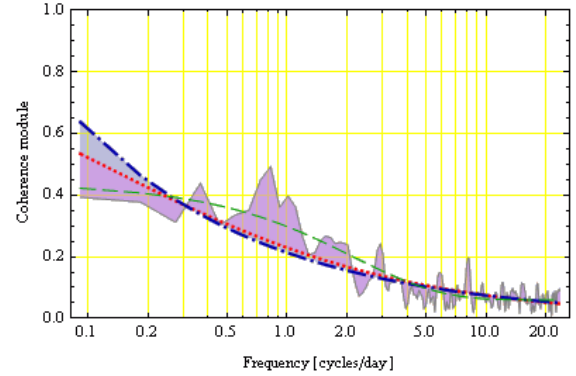
Fractional, power law and exponential models of the coherence module are shown in Fig. 18. The coherence does not follow a clear tendency, and the peaks of the characteristic frequencies $f = 1/3, 0,8, 1$ and 3 cycles/day are not reproduced by the models.

The model that performs better in this particular case is the exponential model (thin, dashed green line in Fig. 18) and it is obtained adjusting two parameters. The fractional model and the exponential model are obtained adjusting only two parameters.

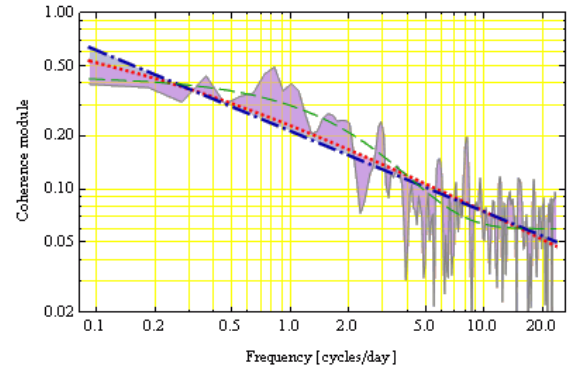
The power law model is quite informative because it indicates the slope and the level of the coherence in a double logarithm plot, even though it overestimates the coherence at low frequencies. The fractional model is included because it is analogous to many wind spectra models found in the literature. For instance, the exponent 0.4573 in the fractional model is about one half of the 5/6 power law of Karman and Kaimal wind spectra.

	Module of coherence[f]	Appearance
Measured coherence	$\frac{ \langle SFFT_1[f,t] \cdot (SFFT_2)^*[f,t] \rangle }{\sqrt{PSD_1[f] PSD_2[f]}}$	thin, grey solid line
Fractional model	$\frac{0.545091}{0.545091 + 1.83456 f^{0.565356}}$	thick, dotted red line
Power law model	$\frac{0.213466}{f^{0.457343}}$	dot-dashed blue line
Exponential model	$0.0596511 + 0.378308 e^{-0.462389 f}$	thin, dashed green line

Comparison of the models in semi-logarithmic plot:



Comparison of the models in double-logarithmic plot:



Quantiles 5%, 25%, 50%, 75% and 95% of the estimated time delay (in days) between the fluctuations in LEZG respect the fluctuations in LELO of the same frequency. (They are fairly constant provided Taylor hypothesis is applicable).

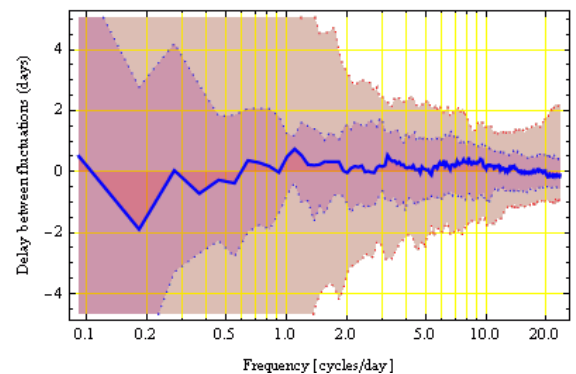


Fig. 18: Comparisons of several coherence models Time lag of oscillations of Zaragoza airport respect the ones of Logroño airport (estimated by WINDFREEDOM program [54]).

However, more meteorological parameters than the single speed modulo at the Zaragoza and Logroño airports is required to explain the variability of the time delays between the fluctuations. Without further information, it should be noticed that the average coherence for oscillations slower than a day is between 30% and 50% and a small time delay in average. This low coherence implies a low correlation of the power injected by wind farms close to the stations considered.

2.4.2. Coherence between Pamplona and Zaragoza airports (Spain, 133,6 km apart)

The second example has been chosen because the distance of Pamplona and Logroño from Zaragoza is comparable and both are quite aligned with the prevailing wind direction in the Ebro River. Pamplona is on the north of the Ebro river valley and closer to the Pyrenees Mountains than Zaragoza and Logroño. However, the coherence between Pamplona and Zaragoza is significantly higher than between Logroño and Zaragoza (see Fig. 19).

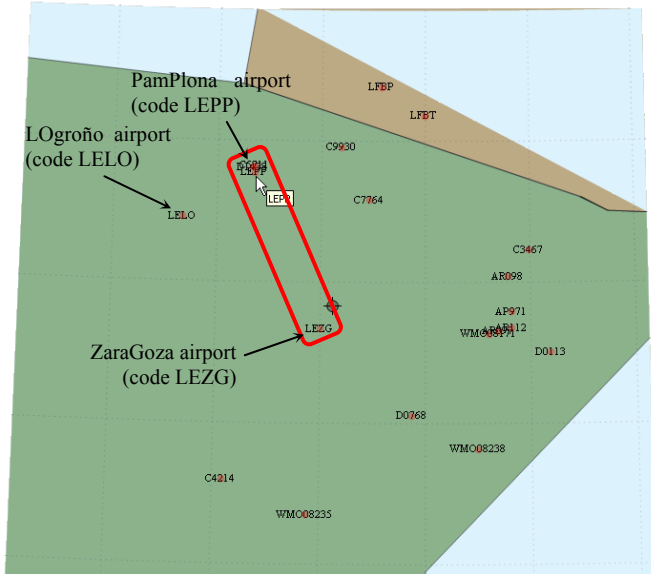


Fig. 19: Map from WINDFREDOM program [54] with the location of Zaragoza and Pamplona in the North of the Iberian Peninsula.

However, the average wind measured at Pamplona is higher than in Logroño. There is no further information on the weather station and the higher wind can be due to the surroundings of the weather stations. The coefficient of variation (standard deviation divided by the mean) is 89% in Pamplona, 87 in Logroño and 70% in Zaragoza.

The periodogram and spectrogram of Pamplona is similar to the one of Logroño. The diurnal variations are more noticeable in Pamplona than in Logroño and in Zaragoza, possibly by the closer presence of the mountains. In contrast, the fluctuations of 3 to 5 days prevail in Zaragoza.

The semi-diurnal pattern clearly seen in Logroño (and in Zaragoza in a lesser extent) but is almost missed in Fig. 20.

The ratio between the periodograms and spectrograms of Fig. 11 and Fig. 20 is shown in Fig. 30. The ratio of oscillations of 3 to 5 days of duration is below the unity in Fig. 30, indicating that they are more noticeable in Zaragoza than in Pamplona. However, the amplitude of the daily fluctuations in Pamplona are almost twice the ones in Zaragoza (the periodogram ratios is a bit lower than 4).

The quartiles of the time series at Pamplona and Zaragoza (lower graph in Fig. 30) show a similar behaviour. The blue shadow indicates the interquartile range of Pamplona and the thick blue line is its median (the red colours correspond to Zaragoza). Even though the median of the wind in Pamplona is 30% ~ 40% smaller than the wind in Zaragoza, the variations match significantly better than between Logroño and Zaragoza. Hence, the coherence between Zaragoza and

Pamplona is significantly bigger than between Zaragoza and Logroño.

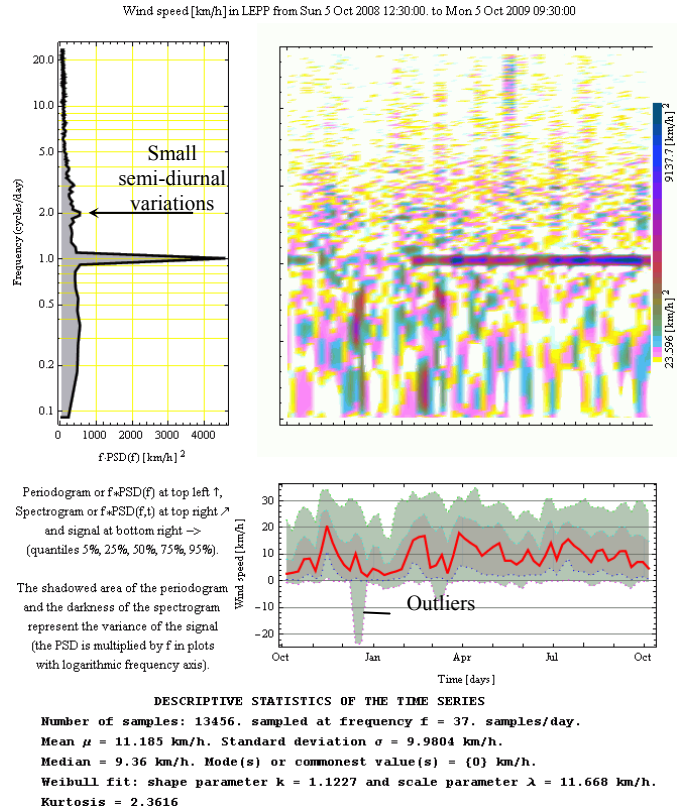


Fig. 20: Periodogram and spectrogram of Logroño airport (Spain) estimated with WINDFREDOM program [54].

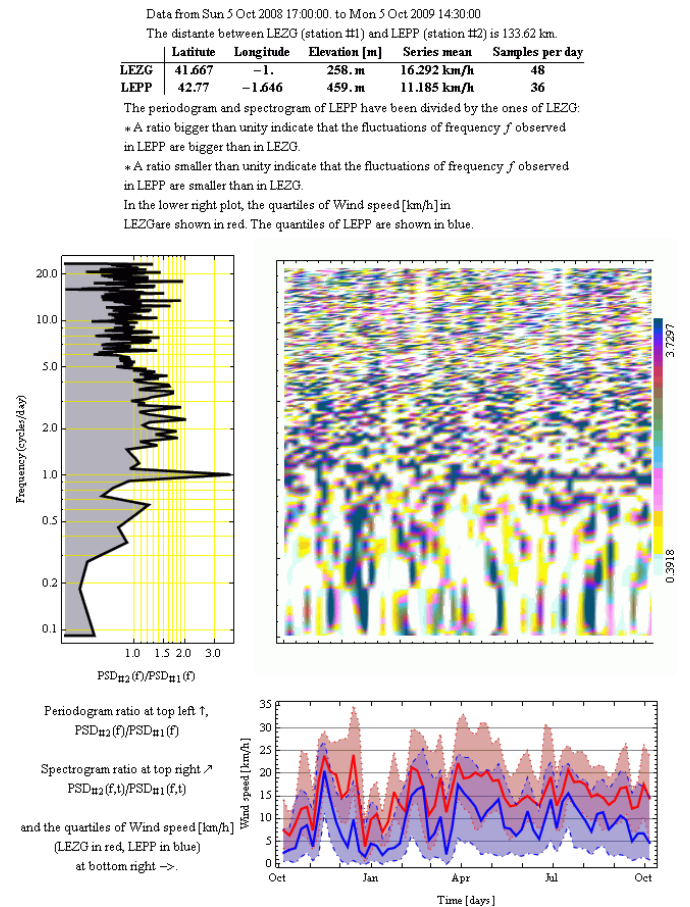


Fig. 21: Periodogram and spectrogram of Pamplona airport divided by the periodogram and spectrogram of Zaragoza airport (estimated by WINDFREDOM program [54]).

In practice, the oscillations observed in one station are seen, in some extent, in other station with some delay or in advance. The time delay between fluctuations of a given frequency is $\tau_{rc} = \varphi / (2\pi f)$, where φ is the phase difference between the spectrums of the two stations.

According to Fig. 22 and Fig. 23, the fluctuations of 5 days ($f = 0,2$ cycles/day) are seen, in median, half day before in Pamplona than in Zaragoza. But the daily fluctuations ($f = 1$ cycles/day) are seen about 19 hours before in Zaragoza than in Pamplona. This is due to the different mechanisms involved in slow and daily oscillations. The actual time lags show big variability (see Fig. 22) except at daily fluctuations. The interquartil range is significantly smaller than the one of Zaragoza and Logroño.

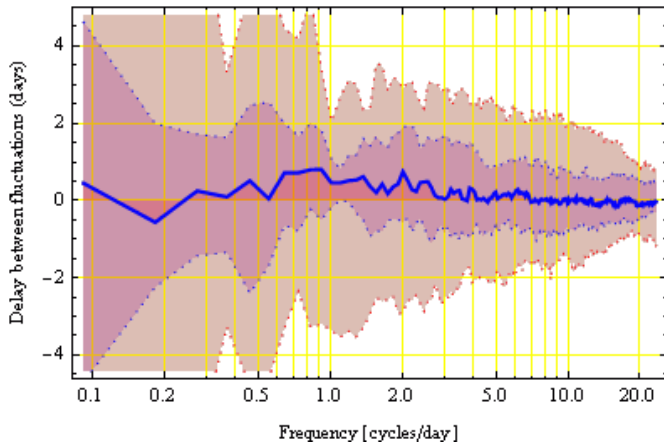


Fig. 22: Quantiles 5%, 25%, 50% and 95% of the estimated time delay (in days) between the fluctuations in Zaragoza airport respect the fluctuations of Pamplona airport of the same frequency.

Data from Mon 6 Oct 2008 21:30:00. to Tue 6 Oct 2009 18:30:00
 The distance between LEZG (station #1) and LEPP (station #2) is 133.62 km.

	Latitude	Longitude	Elevation [m]	(Wind) [m/s]	Samples per day
LEZG	41.667	-1.	258. m	16.342 km/h	48
LEPP	42.77	-1.646	199. m	11.245 km/h	36

The time lag of the the oscillations in LEPP respect LEZG is shown below.
 The time lag is $\text{lag} \approx \text{phase} / (2\pi f)$ with the spectrum phase difference in radians.
 * A time delay positive indicates that the fluctuations of f frequency are observed (in average) first in LEZG and then in LEPP.
 * A time delay negative indicates that the fluctuations of f frequency are observed (in average) first in LEPP and then in LEZG
 => In general, slow fluctuations are observed with a constant time delay between stations.
 * According to the Taylor Hypothesis, the wind direction determines the time delay.
 Thus, different time delays can be due to different wind directions.

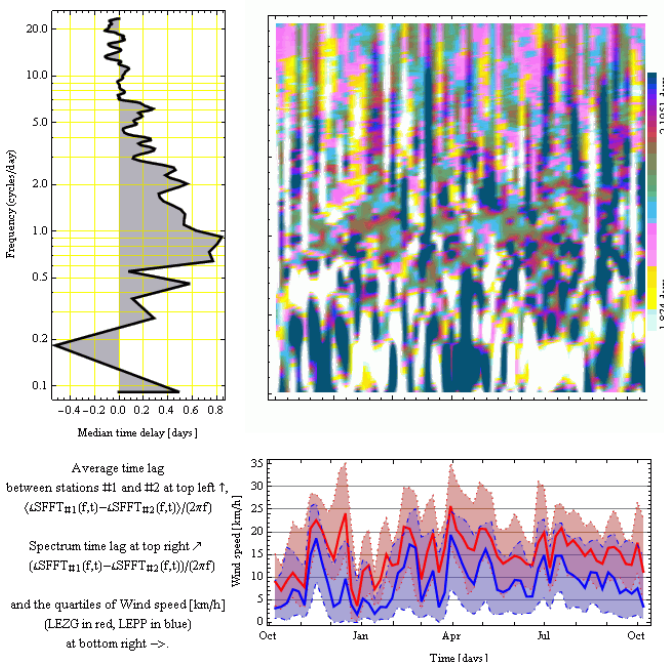


Fig. 23: Time lag of the oscillations of Zaragoza airport respect the ones of Pamplona airport.

The picture in Fig. 23 shows that the commonest delays of the slower fluctuations ($0,1 < f < 0,5$ cycles/day) is -2 days (white colour) or +2 days (indigo colour). The variability decreases at bigger frequencies and the most common colours are cyan (about 0 delay), green (+1/2 day) or pink (-1/2 day).

Fractional, power law and exponential models of the coherence module are shown in Fig. 24. The coherence does not follow a clear tendency, and the peaks of the characteristic frequencies $f = 1/3, 0,8, 1$ and 3 cycles/day are not reproduced by the models.

The model that performs better in this particular case is the exponential model (thin, dashed green line in Fig. 24) and it is obtained adjusting two parameters. The fractional model and the exponential model are obtained adjusting only two parameters. The power law model is quite informative because it indicates the slope and the level of the coherence in a double logarithm plot, even though it overestimates the coherence at low frequencies. The fractional model is included because it is analogous to many wind spectra models found in the literature. For instance, the exponent 0.8978 in the fractional model is comparable to the 5/6 power law of Karman and Kaimal wind spectra.

2.4.3. Coherence between Pamplona and Logroño airports

At low frequencies, the coherence of Zaragoza and Pamplona airports almost doubles the coherence of Zaragoza and Logroño. However, Pamplona and Logroño are in the prevailing wind direction at Zaragoza (North-West) and at similar distances. Furthermore, Fig. 26 shows the low coherence between Logroño and Pamplona airports, only 66,6 km apart. This fact is an example of the complex wind regimes and the value of data measured at weather stations.

Conclusions

This chapter has introduced the concepts relative to wind variation. The most popular characterization of wind turbulence at a point is through the turbulence intensity and the wind spectra.

The Taylor hypothesis of “frozen turbulence”, a simple model that relates about spatial variations and temporal variations of the wind, is discussed. This hypothesis can be used to reconstruct the approximate spatial structure of wind from measurements with an anemometer in a meteorological mast. The accuracy of the Taylor hypothesis of has been tested for long periods and long distances with the program WINDFREEDOM. This hypothesis is an approximated model which allows to obtain the qualitative behaviour of the wind. However, the perturbations evolve along its travel and the time delay between the observations of the events at different locations varies greatly due to different travel speeds (in module and direction) of the weather perturbations.

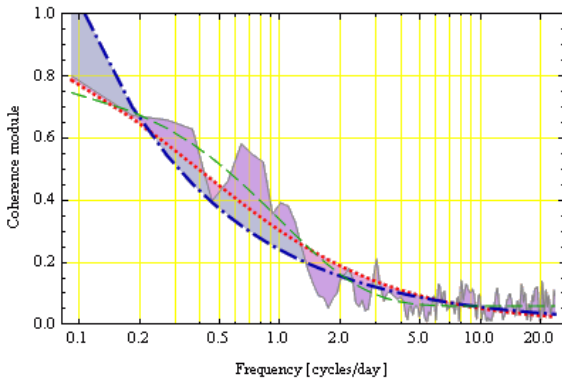
A more advanced concept is the spatial and temporal coherence of the wind, which statistically quantifies the variations of wind in different points in space or in separate moments of time.

The coherence of the wind quantifies the spatial and temporal variability of the wind. The coherence characterizes stochastically the differences of the wind field at different

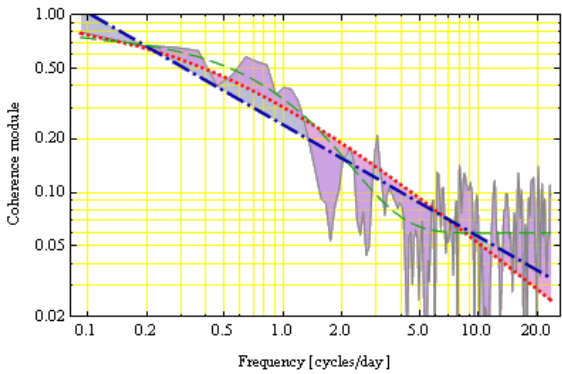
points or at different instants. The computer program WINDFREEDOM retrieves data from the network of institutional meteorological stations and it is able to estimate the coherence of slow wind oscillations (lasting more than an hour) for distances above 30 km. This program is a contribution of this thesis, since the great variety of wind dynamics requires the use of real data to quantify the actual variability of the power generated in a region.

	Module of coherence [f]	Appearance
Measured coherence	$\frac{ \langle SFFT_1[f,t] \cdot (SFFT_2)^*[f,t] \rangle }{\sqrt{PSD_1[f] PSD_2[f]}}$	thin, grey solid line
Fractional model	$\frac{0.658044}{0.658044 + 1.51965 f^{0.897815}}$	thick, dotted red line
Power law model	$\frac{0.241025}{f^{0.629593}}$	dot-dashed blue line
Exponential model	$0.0592189 + 0.7532 e^{-0.997879 f}$	thin, dashed green line

Comparison of the models in semi-logarithmic plot:



Comparison of the models in double-logarithmic plot:



Quantiles 5%, 25%, 50%, 75% and 95% of the estimated time delay (in days) between the fluctuations in LEZG respect the fluctuations in LEPP of the same frequency. (They are fairly constant provided Taylor hypothesis is applicable).

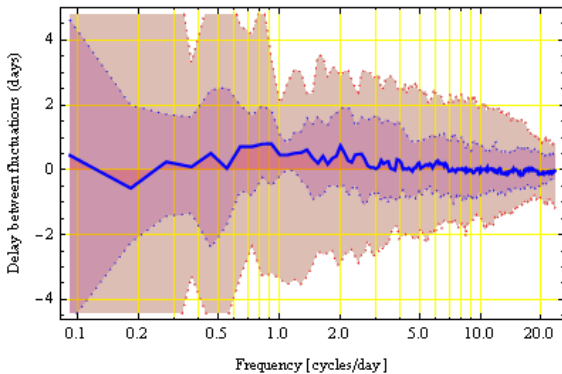


Fig. 24: Comparison of several coherence models Time lag of oscillations of Zaragoza airport respect the ones of Pamplona airport.

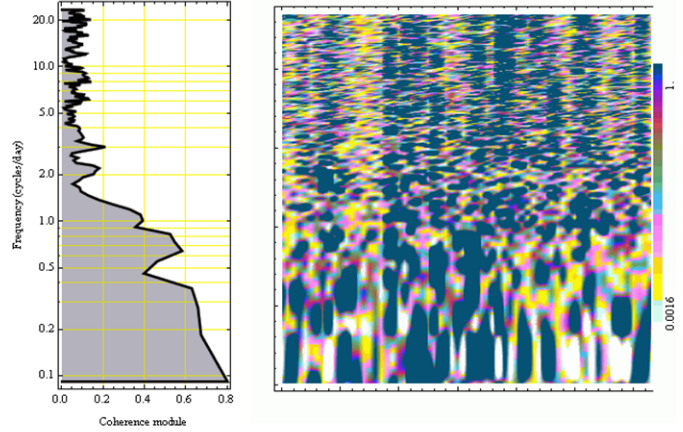
The coherence between the spectrum of LEZG and LEPP indicate the correlation between the oscillation magnitude at a given frequency in both stations.

* A coherence near unity indicate that the fluctuations are almost fully linearly correlated and a coherence near zero indicate that the fluctuations are not linearly correlated.

=> In general, slow fluctuations show a strong correlation (coherence near unity) with a constant time delay between stations.

* A random phase indicates that the fluctuations happen first indifferently in either station without a simple temporal link.

=> In general, fast fluctuations show a low correlation (coherence near zero) and small time delays indicating that fast fluctuations are local.



Average module of coherence between LEZG and LEPP at top left $\frac{|\langle SFFT_1[f,t] \cdot (SFFT_2)^*[f,t] \rangle|}{\sqrt{PSD_1[f] PSD_2[f]}}$ estimated from the top right $\frac{|\langle SFFT_1[f,t] \cdot (SFFT_2)^*[f,t] \rangle|}{\sqrt{PSD_1[f] PSD_2[f]}}$ and the quartiles of Wind speed [km/h] (LEZG in red, LEPP in blue) at bottom right ->

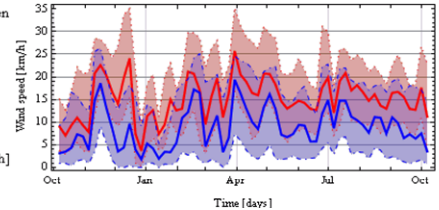


Fig. 25: Coherence of Zaragoza and Pamplona airport winds.

Data from Tue 7 Oct 2008 17:00:00. to Wed 7 Oct 2009 14:00:00

The distance between LELO (station #1) and LEPP (station #2) is 66.643 km.

	Latitude	Longitude	Elevation [m]	(Wind) [m/s]	Samples per day
LELO	42.45	-2.333	363. m	7.911 km/h	36
LEPP	42.77	-1.646	459. m	11.284 km/h	36

	Module of coherence [f]	Appearance
Measured coherence	$\frac{ \langle SFFT_1[f,t] \cdot (SFFT_2)^*[f,t] \rangle }{\sqrt{PSD_1[f] PSD_2[f]}}$	thin, grey solid line
Fractional model	$\frac{0.550442}{0.550442 + 1.81672 f^{0.644491}}$	thick, dotted red line
Power law model	$\frac{0.205964}{f^{0.488016}}$	dot-dashed blue line
Exponential model	$0.0868876 + 0.529343 e^{-1.135 f}$	thin, dashed green line

Comparison of the models in semi-logarithmic plot:

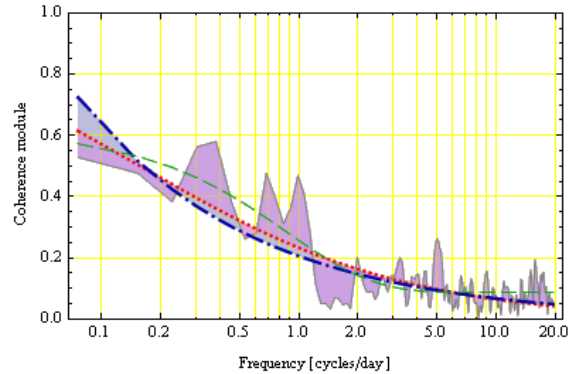


Fig. 26: Coherence of Logroño and Pamplona airport winds.

Chapter 3: The turbine torque and the equivalent wind

3.1. Wind turbine torque

The aim of this work is the characterization and estimation of power output fluctuations. In fact, power oscillations are the ultimate response of generators to torque fluctuations due to spatial and temporal wind variations.

The turbine torque can be estimated from blade theory. Since either the blade section, neither the relative speed nor the angle of attack is constant along the blade from the root to the tip, torque must be integrated along the blade elements. The lift and drag coefficients for the whole blade can be parameterized for blade tip conditions.

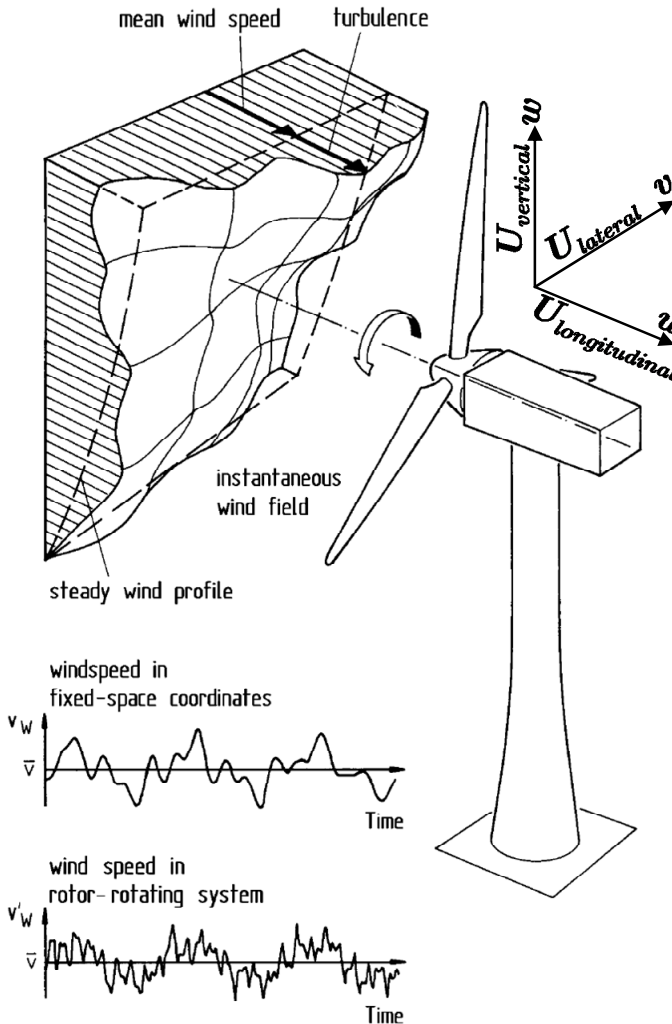


Fig. 27: Effect of an uneven wind-speed distribution over the swept rotor area on the upwind velocity of the rotating rotor blades. The lagrangian motion coordinates are added assuming the turbine is aligned with the wind. Taken from “Dynamic wind turbine models in power system simulation tool DIgSILENT” by Risø National Laboratory [88].

A further simplification is to consider a torque coefficient $C_q(\lambda, \theta)$ depending only on the pitch angle θ and on tip speed ratio λ . In this work, the tip speed ratio is referred to an

equivalent wind speed since the wind conditions vary along the swept area:

$$\lambda = R \Omega_{rotor} / U_{eq} \quad (23)$$

where R is the rotor radius, Ω_{rotor} is the rotor angular speed and U_{eq} is the equivalent wind speed. In a first approximation, U_{eq} is the longitudinal wind speed component averaged along the swept area provided the shaft is aligned with the wind [88, 89].

Thus, the turbine torque is:

$$T_{rotor} = \frac{1}{2} \rho_{air} \pi R^3 U_{eq}^2 C_q(\lambda, \theta) \quad (24)$$

where ρ_{air} is the air density.

In a second approximation, U_{eq} is defined as the wind speed applied to (23) and (24) which produces the same aerodynamic torque T_{rotor} than the real wind field.

A typical curve of rotor torque coefficient can be seen in Fig. 29. Alternatively, the torque coefficient can be computed as the power coefficient (see Fig. 28) divided by the tip speed ratio, $C_q(\lambda, \theta) = C_p(\lambda, \theta) / \lambda$.

3.2. Definition of the equivalent wind, equivalent turbulence and effective quadratic turbulence

3.2.1. Equivalent wind

The *equivalent wind* U_{eq} is an artifice defined as the uniform wind which would produce the same torque as the real wind field. According to (24), it can be computed from real torque as (25):

$$U_{eq} = \sqrt{\frac{2 T_{rotor}}{\rho_{air} \pi R^3 C_q(\lambda, \theta)}} \quad (25)$$

Since the wind varies along the swept area (wind distribution is irregular), the tip speed ratio λ must be computed also from (23). Therefore, the *equivalent wind* U_{eq} is defined as the wind resulting from solving the following equation:

$$C_q\left(\frac{\Omega_{rotor} R}{U_{eq}}, \theta\right) U_{eq}^2 = \frac{2 T_{rotor}}{\rho_{air} \pi R^3} \quad (26)$$

where $C_q(\lambda, \theta)$ is the turbine torque coefficient, T_{rotor} is the torque in the low speed shaft of the wind turbine, R is the rotor radius, Ω_{rotor} is the rotor angular speed and ρ_{air} is the air density.

The *simplification* of using an *equivalent wind* is huge since the non-stationary three-dimensional wind field is approximated by a signal which *produces the same torque*. Apart from accelerating notably the simulations, U_{eq} describes in only one signal the effect of the turbulent flow in the drive train.

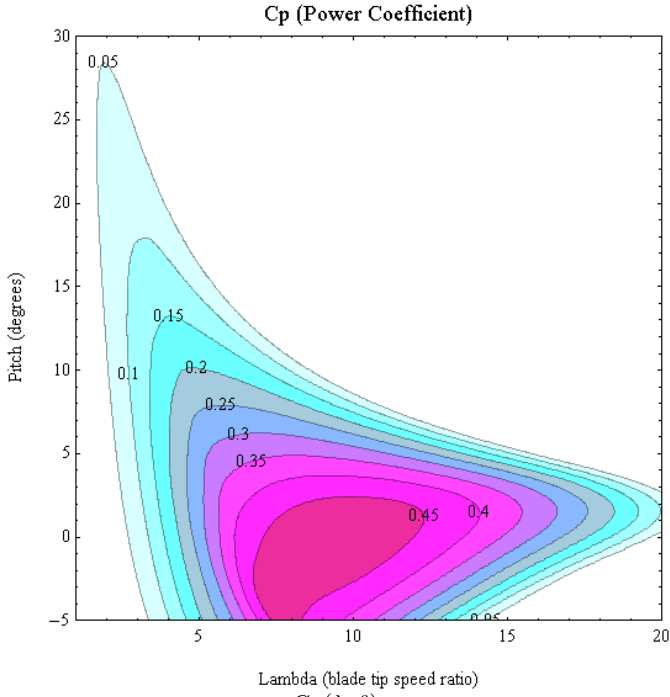


Fig. 28: Rotor power coefficient $C_p(\lambda, \theta)$ for a variable-pitch turbine.

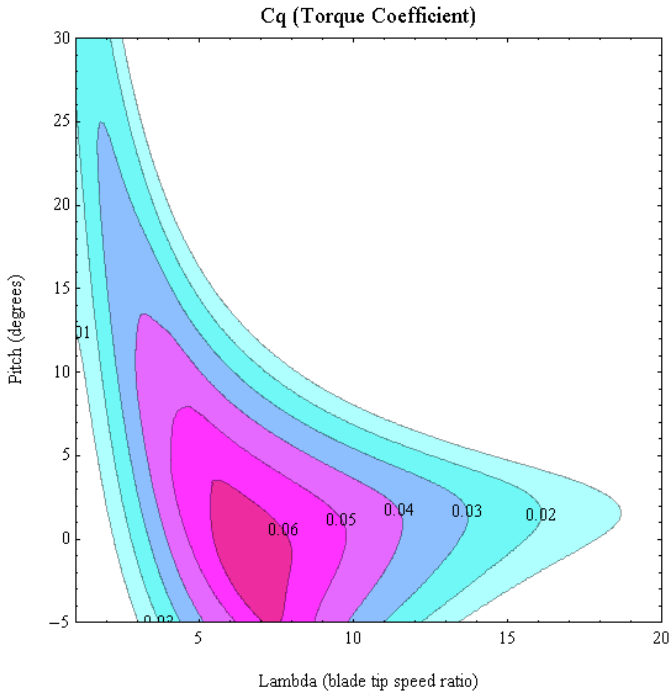


Fig. 29: Rotor torque coefficient $C_q(\lambda, \theta)$ for a variable-pitch turbine.

The actual wind speed U_{wind} is measured at a point by an anemometer whereas the equivalent wind speed U_{eq} is referred to the rotor surface (or more precisely, to the turbine torque). Since the Taylor's hypothesis of "frozen turbulence" is usually applicable, the spatial diversity of wind can be approximated to the point wise time variation of wind times its mean value, $\langle U_{wind} \rangle$, and hence U_{eq} can be considered a low-pass filtered version of U_{wind} (plus the rotational sampling effect due to wind shear and tower shadow effect).

On the one hand, the meteorological science refers to the actual wind speed U_{wind} since the equivalent wind U_{eq} is, in fact, a mathematical artifice. On the other hand, turbine torque or power is customarily referred to the equivalent wind U_{eq} instead of the 3-D wind field for convenience.

A good introduction about the equivalent wind can be found in [177]. The complete characteristics of the wind that the turbine will face during operation can be found in [90].

The equivalent wind speed signal, $U_{eq}(t)$, just describes a smoothed wind speed time series at the swept area. For calculating the influence of wind turbulence into the turbine mechanical torque, it has to be considered the wind distribution along the swept area by a vector field [91]. Blade iteration techniques can be applied for a detailed analysis of torques and forces in the rotor [92]. Thus, the wind shear and tower shadow can be accounted including the rotor position as a parameter in the torque coefficient. Hence, the definition of the equivalent wind accounting the former effects is:

$$C_q \left(\frac{\Omega_{rotor} R}{U_{eq}}, \theta, \varphi \right) U_{eq}^2 = \frac{2 T_{rotor}}{\rho_{air} \pi R^3} \quad (27)$$

where φ is the rotor angle (in the following chapter, a method will be derived to assess the influence of rotor angle in the torque coefficient).

The anemometer dynamic response to fast changes in wind also influences measured wind [93]. Most measurements are taken with cup anemometers, which have a response lengths between 10 and 20 m, corresponding to a frequency cut-off between $f_c = (10 \text{ m/s})/10 \text{ m} = 1 \text{ Hz}$ and $f_c = (10 \text{ m/s})/20 \text{ m} = 0,5 \text{ Hz}$ for 10 m/s average speed.

Apart from metrological issues, the spatial diversity of turbulent wind field reduces its impact in rotor torque. Complete and proved three dimensional wind models are available for estimating aerodynamic behaviour of turbines [82, 94, 95]. Turbulent models are typically used in blade fatigue load.

From the grid point of view, the main effect of spatial diversity is the torque modulation due to wind shear and tower shadow [48]. Vertical wind profile also influences energy yield and it is considered in wind power resource assessment [95].

3.2.2. Equivalent turbulence

Accordingly, the **equivalent turbulence** ΔU_{eq} is the difference between instantaneous value of U_{eq} and its average, $\langle U_{eq} \rangle$ (see Fig. 27).

$$\Delta U_{eq} = U_{eq} - \langle U_{eq} \rangle \quad (28)$$

Since wind is not a stationary process due to weather evolution, the wind average depends on the averaging time $\langle U_{eq} \rangle$. In general, $\langle U_{eq} \rangle$ can be considered the running average of U_{eq} (or alternatively, a smoothed value of U_{eq}). The influence of the constant time in the estimation of $\langle U_{eq} \rangle$ will be considered in subsequent sections of this chapter (some usual values are 1, 10, 15 or 60 minutes, depending on the time span of the analysis).

3.2.3. Effective quadratic turbulence

Since aerodynamic torque is a quadratic function of wind, the deviation of the equivalent wind speed squared (29) is more directly related to power output. The **effective quadratic turbulence** $\Delta(U_{eq}^2)$ is defined as follows:

$$\Delta(U_{eq}^2) = U_{eq}^2 - \langle U_{eq}^2 \rangle \quad (29)$$

For relatively small variations of wind, the *effective quadratic turbulence* $\Delta(U_{eq}^2)$ could be approximated by a normal process (with an almost cyclostationary process superimposed due to the sampling of the quasi-deterministic wind field distribution along the rotor area, see Fig. 27).

Gust dynamics are complex and measured data indicates that small fluctuations are correctly assessed but blasts of air are underestimated with the normal process approximation (independence of wind influences) [214]. During gusts, moment contributions are correlated resulting in a bigger overall wind deviation. Thus, the normal model will be analyzed and modified in the chapter devoted to gusts to fit experimental data of extreme gust.

3.2.4. Linearization of quadratic turbulence

When the wind turbines are generating, a small-signal model based on equivalent wind speed deviations ΔU_{eq} can be obtained since $U_{eq} \gg \Delta U_{eq}$:

$$\begin{aligned} U_{eq}^2 &= [\langle U_{eq} \rangle + \Delta U_{eq}]^2 = \langle U_{eq} \rangle^2 + 2\langle U_{eq} \rangle \Delta U_{eq} + (\Delta U_{eq})^2 \approx \\ &\approx \langle U_{eq} \rangle^2 + 2\langle U_{eq} \rangle \Delta U_{eq} + \langle (\Delta U_{eq})^2 \rangle = \langle U_{eq}^2 \rangle + 2\langle U_{eq} \rangle \Delta U_{eq} \end{aligned} \quad (30)$$

For relatively small variations of wind, the following first-order approximation is valid:

$$\Delta(U_{eq}^2) \approx 2\langle U_{eq} \rangle \Delta U_{eq} \quad (31)$$

Therefore, the relation between the power spectral densities of the equivalent speed and the quadratic turbulence are:

$$PSD_{\Delta(U_{eq}^2)}(f) \approx (2\langle U_{eq} \rangle)^2 PSD_{\Delta U_{eq}}(f) \quad \forall f \neq 0 \quad (32)$$

3.3. Effect of transversal components of wind

The rotor area filters small scale eddies, and thus the relevant eddies for wind turbine power fluctuations are those of larger scales.

The lateral and vertical components of wind affect relative direction and velocity of the air in the blade reference and thus, turbine torque. However, the overall effect of transversal fluctuations to the rotor plane can be neglected in the first instance since the stream wise speed component is significantly bigger than the span wise fluctuations ($U_{lateral}^2 \ll U_{longitudinal}^2$ and $U_{vertical}^2 \ll U_{longitudinal}^2$) [97].

$$|\vec{U}_{wind}|^2 = U_{longitudinal}^2 + U_{vertical}^2 + U_{lateral}^2 \approx U_{longitudinal}^2 \quad (33)$$

Moreover, vertical and lateral turbulence have shorter length scales than the longitudinal component, producing a lower net effect in turbine overall torque. For convenience, only the longitudinal component of the turbulence averaged across the turbine rotor will be considered relevant for power output variations (structural stresses are not studied in this work).

$$U_{eq}^2(t) \approx \langle U_{longitudinal}^2(t) \rangle_{rotor\ area} \quad (34)$$

Nevertheless, the influence of small lateral and vertical components can become eventually important at some pitch

angles where the torque is quite sensitive to changes in attack angle.

3.4. Wind smoothing from turbine rotor and equivalent wind

3.4.1. Fundamentals of spatial filtering in rotor

On the one hand, the spatial and temporal variations of the wind are related to the turbulence structure. On the other hand, the equivalent wind –applied to a simplified aerodynamic model– produces the same torque on the turbine shaft than the real wind distribution across the rotor. The equivalent wind filter models the smoothing of the equivalent wind speed respect the actual measure of an anemometer placed upstream the turbine hub. This filter models the spatial diversity in the area swept by the turbine blades.

The input of this filter is the wind U_{wind} which would be measured at an anemometer installed at the hub height and the output is the estimated equivalent wind, U_{eq1} .

Neglecting the quasi-periodic components in the torque, the equivalent wind smoothing can be expressed as a wind turbine admittance function defined as:

$$|H_1(f)|^2 = \frac{PSD_{U_{wind}}(f)}{PSD_{U_{eq1}}(f)} \quad (35)$$

where $PSD_{U_{wind}}(f)$ is the power spectral density of the wind measured at a point and $PSD_{U_{eq1}}(f)$ is the power spectral density of the equivalent wind (without the periodic components due to the quasi-deterministic variation of torque with rotor angle).

The wind spectrum $PSD_{U_{wind}}(f)$ is equivalent to a low-pass filter with an order around $r' = 5/6$, applied to white noise. In other words, the spectrum decays a bit slower than white noise filtered with a first-order low-pass filter.

The turbine power decreases quicker than the pointwise wind at $f > 0.01$ Hz [52] and this is partially due to the spatial distribution of turbulence, the high rotor inertia and the viscous-elastic coupling between the turbine blades and the generator [96]. In fixed speed, stall regulated turbines, the drivetrain dynamics influences notably the power output. But in variable speed turbines, a simple model with two coupled mass (equivalent to a second-order system) can be precise enough to model the drivetrain since generator control usually damps resonance modes of blades, gearbox and tower.

The ratio on the PSD is the square modulus of the filter, which can be computed from the filter Laplace transform $H_1'(s)$:

$$|H_1(f)|^2 = H_1'(j2\pi f)[H_1'(j2\pi f)]^* \quad (36)$$

The phase of the filter indicates the lag between the wind at the anemometer and the turbine torque. The phase of the filter does not affect $PSD_{U_{eq1}}(f)$ provided the wind could be considered stationary and, accordingly, the phase its spectrum would be arbitrary. The lag difference of equivalent wind among turbines at points r and c will be considered through complex coherence $\bar{\gamma}_{rc}(f)$, irrespective of the argument of $H_1(f)$.

The frequencies of interest for flicker and blade fatigue are in the range of tenths of hertz to 35 Hz. These frequencies

correspond to sub-sound and sound (inertial subrange) and they have wavelengths comparable to the rotor diameter. The assumption that such fluctuations correspond to plane waves travelling in the longitudinal direction and arriving simultaneously at the rotor plane is not realistic. Therefore, quick fluctuations do not reach the rotor disk simultaneously and fluctuations are partially attenuated by spatial diversity. In brief, $H_1'(s)$ is a low-pass filter with meaningless phase.

The smoothing due to the spatial diversity in the rotor area is usually accounted as an aerodynamic filter, basically as a first order low-pass filter of cut-off frequency $\sim 0,1224 \langle U_{wind} \rangle / R$ respect an ideal and unperturbed anemometer measure [44]. For multimegawatt turbines, the rotor filters significantly fluctuations shorter than one minute (cut-off frequency in the order of 1/60 Hz).

The presence of the ground surface hinders vertical development in larger eddies. The lateral turbulence component is responsible for turbulence driven wind direction changes, but it is a secondary factor in turbine torque fluctuations. Moreover, according IEC 61400-1 [97], vertical and transversal turbulence has a significantly smaller length scale and lower magnitude. Thus, the vertical and lateral component of turbulence averaged along the turbine rotor can be neglected in turbine torque in the first instance.

3.4.2. Turbulence models for estimating smoothing of equivalent wind

The spectral coherence of the wind at positions x and y , $Coh(f)$ or $|\bar{\gamma}_{xy}^2(f)|$, is a normalized measure of the correlation between the fluctuations of frequency f on both locations. Note however that the integral of $|\bar{\gamma}_{xy}(f)|$ over all frequencies is different from the correlation coefficient of the wind between both locations.

The coherence is an important quantity when translating Eulerian spectra into spectra in a rotating frame of reference, such as that ‘seen’ at a fixed position on a rotating wind turbine blade [98]. It is quite difficult to measure coherences with sufficient statistical significance and consequently there is a lot of scatter in measured values. Traditionally, very simple exponential models have been used to describe the coherence functions [99]. The coherence for separations perpendicular to the mean wind in neutral conditions, is described reasonably well by the following model, even in wake situations [100]

$$|\bar{\gamma}_{xy}^2(f, \Delta s)| = \text{Exp} \left(-\frac{a_i f \Delta s}{U} \right) \quad (37)$$

where Δs is the longitudinal separation and a_i depend on the velocity component and the direction of separation (vertical or lateral).

The decay constants for the longitudinal wind component are:

- $a_i = 12 + 11 \Delta z / z_{avg}$ (for vertical separation Δz) and
- $a_i = 12 + 11 \Delta y / z$ (for lateral separation Δy)

where Δz is the height difference, z_{avg} is the average of the two heights, and Δy is the lateral separation at the same height z [63]. In the literature, several other models of varying degrees of sophistication can be found [101].

The coherences also depend on stability: the decay constant a_i increases significantly in stable conditions, and decreases slowly with increasing instability.

In strongly stable conditions, the picture is somewhat blurred by the fact that the low-intensity, small-scale turbulent fluctuations are masked by the presence of slow, large-scale, highly coherent, two-dimensional structures. Except for minor differences in average stability (slightly more stable over the sea) there is no reason to believe that the coherences should behave differently over the sea. In complex terrain, however, where we typically see excess turbulence at large scales, one might expect that, like for unstable conditions, the coherences will increase somewhat.

The presence of operating wind turbines in the flow have a significant impact on the flow properties close to the rotor (within 10 diameters), see [102, 103]:

- The wind speed is decreased inside the wake, giving rise to large shear at the top of the wake.
- Turbulence levels are increased inside the wake and, since the mean wind speed is decreased, there is a considerable increase in turbulence intensity.
- The length scale of turbulence is decreased inside the wake because the turbulence produced by the shear layers in the wake is created at length scales of the same magnitude as the cross-wind dimensions of the wake which are typically an order of magnitude smaller than the length scale of the turbulence in the free flow.
- Because of the wake-imposed length scale, turbulence length scales in the wake for the different components of wind speed approach each other.
- In general, second-order statistics are quite perturbed inside the wake. The variances are quite different in the non-equilibrium turbulence and in the usual boundary-layer approximations.
- Spectral coherence in the wake seems to be well described by the usual models except for the near wake (distances $\leq 5D$), see [100].

A) Spatial filter from Sørensen (IEC 61400-1)

For power quality analysis, the equivalent wind speed method described in [153] provides a very good compromise between accuracy and calculation time.

In fact, IEC 61400-1 [97] defines the following coherence function of the wind in the rotor area $\gamma_{IEC}(f)$: (38)

$$\gamma_{IEC}(f, d_{rc}) = \exp \left[-d_{rc} A \sqrt{\left(\frac{f}{\langle U_{wind} \rangle} \right)^2 + \left(\frac{0,12}{\ell_{U_{wind}}} \right)^2} \right] = e^{-\beta d_{rc}} \quad (38)$$

$$\text{where } \beta = A \sqrt{\left(\frac{f}{\langle U_{wind} \rangle} \right)^2 + \left(\frac{0,12}{\ell_{U_{wind}}} \right)^2} \quad (39)$$

A is a decay constant and d_{rc} is the distance between the points r and c . IEC 61400-1 recommends $A \approx 12$; Frandsen et al. [104] recommends $A \approx 5$ and Saranyasoontorn et Al. [82] recommends $A \approx 9,7$ from experimental data in LIST Test site at Bushland, Texas.

The average fluctuation of frequency f at the rotor area (relative to the wind measured at hub nose) is the area integral

of the coherence assuming that point r is the hub nose and point c is in the differential area. Fig. 30 shows the limits for the area integral of the coherence. The fluctuation is assumed to arrive at all the points in the rotor plane at the same time in average or with a random lag and hence $\gamma_{IEC}(f)$ has null argument.

$$\begin{aligned} H_1'(f) &= \int_0^R \int_0^{2\pi} \gamma_{IEC}(f, r) r dr d\varphi = \int_0^R \gamma_{IEC}(f, r) 2\pi r dr = \\ &= 2\pi \int_0^R e^{-\beta r} r dr = \frac{2\pi}{\beta^2} [1 + (\beta R - 1)e^{-\beta R}] \end{aligned} \quad (40)$$

Finally, the transfer function is normalized to have unity gain at very low frequencies (very slow fluctuations affect equally all the rotor area):

$$H_1(f) = \frac{H_1'(f)}{H_1'(0)} = \frac{1}{1 + \left(\frac{\ell_{U_{wind}} f}{0,12 \langle U_{wind} \rangle}\right)^2} \frac{1 + (\beta R - 1)e^{-\beta R}}{1 + \left(\frac{0,12AR}{\ell_{U_{wind}}}\right) e^{-\frac{0,12AR}{\ell_{U_{wind}}}}}$$

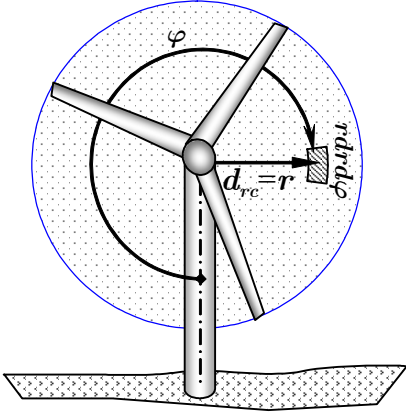


Fig. 30: Differential sector area to compute the average fluctuation along the rotor area.

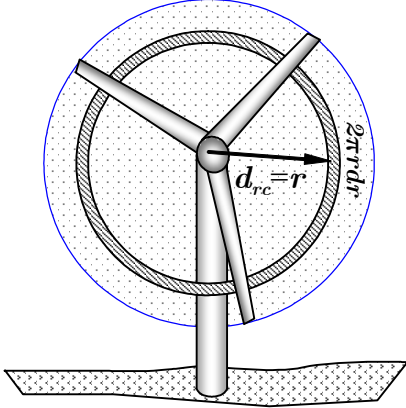


Fig. 31: Differential annular area assuming rotational symmetry.

The admittance function has been solved numerically by Sørensen in [105] for different coherence functions and wind speed weightings in the rotor plane. Calculating the admittance function numerically with the coherence function (38), this admittance function is fitted to the analytical expression

$$|H_1(f)|^2 = \left[1 + \left(\frac{\sqrt{f^2 + f_1^2}}{f_0} \right)^{4/3} \right]^{-3/2} \quad (42)$$

$$f_0 = \frac{\sqrt{2}}{A} \frac{\langle U_{wind} \rangle}{R}, \quad f_1 = 0,12 \frac{\langle U_{wind} \rangle}{\ell_{U_{wind}}} \quad (43)$$

where R is the radius of the wind turbine rotor disk and A is the coherence decay factor, i.e. $A \approx 12$ using the coherence function $\gamma_{IEC}(f)$.

The cut-off frequency of this filter is obtained solving $|H_1(f_{cut})|^2 = 1/2$:

$$f_{cut} = \sqrt{0,4502 f_0^2 - f_1^2} = \frac{\langle U_{wind} \rangle}{A R} \sqrt{0,9 - 0,0144 \frac{A^2 R^2}{\ell_{U_{wind}}^2}}$$

The application of the first filter to the wind produces the following PSD:

$$PSD_{U_{eq1}}(f) = PSD_{U_{wind}}(f) |H_1(f)|^2 \quad (45)$$

where $PSD_{U_{wind}}(f)$ is the power spectral density of the wind measured at a point and $PSD_{U_{eq1}}(f)$ is the power spectral density of the equivalent wind (without the periodic components due to the quasi-deterministic variation of torque with rotor angle).

B) Spatial filter from Wilkie, Leithead and Anderson

Wilkie, Leithead and Anderson proposed in [106] an alternative approach with aerodynamic filters. Since long wind records at hub height and high sampling rate are not usually available, they are randomly generated from a suitable wind model. In the first step, a wind time series at the hub is synthesized with the required properties (i.e., average wind speed, spectrum parameters and turbulence intensity). This signal is the input to the aerodynamic filters, and the output signal is the equivalent wind speed representing the wind field impact in the whole rotor area.

The spatial filter of the rotor disk has the following Laplace transfer function in (46):

$$H_1'(s) = \frac{\sqrt{2} + b \cdot s}{(\sqrt{2} + b \cdot s \sqrt{a})(1 + b \cdot s / \sqrt{a})} \quad (46)$$

where $a = 0,55$, $b = \gamma R / \langle U_{wind} \rangle$, R is the turbine radius, U_{wind} is the average wind speed at the hub height, and γ is the decay factor over the disc ($\gamma = 1,3$) [44].

The square modulus of the filter is:

$$|H_1(f)|^2 = \frac{1 + 2(b \cdot f \cdot \pi)^2}{\left[1 + (2b \cdot f \cdot \pi)^2 / a\right] \left[1 + 2a(b \cdot f \cdot \pi)^2\right]} \quad (47)$$

This filter is almost equivalent to a first-order low pass filter with cut-off frequency $f_{cut} = (2\pi b)^{-1} = 0,1224 \langle U_{wind} \rangle / R$ (compare solid and dot-dashed lines in Fig. 32).

$$|H_1(f)|^2 \approx \frac{1}{1 + 66,72 (f R / \langle U_{wind} \rangle)^2} \quad (48)$$

Notice that for multi-megawatt turbines, the cut-off frequency f_{cut} is a few cents of Hertz, filtering wind oscillations of tens of seconds. However, the filter order is only one and the transition droop is mild. Therefore, the frequency content of the equivalent wind can be noticeable even one decade below the cut-off frequency f_{cut} . However, the effect of the turbulence in the torque is negligible at frequencies $f \gtrsim 0,2$ Hz compared to the drivetrain oscillations due to tower oscillation, wind shear, rotor revolution and tower shadow.

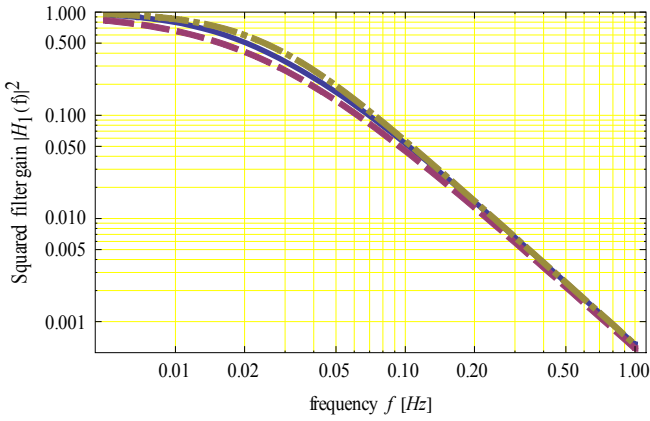


Fig. 32: Comparison of aerodynamic filters (42) –dashed purple line–, (47) –solid blue line– and (48) –dot-dashed brownish line– for a rotor of radius $R = 50$ m, average wind speed $\langle U_{wind} \rangle = 10$ m/s and integral turbulence length $\ell_{U_{wind}} = 1000$ m ($f_{cut} = 0,0245$ Hz approximately).

Fig. 32 shows that the three filters show good agreement. For very short integral turbulence lengths $\ell_{U_{wind}}$, the filter from Sørensen (42) introduces a non-unity gain at very low frequencies, which is not very reasonable. However, the Sørensen filter is more precise than (46) or (48) because the transition is a bit softer and the cut-off frequency depends explicitly of the ratio between the turbulence length scale and the turbine radius.

In short, taking into account the uncertainties in the coherence in the rotor area, the rotor spatial diversity is similar to a first order filter of $f_{cut} \approx A \langle U_{wind} \rangle / (100R)$, where the coherence decay factor A is between 5 (high spatial coherence typical of a stochastic parameter between gusts) and 12 (standard spatial coherence).

C) Spatial average vs. time average

The Taylor's hypothesis of frozen turbulence implies that the spatial averaging along the rotor area is similar to time average during some ΔT interval. In fact, most data loggers record running averages computed during the interval ΔT .

The transfer function of a running average is similar to a second-order filter:

$$H_{\sin c}(f) = \frac{\sin^2(2\pi f \Delta T / 2)}{(2\pi f \Delta T / 2)^2}, \quad f_{cut} \approx \frac{0,443}{\Delta T} \quad (49)$$

and its cut-off frequency is $f_{cut} \approx 0,443/\Delta T$, a bit lower than the Nyquist frequency of the data sampled at ΔT .

Equating the cut-off frequencies of the aerodynamic filter and the running average, $A \langle U_{wind} \rangle / (100R) \approx 0,443/\Delta T$, the characteristic time of the rotor is $\Delta T \approx 44,3R/(A \langle U_{wind} \rangle)$. The gust quicker than ΔT are significantly attenuated by the rotor.

For a rotor of radius $R = 50$ m at an average wind speed $\langle U_{wind} \rangle = 10$ m/s and $A \approx 12$, the characteristic time is $\Delta T \approx 18$ s. This implies that *gust of a few seconds are notably filtered at the low speed rotor shaft of a multimegawatt turbine.*

3.4.3. Average rotor wind speed vs. wind speed at hub height

Wind speed generally increases with height and this variation is termed wind shear. Torque pulsations, and therefore power pulsations, are observed due to the periodic

variations of wind speed seen at different heights. Power and torque oscillate due to the different wind conditions encountered by each blade as it rotates through a complete cycle. For instance, a blade pointing upwards would encounter wind speeds greater than a blade pointing downwards. During each rotation, the torque oscillates three times (in a three bladed turbine) because of each blade passing through minimum and maximum wind. It is therefore important to model these wind shear induced $3p$ torque pulsations when studying a wind turbine system.

If the blades of a rotor have different pitch angles or small differences in their shape or if the rotor mass is unbalanced, then a pulsation at the revolution frequency is also observed in the torque.

The turbulent mixing in the atmosphere may be considered in a similar way to molecular mixing (this is called K theory). Assuming the phenomenon is dominated by mechanical mixing due to shear forces, the following relationship of wind speed with height is derived:

$$U_{wind} \approx \frac{u_*}{k} \text{Ln} \left(\frac{z - D}{z_0} \right) \quad (50)$$

where the friction velocity is u_* , k is the von Karman constant (generally taken as 0.4), z_0 is the roughness length and D is the displacement height.

The roughness length z_0 is related to the vegetation cover of the area and tables of roughness length are available from several sources [107], ranging from $z_0 = 0.0002$ m (sea and lakes) to $z_0 = 0.4$ (urban districts, forests, and farm land with many windbreak). In general, wind vertical profile is heavy dependent on meteorological conditions, specially on stable, unstable and neutral atmosphere (for instance, see Tambke [108]).

The displacement height D is the height above the roughness elements where the flow is free. For most vegetation it is small and is generally treated as zero. For large roughness elements like trees and buildings in towns it is not negligible and is of the order of the average height of the elements (the log law may only be used for heights above D). Turbines are usually sited in isolated places and D is usually taken as zero.

The wind speed at any height z can then be computed provided that the wind speed at a height H is known:

$$\frac{U_{wind}(z)}{U_{wind}(H)} = \frac{\text{Ln}(z/z_0)}{\text{Ln}(H/z_0)} \quad (51)$$

If the wind speed at hub height H is measured, $U_{wind}(H)$, the wind speed at other elevations above ground z can be estimated with (51), without considering the local variations due to turbulence.

The increase in wind speed with height is easier to evaluate if it is described as a power law. A common wind shear model, shown as (52), is taken directly from the literature on wind turbine dynamics [109].

$$U_{wind}(z) = U_{wind}(H) \left(\frac{z}{H} \right)^{\alpha_z} \quad (52)$$

where α_z is an empirical wind shear exponent, which depends on meteorological conditions and site characteristics.

The power law exponent α_z can be estimated from the roughness length z_0 applying logarithms to (51):

$$\alpha_z = \frac{\ln\left[\frac{\ln(z/z_0)}{\ln(H/z_0)}\right]}{\ln(z/H)} = \frac{\ln\left[1 - \frac{\ln(z/H)}{\ln(z_0/H)}\right]}{\ln(z/H)} \quad (53)$$

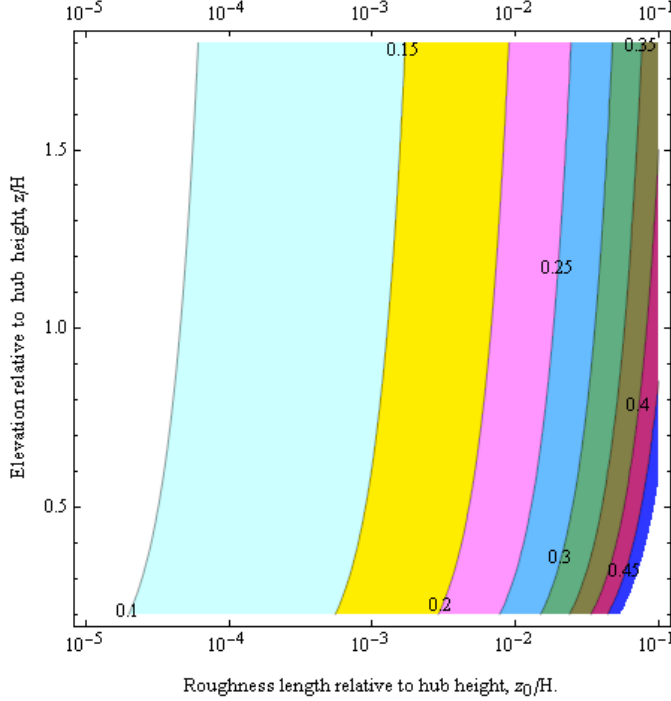


Fig. 33: Shear exponent α_z as a function of roughness length and elevation, relative to hub height from eq. (53).

Fig. 33 indicates that the shear exponent only varies slightly with height (i.e., the contour lines are almost vertical except near the surface). Therefore, the power law and the logarithmic law are similar for points near the rotor hub ($z \sim H$). Taking into account that $\ln(1-x) \approx (\frac{1}{2} - 1/x)^{-1}$, the following approximations are valid:

$$\alpha_z \approx \frac{1}{\ln\left(\frac{\sqrt{zH}}{z_0}\right)} \underset{z \sim H}{\sim} \frac{1}{\ln(H/z_0)} \quad (54)$$

The power law exponent α_z typically varies between 0.1 and 0.4 depending upon the landscape type. According to [110], the wind shear exponent is often assigned a value of 0.143, known as the 1/7th power law, to predict wind profiles in a well-mixed atmosphere over flat, open terrain. However, higher exponent values are normally observed over vegetated surfaces and when wind speeds are light to moderate (i.e., under 7 m/s). For example, Eggers et al. [111] reported exponents up to 0.75 based on wind speed measurements for a considerable period of time in the Midwest and Southwest regions of the United States. It has been reported [112] that findings made at a Colorado wind site indicate shear exponents as high as 1.25 eventually occur at tall tower heights for significant periods of time (up to two hours) at night.

A relationship between wind speed averaged along the rotor disk, $\langle U_{wind} \rangle_{rotor}$, and the hub height wind speed

$U_{wind}(H)$ is required such that tower shadow and wind shear formulas can be combined with only one wind speed term.

$$\langle U_{wind} \rangle_{rotor\ area} = \frac{\int_{H-R}^{H+R} U_{wind}(z) 2\sqrt{R^2 - (H-z)^2} dz}{\pi R^2} \quad (55)$$

where the spatial variation due to the turbulence structure is not considered

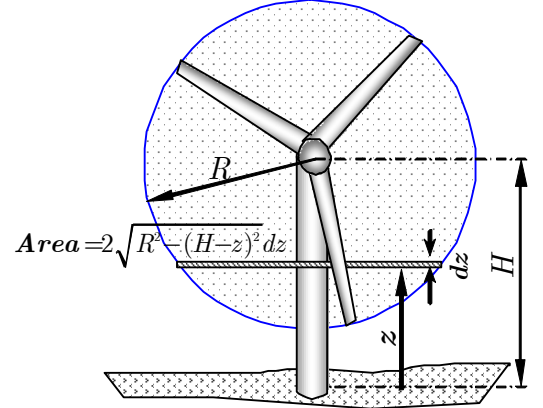


Fig. 34: Differential area assuming dependence only with height.

To calculate spatial average wind speed $\langle U_{wind} \rangle_{rotor}$, the varying wind speed from wind shear is integrated over rotor area and divided by total rotor area (for integration details, see Dolan and Lehn [50]). The ratio of the spatially averaged wind to the hub height wind is:

$$m = \frac{\langle U_{wind} \rangle_{rotor\ area}}{U_{wind}(H)} = \left[1 + \frac{\alpha_z(\alpha_z - 1)}{8} \left(\frac{R}{H}\right)^2 \right] \quad (56)$$

The simplification that $\langle U_{wind} \rangle_{rotor\ area} \approx U_{wind}(H)$ is reasonable since $0.98 < \langle U_{wind} \rangle_{rotor} / U_{wind}(H) \leq 1$, (assuming $R/H < 0.76$ and $0.1 < \alpha_z \leq 1$). For more accuracy, (56) can be used (see Fig. 35).

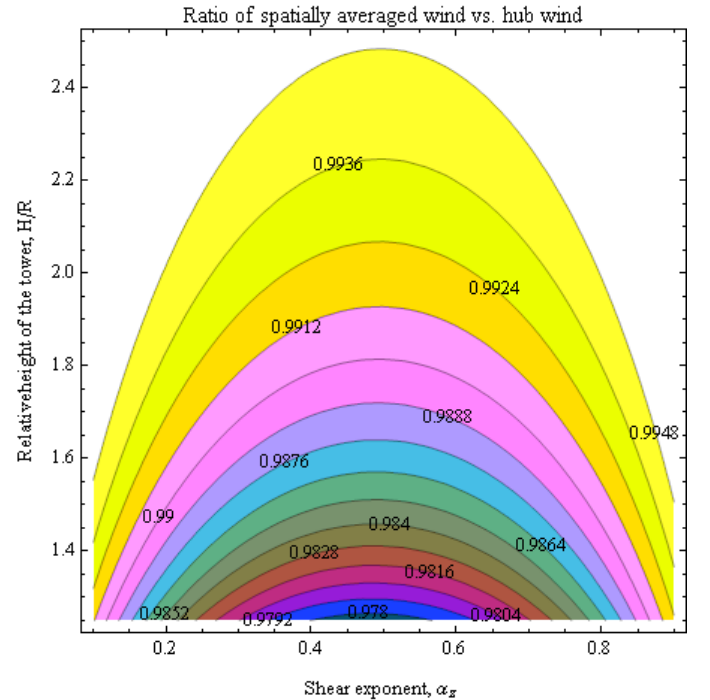


Fig. 35: Ratio $m = \langle U_{wind} \rangle_{rotor} / U_{wind}(H)$ with shear exponent $0 < \alpha_z < 1$ for different tower heights.

Notice that the mean squared wind is proportional to rotor torque. The ratio of squared winds is analogue to (56), but changing α_z by $2\alpha_z$.

$$\frac{\langle U_{wind}^2 \rangle_{rotor\ area}}{U_{wind}^2(H)} = \frac{\int_{H-R}^{H+R} U_{wind}^2(z) 2\sqrt{R^2 - (H-z)^2} dz}{\pi R^2 U_{wind}^2(H)} = \left[1 + \frac{2\alpha_z(2\alpha_z - 1) \left(\frac{R}{H}\right)^2}{8} \right] \quad (57)$$

At partial load, the mean of the wind cubed is proportional to power. The ratio of cubed winds is analogue to (56), but changing α_z by $3\alpha_z$.

$$\frac{\langle U_{wind}^3 \rangle_{rotor\ area}}{U_{wind}^3(H)} = \frac{\int_{H-R}^{H+R} U_{wind}^3(z) 2\sqrt{R^2 - (H-z)^2} dz}{\pi R^2 U_{wind}^3(H)} = \left[1 + \frac{3\alpha_z(3\alpha_z - 1) \left(\frac{R}{H}\right)^2}{8} \right] \quad (58)$$

The uncertainty in the turbine power curve introduced considering hub wind instead of (cubed) wind speed averaged along the rotor can eventually exceed 5% according to Rehman and Al-Abbadi [113]. The average wind speed $\langle U_{wind} \rangle_{rotor\ area}$ is bigger than hub wind speed $U_{wind}(H)$ if $\alpha_z > 1$. Average squared wind speed $\langle U_{wind}^2 \rangle_{rotor\ area}$ is bigger than squared hub wind speed for $U_{wind}^2(H)$ for $\alpha_z > 1/2$. Average cubic wind speed $\langle U_{wind}^3 \rangle_{rotor\ area}$ is bigger than $U_{wind}^3(H)$ for $\alpha_z > 1/3$. Therefore, the power curve of a turbine can vary significantly depending on the shear exponent α_z .

3.5. Calculation of aerodynamic filter based on 3D wind waves

In the previous subsection, the turbulence structure along the rotor disk has been neglected. The equivalent wind has a determinist oscillation due to wind shear and tower shadow and a random oscillation due to turbulence. But even the determinist oscillation can turn into a random oscillation if the blades start vibrating if they have enough flexibility and inertia. Thus, the determinist variation of the real wind along the swept area can introduce random oscillations in the torque and thus, in the equivalent wind.

A naïf approach to estimate the smoothing –due to the spatial variation of turbulence– of the equivalent wind respect the wind measured with an anemometer will be developed in this subsection, just as an illustrative example.

3.5.1. Comparison of 3D wind waves with frozen turbulence

Under the Taylor's assumption of frozen turbulence, the perturbation travels at average wind speed $v_{turb} \approx \langle U_{wind} \rangle$. Thus, the perturbations seen at a fixed point fluctuating with frequency f , have a wavelength $\lambda_{long} = v_{turb}/f \approx \langle U_{wind} \rangle/f$ related to the spatial scale in the longitudinal direction $\ell_{U_{wind}}$. Using the turbulence structure in the standard IEC-61400-1, the cut-off frequency of the equivalent turbulence $f_{cut} \approx A \langle U_{wind} \rangle / (100R)$.

However, the wavelengths in the lateral and vertical directions are smaller due to the surface and the boundary layer presence. For simplicity, we assume a transversal

wavelength $\lambda_{transv} = k_{transv} \lambda_{long}$ for the lateral and vertical directions, slightly smaller than in the longitudinal direction ($0 < k_{transv} \lesssim 1$). Using a sinusoidal perturbation pattern with transversal wavelength λ_{transv} (see Fig. 37), the cut-off frequency in the rotor disk average wind is $f_{cut} \approx k_{transv} \langle U_{wind} \rangle / (6R)$ –this formula will be derived in the next subsection. Equating both estimations, the ratio between the transversal and longitudinal wavelengths can be estimated as $k_{transv} \approx 0,06A$.

Since the coherence decay factor A is a stochastic parameter between 5 (high spatial coherence typical of gusts) and 12 (standard spatial coherence), the ratio between the transversal and longitudinal wavelengths is $v_{turb}/\langle U_{wind} \rangle \approx 0,3\text{--}0,72$. This factor is bellow unity, indicating that the spatial variation of the 3D wind field is bigger in the lateral and vertical directions than in the longitudinal direction.

Thus, the results from Taylor's Hypothesis and from the wind perturbation treated as a wave match. This fact is surprising, especially taking into account the chaotic behaviour of the turbulent flow and the oversimplification of the frozen turbulence hypothesis or the wavelength approach.

3.5.2. Model of 3D wind waves

In a gas, a perturbation generates a pressure wave that transmits in all directions at sound speed. Since macroscopic turbulence implies vortices, that are quite stable flow structures, it is reasonable that they pass floating the turbine. Due to the stability of eddies, their speed of translation is the average flow speed $\langle U_{wind} \rangle$ instead of at sound speed ($v_{sound} = 343$ m/s at standard conditions).

In this sub-section, the source of perturbation will be considered far and the air viscosity (i.e., the attenuation of air waves) will be neglected. With the former simplifications, the longitudinal component of the wind of fluctuating frequency f at the anemometer will have a spatial periodic pattern of wavelength $\lambda_{transv} = k_{transv} \langle U_{wind} \rangle / f$ in the rotor disk (see Fig. 37) travelling in the longitudinal direction at speed $v_{turb} \approx \langle U_{wind} \rangle$.

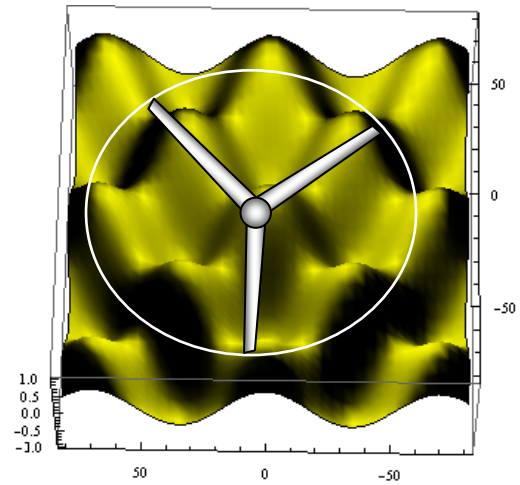


Fig. 36: Plot of the longitudinal wind component corresponding to a 3D wave which at an anemometer appears as a fluctuation of frequency $f = 5$ Hz and a turbine rotor of radius $R = 50$ m.

The longitudinal wind component at frequency f in rectangular coordinates y, z is assumed to be:

$$(59)$$

$$w_i(y, z, f, t) = \gamma_{IEC}(f, \sqrt{y^2 + z^2}) \cdot \text{Cos} \left[\frac{2\pi \langle U_{wind} \rangle (t + t_0)}{\lambda_{long}} \right] \text{Cos} \left[\frac{2\pi(y + y_0)}{\lambda_{transv}} \right] \text{Cos} \left[\frac{2\pi(z + z_0)}{\lambda_{transv}} \right]$$

where $\gamma_{IEC}(f, \sqrt{y^2 + z^2})$ is the amplitude of wind oscillation and t_0, y_0 and z_0 are random values.

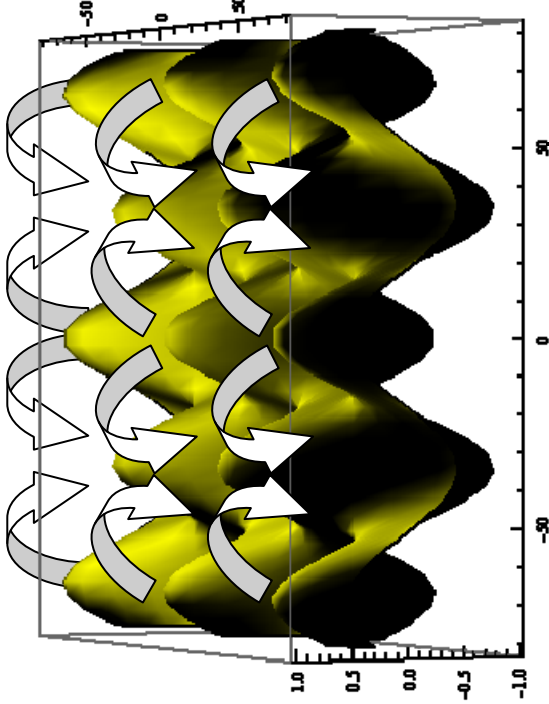


Fig. 37: Flow curls due to the eddies and the corresponding modulation of the longitudinal wind component.

Assuming that initial angle of the first blade is $\varphi = \varphi_0$ at $t = 0$, then the angular position at any time is $\varphi = \Omega_{rotor}t + \varphi_0$, where Ω_{rotor} is the rotor angular speed –for a three bladed turbine, $f_{blade} = 3\Omega_{rotor}/(2\pi)$.

Therefore, the wind field in the blade axis at a distance ρ of the rotor centre is, in polar coordinates:

$$w_i(\rho, \varphi, f, t) = w_i(\rho \text{Cos}(\Omega_{rotor}t + \varphi_0), \rho \text{Sin}(\Omega_{rotor}t + \varphi_0), f, t) \quad (60)$$

If the aerodynamics can be considered linear enough for neglecting small perturbations and the blade aeroelastics, only a sensitivity coefficient of wind in torque or in power needs to be considered. Moreover, the turbine torque would show the same cut-off frequency than the average wind and the equivalent wind.

3.5.3. Spatial turbulence averaged along the blades

Since rotor solidity in a three bladed turbine is low, the equivalent wind can be estimated averaging the wind only along each blade axis, provided the blade is narrow and it is not influenced by the nearby flow.

$$|H_1(f)|^2 = \left\langle \left[\sum_{i=1}^{N_{blades}} \int_{R_{min}}^{R_{max}} \frac{w_i(\rho, \varphi_i, f, t)}{N_{blades}(R_{max} - R_{min})} d\rho \right]^2 \right\rangle \quad (61)$$

Solving the integral for $\beta \approx 0$, this approximation leads to a first-order low-pass filter of the same cut-off frequency f_{cutoff}

$= v_{turb}/(6R) \approx \langle U_{wind} \rangle / (6R)$. Therefore, averaging along the blades instead of along the rotor disk area produces a slower decay (this is sensible since the blade area is smaller than the rotor disk area).

In the one hand, the blade average corresponds to the order $r = 1$ of the aerodynamic filters proposed by Sørensen [105] and Wilkie, Leithead and Anderson [106].

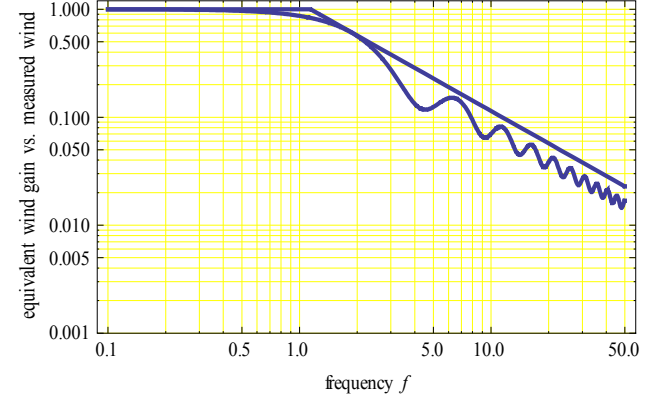


Fig. 38: Averaged wind fluctuation along the blades of a rotor of radius $R = 50$ m, $v_{turb} \approx v_{sound}$ and the asymptotic approximation to a system of order $r=1$.

In the other hand, the cut-off frequency f_{cut} is a few cents of Hertz in multi-megawatt turbines, filtering wind oscillations of tens of seconds. Experimental measurements have shown that the equivalent wind has approximately the same *PSD* as the wind measured at a point and filtered with a second order filter in a multi-megawatt turbine. Since the blades sweep the turbulence many times in the characteristic times corresponding to such low frequencies, it is more sensible to represent the turbine as a disk actuator than only considering the averaging along the blade axis.

3.5.4. Spatial turbulence averaged across the rotor disk area

The cut-off frequency of the rotor filter is very low, typically 0,033 Hz for a megawatt turbine. Such low frequency imply that the fluctuations that happen quicker than 30 s are filtered by the rotor. During such times, the blades sweep many times the wind field perturbation and the rotor can be considered a disk actuator. Thus, the turbulence impact on the equivalent wind is more accurately accounted if the local wind is averaged across the rotor disk area than along the blade axis, assuming a fairly constant blade loading between R_{min} and R_{max} .

The component of mean wind in the rotor area at frequency f gives an idea of the attenuation respect the fluctuation measured with an anemometer due to the averaging of speed in the swept area.

$$|H_1(f)|^2 = \left\langle \left[\int_{R_{min}}^{R_{max}} \int_0^{2\pi} \frac{w_i(\rho, \varphi, f, t)}{\pi(R_{max}^2 - R_{min}^2)} d\varphi d\rho \right]^2 \right\rangle \quad (62)$$

Fig. 39 shows that the averaging is equivalent to a low pass filter. The asymptotic function $\min\{1, f_{cutoff}/f^{3/2}\}$ corresponding to a low-pass filter of order $r=3/2$ and characteristic frequency $f_{cutoff} = v_{turb}/(6R) \approx \langle U_{wind} \rangle / (6R)$ has been added to the plot in Fig. 39 to contrast the system behaviour.

For $\beta \approx 0$, the cut-off frequency due to the rotor averaging is $f_{cut-off} = v_{turb}/(6R) \approx \langle U_{wind} \rangle / (6R)$ and its order is $r=3/2$ (see Fig. 39). For a turbine of radius $R=50$ m and an average wind speed $\langle U_{wind} \rangle \approx 10$ m/s, the cut-off frequency is about $f_{cut-off} \sim 1/(30 \text{ s}) = 0,033$ Hz. In fact, the order r of the filter is bigger than $3/2$ because $\beta > 0$, and the actual filter order estimated from experimental measurements is around $r \sim 2$.

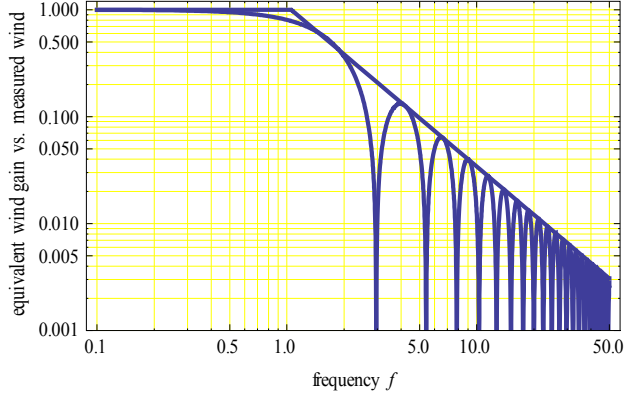


Fig. 39: Averaged wind fluctuation in the area of the rotor disk radius $R=50$ m, $v_{turb} \approx v_{sound}$ and the asymptotic approximation to a system of order $r=3/2$.

In sum, the equivalent wind is similar to the wind measured at the rotor hub filtered with a second-order low-pass filter with cut-off frequency f_{cut} . The effect of the turbulence in the torque is negligible at frequencies $f \gtrsim 0,2$ Hz compared to the drivetrain oscillations due to tower oscillation, wind shear, rotor revolution and tower shadow.

3.6. Torque dependence on rotor position

The analysis of experimental data shows that the turbine torque exhibit quasi-periodic power fluctuations as well as stochastic power pulsations caused by the variations of the wind speed –see Fig. 183 to Fig. 186. The most common are power pulsations at the frequency of the blades passing in front of the tower. These pulsations are caused by the torque modulation due to wind shear and aerodynamic effects as the blades pass in front of the tower.

Wind turbulence induces random changes in wind speed in a very broad frequency range and with high variance. In contrast, torque modulation is an almost systematic torque perturbation but it turns out into a random behaviour due to the interaction with the vibration modes of the blades and drivetrain.

Since the modulation of the torque is almost systematic with a characteristic time-varying frequency and its harmonics, the turbine can be designed and controlled to minimize its effects.

In a variable speed wind turbine (e.g. equipped with a double-output asynchronous generator) the influence of rotor angle in output power is smaller than in a fixed speed turbine. Fast variations in torque and thus power that affect the turbine blades then will result in momentary variations in the turbine speed, momentarily storing real power. Due to the same reason, the variations in power decrease when the induction generator slip is increased, by controlling the power flow in the rotor circuit. Thus, the tower shadow effect and the wind

shear or wind speed gradient usually have a small and deterministic contribution to the observed output power variations ([114] and [186]).

Even though rotational effects concern, first and foremost, the turbine structural integrity and its control, it should be included in the equivalent wind to have a realistic representation of low speed shaft torque.

3.6.1. Cascade rotational sampling filter from Petru and Thiringer

Since wind depends on height due to wind shear, the equivalent wind has a component dependent on rotor angle and hence, at frequency f_{blade} and its harmonics. Near the tower crossing, the air flux is influenced by the presence of the tower, resulting in a small decrease of torque. Thus, the equivalent wind shows amplitude-varying oscillations at the frequency of a blade crossing the tower, f_{blade} , due to spatial sampling at blade positions. The amplitude-varying oscillations can be mathematically decomposed in pulsations of frequency $f_{blade} \pm f(t)$, where the carrier frequency is f_{blade} and $f(t)$ is the modulating frequency, much lower than f_{blade} .

Despite torque varies sharply depending on tower position –see Fig. 311–, this spiky variation is smoothed through the dynamic train flexibility and generator dynamics. Thus final power variations can be characterized primarily through the fundamental sinusoidal fluctuations –see Fig. 190 to Fig. 202.

Petru and Thiringer represented the rotational sampling as a cascade filter applied to the wind spectra. The application of the first and second filter to the wind produces an equivalent wind with the following PSD:

$$\begin{aligned} PSD_{U_{eq}}(f) &= PSD_{U_{eq1}}(f) |H_2(f)|^2 = \\ &= PSD_{U_{wind}}(f) |H_1(f)|^2 |H_2(f)|^2 \end{aligned} \quad (63)$$

where $PSD_{U_{eq}}(f)$ is the equivalent wind, including the rotational sampling effects.

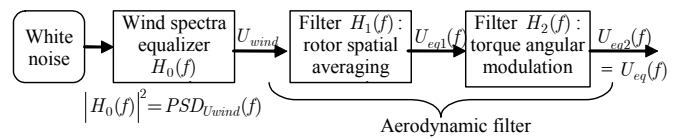


Fig. 40: Block diagram of the cascade model in [43] for off-line equivalent wind time series generation (actual rotor angle φ and pitch angle θ are not considered).

The second filter represents the wind rotational sampling by the turbine rotor and is called the rotational sampling filter, with the general expression (64) taken from [43]:

$$H_2(s) = \frac{[1 + g_d^{-2}](s + 2\pi f_{blade})^2}{[s + 2\pi f_{blade}(g_d^{-1} + j)][s + 2\pi f_{blade}(g_d^{-1} - j)]} \quad (64)$$

where the blade frequency is $f_{blade} = 3\Omega_{rotor}/(2\pi)$ in a three bladed turbine and g_d is the rotor amplification factor at $f = f_{blade}$ respect $H_1(s)$. This filter amplifies the variations at a frequency region around the blade passing frequency. In other regions, this filter has a gain of nearly one. Fig. 41 shows a typical power spectral density for $U=12$ m/s, before and after the application of the aerodynamic filters (46) and (64).

Since signal phase is uniformly distributed, it doesn't affect equivalent wind distribution. The squared modulus of the rotational filter sampling is:

$$|H_2(f)|^2 = \frac{[(1+g_d^2)(f^2+f_{blade}^2)]^2}{f_{blade}^4 + 2f_{blade}^2(f^2+f_{blade}^2)g_d^2 + (f^2-f_{blade}^2)^2 g_d^4} \quad (65)$$

Recall that $g_d = 2\pi f_{blade}/d$ is used instead of the original formula in [43] to obtain simpler expressions related to the equivalent wind. This filter amplifies the equivalent wind variations around the blade passing frequency in an approximate factor g_d . The bandwidth of the filter is $BW \approx f_{blade}/g_d$ approximately and it increases the variance of equivalent wind $U_{eq2}(f)$ in a factor $\sigma_{blade}^2 \approx \pi f_{blade} g_d PSD_{H1}(f_{blade})$.

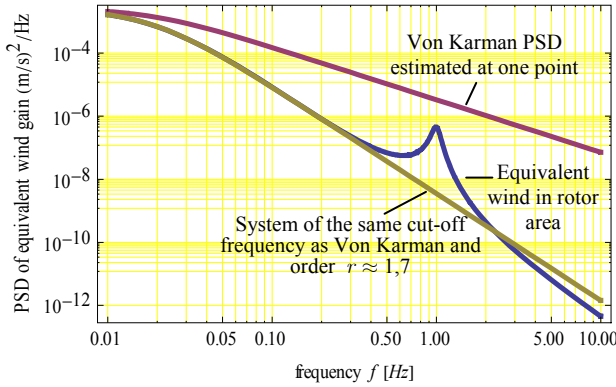


Fig. 41: Wind speed power spectral density before and after the application of aerodynamic filters and a system of fractional order $r = 1.6947$. (Other conditions: von Karman, $U = 10$ m/s, $L2 = 150/2, 329$ m, $I=0.10$, $f_{blade} = 1,0$ Hz, $R=50$ m, $g_d=2\pi f_{blade}/15$).

This rotational sampling filter can be roughly approximated to an ideal narrowband equalizer of unity gain except at f_{blade} , where the gain is approximately $\pi f_{blade} g_d \delta(f-f_{blade}) / PSD_{Ueq1}(f_{blade})$.

$$PSD_{Ueq2}(f) \approx \left[1 + \frac{\pi f_{blade} g_d}{PSD_{Ueq1}(f_{blade})} \delta(f-f_{blade}) \right] \quad (66)$$

Put into words, rotational sampling is modelled in (66) as a deterministic pure tone oscillation. The gain g_d has been deduced equating the variance of the equivalent wind computed with (65) or (66). Notice also that comparing (186) and (66), then the amplitude of the ideal narrowband fundamental component is $g_1 \approx \pi f_{blade} g_d$.

A) Estimation of g_d , σ_{blade} and the bandwidth of the rotational sampling filter

The blade frequency f_{blade} is $3 \Omega_{rotor}/2\pi$ in a three bladed turbine. The average amplitude of the fluctuations due to rotational sampling can be determined from recorded signals or from the model presented in the next section.

The value of g_d can be estimated as $g_d \approx \sigma_{blade}^2 / [\pi f_{blade} PSD_{H1}(f_{blade})]$, where all the parameters are easily estimated. The bandwidth BW in the filter (64) is f_{blade}/g_d (it cannot be adjusted) but the bandwidth can be adjusted in the alternative filter (70) to take into account the variability of f_{blade} and some mechanical vibrations induced by the rotational sampling.

The parameter σ_{blade} is the RMS value of the torque modulation generated by the filter. In order to preserve the amplitude of the torque modulation, σ_{blade} can be estimated alter-

natively as the equivalent wind dip when a blade is crossing the tower divided by $2\sqrt{2}$ and a tiny bandwidth BW .

However, this criteria overestimates the RMS modulation since the loss of torque is very brief (see Fig. 311). If only the fundamental component of the fluctuations are considered, then $\sigma_{blade} \sim Amplitude/\sqrt{2}$ but considering the real shape, $Amplitude/\sigma_{blade} \gg \sqrt{2}$ due to the presence of harmonics in the torque signal.

Since wind is variable, operational conditions vary and consequently the torque signal is not truly stationary. The frequency bandwidth of the oscillations, BW , can be estimated from rotor speed (or f_{blade}) excursions for some given operational conditions and it is a quite small fraction of f_{blade} . The bandwidth BW increases when it is estimated from long records of real data since wind is not really stochastically stationary (f_{blade} varies more in long periods). The bandwidth is an outcome of the interaction of wind turbulence with complex turbine dynamics. In contrast, f_{blade} and σ_{blade} are less affected by estimation method.

If the aerodynamic torque *considering* tower shadow and wind shear is measured or estimated, $\sigma_{blade,(1)}$ is just the RMS value of the bandpass-filtered equivalent wind signal (see Fig. 42).

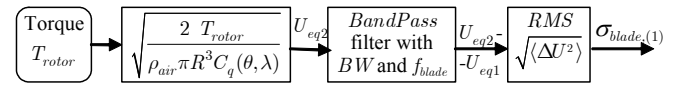


Fig. 42: Estimation of $\sigma_{blade,(1)}$ from the rotor aerodynamic torque.

Analogously to Fig. 42, σ'_{blade} is the RMS value of the bandpass-filtered equivalent wind computed from the aerodynamic torque *without* considering the tower shadow and wind shear. σ'_{blade} can be regarded as the background fluctuation at f_{blade} due exclusively to wind turbulence ($\sigma_{blade,(1)} \gg \sigma'_{blade}$).

Since rotational sampling and wind turbulence are different processes, the fluctuations induced by them can be considered stochastically independent. Therefore, the sole contribution of rotational sampling is $\sigma_{blade}^2 \approx \sigma_{blade,(1)}^2 - \sigma'_{blade}^2$.

B) Rotational effects as a randomly modulated component of carrier frequency f_{blade}

In time domain, the rotor introduces in the equivalent wind a sinusoidal component with approximately Rayleigh-distributed amplitude of parameter $\sigma_{blade} \approx [\pi f_{blade} g_d PSD_{H1}(f_{blade})]^{1/2}$, random phase and approximate frequency f_{blade} . The bandwidth of the filter is related to the modulating frequency of the signal (a rough estimation of the modulating frequency is just the bandwidth, $f_{mod} \approx BW$). Thus, the rotational sampling can be described by the additional term in the temporal signal:

$$H_2(t) \approx A \cos(2\pi f_{blade} t + \varphi_1) \cos(2\pi f_{mod} t + \varphi_2) \quad (67)$$

where φ_1 and φ_2 are random phases uniformly distributed in $[-\pi, +\pi]$ and A is the amplitude, distributed as a Rayleigh random variable of parameter σ_{blade} . This behaviour has been observed in power output of wind turbines, indicating that the assumed approximations are valid (see, for example, Fig. 200 to Fig. 203).

The former expression is suitable for the generation of equivalent wind in time domain simulations, where the rotational speed and f_{blade} can vary depending on the wind and turbine control. If f_{blade} varies in time, (67) transforms into:

$$H_2(t) \approx A \cos(\varphi_1 + \int_0^t 2\pi f_{blade} dt) \cos(2\pi f_{mod} t + \varphi_2) \quad (68)$$

C) Additional filters to increase accuracy

Other filter types can be applied in order to adjust the high frequency components. The induction lag filter is one of them, resulting from the induction lag that occurs when the blades react to a change in wind speed and hence to a changing angle of attack. This change can be modelled as a lag filter with a frequency response represented by (9):

$$H_3(s) = \frac{a_i \tau_i s + 1}{\tau_i s + 1} \quad (69)$$

where $a_i > 1$ for amplifying certain mid-range frequencies. The time constant, τ_i , and the empirical parameter a_i must be obtained through an identification method. According to Petru and Thiringer, omitting the induction lag filter has no detectable impact on the power quality predictions [43]. This can be due to the fact that high frequencies present in rotor torque are highly attenuated by turbine dynamics.

3.6.2. Proposed rotational sampling model

In this, a rotational sampling model is proposed to overcome the limitations of the cascade filters:

- The estimation of the parameters of the rotational sampling filter (64) and its additional filters (69) is intricate. Typically, they are derived from experimental measurements or complex aerodynamic simulations.
- The additional filters introduce harmonic components of random phase, unable to reproduce the shape of the real angular modulation. With several additional filters, a signal with the same frequency content can be obtained, but without its characteristic shape.
- On the one hand, $PSD_{U_{eq1}}(f_{blade})$ depends strongly on wind speed, turbulence length and wind spectra type. On the other hand, the torque modulation depends on rotor angle, average wind speed, pitch angle and shear exponent. The use of cascade filters imply considering rotational components proportional to $PSD_{U_{eq1}}(f_{blade})$ and it is not advisable.
- The essence of the rotational effect is the torque dependence on rotor angle, average wind speed, pitch and speed profile. Therefore, the torque modulation is represented more accurately by an

function dependent on rotor angle, average wind speed, pitch angle and shear exponent.

- The wind field can excite aeroelastic modes of blades, introducing complex behaviour. This behaviour is typically analyzed by specialized programs such as Bladed, Adams, Fast... and it can be introduced either as deterministic or as stochastic terms in the equivalent wind.

Therefore, the rotational sampling will be characterized later in (752) as an angle-dependent torque modulation $f_{pulse}(\varphi)$ whose characteristic shape depends on turbine characteristics and operational conditions (see Fig. 45). The torque modulation $f_{pulse}(\varphi)$ is composed by a sinusoidal oscillation at blade frequency due to wind shear plus a narrow torque dip during the crossing of the blade through the tower (see Fig. 311).

Since rotational sampling produces an angular modulation in torque, an equivalent wind modulation can be defined based on (24). The modulation of equivalent wind speed can be estimated through a small signal model –see (73) to (94) for details on a small-signal model.

Thus, the rotational effects can be accounted as a modulation of equivalent wind speed with approximate shape $f_{pulse}(\varphi)$ and amplitude α .

A) Feedback of actual rotor speed Ω_{rotor} , rotor angle φ and pitch angle θ for better accuracy

Provided U_{wind} and f_{blade} can be considered constant, time series of equivalent wind can be roughly generated regardless of wind turbine dynamics. However, variable speed turbines with blade pitch or active stall regulation or time series with significant wind speed variations requires feedbacking the actual rotor speed Ω_{rotor} , the rotor angle φ and the pitch angle θ to the operating conditions. This is naturally accomplished in the time domain.

Fig. 43 shows a diagram where the mean wind speed $\langle U_{wind} \rangle$ and the turbulence averaged along the rotor $U_{eq1}(t)$ is computed in the time domain without including rotational effects. In fact, the rotational effects are computed from the pitch θ and the effective tip speed ratio $\langle \lambda' \rangle$ –angle brackets indicates that the aerodynamic parameters are averaged along all the blades of the rotor. This approach increases the accuracy on the estimation of aerodynamic behaviour of the rotor without requiring detailed knowledge of rotor details – only torque or power coefficients are needed to compute aerodynamic torque. The use of an effective tip speed ratio $\langle \lambda' \rangle$ have been not found in the literature and it is an original contribution of this work. $\langle \lambda' \rangle$ will be derived from blade

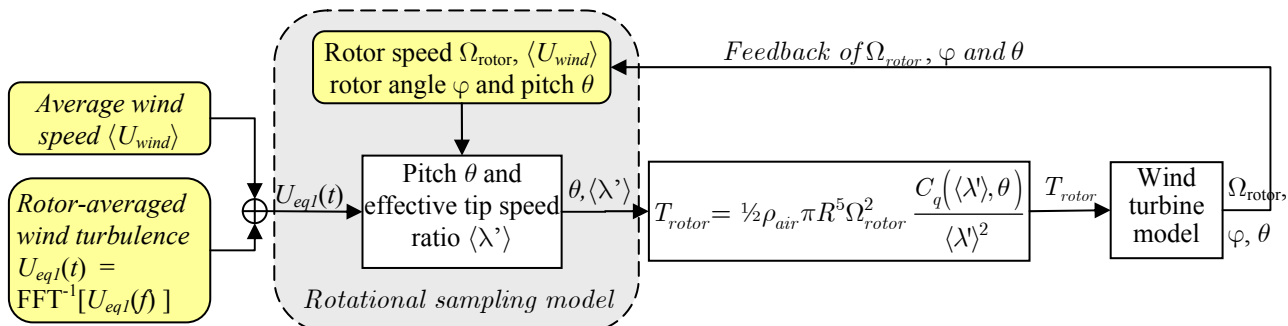


Fig. 43: Diagram of the proposed retrofitted rotational sampling model for the on-line estimation of aerodynamic rotor torque in the time domain

element theory in the next subsection 3.7.

In case the blades experience noticeable aeroelastic twist induced by aerodynamic loads, an equivalent pitch angle $\langle \theta' \rangle$ can be defined analogously.

Fig. 44 shows the simplified diagram of the farm wind model with the interaction between the generated single point wind speed time series, u_{sp} , and the turbine rotational speed.

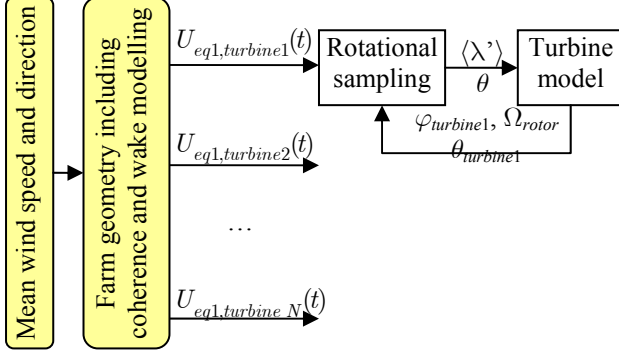


Fig. 44: Diagram of the generation in the time domain of the equivalent wind in a farm.

B) Rotational sampling in the frequency domain

The former methodology can reproduce the shape of the angular dependence of equivalent wind. This methodology is suitable for simulations in the time domain, where turbine parameters evolve.

The studies in the frequency domain usually assume a steady system operation. If f_{blade} and pulse shape is approximately constant, the time model in Fig. 43 transforms into the frequency model in Fig. 45. The frequency model retains the shape of the torque modulation (the phase of $U_{eq2}(f)$ is synthesized) but it does not account for changes in rotor speed, pitch and wind along the simulation.

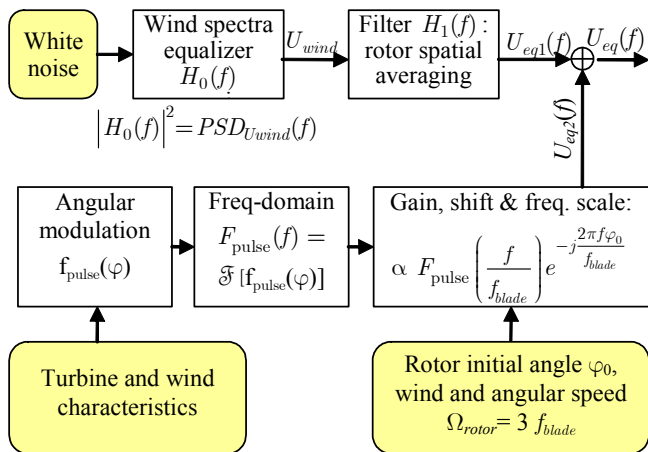


Fig. 45: Diagram of the proposed additive rotational sampling model for the off-line estimation of the equivalent wind in the frequency domain.

Due to the elasticity of the drivetrain and the high inertias in the turbine, the shape of the torque dip at the rotor due to tower shadow is heavily smoothed at the output of the drivetrain. Thus, the main effect of torque modulation –apart from the fatigue on the blades and on the drivetrain– is the excitation of vibration modes of the blades, drivetrain and generator.

Many frequencies of vibration are not harmonic, resulting into stochastic processes characterized primarily by their *PSD*. In such cases, the phase difference between vibrations is random and the original shape of the torque modulation is meaningless (in a linear system, vibration modes are fed by the frequency content of the torque, irrespectively of its original shape).

C) Narrowband filter for coarse simulations

On some studies, higher frequency rotor dynamics can be neglected. In such studies the rotational effects are only represented by its fundamental component.

In such cases, the rotational sampling can be characterized with a narrowband filter around the blade frequency (see Fig. 46) and this approach is comparable to Petru and Thiringer method [43].

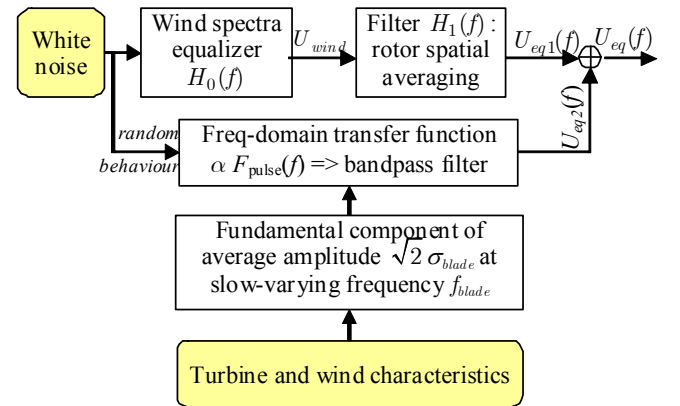


Fig. 46: Simplified block scheme for off-line equivalent wind time series generation (actual rotor angle φ and pitch angle θ are not considered).

A simple second-order bandpass filter can be used. In such case, an extra parameter, the passband bandwidth BW , is used to model how much the rotor speed (and hence, the blade frequency f_{blade}) varies.

$$H_{bandpass}(s) = \frac{2s\sigma_{blade}^2\sqrt{2\pi BW}}{s^2 + 2\pi BWs + (2\pi f_{blade})^2} \quad (70)$$

$$|H_{bandpass}(f)|^2 = \frac{2BWf^2\sigma_{blade}^2/\pi}{BW^2f^2 + (f^2 - f_{blade}^2)^2} \quad (71)$$

$$PSD_{U_{eq}}(f) \approx PSD_{U_{eq_1}}(f) + |H_{bandpass}(f)|^2 \quad (72)$$

In time domain simulations, the full rotational model of Fig. 43 and Fig. 44 is recommended for its low footprint and its high accuracy. The model of Fig. 45 is suitable for frequency domain simulations where the operational conditions of the turbine are known.

When a very simple model of equivalent wind modulation is required, the model of Fig. 46 can be useful. On some circumstances, several band pass filters BW can be connected in parallel to represent the torque harmonics.

3.7. Small signal model of aerodynamic torque

3.7.1. Derivation of the small signal model

A small signal model can be computed using a first-order approximation based on total derivatives of torque T_{rotor} respect squared equivalent wind U_{eq}^2 :

$$\Delta T_{rotor} = T_{rotor} - \langle T_{rotor} \rangle \approx \frac{dT_{rotor}}{d(U_{eq}^2)} \Delta(U_{eq}^2) \quad (73)$$

where $\Delta(U_{eq}^2) = U_{eq}^2 - \langle U_{eq}^2 \rangle$ is the effective quadratic turbulence defined in (29) and ΔT_{rotor} is the turbine torque deviation from its mean, excluding periodic deviations due to rotational sampling (these fluctuations are not related to variations of equivalent wind speed).

Taking into account the torque in function of equivalent wind speed (24) and considering the air density ρ_{air} constant, the total derivative can be computed as:

$$\frac{\Delta T_{rotor}}{\Delta(U_{eq}^2)} \approx \frac{dT_{rotor}}{d(U_{eq}^2)} = \frac{1}{2} \rho_{air} \pi R^3 \frac{d}{d(U_{eq}^2)} [U_{eq}^2 C_q(\lambda, \theta)] \quad (74)$$

where the chain rule can be applied.

$$\frac{d}{d(U_{eq}^2)} [U_{eq}^2 C_q(\lambda, \theta)] = C_q(\lambda, \theta) + U_{eq}^2 \frac{dC_q(\lambda, \theta)}{d(U_{eq}^2)} \quad (75)$$

Based on (74) and (75), the small signal on torque is:

$$\frac{dT_{rotor}}{d(U_{eq}^2)} = \frac{1}{2} \rho_{air} \pi R^3 \left[C_q(\lambda, \theta) + \frac{dC_q(\lambda, \theta)}{d(U_{eq}^2)} U_{eq}^2 \right] \quad (76)$$

The aeroelasticity and the turbine control introduces non-obvious interactions between wind speed through tip speed ratio λ and blade angle θ .

$$\frac{dC_q(\lambda, \theta)}{d(U_{eq}^2)} = \frac{\partial C_q(\lambda, \theta)}{\partial \lambda} \frac{d\lambda}{d(U_{eq}^2)} + \frac{\partial C_q(\lambda, \theta)}{\partial \theta} \frac{d\theta}{d(U_{eq}^2)} \quad (77)$$

Torque fluctuations depend primarily on effective quadratic turbulence. But they depend secondarily on turbine control since the turbine controls θ and Ω_{rotor} .

Tip speed ratio λ and rotor speed Ω_{rotor} are related according to (23). Thus, the first order approximation of aerodynamic torque at the turbine is, in general form: (78)

$$\Delta T_{rotor} \approx \frac{1}{2} \rho_{air} \pi R^3 \Delta(U_{eq}^2) \cdot \left\{ C_q(\lambda, \theta) + U_{eq}^2 \left[\frac{\partial C_q(\lambda, \theta)}{\partial \theta} \frac{d\theta}{d(U_{eq}^2)} + \frac{R}{U_{eq}} \frac{\partial C_q(\lambda, \theta)}{\partial \lambda} \left(\frac{\Omega_{rotor}}{-2U_{eq}^2} + \frac{d\Omega_{rotor}}{d(U_{eq}^2)} \right) \right] \right\}$$

The control influence will be estimated in the following subsections for very slow ($\Delta t \gg 5s$ for a megawatt turbine) or very fast ($\Delta t \ll 5s$ for a megawatt turbine) wind fluctuations.

3.7.2. Classification of turbines according their controllable parameters

A) Speed and blade controlled wind turbine

Controlled turbines can adjust the parameters λ and θ according to the control law. Two main control policies exists

during continuous operation: maximize power output if wind is below rated value and limit power output when wind surpasses rated value. Sometimes, saturable integrators are included in the control scheme to switch smoothly between policies.

B) Fixed speed wind turbine

Squirrel cage induction generators are very reliable, robust, compact and low-cost machines. They have been utilized widespread in wind turbines, directly connected through a soft-starter and sometimes in arrangements which allowed operation at two fixed speeds.

The main drawbacks of fixed speed wind turbines are:

- They operate at low slip (very close to nominal speed). Rotor speed cannot vary significantly to dampen torque oscillations or to optimize aerodynamic efficiency.
- They consume reactive power almost quadratically with load factor, with a significant idle reactive requirement. Capacitor banks are customarily installed in parallel to the generator to control the required power factor.
- They cannot satisfy fault ride-through reactive requirements of most grid codes unless an external system is installed.

Nowadays, the multimegawatt turbines require alleviating structural loads and being able to comply with grid codes. Therefore, fixed speed turbines are less suitable for present turbines and advanced systems allowing bigger speed excursion such as VRIG, DFIG or induction generators connected through power converters are becoming usual (for example, see Hier [115], Sallán-Arasanz [116] or Sanz-Osorio [117]).

In fixed speed turbines, the parameter λ varies inversely proportional to equivalent wind speed and it cannot be controlled.

C) Stall controlled wind turbine

In turbines with variable blade angle θ , it is controlled to achieve maximum power at partial load and limit power at full load. In stall controlled turbines, the blades are designed so that they gradually start stalling their tips at high winds, limiting the power. This concept is robust and reliable but the aerodynamic design is complex, especially in multi-megawatt turbines due to blade fatigue. The stall process is dependent on flow regime and blades are designed so that this process occurs gradually from the tip of the blade. The process of air boundary layer separation present hysteresis and can be characterized through the use of dynamical power or torque coefficients and a state variable (portion of detached flux) to account flow regime.

Stall control of turbines has been widespread in the past and it continues being used in small turbines. However, the need of additional aerodynamic features to stop the turbines has made turbines with variable blade angle θ flavoured by manufactures. Notwithstanding these facts, the control of the turbines decreasing θ at high winds (active stall or stall-induced control) is used by many manufacturers since they present better stability during gusts than conventional pitch control (increasing θ at high winds).

3.7.3. Analysis of fluctuations at characteristic operational points

A) Fast fluctuations at partial generation: $C_P(\lambda, \theta) \approx \text{maximum}$

When the wind U_{eq} increases, the rotor accelerates slowly due to rotor inertia and the tip speed ratio $\lambda = R \Omega_{rotor} / U_{eq}$ changes gradually.

If the turbine is maximizing power output, $\partial C_P(\lambda, \theta) / \partial \lambda \approx 0$ and $\partial C_P(\lambda, \theta) / \partial \theta \approx 0$ since $C_P(\lambda, \theta)$ is maximum. Since the torque coefficient is the power coefficient divided by the tip speed ratio, $C_q(\lambda, \theta) = C_P(\lambda, \theta) / \lambda$, then the following relations holds at maximum $C_P(\lambda, \theta)$:

$$\frac{\partial C_q(\lambda, \theta)}{\partial \theta} = 0 \quad (79)$$

$$\frac{\partial C_q(\lambda, \theta)}{\partial \lambda} = C_P(\theta, \lambda) \frac{\partial \lambda^{-1}}{\partial \lambda} = -\frac{C_q(\lambda, \theta)}{\lambda} \quad (80)$$

$$\frac{dC_q(\lambda, \theta)}{dU_{eq}^2} = C_P(\lambda, \theta) \frac{d\lambda^{-1}}{dU_{eq}^2} = C_q(\lambda, \theta) \left(\frac{1}{2U_{eq}^2} - \Omega_{rotor}^{-1} \frac{d\Omega_{rotor}}{d(U_{eq}^2)} \right) \quad (81)$$

Now, the influence of effective quadratic turbulence on torque can be estimated using the chain rule:

$$\frac{\Delta T_{rotor}}{\Delta(U_{eq}^2)} \approx \frac{1}{2} \rho_{air} \pi R^3 C_q(\lambda, \theta) \left(1 + \frac{1}{2} - \frac{U_{eq}^2}{\Omega_{rotor}} \frac{d\Omega_{rotor}}{d(U_{eq}^2)} \right) \quad (82)$$

Thus, a first-order small-signal model can be estimated from $dT_{rotor}/d(U_{eq}^2)$ in (82), assuming operation at maximum turbine efficiency ($C_P(\lambda, \theta) \approx \text{constant}$ at wind lower than rated speed):

$$\Delta T_{rotor} \approx \frac{1}{2} \rho_{air} \pi R^3 C_q(\lambda, \theta) \left(\frac{3}{2} - \frac{U_{eq}^2}{\Omega_{rotor}} \frac{d\Omega_{rotor}}{d(U_{eq}^2)} \right) \Delta(U_{eq}^2) \quad (83)$$

(assuming turbine operation at maximum efficiency)

For constant speed turbines and for variable speed turbines operating around maximum or minimum rotor speed, $d\Omega_{rotor}/d(U_{eq}^2) \ll \Omega_{rotor}/U_{eq}^2$ and hence:

$$\frac{dC_q(\lambda, \theta)}{dU_{eq}^2} \approx \frac{C_q(\lambda, \theta)}{2U_{eq}^2} \quad (84)$$

Finally, the small signal model (85) has been estimated from (82) assuming $C_P(\theta, \lambda)$ and Ω_{rotor} fairly constant. Thus, fast fluctuations of $\Delta(U_{eq}^2)$ are reflected in turbine tower almost proportionally:

$$\Delta T_{rotor} \approx \frac{3}{4} \rho_{air} \pi R^3 C_q(\lambda, \theta) \Delta(U_{eq}^2) \quad (85)$$

(assuming turbine operation at maximum efficiency and at constant speed)

In other words, the torque variation is approximately proportional to the effective quadratic turbulence $\Delta(U_{eq}^2)$ with gain $\frac{3}{4} \rho_{air} \pi R^3 C_q(\theta, \lambda)$ if the turbine is operating at maximum efficiency and there is not significant energy storage in the rotor.

B) Fast fluctuations at full generation

Beyond rated wind, the generator torque control tries to maintain Ω_{rotor} almost constant varying the generator power.

The rotor torque can be estimated assuming $d\Omega_{rotor}/d(U_{eq}^2) \sim 0$ since a low $d\Omega_{rotor}/d(U_{eq}^2)$ is required for avoiding over-speeding and for limiting the value of $C_P(\lambda, \theta)$.

Moreover, the blade angle θ does not change significantly in very short intervals due to its inertia and its actuator limitations. Therefore, if $d\theta/d(U_{eq}^2) \sim 0$ for short intervals then (78) can be further simplified into:

$$\Delta T_{rotor} \approx \frac{1}{2} \rho_{air} \pi R^3 \Delta(U_{eq}^2) \left[C_q(\lambda, \theta) - \frac{\lambda}{2} \frac{\partial C_q(\lambda, \theta)}{\partial \lambda} \right] \quad (86)$$

(assuming θ and Ω_{rotor} constant)

This approximate formula (86) is valid wherever θ and Ω_{rotor} are judiciously constant.

In pitch regulated turbines, the regulation of $C_q(\lambda, \theta)$ is slower than in active-stall turbines, (i.e. $\partial C_q(\lambda, \theta) / \partial \theta$ and $\partial C_q(\lambda, \theta) / \partial \lambda$ have lower values in pitch regulated turbines).

C) Stall operation

The aerodynamic torque coefficient in (24) is estimated from steady state operating points. The hypothesis that torque coefficient only depends on θ and λ underestimates the actual power fluctuations in the stall region due to flow separation hysteresis. Therefore the aerodynamic model can be improved by taking the dynamic stall effects into account through a dynamic torque coefficient $C_q^{dynamic}(\lambda, \theta)$ –see [118, 119] for details.

D) Slow fluctuations (quasi-static approximation)

During slow wind variations, the control adjusts the blade angle θ and the rotor speed Ω_{rotor} to their optimal values. On the one hand, the torque variations should be computed from the general formula (78) since the variation of θ and Ω_{rotor} cannot be neglected.

On the other hand, wind turbine dynamics are negligible provided the fluctuations are slow enough for the static approximation to remain valid. Thus, the torque can be alternatively estimated based on the power curve in function of the squared effective wind $P_{turbine}(U_{eq}^2)$ and the overall efficiency of the mechanical transmission (mainly the gearbox) and generator, $\eta_{mec+gen}$.

$$T_{rotor} \approx \frac{P_{turbine}(U_{eq}^2)}{\eta_{mec+gen} \Omega_{rotor}} \quad (87)$$

Thus, the small signal model of torque based on the power curve (valid only for slow fluctuations) is:

$$\Delta T_{rotor} \approx \frac{dT_{rotor}}{d(U_{eq}^2)} \Delta(U_{eq}^2) = \frac{\Delta(U_{eq}^2)}{\eta_{mec+gen} \Omega_{rotor}} \left[\frac{dP_{turbine}(U_{eq}^2)}{d(U_{eq}^2)} - \frac{P_{turbine}(U_{eq}^2)}{\Omega_{rotor}} \frac{d\Omega_{rotor}}{d(U_{eq}^2)} \right] \quad (88)$$

(assuming quasi-static operation)

For slower fluctuations bellow rated speed, the turbine can be considered operating at maximum efficiency (control policy: maximize power bellow rated speed). Then λ , θ and $C_P(\theta, \lambda)$ are close to the optimum values and $C_q(\theta, \lambda)$ is approximately constant. Thus, equation (85) is a good approximation and the torque is proportional to the square of the equivalent wind speed.

During slower fluctuations above rated wind speed, the turbine limits the power and rotor speed. Therefore, the torque is unaffected by slower fluctuations beyond rated speed:

$$T_{rotor,limit\ power} \approx \frac{P_{turbine\ max}}{\eta_{mec+gen} \Omega_{rotor,max}} \approx constant \quad (89)$$

Thus, the torque variations are negligible under the quasi-static approximation at constant power:

$$\Delta T_{rotor,limit\ power} \approx -\frac{P_{turbine\ max}}{\Omega_{rotor,max}^2} \frac{d\Omega_{rotor,max}}{d(U_{eq}^2)} \sim 0 \quad (90)$$

(assuming quasi-static operation at constant power)

3.7.4. Small signal approximation of effective quadratic turbulence $\Delta(U_{eq}^2)$ on equivalent turbulence ΔU_{eq} .

When the wind turbines are generating, a small-signal model based on wind speed deviations ΔU_{eq} can be obtained since $U_{eq} \gg \Delta U_{eq}$:

$$U_{eq}^2 = [\langle U_{eq} \rangle + \Delta U_{eq}]^2 = \langle U_{eq} \rangle^2 + 2\langle U_{eq} \rangle \Delta U_{eq} + (\Delta U_{eq})^2 \approx \langle U_{eq} \rangle^2 + 2\langle U_{eq} \rangle \Delta U_{eq} + \langle (\Delta U_{eq})^2 \rangle = \langle U_{eq}^2 \rangle + 2\langle U_{eq} \rangle \Delta U_{eq} \quad (91)$$

Notice that the average of $(\Delta U_{eq})^2$ is the equivalent turbulence parameter or more precise, the variance of the equivalent wind, $\langle (\Delta U_{eq})^2 \rangle = \langle U_{eq}^2 \rangle - \langle U_{eq} \rangle^2$. Therefore the following relationship is also hold:

$$\Delta(U_{eq}^2) = U_{eq}^2 - \langle U_{eq}^2 \rangle = U_{eq}^2 - \langle U_{eq} \rangle^2 - \langle (\Delta U_{eq})^2 \rangle = 2\Delta U_{eq} \langle U_{eq} \rangle + (\Delta U_{eq})^2 - \langle (\Delta U_{eq})^2 \rangle \quad (92)$$

For relatively small variations of wind, the following first-order approximation is valid:

$$\Delta(U_{eq}^2) \approx 2\langle U_{eq} \rangle \Delta U_{eq} \quad (93)$$

Therefore, the relation between the power spectral densities of the equivalent speed and its square are:

$$PSD_{\Delta(U_{eq}^2)}(f) \approx (2\langle U_{eq} \rangle)^2 PSD_{\Delta U_{eq}}(f) \quad \forall f \neq 0 \quad (94)$$

3.7.5. Influence of turbine control

The measurement system shown in the second chapter has been installed on two models of doubly-fed induction generator (DFIG) wind turbines (WT) from GAMESA with several control configurations, in a variable resistor induction generator (VRIG) turbine from VESTAS and two models of squirrel cage induction generator (SQIG) turbine from TAIM-NEG MICON (now VESTAS).

The turbine behaviour relies heavily on the control scheme and their fine-tuned parameters. The usual schemes are available in the literature (see the thesis of Comech-Moreno [120] and Akhmatov [121], or the book from Bianchi, De Battista and Mantz [122]) but the turbine manufacturers are very reluctant to provide the control parameters.

The derivatives $d\theta/d(U_{eq}^2)$ or $d\Omega_{rotor}/d(U_{eq}^2)$ in (78) are difficult to estimate analytically since they depend on turbine control. If no information on the control is available, it can be

assumed that the dynamic of θ and Ω_{rotor} are dominated by the blade and rotor inertias, respectively.

Neither the drivetrain nor the generator is modelled in this work due to unavailability of the turbine and its control characteristics. The transfer functions in this thesis are estimated only from measurements since full turbine simulations are out of the scope of this thesis.

For small torque variations, a linear model can be enough. Inertia constant of multimegawatt turbines is in the range of 8 s (ratio of kinetic energy in the drivetrain to turbine assigned power). The drivetrain, with its torsion stiffness and its small damping is often modelled as a second order (see for example Comech [120]). The electromagnetic transients are usually fast compared to turbulence and to the inertia. The control influences notably the dynamics. In some turbines, it has been observed experimentally the noticeable changes in the behaviour after updating control parameters and/or software.

Some turbine transfer functions are available in the literature for induction generators (see for example the book from Ong [123] and Lesieutre [124]), self-excited induction generator (see for example the review from [125], Melkebeek [126] and Uçtug [127]), doubly-fed induction generator (see Comech-Moreno [120], Akhmatov [121], Wu [128], Nagaria [129] and the book from Bianchi et al. [122]), full converter generators (see for example Erikson [130] and [131]) and hybrid configurations (see for example Sallán-Arasanz [116] or Sanz-Osorio [117]).

3.8. Equivalent wind of turbine clusters

3.8.1. Equivalent wind of a farm

A) Average farm behaviour

Sometimes, a reduced model of the whole wind farm is very useful for simulating a wind farm in the grid. The behaviour of a network with wind generation can be studied supplying the farm equivalent wind as input to a conventional turbine model connected to the equivalent grid.

The foundations of these models, their usual conventions and their limitations can be seen in [120, 132, 133, 134]. The average power and torque in the turbines and in the farm are the same on per unit values. This can be a significant advantage for the simulation since most parameters do not have to be scaled. Notice that if electrical values are not expressed *per unit*, currents and network parameters have to be properly scaled.

For convenience, all the N turbines of a wind farm are represented with a single turbine of radius R_{farm} spinning at angular speed Ω_{farm} . The equivalent power, torque, wind, rotor speed, pitch and voltage are their average among the turbines of the farm. Thus, the equivalent turbine represents the average operation among the farm turbines.

If the turbines are different or their operational conditions are dissimilar, the averages are weighted by the turbine power (because the aim of this work is to reproduce the power output of farms). Elsewhere, the farm averaged parameters can be approximated by a conventional arithmetic mean. The average along the turbines will be notated as $\langle x_i \rangle_{turbines}$.

The equivalent farm mechanical power P_{farm} is the average of the individual mechanical powers along turbine rotors:

$$P_{farm} = \langle P_i \rangle_{turbines} = \sum_{i=1}^N \frac{P_{turbine,i}}{N} \quad (95)$$

where subindex i indicate that the parameters refer to the turbine i .

The equivalent farm torque can be derived from farm power:

$$(95) \Rightarrow \Omega_{farm} T_{farm} = \sum_{i=1}^N \frac{\Omega_{rotor,i} T_{rotor,i}}{N} \quad (96)$$

Thus, farm torque can be defined as:

$$\begin{aligned} T_{farm} &= \langle T_{rotor,i} \rangle_{turbines} = \frac{\sum_{i=1}^N P_{turbine,i}}{\Omega_{farm} N} \\ &= \frac{\sum_{i=1}^N \Omega_{rotor,i} T_{rotor,i}}{\Omega_{farm} N} \end{aligned} \quad (97)$$

Taking into account relationship (24), the farm torque is:

$$T_{farm} = \frac{1}{2} \rho_{air} \pi \sum_{i=1}^N U_{eq,i}^2 \frac{\Omega_{rotor,i}}{\Omega_{farm} N} R_i^3 C_{q,i}(\lambda_i, \theta_i) \quad (98)$$

The equivalent farm wind is derived assuming a similar relationship to (24) with an equivalent wind farm torque coefficient $C'_q(\theta_{farm}, \lambda_{farm})$:

$$T_{farm} = \frac{1}{2} \rho_{air} \pi U_{eq,farm}^2 R_{farm}^3 N C'_q(\lambda_{farm}, \theta_{farm}) \quad (99)$$

The average tip speed ratio λ_{farm} , the equivalent rotor speed Ω_{farm} and the average blade angle θ_{farm} are typically estimated in the turbine model. However, they can be alternatively estimated as the weighted average of the actual turbine values according to formulas (100) and (102).

$$\langle \theta_i \rangle_{turbines} = \frac{\sum_{i=1}^N P_{turbine,i} \theta_i}{P_{farm} N} \approx \theta_{farm} \quad (100)$$

$$\langle \lambda_i \rangle_{turbines} = \frac{\sum_{i=1}^N P_{turbine,i} \lambda_i}{P_{farm} N} \approx \lambda_{farm} \quad (101)$$

$$\langle \Omega_{rotor,i} \rangle_{turbines} = \frac{\sum_{i=1}^N P_{turbine,i} \Omega_{rotor,i}}{P_{farm} N} \approx \Omega_{farm} \quad (102)$$

The power considered for computing the weighted averages (100) to (103) can be the mechanical power at the turbine rotor, the electrical power output and the nominal power output (in decreasing order of model accuracy). Notice that even if $P_{turbine,i}$ were considered the electrical power output of the turbine, then P_{farm} would be the output of the farm plus the losses inside the farm grid. Notice that whichever representation is selected for $P_{turbine,i}$, the calculus of the rest of global parameters must be congruent.

The turbine radius is a constructive property of the turbine. If a wind farm is composed by several types of turbines, the equivalent radius can be computed as the average of rotor areas weighted by the turbine nominal power (other constructive parameter):

$$R_{farm} = \langle R_i \rangle_{turbines} = \frac{\sum_{i=1}^N P_{turbine,i} R_i}{P_{farm} N} \quad (103)$$

The weighted average of squared radius produces a higher fidelity in power (104) whereas the linear average (103) produce more accuracy of tip speed ratio.

$$R_{farm}^2 = \langle R_i^2 \rangle_{turbines} = \frac{\sum_{i=1}^N P_{turbine,i} R_i^2}{P_{farm} N} \quad (104)$$

The standard IEC 61400-123 defines a methodology to compute the power curve of a whole wind farm. Based in this power curve, a wind farm torque coefficient $C'_q(\lambda_{farm}, \theta_{farm})$ can be estimated. Basically, $C'_q(\lambda_{farm}, \theta_{farm})$ is the turbine torque coefficient $C_{q,i}(\lambda_i, \theta_i)$ scaled and smoothed to take into account the diverse operational points of the different wind turbines.

$$C'_q(\lambda_{farm}, \theta_{farm}) = \frac{\sum_{i=1}^N \Omega_{rotor,i} R_i^3 C_{q,i}(\lambda_i, \theta_i)}{\Omega_{farm} R_{farm}^3 N} \sim \sum_{i=1}^N \frac{C_{q,i}(\lambda_i, \theta_i)}{N} \quad (105)$$

$$C'_q(\lambda_{farm}, \theta_{farm}) \sim \langle C_{q,i}(\lambda_i, \theta_i) \rangle_{turbines} \quad (106)$$

The wind farm equivalent wind is implicitly defined from the previous relationship as:

$$U_{eq,farm}^2 = \frac{\sum_{i=1}^N \Omega_{rotor,i} R_i^3 C_{q,i}(\lambda_i, \theta_i) U_{eq,i}^2}{N \Omega_{farm} R_{farm}^3 C'_q(\lambda_{farm}, \theta_{farm})} \approx \langle U_{eq,i}^2 \rangle_{turbines}$$

or, equivalently, as:

$$U_{eq,farm}^2 = \frac{\sum_{i=1}^N P_{turbine,rotor,i} / N}{\frac{1}{2} \rho_{air} \pi \Omega_{farm} R_{farm}^3 C'_q(\lambda_{farm}, \theta_{farm})} \quad (108)$$

The effective quadratic turbulence of the wind farm $\Delta(U_{eq,farm}^2)$ is defined as:

$$\Delta(U_{eq,farm}^2) = \frac{\sum_{i=1}^N \Omega_{rotor,i} R_i^3 C_{q,i}(\lambda_i, \theta_i) \Delta U_{eq,i}^2}{N \Omega_{farm} R_{farm}^3 C'_q(\lambda_{farm}, \theta_{farm})} \quad (109)$$

or, equivalently, as:

$$\Delta(U_{eq,farm}^2) = \frac{\sum_{i=1}^N \Delta P_{turbine,rotor,i} / N}{\frac{1}{2} \rho_{air} \pi \Omega_{farm} R_{farm}^3 C'_q(\lambda_{farm}, \theta_{farm})} \quad (110)$$

A small-signal model of the wind farm can be derived from the previous relationships:

$$\Delta(U_{eq,farm}^2) \approx \sum_{i=1}^N b_i \Delta(U_{eq,i}^2) \quad (111)$$

where the sensitivity factor of wind farm equivalent wind respect turbine equivalent wind b_i is:

$$b_i = \frac{d U_{eq,farm}^2}{d U_{eq,i}^2} = \frac{\sum_{i=1}^N \Omega_{rotor,i} R_i^3 C_{q,i}(\lambda_i, \theta_i) / N}{\Omega_{farm} R_{farm}^3 C'_q(\lambda_{farm}, \theta_{farm})} \quad (112)$$

and the farm sensitivity vector is notated $\vec{b}_{farm} = [b_i]$.

The equivalent farm wind can be estimated as a weighted sum of joint Gaussian processes [135, 136] corresponding to the equivalent squared turbine wind. Thus, the turbine wind spectra $\Delta U_{eq,i}(f)$ are joint complex normal random variables $\forall 1 \leq i \leq N$ and the coherence can be used to compute an equivalent wind speed for the whole wind farm according to (22).

If all the turbines are equal and they are operating near the same operational points — $\theta_i(t) \approx \theta_{farm}(t) = \theta(t)$ and $\lambda_i(t) \approx \lambda_{farm}(t) \approx \lambda(t)$ — then $b_i \approx 1/N$. (113)

a) Model based in equivalent squared wind

In general, $\Delta(U_{eq,farm}^2)(t)$ —defined analogously to (73)— is not a Gaussian process. However, an instantaneous transformation can be used to obtain a process with the same stationary probability as the actual one.

Assuming that the equivalent squared wind at the different wind turbines behaves as a multivariate Gaussian process with spectral covariance matrix:

$$\Xi_{U^2_{eq}}(f) = \left[\vec{\gamma}'_{ij}(f) \sqrt{PSD_{U^2_{eq,i}}(f) PSD_{U^2_{eq,j}}(f)} \right] \quad (114)$$

Thus, the $PSD_{U^2_{eq,farm}}(f)$ of the equivalent squared wind for the farm can be computed as:

$$\begin{aligned} PSD_{U^2_{eq,farm}}(f) &= \vec{b}_{farm}^T \Xi_{U^2_{eq}}(f) \vec{b}_{farm} \\ &= \sum_{i=1}^N \sum_{j=1}^N b_i b_j \vec{\gamma}'_{ij}(f) \sqrt{PSD_{U^2_{eq,i}}(f) PSD_{U^2_{eq,j}}(f)} \end{aligned} \quad (115)$$

where $\vec{\gamma}'_{ij}(f)$ is the complex coherence of effective quadratic turbulence at frequency f .

If all the turbines experience similar equivalent squared wind spectra — $PSD_{U^2_{eq,i}}(f) \approx PSD_{U^2_{eq}}(f)$ — and their contribution to the farm is similar — $b_i \approx 1/N$ — then the following approximate formula is valid:

$$PSD_{U^2_{eq,farm}}(f) \approx \frac{PSD_{U^2_{eq}}(f)}{N^2} \sum_{i=1}^N \sum_{j=1}^N \vec{\gamma}'_{ij}(f) \quad (116)$$

Notice that $\vec{\gamma}'_{ii}(f) = 1$ and $0 \leq |\vec{\gamma}'_{ij}(f)| \leq 1$. Since the real part of $\vec{\gamma}'_{ij}(f)$ is usually positive or close to zero (i.e., non-negative correlation of fluctuations), $PSD_{U^2_{eq,farm}}(f)$ is generally between the behaviour of perfectly correlated and independent fluctuations at the turbines.

$$\frac{PSD_{U^2_{eq}}(f)}{N} \lesssim PSD_{U^2_{eq,farm}}(f) \leq \frac{PSD_{U^2_{eq}}(f)}{N^2} \quad (117)$$

if $0 \lesssim \text{Re}[\vec{\gamma}'_{ij}(f)]$

b) Model based in equivalent wind

The properties of the effective quadratic turbulence are not available usually. A second-order approximation based on (93) and (118) can be used to obtain its characteristics:

$$\Delta(U_{eq,farm}^2)(t) \approx 2 \Delta U_{eq,farm}(t) \langle U_{eq,farm} \rangle \quad (118)$$

The wind farm model based in equivalent wind speed assumes that the equivalent wind at the wind turbines behaves as a multivariate Gaussian process with covariance matrix:

$$\Xi'_{U^2_{eq}}(f) = \left[4 \langle U_{eq,i} \rangle \langle U_{eq,j} \rangle \vec{\gamma}_{ij}(f) \sqrt{PSD_{U_{eq,i}}(f) PSD_{U_{eq,j}}(f)} \right] \quad (119)$$

where $\vec{\gamma}_{ij}(f)$ is the complex coherence of equivalent turbulence at frequency f —as the coherence for Høvsøre (22)— and $PSD_{U^2_{eq,i}}(f)$ can be computed through (45).

The equivalent turbulence coherence and the effective quadratic coherence are roughly equivalent, $\vec{\gamma}'_{ij}(f) \approx \vec{\gamma}_{ij}(f)$, provided the second-order approximations (93) and (118) are valid:

$$\begin{aligned} \vec{\gamma}'_{ij}(f) &= \frac{\left\langle \overrightarrow{U_{eq,i}^2}(f) \cdot \overrightarrow{U_{eq,j}^2}(f)^* \right\rangle}{\sqrt{\left\langle \left| \overrightarrow{U_{eq,i}^2}(f) \right|^2 \right\rangle \left\langle \left| \overrightarrow{U_{eq,j}^2}(f) \right|^2 \right\rangle}} \approx \\ &\approx \frac{4 \langle U_{eq,i} \rangle \langle U_{eq,j} \rangle \left\langle \overrightarrow{U_{eq,i}}(f) \cdot \overrightarrow{U_{eq,j}}(f)^* \right\rangle}{4 \langle U_{eq,i} \rangle \langle U_{eq,j} \rangle \sqrt{\left\langle \left| \overrightarrow{U_{eq,i}}(f) \right|^2 \right\rangle \left\langle \left| \overrightarrow{U_{eq,j}}(f) \right|^2 \right\rangle}} = \vec{\gamma}_{ij}(f) \end{aligned} \quad (120)$$

And the spectral density of quadratic coherence, expressed with equivalent turbulence complex coherence, is: (121)

$$\begin{aligned} PSD_{U^2_{eq,farm}}(f) &= \vec{b}_{farm}^T \Xi'_{U^2_{eq}}(f) \vec{b}_{farm} \\ &= \sum_{i=1}^N \sum_{j=1}^N 4 \langle U_{eq,i} \rangle \langle U_{eq,j} \rangle \vec{\gamma}_{ij}(f) b_i b_j \sqrt{PSD_{U_{eq,i}}(f) PSD_{U_{eq,j}}(f)} \end{aligned}$$

If the turbines experience the same equivalent wind spectra, $PSD_{U_{eq,i}}(f) \approx PSD_{U_{eq}}(f)$, their equivalent average wind speed is similar, $\langle U_{eq,i} \rangle \approx \langle U_{eq} \rangle$, and their contribution to the farm is similar ($b_i \approx 1/N$), then the following approximate formula for the effective quadratic wind speed is valid: (122)

$$PSD_{U^2_{eq,farm}}(f) \approx 4 \langle U_{eq} \rangle^2 \frac{PSD_{U_{eq}}(f)}{N^2} \sum_{i=1}^N \sum_{j=1}^N \vec{\gamma}_{ij}(f)$$

Assuming that $\langle U_{eq} \rangle \approx \langle U_{eq,farm} \rangle$, then the model for the equivalent speed is valid:

$$PSD_{U_{eq,farm}}(f) \approx \frac{PSD_{U_{eq}}(f)}{N^2} \sum_{i=1}^N \sum_{j=1}^N \vec{\gamma}_{ij}(f) \quad (123)$$

and

$$\frac{PSD_{U_{eq}}(f)}{N} \lesssim PSD_{U_{eq,farm}}(f) \leq \frac{PSD_{U_{eq}}(f)}{N^2} \quad (124)$$

B) Equivalent wind farm filter

The rotor angle of each turbine is random and independent of the rest of the turbines due to the lack of noticeable synchronizing forces. The torque modulation of many turbines with random phases is a stochastic process that will be studied in detail in the next section.

Since the tower shadow is quite narrow (the blades and the tower are quite slim), the probability of several simultaneous tower shadows is small. Moreover, the shape of the torque dip at the rotor due to tower shadow is heavily smoothed at the output of the drivetrain due to the elasticity of the drivetrain and the high inertias in the turbine.

Thus, the main effect of torque modulation —apart from the fatigue on the blades and on the drivetrain— is the excitation of vibration modes of the blades, drivetrain and generator of each turbine. Many frequencies of vibration are not harmonic, resulting into stochastic processes characterized primarily by their PSD (in a linear system, vibration modes are fed by the frequency content of the torque, irrespectively of its original shape).

Thus, it is sensible to model rotational sampling only by the PSD of the equivalent wind modulation. Since each turbine angle is independent of the rest of the turbines, there is a partial cancelation of power fluctuations along the farm. Thus, the equivalent wind will present —in average— an

angular modulation inversely proportional to the number of turbines of the farm.

If different turbines are installed in the farm, an average shape of the torque modulation can be estimated but, in many cases, it would be more practical to simulate the turbines aggregated in groups of the same characteristics.

In Fig. 52, the spatial diversity smoothing filter $H_3(f)$ and the aerodynamic rotor filter $H_1(f)$ account for the spatial variation of wind computed in a region or in the turbine rotor, respectively. $H_3(f)$ is related to the PSD of the equivalent wind of a representative turbine and of the wind farm:

$$|H_3(f)|^2 = \frac{PSD_{U_{eq, farm}}(f)}{PSD_{U_{eq}}(f)} \approx \frac{1}{N^2} \sum_{i=1}^N \sum_{j=1}^N \tilde{\gamma}_{ij}(f) \quad (125)$$

For simplicity, $H_3(f)$ can be estimated from the equivalent turbulence coherences among turbines. Since the phase of the white noise is random, the phase of the filter $H_3(f)$ do not alter the statistical properties of the farm wind. According to (123), a simple estimation of $H_3(f)$ is:

$$H_3(f) \approx \frac{1}{N} \sqrt{\sum_{i=1}^N \sum_{j=1}^N \tilde{\gamma}_{ij}(f)} \quad (126)$$

3.8.2. Equivalent wind of turbines distributed along a geographical area

The turbines are grouped into farms, and some farms are concentrated around the geographical spots with higher wind potential. Thus, the approach used to compute the equivalent wind of a wind farm can be iterated for a cluster of wind farms.

However, this subsection presents another approach valid when the wind farms are fairly distributed across a region. This approach accounts the asymptotic wind smoothing due to geographical dispersion of the wind farms. This subsection relates the dimensions of a geographical area with the smoothing of the equivalent wind of that area.

In (22), a model of complex root coherence $\tilde{\gamma}_{rc}(f)$ was introduced based on the works of Schlez and Infield [45] in the Rutherford Appleton Laboratory and Sørensen et Al. [85] in the Høvsøre offshore wind farm. In (116), a formula was derived assuming all the turbines experience a similar wind and they have similar characteristics.

In this section, the decrease of variability of the equivalent wind of a geographical area due to its spatial diversity is computed in (127) from the variability at a single turbine or a single farm and from the complex root coherence $\tilde{\gamma}_{rc}(f)$.

Formula (127) assumes that wind turbines are approximately evenly spread over the area corresponding to the integrating limits. Even though the former assumptions are oversimplifications of the complex meteorological behaviour and wakes have been neglected, (127) indicates the general trend in the decrease of wind power variability due to spatial diversity in bigger areas. Notice that $PSD_{U_{eq, turbine}}(f)$ is assumed to be representative of the average turbulence experienced by turbines in the region and hence, it must account average wake effects. Even though the model is not accurate enough for most applications, it leads to expression (132) that links the smoothing effect of the spatial diversity of wind generators in an area and its dimensions.

Since $\tilde{\gamma}_{rc}(f)$ in (22) is expressed in terms of the power spectral density of the wind, $PSD_{U_{eq}}(f)$, the model presented here will be also referred to $PSD_{U_{eq}}(f)$, which is more usual than $PSD_{U_{eq}^2}(f)$ –which is more closely related to aerodynamic force and torque fluctuations. Notice that the variations of the wind and the variations of its square are closely related through the first order approximation $\Delta(U_{eq}^2) \approx 2\langle U_{eq} \rangle \Delta U_{eq}$ (31) and thus $PSD_{\Delta(U_{eq}^2)}(f) \approx 4\langle U_{eq} \rangle^2 PSD_{\Delta U_{eq}}(f)$ (32).

The coherence $\tilde{\gamma}_{rc}(f)$ between points $r=(x_1, y_1)$ and $c=(x_2, y_2)$ inside the wind farm can be derived from Fig. 47 and formulas (20), (21) and (22). The geometric distance between them is $d_{rc}=|(x_2, y_2)-(x_1, y_1)|= [(y_2-y_1)^2 + (x_2-x_1)^2]^{1/2}$ and the angle between the line that links the two points and the wind direction is $\alpha_{rc}=\beta - \text{ArcTan}[(y_2-y_1)/(x_2-x_1)]$. In the general case, the equivalent wind taking into account the spatial diversity can be computed extending formula (123) to the continuous case:

$$\frac{PSD_{U_{eq, area}}(f)}{PSD_{U_{eq, turb}}(f)} \approx \frac{\int_{-b/2}^{b/2} \int_{-a/2}^{a/2} \int_{-b/2}^{b/2} \int_{-a/2}^{a/2} \tilde{\gamma}_{rc}(f, d_{rc}, \alpha_{rc}) dx_2 dx_1 dy_2 dy_1}{\int_{-b/2}^{b/2} \int_{-a/2}^{a/2} dx_2 dx_1 dy_2 dy_1}$$

where the quadruple integral in the denominator is a fourth of the squared area, i.e., $a^2 b^2/4$.

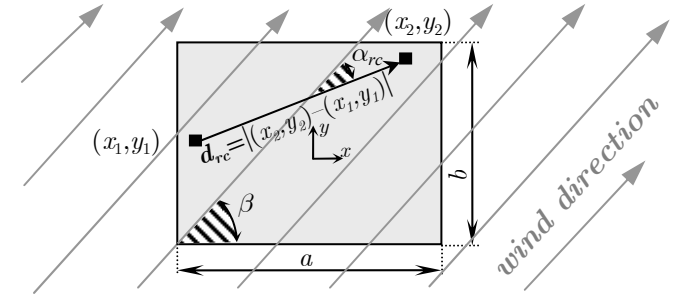


Fig. 47: Wind farm dimensions, angles and distances among wind farm points for the general case.

Due to the complexity of d_{rc} and α_{rc} and the estimation of $\tilde{\gamma}_{rc}(f, d_{rc}, \alpha_{rc})$ in formula (22), no analytical closed form of (127) have been found for the general case.

In case wind has x direction as in Fig. 48, then the coherence has a simpler expression:

$$\tilde{\gamma}_{rc}(f, d_{rc}, \alpha_{rc}) = \exp \left[\frac{-f}{\langle U_{wind} \rangle} \left(\sqrt{[A_{long}(x_2-x_1)]^2 + [A_{lat}(y_2-y_1)]^2} + j2\pi(x_2-x_1) \right) \right] \quad (128)$$

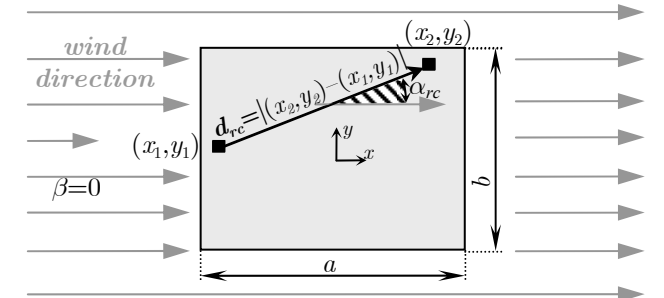


Fig. 48: Wind farm parameters when wind has the x direction ($\beta=0$).

The presence of the squared root in (128) prevents from obtaining an analytical $PSD_{U_{eq,area}}(f)$. In case $aA_{long} \ll bA_{lat}$ the region can be considered a thin column of turbines transversally aligned to the wind. This is the case of many wind farms where turbine layout has been designed to minimize wake loss (see Fig. 50) and areas where wind farms or turbines are sited in mountain ridges, in seashores and in cliff tops perpendicular to the wind. Since $A_{long}(x_2-x_1) \ll A_{lat}(y_2-y_1)$, then $PSD_{U_{eq,area}}(f)$ can be computed analytically as:

$$\frac{PSD_{U_{eq,lat\ area}}(f)}{PSD_{U_{eq,turb}}(f)} \approx f_7 \left(\frac{A_{lat} b f}{\langle U_{wind} \rangle} \right) \quad (129)$$

where $f_7(x) = 2(-1 + e^{-x} + x) / x^2$

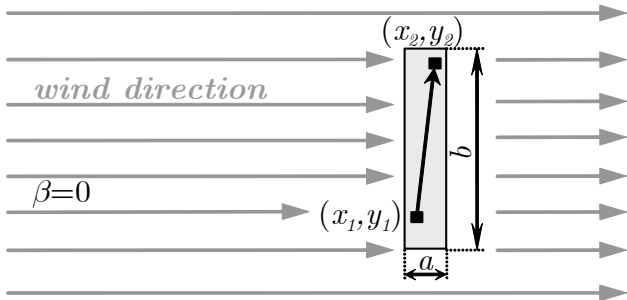


Fig. 49: Wind farm with turbines aligned transversally to the wind.

In case $aA_{long} \gg bA_{lat}$, the region can be considered a thin row of wind farms longitudinally aligned to the wind. This is the case of many areas where wind farms are disposed in a gorge, canyon, valley or similar where wind is directed in the feature direction (see Fig. 50). Since $A_{long}(x_2-x_1) \gg A_{lat}(y_2-y_1)$, then $PSD_{U_{eq,area}}(f)$ can be computed analytically as:

$$\frac{PSD_{U_{eq,long\ area}}(f)}{PSD_{U_{eq,turb}}(f)} \approx \text{Re} \left\{ f_7 \left(\frac{(A_{long} + j2\pi) a f}{\langle U_{wind} \rangle} \right) \right\} \quad (130)$$

where $\text{Re} \left\{ f_7 \left(\frac{(A_{long} + j2\pi) a f}{\langle U_{wind} \rangle} \right) \right\} = f_8 \left(\frac{A_{long} a f}{\langle U_{wind} \rangle}, A_{long} \right)$

which can be expressed with real functions as:

$$f_8(\nu, A_{long}) = \quad (131)$$

$$\frac{(\nu-1) + (\nu+1) \left(\frac{2\pi}{A_{long}} \right)^2 + \frac{\left\{ \left[1 - \left(\frac{2\pi}{A_{long}} \right)^2 \right] \text{Cos} \left[\frac{2\pi\nu}{A_{long}} \right] - \frac{4\pi}{A_{long}} \text{Sin} \left[\frac{2\pi\nu}{A_{long}} \right] \right\}}{e^\nu}}{\frac{1}{2} \nu^2 \left(1 + \left(\frac{2\pi}{A_{long}} \right)^2 \right)^2}$$

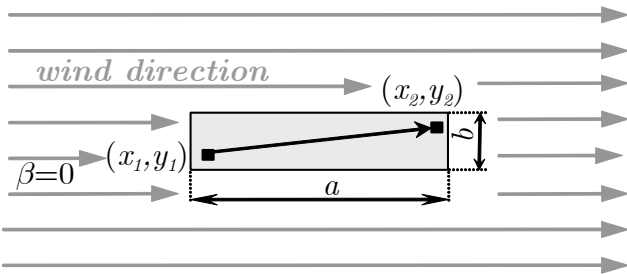


Fig. 50: Wind farm with turbines aligned longitudinally to the wind.

Notice that (130) includes an imaginary part that is due to the frozen turbulence model in formula (22). A wind wave travels at wind speed, producing an spatially average PSD

that depends on the longitudinal length a relative to the wavelength. For long wavelengths compared to the longitudinal dimension of the area ($A_{long} \gg 2\pi$), the imaginary part in (130) can be neglected and (130) simplifies to (129). This is the case of the Rutherford Appleton Laboratory, where Schlez and Infield [45] fitted the longitudinal decay factor to $A_{long} \approx (15 \pm 5) \langle U_{wind} \rangle / \sigma_{U_{wind}}$ for distances up to 102 m.

But when the wavelengths are similar or smaller than the longitudinal dimension, ($A_{long} \lesssim 2\pi$), then the fluctuations are notably smoothed. This is the case of the Høvsøre offshore wind farm, where Sørensen et Al. [85] fitted the longitudinal decay factor to $A_{long} = 4$ for distances up to 2 km. In plain words, the disturbances travels at wind speed in the longitudinal direction, not arriving at all the points of the area simultaneously (see Fig. 5 for clarity) and thus, producing an average wind smoother in longitudinal areas than in transversal regions.

In the normalized longitudinal and transversal distances have the same order, then (127) can be estimated as the compound of many stacked longitudinal or transversal areas (see Fig. 51):

$$\frac{PSD_{U_{eq,rect\ area}}(f)}{PSD_{U_{eq,turb}}(f)} = \frac{PSD_{U_{eq,long\ area}}(f)}{PSD_{U_{eq,lat\ area}}(f)} \frac{PSD_{U_{eq,lat\ area}}(f)}{PSD_{U_{eq,turb}}(f)} \approx \quad (132)$$

$$\approx f_7 \left(\frac{A_{lat} b f}{\langle U_{wind} \rangle} \right) f_8 \left(\frac{A_{long} a f}{\langle U_{wind} \rangle}, A_{long} \right) = |H_3(f)|^2$$

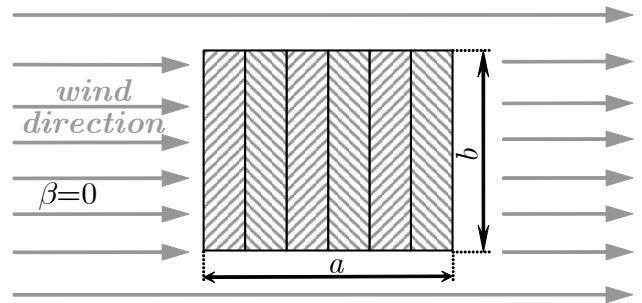


Fig. 51: Rectangular area divided in smaller transversal areas.

The approximation (132) is equivalent to consider the Manhattan distance (L_1 or city-block metric) instead of the Euclidean distance (L_2 metric) in the coherence $\vec{\gamma}_{rc}$ (128):

$$\sqrt{[A_{long}(x_2-x_1)]^2 + [A_{lat}(y_2-y_1)]^2} \sim A_{long}(x_2-x_1) + A_{lat}(y_2-y_1) \quad (133)$$

3.8.3. Equivalent wind smoothing due to turbine spatial layout

Expression (132) is the squared modulus of the transfer function of the spatial diversity smoothing in the area. $H_3(f)$ corresponds to the low-pass filters in Fig. 53 with cut-off frequencies inversely proportional to the region dimensions.

The overall cut-off frequency of the spatially averaged wind is obtained solving $|H_3(f)|^2 = 1/4$. Thus, the cut-off frequency of transversal wind farms (solid black line in Fig. 53) is:

$$f_{cut,lat} = 6.83 \frac{\langle U_{wind} \rangle}{bA_{lat}} \quad (134)$$

In the Rutherford Appleton Laboratory (RAL), $A_{lat} \approx (17,5 \pm 5)(\text{m/s})^{-1} \sigma_{U_{wind}}$ and hence $f_{cut,lat} \approx (0,42 \pm 0,12) \langle U_{wind} \rangle / (\sigma_{U_{wind}} b)$. A typical value of the turbulence intensity $\sigma_{U_{wind}} / \langle U_{wind} \rangle$ is around 0,12 and for such value $f_{cut,lat} \sim (3,5 \pm 1)/b$, where b is the lateral dimension of the area in meters. For a lateral dimension of a wind farm of $b = 3$ km, the cut-off frequency is in the order of 1,16 mHz.

In the Høvsøre wind farm, $A_{lat} = \langle U_{wind} \rangle / (2 \text{ m/s})$ and hence $f_{cut,lat} \approx 13,66/b$, where b is a constant expressed in meters. For a wind farm of $b = 3$ km, the cut-off frequency is in the order of 4,5 mHz (about four times the estimation from RAL).

In RAL, $A_{long} \approx (15 \pm 5) \sigma_{U_{wind}} / \langle U_{wind} \rangle$. A typical value of the turbulence intensity $\sigma_{U_{wind}} / \langle U_{wind} \rangle$ is around 0,12 and for such value $A_{long} \approx (1,8 \pm 0,6)$.

$$f_{cut,long} = 1,1839 \frac{\langle U_{wind} \rangle}{a A_{long}} \approx 0,6577 \frac{\langle U_{wind} \rangle}{a} \quad (135)$$

For a significative wind speed of $\langle U_{wind} \rangle \sim 10$ m/s and a wind farm of $a = 3$ km longitudinal dimension, the cut-off frequency is in the order of 2,19 mHz.

In the Høvsøre wind farm, $A_{long} = 4$ (about twice the value from RAL). The cut-off frequency of a longitudinal area with A_{long} around 4 (dashed gray line in Fig. 53) is:

$$f_{cut,long} = 2,7217 \frac{\langle U_{wind} \rangle}{a A_{long}} \approx 0,6804 \frac{\langle U_{wind} \rangle}{a} \quad (136)$$

For a significative wind speed of $\langle U_{wind} \rangle \sim 10$ m/s and a wind farm of $a = 3$ km longitudinal dimension, the cut-off frequency is in the order of 2,26 mHz.

In accordance with experimental measurements, turbulence fluctuations quicker than a few minutes are notably smoothed in the wind farm output. This relation is proportional to the dimensions of the area where the wind turbines are sited. That is, if the dimensions of the zone are doubled, the area is four times the original region and the cut-off frequencies are halved. In other words, *the smoothing of the aggregated wind is proportional to the longitudinal and lateral distances of the zone* (and thus, related to the square root of the area if zone shape is maintained).

In sum, the lateral cut-off frequency is inversely proportional to the site parameters A_{lat} and the longitudinal cut-off frequency is only slightly dependent on A_{long} . Note that the longitudinal cut-off frequency show closer

agreement for Høvsøre and RAL since it is dominated by frozen turbulence hypothesis.

However, if transversal or longitudinal smoothing dominates, then the cut-off frequency is approximately the minimum of $f_{cut,lat}$ and $f_{cut,long}$. The system behaves as a first order system at frequencies above both cut-off frequencies, and similar to $1/2$ order system in between $f_{cut,lat}$ and $f_{cut,long}$.

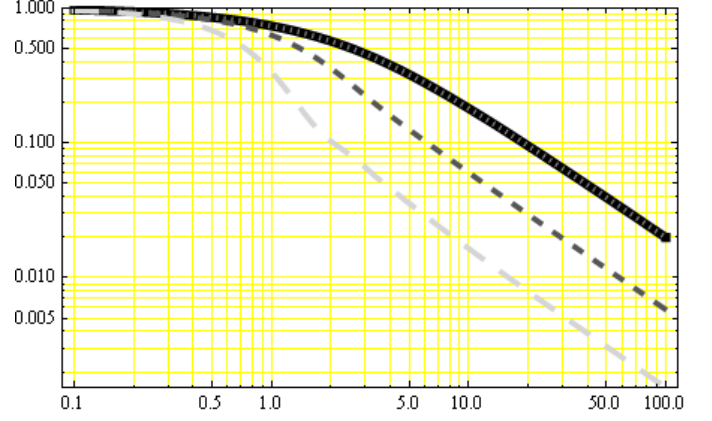


Fig. 53: Normalized ratio $PSD_{U_{eq,area}}(f) / PSD_{U_{eq,turbine}}(f)$ for transversal (solid thick black line) and longitudinal areas (dashed dark gray line for $A_{long} = 4$, long dashed light gray line for $A_{long} = 1,8$). Horizontal axis is expressed in either longitudinal and lateral adimensional frequency $a A_{long} f / \langle U_{wind} \rangle$ or $b A_{lat} f / \langle U_{wind} \rangle$.

Conclusions

This chapter has introduced a simplified small signal model of the torque variation based on the wind variation. The simplified calculation of the aerodynamic torque coefficient based on the torque of the turbine, which assumes that the wind is uniform in the area swept by the turbine. From this formula, a simplified small signal model has been derived to estimate the torque when the wind conditions in the swept area are not uniform.

Based on this approximation, the equivalent wind has been defined as the one that produce the same effects that the non-uniform real wind field. This simplification implies that the effects of the wind field, which cannot be measured directly, can be estimated from an equivalent wind, usually estimated from the measurements of an anemometer.

Thus, the aerodynamic torque has been computed approximately with a simple formula from the torque

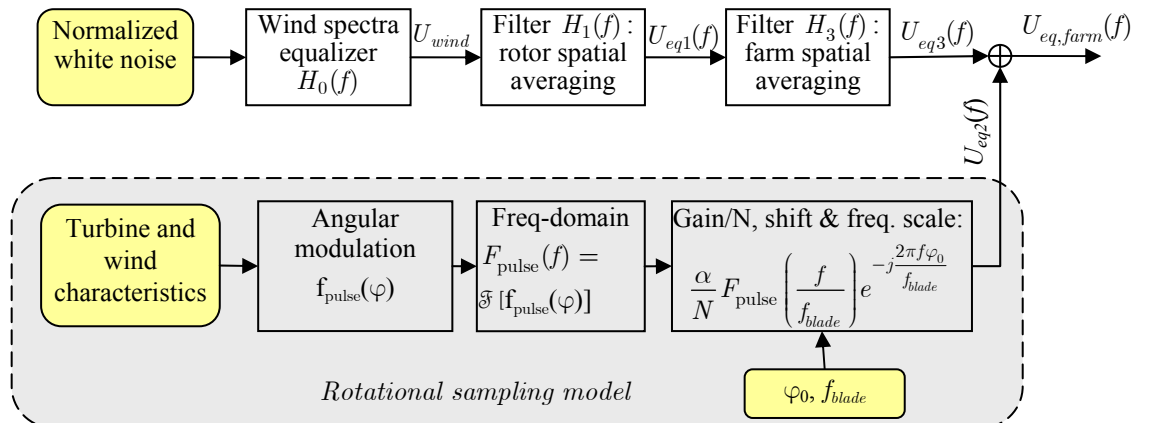


Fig. 52: Diagram of the proposed additive rotational sampling model for the off-line estimation of the equivalent wind in the frequency domain.

coefficient and from the equivalent wind, derived from the measured wind.

The equivalent wind speed contains a stochastic component due to the effects of turbulence, a rotational component due to the wind shear and the tower shadow and the average value of the wind in the swept area, considered constant in short intervals. The fluctuations in the aerodynamic torque due to the real wind field along the swept rotor area are introduced in the equivalent wind modifying its spectra. This oversimplification works relatively well since the vibrational turbine dynamics randomize the real dependence of the generator torque with the rotor angle.

The combination of the small signal model and the wind coherence permits to derive the spatial averaging of random wind variations. A stochastic model that links the overall behaviour of a large number of turbines is derived from the behaviour of a single turbine.

The power spectral density of the equivalent wind of a cluster of turbines is estimated from parameters of an isolated turbine, lateral and longitudinal dimensions of the cluster region and the decay factor of the spatial coherence.

Although the proposed model is an oversimplification of the actual behaviour of a group of turbines scattered across the area, this model quantifies the influence of the spatial distribution of the turbines in the smoothing and in the frequency content of the aggregated power. This stochastic model is in agreement with the experimental observation that slow changes are highly correlated among a turbine cluster while fast changes are poorly correlated.

The small signal model used in this chapter is derived mathematically. In the next chapter, a model based on the blade element theory is presented. That model predicts torque oscillations based on the wind field perturbation due to the surface and the tower.

Chapter 4:

Variability of Power

in the Frequency Domain

4.1. Introduction

In previous chapters, the wind has been analyzed to estimate the variations of aerodynamic torque. However, the structural and drive-train vibrations result into stochastic fluctuations in the generator speed.

The complexity of the mechanical vibrations, the turbine control and the non-linearity of the generator power electronics interactions affects notably the generator electromagnetic torque and the turbine power fluctuations, specially in the frequency range from tenths of Hertz to grid frequency.

There are many dynamic turbine models described in the literature. Most megawatt turbine share the following behaviour, considering the aerodynamic torque as the system input and the power injected in the grid as the system output: [212, 120, 122]

- Between the cut-in and rated wind speeds, the system usually behaves as a low frequency filter of first order with a time constant between 1 and 10 s.
- Between the rated and cut-out wind speeds, the system usually behaves as an asymmetric band pass filter of characteristic frequency around 0,3 Hz due to the combined action of the slow action of the pitch/active stall and the quicker speed controllers.
- At some characteristic frequencies, the turbine mechanical vibrations, the power electronics and the generator dynamics modify the general trend of the transfer function. Generally, these effects are not linearly related to the wind and the ratio of the output signal divided by the input signal in the frequency domain is not constant.

There are many specific characteristics that impact notably in the power fluctuations between the first tower frequency (usually some tenths of Hertz) and the grid frequency. The realistic reproduction of power fluctuations needs a comprehensive model of each turbine.

The details of the control, the structural details and the power electronics implemented in the turbines are proprietary and they are not available. In contrast, the electrical power injected by a turbine can be measured relatively easily.

Moreover, some fluctuations in power are not proportional to the fluctuations in wind or aerodynamic torque. Thus, a general transfer function cannot be obtained for the power oscillation, respect the equivalent wind or the aerodynamic torque, unless big errors are allowed.

The approach taken in this chapter is primarily phenomenological: the power fluctuations during the continuous operation of the turbines are measured and characterized for timescales in the range of minutes to fractions of seconds. Thus, one contribution of this chapter is the experimental characterization of the power fluctuations of three commercial turbines. Some experimental measurements in the joint time-frequency domain are presented to test the mathematical model of the fluctuations.

A literature review on experimental data of Power Spectral Densities (PSD) and periodograms (averaged spectrum) of power output of wind turbines or wind farms are presented at the end of the chapter. The variability of PSD is also studied in the joint time-frequency domain through spectrograms.

Other contribution of this chapter is the admittance of the wind farm: the oscillations from a wind farm are compared to the fluctuations from a single turbine, representative of the operation of the turbines in the farm. The partial cancellation of power fluctuations in a wind farm are estimated from the ratio of the farm fluctuation relative to the fluctuation of one representative turbine. Some stochastic models are derived in the frequency domain to link the overall behaviour of a large number of wind turbines from the operation of a single turbine.

This chapter is based mostly on the experience designing, programming, mounting and analyzing two multipurpose measuring system installed in several wind farms through the years 1998 to 2002 [52, 53, 137, 138, 139, 140, 141, 142, 143, 144, 145]. During that years, a set of programs developed in LabVIEW [146], C++ [147], a set of spreadsheets and algorithms [148] and an analysis methodology was developed. According to the CIRCE Foundation [149], this measuring system and its procedures has been the first prototype of a multipurpose data logger, now called AIRE (Analizador Integral de Recursos Energéticos), that is commercialized by Inycom and CIRCE [150].

4.2. Overview of wind power fluctuations

The power from a cluster of turbines is the sum of powers from their turbines less the transmission losses. Since the losses are usually small, the power fluctuations of clusters are, basically, the sum of turbine contributions –or if a small signal of power losses is used, a linear combination of turbine powers [204].

The interaction between the wind fluctuations and the turbine is very complex and a thorough model of the turbine,

generator and control system is needed for simulating the influence of wind turbulence in power output [151, 152]. The control scheme and its optimized parameters are proprietary and difficult to obtain from manufacturers and complex to guess from measurements usually available.

The turbine and micro-meteorological dynamics transforms the combination of periodic and random wind variations into stochastic fluctuations in the power.

This chapter is focused in the variations of power in the frequency domain, which is linked to equivalent wind variations and to the distribution of almost periodic events such as vibration, blade positions, etc. The spatial sampling of the wind in the rotor and the frequency content of the equivalent wind has been carefully considered in the previous chapter. In the next chapter, the distribution of almost periodic events such as the blade shadow and is studied.

Wind distribution inside the wind farm is studied in the micro-sitting to optimize the wind farm layout. Wind spectrum and coherence between turbines has been analyzed in the previous chapters. Turbulence, turbine wakes, gusts... are highly random and don't show a definite frequency [46, 153]. Non-cyclic variations in the power are usually regarded as the outcome of the random component of the wind. They concern the control (short term prediction) and the forecast (long horizon prediction). Artificial Intelligence techniques and advanced filtering have been used for forecasting. Power fluctuations of frequency around 8 Hz can eventually produce flicker in very weak networks [154, 155].

An alternative to Fourier analysis is time series. Time series are quite popular in stochastic models since its parameters and its properties can be easily estimated [156, 157]. Even though the two mathematical techniques are quite related, the study of periodic behaviour is more direct through Fourier approach whereas the time series approach is more appropriate for the study of non-systematic behaviour.

Both current and power can be measured directly, they can be statistically characterized and they are straightforward related to power quality. Current is transformed and its level depends on transformer ratio and actual network voltage. In contrast, power flows along transformers and networks without being altered except for some efficiency losses in the elements. That is why linealized power flows in the frequency domain are used in this chapter for characterizing experimentally the electrical behaviour of wind turbines.

4.2.1. Random and cyclic fluctuations

Fluctuations of power output can be divided into cyclic components (tower shadow, wind shear, modal vibrations, etc.), wind farm weather dynamics and events (connection or disconnection of the turbine, change in generator configuration, etc.). The customary treatment of these fluctuations is done through Fourier transform.

Cyclic fluctuations due to tower shadow, wind shear, etc. present more systematic behaviour than weather related variations. Cyclic fluctuations are almost periodic and they present definite frequencies. Almost periodic means in this context that the signal can be decomposed in a set of sinoidal components (some of them non-harmonically related) with additive (stationary) noise (i.e., polycyclostationary signals). Since some frequencies cannot be expressed as multiple of

the others, the signal is not periodic in the conventional sense (see Fig. 204).

Cyclic time variations are usually characterized from the signal *PSD* (see for example the review from Gardner et al. [158]). The magnitude and frequency of the cyclic fluctuations can be characterized for each turbine model and wind regime [52]. Thus, the cyclic fluctuations can be represented by spectral density phasors revolving at the oscillation frequency.

Turbulence has been previously characterized through its power spectral density, which is basically the Fourier transform of its autocorrelation. Thus, turbulence can be represented by *power* spectral density phasors revolving at the oscillation frequency with a random phase since turbulence does exhibit neither a characteristic shape nor timing.

Weather evolution is the outcome of slow and complex atmospheric processes. Since weather evolution has a strong non-linear behaviour, it not considered in this section. An alternative statistical characterization of wind power variability based on Markov chains, which suits better the complex non-linear weather behaviour, will be presented in the following chapter.

4.2.2. Major difficulties on the fluctuation characterization

The torque drop due to rotor spatial sampling has a characteristic shape (see Fig. 311 or Fig. 59). This torque is filtered by turbine dynamics and the influence in output power can be complex (see Fig. 204). The signals cannot be considered truly periodic neither the characteristic frequencies are constant (rotor speed is not constant due to the wind) nor frequencies are harmonically related (some frequencies cannot be expressed as multiple of the others). Under some conditions –steady wind, short data length, etc– the power can be considered a set of periodic signals decomposable in their fundamental component $f_{1,i}$ and their harmonics $k \cdot f_{1,i}$.

The structural resonance modes of the tower, blades and cinematic train present a vibration behaviour with frequencies different from the blade passing the tower frequency, f_{blade} .

The turbulence adds a “coloured noise” overimposed to the former oscillatory modes, modulating cyclic vibrations and influencing rotor speed. The actual power is the outcome of many processes that interacts and the analysis in the frequency domain is a simplifying approximation of a system driven by stochastic differential equations.

The first problem when analyzing power variations is that the contributions from rotor sampling, vibrational modes and turbulence-driven variations are aggregated.

The second difficulty is the fact that frequencies of almost cyclic contributions are neither fixed nor are they multiple. Fourier coefficients are defined for periodic signals, but a signal with components not harmonically related is not longer periodic.

The third difficulty is that frequencies of contributions are overlapped. Fortunately, characteristic frequencies (resonance and blade frequencies and its harmonics) have narrow margins for given operational conditions, producing peaks in

the spectrum where one contribution usually predominates over the rest.

The fourth difficulty is the turbulence, that introduces a non-periodic stochastic behaviour interacting with periodic signals. Different mathematical tools are customarily used for periodic and stochastic signals, increasing the difficulty of the analysis of these mixed-type signals.

The cyclic fluctuations of the turbine power can be considered in the *fraction-of-time (FOT)* probability framework as the sum of sets of signals with different periods with additive stationary coloured noise and, hence, almost cyclostationary (see the review from Gardner et al. [158]). Since wind power is formed by the superposition of several almost cyclostationary signals whose periods are not harmonically related, wind power is *polycyclostationary*.

Therefore, thorough models of the wind turbines and turbulence are needed for the analysis of power fluctuations. In the following sections, a phenomenological and pragmatic approach will be applied to draw some conclusions and to extrapolate results from specific measurements to general cases.

4.3. Mathematical framework

4.3.1. Definitions

According to [159], a very steady and a very uniformly distributed wind together with a weak electrical network is necessary for synchronisation to happen driven by voltage drops. Experimental measurements [52] have corroborated that the synchronisation of the blades is unusual. In addition, the spectral model of the turbulence (128) showed that wind fluctuations at frequencies much higher than $f_{cut,lat}$ and $f_{cut,long}$ defined in (134) to (136) can be considered independent because its coherence is very small.

Thus, fast fluctuations can be considered statistically independent whereas slower fluctuations are linked basically to weather dynamics. Fortunately, slow fluctuations can be linked to equivalent wind fluctuations through a quasi-static approximation based on the power curve of the turbines.

A) Aggregation of uncorrelated almost-cyclic signals results on stochastic signals

As main wind characteristics are similar inside the farm, the typical magnitude of the cyclic components would be similar in all turbines. If the turbines blades are not synchronized, the cyclic uncorrelated fluctuations due to rotor movement have random phases.

Thus, the aggregation of cyclic fluctuations from the turbines in a wind farm or in an area turns out to have a stochastic behaviour. Moreover, the correlated fluctuations in a wind farm or in an area are due to meteorology. Both turbulence and weather have strong stochastic nature.

As an outcome, the total fluctuation from an area is best characterized as a stochastic signal even though the fluctuations from single turbines have strong cyclic components. The properties of the total fluctuation can be derived from the turbine fluctuations and their relationship (especially the coherence among turbines).

In sum, the transformation of cyclic components into stochastic components eases the treatment of area fluctuations.

B) Dependence on the data length of the Fourier transform of random and cyclic signals.

The Fourier transform of a signal of active power $P(t)$, recorded in $0 \leq t \leq T$, is $\vec{P}_T(f)$:

$$\vec{P}_T(f) = \int_0^T P(t) e^{-j2\pi f t} dt = \mathfrak{F}\{P(t)\} \quad (137)$$

The units of $\vec{P}_T(f)$ are the same than the ones of $P(t)$ per Hertz. Thus, if $P(t)$ is in MW, then $\vec{P}_T(f)$ is in MW/Hz and if $P(t)$ is in p.u. (per unit system), then $\vec{P}_T(f)$ is in p.u./Hz. The subindex notation in $\vec{P}_T(f)$ indicate the sample duration T of the original time series and it is used in this chapter to distinguish the Fourier transforms, the Fourier coefficients and the stochastic spectral phasor densities.

If $P(t)$ is a periodic component of period $T = 1/f_1$ in the active power, its Fourier transform is a modulated Dirac comb. The complex Fourier coefficient of order k , \vec{P}_k , is the conventional Fourier transform of the signal during a period, scaled by the period, at harmonic frequency $f = k f_1 = k/T$ $\forall k \in \mathbb{Z}$:

$$\vec{P}_k = \frac{1}{T} \int_0^T P(t) e^{-j\frac{2\pi k t}{T}} dt = \frac{1}{T} \mathfrak{F}\{P(t)\} = \frac{1}{T} \vec{P}_T(f = k f_1) \quad (138)$$

The units of \vec{P}_k is the same than $P_T(t)$. The amplitude of the fluctuation of harmonic k is $|\vec{P}_k + \vec{P}_{-k}^*| = 2|\vec{P}_k|$ in peak values and its initial phase is $\text{Arg}[\vec{P}_k]$. The Fourier coefficients are notated with the k subscript to distinguish them from the Fourier transform.

Notice that the active power can be considered the aggregation of stochastic noise and periodic components. Since periodic components can be considered deterministic with period T under the *FOT* probability framework, its Fourier coefficients can be computed.

If $P(t)$ is the stochastic component in the active power recorded in $0 \leq t \leq T$, the conventional Fourier transform, denoted by \mathfrak{F} , is scaled by a factor \sqrt{T} to achieve an spectral measure whose main statistical properties do not depend on the sample duration T .

$$\vec{P}_\sigma(f) \equiv \frac{1}{\sqrt{T}} \int_0^T P(t) e^{-j2\pi f t} dt = \frac{1}{\sqrt{T}} \mathfrak{F}\{P(t)\} = \frac{1}{\sqrt{T}} \vec{P}_T(f) \quad (139)$$

The factor $1/\sqrt{T}$ applied to the conventional Fourier transform $\vec{P}_T(f)$ to obtain $\vec{P}_\sigma(f)$ is between unity –used for pulses and signals of bounded energy– and $1/T$ –the Fourier coefficients \vec{P}_k used for pure periodic signals–.

Fortunately, the definition (791) has the advantage that the variance of $\vec{P}_\sigma(f)$ is the two-sided power spectral density, $\langle |\vec{P}_\sigma(f)|^2 \rangle = PSD_P(f)$, which is independent of the sample length T and it characterizes the process. $\vec{P}_\sigma(f)$ will be referred as stochastic spectral phasor density of the active power or just the (stochastic) phasor for short.

Notice that the text or the subscript indicates the scaling factor applied to the Fourier transform. If nothing is stated, then $\vec{P}(f)$ should be interpreted *in this chapter* just as $\vec{P}_\sigma(f)$, the *stochastic spectral phasor density*.

C) Stochastic spectral phasor density of the active power

The instantaneous output of a wind farm or turbine can be expressed in frequency components using stochastic spectral phasor densities. As aforementioned, experimental measurements indicate that wind power nature is basically stochastic with noticeable fluctuating periodic components.

The stochastic spectral phasor density of a power output time series $P(t)$ with duration T and zero initial time is:

$$\vec{P}_\sigma(f) = P_\sigma(f) e^{j\varphi(f)} = \frac{1}{\sqrt{T}} \int_0^T P(t) e^{-j2\pi f t} dt \quad (140)$$

The signal in the time domain can be computed from the inverse Fourier transform:

$$\begin{aligned} P_\sigma(t) &= \sqrt{T} \int_{-\infty}^{\infty} \vec{P}_\sigma(f) e^{j2\pi f t} df \stackrel{\vec{P}_\sigma(f) = \vec{P}_\sigma^*(-f)}{=} \\ &= 2\sqrt{T} \operatorname{Re} \left[\int_0^{\infty} \vec{P}_\sigma(f) e^{j2\pi f t} df \right] = \\ &= 2\sqrt{T} \int_0^{\infty} P_\sigma(f) \cos[2\pi f t + \varphi(f)] df \end{aligned} \quad (141)$$

where e is the base of the natural logarithm, j is the imaginary unit, Re states for the real part of a complex number and $*$ stands for complex conjugate. An analogue relation can be derived for reactive power and wind, both for continuous and discrete time.

Standard FFT algorithms use two sided spectra, with negative frequencies in the last half of the output vector. Thus, calculus will be based on two-sided spectra unless otherwise stated, as in (141). In real signals, the negative frequency components are the complex conjugate of the positive one and a $1/2$ scale factor may be applied to transform one to two-sided magnitudes.

Fluctuations at the point of common coupling (PCC) of the wind farm can be obtained from power balance equations for the average complex power of the wind farm.

Neglecting the increase of power losses in the grid due to fluctuating generation, the sum of oscillating power from the turbines equals the farm output undulation. Therefore, the complex sum of the frequency components of each turbine $P_{\text{turbine } i}(f)$ totals the approximate farm output, $P_{\text{farm}}(f)$:

$$\vec{P}_{\text{farm}}(f) = \sum_{i=1}^{N_{\text{turbines}}} \vec{P}_{\text{turbine } i}(f) = \sum_{i=1}^{N_{\text{turbines}}} P_{\text{turbine } i}(f) e^{j\varphi_i(f)} \quad (142)$$

For usual wind farm configurations, total real losses at full power are less than 2% and reactive losses are less than 20%, showing a quadratic behaviour with generation level [160]. A small-signal model of power losses due to fluctuations inside the wind farm can be derived [161], but since they are expected to be up to 2% of the fluctuation, the increase of power losses due to oscillations can be neglected in the first instance. A small signal model can be used to take into account the network losses multiplying the turbine phasors in (142) by the sensitivity factors $\partial P_{\text{farm}} / \partial P_{\text{turbine } i}$ estimated from power flows with small variations from the mean values using methodologies as the point-estimate method [162, 163].

4.3.2. Statistical properties of the sum of stochastic spectral phasor densities

Periodic fluctuations appear as narrow peaks at their harmonic frequencies in the spectrum, whereas random fluctuations (which have neither a periodic pattern nor a characteristic frequency) can be associated with the tendency of the smoothed spectrum.

The discrete Fourier transform (DFT) divided by \sqrt{T} (the square root of the sample duration) is the phasor $\vec{P}_\sigma(f, t)$ which vary randomly in time (even though f and t are discrete in logged data, the notation is maintained as if frequency and time were continuous for convenience). The squared modulus of the DFT divided by T is an estimate of the power spectrum density $|\vec{P}_\sigma(f, t)|^2$ in grey in *PSD* plots –such as **Fig. 205**– which varies in time since wind is stochastic. However, its time average $\langle |\vec{P}_\sigma(f, t)|^2 \rangle = \langle |\vec{P}_\sigma(f)|^2 \rangle$ is approximately constant for certain operational conditions and it is an estimation of the actual $PSD_P(f)$ (see black thin line in *PSD* plots).

The $PSD_{P_{\text{farm}}}(f)$ is the Fourier transform of the autocorrelation function, $R_{P_{\text{farm}}}(\tau)$ provided the power output of the farm can be considered a stationary random process. A basic estimation of the power spectral density is $PSD_P(f) = P^2(f)/\Delta f$, where $\Delta f = 1/T$ is the inverse of the duration of the record and $P^2(f)$ is the square of the spectrum density, smoothed in the frequency domain to decrease the variance of the *PSD* estimate [164, 165, 166]. Wind farm or turbine *PSD*, $\langle |\vec{P}_{\text{farm}}(f)|^2 \rangle$ or $\langle |\vec{P}_{\text{turbine } i}(f)|^2 \rangle$, has been estimated as the averaged squared *DFT* modulus of power output, scaled by period T . This technique is called “averaged periodogram” and its properties can be found in [167, 168, 169].

In *PSD* plots such as **Fig. 205**, the original power spectrum is plotted in grey whereas the estimated *PSD* is in thin black (linearly averaged periodogram in squared effective watts of real power per hertz). Since the required frequency resolution in this application is low, the power spectrum has been smoothed in order to lower the *PSD* variance (the frequency resolution Δf has decreased $N_{\text{aver.}}$ times to reduce the *PSD* uncertainty in the factor $\sqrt{N_{\text{aver.}}}$). In the analyzed cases where power is measured each grid cycle, the values $10 < N_{\text{aver.}} < 100$ have been suitable tradeoffs between frequency resolution and variance of the estimated *PSD*. The *PSD* has been estimated in the figures with $N_{\text{aver.}}=20$ if nothing else is stated.

The fluctuation of power output of the farm is the sum of contributions from many turbines (142), which are mainly uncorrelated. The sum of N independent phasors of random angle of N turbines in the farm asymptotically converges to a complex Gaussian distribution, $\vec{P}_{\text{farm}}(f) \sim \mathcal{CN}[0, \sigma_{P_{\text{farm}}}(f)]$, of null mean and standard deviation $\sigma_{P_{\text{farm}}}(f) = \sqrt{N}\sigma_1(f)$, where $\sigma_1(f)$ is the mean *RMS* fluctuation at a single turbine at frequency f . To be precise, the variance $\sigma_1^2(f)$ is half the mean squared fluctuation amplitude at frequency f , $\sigma_1^2(f) = \frac{1}{2} \langle |\vec{P}_{\text{turbine } i}(f)|^2 \rangle = \langle \operatorname{Re}^2[\vec{P}_{\text{turbine } i}(f)] \rangle = \langle \operatorname{Im}^2[\vec{P}_{\text{turbine } i}(f)] \rangle$. Therefore, the real and imaginary phasor components $\operatorname{Re}[\vec{P}_{\text{farm}}(f)]$ and $\operatorname{Im}[\vec{P}_{\text{farm}}(f)]$ are independent real Gaussian random variables of standard deviation $\sigma_{P_{\text{farm}}}(f)$ and null mean since phasor angle is uniformly distributed in $[-\pi, +\pi]$. Moreover, the phasor modulus $|\vec{P}_{\text{farm}}(f)|$ has *Rayleigh* $[\sigma_{P_{\text{farm}}}(f)]$ distribution. The double-sided power

spectrum $|\vec{P}_{farm}(f)|^2$ is an *Exponential* $[\lambda = \frac{1}{2}\sigma_{P_{farm}(f)}^{-2}]$ random vector of mean $\langle |\vec{P}_{farm}(f)|^2 \rangle = 2\sigma_{P_{farm}(f)}^2 = \frac{1}{2}PSD_{P_{farm}(f)}$ (the double-sided power spectral density is half the one-sided power spectral density) [170, 171].

The estimate from the periodogram is the moving average of N_{aver} exponential random variables corresponding to adjacent frequencies in the power spectrum vector. The estimate is a Gamma random variable. If the *PSD* is sensibly constant on $N_{aver}\Delta f$ bandwidth, then the *PSD* estimate has the same mean as the original *PSD* and the standard deviation is $\sqrt{N_{aver}}$ times smaller (i.e., the estimate has lower uncertainty at the cost of lower frequency resolution).

A comprehensive literature survey on the sum of random vectors can be reviewed in [172]. The statistical properties of the wind power spectrum will be further analyzed in this chapter.

A) Sum of two phasors with random angle and the same modulus

Fig. 54 shows the instantaneous phasor diagram of a wind farm with four turbines with similar uncorrelated fluctuation level at angular frequency f . Recall that the *stochastic spectral phasor density* $\vec{P}_\sigma(f)$ has been notated as $\vec{P}(f)$ for simplicity. Phases $\varphi_1, \varphi_2, \varphi_3$ and φ_4 , are random and its value is uniformly distributed in $[-\pi, +\pi]$ (uncorrelated fluctuations). It should be noted that the phases of each turbine are random when compared to the others because each turbine has its own blade reference.

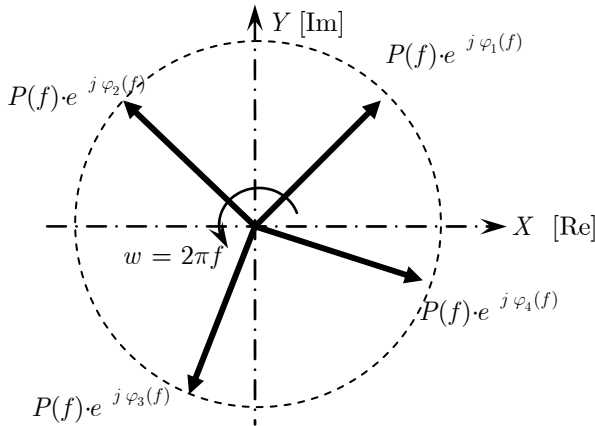


Fig. 54: Model of the phasor diagram at frequency f of a park with four turbines with similar uncorrelated fluctuation level $P(f)$.

The sum of phasors of equal frequency is another phasor with a statistical distribution which will be derived in the next sections. Finally, an expression for the phasor of a wind farm will be obtained in function of the number of turbines N and the frequency component of a single turbine, $P(f)$.

Each phasor will be decomposed in real and imaginary components, that correspond to the projection on horizontal and vertical axis in Fig. 54. For convenience, the phasors will be treated as complex random variables with some modulus distribution in p.u. or in standardized variables and uniformly distributed angle $[-\pi, +\pi]$.

B) Sum of two phasors with the same modulus

The sum of two phasor i and k is another phasor with random phase and amplitude $2P(f) \cdot \left| \cos\left[\frac{\varphi_i - \varphi_k}{2}\right] \right|$

The modulus of the sum of phasors $\vec{P}_{i+k} = \vec{P}_i + \vec{P}_k$ of the same amplitude $P(f)$ is:

$$\begin{aligned} |\vec{P}_{i+k}(f)| &= P_{i+k}(f) = \left| P(f) \cdot e^{j\varphi_i} + P(f) \cdot e^{j\varphi_k} \right| = \\ &= 2 \left| P(f) \cdot \left| \cos\left(\frac{\varphi_i - \varphi_k}{2}\right) \right| \right| \end{aligned} \quad (143)$$

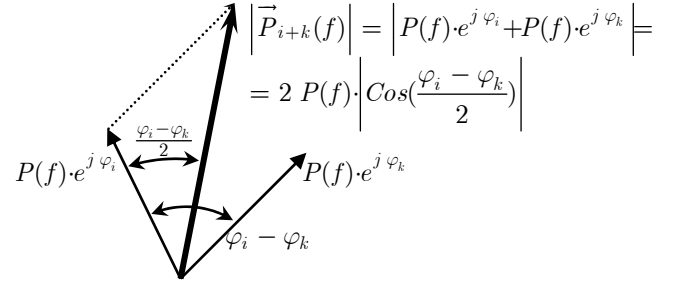


Fig. 55: Sum of two phasors with same magnitude.

The cumulative density function (*CDF*) of the amplitude of the sum of two uncorrelated turbines is:

$$\begin{aligned} CDF_{P_{i+k}(f)}(x) &= \\ &= \Pr\left\{ \left| P_{i+k} \right| \leq x \right\} = \Pr\left\{ 2P(f) \left| \cos\left(\frac{\varphi_i - \varphi_k}{2}\right) \right| \leq x \right\} = \\ &= \Pr\left\{ \left| \cos\left(\frac{\varphi_i - \varphi_k}{2}\right) \right| \geq \left| \text{ArcCos}\left(\frac{x}{2P(f)}\right) \right| \right\} = \\ &= 1 - \frac{2}{\pi} \text{ArcCos}\left(\frac{x}{2P(f)}\right) \end{aligned} \quad (144)$$

The probability density function (*PDF*) of the sum amplitude can be derived from its *CDF*:

$$PDF_{P_{i+k}(f)}(x) = \frac{d}{dx} CDF_{P_{i+k}(f)}(x) = \frac{1}{\pi \sqrt{P^2(f) - \left(\frac{x}{2}\right)^2}} \quad (145)$$

C) Sum of two phasors with different modulus

The sum of four phasors can be computed iteratively from the former subsection.

$$\begin{aligned} \vec{P}_{i+k+l+m}(f) &= \vec{P}_{i+k}(f) + \vec{P}_{l+m}(f) = \\ &= \left[\vec{P}_i(f) + \vec{P}_k(f) \right] + \left[\vec{P}_l(f) + \vec{P}_m(f) \right] \end{aligned} \quad (146)$$

The phasors obtained in the former subsection have different modules and the result is a bit different from the previous paragraphs. The modulus of the sum will be derived by trigonometry. The projection of the phasor $\vec{P}_{i+k}(f)$ of the turbines i and k in the axis of the sum of the four turbine phasors is $|\vec{P}_{i+k}(f)| \cos \varphi_{i+k}(f)$. The projection of the phasor $\vec{P}_{l+m}(f)$ of the turbines l and m in the axis of the sum of the four turbine phasors is $|\vec{P}_{l+m}(f)| \cos \varphi_{l+m}(f)$.

The phases $\varphi_{i+k}(f)$ and $\varphi_{l+m}(f)$ are uniformly distributed in $[-\pi, \pi]$ and the function $\text{ArcCos}(\varphi)$ returns a number in $[0, \pi]$. The modulus of two vectors $\vec{P}_{i+k}(f)$ and $\vec{P}_{l+m}(f)$ are distributed according to (145).

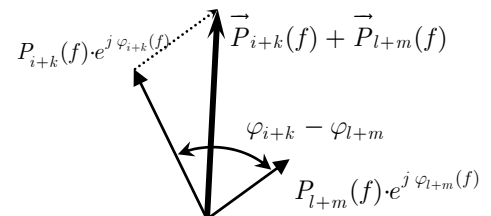


Fig. 56: Sum of two phasors with different magnitude.

Therefore the cumulative density function (CDF) of the modulus of the phasor of the sum of four turbines is: (147)

$$\begin{aligned} CDF_{P_{i+k+l+m}}(y) &= \Pr(|\vec{P}_i(f) + \vec{P}_k(f) + \vec{P}_l(f) + \vec{P}_m(f)| \leq y) = \\ &= \Pr(|\vec{P}_{i+k}(f)| \cos(\varphi_{i+k}(f) - \varphi_{i+k+l+m}(f)) + \\ &\quad + |\vec{P}_{l+m}(f)| \cos(\varphi_{l+m}(f) - \varphi_{i+k+l+m}(f)) \leq y) \end{aligned}$$

For the rest of this subsection, the dependence of parameters with frequency will not be indicated explicitly to shorten expressions. The projection of a phasor of modulus P_{i+k} in the direction of the overall sum is x_{i+k} and it has the following conditional CDF (the explicitly notation of the dependence of variables with frequency f has been dropped for simplicity): (148)

$$\begin{aligned} CDF_{x_{i+k}|r_{i+k}}(x|P_{i+k}) &= \Pr(P_{i+k} \cos(\varphi_{i+k}) \leq x) = \\ &= \Pr\left(\cos(\varphi_{i+k}) \leq \frac{x}{P_{i+k}}\right) = \Pr\left[\varphi_{i+k} \leq \text{ArcCos}\left(\frac{x}{P_{i+k}}\right)\right] = \\ &= 1 - \frac{\text{ArcCos}(x/P_{i+k})}{\pi} \end{aligned}$$

The conditional probability density function (PDF) of the projection, given P_i can be derived from CDF: (149)

$$PDF_{x_{i+k}|r_{i+k}}(x|P_{i+k}) = \frac{d}{dx} CDF_{x_{i+k}|r_{i+k}}(x) = \frac{1}{\pi \sqrt{P_{i+k}^2 - x^2}}$$

Taken into account that the distribution of modulus r_i of the sum of two vectors has been obtained previously, the total PDF of x_{i+k} can be computed by integration. (150)

$$\begin{aligned} PDF_{x_{i+k}}(x) &= \int_x^{2P(f)} PDF_{x_{i+k}|r_{i+k}}(x|P_{i+k}) \cdot PDF_2(P_{i+k}) dP_i = \\ &= \int_x^{2P(f)} \frac{1}{\pi P_{i+k} \sqrt{1 - \left(\frac{x}{P_{i+k}}\right)^2}} \cdot \frac{1}{\pi \sqrt{1 - \left(\frac{P_{i+k}}{2}\right)^2}} dP_i = \\ &= \frac{-2}{\pi^2 |x|} \text{Im} \left\{ \text{EllipticK} \left[\left(\frac{2P(f)}{x} \right)^2 \right] \right\} \end{aligned}$$

Finally, the total PDF of the relative modulus of the sum of the four phasor is: (151)

$$PDF_{S_{i+k+l+m}}(y) = 2 \int_{-2P(f)+y}^{2P(f)} PDF_{x_{i+k}}(y-x) \cdot PDF_{x_{i+k}}(x) dx$$

where $0 < y < 4P(f)$ and factor 2 take account that $\varphi_{i+k}(f)$ and $\varphi_{l+m}(f)$ are uniformly distributed in $[-\pi, \pi]$ whereas $\text{ArcCos}(\varphi)$ returns a number in $[0, \pi]$, half the interval.

The integral (151) doesn't have a simple analytic solution and must be computed numerically. The calculus of the sum of phasors can be done iteratively. However, the integrals cannot be solved analytically and the accumulated numerical error can be noticeable for farms with more than 32 turbines. The next subsection employs a general method to compute the sum of any number of phasors using the characteristic function of the modulus of fluctuation phasors.

D) Sum of any number of phasors

In some applications, we encounter a random signal that is composed of the sum of several random sinusoidal signals, e.g., multipath fading in communication channels, clutter and target cross section in radars, interference in communication

systems, wave propagation in random media and channels, laser speckle patterns and light scattering and summation of random current harmonics such as the ones produced by high frequency power converters of wind turbines [173, 174].

Any random sinusoidal signal can be considered as a random phasor, i.e., a vector with random length and angle. In this way, the sum of random sinusoidal signals is transformed into the sum of 2-D random vectors. So, irrespective of the type of application, we encounter the following general mathematical problem: there are vectors with lengths $P_{i, \text{uncorr}} = |P_{i, \text{uncorr}}|$ and angles $\varphi_i = \text{Arg}(P_{i, \text{uncorr}})$, in polar coordinates, where $P_{i, \text{uncorr}}$ and φ_i are random variables. It is desired to obtain the probability density function (pdf) of the length of the resulting vector.

$$P_N = \left| \vec{P}_{\text{farm, uncorr}} \right| = \left| \sum_{i=1}^{N_{\text{turbines}}} \vec{P}_{i, \text{uncorr}} \right| = \left| \sum_{i=1}^{N_{\text{turbines}}} P_{i, \text{uncorr}} \cdot e^{j\varphi_i} \right| \quad (152)$$

A comprehensive literature survey on the sum of random vectors can be obtained from [172]. This problem is often solved through the joint characteristic function of the modulus of $P_{i, \text{uncorr}}$.

If the turbines $i = 1$ to N have approximately the same phasor density modulus, $P_{i, \text{uncorr}} = P_i$, then the PDF of the modulus of the sum $P_N = |P_N|$ can be computed according to equations (9), (10) and (29) from [172] as:

$$PDF_{\sum P_i}(x) = \frac{x}{P_1} \int_0^\infty \rho J_0\left(\frac{x}{P_1} \rho\right) \left[J_0(\rho)\right]^N d\rho \quad (153)$$

where J_0 denotes the zeroth-order Bessel function.

An analytical PDF can be obtained accurate enough for $N > 4$ (farms with more than 4 turbines) using the asymptotic approximation $\lim_{N \rightarrow \infty} J_0^N(\rho) = e^{-N\rho^2/4}$.

$$\begin{aligned} PDF_{\sum P_i}(x) &\simeq \frac{x}{P_1} \int_0^\infty \rho J_0\left(\frac{x}{P_1} \rho\right) e^{-N\rho^2/4} d\rho = \\ &= \frac{x}{\left(\sqrt{N/2} P_1\right)^2} \exp\left[-\frac{1}{2} \left(\frac{x}{\sqrt{N/2} P_1}\right)^2\right] \end{aligned} \quad (154)$$

The $PDF_N(P_N)$ for wind farms with $N = 8, 16$ or 32 turbines computed from exact formula (153) or computed from the approximation (154) is very similar, as can be seeing in Fig. 57. The approximate PDF of the modulus (shown in red) corresponds to a Rayleigh distribution with parameter $\sigma_N = \sqrt{N/2} P_1$.

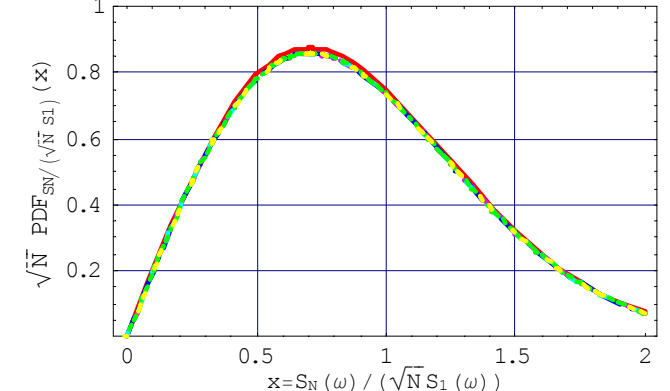


Fig. 57: Normalized $PDF_N(P_N)$ for wind farms with $N = 8, 16$ and 32 turbines.

E) Projection of the phasor in the horizontal axis

The projection of a phasor in the horizontal (or real) axis corresponds to the instantaneous value represented by phasors. $P_N \cos \varphi_N$ is the instantaneous value of the fluctuation (at frequency f).

If the modulus and the angle are independent random variables and the angle is uniformly distributed in $[0, 2\pi]$, all the odd moments are zero. The $2r$ order absolute moments of the projection, $M_{2r, \text{proj}}$, can be computed as:

$$M_{2r, \text{proj}} = \int_0^{\text{Max } |S_N|} \int_0^{2\pi} \left(|\vec{P}_N| \cos(\varphi) \right)^{2r} PDF_{|\vec{P}_N|} \left(|\vec{P}_N| \right) \frac{1}{2\pi} d\varphi d|\vec{P}_N| \quad (155)$$

The relation between absolute moments of the phasor modulus $M'_{2r, \text{mod}}$ (respect 0) and the absolute moments of the phasor projection $M_{2r, \text{proj}}$ is:

$$M_{2r, \text{proj}} = \int_0^{\text{Max } |\vec{P}_N|} |\vec{P}_N|^{2r} PDF_{|\vec{P}_N|} \left(|\vec{P}_N| \right) d|\vec{P}_N| \cdot \int_0^{2\pi} \frac{\cos(\varphi)^{2r}}{2\pi} d\varphi = a M'_{2r, \text{mod}} \quad (156)$$

where $a = 1/2, 3/8, 5/16, 35/128, 63/256 \dots$ for $2r = 2, 4, 6, 8, 10 \dots$ (odd moments are null)

For example, the quadratic value of the projection –i.e., the quadratic average of time-domain signal– is half the squared amplitude. Hence, the RMS value of a phasor is its amplitude divided by $\sqrt{2}$.

The distribution of the projection can be computed by integration:

$$CDF_{\text{proj}}(x) = \frac{1}{2\pi} \int_0^{2\pi} CDF_{|\vec{P}_N|}(x/\cos(\varphi)) d\varphi \quad (157)$$

The projection in the real axis of a phasor with Rayleigh distributed modulus and parameter σ_N is distributed normally with zero mean and standard deviation σ_N .

The real and imaginary part of a phasor with random (equally probable) phase angle and its modulus Rayleigh distributed are two identically distributed and independent real Gaussian random variables. Thus, the squared modulus has an exponential distribution with rate parameter $\lambda = 1/(2\sigma_N)$ (also equivalent to a gamma distribution with unity shape factor and scale parameter $2\sigma_N$).

4.3.3. Spectral density of uncorrelated oscillations in a group of turbines

The fluctuations of a group of turbines can be divided into the correlated and the uncorrelated components. According to Fig. 57, the Central Limit is applicable for the sum of uncorrelated spectral components of more than 8 turbine phasor densities and the sum distribution converges asymptotically to a complex normal distribution.

The correlated fluctuation components are usually linked to slow meteorological dynamics and they have been characterized in the former chapter –see (115) and (127). Thus, the correlated components are not considered in this section.

The one-sided stochastic spectral phasor density of the active power of a cluster of N turbines at frequency f is $|\vec{P}_N^+(f)| = |\vec{P}_N(f)| + |\vec{P}_N(-f)| = 2|\vec{P}_N(f)|$. In plain words,

the one-sided density is twice the two-sided density. The amplitude of fluctuations at frequencies between $f - \Delta f/2$ and $f + \Delta f/2$ is $|\vec{P}_N^+(f)| \cdot \sqrt{\Delta f}$.

The one-sided amplitude density of fluctuations at frequency f , $|\vec{P}_N^+(f)|$, is a Rayleigh distribution of scale parameter $\sigma_N(f) = \langle |\vec{P}_N^+(f)| \rangle \sqrt{2/\pi}$, where angle brackets $\langle \cdot \rangle$ denotes averaging. In other words, the mean of $|\vec{P}_N^+(f)|^2$ is $\langle |\vec{P}_N^+(f)|^2 \rangle = \sqrt{\pi/2} \sigma_N(f)$ where $\sigma_N(f)$ is the RMS value of the phasor projection.

The RMS value of the phasor projection $\sigma_N(f)$ is also related to the one and two sided PSD of the active power:

$$\sigma_N(f) = \sqrt{2PSD_{P_N}(f)} = \sqrt{PSD_{P_N}^+(f)} \quad (158)$$

Put into words, the phasor density of the oscillation, $|\vec{P}_N^+(f)|$, has a Rayleigh distribution of scale parameter $\sigma_N(f)$ equal to the square root of the one-sided power spectral density.

For convenience, effective values are usually used instead of amplitude. The effective value of a sinusoid (or its root mean square value, RMS for short) is the amplitude divided by $\sqrt{2}$. Thus, the average quadratic value of the fluctuation of a wind farm at frequency f is, according to (156):

$$\left\langle \left| \vec{P}_N^+(f)/\sqrt{2} \right|^2 \right\rangle = \left\langle \left| \vec{P}_N^+(f) \right|^2 \right\rangle / 2 = \sigma_N^2(f) = PSD_{P_N}^+(f) \quad (159)$$

Rayleigh($\sigma_N(f)$)

If a fast Fourier transform is used as ideal narrowband filter and the Parseval's Theorem is applied, an estimate of $\sigma_N(f)$ is $\sqrt{2\Delta f} \cdot \langle |FFT_{n=f/\Delta f} \{P(k\Delta t)\}|^2 \rangle^{1/2}$ (in Bartlett or Welch methods, some smoothing or averaging is applied to obtain a consistent estimate).

If fluctuations at a cluster of N turbines are independent, then $\sigma_N(f) \approx \sqrt{N} \sigma_1(f)$, where $\sigma_1(f)$ is the mean RMS fluctuation density at a single turbine and at frequency f . The mean phasor density is:

$$\langle |\vec{P}_N^+(f)| \rangle_{\text{Rayleigh}(\sigma_N(f))} = \sqrt{\frac{\pi}{2}} \sigma_N(f) = \sqrt{N} \frac{\pi}{2} \sigma_1(f) = \sqrt{N} \langle |\vec{P}_1^+(f)| \rangle \quad (160)$$

If the real power of the turbine cluster is filtered with an ideal narrowband filter tuned at frequency f and bandwidth Δf , then the average effective value of the filtered signal is $\sigma_N(f) \sqrt{\Delta f}$ and the average amplitude of the oscillations is $\langle |\vec{P}_N^+(f)| \rangle \sqrt{\Delta f} = \sigma_N(f) \sqrt{\Delta f} \cdot \pi/2$. The instantaneous value of the filtered signal $\vec{P}_{N,f,\Delta f}(t)$ is the projection of the phasor $\vec{P}_N^+(f) \cdot e^{j2\pi f t} \sqrt{\Delta f}$ in the real axis. The instantaneous value of the filtered signal squared, $P_{N,f,\Delta f}^2(t)$, is an exponential random variable of parameter $\lambda = [N\sigma_1^2(f)\Delta f]^{-1}$. Taking into account the properties of the exponential distribution:

$$\left\langle P_{N,f,\Delta f}^2(t) \right\rangle_{\text{Exp distribution}} = N\sigma_1^2(f)\Delta f \quad (161)$$

The RMS oscillation resulting from all the discrete frequency components of uncorrelated fluctuations is the sum of the contributions of each characteristic frequency. For a discretized spectrum, the Parseval's theorem is:

* Comparison note: if the amplitude density $|\vec{P}_N^+(f)|$ is deterministic, then $\langle |\vec{P}_N^+(f)| \rangle = |\vec{P}_N^+(f)| = \sqrt{2} \sigma_N(f)$, slightly bigger than if $|\vec{P}_N^+(f)|$ is Rayleigh distributed. During a short record, $|\vec{P}_N^+(f)|$ can be fairly constant and thus the average sample amplitude density would be $\sqrt{\pi/2} \sigma_N(f) \leq \langle |\vec{P}_N^+(f)| \rangle \leq \sqrt{2} \sigma_N(f)$.

$$\begin{aligned} \left\langle P_{uncorr\ fluctuation}^2(t) \right\rangle &= \frac{1}{2} \left\langle \sum_{k=1}^{\infty} |\vec{P}^{+2}(k\Delta f)| \Delta f \right\rangle = \\ &= \frac{1}{2} \sum_{k=1}^{\infty} \langle |\vec{P}^{+2}(k\Delta f)| \rangle \Delta f = \sum_{k=1}^{\infty} \sigma^2(k\Delta f) \Delta f \end{aligned} \quad (162)$$

Notice that the factor 1/2 must be changed into 2 if two-sided phasors densities are used. For a continuous PSD, the sum transforms into an integral:

$$\begin{aligned} \left\langle P_{uncorr\ fluctuation}^2(t) \right\rangle &= \frac{1}{2} \left\langle \int_{1/T}^{f_{grid}} |\vec{P}^{+2}(k\Delta f)| df \right\rangle = \\ &= \frac{1}{2} \int_{1/T}^{f_{grid}} \langle |\vec{P}^{+2}(k\Delta f)| \rangle df = \int_{1/T}^{f_{grid}} \sigma^2(f) df \end{aligned} \quad (163)$$

According to (160) and (163), both the RMS value and the spectral phasor density of uncorrelated fluctuations scale up in a wind farm with a factor \sqrt{N} .

The distribution of $\left\langle P_{uncorr\ fluctuation}^2(t) \right\rangle$ can be derived in the time or in the frequency domain. In both cases, $\left\langle P_{uncorr\ fluctuation}^2(t) \right\rangle$ is the sum of infinitesimal Exponential random variables.

If the modulus and phase of $\vec{P}^+(f_k)$ are not linearly correlated at different frequencies f_k , then $\left\langle P_{uncorr\ fluctuation}^2(t) \right\rangle$ in (163) can be computed as the sum of independent infinitesimal random variables with exponential distribution. If $\sigma(f)$ is constant $\forall f_1 \leq f \leq f_2$ and null otherwise, the resulting distribution converges to a normal distribution with mean $\left\langle P_{uncorr\ fluctuation}^2(t) \right\rangle$ and standard deviation $\sqrt{2} \left\langle P_{uncorr\ fluctuation}^2(t) \right\rangle$. In practice, the fluctuation spectral density $\sigma(f)$ do depend on frequency and the sum of correlated gammas with different scale parameters can be computed with algorithm proposed in [175].

Power dips due to a blade passing in front of a turbine resembles pulse dips, which have a wide frequency spectrum. The correlation coefficients of frequency components will be derived in the second part of this work.

One or two sided sums of phasors are consistent –provided all values refer exclusively either to one or to two side spectra. Most differences do appear in integral or summation formulas – if two-sided spectra is used, a factor 2 may appear in some formulas and the integration limits may change from positive frequencies to positive and negative frequencies, as in (163).

4.4. Sum of partially correlated phasor densities of power from several turbines

4.4.1. Sum of fully correlated and fully uncorrelated spectral components

On the one hand, slow fluctuations ($f < 10^{-3}$ Hz) are mainly due to meteorological dynamics and they are widely correlated spatially and temporally. Slow fluctuations in power output of nearby farms are quite correlated –see (115) and (127)– and wind forecast models try to predict them to optimize power dispatch.

On the other hand, fast wind speed fluctuations are mainly due to turbulence and microsite dynamics [176]. They are local in time and space and they can affect turbine control and cause flicker [177]. Tower shadow is probably the more noticeable fluctuation of a turbine. It has a definite frequency

and, if the blades of all turbines of an area became eventually synchronized, it could be a power quality issue. But synchronization is very rare since the only synchronizing forces might be turbine wakes and voltage drops in the grid.

The phase $\varphi_i(f)$ implies the use of a time reference. Since fluctuations are random events, there is not an unequivocal time reference for use it as angle reference. Since fluctuations can happen at any time with the same probability –there is no preferred angle $\varphi_i(f)$ –, the phasor angles are random variables uniformly distributed in $[-\pi, +\pi]$ (i.e., the system exhibits circular symmetry and the stochastic process is cyclostationary). Therefore, the relevant information contained in $\varphi_i(f)$ is the relative angle difference among the turbines of the farm [178] in the range $[-\pi, +\pi]$, which is linked to the time lag among fluctuations at the turbines.

If the N turbine fluctuations at frequency f are completely synchronized, all the phases have the same value $\varphi_i(f)$ and the modulus of fully correlated fluctuations $|\vec{P}_{i, corr}^+(f)|$ sum arithmetically.

$$|\vec{P}_{farm, corr}^+(f)| = \left| \sum_{i=1}^N \vec{P}_{i, corr}^+(f) \right| = \sum_{i=1}^N |\vec{P}_{i, corr}^+(f)| \quad (164)$$

If there is no synchronization at all, the fluctuation angles $\varphi_i(f)$ at the turbines are stochastically independent. Since $\vec{P}_{i, uncorr}^+(f)$ has a random argument, its sum across the wind farm will partially cancel and inequality (165) holds true.

$$|\vec{P}_{farm, uncorr}^+(f)| = \left| \sum_{i=1}^N \vec{P}_{i, uncorr}^+(f) \right| < \sum_{i=1}^N |\vec{P}_{i, uncorr}^+(f)| \quad (165)$$

If there is no synchronization at all, the fluctuation angles $\varphi_i(f)$ at the turbines are stochastically independent. If the number of turbines $N > 4$, the central limit for the sum of phasors is a good approximation and (160) is applicable.

This approach remarks that correlated fluctuations adds arithmetically and they can be an issue for the network operation whereas uncorrelated fluctuations diminish in relative terms when considering many turbines (even if they are eventually very noticeable at turbine terminals).

4.4.2. Sum of partially linearly correlated spectral components

Inside a farm, all the turbines exhibit a similar behaviour for a given frequency f and the PSD of each turbine is expected to be quite similar. However, the phase differences among turbines do vary with frequency. Slow meteorological variations affect all the turbines with negligible time lag, compared to characteristic time frame of weather systems (i.e., the phasors $\vec{P}_{turbine}^+(f)$ have the same phase). Turbulences with scales significantly smaller than the turbine distances have uncorrelated phases. Fluctuations due to rotor positions also show uncorrelated phases provided turbines are not synchronized.

$$\left\langle P_{turbine}^+(f) \right\rangle^2 = \left\langle P_{turb, corr}^+(f) \right\rangle^2 + \left\langle P_{turb, uncorr}^+(f) \right\rangle^2 \quad (166)$$

If the number of turbines $N > 4$ and the correlation among turbines are linear, the central limit is a good approximation. The correlated and uncorrelated components sums quadratically and the following relation is applicable: (167)

$$\left\langle \left| \vec{P}_{farm}^+(f) \right|^2 \right\rangle \approx N^2 \left\langle \left| \vec{P}_{turb, corr}^+(f) \right|^2 \right\rangle + N \left\langle \left| \vec{P}_{turb, uncorr}^+(f) \right|^2 \right\rangle$$

where N is the number of turbines in the farm (or in a group of close farms). Since phasor densities sums quadratically, (166) and (167) are concisely expressed in terms of the PSD of correlated and uncorrelated components of phasor density:

$$PSD_{farm}(f) \approx N^2 PSD_{turb, corr}(f) + N \cdot PSD_{turb, uncorr}(f) \quad (168)$$

$$PSD_{turb}(f) = PSD_{turb, corr}(f) + PSD_{turb, uncorr}(f) \quad (169)$$

The correlated components of the fluctuations are the main

source of fluctuation in large clusters of turbines. The cluster admittance $J(f)$ is the relative transfer function of the mean fluctuation density of the farm, $\left\langle \left| \vec{P}_{farm}^+(f) \right|^2 \right\rangle$, respect the mean turbine fluctuation density, $\left\langle \left| \vec{P}_{turbine}^+(f) \right|^2 \right\rangle$.

$$J(f) = \frac{\left\langle P_{farm}^+(f) \right\rangle}{\left\langle P_{turbine}^+(f) \right\rangle} \approx \sqrt{\frac{PSD_{P_{farm}}(f)}{PSD_{P_{turbine}}(f)}} \quad (170)$$

Note that the phase of the transfer function $J(f)$ has been omitted since the phase lag between the oscillations at the cluster and at a generic turbine is meaningless if the turbine position is not specified.

TABLE II: SUMMARY OF STATISTICAL PROPERTIES OF UNCORRELATED SINUSOIDAL FLUCTUATIONS IN A CLUSTER OF N TURBINES

Assumptions	Spectral fluctuation density is deterministic and can happen at any time => phasor $\vec{P}_1^+(f)$ of fixed modulus and random angle.	Instantaneous fluctuation of frequency f at time t $\vec{P}_1^+(f)$ has normal complex distribution
1 turbine in the wind farm	Phasor $\vec{P}_1^+(f)$ of fixed modulus and random angle. $PDF_{ \vec{P}_1^+(f) }(x) = \delta(\vec{P}_1^+(f) - x)$; $\delta(\cdot)$ is the Dirac Delta $\sigma_1(f) = \vec{P}_1^+(f) /\sqrt{2}$ = standard deviation of the projection of the phasor $\vec{P}_1^+(f) e^{j2\pi f t}$ = mean RMS density of the instantaneous fluctuation at frequency f in one turbine $PDF_{ \vec{P}_1^+(f) e^{j2\pi f t} }(x) = \frac{1}{\pi \sqrt{2\sigma_1^2(f) - x^2}} \quad \forall 0 \leq x \leq \sqrt{2} \sigma_1(f)$	$\vec{P}_1^+(f)$ is a complex Gaussian random variable with zero mean and standard deviation $\sigma_1(f)$, $\vec{P}_1^+(f) \sim \mathbb{C}N(0, \sigma_1(f))$ $P_{1,f}(t) = \text{Re}[\vec{P}_1^+(f) e^{j2\pi f t}] \sim N(0, \sigma_1(f))$ $ \vec{P}_1^+(f) \sim \text{Rayleigh}(\sigma_1(f))$ $PDF_{ \vec{P}_1^+(f) }(x) = \frac{x}{\sigma_1^2(f)} \exp\left[-\frac{1}{2} \left(\frac{x}{\sigma_1(f)}\right)^2\right]$
2 turbines in the wind farm, statistically uncorrelated $\vec{P}_2^+(f) = \vec{P}_a^+(f) + \vec{P}_b^+(f)$	$PDF_{ \vec{P}_2^+(f) }(x) = \frac{1}{\pi \sqrt{2\sigma_2^2(f) - x^2}} \quad \forall 0 \leq x \leq \sqrt{2} \sigma_2(f)$ $\sigma_2(f) = \vec{P}_1^+(f) = \sqrt{2} \sigma_1(f)$ $PDF_{\vec{P}_2^+(f) e^{j2\pi f t}}(x) = \frac{-2\sigma_2(f)}{\pi^2 x } \text{Im} \left[\text{EllipticK} \left(\frac{2\sigma_2(f)}{x^2} \right) \right]$	$\vec{P}_2^+(f)$ is a complex Gaussian random variable with zero mean and standard deviation $\sigma_2(f)$, $\sigma_2(f) = \sqrt{2} \sigma_1(f)$ $\vec{P}_2^+(f) \sim \mathbb{C}N(0, \sqrt{2} \sigma_1(f))$ $P_{2,f}(t) = \text{Re}[\vec{P}_2^+(f) e^{j2\pi f t}] \sim N(0, \sqrt{2} \sigma_1(f))$ $ \vec{P}_2^+(f) \sim \text{Rayleigh}(0, \sqrt{2} \sigma_1(f))$
N turbines in the wind farm, statistically uncorrelated ($N > 4$) $\vec{P}_N^+(f) = \sum_{i=1}^N \vec{P}_i^+(f)$	<ul style="list-style-type: none"> $\vec{P}_N^+(f)$ is (or converges to) a complex Gaussian random variable with zero mean and stdev. $\sigma_N(f) = \sqrt{N} \sigma_1(f)$: $\Rightarrow \vec{P}_N^+(f) \sim \mathbb{C}N(0, \sqrt{N} \sigma_1(f))$; $\Rightarrow \text{Re}[\vec{P}_N^+(f)]$ and $\text{Im}[\vec{P}_N^+(f)]$ are independents with normal distribution: $N(0, \sqrt{N} \sigma_1(f))$; The instantaneous <i>uncorrelated</i> fluctuation amplitude density at frequency f is: $\vec{P}_N^+(f) \sim \text{Rayleigh}(\sqrt{N} \sigma_1(f))$ \Rightarrow The mean fluctuation amplitude density is $\langle \vec{P}_N^+(f) \rangle = \sqrt{2} \sigma_N(f) \sqrt{\pi/2} = 1,253 \sqrt{N} \sigma_1(f)$ \Rightarrow The mean fluctuation amplitude density squared is $\langle \vec{P}_N^+(f) ^2 \rangle \sim \text{Exponential} \left[\left(2 N \sigma_1^2(f) \right)^{-1} \right]$ The instantaneous <i>uncorrelated</i> fluctuation density at freq. f is $P_{N,f}(t) = \text{Re} \left[\vec{P}_N^+(f) e^{-j2\pi f t} \right] \sim N(0, \sqrt{N} \sigma_1(f))$ The variance of instantaneous power output in time interval T is $\int_{T-1}^{f_{\max}} \frac{1}{2} \langle \vec{P}_N^+(f) ^2 \rangle df$ The one-sided power spectral density of the wind farm fluctuation is $PSD_P^+(f) = \sigma_N^2(f)$ If the real power of the turbine cluster is filtered with an ideal <i>narrowband filter</i> tuned at frequency f and bandwidth Δf, then the average RMS value of the filtered signal is $\sigma_1(f) \sqrt{N \Delta f}$ and the average amplitude of the oscillations is $\sigma_1(f) \sqrt{N \Delta f \cdot \pi/2}$. 	

Since turbine clusters are usually not negatively correlated, then the following inequality is valid:

$$\sqrt{N} \lesssim J(f) \lesssim N \quad (171)$$

The squared modulus of the admittance $J(f)$ is conveniently estimated from the PSD of the turbine cluster and a representative turbine using the cross-correlation method and discarding the phase information [179]:

$$J^2(f) = \frac{PSD_{Pfarm}(f)}{PSD_{P_{turb}}(f)} = N^2 \frac{PSD_{turb,corr}(f)}{PSD_{turb}(f)} + N \frac{PSD_{turb,uncorr}(f)}{PSD_{turb}(f)} \quad (172)$$

If the PSD of a representative turbine, $PSD_{P_{turb}}(f)$, and the PSD of the farm $PSD_{Pfarm}(f)$ is available, the components $PSD_{turb,corr}(f)$ and $PSD_{turb,uncorr}(f)$ can be estimated from (168) and (169) provided the behaviour of the turbines is similar.

At $f \ll 0,01$ Hz, fluctuations are mainly correlated due to slow weather dynamics, $PSD_{turb,uncorr}(f) \ll PSD_{turb,corr}(f)$, and the slow fluctuations scale proportionally $PSD_{Pfarm}(f) \approx N^2 PSD_{turb,corr}(f)$. At high frequencies $f > 0,01$ Hz, individual fluctuations are statistically independent, $PSD_{turb,uncorr}(f) \gg PSD_{turb,corr}(f)$, and fast fluctuations are partially attenuated, $PSD_{Pfarm}(f) \approx N \cdot PSD_{turb,uncorr}(f)$.

An analogous procedure can be replicated to sum fluctuations of wind farms of a geographical area, obtaining the correlated $PSD_{farm,corr}(f)$ and uncorrelated $PSD_{farm,uncorr}(f)$ components. The main difference in the regional model –apart from the scattered spatial region and the different turbine models– is that wind farms must be normalized and an average farm model must be estimated for reference. Therefore, the average farm behaviour is a weighted average of individual farms [180] with lower characteristic frequencies. Recall that if hourly or even slower fluctuations are studied, meteorological dynamics are dominant and other approaches are more suitable.

4.4.3. Estimation of wind farm power admittance

In the previous sections, the equivalent farm squared wind has been derived assuming that equivalent squared wind is a multivariate Gaussian process with spectral covariance matrix $\Xi_{U^2_{eq}}(f)$.

According to (99), wind farm admittance $J(f)$ can be estimated from the equivalent farm squared wind (115) or from the equivalent farm wind (121).

$$J(f) \approx \sqrt{\frac{PSD_{Pfarm}(f)}{PSD_{P_{turbine}}(f)}} = \frac{\Omega_{farm}}{\Omega_{turb}} \sqrt{\frac{PSD_{Tfarm}(f)}{PSD_{T_{turbine}}(f)}} = \frac{\left\langle \frac{1}{2} \rho_{air} \pi \Omega_{farm} R_{farm}^3 N C'_q(\theta_{farm}, \lambda_{farm}) \right\rangle}{\left\langle \frac{1}{2} \rho_{air} \pi \Omega_{turb} R_{turb}^3 C_q(\theta_{turb}, \lambda_{turb}) \right\rangle} \sqrt{\frac{PSD_{U^2_{eq,farm}}(f)}{PSD_{U^2_{eq,turb}}(f)}} \quad (173)$$

In a wind farm with turbines of the same model and functioning at similar operational points:

$$\Omega_{farm} = \langle \Omega_{rotor,i} \rangle_{turbines} = \Omega \quad (174)$$

$$\lambda_{farm} = \langle \lambda_i \rangle_{turbines} = \lambda \quad (175)$$

$$\theta_{farm} = \langle \theta_i \rangle_{turbines} = \theta \quad (176)$$

$$R_{farm}^2 = \langle R_i^2 \rangle_{turbines} = R^2 \quad (177)$$

$$C'_q(\theta_{farm}, \lambda_{farm}) = \langle C_{q,i}(\theta_i, \lambda_i) \rangle_{turbines} = C_q(\theta, \lambda) \quad (178)$$

$$J(f) = \frac{\Omega_{farm} R_{farm}^3 N C'_q(\theta, \lambda) \sqrt{PSD_{U^2_{eq,farm}}(f)}}{\Omega_{turb} R_{turb}^3 C_q(\theta, \lambda) \sqrt{PSD_{U^2_{eq,turb}}(f)}} = \frac{N C'_q(\theta, \lambda) \sqrt{PSD_{U^2_{eq,farm}}(f)}}{C_q(\theta, \lambda) \sqrt{PSD_{U^2_{eq,turb}}(f)}} = N \sqrt{\frac{PSD_{U^2_{eq,farm}}(f)}{PSD_{U^2_{eq,turb}}(f)}} \quad (179)$$

If all the turbines experience similar equivalent squared wind spectra, i.e. $PSD_{U^2_{eq,i}}(f) \approx PSD_{U^2_{eq}}(f)$, then approximation (116) is valid and the following ratio can be computed:

$$\frac{PSD_{U^2_{eq,farm}}(f)}{PSD_{U^2_{eq,turb}}(f)} \approx \frac{1}{N^2} \sum_{i=1}^N \sum_{j=1}^N \tilde{\gamma}'_{ij}(f) \quad (180)$$

where $\tilde{\gamma}'_{ij}(f)$ is the complex coherence of effective quadratic turbulence at frequency f and at turbines i and j .

Therefore, the wind farm power admittance $J(f)$ is the sum of the complex coherence of effective quadratic turbulence among turbines:

$$J(f) \approx \sqrt{\sum_{i=1}^N \sum_{j=1}^N \tilde{\gamma}'_{ij}(f)} \quad (181)$$

As stated in (120), the equivalent turbulence and effective quadratic coherence are roughly equivalent, $\tilde{\gamma}'_{ij}(f) \approx \tilde{\gamma}_{ij}(f)$, provided the second-order approximations (93) and (118) are valid.

Thus, the admittance $J(f)$ can be estimated as $PSD_{Ueq,area}(f) / PSD_{Ueq,turbine}(f)$, the smoothing factor of the area (132). For the rectangular region shown in Fig. 51, the admittance is:

$$J(f) \approx f_\tau \left(\frac{A_{lat} b f}{\langle U_{wind} \rangle} \right) f_8 \left(\frac{A_{long} a f}{\langle U_{wind} \rangle}, A_{long} \right) \quad (182)$$

4.5. Parameterization of the power output spectrum

The actual spectrum of power from a wind turbine depends on many parameters such as turbine technology and wind regime. Kaimal (11) and Von Karman (14) wind turbulence spectra corresponds to a low pass filter of fractional order $r = 5/6$ and cut-off frequency related to the integral time [153]. The peak of wind PSD has a characteristic time usually in the order of minutes and the turbine dynamics are negligible at such slow frequencies (a quasi-static approach can be precise enough in most cases).

A simple model (183) will be used to characterize power fluctuations in partial load generation from the grid point of view. It will be used also to compare spectrum main characteristic of spectra available in the literature.

$$PSD_P(f) = \langle P_\sigma^2(f) \rangle \approx \frac{1}{2} H^+(f) G(f) \quad (183)$$

where either $PSD_P(f)$ or $\langle P_\sigma^2(f) \rangle$ are the two-sided PSD of the turbine or the farm real power. The factor $\frac{1}{2}$ has been introduced since $PSD_P(f)$ is the two-sided PSD and $H^+(f)$ corresponds to one-sided representation ($f \geq 0$). The one-sided representation of $H^+(f)$ have been selected to compare more easily the parameters from the literature, where one-sided plots are the standard for real signals and because only

positive frequencies are customarily considered in transfer functions.

$H^+(f)$ is the smooth part of the PSD due to turbulence and $G(f)$ is the squared gain which models the periodic components (PSD peaks at f_{blade} and its harmonics). $G(f)$ can be understood as the squared module of a filter bank that amplifies turbulence at some characteristic frequencies (blade frequency, tower resonance frequency, etc.) to match experimental data.

$H^+(f)$ can be parameterized approximately in the range from milihertz to 35 Hz as:

$$H^+(f) = P_1' \left(\frac{1 + (f/f_2)^2}{f_1^2 + f^2} \right)^{r'} \quad (184)$$

where r' , f_1 , f_2 and P_1' are parameters adjusted from experimental PSD.

The PSD of real or reactive power output has several components:

- Output of a system of fractional order r' slightly usually bigger than unity ($1 < r' < 1,75$). The slope of $|H(f)|$ in a double logarithmic plot at mid frequencies (10^{-2} Hz $< f < 10$ Hz) is r' . In all measurements and in almost all analyzed references, the order of power output is superior to the usual wind order $r' = 5/6 = 0,833$ from von Karman, Davenport or Kaimal PSDs. This indicates that the turbines attenuate wind oscillations of high frequency.
- The cut-off frequency $f_1 = 1/\tau_1$ indicates the transition of constant PSD to the constant slope $1/(2r')$ in a double logarithm plot. Frequency f_1 is usually in the range of milihertz (first time constant τ_1 is in the range of minutes). If PSD has a constant slope in low and middle frequencies, $f_1 \approx 0$.
- The scale factor is P_1' . At 1 Hz, the PSD is approximately P_1' and at very low frequencies, PSD is approximately constant with value $P_1' \cdot f_1^{-2r'}$.
- In some turbines, the PSD is approximately constant at frequencies higher than f_2 . At $f \gg f_2$ the noise floor is $P_1' \cdot f_2^{-2r'}$. If PSD decays with the same slope in a double logarithmic plot at middle and higher frequencies, the noise floor is negligible and the second time constant is very small, $\tau_2 = 1/f_2 \approx 0$.

Since $1 < r' < 1,75$, $H(f)$ can be approximated for $f \gg f_1$ (i.e., $f \geq 10^{-2}$ Hz) by:

$$H^+(f) \underset{f \gg f_1}{\approx} P_1' f^{-2r'} + P_2 \quad (185)$$

where $r \approx r'$ is the approximate order of the system and it can be computed as the slope of $|H(f)|$ in a double logarithmic plot at mid frequencies, $f_1 < f < f_2$. If PSD remains approximately constant at high frequencies, the value of noise floor for frequencies between $f_2 = 1/\tau_2$ and 35 Hz (maximum frequency of interest in flicker analysis) is $P_2 \approx (2^r - 1) P_1 \tau_2^{2r}$.

The deviation of the actual system from the spectrum trend is modeled as a multiplicative factor $G(f)$, which can be considered approximately unity except at blade frequency $f_{blade} = 3f_{rotor} = 3p$ (for a rotor with three blades) and its harmonics. $G(f)$ is significantly above unity at frequencies f where the system presents a periodic pattern. If turbine

dynamics and its control damp fluctuations of some frequency range, $G(f)$ is bellow unity at those frequencies.

PSD shows peaks at blade frequency ($f_{blade} = 3\Omega_{rotor}/(2\pi) = 3p$ for a rotor with three blades) and its harmonics due to wind shear and aerodynamic effects as the blades pass in front of the tower.

Exact frequency of fluctuations can be very important for avoiding mechanical resonance modes in the design of a wind turbine, but they play a secondary role in the grid. The main power quality concern due to fluctuations is flicker level. Since weighting filter on flickermeter varies smoothly with frequency, the frequency value of is not as important as in mechanical resonance studies. Moreover, the PSD shows some wide peaks at blade frequency harmonics indicating modulation (i.e., periodic fluctuations have actually variable frequency and amplitude). A simplified admittance function $G(f)$ with a few harmonics of blade frequency f_{blade} can have enough precision in most cases: (186)

$$G(f) = 1 + \sum g_k \delta(f - k f_{blade}) \approx \approx 1 + \frac{\langle P(t) \rangle^2}{S_1^2} \delta(f) + g_1 \delta(f - f_{blade}) + g_3^2 \delta(f - 3f_{blade})$$

where δ is the delta of Dirac function. $G(f)$ concentrates the accumulated relative error of $H(f)$ at the center of the frequency band $(k - \frac{1}{2})f_{blade} < f < (k + \frac{1}{2})f_{blade}$. If the modulation of the fluctuations needs to be represented, then $\delta(f - f_{blade})$ can be replaced by a notch filter such as:

$$\delta(f - f_{blade}) \sim \underset{BandWidth \rightarrow 0}{Lim} \frac{2 / \pi}{1 + \frac{(f^2 - f_{blade}^2)^2}{BandWidth \cdot f^2}} \quad (187)$$

where the bandwidth parameter (in Hertz) controls the modulation of the fluctuations.

The delta impulse at origin is due to the mean value of power, $\langle P(t) \rangle$. The rest of terms can be estimated with the following expression:

$$g_k = \frac{2 \int_{(k-\frac{1}{2})f_{blade}}^{(k+\frac{1}{2})f_{blade}} PSD_P(f) df - \int_{(k-\frac{1}{2})f_{blade}}^{(k+\frac{1}{2})f_{blade}} H^+(f) df}{H^+(k f_{blade})} \quad (188)$$

where the factor 2 is due that $PSD_P(f)$ is the two-sided PSD –symmetric respect origin–, integration limits corresponds only to positive frequencies and g_k corresponds to one-sided representation ($k > 0$).

At full load generation, wind fluctuations of frequencies bellow 0,05 Hz are strongly attenuated in electrical power output. Recall that frequency analysis must be used with care because wind is a stationary stochastic process only if meteorological conditions do not vary significantly. In general, parameters P_1 , P_2 , r , τ_1 , τ_2 and g_k must be estimated for the fundamental operational modes of the turbines. Since the turbine dynamics at very low frequencies is driven by the meteorological evolution where operational conditions do change, non-linear models can be more appropriate to model very slow changes.

4.5.1. Estimation of power variance during a time interval

Often, the variance is computed not from instantaneous power but from mean averages integrated during a short period Δt multiple of half grid period. Since the available data in this work is measured based on half grid periods, then the corresponding Nyquist frequency is $f_{Nyquist} = 1/(2\Delta t) \leq f_{grid}$. The maximum frequency considered in the flicker standard IEC 61000-4-15 [181] is 35 Hz. Power oscillations of frequency higher than the network frequency ($f_{grid}=50$ or 60 Hz) has negligible influence in flicker and it can be considered as waveform distortions (their interaction with the grid is different than slower fluctuations).

The variance of power computed during a time interval T from data recorded each Δt seconds can be computed from (185) and (186) through Parseval's theorem, assuming that fluctuations of different frequencies $f > 0,01$ Hz typically have uncorrelated phases:

$$\begin{aligned} \sigma_{P,T,\Delta t}^2 &= 2 \int_{1/T}^{1/2\Delta t} PSD_P(f) df \approx \int_{1/T}^{1/2\Delta t} H^+(f)G(f) df \approx \\ &\approx P_1 \frac{T^{2r-1}-(2\Delta t)^{2r-1}}{2r-1} + P_2 \left(\frac{1}{2\Delta t} - \frac{1}{T} \right) + \sum_k g_k^2 H^+(k f_{blade}) \end{aligned} \quad (189)$$

where 2 factor has been included since $PSD_P(f)$ is two-sided and only positive frequencies are considered in the integral limits. If $\sigma_{P,T,\Delta t}^2$ is computed directly from discrete $PSD_P(f)$, take into account that the integral transforms into a sum, DC term should be excluded and Nyquist frequency should be accounted only once (without the 2 factor).

If the model is extrapolated up to the maximum frequency of interest f_{grid} the variance of power can be estimated as:

$$\sigma_{P,T}^2 \approx P_1 \frac{T^{2r-1}-f_{grid}^{1-2r}}{2r-1} + P_2 \left(f_{grid} - \frac{1}{T} \right) + \sum_k g_k^2 H^+(k f_{blade}) \quad (190)$$

Taking into account the actual uncertainty of estimated parameters P_1 , P_2 , r and $g_k f_{blade}$ and the fact that $f_{grid} \gg T$, the following approximate expression is suitable:

$$\sigma_{P,T}^2 \approx P_1 \frac{T^{2r-1}}{2r-1} + P_2 f_{grid} + \sum_k g_k^2 H^+(k f_{blade}) \quad (191)$$

Since wind evolves due to meteorological dynamics, wind is not a truly stationary stochastic process. The weather evolution increases the variance in power output. In fact, if P_1 has been estimated from raw power output (without detrending the weather evolution), formulas (190) and (191) include variance due to meteorological dynamics. If weather forecast is employed as an input of the variability model, the variance due to the unpredictable component of the wind (i.e. stochastic wind turbulence) and foreseeable wind evolution (i.e., slow weather evolution) should be accounted separately. In fact, this approach improves the estimation of P_1 and the turbulence length of the wind in Kaimal and von Karman turbulence models. In [182], a method to detrend turbulence and weather evolution in measured wind variance is presented (a similar approach can be used for power output data).

Since fluctuations of different frequencies typically have uncorrelated phases during continuous operation, the variance of instantaneous power is half the integral of the power spectrum. In other words, the expected variance of instantaneous power is half the area beneath the PSD plot in

linear axis plot. Moreover, the linear averaging of power spectrum (used to estimate the PSD) does not change the variability of instantaneous power.

The value and bandwidth of PSD peaks are influenced by frequency resolution, recorded signal, window function and the estimation method (Welch's periodogram, ARIMA models, etc). Fortunately, the variability content in a frequency band has lower uncertainty than the PSD estimation at a single frequency.

For time spans of minutes or smaller, the fluctuations of different turbines are highly uncorrelated and the PSD of the turbines sums the wind farm PSD (i.e., the PSD in p.u. units of turbines and the farm is the same at $f > 0.001$ Hz).

For time spans of quarters of hour ($f < 0.001$ Hz), the fluctuations of turbines inside a farm are quite correlated and the simple spectrum of the turbines (i.e., the modulus of the Fourier transform of the instantaneous power) sums the simple spectrum of the farm.

If all the phasors had had the same angles, the standard deviation of instantaneous power would have been half the integral of the simple spectrum. In such case, the frequency analysis would have been based on the spectrum modulus instead of the PSD. Measurements have shown that the angles of phasors are significantly correlated only at the tripping of turbines or wind farms or at very low frequencies (for example, in a gradual weather change leading to the evolution from no generation to full generation or the reverse). Fluctuations of very low frequency are related to meteorological dynamics, which are out of the scope of this work. Abrupt changes of instantaneous power will be studied in time domain with Markov chains in the following chapter.

In conclusion, the PSD is a consistent estimator of wind power variability for the time span of interest.

4.6. Estimation of parameters from measured data

4.6.1. General features of measured data

The smoothed periodogram (module averaged Power Spectrum Density) has proved suitable PSD estimator. There is a trade-off between removing noise and frequency resolution, but a data record of several minutes measured at 50 Hz is usually enough to obtain a good PSD estimation.

The PSD of the wind agrees, up to some extent, to the usual Kaimal wind spectra (i.e., system order $\sim 5/6$).

Slow fluctuations are prevalent in the turbine power (the spectrum quickly decreases at frequencies beyond f_{blade} since both wind spectra decreases and turbine dynamics act as a low-pass filter). The fluctuations do not have a narrow frequency margin; they are spread in wide frequency bands.

Even though rotor torque at low-speed shaft has strong periodic components due to rotor position (see Fig. 311), this modulation is largely filtered by the gearbox, the drive train and the generator dynamics. The resulting power fluctuations have neither the characteristic shape of Fig. 311 nor a true periodic signal. The fluctuations in power vary their frequency and amplitude slowly, probably because the randomness of the wind interacts with turbine resonance

modes of frequency similar to blade frequency (interference of two oscillations of similar frequency). The rotor speed of the turbines varies slightly and the sum of the fluctuations due to turbine modes and blade frequency modulates instantaneous power output (see for example Fig. 190). The PSD of power show peaks at rotor and tower resonance frequencies and their harmonics (see Fig. 205 and Fig. 206). In some turbines, sub-harmonic $2/3$ ($f = 2f_{rotor}$), sub-harmonic $1/2$ ($f = 2/3f_{rotor}$), and sub-harmonic $1/3$ ($f = f_{rotor}$), have been found, probably related misalignments in the blades and excitation of low frequency turbine oscillation modes.

Superposed to the almost periodic component, there are random variations due to wind turbulence that can be identified as the background spectrum trend after removal of cyclical oscillations. The power output PSD background corresponds to a system of fractional order between 1 and 2.

The switching events can be clearly noticed in the WT, but the effect in the substation of the park is quite weak. This is mainly due to the independent operation of the WT in a farm and the diverse wind conditions that each WT experiences. Thus, if switching events are fast enough, there is low probability that more than two turbines are connecting their generators at the same time.

There is a small probability of resonance or turbine synchronization along a wind farm. A time-frequency analysis has been performed to detect a possible resonance. Some methods with large time-frequency resolution as Wigner-Ville Distribution (WVD) and S-Method (SM) have been tested, but they generate cross-terms because of the wide range of frequencies in the signal. In fact, the Short Fast Fourier Transform (SFFT) is the method more stable and less influenced by cross-terms of the tested techniques. In the SFFT, the Fourier Transform is applied to a small window of the signal. If a frequency appears remarkably perceptible in the correlogram, an eventual resonance of that frequency has happened during that elapse. Finally, some examples of the application of the time-frequency analysis to wind power are shown in this chapter using SFFT.

4.6.2. Procedure to estimate model parameters

The adjustment of parameters of the model (184) is somewhat subjective, since the standard least square fitting method overweight frequencies where PSD is bigger and where the spectrum has more points per decade. Generally, low frequency deviations have more influence in total fit error.

Several fitting methods have been tested for fitting P_1' , r' , f_1 and f_2 whilst minimizing $\sum g_k^2$ using standard mathematical tools. One method has been developed based on the manual fit procedure (see Fig. 58). This procedure is quite simple and it gives reasonable performance for the estimation of P_1' , r' although the estimation of f_1 and f_2 can be further improved.

Sample $PSD_p^+(f)$ units are effective square Watts per Hertz and it is plotted in light gray (see Fig. 187). The term effective or rms refers to the fact that the integral bellow the $PSD_p^+(f)$ is the signal variance according to (192). These units are consistent with the effective or rms values of voltages and currents.

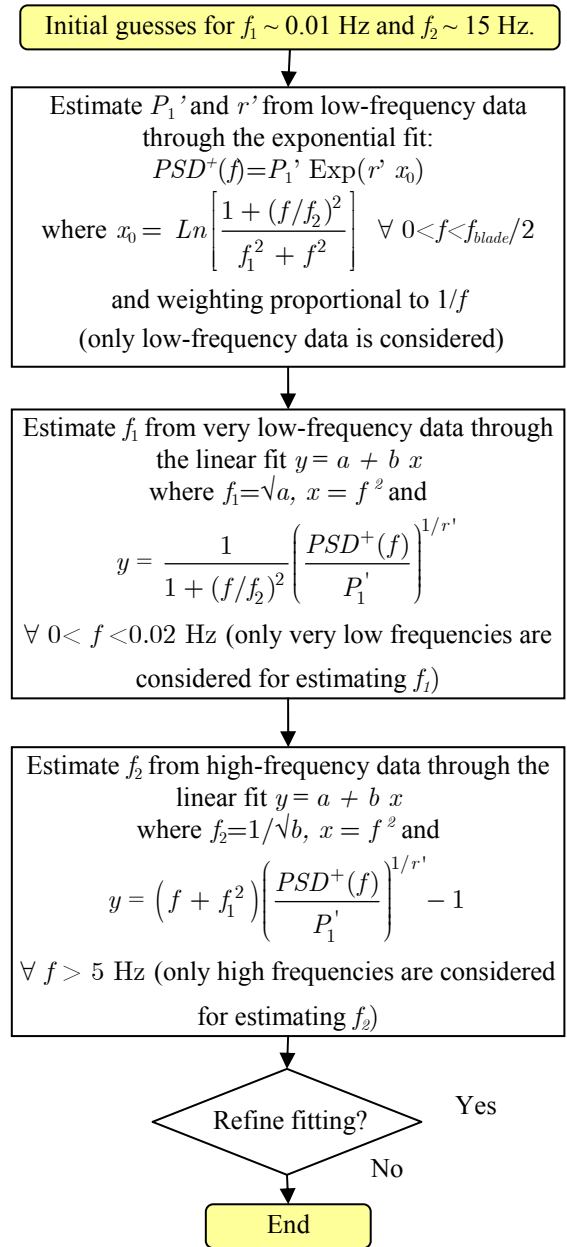


Fig. 58: Basic procedure for estimating P_1' , r' , f_1 and f_2 .

The running average of $PSD_p^+(f)$ is the smoothed *periodogram* and it is plotted in black. The average blade frequency is indicated in vertical yellow line. Red line is the model (184) (the output of a system of fractional order r between 1 to 1,75 with a zero and a pole excited by white noise). In the cases analyzed, the frequency of the pole is generally in the range $f_1 \lesssim 10^{-2} \sim 10^{-3}$ Hz and the zero frequency is usually $f_2 \gtrsim 7$ Hz.

On the one hand, the zero characterizes the frequency where the spectrum no longer decreases, i.e. the noise floor of the spectrum (if there is no noise floor, then $f_2 \approx \infty$). Since the noise floor is quite small, it is influenced by the measurement accuracy.

On the other hand, the pole characterizes the frequency where the spectrum starts decreasing. Since it occurs at very low frequencies, it is biased by the duration of the sample. If $f_1 \leq N_{smoothing}/T$, where T is the duration of the sample and $N_{smoothing}$ is the effective number of samples in the smoothing filter applied to the spectrum to decrease its uncertainty, then the estimate of f_1 is unreliable and only upper bound of f_1 can

be given. In the cases presented in this section, T is from 200 s to 800 s and the effective smoothing is $N_{smoothing} = 0,443 \cdot 20 = 8,86$ samples (cut-off frequency of a moving average of 20 samples, in sample units). Therefore, pole frequencies below 0,01 to 0,04 Hz (depending on the sample duration) cannot be estimated from these short samples.

However, f_1 can be estimated from data of lower time resolution but with longer duration records. During the measuring campaign, only the average values of one or two second spans were recorded during several days due to storage limitations. These records allow to study very low frequency behaviour, up to the Nyquist frequency (0,5 or 0,25 Hz). For very long series, the number of samples in the original series is very big and special techniques may be applied to avoid running out of memory while the PSD is being estimated. Note also that very long records can include meteorological changes and different operational modes of the turbine (these features will be analyzed in the last chapter).

A dark blue line is added sometimes to indicate the variance $\sigma_{P,T,f}^2$ of the signal filtered up to frequency f .

$$\sigma_{P,T,f}^2 = \int_{1/T}^f PSD_P^+(f) df \quad (192)$$

Sometimes, a green line is added to indicate the accumulated error of the model from frequency f up to the Nyquist frequency (25 Hz).

$$accumulated\ error = \int_f^{1/2\Delta t} PSD_P^+(f) df - \int_f^{1/2\Delta t} H(f) df$$

In PSD plots such as Fig. 187, the bar chart are the values of $g_k \forall k > 0$ computed from (188) and the color of the bar indicates that g_k is positive (red) or negative (blue).

4.7. Estimation of parameters from the literature

A literature review on experimental data of power output PSD from wind turbines or wind farms are presented. In most cases, the fluctuation level S_1' can not be computed from the literature data. Recall that many papers show the discrete Fourier Transform of real power, which is essentially the squared root of the PSD times the frequency resolution Δf . If Δf is not stated, the PSD normalization constant is unknown. In other cases, the units of PSD are not pointed out. Even though the PSD depends on the employed estimation method –specially its peak values at periodic frequencies–, the power content in a frequency band is less sensible and therefore, suitable for comparing fluctuations at different locations.

Table III shows the adjusted parameters of (183) from measurements taken by the author or estimated from the references. Unfortunately, there is not enough information in most references to estimate S_1 , f_1 or the interval variance of power $\sigma_{P,T}^2$.

Finally, recall that the turbine or farm can be approximated by a system with transfer function $S(f)$ excited with white noise of unity variance plus a unity DC component.

4.8. Conclusions

In the former chapters, the wind has been analyzed to estimate the variations of aerodynamic torque. However, the aerodynamic torque interacts with the structural and drive-train vibrations. Consequently, the power injected in the grid has a stochastic nature even in total absence of turbulence.

There are many specific characteristics that impact notably in the power fluctuations between the first tower frequency (usually some tenths of Hertz) and the grid frequency. The realistic reproduction of power fluctuations needs a comprehensive model of each turbine, that is usually confidential and private.

One contribution of this chapter is the experimental characterization of the power fluctuations of three commercial turbines with a multipurpose data logger designed and installed by the author of this thesis. This multipurpose data logger has posteriorly evolved into a commercial product called AIRE (Analizador Integral de Recursos Energéticos).

The variations of power during the continuous operation of turbines are measured and experimentally characterized for timescales in the range of minutes to fractions of seconds. Some experimental measurements in the joint time-frequency domain are presented to test the mathematical model of the fluctuations.

The admittance of the wind farm is defined as the ratio of the oscillations from a wind farm compared to the fluctuations from a single turbine, representative of the operation of the turbines in the farm. The partial cancellation of power fluctuations in a wind farm are estimated from the ratio of the farm fluctuation relative to the fluctuation of one representative turbine. Some stochastic models are derived in the frequency domain to link the overall behaviour of a large number of wind turbines from the operation of a single turbine.

A literature review on Power Spectral Densities (PSD) and periodograms (averaged spectrum) of wind power are presented. The variability of PSD is also studied, a step ahead from the literature, in the joint time-frequency domain through spectrograms.

TABLE III: COMPARISON OF SPECTRUM PARAMETERS OF POWER OUTPUT

Source	r	S_1' (kW ² /Hz)	τ_2 (s)	Remarks
[52], NM-750 kW, SCIG	1,35	$1.4 \cdot 10^3$	0	Fixed speed, stall regulated turbine at Valdecuadros.
[52], Gamesa DFIG 640 kW	1,23	$6 \cdot 10^3$	0,5	Variable speed, pitch wind turbine at Remolinos, S_1 high
[52], 17 x 640 kW wind farm, Gamesa pitch contr. DFIG	1,23	10^5	0,5	Remolinos wind farm with variable speed, pitch controlled wind turbines, S_1 high.
[52], 27x600 kW turbines, Vestas pitch controlled VRIG	1,1	10^4	0	Borja wind farm, pitch control and almost fixed speed (opti-slip control), S_1 high.
[183], 5 x 500kW stall-regulated offshore wind farm	$\sim 1,9$		0	Bockstigen stall-regulated offshore wind park with variable speed turbines at low winds
[183], 5 x 500kW offshore	$\sim 1,6$		0.2	Constant speed operation at medium or high winds
[184], 2,5 MW wind farm operating at 500 kW, fixed speed	0.63		0	Fixed speed operation. Noticeable tower shadow pulsation.
[184], 2,5 MW wind farm operating at 500 kW, variable speed	1.3		0.8	Good agreement also for $r \sim 1$ and $\tau_2=0$. Anti-flicker algorithm avoids tower shadow pulsation
[185] 2x225 kW wind farm	1,03			Two 225 kW pitch-controlled turbines.
[186], 4 x 180 kW Alsvik wind farm	1*		0.24	$v_{\text{wind}} \approx 14$ m/s, low turbulence wind at Gotland
[186], 4 x 180 kW Alsvik wind farm	1,1*		0.24	$v_{\text{wind}} \approx 14$ m/s, wake operation
[186], 4 x 180 kW Alsvik wind	1,15		0.24	$v_{\text{wind}} \approx 10$ m/s, low turbulence wind
[187], 10 x 500 kW wind farm	1		0	Spectrum of real power, fixed-speed, stall-regulated
[187], 10 x 500 kW wind farm	0.86		0	Spectrum of reactive power, fixed-speed, stall-regulated
[188] 7 x 1.5 MW ENRONWIND EW offshore wind farm at Utgrunden	0.7~ 1.4		10- 20	At full power, almost constant PSD from 0,05 Hz (at medium and low power, constant PSD from 0,1 Hz)
[189] 7 x 1.5 MW ENRONWIND EW offshore wind farm at Utgrunden	~ 1.5			Real and reactive power shows an almost linear relationship up to 17 Hz: $\Delta Q \sim \Delta P / 10$
[152], MADE AE46/I, 660 kW	1		0	Stall regulated turbine, fixed speed, SCIG
[190], 4 x 180 kW, Alsvik wind farm, Fig. 5.2 a=	~ 1		0	Spectrum of real power. Generator fluctuations near 10 Hz.
[190], 4 x 180 kW, Fig. 5.2 b)	$\sim 0,8$		0	Stall regulated turbine, spectrum of reactive power at Alsvik.
[43], 180 kW, constant speed, soft shaft	1.1		0	Soft shaft damps high frequency oscillations down
[43], 180 kW, constant speed, stiff shaft	1.1		3	Stiff shaft increases oscillations faster than 1 Hz
[191], [192] or [193], 2 MW, NM2000/72 turbine at 9 m/s	1,04~ 1,17	~ 158	0	Medium power operation (8~9 m/s)
[191], [192] or [193], 2 MW, NM2000/72 turbine at rated wind speed	1,04~ 1,1	~ 16	0	Rated power operation (14~15 m/s)
[44], 500 kW stall regulated turbine	$\sim 1,5$	~ 20	0	Constant speed, stall regulated wind turbine
[194] multi-megawatt turbine, coordinated pitch controller	~ 0.7	~ 500	0	Simulation results without reference to real measurements
[194] multi-megawatt turbine, traditional controller	1	~ 300	0	Simulation results without reference to real measurements, K_1 high.
[195], 2-bladed, teeter hub, down wind, stall controlled 11 kW turbine	1,15~ 1,24	25~80	0	PSD of the turbine operating in a wind-diesel autonomous system is 3 times bigger than operating connected to the grid.
[196], 500 kW fixed-speed, stall-controlled wind turbine	1,45	$\sim 4,6$	0	Wind farm and turbine power output shows a \sqrt{N} ratio for $f > 0.07$ Hz
[197], simulated PSD (not experimentally measured PSD)	1,15	$\sim 10^{-4}$ pu ² /Hz	0	At high winds, PSD decreases in a factor of 10.
[47], 8 x 55 kW ENERCON-16 turbines at Cuxhaven wind farm	0.62	$\sim 10^{-4,2}$ pu ² /Hz	0	Wind farm and turbine fluctuations show \sqrt{N} ratio for $f > 0.09$ Hz and N ratio for $f < 0.03$ Hz
[198], 4 x 180 kW wind farm at Gotland	1,25	~ 64	0,17	Spectrum of real power. Stall-regulated, fixed speed.
[198], 4 x 180 kW wind farm at Gotland	0.8~1	~ 6.4	0	Spectrum of reactive power
[199], GE 3.6 MW, DFIG, pitch regulated	1.025		0	Spectrum of mechanical power at low winds (not electrical power output)
[199], GE 3.6 MW, DFIG, pitch regulated	1,6		0	Slow mechanical fluctuations are attenuated by constant power control at high winds.

* The spectrum fit neither a single slope in the double-logarithmic plot nor a slope and a horizontal zone at high frequencies. The value indicated is the mean slope, but they should be considered carefully.

Chapter 5:

Almost Periodic Fluctuations

In The Time Domain

5.1. Blade angle difference among turbines in a wind farm

The nature of turbulence and vibrations are different. The equivalent wind fluctuations due to the turbulence are broadband stochastic processes with no characteristic frequencies. However, vibrations and electrical oscillations are almost cyclostationary stochastic processes, usually with several noticeable narrowband components.

The influence of blade position in a single turbine power output has been analyzed in the annex C and in the literature [43, 44, 81, 154, 207, 208]. The almost deterministic behaviour used in the annex C and in the reference does not represent the real stochastic nature of the turbine torque, that is the outcome of many random vibrations, most of them fueled by the rotor spinning. Moreover, the electrical system interacts with the mechanical vibrations, damping some frequencies and introducing new oscillations.

This chapter focuses on the instantaneous overall effect in a cluster of turbines, assuming a deterministic behaviour of the turbine torque or power, which is a more conservative than actual random fluctuations. In any case, it will be derived that the sum of the power variations from more than four turbines converges approximately to a Gaussian process despite of the process nature (deterministic, stochastic, broadband or narrowband), analogously to the martingale central limit theorem. The only required condition is the negligible effect of synchronization forces among turbine oscillations.

According to [159], a very steady and very uniformly distributed wind together with a weak electrical network is necessary for synchronisation to happen driven by voltage drops. Experimental measurements [52] have corroborated that the synchronisation of the blades is unusual. In addition, the spectral model of the turbulence (128) showed that wind fluctuations at the frequency of the blades crosses the tower can be considered independent because it is much higher than $f_{cut,lat}$ and $f_{cut,long}$, defined in (134) to (136).

If the synchronization forces are negligible, the cyclic uncorrelated fluctuations due to rotor position have random phases. As wind characteristics are similar inside the farm, the magnitude of the cyclic components would be similar in all turbines. The angle (or phase) difference between blades of turbines i and j is $\varphi_{i,j}/3$ and it is uniformly distributed in $[-\pi, +\pi]$. Therefore, phase difference of harmonic k in turbines i and j is $k \varphi_{i,j}$, which is also uniformly distributed in $[-\pi, +\pi]$.

The frequency decomposition poses the burden of computing phase relationships and time-domain approaches are advantageous. However, they are closely related and some interesting results will be derived. For example, the approximate flicker emission of a wind farm is derived from measurements of a single turbine.

5.2. Tower shadow and wind shear effect in the wind farm power

In the third chapter, a method to compute the relation of blade angle on rotor torque has been computed –see for example **Fig. 311**. The interaction between the rotor torque fluctuations and the turbine is very complex and a thorough model of the turbine, generator and control system is needed for simulating the influence of wind turbulence in power output. The control scheme and its optimized parameters are proprietary and difficult to obtain from manufacturers and complex to guess from measurements usually available.

This chapter is focused in almost periodic variations of power in the time domain, such as the blade shadow, from a phenomenological point of view.

Both current and power are straightforward related to power quality. Current is transformed and its level depends on transformer ratio and actual network voltage. In contrast, power flows along transformers and networks without being altered except for some efficiency losses in the elements. Since real and reactive power is less affected by the factors external to the self turbines, the parameters selected to characterize the electrical output of wind turbines are the real and reactive power. Notwithstanding this fact, the model is also applicable to the rotor torque in case the drivetrain and generator can be assimilated to a linear, time-invariant dynamic system.

The power dips due to blade position will be represented by negative pulses in real power. Since all blade angles are equally probable, the pulse is distributed uniformly in time $t \in [0, T]$, where T is the period of the pulses (the period in Fig. 59 is $T=1$ s).

For a turbine of three blades, the period in seconds is $T = 20 / \Omega_{rotor}$, where Ω_{rotor} is the rotor in r.p.m. and the conversion factor is 60 s/min divided by 3 blades in the rotor, equal to 20 blades/r.p.m. The effective period of a wind farm –whose turbines can have different Ω_{rotor} – is the average of the periods of its turbines.

Since the occurrence of pulses is not correlated, usual techniques for the computation of the sum of identically

distributed independent random variables are applicable. They involve iterative computation of convolutions or the inverse Fourier transform of the characteristic function to the power N .

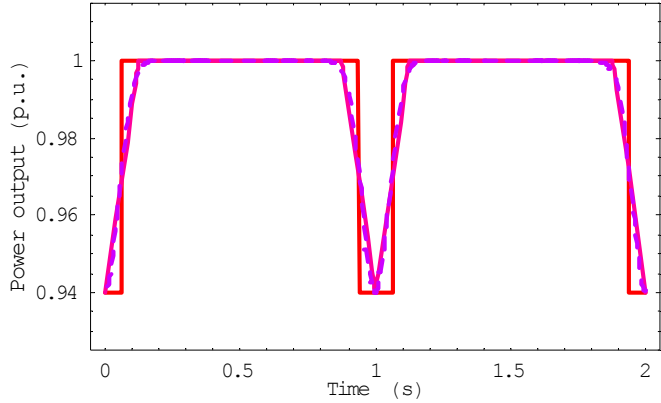


Fig. 59: Power output at a single turbine with blade rate 1 Hz, depth of tower shadow $\alpha = 0,06$ p.u. and average power loss $= \alpha \tau / T = 0,0075$ p.u. (the power dip shapes are rectangular, triangular and Gaussian).

TABLE IV: PROCESS OF COMPUTING THE DISTRIBUTION OF FLUCTUATIONS IN A WIND FARM DUE TO TOWER SHADOW.

1. Compute the PDF of the pulse.
2. Compute continuous Fourier transform of the PDF.

$$\phi_{\text{pulse}}^*(f) = \mathcal{F}\{PDF_{\text{pulse}}(y)\}$$
3. Compute the PDF of the wind farm as the inverse Fourier transform of the PDF Fourier transform to the power N ,

$$\phi_{\text{wind farm}}^*(f) = [\phi_{\text{pulse}}^*(f)]^N$$
 (N = the number of turbines in the wind farm).
4. Quantify the power quality of the wind farm from its PDF.

$$PDF_{\text{wind farm}}(y) = \mathcal{F}^{-1}\{\phi_{\text{wind farm}}^*(f)\}$$

Note that $F_{\text{pulse}}(f)$ is the conjugate of the characteristic function of the pulse distribution, $\phi(f)$. Note also that $\mathcal{F}\{PDF_{\text{pulse}}(y)\}$ can only be computed analytically in a few cases.

The pulse will be characterized by its energy loss $\alpha \tau$ (area between power pulse and unperturbed power) and its maximum depth α .

Tower shadow of shapes rectangular, triangular, cosine and Gaussian have been compared to test the shape influence in overall behaviour of the farm.

$$P_{\text{turbine}}(t) = P_0 - f_{\text{pulse}}(t) \quad (194)$$

$$f_{\text{pulse}\Delta}(t) = \begin{cases} \alpha \left(1 - \frac{|t-\mu|}{\tau}\right) & |t-\mu| < \tau \\ 0 & |t-\mu| \geq \tau \end{cases} \quad (\tau < T/2) \quad (195)$$

$$f_{\text{pulse}\square}(t) = \begin{cases} \alpha & |t-\mu| < \tau/2 \\ 0 & |t-\mu| \geq \tau/2 \end{cases} \quad (\tau < T) \quad (196)$$

$$f_{\text{gaussian pulse}}(t) = \alpha e^{-\left(\sqrt{\pi}(t-\mu)/\tau\right)^2} \quad (\sigma = \tau/\sqrt{2\pi}) \quad (197)$$

$$f_{\text{cos pulse}}(t) = \begin{cases} \frac{\alpha}{2} \left[1 + \cos\left(\frac{\pi(t-\mu)}{\tau}\right)\right] & |t-\mu| < \tau \\ 0 & |t-\mu| \geq \tau \end{cases} \quad (198)$$

$$\text{Max}(f_{\text{pulse}}(t)) = \alpha; \quad (199)$$

$$\text{Pulse Energy Loss} = \int_{\mu-T/2}^{\mu+T/2} f_{\text{pulse}}(t) dt = \alpha \tau \quad (200)$$

$$\text{Average Power Loss} = \frac{\text{Pulse Energy Loss}}{\text{time between pulses}} = \alpha \frac{\tau}{T} \quad (201)$$

where α is the depth of the pulse, τ is the characteristic width and μ is the time position of the pulse. For convenience, the origin of time will be chosen in the center of the pulse ($\mu=0$). Tower shadow duration is small, in the order of $1/8$ of period according to [50] and Fig. 311, because the solidity of the blades and the tower radius are small. The torque pulse depth depends on the blade pitch, rotor speed and wind speed. The power pulse depth, α , depends additionally on turbine inertia, type and control of the generator.

5.2.1. Distribution of the fluctuation

The first step is the computation of the distribution of the pulse. If the pulse is symmetrical about its mass center, its PDF is the inverse function divided by half the pulse energy. Then, the CDF can be computed, taking into account the symmetry of the pulse and taking the positive branch ($t > 0$) of the inverse function of $f_{\text{pulse}}(t)$.

$$\begin{aligned} \text{CDF}_{\text{pulse}}(y) &= \Pr[f_{\text{pulse}}(t) < y] = \\ &= \Pr[t > f_{\text{pulse}}^{-1}(y) | 0 < t < T/2] \end{aligned} \quad (202)$$

Assuming $0 < t < T/2$, $0 \leq y \leq \alpha$ and $\mu=0$ (symmetric pulse centered in time origin), the general formula is:

$$\text{CDF}_{\text{pulse}}(y) = 1 - \frac{f_{\text{pulse}|\mu=0}^{-1}(y)}{T/2} \quad (203)$$

From (203), the distributions of fluctuations of a single turbine due to triangular, rectangular and Gaussian pulses are:

$$\begin{aligned} \text{CDF}_{\text{pulse}\Delta}(y) &= 1 - \frac{\tau(1-y/\alpha)}{T/2} \\ \Rightarrow \text{PDF}_{\text{pulse}\Delta}(y) &= \frac{2\tau}{\alpha T} + \left(1 - \frac{2\tau}{\alpha T}\right) \delta(y) \end{aligned} \quad (204)$$

$$\begin{aligned} \text{CDF}_{\text{pulse}\square}(y) &= \begin{cases} 1 - \frac{\tau}{T} & y \geq \alpha \\ 1 - \frac{\tau}{T} & 0 \leq y < \alpha \end{cases} \\ \Rightarrow \text{PDF}_{\text{pulse}\square}(y) &= \left(1 - \frac{\tau}{T}\right) \delta(y) + \frac{\tau}{T} \delta(y - \alpha) \end{aligned} \quad (205)$$

$$\begin{aligned} \text{CDF}_{\text{pulse gaussian}}(y) &= 1 - \frac{\tau}{T/2} \sqrt{\frac{\text{Ln}(\alpha/y)}{\pi}} \\ \Rightarrow \text{PDF}_{\text{pulse gaussian}}(y) &= \frac{\tau}{T y \sqrt{\pi \text{Ln}(\alpha/y)}} \end{aligned} \quad (206)$$

where U states for the Heaviside unit step function and δ for the delta of Dirac.

The characteristic function $\phi(w)$ of this distribution is the complex conjugate of the continuous Fourier transform of $PDF_{\text{pulse}}(y)$:

$$\phi_{\text{turbine}}^*(w) = \int_0^\alpha e^{-jwy} PDF_{\text{pulse}}(y) dy \quad (207)$$

where the asterisk denotes complex conjugation and j denotes the imaginary unit. Since the tangent of the pulse is horizontal at some points (at least at the maximums and minimums), $PDF_{\text{pulse}}(y)$ contains essential singularities. Therefore, the Fourier transform of $PDF_{\text{pulse}}(y)$ should be computed analytically.

The pulsating power of a wind farm with N turbines is the sum of individual power pulses, supposed identically distributed independent random events. The corresponding characteristic function is $\phi_{\text{turbine}}^N(w) = \phi_{\text{wind farm}}(w)$. Thus, the PDF of the wind farm deviation can be computed as inverse Fourier transform of the complex conjugate of $\phi_{\text{wind farm}}(w)$:

$$PDF_{\Delta P_{\text{wind farm}}}(y) = \frac{1}{2\pi} \int_{-\infty}^{+\infty} e^{jwy} [\phi_{\text{turbine}}^*(w)]^N dw \quad (208)$$

The characteristic function of a wind farm with rectangular power dips shown at Fig. 59 corresponds to a binomial distribution. This makes sense since the number of simultaneous pulses in a wind farm is the probability of the number of successes in a sequence of N independent “pulse” / “no pulse” experiments with success probability $p = \tau / T$ (the relative width of the pulse). Therefore, the instantaneous fluctuation in the wind farm follows a Binomial distribution:

$$PDF_{\Delta P_{\text{wind farm}}}(y) = \binom{N}{y/\alpha} \left(\frac{\tau}{T}\right)^{y/\alpha} \left(1 - \frac{\tau}{T}\right)^{N-y/\alpha} \quad (209)$$

$$CDF_{\Delta P_{\text{wind farm}}}(y) = I_{1-\tau/T}(N - y/\alpha, y/\alpha + 1) \quad (210)$$

where $I_{1-\tau/T}$ is the regularized incomplete beta function.

Fig. 60 shows the CDF of the deviation of power output at a wind farm due to tower shadow effect. *Pulse sum (p.u.)* is the ratio of the experienced power deviation relative to the maximum deviation which occurs when all tower shadows happen simultaneously. As the number of turbines in the wind farm increases, the relative deviation is more stable and it tends to its average, $\langle y \rangle = \alpha \langle y/\alpha \rangle = \alpha N p$.

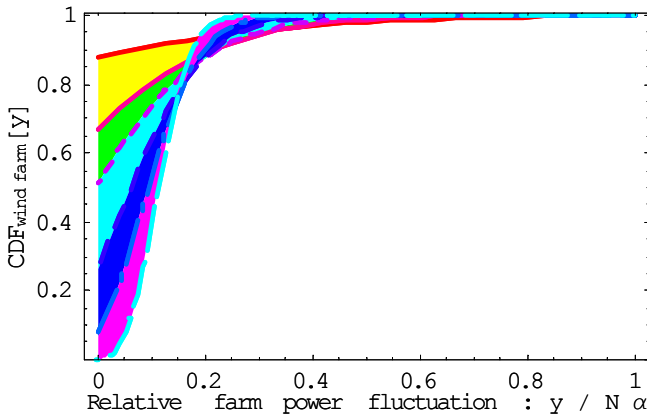


Fig. 60: CDF of pulses at a wind farms of 1, 3, 5, 10, 20 and 50 turbines (starting from upper part at zero fluctuation). The parameters of the pulses correspond to Fig. 59 and rectangular shape ($p = \tau / T = 0,125$). The discrete CDF (210) has been evaluated at midpoints to account that real pulses are continuous and derivable.

The standard deviation of the wind farm power output y is:

$$\sigma_y = \alpha \sigma_{y/\alpha} = \alpha \sqrt{N p (1-p)} = \alpha \frac{\tau}{T} \sqrt{N} \sqrt{\frac{\tau}{T} - 1} \quad (211)$$

which scales with \sqrt{N} instead of being proportional to the number of turbines N . The probability of simultaneous tower shadows events at most turbines is very low, as can be seen in the figure, $CDF_{\text{pulse}}(3\langle y \rangle) \approx 1$. The probability of exceeding a certain amount of power dip is the complementary CDF:

$$\Pr[\Delta P_{\text{wind farm}} > y] = 1 - CDF_{\Delta P_{\text{wind farm}}}(y) = I_{\tau/T}\left(\frac{y}{\alpha} + 1, N - \frac{y}{\alpha}\right) \quad (212)$$

The average power loss due to tower shadow is $\langle y \rangle$ (there are exactly N pulses in a period T).

$$\langle y \rangle = \frac{N}{T} \int_{-T/2}^{+T/2} f_{\text{pulse}}^{\text{single}}(t) dt = \frac{N}{T} \alpha \tau \quad (213)$$

Since turbine rotor angles are independent random variables, the variance of wind farm power output due to turbine blade position, σ_y^2 , can be computed as:

$$\sigma_y^2 = N \left[\frac{1}{T} \int_{-T/2}^{+T/2} f_{\text{pulse}}^{\text{single}}{}^2(t) dt - \left(\frac{1}{T} \int_{-T/2}^{+T/2} f_{\text{pulse}}^{\text{single}}(t) dt \right)^2 \right]$$

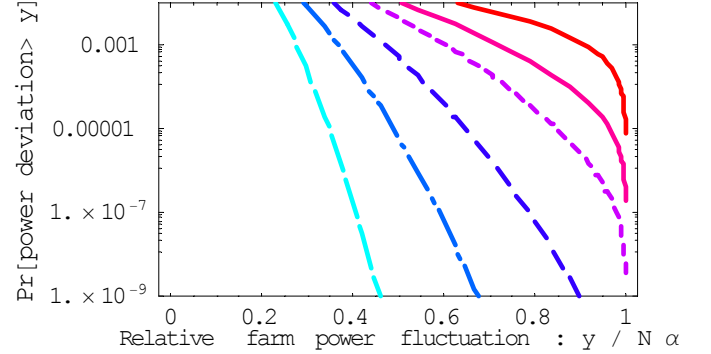


Fig. 61: Probability of farm output exceeding the normalized deviation $y/N\alpha$ for farms with of 1, 3, 5, 10, 20 and 50 turbines as in the previous figure.

A) Numerical computation of tower shadow effect.

In most cases, integrals (207) and (208) cannot be computed analytically. In such cases, the convolution can be computed numerically through discrete FFT or numerical integration.

Since $PDF_{\text{pulse}}(x)$ contains essential singularities whichever shape it has, the spectrum does not vanish at high frequencies and the numerical Fourier transform is not accurate (only analytical transform is suitable). The computation of N -fold convolution through repetitive direct numerical integration also introduces significant errors at essential discontinuities, aggravated by the iterative process of calculus.

Thus, usual numerical methods to compute $PDF_{\text{wind farm}}(y)$ such as FFT and numerical integration introduce significant errors. If the number of turbines is big, the distribution of power output can be approximated by a normal distribution of average power loss (213) and variance (214).

If the number of turbines is small, the second order approximation can be not enough precise. The following approach is based in the discretization of the pulse silhouette into segments and it is valid even for small wind farms. A rectangular pulse can be decomposed into two segments (up and down). The number of turbines in the “down” state follows a binomial distribution (the multinomial distribution for two options). Therefore, the farm fluctuation is the pulse height α times the number of turbines experiencing tower shadow effect.

If the pulse is approximated by more piecewise segments, the combinations of segments obey a multinomial distribution instead a binomial distribution.

For instance, the turbine pulse of Fig. 62 is approximated by tree segments (notice that for convenience, the shape has

been inverted vertically to operate with usual pulses instead of power dips). Therefore, the wind farm CDF of the power deviation can be computed summing probabilities corresponding to the combinations of segments which generate an output below level y .

$$\begin{aligned} CDF_{\Delta P_{wind\ farm\ multinomial}}(y) &= \frac{y}{y - i_1 y_1} \\ &= \sum_{i_1=0}^{y_1} \sum_{i_2=0}^{y_2} \binom{n - i_1 - i_2}{i_1, i_2, n - i_1 - i_2} a_1^{i_1} a_2^{i_2} a_3^{n - i_1 - i_2} \end{aligned} \quad (215)$$

where the multinomial coefficient is:

$$\binom{n}{i_1, i_2, n - i_1 - i_2} = \frac{n!}{i_1! i_2! (n - i_1 - i_2)!} \quad (216)$$

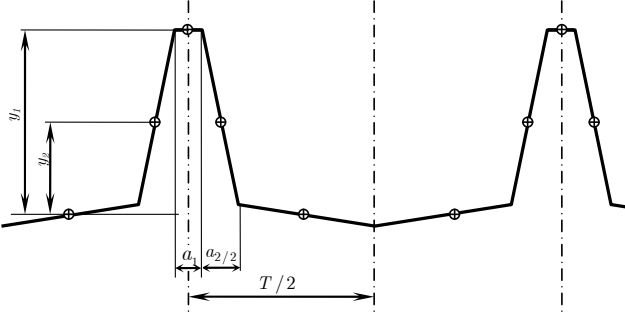


Fig. 62: Discretization of a pulse dip into three segments taking the mass center of each segment.

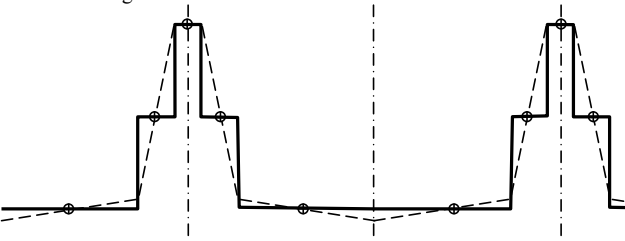


Fig. 63: Discrete counterpart of the continuous pulse dip of Fig. 62. Notice that the energy power loss (area beneath the pulse) of both pulses are the same.

The discretization of a continuous pulse has the following advantages:

- The computation of $PDF_{pulse}(y)$ is avoided. Moreover, if $PDF_{pulse}(y)$ is needed, it can be computed as the probability mass function $PMF_{pulse}(y)$ of the segmented pulse.
- Since a wind farm usually has more than 10 turbines, the approximation of the continuous pulse shape with its discrete counterpart does not introduce significant error. Furthermore, the discrete $CDF_{wind\ farm}(y)$ can be interpolated to account that real pulses are, actually, continuous and derivable, as in Fig. 60 or Fig. 61.
- The sums in (215) can be computed efficiently and the CDF of the wind farm does neither degenerate nor loss accuracy for wind farms with many turbines. In addition, this algorithm is numerically stable since the essential singularities are avoided.
- For wind farms with many turbines, the pulse shape can be approximated to a rectangle with relatively small error in $CDF_{wind\ farm}(y)$ because the shape of the turbine pulses is blurred in the wind farm output (both distributions converge for wind farms with increasing number of turbines provided the two pulses has the same energy loss). Therefore, a reduced number of segments are enough to characterize the pulse shape.

- A similar method can be used to compute the distribution of the power gradient. This can be helpful to assess the variability of power output due to blade position instead of the power deviation.

5.2.2. Rate of tower shadow events

The alignments of blades with their tower axis are [tower shadow] events whose time occurrence can be modeled as a stochastic process. The number of tower shadow events in the period T is the number of turbines in a wind farm, N .

The event rate or event *intensity* $\lambda(t)$ is the number of events per unit time and its average can be computed as $\lambda_0 = \langle \lambda(t) \rangle = N/T$ since in one period exactly one blade of all turbines of the wind farm passes in front of its tower (provided all turbines were spinning approximately at the same speed). The event rate λ_0 can be thought of as the probability that a blade alignment occurs in a specified interval.

A) Prior probability distributions

Since there is no explicit time origin and there are no appreciable synchronizing forces, the event can occur at any instant with the same likelihood and λ_0 is constant. This implies that the time between consecutive events (called *interarrival* times) are independent random variables. The only interarrival time distribution with constant hazard rate is the exponential. The waiting time Δt until the first occurrence is a continuous random variable with an exponential distribution (with parameter λ_0). This probability distribution may be deduced from the fact that

$$\begin{aligned} \Pr(\Delta t_{interarrival} > t) &= \Pr(N_{events} = 0 \text{ in interval } (0, t]) = \\ &= e^{-\lambda_0 t} = 1 - CDF_{Exponential(\lambda_0)}(t) \end{aligned} \quad (217)$$

For exponentially distributed events, the Poisson distribution is the probability distribution of the number of events that would occur within a preset time t .

$$\begin{aligned} \Pr(N_{events} = k \text{ in interval } (0, t]) &= \\ &= PDF_{Poisson(\lambda_0 t)}(k) = \frac{e^{-\lambda_0 t} (\lambda_0 t)^k}{k!} \end{aligned} \quad (218)$$

The Erlang distribution describes the waiting time until k tower shadow events have occurred when inter-event time is distributed exponentially (the Erlang distribution is the distribution of the sum of k independent identically distributed random variables each having an exponential scattering). The probability density function of the Erlang random variable is:

$$\begin{aligned} \Pr(\Delta t_{waiting} \leq t \mid N_{events} = k) &= \\ &= CDF_{Erlang(k, \lambda_0)}(t) = \frac{\gamma(k, \lambda_0 t)}{(k-1)!} \end{aligned} \quad (219)$$

where $\gamma(\cdot)$ is the lower incomplete gamma function. The probability density is:

$$PDF_{Erlang(k, \lambda_0)}(t) = \frac{\lambda_0^k t^{k-1} e^{-\lambda_0 t}}{(k-1)!} \quad (220)$$

B) Including periodicity in probability distributions

During normal operation, turbine speed fluctuates slightly. Multi-megawatt turbines spin at $\Omega_{rotor} = 8\text{-}20$ rpm, implying

blade periods $T = 1\sim 2,5$ s. During a short time interval, the turbine speed can be considered constant and the time interval between two consecutive tower shadow events of the same turbine is (approximately) T . If all turbines of a wind farm rotate at the same approximate speed Ω_{rotor} , each turbine must experience one and only one tower shadow event in the interval $(0, T]$ with uniform probability.

The implications of periodicity can be included in the probability of the number of tower shadow events in a time interval Δt using Bayes' theorem, provided $0 \leq \Delta t < T$ and $0 \leq k \leq N$:

$$\begin{aligned} & \Pr(N_{events} = k \text{ in } (0, t] | N_{events} = N \text{ in } (0, T]) = \\ &= \frac{\Pr(N_{events} = k \text{ in } (0, t]) \cdot \Pr(N_{events} = N \text{ in } (0, T] | N_{events} = k \text{ in } (0, t])}{\Pr(N_{events} = N \text{ in } (0, T])} \\ &= \frac{PDF_{Poisson}(\lambda_0 t)(k) \cdot PDF_{Poisson}(\lambda_0 (T-t))(N-k)}{PDF_{Poisson}(\lambda_0 T)(N)} = \\ &= \binom{N}{k} \left(\frac{t}{T}\right)^k \left(1 - \frac{t}{T}\right)^{N-k} \end{aligned} \quad (221)$$

The PDF of the number of tower shadow events in an interval t is a binomial distribution of N trials, k events and event probability $p = t/T$. (This equation is equivalent to (209), where the pulse width τ has been replaced by the interval time t , and the depth ratio of the power dip at the farm y/α has been replaced by the number of pulses, k).

The probability density of the waiting time t_k until the k^{th} occurrence can be computed using Bayes' theorem, provided $0 < t < T$ and $0 < k < N$:

$$\begin{aligned} & PDF(\text{waiting time } t \text{ for } k \text{ events} | N_{events} = N \text{ in } (0, T]) = \\ &= \frac{PDF_{\text{waiting time for } k \text{ events}}(t) \cdot PDF_{\text{waiting time for } N-k \text{ events}}(T-t | N_{events} = N \text{ in } (0, T])}{PDF_{\text{waiting time for } N \text{ events}}(T)} = \\ &= \frac{PDF_{Erlang}(k, \lambda_0)(t) \cdot PDF_{Erlang}(N-k, \lambda_0)(T-t)}{PDF_{Poisson}(\lambda_0 T)(N)} = \\ &= \frac{N-1}{T} \binom{N-2}{k-1} \left(\frac{t}{T}\right)^{k-1} \left(1 - \frac{t}{T}\right)^{N-k-1} \end{aligned} \quad (222)$$

The PDF of the waiting time t resembles the binomial distribution of $N-2$ trials, $k-1$ successes and success probability $p = t/T$, multiplied by a normalizing factor.

C) Evenly distributed tower shadow events

The interarrival time between pulses k and $k+1$ will be denoted $\Delta t(k) = \Delta t_{k,k+1}$. The interarrival times are not constant, but it has a mean value $\langle \Delta t(k) \rangle = \Delta t_0 = T/N$.

The expected number of tower shadow occurrences during the time unit is the inverse of the mean interarrival time, $\lambda_0 = 1/\Delta t_0 = N/T$ and λ_0 is also the average frequency of occurrence, measured in hertz, and the average blade rate of the wind farm. At an instant t between pulses k and $k+1$, the instantaneous frequency $\lambda(t)$ of tower shadow events at the wind farm output can be computed as $\lambda(t) = 1/\Delta t_{k,k+1}$. In Poisson process theory [200], the event rate $\lambda(t)$ is the process parameter, whereas the interarrival time $\Delta t(k)$ is an

outcome of the process. When the number of wind turbines is big ($N > T/\tau$ or $\lambda_0 \tau > 1$), the density of blade events $\lambda(t)$ is more significant than the interarrival time $\Delta t_{k,k+1}$.

At an instant between pulses k and $k+1$, the instantaneous angular frequency w_1 of tower shadow at wind farm output can be computed as $w_1(t) = 2\pi \lambda(t) = 2\pi / \Delta t_{k,k+1}$. The angular frequency will oscillate around its average value $\langle w_1(t) \rangle = 2\pi \lambda_0 = 2\pi N/T$.

The spectrum of a time interval will show a somewhat wide peak, revealing that tower shadow frequency is not definite. Thus, the spectrum at the wind farm output will resemble a frequency modulated signal of carrier frequency $f = \lambda_0$.

If two blades are crossing the tower with a time delay λ less than the pulse width τ , the averaged frequency will be $\langle w_1(t) \rangle = 2\pi (N-1)/T$. Tower shadow events are considered approximately simultaneous if $\Delta t_{k,k+1} < \tau$ and it can happen several times during a period T . If this phenomenon occur several times in a period T , the averaged frequency will be $\langle w_1(t) \rangle = 2\pi (N-k)/T$, where k is the number of approximately simultaneous tower shadows in the period. The probability of $\lambda(t) < 1/\tau$ can be computed with the interarrival distribution (217). In a wind farm with many turbines, k can likely have appreciable values.

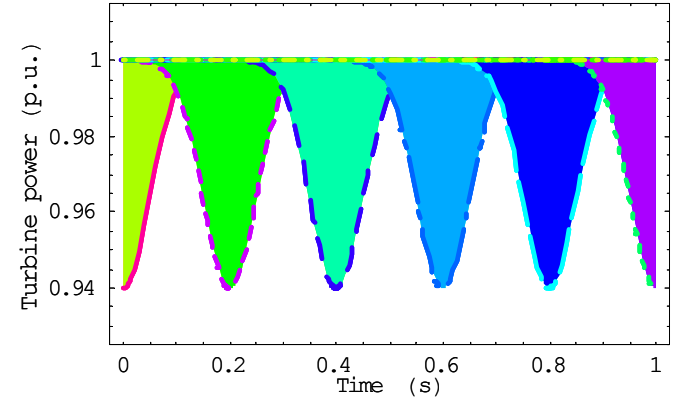


Fig. 64: Power output of 5 turbines with blade position uniformly distributed. The parameters of the pulses correspond to Fig. 59 and Gaussian shape.

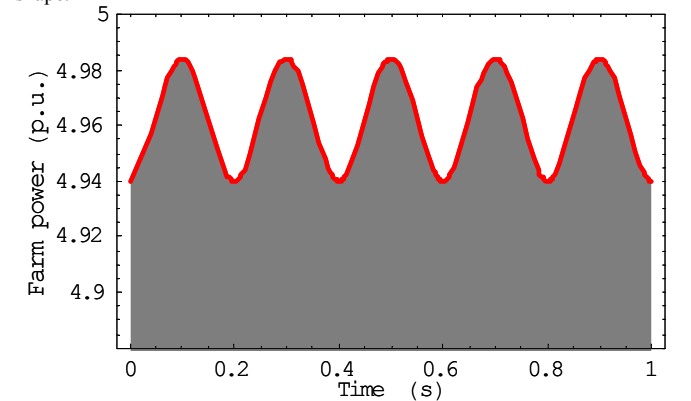


Fig. 65: Overall tower shadow effect at the wind farm output as the sum of individual turbine power of Fig. 64.

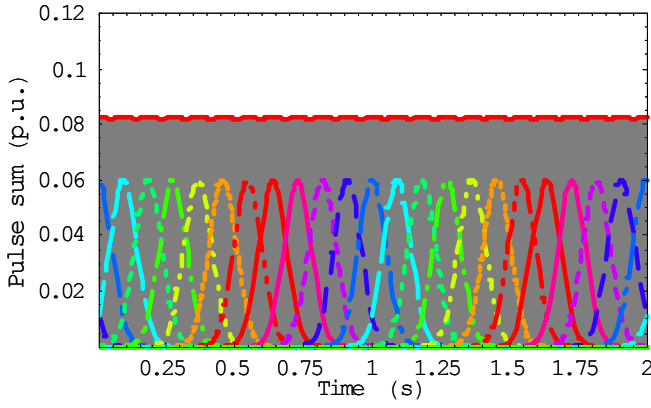


Fig. 66: Individual tower shadow pulses of Fig. 64 and their sum (notice the diminution of fluctuation due to the smoothness of Gaussian pulses).

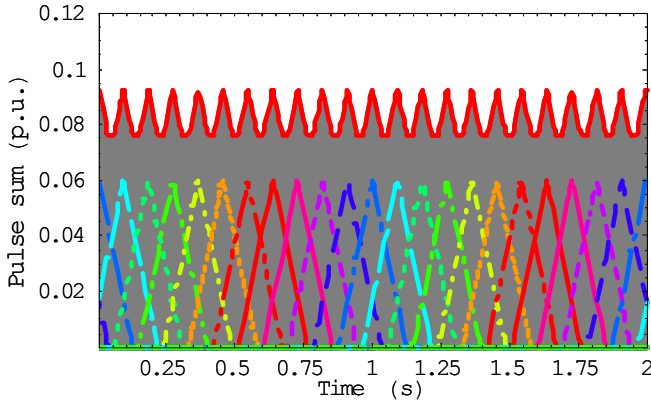


Fig. 67: Individual tower shadow pulses of Fig. 64 with triangular shape and their sum (notice that the fluctuation of the pulse sum increases with the sharpness of individual fluctuations shape).

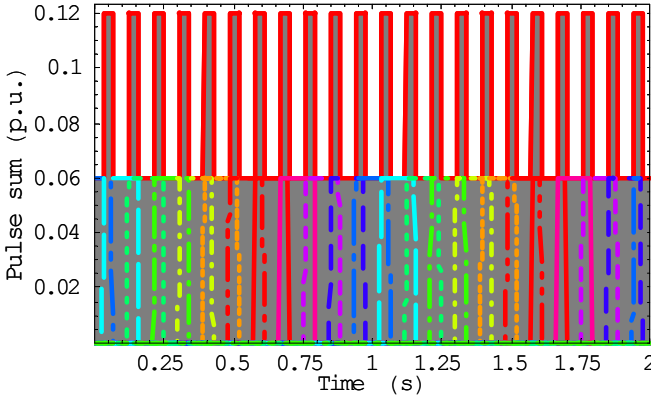


Fig. 68: Individual tower shadow pulses of Fig. 64 with rectangular shape and their sum (notice that rectangular pulse shape is the contour that produces the most variable output at the wind farm).

D) Calculus of the instantaneous frequency harmonics with evenly distributed pulses.

The continuous Fourier transform of a single pulse centred in time origin and symmetric is:

$$\begin{aligned} F_{\text{single pulse}}(f) &= \mathcal{F}\{f_{\text{pulse}}(t)\} = \int_{-t_{\text{max}}}^{t_{\text{max}}} f_{\text{pulse}}(t) e^{-j2\pi f t} dt = \\ &= 2 \int_0^{t_{\text{max}}} f_{\text{pulse}}(t) \cos(2\pi f t) dt \end{aligned} \quad (223)$$

even symmetry

The continuous transforms of the rectangular, triangular and Gaussian shapes are:

$$F_{1 \text{ pulse}\square}(f) = 2 \int_0^{\tau/2} \alpha \cos(2\pi f t) dt = \frac{\alpha}{\pi f} \sin(\pi f \tau) \quad (224)$$

$$\begin{aligned} F_{1 \text{ pulse}\Delta}(f) &= 2 \int_0^{\tau} \alpha \left(1 - \frac{|t|}{\tau}\right) \cos(2\pi f t) dt = \\ &= \frac{2\alpha [1 - \cos(2\pi f \tau)]}{(2\pi f)^2 \tau} \end{aligned} \quad (225)$$

$$F_{1 \text{ pulse}}^{\text{gaussian}}(f) = 2 \int_0^{\infty} \alpha e^{-\left(\frac{\sqrt{\pi} t}{\tau}\right)^2} \cos(2\pi f t) dt = \alpha \tau e^{-\pi f^2 \tau^2} \quad (226)$$

The frequency spectrum of the tower shadow can be computed considering the sum of the wind farm as the convolution of one pulse with a train of pulses (comb function) at the interarrival time λ rate. The convolution is equivalent to multiplication of the Fourier transforms. The transform of the tower shadow pulses at constant rate λ is another train of pulses at frequencies $f_m = \lambda m$ and amplitude $\lambda F_{\text{pulse}}(\lambda m)$. Therefore, the coefficients c_m of the new Fourier series are $c_m = 2\lambda F_{1 \text{ pulse}}(\lambda m)$ [201].

$$\begin{aligned} P_{\text{farm}}(t) &= \langle P_{\text{farm}} \rangle - \sum_{m=1}^{\infty} c_m \cos(2\pi \lambda m t) + \\ &+ \text{Re} \left\{ \int_0^{\infty} \left[N \vec{S}_{i \text{ corr}}(w) + \mathbb{C}N \left(0, \sqrt{\frac{N}{2}} \vec{S}_{i \text{ uncorr}}(w) \right) \right] e^{jw t} dw \right\} \end{aligned} \quad (227)$$

(except shear and tower shadow)

Where :

$\langle P_{\text{farm}} \rangle$ = mean power output. It includes the average power loss due to wind shear and tower shadow (DC term component of the Fourier series of tower shadow undulation, $c_0 / 2 = \alpha \tau \lambda$).

$\lambda = \lambda(t)$ = instantaneous blade rate of the wind farm. The fluctuation of $\lambda(t)$ can be modelled as a modulation of the tower shadow oscillation.

$F_{\text{single pulse}}(\lambda m)$ = continuous Fourier transform of a single, centred pulse at frequency $f_m(t) = m \lambda(t)$.

$c_m = 2\lambda F_{\text{pulse}}(\lambda m)$ = coefficient m of the Fourier series or the fluctuation at harmonic m of the blade rate. The tower shadow fluctuation usually decrease with blade rate λ , as can be derived from (228).

$$c_m = \begin{cases} \frac{2\alpha}{\pi m} \sin(\pi \lambda \tau m) & \text{rectangular pulse} \\ \frac{\alpha}{\pi^2 m^2 \lambda \tau} [1 - \cos(2\pi \lambda \tau m)] & \text{triangular pulse} \\ 2\alpha \tau \lambda e^{-\pi(\lambda \tau m)^2} & \text{gaussian pulse} \end{cases} \quad (228)$$

c_0 = twice the average power loss due to tower shadow events:

$$\begin{aligned} c_0 &= \lim_{f \rightarrow 0} F_{\text{single pulse}}(f) = 2\lambda \int_{-\infty}^{+\infty} f_{\text{single pulse}}(t) dt = \\ &= 2 \left(\text{Average Power Loss} \right) = 2\alpha \frac{\tau}{T} \end{aligned} \quad (229)$$

$\vec{P}_{i \text{ corr}}(f)$ = turbine power fluctuation at frequency f , correlated with the rest of turbines in the wind farm. Its modulus is the correlated component amplitude and its argument is the phase difference referred to the time origin.

$\vec{P}_{i \text{ uncorr}}(f)$ = turbine power fluctuation at frequency f , uncorrelated with the rest of turbines in the wind farm.

$\mathcal{CN}(0, \sqrt{N} \overline{P}_{i,uncorr}(f))$ is a complex normal random number with zero mean and standard deviation $\sqrt{N} \overline{P}_{i,uncorr}(f)$ (i.e., the modulus follows a Rayleigh distribution and the argument is uniformly distributed in $[-\pi, +\pi]$).

The tower shadow oscillation frequency $\langle f_{blade}(t) \rangle$ scale linearly with the number of turbines of a wind farm, but its amplitude do not scale in factors N or \sqrt{N} . Rectangular power pulses have Fourier coefficients that generally do not increase with the number of turbines. Triangular power pulses have Fourier coefficients that generally decrease with the number of turbines since $\langle \lambda(t) \rangle = N/T$. For some values of λ , the effect of wind shear and tower shadow is minimum (for instance, $F_{pulse}(w_n(t)) = 0$ when $\lambda = 2\tau$ -rectangular pulses- or $\lambda = \tau$ -triangular and rectangular pulses-).

Note that $\langle P_{farm} \rangle$, λ and $\overline{P}_i(f)$ are parameters of a stochastic process and their values varies according to the system operation. The explicit dependence of time has been dropped to simplify notation. Note also that N is the number of turbines functioning, which can be different of the number of installed turbines in the wind farm.

One important result of this section is that the effect of the tower shadows at a wind farm can be eventually compensated if the turbines could be controlled to distribute their rotor angle evenly. However this is not practical because this control would impose the same wind speed at all turbines.

5.2.3. Modulation of the pulse density at the wind farm with randomly distributed pulses.

When $N > T/\tau$ (or equivalently $\lambda_0 \tau > 1$), the effects due to the sharp shape of the pulse diminish and the main contribution to wind farm fluctuations is due to the possible concentration of tower shadow events in a part of the period T .

In a real wind farm, the pulse rate λ is not constant in the period. Fundamental harmonic ($m = 1$) measures how much the pulses are concentrated in half period. The order 2 harmonic ($m = 2$) measures if the tower shadow events occurs preferably every $T/4$ seconds.

The event density at a given time t is $\lambda(t)$ (this will be used in the next subsection for computing the modulation of power output).

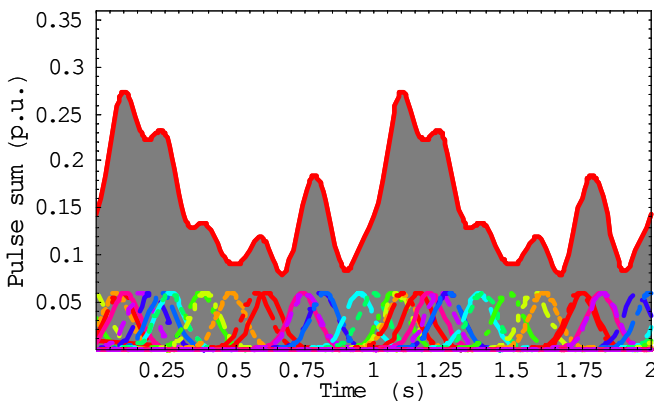


Fig. 69: Individual tower shadow pulses with Gaussian shape and random blade position corresponding to a wind farm with $N = 20$ turbines spinning at $\Omega = 20$ rpm (1 blade/s).

A) Estimation of coefficients of Fourier series of random pulses

Blade positions inside a turbine can be understand as random. However, each $1/3$ rotor revolution, a blade crosses the tower. The rate of tower shadow pulses is the number of blades divided by the mean rotor speed, $\lambda = \text{blades} / \Omega_{rotor}$. The instantaneous power due to tower shadow and wind shear is periodic with period $T = 1/\lambda$. In general, the pulse is not centred at the time origin and the Fourier coefficients will be complex numbers except the DC component (term of zero order).

If turbine speeds are equal, power is cyclic with period T and there are N tower shadow events in each cycle. Therefore, power can be decomposed in its Fourier series of harmonics of fundamental angular frequency $f_{blade} = 1/T$. As power is a stochastic magnitude, the coefficients of Fourier series are stochastic complex values (coefficients are not real since instantaneous power is not symmetric with respect to time origin).

$$P_{farm}(t) = \sum_{m=-\infty}^{\infty} \text{Re} \left[\overline{c}_m e^{j2\pi f_{blade} m t} \right] \quad (230)$$

The distribution of the complex Fourier coefficients \overline{c}_m , $m \neq 0$, can be estimated taken into account that:

- Fourier transform is linear and, thus, the transform of wind farm output is the sum of the transform of the individual turbines:

$$\mathcal{F} \left\{ \sum_{i=1}^N f_{\text{pulse turbine } i}(t - \mu_i) \right\} = \sum_{i=1}^N \mathcal{F} \left\{ f_{\text{pulse turbine } i}(t - \mu_i) \right\} \quad (231)$$

- The Fourier coefficient for a single turbine whose tower shadow event coincides with time origin can be obtained from the continuous Fourier transform of a single pulse, centred in time origin, $F_{\text{single pulse}}(w)$.

$$\overline{c}_m \Big|_{\text{single turbine with pulses at } t=0, T, 2T, 3T, \dots} = 2\lambda F_{\text{single pulse}} \left(\frac{2\pi m}{T} \right) = \frac{2}{T} F_{\text{single pulse}} \left(\frac{2\pi m}{T} \right) \quad (232)$$

- The tower shadow can occur at turbine i at any time μ_i with equal probability. Hence μ_i is uniformly distributed in the period $[0, T]$.
- The circular time shift property of Fourier transform implies that $\mathcal{F} \{ f_{\text{pulses}}(t - \mu_i) \} = e^{-jw \mu_i} \mathcal{F} \{ f_{\text{pulses}}(t) \}$, where $f_{\text{pulses}}(t)$ is the pulse train centered in the time origin, $f_{\text{pulses}}(t - \mu_i)$ is the pulse train displaced μ_i time and w is the angular frequency.

$$\mathcal{F} \left\{ f_{\text{pulse turbine } i}(t - \mu_i) \right\} = e^{-jw \mu_i} \mathcal{F} \left\{ f_{\text{pulse train centered in time origin}}(t) \right\} \quad (233)$$

$$\Rightarrow \left| \mathcal{F} \left\{ f_{\text{pulse turbine } i}(t - \mu_i) \right\} \right| = \left| \mathcal{F} \left\{ f_{\text{pulse train centered in time origin}}(t) \right\} \right| \quad (234)$$

- Therefore, the module of the Fourier transform of a pulse is independent of its position and can be easily calculated:

$$\left| \overline{c}_m \Big|_{\text{turbine}} \right| = \frac{2}{T} \left| F_{\text{single pulse}} \left(\frac{2\pi m}{T} \right) \right| \quad (235)$$

- Since μ_i is uniformly distributed in $[0, T]$, the argument of $\mathcal{F} \{ f_{\text{pulses}}(t - \mu_i) \}$ is also uniformly distributed in

$[-\pi, +\pi]$. Thus, the angles $2\pi\mu_i/T$ and $2\pi\mu_k/T$ at which pulses i and k occur are independent random variables.

$$\mu_i \sim \text{Uniform}[0, T] \Rightarrow \frac{2\pi}{T} \mu_i \sim \text{Uniform}[0, 2\pi] \quad (236)$$

- If $m \neq 0$ and $m \in \mathbb{N}$, $e^{j2\pi m\mu_i/T}$ is a phasor of unity modulus and random argument. For the usual number of turbines in a wind farm ($N > 4$), the sum of these phasors, $\sum e^{j2\pi m\mu_i/T}$, is approximately a complex normal random variable with zero mean and standard deviation $\sqrt{N/2}$ (see Fig. 57 and

- Table II).

$$\sum_{i=1}^N e^{+j\frac{2\pi m}{T}\mu_i} \sim \mathbb{CN}(0, \sqrt{N/2}) \quad m \neq 0, \quad m \in \mathbb{N} \quad (237)$$

- If $m \neq 0$, \vec{c}_m is the sum of N phasors of random argument and fixed module.

$$\vec{c}_m = -\frac{2}{T} F_{\text{pulse}}^{\text{single}} \left(\frac{2\pi m}{T} \right) \sum_{i=1}^N e^{+j\frac{2\pi m}{T}\mu_i} \quad (238)$$

- Summarizing, the complex Fourier coefficients \vec{c}_m are, approximately, complex normal random variables with zero mean and standard deviation $\sigma_{\vec{c}_m}$.

$$\vec{c}_m \sim \mathbb{CN}(0, \sigma_{\vec{c}_m}) \quad (239)$$

$$\sigma_{\vec{c}_m} = \frac{\sqrt{2N}}{T} F_{\text{pulse}}^{\text{single}} \left(\frac{2\pi m}{T} \right) \quad \forall m \neq 0 \quad (240)$$

The argument of \vec{c}_m is uniformly distributed in $[-\pi, +\pi]$ and the modulus $|\vec{c}_m|$ has a Rayleigh distribution with parameter $\sigma_{\vec{c}_m}$.

The zero order coefficient \vec{c}_0 or c_0 is twice the DC component of the signal (i.e., twice the average wind farm power).

$$\langle c_0 \rangle = 2 \langle P_{\text{farm}} \rangle \quad (241)$$

a) Product of complex coefficients of Fourier series.

The covariance of two complex Fourier coefficients \vec{c}_m and \vec{c}_n is:

$$\begin{aligned} \text{Cov}[\vec{c}_m, \vec{c}_n] &\triangleq \left\langle \left(\vec{c}_m - \langle \vec{c}_m \rangle \right) \cdot \left(\vec{c}_n - \langle \vec{c}_n \rangle \right)^* \right\rangle = \left\langle \vec{c}_m \cdot \vec{c}_n^* \right\rangle \\ &= \left\langle \left(F_{\text{pulse}} \left(\frac{2\pi n}{T} \right) \sum_{i=1}^N e^{-j\frac{2\pi n}{T}\mu_i} \right) \left(F_{\text{pulse}} \left(\frac{2\pi m}{T} \right) \sum_{i=1}^N e^{+j\frac{2\pi m}{T}\mu_i} \right) \right\rangle \\ &= F_{\text{pulse}} \left(\frac{2\pi m}{T} \right) F_{\text{pulse}} \left(\frac{2\pi n}{T} \right) \left\langle \left(\sum_{i=1}^N e^{-j\frac{2\pi n}{T}\mu_i} \right) \left(\sum_{i=1}^N e^{+j\frac{2\pi m}{T}\mu_i} \right) \right\rangle \end{aligned}$$

The case $m = 0$ or $n = 0$ is the multiplication of the DC component of the signal, which is a real number. Mean power during a blade period T and tower shadow can be marginally considered low correlated and almost statistically independent given some operation conditions. Therefore, the covariance of a phasor and the zero order Fourier component is null:

$$\text{Cov}[\vec{c}_m, c_0] = 0 \quad (\text{independent random variables}) \quad (243)$$

Notwithstanding this fact, the product of any Fourier Coefficient by a constant such as c_0 has non-null variance.

$$\text{Var}[c_0 \vec{c}_m]_{\langle c_0 \rangle \gg \sigma_0} \approx \langle c_0 \rangle^2 \text{Var}[\vec{c}_m] \quad (244)$$

If $n \neq m$, the covariance is zero because $\vec{c}_m \cdot \vec{c}_n^*$ has a random argument uniformly distributed (circular symmetry) [202].

$$\text{Cov}[\vec{c}_m, \vec{c}_n] = 0 \quad m \neq n \quad \text{or} \quad m=0 \quad \text{or} \quad n=0 \quad (245)$$

The only non-null covariance case is $n = m \neq 0$ because $\vec{c}_m \cdot \vec{c}_m^* = |\vec{c}_m|^2$ and the product is a non-negative real random variable and its average is non-zero and positive. It is also special because $|\vec{c}_m|$ and itself is fully correlated.

The pseudo-covariance can be also computed (it can be used to derive the flicker contribution of turbine tower shadows).

$$\begin{aligned} \widetilde{\text{Cov}}[\vec{c}_m, \vec{c}_n] &= \left\langle \left(\vec{c}_m - \langle \vec{c}_m \rangle \right) \cdot \left(\vec{c}_n - \langle \vec{c}_n \rangle \right) \right\rangle = \left\langle \vec{c}_m \cdot \vec{c}_n \right\rangle = \\ &= \left\langle \left(F_{\text{pulse}} \left(\frac{2\pi n}{T} \right) \sum_{i=1}^N e^{-j\frac{2\pi n}{T}\mu_i} \right) \left(F_{\text{pulse}} \left(\frac{2\pi m}{T} \right) \sum_{i=1}^N e^{-j\frac{2\pi m}{T}\mu_i} \right) \right\rangle = \\ &= F_{\text{pulse}} \left(\frac{2\pi m}{T} \right) F_{\text{pulse}} \left(\frac{2\pi n}{T} \right) \left\langle \left(\sum_{i=1}^N e^{-j\frac{2\pi n}{T}\mu_i} \right) \left(\sum_{i=1}^N e^{-j\frac{2\pi m}{T}\mu_i} \right) \right\rangle \end{aligned}$$

Except if $m = 0$, $e^{j2\pi m\mu_i/T}$ is a phasor of unity modulus and random argument since $m \in \mathbb{N}$. Therefore, the pseudo-covariance is always zero due to its circular symmetry

$$\widetilde{\text{Cov}}[\vec{c}_m, \vec{c}_n] = 0 \quad \forall m, \forall n \quad (247)$$

for any value (even for $m = n$).

The product of independent complex normal variables with zero mean is another random variable with circular symmetry but the modulus is not Rayleigh-distributed. Therefore, the product of two independent complex normal random variables is not another normal.

$$\begin{aligned} \text{Pr} \left(\left| \vec{c}_m \cdot \vec{c}_n^* \right| \leq y \right) &= \\ &= \text{CDF}_{\left| \vec{c}_m \cdot \vec{c}_n^* \right|} (y) = \text{CDF}_{\left| \vec{c}_m \right| \left| \vec{c}_n \right|} (y) = \text{CDF}_{\left| \vec{c}_m \right| \left| \vec{c}_n \right|} (y) = \\ &= \int_0^\infty \int_0^{y/|\vec{c}_n|} \text{PDF}_{\text{Rayleigh}}(|\vec{c}_m|) \text{PDF}_{\text{Rayleigh}}(|\vec{c}_n|) d|\vec{c}_m| d|\vec{c}_n| = \\ &= 1 - \frac{y}{\sigma_{\vec{c}_m} \sigma_{\vec{c}_n}} K_1 \left(\frac{y}{\sigma_{\vec{c}_m} \sigma_{\vec{c}_n}} \right) \quad \forall n \neq m \end{aligned} \quad (248)$$

where K_1 is the modified Bessel function of second kind and unity order. This distribution is similar to a Gamma with shape parameter between 1 (exponential case) and 2 (Rayleigh case). Its PDF is:

$$\begin{aligned} \text{PDF}_{\left| \vec{c}_n \right| \left| \vec{c}_m \right|} (y) &= \frac{d}{dt} \text{CDF}_{\left| \vec{c}_n \right| \left| \vec{c}_m \right|} (y) = \\ &= \frac{y}{\sigma_{\vec{c}_m}^2 \sigma_{\vec{c}_n}^2} K_0 \left(\frac{y}{\sigma_{\vec{c}_m} \sigma_{\vec{c}_n}} \right) \quad \forall n \neq m \end{aligned} \quad (249)$$

where K_0 is the modified Bessel function of second kind and zero order.

In conclusion, the product of Fourier coefficients (conjugated or not) of different order ($n \neq m$) is a complex random variable with circular symmetry and modulus distributed as:

$$\left| \vec{c}_m \cdot \vec{c}_n \right| = \left| \vec{c}_n \right| \left| \vec{c}_m \right| \sim \frac{y}{\sigma_{\vec{c}_m}^2 \sigma_{\vec{c}_n}^2} K_0 \left(\frac{y}{\sigma_{\vec{c}_m} \sigma_{\vec{c}_n}} \right) \quad (250)$$

The average of the modulus of the product of the Fourier coefficients is computed by integration:

$$\begin{aligned} \left\langle \left| \overrightarrow{c_m} \cdot \overrightarrow{c_n}^* \right| \right\rangle &= \left\langle \left| \overrightarrow{c_m} \cdot \overrightarrow{c_n} \right| \right\rangle = \left\langle \left| \overrightarrow{c_m} \right| \left| \overrightarrow{c_n} \right| \right\rangle = \\ &= \int_0^\infty y \text{PDF}_{\left| \overrightarrow{c_n} \right| \left| \overrightarrow{c_m} \right|} (y) dy = \frac{\pi}{2} \sigma_{\overrightarrow{c_m}} \sigma_{\overrightarrow{c_n}} \quad \forall n \neq m \end{aligned} \quad (251)$$

The second order centered moment of the modulus of the product of the Fourier coefficients is:

$$\left\langle \left(\left| \overrightarrow{c_m} \right| \left| \overrightarrow{c_n} \right| \right)^2 \right\rangle = \int_0^\infty y^2 \text{PDF}_{\left| \overrightarrow{c_n} \right| \left| \overrightarrow{c_m} \right|} (y) dy = 4\sigma_{\overrightarrow{c_m}}^2 \sigma_{\overrightarrow{c_n}}^2 \quad n \neq m \quad (252)$$

In the convolution of Fourier coefficients, many of these complex variables must be summed and they can be replaced by complex normal variables with the same standard deviation (the second order approximation of the random variables). According to (155) and (252), the second order statistical approximation of the product $\overrightarrow{c_m} \cdot \overrightarrow{c_n}$ or $\overrightarrow{c_m} \cdot \overrightarrow{c_n}^*$ is a complex normal with the same average than its projection (zero) and variance equal to the second order centered moment divided by two:

$$\overrightarrow{c_m} \cdot \overrightarrow{c_n}^* \sim \overrightarrow{c_m} \cdot \overrightarrow{c_n} \underset{\text{approx}}{\sim} \mathbb{CN} \left(0, \sqrt{2} \sigma_{\overrightarrow{c_m}} \sigma_{\overrightarrow{c_n}} \right) \quad n \neq m, n \neq 0, m \neq 0 \quad (253)$$

The product of a harmonic coefficient and the zero order term, which is a constant, has the complex normal distribution:

$$c_0 \overrightarrow{c_m} \sim \mathbb{CN} \left(0, c_0 \sigma_{\overrightarrow{c_m}} \right) \quad (254)$$

The case where $n = m \neq 0$ is special because $\overrightarrow{c_m} \cdot \overrightarrow{c_m}^* = |\overrightarrow{c_m}|^2$ and the product is a non-negative real random variable (no longer circular symmetry). It is also special because $|\overrightarrow{c_m}|$ and itself is fully correlated and the conditions used in to derive the CDF of the product does not hold for the product of Fourier coefficients of the same order.

$$\begin{aligned} \Pr \left(\left| \overrightarrow{c_m} \cdot \overrightarrow{c_m}^* \right| \leq y \right) &= \Pr \left(\left| \overrightarrow{c_m} \right|^2 \leq y \right) = \text{CDF}_{\left| \overrightarrow{c_m} \right|^2} (y) = \\ &= \Pr \left(\left| \overrightarrow{c_m} \right| \leq \sqrt{y} \right) = \text{CDF}_{\left| \overrightarrow{c_m} \right|} (\sqrt{y}) = \text{CDF}_{\text{Rayleigh}} (\sqrt{y}) = \\ &= 1 - \exp \left(-\frac{y}{2\sigma_{\overrightarrow{c_m}}^2} \right) \end{aligned} \quad (255)$$

which corresponds to an exponential random variable with rate parameter λ and mean $\lambda^{-1} = 2\sigma_{\overrightarrow{c_m}}^2$. Thus, $|\overrightarrow{c_m}|^2$ is an exponential random variable:

$$\overrightarrow{c_m} \cdot \overrightarrow{c_m}^* = \left| \overrightarrow{c_m} \right|^2 \sim \text{Exponential} \left(2\sigma_{\overrightarrow{c_m}}^2 \right) \quad m \neq 0 \quad (256)$$

The average of $\overrightarrow{c_m} \cdot \overrightarrow{c_m}^*$ is not null:

$$\left\langle \left| \overrightarrow{c_m} \cdot \overrightarrow{c_m}^* \right| \right\rangle = \left\langle \left| \overrightarrow{c_m} \right|^2 \right\rangle_{\text{Exponential distr.}} = 2\sigma_{\overrightarrow{c_m}}^2 \quad m \neq 0 \quad (257)$$

Therefore, the variance of $\overrightarrow{c_m}$ is:

$$\text{Var}[\overrightarrow{c_m}] = \text{Cov}[\overrightarrow{c_m}, \overrightarrow{c_m}] = \left\langle \left| \overrightarrow{c_m} \cdot \overrightarrow{c_m}^* \right| \right\rangle = 2\sigma_{\overrightarrow{c_m}}^2 \quad m \neq 0 \quad (258)$$

Summarizing, the covariance between Fourier coefficients are:

$$\text{Cov}[\overrightarrow{c_m}, \overrightarrow{c_n}] = \begin{cases} 0 & m \neq n \text{ or } m = n = 0 \\ 2\sigma_{\overrightarrow{c_m}}^2 & m = n \neq 0 \end{cases} \quad (259)$$

The second order centered moment of the product of the Fourier coefficients of the same order is:

$$\left\langle \left| \overrightarrow{c_m} \right|^4 \right\rangle = \int_0^\infty y^4 \text{PDF}_{\text{Exponential}(2\sigma_{\overrightarrow{c_m}}^2)} (y) dy = 8\sigma_{\overrightarrow{c_m}}^4 \quad (260)$$

and its variance is:

$$\text{Var}[\left| \overrightarrow{c_m} \right|^2] = \left\langle \left| \overrightarrow{c_m} \right|^4 \right\rangle - \left\langle \left| \overrightarrow{c_m} \right|^2 \right\rangle^2 = 4\sigma_{\overrightarrow{c_m}}^4 \quad (261)$$

The product $|\overrightarrow{c_m}|^2$ is a real number distributed exponentially. Even if exponential distribution is significantly different from a real normal distribution, the second order approximation can be acceptable in sums of a high number of random variables. The second order statistical approximation of $|\overrightarrow{c_m}|^2$ is:

$$\left| \overrightarrow{c_m} \right|^2 \underset{\text{approx}}{\sim} \text{Exponential} \left(2\sigma_{\overrightarrow{c_m}}^2 \right) \underset{\text{approx}}{\sim} N \left(2\sigma_{\overrightarrow{c_m}}^2, 2\sigma_{\overrightarrow{c_m}}^2 \right) \quad m \neq 0$$

According to (155) and (260), the second order statistical approximation of the phasor product $\overrightarrow{c_m}^2$ is a complex normal with zero average and variance:

$$\overrightarrow{c_m}^2 \underset{\text{approx}}{\sim} \mathbb{CN} \left(0, \sqrt{2} \sigma_{\overrightarrow{c_m}}^2 \right) \quad m \neq 0 \quad (263)$$

B) Experimental variance of mean power in interval T

It is convenient to define c_0 as twice the power for one period given some operational conditions. Most standards assume that the operation conditions for the turbine remain roughly the same during $T_{int} = 10$ minutes. For usual distances inside a wind farm, uncorrelated fluctuations predominate for smaller timescales than T_{int} , whereas power variations with longer characteristic times are mostly correlated (see p. 79 of [44]). Since there are exactly N tower shadow events in each cycle, the tower shadow power loss per cycle is constant and c_0 do not vary with tower shadow distribution.

If operational conditions of a turbine during 10 minutes remain constant approximately, the variance of mean power during each interval $\sigma_{c_0}^2/4$ is:

$$\text{Var} \left[\frac{c_0}{2} \right] = \frac{\sigma_{c_0}^2}{4} = \left\langle P_{farm}^2 \right\rangle - \left\langle P_{farm} \right\rangle^2 - \left\langle \sum_{m=1}^{\infty} \left| \overrightarrow{c_m} \right|^2 \right\rangle \quad (264)$$

The variance $\sigma_{c_0}^2$ can be estimated as the sample variance $\hat{\sigma}_{c_0}^2$:

$$\frac{\sigma_{c_0}^2}{4} = \frac{T}{600} \sum_{k=1}^{600/T} \overline{P_{turb}^2}(k) - \left[\frac{T}{600} \sum_{k=1}^{600/T} \overline{P_{turb}}(k) \right]^2 \quad (265)$$

where $\overline{P_{turb}}(k)$ is the average power of interval k of the 10 minute interval (600 seconds or $600/T$ periods).

Alternatively, the variance of the coefficient is the energy in the frequency range $1/600$ Hz to $1/2T$ Hz. If the periodogram of the real power $\left\langle |S_{P_{farm}}(f)|^2 \right\rangle$ is available (averaged power spectrum density or PSD), $\sigma_{c_0}^2/4$ is:

$$\frac{\sigma_{c_0}^2}{4} = \frac{1}{2} \int_{1/600}^{1/2T} \left\langle |S_{P_{farm}}(f)|^2 \right\rangle df \quad (266)$$

The zero-order phasor can be understood as a phasor with random phase (but it approximately does not vary during the interval T) and modulus with absolute second moment $M'_{r, \text{mod}} = 2\sigma_{c_0}^2$. In fact, the zero-order phasor correspond to a stochastic process with frequencies between the range $1/600$ Hz to $1/2T$ Hz. Taking into account that these frequencies are very low, the dynamic characteristic

$\partial P_{farm} / \partial v$ can be used to estimate the variance of power from the spectrum of wind speed v .

C) Root Mean Square (RMS) value of the power fluctuations due to tower shadow and wind shear at the wind farm output

The Root Mean Square (RMS) value of the power fluctuations, RMS_{farm} , is a figure that characterizes the overall oscillation of a the wind farm output due to tower shadow and wind shear. It is the standard deviation of the sum of power pulses or the root of the squared sum of the modulus of Fourier coefficients. The calculus of RMS_{farm} from Fourier coefficients can be derived using Parseval's Theorem.

$$RMS_{\Delta P_{farm}}^2 = \frac{1}{2} \sum_{m=1}^{\infty} |c_m|^2 = \frac{1}{2} \sum_{m=1}^{\infty} \overline{c_m} \cdot \overline{c_m}^* \quad (267)$$

$$\begin{aligned} \langle RMS_{\Delta P_{farm}}^2 \rangle &= \frac{1}{2} \sum_{m=1}^{\infty} \langle \overline{c_m} \cdot \overline{c_m}^* \rangle = \frac{1}{2} \sum_{m=1}^{\infty} Cov[\overline{c_m}, \overline{c_m}] = \\ &= \sum_{m=1}^{\infty} \sigma_m^2 = \sum_{m=1}^{\infty} \left[\frac{\sqrt{2N}}{T} F_{pulse}(2\pi m / T) \right]^2 \end{aligned} \quad (268)$$

The RMS value of fluctuations can be also equivalently derived for any single pulse shape using the following relationship:

$$\begin{aligned} \langle RMS_{\Delta P_{farm}}^2 \rangle &= \\ &= N \left[\frac{1}{T} \int_{-T/2}^{+T/2} f_{pulse}^2(t) dt - \left(\frac{1}{T} \int_{-T/2}^{+T/2} f_{pulse}(t) dt \right)^2 \right] \end{aligned} \quad (269)$$

Mean value of squared RMS_{farm} for rectangular, triangular and Gaussian shape of pulses as defined in (194) to (201) is:

$$\langle RMS_{\Delta P_{farm}}^2 \rangle = N \left(\frac{\alpha \tau}{T} \right)^2 \left(k \frac{T}{\tau} - 1 \right) \quad (270)$$

where the constant k depends on the pulse shape

$$k = \frac{T}{\alpha^2 \tau} \int_{-T/2}^{+T/2} f_{pulse}^2(t) dt = \begin{cases} 1 & \text{rectangular pulse} \\ 2/3 & \text{triangular pulse} \\ 1/\sqrt{2} & \text{gaussian pulse} \end{cases} \quad (271)$$

The distribution of RMS_{farm}^2 can be derived from the distribution of wind farm power output.

$$CDF_{RMS^2 \Delta P_{farm}}(x) = CDF_{\Delta P_{wind farm}}(\sqrt{x} + N\alpha \tau / T) \quad (272)$$

where $CDF_{\Delta P_{wind farm}}(x)$ has been computed for rectangular and discretized pulses in (210) and (215), respectively. Recall that the standard deviation of farm power has been calculated also for rectangular pulses in (211) and all results coincide.

In farms with a many turbines, the distribution of farm output y due to tower shadow converges asymptotically to a normal distribution with mean $\langle y \rangle = N\alpha \tau / T$ and variance $Var(y) = \langle y^2 - \langle y \rangle^2 \rangle = \langle RMS_{\Delta P_{farm}}^2 \rangle$. Thus, the modulus of the fluctuation, $RMS_{\Delta P_{farm}}$, is distributed as a Rayleigh random variable with scale parameter equal to standard deviation of the underlying cyclic stochastic process [203].

$$\lim_{N \rightarrow \infty} RMS_{\Delta P_{farm}} \rightarrow Rayleigh(\sqrt{\langle RMS_{\Delta P_{farm}}^2 \rangle}) \quad (273)$$

The average of RMS_{farm} is a bit smaller than the squared root of the RMS_{farm}^2 mean since quadratic averages weigh up larger values.

$$\langle RMS_{\Delta P_{farm}} \rangle \approx \sqrt{\frac{\pi}{2}} \sqrt{\langle RMS_{\Delta P_{farm}}^2 \rangle} < \sqrt{\langle RMS_{\Delta P_{farm}}^2 \rangle} \quad (274)$$

Mean RMS_{farm} for rectangular, triangular and Gaussian pulses is shown below.

$$\langle RMS_{\Delta P_{farm}} \rangle \approx \frac{\alpha \tau}{T} \sqrt{N} \sqrt{\frac{\pi}{2}} \sqrt{k \frac{T}{\tau} - 1} \quad (275)$$

Since usually $1 \ll T/\tau \approx 6 \sim 10$, the fluctuation is also proportional to the square root of the relative width of the pulse $\sqrt{\tau/T}$, approximately.

$$\langle RMS_{\Delta P_{farm}} \rangle \approx_{approx} \alpha \sqrt{N} \sqrt{\frac{\tau}{T}} \sqrt{\frac{k\pi}{2}} \quad (276)$$

Notice that $RMS_{\Delta P_{farm}}$ is proportional to the pulse power dip amplitude α and to the square root of the number of turbines \sqrt{N} and the relative width of the pulse, $\sqrt{\tau/T}$.

D) Distribution of the gradient of power (time derivative of power) due to tower shadow effect

The derivative of farm power is a measure of the variability of farm output with time. Whereas RMS_{farm} only account the deviation from the average of the power output, the distribution of time gradient of power dP_{farm}/dt measures how quickly are the oscillations due to the position of the turbine blades.

The distribution of the gradient of power (time derivative of power) can be computed using properties of Fourier transforms in a similar fashion to the previous section.

$$\frac{dP_{farm}}{dt} = \text{Re} \left(\sum_{m=1}^{\infty} j \frac{2\pi m}{T} \overline{c_m} e^{j \frac{2\pi m}{T} t} \right) \quad (277)$$

$$\left\langle \frac{dP_{farm}^2}{dt} \right\rangle = \frac{1}{2} \sum_{m=1}^{\infty} \left(\frac{2\pi m}{T} \right)^2 \langle \overline{c_m} \cdot \overline{c_m}^* \rangle = \quad (278)$$

$$= \frac{1}{2} \sum_{m=1}^{\infty} \left(\frac{2\pi m}{T} \right)^2 Cov[\overline{c_m}, \overline{c_m}] = \sum_{m=1}^{\infty} \left(\frac{2\pi m}{T} \sigma_m \right)^2$$

Using the results form (240) and (265), the sum is:

$$\left\langle \frac{dP_{farm}^2}{dt} \right\rangle = \sum_{m=1}^{\infty} \left[\frac{2\pi m}{T} \frac{\sqrt{2N}}{T} F_{pulse} \left(\frac{2\pi m}{T} \right) \right]^2 \quad (279)$$

Notice that square pulses presents infinite derivative at flanks and its quadratic average is infinite (real pulse are continuous functions). For triangular and Gaussian pulses, the RMS value of the time derivative is:

$$\sqrt{\left\langle \frac{dP_{farm}^2}{dt} \right\rangle} = \begin{cases} \alpha \sqrt{2 \frac{N}{\tau \cdot T}} & \text{triangular shape} \\ \alpha \sqrt{\frac{\pi}{\sqrt{2}} \frac{N}{\tau \cdot T}} & \text{gaussian shape} \end{cases} \quad (280)$$

The RMS value of the derivative of farm power is proportional to turbine pulse height α and to the square root of the number of turbines \sqrt{N} . Notice that the time derivative of farm power is inversely proportional to *square root* of the product of turbine time constants. If the turbine pulse is symmetric respect its peak, as all the pulses presented in this work, the distribution of power gradient is also symmetric respect to zero level.

5.3. Contribution of periodic components to Flicker

The fluctuations in voltage are strongly influenced by the external grid and they are several orders of magnitude smaller than the power fluctuations. Due to these difficulties, IEC 61400-21 measures current and then voltage fluctuations are derived from the current, instead of using directly voltage measurements.

5.3.1. Voltage variations of induced by power fluctuations

The approach followed in this section is based in [204], where a simplified model of the wind farm is derived based on the fourth-pole equivalent representation of the electrical elements, the distributed layout of the turbines, the stochastic nature of power output and small-signal analysis of the grid. The model is based on the circuit of Fig. 70 and its parameters can be obtained from [160] (see annex A for further information).

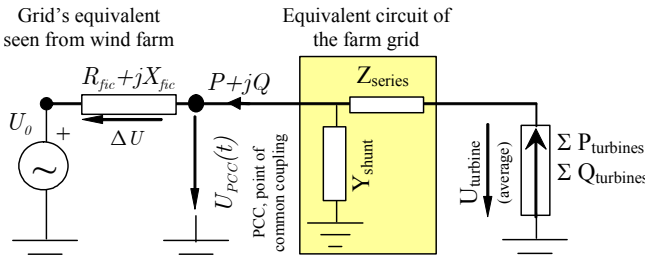


Fig. 70: Small signal model of the farm.

The approximated voltage variation can be obtained from the small signal model:

$$\Delta U \underset{\text{approx}}{\simeq} \frac{R_{fic} \cdot P + X_{fic} \cdot Q}{U_{PCC}} \quad (281)$$

where P and Q are the real and reactive generated power of the wind farm at the point of common coupling with the grid (PCC), U_n is the nominal voltage at PCC, R_{fic} and X_{fic} are the equivalent resistance and reactance at PCC.

A) General model

According to (281), the voltage drop in the fictitious grid can be computed approximately as a linear combination of the real and reactive power spectra:

$$\Delta U(f) \underset{\text{approx}}{\simeq} \frac{R_{fic}}{U_{PCC}} P(f) + \frac{X_{fic}}{U_{PCC}} Q(f) \quad (282)$$

During continuous operation, the variations of real power are bigger than the oscillations of reactive power. However, it is usual that $R_{fic} \ll X_{fic}$ at high voltage (see Table XV) and reactive power variations can influence notably $\Delta U(f)$.

If the dynamics of reactive power are important, then the characterization of pulses (Section II of this chapter) should be based on the fictitious voltage drop $\Delta U(f)$ instead of real power $P(f)$. Moreover, the modeling of stochastic fluctuations should be based on $PSD_{\Delta U}(f)$ instead of $PSD_P(f)$. Elsewhere the methodology remains the same.

For convenience, a fictitious power fluctuation can be computed as:

$$S = P + \frac{X_{fic}}{R_{fic}} Q \quad (283)$$

Thus, the voltage at the PPC of the farm can be expressed according to Fig. 70:

$$\begin{aligned} U_{PCC}(t) &= U_0 + \Delta U \simeq U_0 + \beta U_{PCC} \left(P(t) + \frac{X_{fic}}{R_{fic}} Q(t) \right) = \\ &= U_0 + \beta U_{PCC} \left(\langle P \rangle + \frac{X_{fic}}{R_{fic}} \langle Q \rangle + \Delta P(t) + \frac{X_{fic}}{R_{fic}} \Delta Q(t) \right) = \\ &= U_0 + \beta U_{PCC} \langle S \rangle + \beta U_{PCC} \Delta S(t) = \\ &= \langle U_{PCC} \rangle - \beta U_{PCC} \sum_{m=1}^{\infty} \text{Re} \left[\vec{c}_m e^{jm\omega t} \right] \end{aligned} \quad (284)$$

where \vec{c}_m are the phasors of the almost periodic voltage fluctuations based on the fictitious power S instead of P . The voltage sensitivity coefficient respect the fictitious power is β . It can be expressed in terms of the apparent short-circuit power $S_{k, fic}$ and the network impedance angle ψ_k .

$$\beta = \frac{R_{fic}}{U_{PCC}^2} = \frac{\cos(\psi_k)}{S_{k, fic}} \quad (285)$$

B) Model for constant power factor

At frequencies $f \ll f_{grid}$ the dynamics of reactive power can be discarded. Thus, a quasistatic relationship between active and reactive power is sometimes accurate enough.

Assuming that the voltage-current lag angle $\varphi(f) = \arctan(Q(f) / P(f))$ at PCC is approximately constant under some operational conditions, then voltage deviations are proportional to power deviations:

$$\Delta U \underset{\text{approx}}{\simeq} \frac{R_{fic} + X_{fic} \cdot \tan(\varphi)}{U_{PCC}} P = \beta U_{PCC} P \quad (286)$$

where β is a sensitivity coefficient of voltage to power fluctuations. It can be expressed in terms of apparent short-circuit power $S_{k, fic}$, its network impedance angle ψ_k and voltage-current lag angle φ .

$$\beta = \frac{R_{fic} + X_{fic} \tan(\varphi)}{U_{PCC}^2} = \frac{\cos(\psi_k) + \sin(\psi_k) \tan(\varphi)}{S_{k, fic}} \quad (287)$$

Thus, the voltage at the PPC of the farm can be expressed with random phasors, according to Fig. 70:

$$\begin{aligned} U_{PCC}(t) &= U_0 + \Delta U \simeq U_0 + \beta U_{PCC} P(t) = \\ &= U_0 + \beta U_{PCC} (\langle P \rangle + \Delta P(t)) = \\ &= \langle U_{PCC} \rangle - \beta U_{PCC} \sum_{m=1}^{\infty} \text{Re} \left[\vec{c}_m e^{jm\omega t} \right] \end{aligned} \quad (288)$$

where $\langle U_{PCC} \rangle = U_0 + \beta U_{PCC} \langle P \rangle$ is the average voltage for the given operational condition. In fact, (288) is the small signal model for voltage respect its mean value $\langle U_{PCC} \rangle$. The parameters $\langle U_{PCC} \rangle$ and β are actually random variables which depend on nearby loads, generators and grid configuration. Their characteristics can be estimated from measurements or from power flow simulations and they can be considered constant during blade period T (around 1 s).

5.3.2. Standard IEC 61400-21 approach to flicker emission from wind farms

Standard IEC 61400-21 [205] states flicker emission assuming flicker is inversely proportional to $S_{k, fic}$ and computing separate flicker contribution of continuous operation (mainly due to tower shadow and wind variability) and contribution of switching events (such as connection and disconnection of turbines and other components) [206, 207, 208].

The flicker coefficient for continuous operation, $c(\psi_k)$, is the normalized short term flicker for 10 minutes measuring interval and $S_{k, fic} = 1 \text{ p.u.}$ in (287), i.e., sensitivity coefficient $\beta = \cos(\psi) + \sin(\psi) \tan(\varphi)$. The flicker coefficient for continuous operation and annual average wind speed v_a , $c(\psi_k, v_a)$, is the averaged 99th percentile of $c(\psi_k)$ for and voltage. Nonetheless, for usual real network impedance values at PCC of a wind farm, β range from 0.1 to 0.005 for p.u. power values.

Since the distribution of the Fourier coefficients has been derived, it is possible to compute the Flicker that a wind farm would produce in a fictitious grid as defined in IEC61400-21.

A) Flickermeter functional blocks

According to IEC 61000-4-15 [209], the flickermeter is divided into functional blocks (see Fig. 71). The first block is a normalizing voltage adaptor with proportional constant $1/\langle U_{PCC} \rangle$. The output of the first block is a signal proportional to voltage and unity mean (i.e., per unit voltage respect its average).

$$U_{pu}(t) \simeq 1 - \beta \sum_{m=0}^{\infty} \text{Re} \left[\overrightarrow{c_m} e^{jm\omega_1 t} \right] \quad (289)$$

The more difficult blocks to compute in the frequency domain are the quadratic demodulator (block 2) and quadratic multiplier (block 4) since squaring in the time domain is equivalent to convolving in the frequency domain. The convolution in the frequency domain requires the summation of the product of Fourier coefficients. Taking into account the transforms of the sines and cosines of the Fourier series, the Fourier coefficients of the squared input at block 2 can be computed from the auto-convolution of the farm power output

The Fourier coefficients of a squared voltage $\overrightarrow{d_k}$ can be computed from the coefficients of the original signal $\overrightarrow{c_m}$.

$$U_{pu}^2(t) \simeq d(t) = 1 - 2\beta \sum_{m=0}^{\infty} \text{Re} \left[\overrightarrow{c_m} e^{jm\omega_1 t} \right] + \left(\beta \sum_{m=0}^{\infty} \text{Re} \left[\overrightarrow{c_m} e^{jm\omega_1 t} \right] \right)^2 = \frac{d_0}{2} + \sum_{m=0}^{\infty} \text{Re} \left[\overrightarrow{d_m} e^{jm\omega_1 t} \right] \quad (290)$$

The odd order coefficients of the squared voltage are:

$$\overrightarrow{d_k} = -2\beta \overrightarrow{c_k} + \beta^2 \left(\sum_{m=(k+1)/2}^k \overrightarrow{c_m} \cdot \overrightarrow{c_{k-m}} + \sum_{m=k+1}^{\infty} \overrightarrow{c_{m-k}} \cdot \overrightarrow{c_m} \right) \quad (k \text{ odd}) \quad (291)$$

The even order coefficients of the squared voltage are:

$$\overrightarrow{d_k} = -2\beta \overrightarrow{c_k} + \beta^2 \left(\frac{1}{2} \overrightarrow{c_{k/2}}^2 + \sum_{m=(k/2)+1}^k \overrightarrow{c_m} \cdot \overrightarrow{c_{k-m}} + \sum_{m=k+1}^{\infty} \overrightarrow{c_{m-k}} \cdot \overrightarrow{c_m} \right) \quad (k \text{ even}) \quad (292)$$

The statistical distribution of phasors can be computed from results from previous chapters. As the stochastic sum includes infinite terms and distributions of different types, the Central Limit can be applied to substitute exact distributions with approximated normalized random variables (i.e., second order statistical approximation). Notice that the main contribution to $\overrightarrow{d_k}$ is $2\beta \overrightarrow{c_k}$, which is a complex normal quantity of zero mean. The sum of components of $\overrightarrow{d_k}$ can be neglected since $\beta \sigma_{\overrightarrow{d_k}} \ll 1$. This is equivalent to the approximation:

$$\left(\langle U \rangle - \Delta U \right)^2 = \langle U \rangle^2 - 2\Delta U \langle U \rangle + \Delta U^2 \simeq \langle U \rangle^2 - 2\Delta U \langle U \rangle \quad (293)$$

For usual network configurations, the fluctuating voltage deviation due to periodic components in wind power at PCC is $\Delta U_{PCC} < 10^{-3}$ p.u. and therefore, $\Delta U_{PCC}^2 < 10^{-6}$ p.u.

The linear approximation (293) is implicit when standard IEC61400-21 states that flicker level is proportional to the short-circuit impedance at PCC, the high ratio $S_{k, fic} / S_{n \text{ turb}}$ recommended or the independent flicker contribution of continuous and switching operation.

Using the properties of complex normal variables, the output of block 2 (quadratic demodulator) at harmonic k $\overrightarrow{d_k}$ for $k \neq 0$ will be approximately a normal random variable with zero mean and variance $\sigma_{\overrightarrow{d_k}}^2$:

$$\overrightarrow{d_k} \underset{2^{nd} \text{ order approx}}{\sim} \mathcal{CN} \left(0, \sigma_{\overrightarrow{d_k}}^2 \right) \quad \forall k \neq 0 \quad (294)$$

• k is odd.

$$\sigma_{\overrightarrow{d_k}}^2 = 4\beta^2 \sigma_{\overrightarrow{c_k}}^2 + \beta^4 \sum_{m=(k+1)/2}^{k-1} 2\sigma_{\overrightarrow{c_m}}^2 \sigma_{\overrightarrow{c_{k-m}}}^2 + \beta^4 \sum_{m=k+1}^{\infty} 2\sigma_{\overrightarrow{c_{m-k}}}^2 \sigma_{\overrightarrow{c_m}}^2 \approx 4\beta^2 \sigma_{\overrightarrow{c_k}}^2 \quad (295)$$

• k is even.

$$\sigma_{\overrightarrow{d_k}}^2 = 4\beta^2 \sigma_{\overrightarrow{c_k}}^2 + \beta^4 \sigma_{\overrightarrow{c_{k/2}}}^4 + \beta^4 \sum_{m=(k/2)+1}^k 2\sigma_{\overrightarrow{c_m}}^2 \sigma_{\overrightarrow{c_{k-m}}}^2 + \beta^4 \sum_{m=k+1}^{\infty} 2\sigma_{\overrightarrow{c_{m-k}}}^2 \sigma_{\overrightarrow{c_m}}^2 \approx 4\beta^2 \sigma_{\overrightarrow{c_k}}^2 \quad (296)$$

• $k = 0$. The DC component d_0 is a special case because it

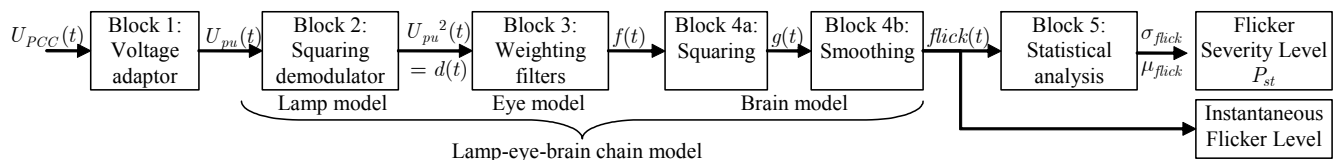


Fig. 71: Simplified block diagram of IEC Flickermeter according to IEC 61000-4-15

is not a phasor, it is a real number with nonzero mean.

$$d_0 = 2 + \beta^2 \sum_{m=0}^{\infty} \text{Exponential}(\lambda_m^{-1} = 2\sigma_{\vec{c}_m}^2) \quad (297)$$

The finite sum of independent exponential variables of the same scale parameter λ_m^{-1} is a gamma distribution. This is not the case because λ_m^{-1} decreases with m (the spectrum vanishes for high frequencies). Since the number of independent random variables to be summed is infinite, the second order approximation is suitable. The average of d_0 is $\langle d_0 \rangle$.

$$\langle d_0 \rangle = \left\langle 2 + \beta^2 \sum_{m=0}^{\infty} |\vec{c}_m|^2 \right\rangle = 2 \left(1 + \beta^2 \langle \text{RMS}_{\Delta Sfarm}^2 \rangle \right) \quad (298)$$

where $\langle \text{RMS}_{\Delta Sfarm}^2 \rangle$ is the average quadratic fluctuation of the wind farm fictitious power output, defined in (268), and $\sigma_{\vec{c}_m}$ is the standard deviation of \vec{c}_m , defined in (240).

The variance of d_0 is $\sigma_{d_0}^2$, the sum of the variances of the independent exponential random variables:

$$\sigma_{d_0}^2 = \beta^4 \sum_{m=0}^{\infty} 4\sigma_{\vec{c}_m}^4 \quad (299)$$

Thus, the second order approximation of d_0 is a normal real variable with the same average and standard deviation:

$$d_0 \sim N(\langle d_0 \rangle, \sigma_{d_0}) \quad (300)$$

The weighting filters of block 3, as named in IEC 61000-4-15, is equivalent to the multiplication of Fourier coefficients by the filter transfer function at the harmonic frequency. The phase displacement introduced by a filter in a stochastic signal with circular symmetry does not alter its statistical properties since the phase of the signals is random [203]. Therefore, the variance is multiplied by the modulus of the transfer function, $F_{block\ 3}(w)$, squared at the corresponding frequency, $f(t) = \mathcal{F}^{-1} \left[U_{PCC}^2(w) * F_{block\ 3}(w) \right]$.

$$\begin{aligned} f(t) &= \sum_{0,05T < k < 35T} \text{Re} \left[\vec{f}_k e^{jk \frac{2\pi}{T} t} \right] = \\ &= \sum_{0,05T < k < 35T} \text{Re} \left[\vec{d}_k F_{block\ 3} \left(k \frac{2\pi}{T} \right) e^{jk \frac{2\pi}{T} t} \right] \end{aligned} \quad (301)$$

• $0,05 T < k < 35 T$.

$$\sigma_{\vec{f}_k}^2 = \sigma_{\vec{d}_k}^2 \left| F_{block\ 3} \left(\frac{2\pi k}{T} \right) \right|^2 \approx 4\beta^2 \sigma_{\vec{c}_k}^2 \left| F_{block\ 3} \left(\frac{2\pi k}{T} \right) \right|^2 \quad (302)$$

where $\sigma_{\vec{f}_k}^2$ is the variance of the Fourier coefficient k of the weighted voltage fluctuation (output of block 3) and $F_{block\ 3}(w)$ is the weighting transfer function defined in [209] between 0,05 Hz and 35 Hz and zero elsewhere (ideal pass-band sinc filter). Recall that the pass-band filter removes the DC component of the signal.

The fourth block is another quadratic multiplier and its output can be computed with formulas (295) to (296), taking into account that now its input signal, $g(t)$, is band limited. Using the properties of complex normal variables, the k Fourier coefficients of the output of the of block 4 (quadratic multiplier), \vec{g}_k , will be approximated by normal random variable with zero mean and variance $\sigma_{\vec{d}_k}^2$ for $k \neq 0$:

$$g(t) = \sum_{k=0}^{\text{Floor}(35T)} \text{Re} \left[\vec{g}_k e^{jk \frac{2\pi}{T} t} \right] \quad (303)$$

$$\vec{g}_k \underset{\text{2nd order approximation}}{\sim} \mathbb{CN}(0, \sigma_{\vec{g}_k}) \quad k \neq 0 \quad (304)$$

where floor means rounded towards the smaller integer.

• k is odd.

$$\sigma_{\vec{g}_k}^2 = \sum_{m=(k+1)/2}^k 2\sigma_{\vec{f}_m}^2 \sigma_{\vec{f}_{k-m}}^2 + \sum_{m=k+1}^{\text{Floor}(35T)} 2\sigma_{\vec{f}_{m-k}}^2 \sigma_{\vec{f}_m}^2 \quad (305)$$

• k is even and $k \neq 0$.

$$\sigma_{\vec{g}_k}^2 = \sum_{m=(k/2)+1}^k 2\sigma_{\vec{f}_m}^2 \sigma_{\vec{f}_{k-m}}^2 + \sum_{m=k+1}^{\text{Floor}(35T)} 2\sigma_{\vec{f}_{m-k}}^2 \sigma_{\vec{f}_m}^2 + \sigma_{\vec{f}_{k/2}}^4 \quad (306)$$

The DC component $g_0 = 2 \langle g(t) \rangle$ is a special case because it is not a phasor, it is a real number. The average of g_0 is $\langle g_0 \rangle$ and its variance is $\sigma_{g_0}^2$.

$$\langle g_0 \rangle = \left\langle \sum_{m=0}^{\infty} \text{Exponential}(\lambda_m^{-1} = 2\sigma_{\vec{f}_m}^2) \right\rangle = \sum_{0,05T < m < 35T} 2\sigma_{\vec{f}_m}^2$$

$$\sigma_{g_0}^2 = \sum_{0,05T < m < 35T} 4\sigma_{\vec{f}_m}^4 \quad (307)$$

After performing the squaring, a first order low-pass filter must be applied. Therefore, the output of block 4 can be computed as:

$$\sigma_{flick, k}^2 = \sigma_{\vec{g}_k}^2 \left| F_{block\ 4} \left(\frac{2\pi k}{T} \right) \right|^2 \quad (308)$$

where $\sigma_{flick, k}^2$ is the variance of the instantaneous flicker coefficient k . $F_{block\ 4}(w)$ is the transfer function of the first order displacement filter.

B) Stochastic characterization of instantaneous flicker

Block 5 is a statistical classifier. Since the stochastic characteristics of the signals have been tracked along each block, the percentiles of the instantaneous flicker can be computed from the variance of Fourier coefficients of instantaneous flicker and the mean and variance of DC component.

The Fourier coefficients of the instantaneous flicker $flick(t)$ are the result of two stochastic sums of complex normal and non-normal distributions followed by weightings. The result of this process can be approximated by a normal.

$$flick(t) \sim N(\mu_{flick}, \sigma_{flick}) \quad (309)$$

where μ_{flick} is the average of the instantaneous flicker level and $\sigma_{flick, m}^2$ is the variance of the instantaneous flicker (output of quadratic demodulator).

The complex coefficients \vec{g}_k have null mean except the zero order component, g_0 . The average of the instantaneous flicker μ_{flick} is just half the zero order coefficient of $g(t)$ since the block 4 does not alter DC value.

$$\mu_{flick} = \langle flick(t) \rangle = \frac{1}{2} \langle g_0 \rangle = \sum_{0,05T < m < 35T} \sigma_{\vec{f}_m}^2 \quad (310)$$

The variance of the instantaneous flicker, σ_{flick}^2 , is the sum of the variance of the mean flicker, $\sigma_{g_0}^2/4$, plus the variance due to the projection of the phasors in the real axis. According to (156), the variance due to the m phasor projection is half the sum of the second order central moment of the Fourier coefficient modulus divided by two, i.e. $\sigma_{flick, m}^2$.

$$\sigma_{flick}^2 = \frac{1}{4} \sigma_{g0}^2 + \sum_{m=1}^{\text{Round}(35T)} \sigma_{flick, m}^2 \quad (311)$$

Therefore, assuming normal distribution of the instantaneous flicker (309), the short-time flicker P_{st} is:

$$P_{st} = \sqrt{0,5096 \mu_{flick} + 0,6879 \sigma_{flick}^2} \quad (312)$$

Since the terms multiplied by β^4 are negligible respect the term multiplied by $4\beta^2$ in (295) to (296), the blocks 1 to 3 of the flickermeter behaves almost linearly. The mean μ_{flick} and the standard deviation σ_{flick} of the instantaneous flicker are approximately proportional to $\alpha^2 \beta^2 N/T$. Thus, P_{st} is approximately proportional to $\sqrt{N/T} \alpha \beta$ and P_{st} can be estimated as:

$$P_{st} = \alpha \beta \sqrt{\frac{N}{T}} Coef_1(T, \tau) \quad (313)$$

Or alternatively, it can be expressed in grid parameters:

$$P_{st} = Coef_1(T, \tau) \frac{\alpha}{S_{k, fict}} \sqrt{\frac{N}{T}} [\cos(\psi_k) + \sin(\psi_k) \tan(\varphi)]$$

Where:

- $Coef(T, \tau)$ is a coefficient that depends on the tower shadow shape, its characteristic width τ and the blade period T . It is usually between 0,1 and 0,2.
- $\alpha/S_{k, fict}$ is the relative depth of the tower shadow α compared to the short circuit ratio at PCC, $S_{k, fict}$. This factor is usually bellow $0,03/N$ for grid connected wind farms (according to typical tower shadow effect and usual grid codes).
- N/T is the wind farm blade frequency. The formula (313) has been derived with all the N turbines spinning at the same speed, but it can be extended substituting N/T by the average number of blades that crosses a tower per second, $\langle \lambda \rangle$.
- $\cos(\psi_k) + \sin(\psi_k) \tan(\varphi)$ is the functional dependence of flicker with impedance angle ψ_k and voltage-current lag angle φ . This factor is usually bellow 0,5 for high voltage grids (see Table XV).

Recall that for usual conditions, the flicker emission of continuous at PCC is far below 1 for grid connected wind farms.

$$P_{st} < 0.004/\sqrt{N} \quad (\text{emission at PCC}) \quad (314)$$

At medium voltage and high voltage, the capacity of the grid to be perturbed is shared among generators and loads (IEC 1000-3-7 [210] asses this capacity). As tower shadow is a continuous process and it has been computed through the mean and variance of instantaneous flicker, the quadratic summation law is more suitable than the cubic summation.

The low flicker emission at PCC makes very difficult to relate measured flicker and the output of near wind farms. The authors of this article performed several test in various wind farms with a conventional flickermeter and the influence of nearby loads masked the influence of the farm.

The flicker coefficient $c(\psi_k)$ defined in Standard IEC 61400-21 is the flicker that the farm would emit if it is connected at a PCC with 1 p.u. short-circuit impedance and impedance angle ψ . Notice also if $c(\psi_k)$ is given for some

ψ_k and φ , the flicker for other operational conditions can be computed. (315)

$$c(\psi_k) = P_{st, fic} \cdot \frac{S_{k, fic}}{S_n} = Coef_1(T, \tau) \frac{\alpha}{S_n} \sqrt{\frac{N}{T}} [\cos(\psi_k) + \sin(\psi_k) \tan(\varphi)]$$

where α/S_n is the relative depth of the tower shadow α compared to the nominal power of the turbine.

The wind farm flicker coefficient $c_{wind\ farm}(\psi_k)$ can be obtained from the flicker coefficient of a single turbine, $c_{wind\ turbine}(\psi_k)$:

$$c_{wind\ farm}(\psi_k) = \frac{S_{n\ turbine}}{S_{n\ farm}} \sqrt{N} c_{wind\ turbine}(\psi_k) = \frac{1}{\sqrt{N}} c_{wind\ turbine}(\psi_k)$$

IEC61400-21 also defines the flicker coefficient for continuous operation, $c(\psi_k, v_a)$, which is the 99% percentile of $c(\psi_k)$ and can be obtained also applying the $1/\sqrt{N}$ factor.

In Table V, $Coef(T, \tau)$ has been adjusted with an even mesh of 198 points with blade period $0,5\ s \leq T \leq 1,5\ s$ and characteristic rate $0,05\ s \leq \tau \leq 0,25\ s$.

TABLE V: APPROXIMATED TOWER SHADOW EFFECT ON FLICKER

	$Coef_1(T, \tau)$	MSE
Gaussian	$\frac{0.100711}{T^{0.0673857} \tau^{0.218744}}$	$3,4 \cdot 10^{-5}$
Triangular	$\frac{0.251499 \tau^{0.0216745}}{T^{0.0607005}}$	$4,3 \cdot 10^{-6}$
Rectangular	$\frac{0.091558}{T^{0.0698291} \tau^{0.226092}}$	$4,3 \cdot 10^{-5}$

C) Gaussian pulse

The fitted model (with $3,4 \cdot 10^{-5}$ mean square error) of the flicker produced by Gaussian pulses of fictitious voltage (or power) is:

$$Coef_1(T, \tau) = \frac{0,100711}{T^{0,0673857} \tau^{0,218744}} \approx \frac{0,2}{\sqrt{T}} - \frac{0,32\tau}{\sqrt[4]{T}} \quad (317)$$

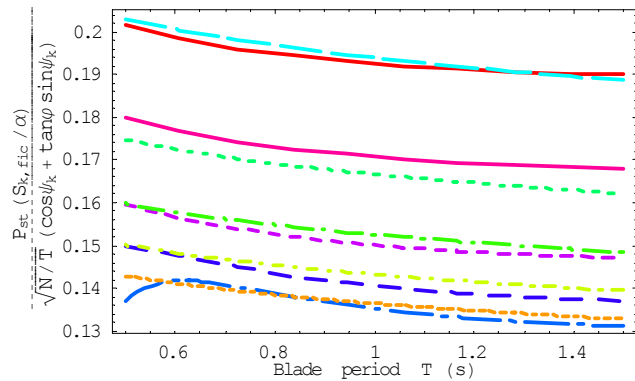


Fig. 72: Flicker coefficient for a farm with Gaussian rotational effect.

D) Rectangular pulse

The fitted model (with $4,3 \cdot 10^{-5}$ mean square error) of the flicker produced by rectangular pulses of fictitious voltage (or power) is:

$$Coef_1(T, \tau) = \frac{0,251499\tau^{0,0216745}}{T^{0,0607005}} \approx \frac{0,24}{\sqrt{T}} \quad (318)$$

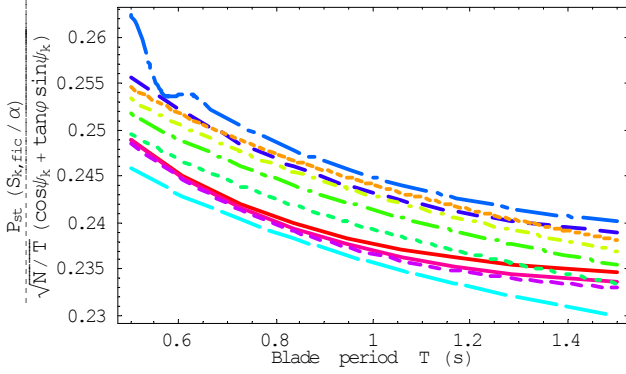


Fig. 73: Flicker coefficient for a farm with rectangular rotational effect.

E) Triangular pulse

The fitted model (with $4,3 \cdot 10^{-6}$ mean square error) of the flicker produced by rectangular pulses of fictitious voltage (or power) is:

$$Coef_1(T, \tau) = \frac{0,091558}{T^{0,069829}\tau^{0,226092}} \approx \frac{0,242}{\sqrt{T}} - 0,205 \left(\frac{\tau}{T} \right)^{0,38} \quad (319)$$

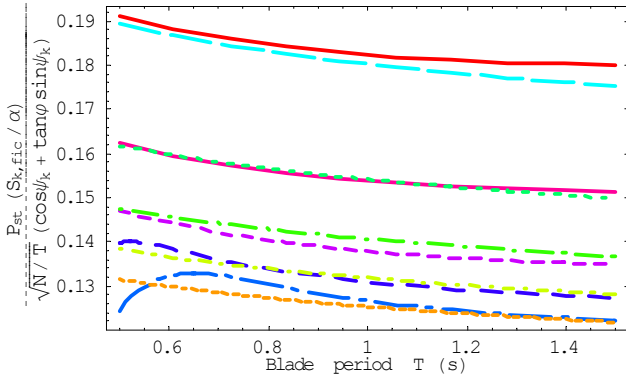


Fig. 74: Flicker coefficient for a farm with triangular rotational effect.

The lower percentiles 0,1% and 1% in the fifth functional block of the flickermeter are more dependent on the exact statistical distribution of instantaneous flicker. The non-linear behaviour of squaring blocks and the actual non-normal distribution of instantaneous flicker are supposed to be an important source of uncertainty. The authors plan to work further to asses the uncertainty introduced by the approximations used in this approach, comparing this model with the results of Monte Carlo simulations.

5.4. Contribution of aperiodic components to Flicker

5.4.1. Simplified PSD for flicker estimation

Since very slow and DC components ($f \ll 0,05$ Hz) of PSD don't influence flicker, the model (184) has been simplified for $0,05$ Hz $< f \leq 35$ Hz. In Fig. 205, the PSD shows a wide peak at blade frequency due to the varying amplitude and frequency with harmonics and sub-harmonics.

Their effect on flicker depends on the product of sensitivity of flicker to that frequency $|F_{weight}(f)|$ defined in [209], times the power content of the frequency range (i.e., product of the width by the amplitude of the peak).

Thus, the PSD can be approximated by the spectrum of a system of fractional order r ($1 \leq r \leq 1,75$), plus the tower shadow effect S_0 (a delta impulse δ_0 at frequency f_0) and the noise floor S_2 . In the frequencies of interest for flicker analysis, $0,05$ Hz $< f \leq 35$ Hz, the following approximations are valid:

$$\langle S_{farm}^2(f) \rangle \approx N S_1 (S_0 \delta_0(f-f_0) + f^{-2r} + S_2) \quad (320)$$

$$\sigma_{farm}^2(f) = \frac{1}{2} \langle S_{farm}^2(f) \rangle \quad (321)$$

$$\vec{S}_{farm}(f) \sim \mathcal{CN}[0, \sigma_{farm}(f)] \quad (322)$$

$$S_{farm}(f) \sim \text{Rayleigh}[\sigma_{farm}(f)] \quad (323)$$

Typical values for r, f_0, S_0, S_1 and S_2 can be derived from the PSD (see Fig. 205 to Fig. 271) by regression analysis.

TABLE VI: PARAMETERS OF THE PSD MODEL OF REAL POWER TURBINE OUTPUT (321)

	Significance	Range
r	System order of the turbine real power output excited by the wind turbulence (i.e., half the slope trend of PSD in a double logarithmic plot)	1 ~ 1.7
$\frac{S_1}{S_n^2}$	Overall fluctuation level of the turbine (i.e., the PSD trend line at 1 Hz) in p.u. units	10^{-4} $\sim 10^{-2}$
S_0	Squared average of tower shadow power oscillation relative to S_1	5~100
f_0	Mean tower shadow frequency	0.5~2 Hz
S_2	Squared noise level on power output relative to S_1	0~0.01
S_n	Nominal power of the turbine	0,3~5 MW
N	Number of equivalent turbines in the farm	1~50

Notice that in general, harmonic peaks are narrow and their power content is low. Sub-harmonics can have noticeable power, but their flicker sensitivity is low. These terms can be added explicitly to (320) as delta impulses. Nevertheless, models more complex than (320) are also suitable. For the sake of simplicity, S_0 can include not only tower shadow but also its harmonics and sub-harmonics approximate effect if the following estimation is used:

$$\begin{aligned} S_0 &= \int_{0,05\text{Hz}}^{8,8\text{Hz}} \left(\frac{1}{S_1} \langle S_{farm}^2(f) \rangle - f^{-2r} - S_2 \right) \frac{|F_{weight}(f)|^2}{|F_{weight}(f_0)|^2} df \approx \\ &\approx \int_{0,05\text{Hz}}^{8,8\text{Hz}} \left(\frac{1}{S_1} \langle S_{farm}^2(f) \rangle - f^{-2r} - S_2 \right) \frac{f^2}{f_0^2} df \end{aligned} \quad (324)$$

If PSD does not fit the model (320) at frequencies between 8,8 Hz and 35 Hz, another delta impulse term S_3 at frequency $8,8$ Hz $< f_3 < 35$ Hz can be included in (320):

$$S_3 = \int_{8,8\text{Hz}}^{35\text{Hz}} \left(\frac{1}{S_1} \langle S_{farm}^2(f) \rangle - f^{-2r} - S_2 \right) \frac{|F_{weight}(f)|^2}{|F_{weight}(f_3)|^2} df S_3 \approx$$

$$\approx \int_{8,8\text{Hz}}^{35\text{Hz}} \left(\frac{1}{S_1} \langle S_{farm}^2(f) \rangle - f^{-2r} - S_2 \right) \frac{f^{-3}}{f_3^{-3}} df \quad (325)$$

Approximations (324) or (325) assume no correlation of fluctuations included in terms S_0 or S_3 . If this assumption does not hold, formulas must be modified accordingly.

These formula indicate that the relative importance of fluctuations is proportional to f^2 up to 8,8 Hz and then proportional to f^{-3} .

Spectrum angle $\varphi_{farm}(f)$ is a random variable uniformly distributed in $[-\pi, +\pi]$. Consequently, the complex phasor $\vec{S}_{farm}(f)$ is a complex Gaussian random variable of zero mean and standard deviation $\sigma_{farm}(f)$:

$$\vec{S}_{farm}(f) \sim \mathbb{C}N[0, \sigma_{farm}(f)] \quad (326)$$

5.4.2. Flicker contribution from a parameterized PSD

The computation of flicker from a PSD is analogous to the computation from Fourier Coefficients, except that the coefficient variances are replaced by spectral densities and some sums are transformed into integrals. Since the derivation of the linearized model has been carefully derived previously, only the main results are outlined. The PSD of the squaring demodulator (block 2) is:

$$PSD_f^+(f) \approx 4\beta^2 PSD_S^+(f) \left| F_{block\ 3}(2\pi f) \right|^2 \quad (327)$$

The average of the instantaneous flicker, σ_{flick}^2 , can be computed integrating PSD_f^+ :

$$\mu_{flick} \approx \int_{0,05\text{Hz}}^{8,8\text{Hz}} PSD_f^+(f) df \quad (328)$$

The PSD of the instantaneous flicker at low frequencies, $0,10\text{ Hz} \leq f \leq 34,95\text{ Hz}$, is:

$$PSD_{flick}^+(f) \approx 2 \left| F_{block\ 4}(2\pi f) \right|^2 \cdot \left(\int_{f/2}^f PSD_f^+(f-\vartheta) \cdot PSD_f^+(\vartheta) d\vartheta + \int_f^{35\text{Hz}} PSD_f^+(\vartheta-f) \cdot PSD_f^+(\vartheta) d\vartheta \right) \quad \forall \quad 0,10\text{Hz} \leq f \leq 34,95\text{Hz}$$

The PSD of the instantaneous flicker at higher frequencies, $35,05\text{ Hz} \leq f \leq 70\text{ Hz}$, is significantly smaller since block 4 attenuates notably these frequencies:

$$PSD_{flick}^+(f) \approx 2 \left| F_{block\ 4}(2\pi f) \right|^2 \int_{f/2}^{35\text{Hz}} PSD_f^+(f-\vartheta) \cdot PSD_f^+(\vartheta) d\vartheta \quad \forall \quad 35,05\text{Hz} \leq f \leq 70\text{Hz}$$

The variance of the instantaneous flicker, σ_{flick}^2 , can be computed by integration:

$$\sigma_{flick}^2 \approx \int_{0,05\text{Hz}}^{35\text{Hz}} PSD_f^{+2}(f) df + \int_{0,10\text{Hz}}^{70\text{Hz}} PSD_{flick}^+(f) \quad (331)$$

Thus, the flicker level can be estimated through (312) and another coefficient depending on r can be computed provided the tower shadow is computed separately and noise floor is small.

$$P_{st} = \beta \sqrt{S_1 N} \text{Coef}_2(r) \quad (332)$$

where $\text{Coef}_2(r) \approx 5,06051 - 6,96771r + 2,86515r^2$

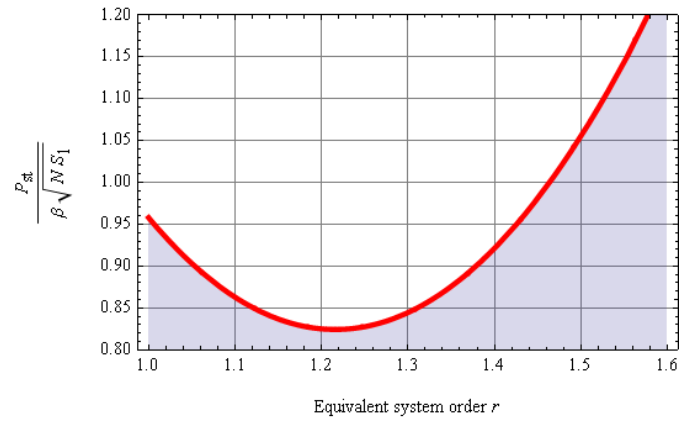


Fig. 75: Flicker coefficient (332) for a farm with simple PSD

5.4.3. Estimation of total flicker during continuous operation (periodic and aperiodic)

A) Continuous operation

Even though both periodic and aperiodic components are present in the fictitious power, both components are statistically independent. Assuming the linearization of the quadratic block and second order statistics, the total flicker can be estimated from the individual components.

The second order approximation for the instantaneous flicker is:

$$flick_{contop}(t) \sim N\left(\mu_{flick,1} + \mu_{flick,2}, \sqrt{\sigma_{flick,1}^2 + \sigma_{flick,2}^2}\right) \quad (333)$$

Thus, the flicker level can be computed assuming normality and approximate sum of variances:

$$P_{st,contop} \approx \zeta \sqrt{0,5096(\mu_{flick,1} + \mu_{flick,2}) + 0,6879 \sqrt{\sigma_{flick,1}^2 + \sigma_{flick,2}^2}} \quad (334)$$

where ζ is a scaling factor added to fit the flickermeter tests. It is required to give a maximum perceptibility output of 1 for a $\Delta V/V$ of 0.25 % at a modulation frequency, f_f of 8.8 Hz. (this is the modulation frequency at which we are most sensitive to flicker from an incandescent light bulb).

The factor ζ varies from 750 to 1850 depending on the applied calibration signal since this model is intended for stochastic input signals instead of deterministic ones. The accuracy can be increased if all filters are fully implemented since some filters in this model have been replaced with ideal filters for conceptual simplicity. However, a full implementation –non stochastic– of the frequential flickermeter is required to decrease notably the uncertainty in $P_{st,contop}$ with deterministic signals.

Since the linearization of quadratic block slightly underestimates the flicker, an assumable approximation, specially valid if one variance is significantly bigger than the other, is:

$$\sqrt{\sigma_{flick,1}^2 + \sigma_{flick,2}^2} \lesssim \sigma_{flick,1} + \sigma_{flick,2} \quad (335)$$

The former approximation is sensible since some assumptions made in this work may underestimate a little the flicker coefficient (independence of fluctuations, neglected terms in convolutions, and $N > 4$). In fact, (335) assumes some correlation between periodic and aperiodic fluctuations:

$$P_{st,contop} \approx \zeta \sqrt{0,5096(\mu_{flick,1} + \mu_{flick,2}) + 0,6879(\sigma_{flick,1} + \sigma_{flick,2})} \approx \sqrt{P_{st,1}^2 + P_{st,2}^2} \quad (336)$$

Finally, the contribution from periodic and aperiodic sums quadratically assuming the upper bound (335):

$$P_{st,contop} \approx \sqrt{P_{st,1}^2 + P_{st,2}^2} = \zeta \beta \sqrt{N} \sqrt{\frac{\alpha^2}{T} Coef_1^2(T, \tau) + S_1 Coef_2^2(r)} \quad (337)$$

According to (285) or (287), the actual sensitivity coefficient of voltage to power fluctuations β can be expressed in terms of SCR , power factor angle φ and the network impedance angle ψ_k as:

$$\beta = \frac{\cos(\psi_k) + \sin(\psi_k) \tan(\varphi)}{SCR \cdot S_n \cdot N} \quad (338)$$

Thus, the flicker level for continuous operation is: (339)

$$P_{st,total} \approx \frac{\cos(\psi_k) + \sin(\psi_k) \tan(\varphi)}{SCR \cdot S_n \cdot \sqrt{N}} \zeta \sqrt{\frac{\alpha^2}{T} Coef_1^2(T, \tau) + S_1 Coef_2^2(r)}$$

Assuming typical values for high voltage according to see Table XV and Spanish minimum value of SCR , the upper bound is:

$$P_{st,contop} < \zeta \sqrt{\frac{\frac{\alpha^2}{S_n^2 T} Coef_1^2(T, \tau) + \frac{S_1}{S_n^2} Coef_2^2(r)}{40\sqrt{N}}} \quad (340)$$

B) Decreasing annoyance due to Flicker in turbine clusters

Flicker levels can be eventually noticeable at nodes electrically close to wind turbines with stiff drivetrains and squirrel cage induction generators connected directly to very weak grids or in stand alone applications. But these conditions are not common and the flicker contribution of wind power is rarely an annoyance.

On the one hand, actual turbines have massive inertias, relatively soft drivetrains and electronically controlled generators. Thus, the torque periodic components are transformed in a kind of stochastic fluctuations in active and reactive power of lesser magnitude (i.e., real power fluctuations from those turbines do no longer resemble pulses).

On the other hand, grid codes usually require a minimum Short Circuit Ratio, SCR . It is the ratio of the short circuit power at the point of common coupling of the grid, $S_{k,PCC}$ to the installed wind power, $N \cdot S_n$ in a cluster of N turbines.

$$SCR = \frac{S_{k,PCC}}{S_n \cdot N} \quad (341)$$

For example, the Spanish regulation [211] requires $SCR \geq 20$. In order to meet this requirement, big clusters of wind turbines are connected to high voltage nodes where $S_{k,PCC}$ are bigger (see Table VII).

TABLE VII: TYPICAL SHORT CIRCUIT VALUES (FROM [212]).

Substation voltage	Typical value of $S_{k,PCC}$
400 kV	30.000 MVA
150 kV	10.000 MVA

70 kV	2.500 MVA
30 kV	1.300 MVA
15 kV	500 MVA
10 kV	400 MVA
400 V	16 MVA

The short time wind farm flicker level can be obtained from the farm coefficient $c_{wind\ farm}(\psi_k)$:

$$P_{st,PCC} = c_{wind\ farm}(\psi_k) \frac{S_{n,windfarm}}{S_{k,PCC}} = \frac{c_{wind\ turbine}(\psi_k)}{\sqrt{N}} \frac{S_n \cdot N}{SCR \cdot S_n \cdot N} = \frac{c_{wind\ turbine}(\psi_k)}{SCR \cdot \sqrt{N}} \quad (342)$$

Since flicker coefficients for a single turbine $c_{wind\ farm}(\psi_k)$ are typically between 4 to 10 [205, 213] and typically $SCR \geq 20$ in Spain, the flicker level in a farm is expected to be low:

$$P_{st,PCC} \leq \frac{1}{2\sqrt{N}} < 1 \quad (343)$$

Therefore, the flicker level during continuous operation at PCC is usually bellow unity and power fluctuations do not produce major irritating flicker.

5.5. Spectrum of the eye output and the average instantaneous flicker

The average instantaneous flicker level can be computed from (302) or (310). Taking into account that first three blocks are almost linear and considering that the PSD has random phase, it is possible to estimate the contribution of each frequency to instantaneous flicker. In the following graphs, the blue lines are the PSD of the eye model output $f(t)$ and the red line is the area beneath the PSD from the left, which equates at the right μ_{flick} the mean instantaneous flicker level. The frequencies that contribute more to flicker are where red line increases quickly.

For the fixed speed, stall turbine the principal contribution to flicker is due to tower shadow (rotor and blade frequencies). The contribution of frequencies 5-7,5 Hz is small.

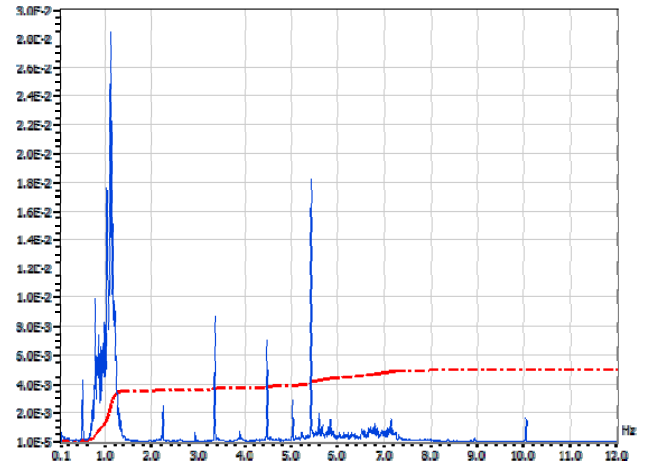


Fig. 76: PSD of squared voltage variations $f(t)$ and its integral g_0 ($\beta = 0.001$) for a SCIG (fixed speed, stall regulated) wind turbine.

In the 600 kW Vestas opti-slip turbine (variable resistor induction generator with pitch control), the influence of tower shadow (rotor and blade frequencies) is negligible. The flicker levels are the lower of the measured turbines and its due mainly to frequencies 4-12 Hz (see Fig. 77)

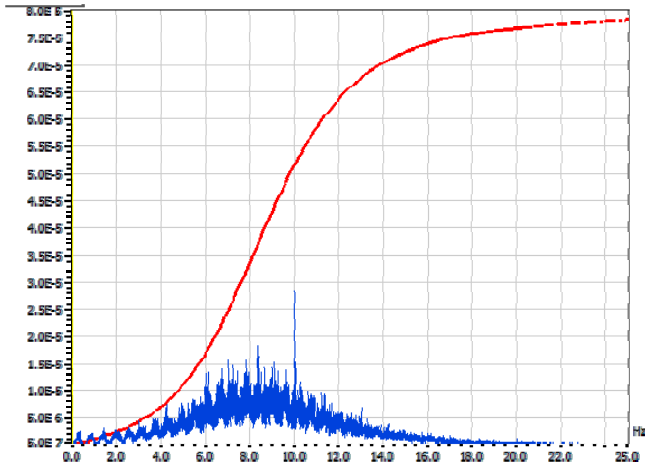


Fig. 77: PSD of squared voltage variations $f(t)$ and its integral g_0 ($\beta = 0.001$) for a VRIG (opti-slip) wind turbine.

In the doubly fed induction generator, Fig. 78, pitch regulated turbine, the influence of tower shadow (rotor and blade frequencies) is small. The flicker is due mainly to frequencies 4-14 Hz.

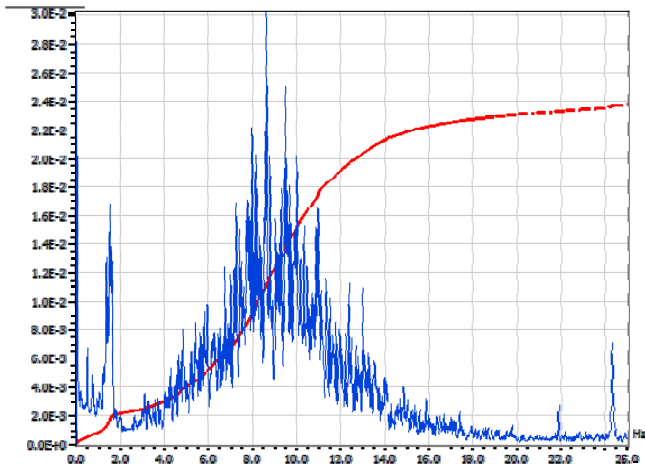


Fig. 78: PSD of squared voltage variations $f(t)$ and its integral g_0 ($\beta = 0.001$) for a DFIG (variable speed) wind turbine.

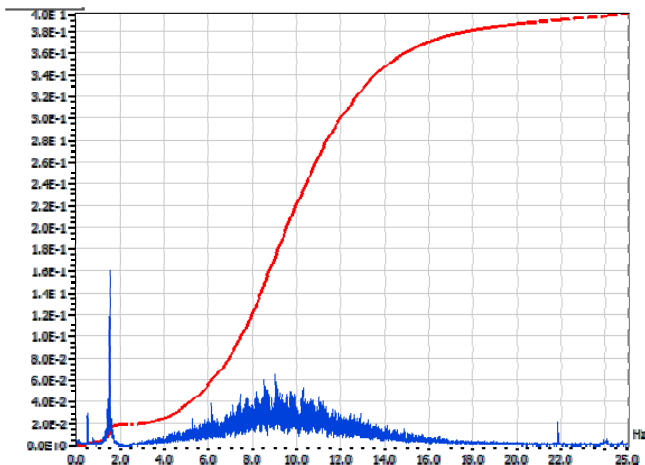


Fig. 79: PSD of squared voltage variations $f(t)$ and its integral g_0 ($\beta = 0.001$) for Remolinos wind farm.

The Remolinos wind farm, Fig. 79, shows a similar behaviour than the single turbine. The average instantaneous flicker level μ_{flick} in the wind farm is approximately the value of measured wind turbine times the number of turbines in the wind farm (18). Since P_{st} is fairly proportional to $\sqrt{\mu_{flick}}$, the flicker emission of the wind farm can be computed from measurements of single turbines: $P_{st, farm} \approx \sqrt{N} P_{st, turbine}$

provided the short circuit power is the same at the turbine and at the point of common coupling (PCC) of the farm.

Actually, the short circuit power at the farm PCC is, to some extent, proportional to the number of turbines. In terms of the short circuit ratio (SCR), the farm flicker emission is:

$$P_{st, farm} \approx \frac{P_{st, turbine}}{SCR \cdot \sqrt{N}} \quad (344)$$

In other words, the flicker emission of a farm is reduced typically in a factor \sqrt{N} respect the turbine emission. Moreover, the flicker is rarely a power quality problem in farms because the short circuit ratio is high due to transmission network requirements ($SCR \geq 20$ habitually).

5.6. Conclusions

Power fluctuations in a farm are related to relative blade positions of the turbines and wind turbulence. The rotor can have any angle with approximately the same probability and turbulence is mostly uncorrelated for different wind turbines. Thus, the overall behaviour of a large number of wind turbines can be derived from the operation of a single turbine.

Correlated fluctuations scales proportional to the number of turbines N whereas linearly uncorrelated fluctuations cancel partially among turbines and they scale up typically in a factor \sqrt{N} . Oscillations from fractions of hertz to power supply frequency are mainly uncorrelated and their sum across a wind farm can be estimated using stochastic analysis commonly applied in other areas such as multipath fading in communication channels, clutter and target cross section in radars, interference in communication systems, etc. but its use in wind energy is novel.

The distribution of power deviations, the speed of power output variations, the distribution of blade position in the turbines and the flicker emission due to blade position are estimated using analytic formulas and a few parameters of the turbines. The model can be completed with small-scale site models to extend its applicability and improve its accuracy.

The flicker emission of a farm is reduced typically in a factor \sqrt{N} respect the turbine emission. Moreover, the flicker is rarely a power quality problem in farms because the short circuit ratio is high due to transmission network requirements.

The wind farm oscillation amplitude due to uncorrelated sinusoidal turbine fluctuations is a Rayleigh random variable of with scale parameter \sqrt{N} times the uncorrelated fluctuation of a single turbine. The instantaneous fluctuation is distributed normally with standard deviation \sqrt{N} times the turbine uncorrelated fluctuation. The squared instantaneous fluctuation shows a gamma distribution with unity shape factor.

The power fluctuation when a blade passes in front of the tower can be represented by power dips. The number of simultaneous tower shadows happening at an instant is a binomial random variable. Tower shadow events are characterized as a generalized Poisson process and its average frequency is N times the tower shadow frequency of a single turbine.

Chapter 6:

Characterization of wind gusts in the time domain

6.1. Introduction

The wind speed fluctuations are defined in this chapter as the deviation of the instantaneous wind speed in the longitudinal direction, ΔU_{wind} , from the average value, $\langle U_{wind} \rangle$, (usually computed averaging 5-60 minutes). The changes in the wind direction are not considered since the wind speed has a more steady behaviour than its module.

Although the probability distributions of wind speed fluctuations, ΔU_{wind} , fits a Normal distribution respect the average $\langle U_{wind} \rangle$ during periods shorter than one hour, the observed accelerations have wider distributions ('longer tails') in general [221].

In words, the probability of extreme accelerations is bigger in reality than the predicted by a normal model and the real sample distribution has bigger extreme values than a normal process with the same average and variance.

Despite these deviations from the normal behaviour and because of the lack of a better description, the gust, defined as the maximum wind speed during a measurement period of 5-60 minutes, is often calculated using a Gaussian process as an approximation and then a transformation is usually applied [223].

The characteristic shapes of gust events are described in [214, 215, 216]. For calculations of the mechanical loads on a wind turbine rotor, it is necessary to have detailed information about the spatial structure of the 3-D wind field. The Mann turbulence model [94] is actually preferred to the Veers model [217].

The interactive program EquiWind [218] for the generation of random samples of equivalent wind gust has been developed. Many of the graphs presented in this chapter have been obtained with this program.

6.2. Statistical distribution of wind variations depending on turbulence mechanism

On one hand, the approximating the equivalent wind as a Gaussian process is a reasonable estimation for small disturbances since small-scale turbulence is the outcome of many independent (considerably low correlated) contributions. On the other hand, big wind variations (big-scale turbulence) are due to external forces which are *correlated* and hence, the experimental probability tails of extreme events are remarkably heavier than the ones from a Gaussian distribution.

One of the key points in the probability theory is the Central Limit Theorem, that states that under quite general conditions, the distribution of the sum of many independent random variables converges to a Gaussian distribution. According to this theorem, the Gaussian distribution (also known as Normal distribution) is suitable for describing a wide range of experiments and experimental data [219].

The wind difference $\Delta U_{wind} = U_{wind} - \langle U_{wind} \rangle$ for lags of a few seconds is, according to [214], *leptokurtic* (positive excess kurtosis ranging from 0 to 3) and quite symmetric (skewness ranging from -0.4 to 0.3). For short time scales, a normal process is a reasonable approximation for small wind variations but it underestimates bigger gust by more than an order of magnitude comparing to real measures, especially at complex sites since wind deviations are leptokurtic.

The measure of the frequency of occurrence of rare events requires long records, but these records are not customarily available and some assumptions must be made to guess a fair probability from limited data.

Extreme weather conditions are due to the chaotic atmospheric behaviour. The statistical distribution of extreme wind variations depends on the prevailing mechanism involved in gusts: the macroscopic wind speed depends on microscopic system dynamics with strong interactions ranging from tiny to very large scales and this is a challenge for meteorologists and chaos theorists. Despite the abundant research done in atmospheric turbulence, this topic is far from concluded and it is out of the aim of this thesis.

Notwithstanding these facts, normality could be a compromise between accuracy and traceability and a sensible choice for its remarkable theoretical properties. However, the estimation of extreme events should be corrected to account the real behaviour of the wind.

In general, the normal approximation is an adequate estimate of the probability of the more frequent wind variations (deviations from the wind, in relative terms, less than two times the intensity of turbulence). However, experimental measurements have shown that the extreme variations of wind ($|\Delta U_{wind}| / \langle U_{wind} \rangle > 2 \sigma_{U_{wind}}$) are underestimated by the normal distribution. The PDF of wind deviations during a few seconds is close to a broken line in logarithmic scale at larger deviations (i.e., double exponential tails) [220, 221, 222, 223, 224]. The probability density in a semilogarithmic-scale converges to two lines –typical of the Laplacian distribution, also called double exponential distribution – instead of converging to a parabola –Gaussian or normal distribution.

In the subsequent subsections, some turbulence mechanisms are compared to the observed distribution of wind turbulence. A naïve analysis of the turbulence will be shown, where some mechanisms are negligible; others are important or even dominant at certain scales or in some events.

6.2.1. Wind distributions in the literature

The results of an extensive measuring campaign with a LIDAR sensor of wind between 40 m to 220 m above the roof of the Institute of Aeronautical Design at the University of Stuttgart can be seen in the report [225]. In Fig. 80, the distribution of wind speed variations ΔU_{wind} respect the average at 120 m in intervals of duration $T = 1,5$ s, 4,5 s, 15 s, 48 s y 162 s (graphs displaced from top to bottom) show that the average occurrence frequency resemble a broken line to two lines that meet at the average semi-logarithmic scale. To avoid overlapping charts, the graphs have been shifted downward. The points correspond to the measured occurrence frequency and the lines correspond to the fitted probability density function in [226]. According to Fig. 80, the wind speed variation ΔU_{wind} follow a Laplacian distribution instead of a Gaussian distribution.

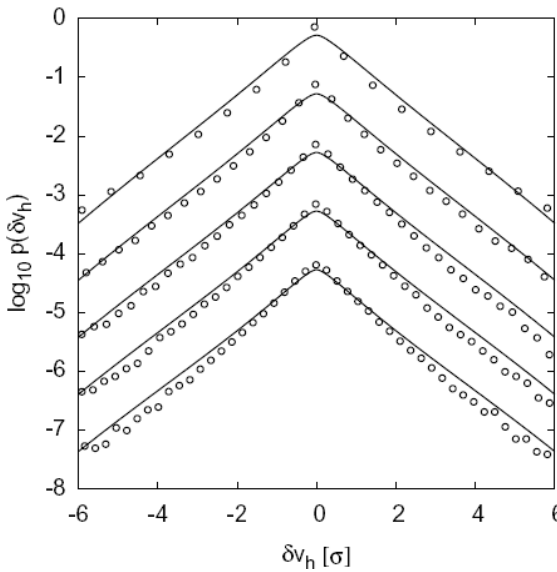


Fig. 80: Measured and fitted probability density of instantaneous wind minus the instantaneous wind at $T = 1,5$ s, 4,5 s, 15 s, 48 s and 162 seconds before (from top to bottom). For great clarity, the plots are displaced downwards. Reproduced from M. Wächter et al. [225].

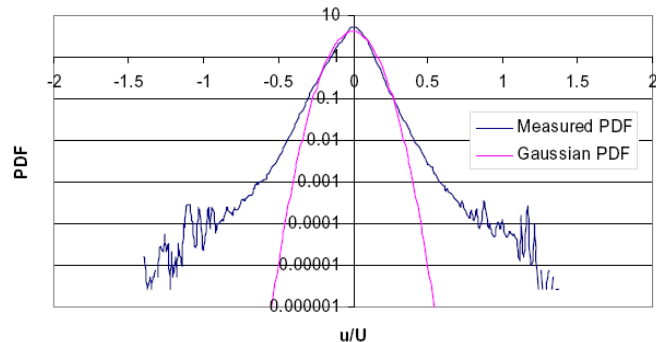


Fig. 81: Probability distribution of longitudinal wind variations (u) respect the average longitudinal velocity (U) in Oak Creek (California) at 80 m. The dark blue line corresponds to the actual probability density and the light pink line corresponds to the normal distribution fitted from data (the vertical axis is in logarithmic scale). Reproduced from G. C. Larsen, [221].

The Fig. 81 shows the wind speed variations ΔU_{wind} in Oak Creek (California) at 80 m above the surface. The wind speed variations ΔU_{wind} are adequately characterized by the normal distribution up to $|\Delta U_{wind}| / \langle U_{wind} \rangle < 2,8 \sigma_{U_{wind}}$ but bigger wind variations are underestimated by several orders of magnitude.

The actual distribution of wind variations can be obtained transforming the normal process to other process with the target probability distribution. The simplest memory-less transformation is a continuous and strictly monotone function that maps each point of the actual distribution into a point of a normal process with the same mean and variance.

The distribution of the lateral wind component in Fig. 82 fits even better to a broken line than the longitudinal wind. Thus, the lateral wind has a Laplacian distribution, also called double exponential distribution. For example, the transformation (352) convert the normal process $x(t)$ into the observed process $y(t)$, which has a Laplacian Distribution, that some authors consider that belongs to the family of generalized Gaussian distributions [227].

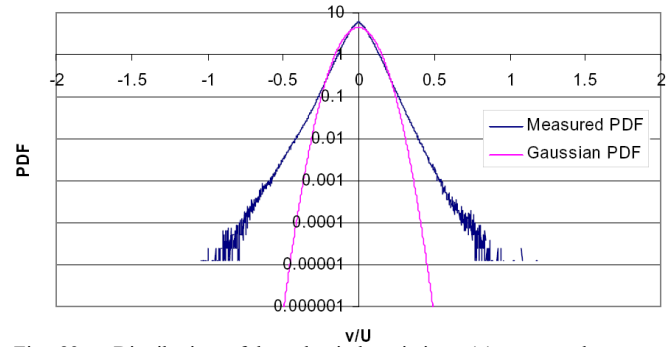


Fig. 82: Distribution of lateral wind variations (v) respect the average longitudinal velocity (U) in Oak Creek (California) at 80 m. The dark blue line corresponds to the measured probability density and the light pink line corresponds to the normal distribution fitted from data (the vertical axis is in logarithmic scale). Reproduced from G. C. Larsen, [221].

In fact, Fig. 83 from [228] shows a very good fit of power generated hourly in a wind farm and in Western Denmark to a double exponential distribution.

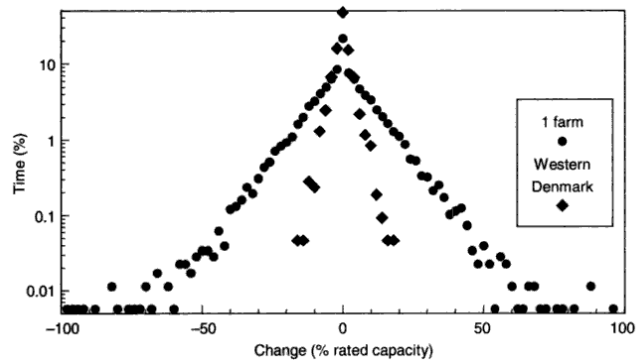


Fig. 83: Changes in average generated output from wind farms, based on hourly averages. Reproduced from B. Fox et al. [228].

The data measured at the airport of Florence in [229, 230] also show a Laplacian distribution of ΔU_{longr} . In those works, a model based on superstatistics was used (this term is used to refer to the stochastic properties of the statistical parameters). Those works present a generalized Boltzmann factor which fits a generalized q-exponential distribution from the measured quantiles. A Laplacian distribution has been added in the experimental distribution of Fig. 84 for comparison with the normal distribution and the q-exponential.

Other authors [231, 232, 233] have fitted the experimental data to a family of stable distributions. For instance, Fig. 85 shows the wind speed deviations during a 58 day measuring campaign during the years 1998-1999 in the Dansk platform Roedsand at 30 m above the Baltic Sea.

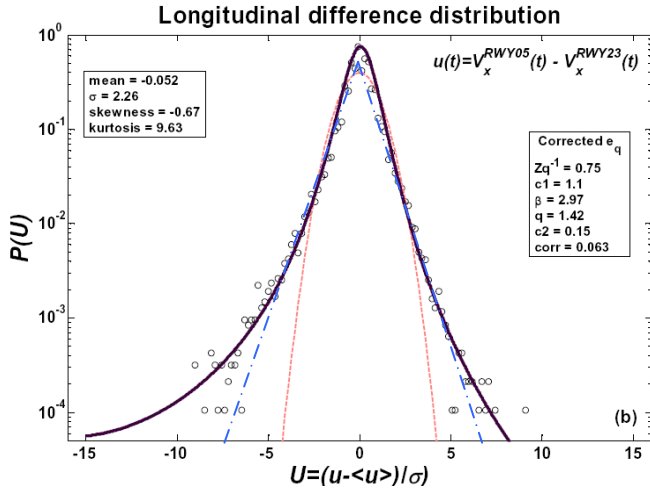


Fig. 84: Comparison of the experimental probability distribution of ΔU_{long} (circles), the Gaussian distribution (dashed red curve), the q-exponential distribution for $q=1.42$ (solid thick black curve) and the Laplacian distribution (a blue dot-dashed broken line) in the Florence Airport. Reproduced from S. Rizzo and A. Rapisarda [230].

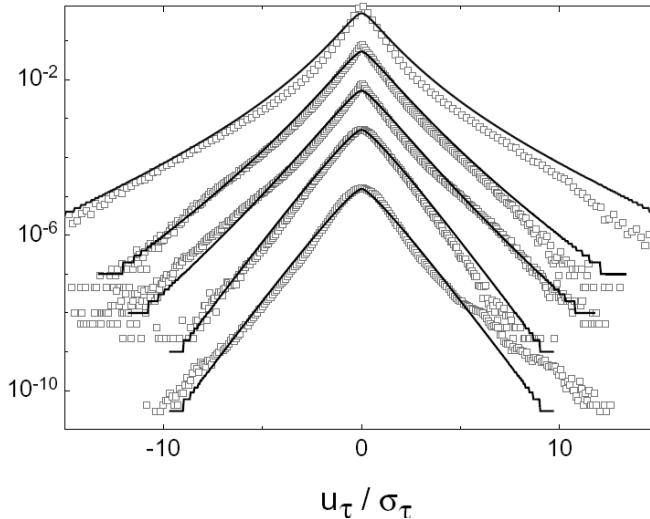


Fig. 85: Measured and fitted probability density of instantaneous wind minus the instantaneous wind at $T = 10, 2, 10, 20, 200, 2000$ seconds (from top to bottom). For great clarity, the plots are displaced downwards. Reproduced from F. Böttcher, St. Barth, and J. Peinke [231].

In a generic case, an adjustable distribution (such as the generalized Gaussian distribution, the q-exponential distribution, the Type IV Pearson distribution, stable distributions or the type I Gumbel distribution for extreme value) could be adapted reasonably well to the frequency of occurrence of wind variations in a pilot site. The transformation f of the normal process observed is obtained by equating the cumulative probability distribution of the adjusted observed process $y(t)$ and the distribution standard process $x(t)$:

$$CDF_{y(t)}[y(t)] = CDF_{x(t)}[x(t)] \quad \forall y(t) = f[x(t)] \quad (345)$$

In the following sections, some mechanisms involved in the turbulence will be analyzed to discern the complex relationships that emerge. To understand the atmospheric interactions, the main mechanisms will be compared, indicating their importance and scale of influence.

6.2.2. Simplistic models based on energy or momentum transfer

A) Wind distribution driven by geostrophic wind

In the free atmosphere (at 1 km or higher above the surface level), the geostrophic wind has a low vertical component and the influence of the orography is smaller. At higher levels of the atmosphere, the wind can be considered a 2-D random vector $\vec{U}_{wind, free atmosphere}$ and it can be modelled by a complex normal random variable, which has circular symmetry (all directions are equiprobable) and Rayleigh modulus distribution.

The wind direction changes in the surface layer due to orography and Coriolis forces (Ekman spiral), resulting in some preferred wind directions. However, the modulus of the speed at the atmospheric boundary layer $|\vec{U}_{wind}| = U_{wind}$ can be considered a fraction of the speed at geostrophic layer due to the momentum transfer due to air viscosity. If the proportional factor is fairly constant, then the modulus of the wind speed at geostrophic and boundary layer has the same type of distribution, i.e., a Rayleigh distribution.

Since the previous assumptions are oversimplifications, real wind modulus distribution at atmospheric surface layer is usually represented by a Weibull distribution, which is the generalization with one extra parameter of the Rayleigh distribution. The Rayleigh distribution is a particular case of the Weibull distribution with a shape factor $k = 2$, typical of the wind distribution in mild climates.

B) Turbulence driven by momentum exchanges

Notice that considering the wind a normal process is equivalent to assume that speed deviations in the considered direction are due primarily to random momentum exchanges (neither pressure differences nor energy exchanges).

In laminar regime, friction governs the fluid and then the prevailing process is the momentum exchanges by viscous forces, which are proportional to relative velocity differences in the flow. Laminar regime happens at low wind speeds, stable meteorological conditions and low roughness surfaces. In such regime, flux speed is primarily the outcome of the sum of many momentum exchanges.

The momentum exchanges can be in the same direction than the wind (longitudinal direction) or transversal (vertical or lateral). However, only the stream wise components produce noticeable effective turbulence, as aforementioned.

Since momentum is proportional to wind speed and momentum frictional exchanges are proportional to wind speed curl (a linear operator on spatial speed differences), the central limit indicates that ΔU_{wind} is approximately a Gaussian process if the momentum exchanges due to viscosity are uncorrelated.

C) Turbulence driven by power exchanges or by static pressure changes

In turbulent flux (typical of high wind speeds, gusty wind, unstable conditions or rough surfaces as brave sea and dense vegetation) the viscous forces decreases. In such situations, the fluid can be dominated by power exchanges and energy balance.

Since the mass density of the air near the ground surface is fairly constant and the wind speeds are much smaller than sound speed, then the air flow is fairly incompressible. Given that the viscous forces are small in comparison to inertial forces in the stream, then the viscosity of the flow can be neglected (inviscid flow). Then the energy per unit volume along a streamline is fairly constant provided there is no heat or energy contribution and the Bernoulli equation is applicable to any streamline in an Eulerian reference:

$$p + \frac{1}{2} \rho_{air} |\vec{U}_{wind}|^2 + \rho_{air} g h \approx \text{energy per unit volume} \quad (346)$$

where U_{wind} is the speed measured in an Eulerian reference (i.e., the wind speed measured with an anemometer) and the static pressure is p .

The air density ρ_{air} is almost constant in the atmospheric boundary layer for short lapses. In a fixed reference, the height h and the gravity constant g in the anemometer are constant. However, the height h and the pressure p can change along the streamline and the streamline is not constant along the time.

If there is a power or heat transfer in the flow, the volumetric density of power exchange can be computed deriving the former expression:

$$\begin{aligned} \text{Volumetric density of power exchange} &\approx \\ &\approx \frac{d}{dt} \left[p + \frac{1}{2} \rho_{air} |\vec{U}_{wind}|^2 + \rho_{air} g h \right] = \\ &= \rho_{air} a |\vec{U}_{wind}| + \frac{dp}{dt} + \rho_{air} g \frac{dh}{dt} \end{aligned} \quad (347)$$

where the modulus of the wind acceleration is $a = d|\vec{U}_{wind}|/dt$.

The kinetic energy density is, expressed in the longitudinal, vertical and lateral components (see Fig. 86):

$$\rho_{air} |\vec{U}_{wind}|^2 / 2 = \rho_{air} (U_{long}^2 + U_{vertical}^2 + U_{lateral}^2) / 2 \quad (348)$$

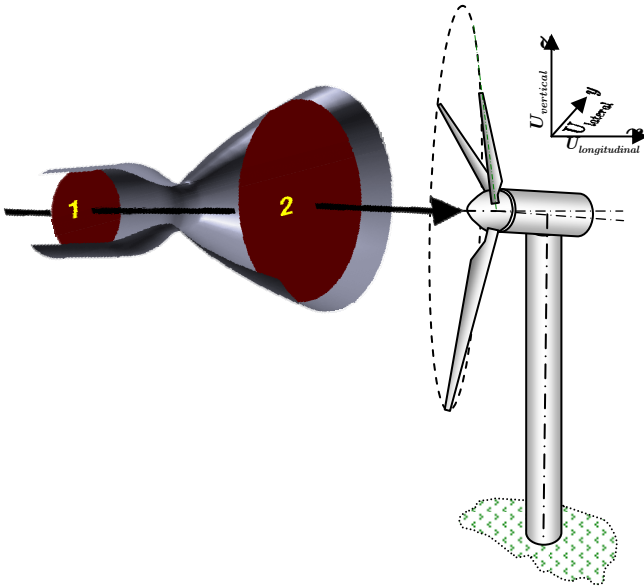


Fig. 86: Control volume laterally limited by stream lines upstream the turbine.

The kinetic energy in terms of the wind components is:

$$\begin{aligned} \Delta(U_{wind}^2) &= U_{wind}^2 - \langle U_{wind}^2 \rangle = U_{long}^2 + U_{vertical}^2 + U_{lateral}^2 - \langle U_{wind}^2 \rangle \\ &\approx U_{long}^2 - \langle U_{long}^2 \rangle + \xi, \end{aligned} \quad (349)$$

where ξ is the random variable $\xi = U_{vertical}^2 + U_{lateral}^2 + \langle U_{long}^2 \rangle - \langle U_{wind}^2 \rangle$.

The kinetic energy density variations are due to potential energy density and local pressure deviations.

- If the squared longitudinal wind component U_{long}^2 and the wind speed modulo $\Delta(U_{wind}^2)$ could be considered the outcome of many uncorrelated contributions, including ξ , then U_{long}^2 and $\Delta(U_{wind}^2)$ could be considered a Gaussian process. In that case, U_{long} would be distributed as a non-central chi random variable. Since $U_{long}^2 \gg \Delta(U_{long}^2)$ and $U_{wind}^2 \gg \Delta(U_{wind}^2)$, the quadratic relationship can be linearized without much error and both U_{long} and U_{wind} would be approximately normal processes.
- However, for small relative changes in velocity, acceleration of the wind could be considered a normal process. Then, the acceleration integral, U_{long} , would be also a normal process.

The slight asymmetry of U_{long}^2 can be explained from energetic arguments. However, the general model of energy transfer is too complex for the purposes pursued in this work it would require a dynamic model of energy transfer and the estimation of parameters usually not available.

D) Turbulence driven by dynamic pressure gradients respect the flow

According to the Taylor's Hypothesis, the total derivative of any conserved field variable is negligible in a Lagrangian framework. If the energy per unit volume is computed in a Lagrangian reference [234] moving at the average stream speed $\langle U_{wind} \rangle$ respect an Eulerian reference, such as Fig. 86, then the energy per unit volume is:

$$\begin{aligned} \text{energy per unit volume} &\approx \\ &\approx p_{(U_{wind})} \pm \frac{1}{2} \rho_{air} (\Delta U_{wind})^2 + \rho_{air} g h \end{aligned} \quad (350)$$

The static pressure in such reference is $p_{(U_{wind})}$. The dynamic pressure is $\pm \frac{1}{2} \rho \Delta U_{wind}^2$, where ΔU_{wind} is the deviation from the average flow speed and \pm is the shortened notation of $Sign(\Delta U_{wind})$. Even though total negative pressure must be always positive, negative dynamic pressures are possible.

If the Bernoulli equation is applied in the Lagrangian reference assuming applicable the Taylor's Hypothesis, the total energy (350) would be fairly constant –neglecting power transfers. In the new reference, the streamlines corresponds to eddies floating in the stream. If the vertical size of the eddies is small, the height influence is negligible. This is equivalent to assuming that the total pressure (the sum of static and dynamic pressure) is fairly constant along the stream lines. Under the Bernoulli assumptions, an increase in the static pressure would imply a decrease in dynamic pressure and vice versa.

The dynamic pressure in the Lagrangian reference moving with mean flow speed is $\pm \rho_{air} (\Delta U_{wind})^2 / 2$, where the signed deviation from the mean speed, squared, is $\pm (\Delta U_{wind})^2 = Sign(U_{wind} - \langle U_{wind} \rangle) (U_{wind} - \langle U_{wind} \rangle)^2$.

The speed deviation from average flow, squared and projected in the longitudinal axis, $\cos(\varphi)(\Delta U_{wind})^2$ is expected to be proportional to the dynamic pressure imbalance streamwise respect the vicinity (i.e., the mean flow) in incompressible air.

If dynamic pressure were the main driving mechanism in turbulence and this pressure were the sum of many random and independent contributions, then $\cos(\varphi)(\Delta U_{wind})^2$ could be approximated by a Gaussian process. In such case, the wind distribution might be interpreted as the signed squared root of a normal process corresponding to the dynamic pressure surplus (plus sign) or deficit (negative sign) respect the vicinity (i.e., the dynamic pressure computed from the flow speed in a Lagrangian reference moving at the mean flow rate).

Fig. 87 shows that if $\cos(\varphi)(\Delta U_{wind})^2$ were normal, then extreme values of ΔU_{wind} would have lower probability, contradicting the measurements. In other words, its probability tails would be lighter than those from a Gaussian distribution (i.e., extreme events would be even more underestimated!). In addition, the distribution would be bimodal, in contradiction with the real measures.

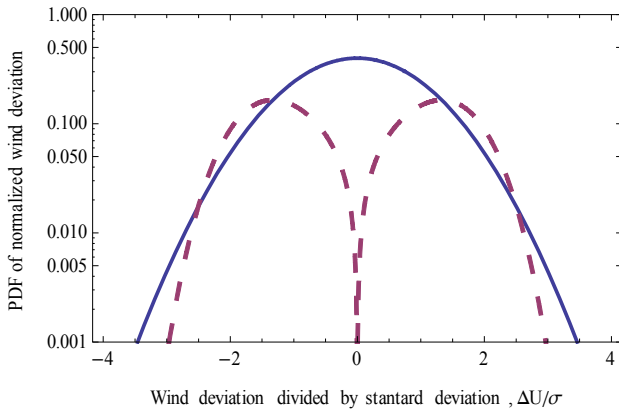


Fig. 87: PDF of a normal random variable X (solid blue line) and the distribution of $\pm X^{1/2}$ where X is normal (dashed purple line). Both distributions have unity variance and zero mean

E) Distribution of ΔU_{wind} assuming $\pm(\Delta U_{wind})^{1/2}$ is normal

If the behaviour of $\pm(\Delta U_{wind})^{1/2}$ were normal, then the extreme deviations of the wind speed ΔU_{wind} would be more probable (see Fig. 88). However, the distribution of ΔU_{wind} would be very leptokurtic, overestimating the probability of extreme events (the actual kurtosis [214] ranges from 0 to 3 but the kurtosis of the rooted model is 8,67). In other words, the actual distribution of ΔU_{wind} is not as sharp at the mode as the rooted model (purple dashed line in Fig. 88) neither as smooth as the normal distribution (blue solid line in Fig. 88).

Therefore, the $\pm(\Delta U_{wind})^{1/2}$ model can represent the extreme wind deviations due to the linearly logarithmic asymptotic tail probability. However, this model does not represent adequately the small wind deviations, more related to the viscosity.

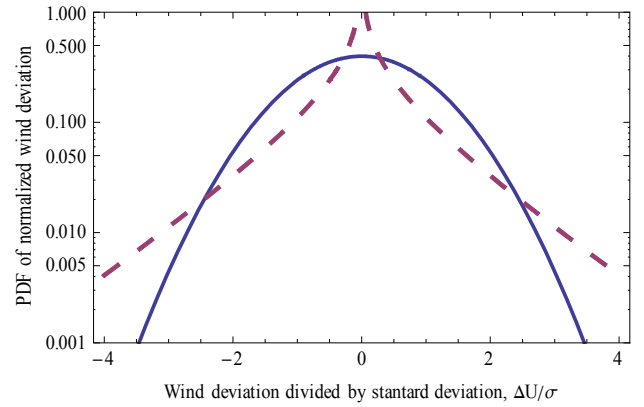


Fig. 88: PDF of a normal random variable X (solid blue line) and the distribution of $\pm X^2$ where X is normal (dashed purple line). Both distributions have unity variance and zero mean.

6.2.3. Constant probability of acceleration direction change

The speed in one direction has a maximum or local minimum whenever the acceleration changes its direction. The multiplicative process in the turbulence leads to a probability of acceleration reversal fairly constant.

Moreover, if the acceleration component in one direction (e.g. longitudinal) has a constant probability of sign change, the velocity (its integral) will have a Laplacian or double exponential distribution. In other words, if the probability of having a maximum or minimum speed is constant, then the resulting distribution of the maxima and minima will be Laplacian.

The small deviations related to small scale turbulence are not so leptokurtic [221]. The wind variations related to greater scales, such as the hourly wind differences usually have bigger kurtosis [228] and its probability is more similar to the Laplacian distribution.

6.2.4. Multiplicative processes in turbulence due to energy cascade

The difference of turbulence velocity is typically modelled as a multiplicative process, which is meant to capture the basic picture of energy cascade in turbulence. The turbulence have a multifractal nature due to the energy transfer involved in the eddies. Experimental studies have shown that the turbulence velocity field in the inertial range can be described reasonably by power law scaling [250].

According to Tabeling [235], flows in the atmosphere and in the ocean develop in thin rotating stratified layers, and it is known that rotation, stratification and confinement are efficient vectors conveying two-dimensionality. In the simplest cases, pure two-dimensional equations must be amended by the addition of an extra-term, characterizing the effect of Coriolis forces, to represent physically relevant situations. This term generates waves which radiate energy, a mechanism absent in pure two-dimensional systems. In more realistic cases, topography, thermodynamics, stratification, must be incorporated in the analysis, and indeed full two-dimensional approximation hardly encompasses the variety of phenomena generated by these additional terms.

Approximation in the form of homogeneous and isotropic turbulence is quite crude for describing many geophysical applications. Usually, there are two reasons why this approximation can be violated. One of them is a rapid daily rotation characterized by a small Rossby number, $Ro \ll 1$. This case is typical for problems of meteorology and physics of the ocean where its influence is principal [236].

The introduction of rotation leads to substantial rearranging of the flow, both in the physical and in the wave spaces. In spite of this, the Coriolis force itself does not produce work. It can redistribute the energy between the scales and lead to inverse cascades, which is known in direct numerical simulations (DNS) as an increase of the kinetic energy on large scales [237] predicted in the renormalization group theory [238]. As a result, the slope of the spectrum of the kinetic energy changes from $-5/3$ to -2 [239, 240]. This change is closely related to the break of the energy transfer over the spectrum [239].

Moreover, the addition of heat transfer leads to the transformation of cellular convection to the cyclonic convection.

6.3. Conclusion on turbulence mechanisms

Experimental studies have shown that the turbulence velocity field in the inertial range can be described reasonably by power law scaling [250] related to multiplicative processes.

The flow rotation increases the kinetic energy on large scales [237] predicted in the renormalization group theory [238]. As a result, the slope of the spectrum of the kinetic energy changes from $-5/3$ to -2 [25, 240].

The atmosphere shows transitions between stable conditions that can last a few days. A normal process does not reflect the non-stationary wind behaviour during long intervals of time [247].

In [241, 242], a model based on superstatistics and the generalized Boltzmann factor is derived, obtaining a q-exponential curve distribution. In [243, 244, 245], a model to fit stable distributions is derived from wind variation data. In [246] extensive measures are performed.

Some authors claim that a normal process scarcely reflects the non-stationary behaviour of the weather during long time spans, which shows transitions between stable meteorological conditions lasting a few days. Gusts also have an intermittent behaviour [247].

In [247], a non-Gaussian wind model based on wind intermittency and continuous random walks has been proposed. This effect is due to weather dynamics and can be treated as a Markov process with state jumps [248]. Alternatively, a simulation method of inhomogeneous, non-stationary and non-Gaussian turbulent winds is presented in [249] based in the coherence.

The exponential behaviour of larger variations is a symptom of multiplicative processes, producing air acceleration direction changes fairly constant.

Thus, a double exponential distribution will be used for the calculus of probability of *extreme events*. This distribution implies a multiplicative mechanism in the turbulence

according to Eggers [250], leading to stable rates of change between accelerations and decelerations of the air.

According to Eggers [250], if wind speed difference ΔU_{long} is computed subtracting the simultaneous measurements at two separate points, its statistical distribution slowly converges to Gaussian for distances greater than the turbulence length scale. Conversely, if wind speed difference is computed subtracting the measurements at two separate instants, its statistical distribution slowly converges to Gaussian for time gaps greater than the turbulence time scale.

The second chapter of this thesis pointed out that the lengths and the times involved in turbulence in the atmospheric boundary layer can exceed 10 km and 250 s, respectively. The length and time scales involved in meteorology dynamics are even greater. Thus, the distribution of ΔU_{long} is more similar to the Laplacian than to the Gaussian in most practical cases.

In the seventh chapter, the Laplacian process will be obtained using a Markov chain approximation to model the multiplicative stochastic dynamics. However, in this chapter the Laplacian process will be approximated through a memory-less transformation of the Gaussian process based on section 3.3 of [214].

The shape of the gusts will be estimated from the point-to-point bijective transformation. Since the transformation is strictly monotone, the estimation of the gust probabilities is straightforward from the properties of the normal processes.

The advantages of working with normal processes and, after all, transforming them into processes with the wind characteristics are:

- You can take advantage of the substantial theoretical properties of the normal processes to deduce properties of the actual process.
- The bijective and strictly monotone transformation from normal to real and vice versa is simple and numerically efficient. The transformation is derived from the probability distribution of ΔU_{long} in any site.
- Larsen, Bierbooms et Al. have studied the average wind gust shapes in various locations in the excellent work [214]. They validated the overall approach of the normal process. However, the normal process are symmetric and the gust usually are slightly asymmetric (the front ramp is steeper than the down ramp). A memory-less transformation of a normal process cannot generate itself an asymmetric process and a filter can be used to mimic the actual behaviour.
- The stochastic properties of the equivalent wind can be obtained with this approach. Instead of using the $PSD_{U_{long}}(f)$ of the actual wind, the $PSD_{U_{eq}}(f)$ of the equivalent wind is employed to derive the characteristic of the equivalent wind gusts.
- The $PSD_{U_{eq}}(f)$ of the equivalent wind is obtained multiplying the $PSD_{U_{long}}(f)$ of the longitudinal component of the conventional wind by the squared modulo of the equivalent spatial filter of the rotor, $|H_1(f)|^2$ (see Chapter 3 for more details).
- Analogously, this approach can be extended for wind farms. The characteristics of the equivalent wind of a farm

can be computed from $PSD_{U_{eq, farm}}(f)$. It is the power spectral density of the equivalent wind, $PSD_{U_{eq}}(f)$, multiplied by the squared modulo of the spatial diversity smoothing filter, $|H_3(f)|^2$, defined at the end of the third chapter.

- Moreover, this approach can be extended to derive the characteristic gusts of the equivalent wind of a geographical area. The power spectral density of the area, $PSD_{U_{eq, area}}(f)$, can be obtained analogously to the wind farm case (see the end of Chapter 3 for more details).

6.4. Memory-less transformation of the Gaussian process

Several techniques have been suggested for simulation of non-Gaussian processes –see e.g. the review [251] or the book [252]. The bijective monotonic transformation has been selected for this work because it is a simple technique for achieving the required distribution of speed variations.

Memoryless processes have the same properties if time is scanned forward or reverse. Therefore, if the rising time of gust is smaller than the decreasing time or if the process shows characteristic shapes or intermittency, a more advanced model should be used. Fortunately, even though the signal from separate turbines shows characteristic shapes, their sum tends to lose those features and they tends to a Gaussian process if the signals are not synchronised (Central Limit Theorem for the sum of independent processes).

A) Static monotone transform

The method used in this work is a memoryless transformation from an auxiliary Gaussian processes $x(t)$ of mean μ and standard deviation σ (blue solid line in Fig. 91) to a double exponential $y(t)$ of the same mean and standard deviation (purple long dashed line in Fig. 91). Imposing that the CDF of the normal is transformed into the CDF of a Laplace distribution (351), the following relation has been obtained:

$$CDF_{y(t)}[y(t)] = CDF_{x(t)}[x(t)] \quad \forall y(t) = f[x(t)] \quad (351)$$

$$y(t) = f[x(t)] =$$

$$= \mu - \text{Sign}[x(t) - \mu] \frac{\sigma}{\sqrt{2}} \text{Ln} \left[1 - \text{Erf} \left(\frac{|x(t) - \mu|}{\sqrt{2}\sigma} \right) \right] \quad (352)$$

where Erf is the error function.

Analogously, the auxiliary Gaussian process $x(t)$ can be obtained from the measured wind speed $y(t)$ applying the reverse transformation of (352):

$$\begin{aligned} x(t) &= f^{-1}[y(t)] = \\ &= \mu + \sqrt{2}\sigma \text{Sign}[y(t) - \mu] \text{InverseErf} \left(1 - e^{-\sqrt{2}|y(t) - \mu|/\sigma} \right) \end{aligned} \quad (353)$$

Larsen proposed in [221] a signed quadratic transformation. The relationship for this transformation is:

$$y(t) = f[x(t)] = \mu + \text{Sign}[x(t) - \mu] \frac{[x(t) - \mu]^2}{\sqrt{3}\sigma} \quad (354)$$

$$x(t) = f^{-1}[y(t)] = \mu + \text{Sign}[y(t) - \mu] \sqrt{\sqrt{3}\sigma |y(t) - \mu|} \quad (355)$$

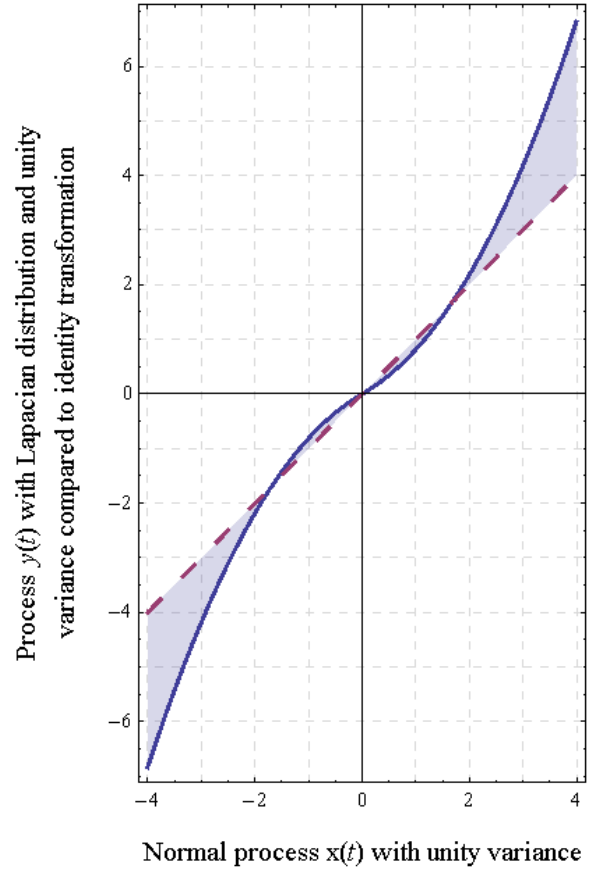


Fig. 89: Graph of the bijective transformation of the auxiliary Gaussian process $x(t)$ into the real process $y(t)$, with Laplacian distribution, compared to the identity transformation.

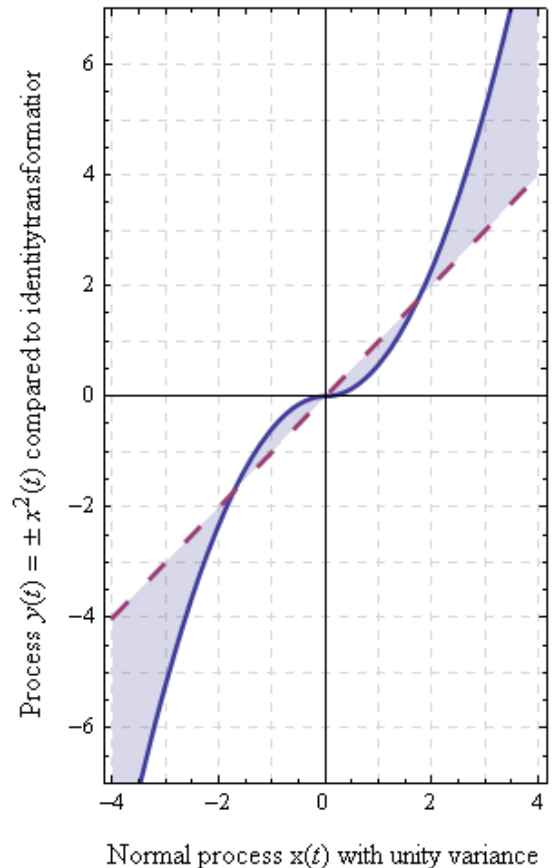


Fig. 90: Graph of the bijective transformation of the auxiliary Gaussian process $x(t)$ into the real process $y(t)$, with signed Chi-Squared distribution, compared to the identity transformation

The probability of deviations smaller than 2σ in absolute value are similar for the auxiliary Gaussian process $x(t)$ and for the real process $y(t)$ in Fig. 90: both processes stay within this limit around 96% of the time. But the differences are remarkable for extreme deviations ($|x(t)| \gg 2\sigma$). The real process $y(t)$ experience bigger probability of extreme deviations.

This method can be applied to obtain any continuous distribution. If wind records measured at greater period than the average duration of wind gusts are available, the experimental distribution of wind variations can be obtained and a transformation can be fitted. The experimental distribution can be approximated to a suitable parametric distribution such as q-exponential, Pearson type IV, stable distribution or Gumbel type I for extreme values.

For example, Fig. 91 shows other transformations of the normal distribution: the square of a normal random variable (brownish dot-dashed line) and the 1,2 power of a normal random variable (green dotted line). Generally, a power law transformation or a type IV Pearson distribution can be used to closely mimic measured distributions.

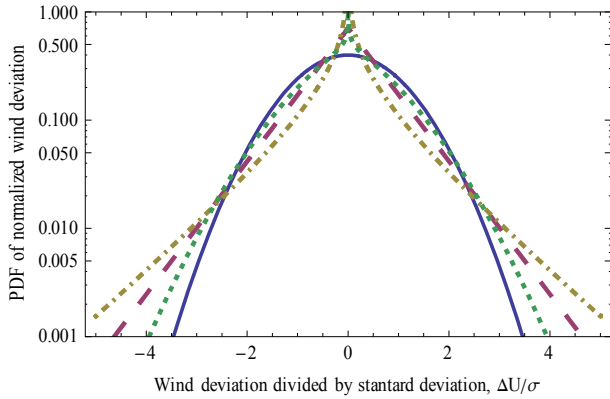


Fig. 91: PDF for different distributions (Normal: solid line; Laplacian: purple long dashed; X^2 distribution where X is a zero mean normal: brownish dot-dashed line; $X^{6/5}$ distribution: green dotted line). All the distributions have been adjusted to unity variance and zero mean.

The original and the transformed process have the same mean and variance (i.e. this is a second-order statistical approach of the real process). Hence, the remarkable properties of normal processes are used to make the problem tractable and finally, the non-linear transformation is applied to achieve a process with the target distribution.

This transformation can be used to infer properties such of occurrence probability of analyzing extreme events from the properties of a Gaussian process.

On the one hand, a normal distribution fit of wind speed represents accurately small deviations, it underestimates rare events. On the other hand, a Laplacian distribution fit of wind speed represents accurately rare events but it underestimates common events.

In general, second order statistics will be used and normality will be assumed unless otherwise stated. For convenience, the *effective wind speed* in this chapter will be treated as a *Gaussian process unless for the study of extreme events and gusts*, where the memory-less transformation to a *double exponential* distribution will be applied. This is a conservative approach which makes the wind variations

tractable and it tends to overestimate slightly rare events. Fig. 92 represents the normalized distribution of the powers of equivalent turbulence using a double exponential model for the effective wind speed.

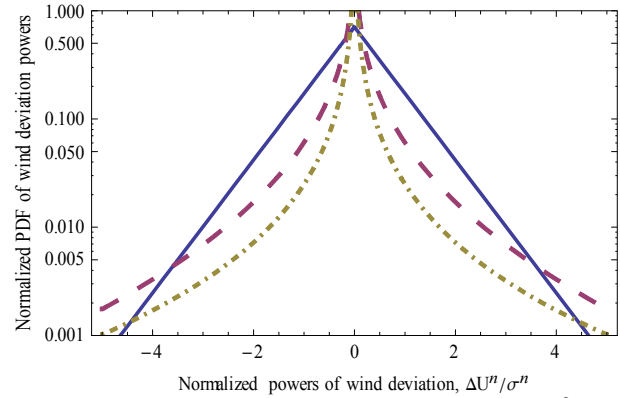


Fig. 92: Normalized PDF of ΔU_{wind} in blue solid line, $\Delta(U_{eq}^2)$ in purple dashed line and $\Delta(U_{eq}^3)$ in brownish dot-dashed line. The distribution of ΔU_{eq} is assumed to be Laplacian (double exponential) and the three PDFs have been scaled to have unity variance.

B) Alternative dynamic models

Other limitation of the memory-less model is that the transformed process cannot reproduce accurately the very slow dynamics of stable weather [253]. These patterns affect wide areas and their influence in power production is highly correlated. Therefore, the transformed process is valid only up to medium horizons. For longer horizons, other approaches as the stochastic differential equations (SDE) are more suitable.

SDE can be approximated by Markov chains [254], and the properties of the process are usually obtained applying matrix algebra. The Markov process is indeed multiplicative and hence, it is suitable for modelling wind fluctuations, that exhibit this behaviour.

In the following chapter, a simplified approach to account slow weather dynamics based on Markov chains will be presented. The Markov chains are strongly connected to exponential distributions and they are a tractable discretization of diffusive stochastic differential equations with jumps [255].

C) Conventions and assumptions in the rest of this chapter

The experimental probability distribution of ΔU_{wind} is primarily Laplacian [221, 223, 224] –a broken line in logarithmic probability scale–. Thus, the bijective transformation (352) and its inverse transformation (353) will be used, unless stated otherwise.

The gusts of the real process $y(t)$ are usually characterized in the time domain. Then, the equivalent parameters of the auxiliary Gaussian process $x(t)$ are obtained from (353) in the time domain. Then, the properties are determined from the power spectral density of $x(t)$, $PSD_x(f)$, that is assumed to be similar to the $PSD_y(f)$ of $y(t)$ (second order statistical approximation).

This approximation is conservative, since it does not underestimate extreme events and the main characteristics of wind variations can be derived.

6.4.2. Maximum speed expected in a register of length T

The maximum wind speed in an interval can be estimated from the theoretical properties of the stochastic processes. The stochastic theory related to local maximums has been extensively developed. The pioneering work of S.O. Rice in [256] initiated a new approach to characterize the extremes of a stochastic process. D.E. Cartwright enhanced the properties of the maximums of normal processes in [257].

The work of G.C. Larsen, W. Bierbooms y K.S. Larsen in [258] is focused in the statistical properties of wind gusts, comparing the analytical results and the measurements in several sites of the database www.winddata.com [259].

A) Case I: the equivalent wind difference ΔU_{eq} has a Gaussian distribution

In this subsection, the equivalent wind $U_{eq}(t)$ will be assumed stationary (the properties of $U_{eq}(t)$ does not vary in time and therefore, the weather evolution will be neglected). It will be also assumed that $U_{eq}(t)$ can be considered a broadband normal process since the spectrum of the wind have a wide range of frequency components.

Under such assumptions, the expected maximum of $\Delta U_{eq}(t)$ in a record of duration T_0 is:

$$\Delta U_{\max, Normal} = \sigma_{U_{eq}} \sqrt{2 \ln \left[\frac{T_0}{2\pi} \frac{\sigma_{dU_{eq}/dt}}{\sigma_{U_{eq}}} \right]} \quad (356)$$

where the standard deviation of the equivalent wind speed, $\sigma_{U_{eq}}$ and the standard deviation of the equivalent air acceleration, $\sigma_{dU_{eq}/dt}$, can be computed from the equation (6) of [63].

In practice, $\sigma_{U_{eq}}$ and $\sigma_{dU_{eq}/dt}$ in (356) must be estimated from records of duration T_0 and where there is not a significant weather change (the standard deviations increase with the interval duration because the variance due to the meteorological dynamics increases for longer durations).

It should be noted also that the equivalent speed (referring to a single turbine rotor or a set of turbines) is filtered respect the wind that would be measured with an anemometer of instantaneous response. Therefore, the more smoothed is the equivalent wind, the smaller is the maximum expected deviation.

Moreover, the instantaneous speed can contain a very brief maximum due to microturbulence. However, this ephemeral maximum correspond to a very small area of the rotor and this maximum does not have greater importance in our study nor could post due to the limitations of the real anemometers (they have a non-negligible inertia and they measure the speed of a certain air volume).

In **Fig. 32**, the cut-off frequency is $f_{cutoff} = 0,0245$ Hz for mean wind speeds $\langle U_{wind} \rangle = 10$ m/s y and integral turbulent length scale $\ell_{U_{wind}} = 1000$ m and rotor radius $R = 50$ m. In **Fig. 39**, the cut-off frequency is $f_{cutoff} \approx \langle U_{wind} \rangle / (6R) \approx 0,033$ Hz for $\beta \approx 0$ and the same $\langle U_{wind} \rangle$ and R . This indicates that faster wind fluctuations than $\tau_{oyt} \approx 1/f_{cut} \sim 40$ s are filtered due to the spatial structure of the turbulence and the size of the rotor.

Experimental measures have shown that the wind turbulence is averaged along the rotor disk area and the actual filter order is $r \sim 2$. The fluctuations of the equivalent wind at $10f_{cutoff}$ are attenuated 20 times respect the instantaneous wind speed measured with an ideal anemometer.

Most meteorological anemometers and data loggers systems have a maximum frequency response $f_{max} \leq 1$ Hz. Thus, the quicker gust that can be considered is half cycle at the maximum frequency, $\tau_{min} \approx (2f_{max})^{-1} > 0,5$ s. In fact, the average gust duration of a turbine with $R = 50$ m and $\langle U_{wind} \rangle = 10$ m/s is many times τ_{min} (see Fig. 93). A synthesized equivalent gust for $R = 50$ m and $\langle U_{wind} \rangle = 10$ m/s is shown in Fig. 93 (thick line) with the average shape (dot-dashed line) along its standard deviation (dashed lines). In average, the gust is inside the dotted range the 68,2 % of time.

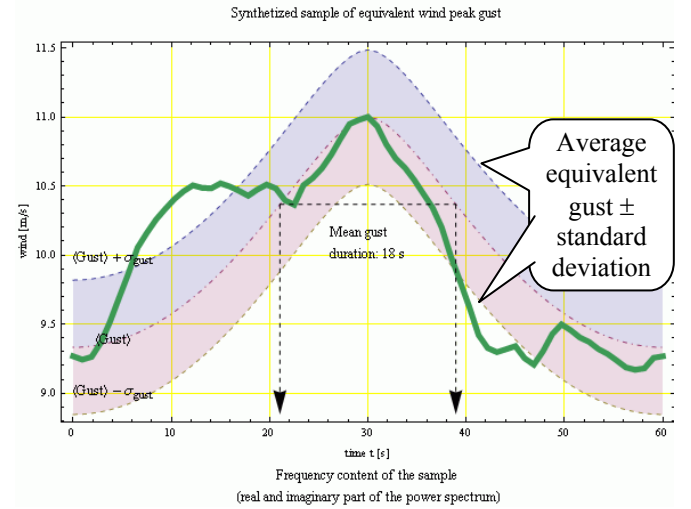


Fig. 93: Equivalent peak gust of $\Delta U_{eq} = 1$ m/s, generated from $PSD_{U_{eq}}(f)$.

Thus, the standard deviation of the equivalent wind speed $\sigma_{U_{eq}}$ and the equivalent air acceleration $\sigma_{dU_{eq}/dt}$ must be estimated considering only the variations in the range from $f_{min} = 1/T_0$ to $f_{max} \approx 0,5/\tau_{min}$.

$$\sigma_{U_{eq}}^2 = \int_{f_{min}}^{f_{max}} PSD_{U_{eq}}^+(f) df \quad (357)$$

$$\sigma_{dU_{eq}/dt}^2 = \int_{f_{min}}^{f_{max}} (2\pi f)^2 PSD_{U_{eq}}^+(f) df \quad (358)$$

If f_{max} is infinite and the estimated $PSD_{U_{eq}}(f)$ does not decrease quicker than f^2 at high frequencies, the integral (358) may not converge, as pointed in [223]. However, the air acceleration is bounded and physically $\sigma_{dU_{eq}/dt}$ is finite due to the air viscosity and compressibility. Since τ_{min} is much smaller than the actual gust duration, the value f_{max} only has a residual effect in (356) to (358).

The expected maximum deviation of the longitudinal wind during a minute, measured with an ideal anemometer, is between 2 and 3 times its standard deviation: $\Delta U_{long, max, T, Normal} / \sigma_{U_{long, T=60s}} \approx 2,1$ y $2,7$. This value has been obtained for the usual wind spectra defined in the first chapter of this thesis.

The equivalent wind speed is smoother and the ratio $\Delta U_{eq, max, Normal} / \sigma_{U_{eq, T=60s}}$ is typically between 1,4 y 1,9 for a multi megawatt turbine.

The formula (356) is fair for the longitudinal wind difference in a point, ΔU_{long} . However, the expression (356) underestimates slightly the equivalent wind difference ΔU_{eq} for periods smaller than one minute because the actual $PSD_{U_{eq}}(f)$ does not correspond to a true broadband process in the frequency range between $f_{min} = 1/60$ Hz and f_{max} (the frequency content is very biased towards the low frequency range).

The probability of staying within a range corresponds to the normal distribution in a Gaussian process (see Fig. 94).

The area shaded in pink corresponds to less than a standard deviation offsets respect the average. A normal process has a swing less than a standard the 68,2 % of the time (probability of the pink region: 34,1 % + 34,1 % = 68,2 %). The process stays within two standard deviations the 95,4 % of time (pink and beige regions: 13,6 % + 34,1 % + 34,1 % + 13,6 % = 95,4 %). The process stays within three standard deviations the 99,7 % of time (pink, beige and green regions).

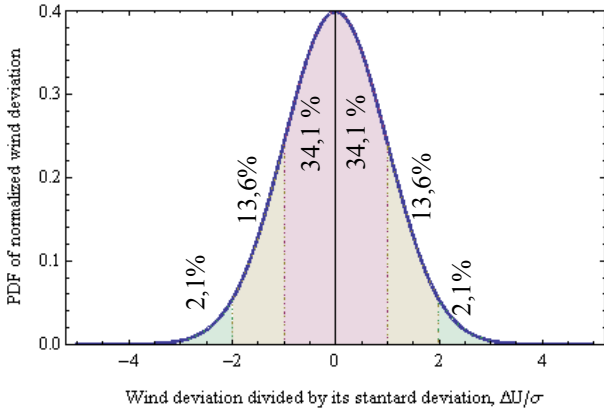


Fig. 94: PDF de la distribución normal.

Finally, it should be noted that normal processes are symmetrical. Hence, the minimum value expected in an interval of duration T_0 is $\Delta U_{min} = -\Delta U_{max}$.

B) Case II: the equivalent wind difference $\Delta U'_{eq}$ has a Laplacian distribution

Since the transformation (352) is monotone rising, the expected value of the Laplacian process can be obtained from (352) and (356), substituting $\mu = 0$ and $\sigma = \sigma_{U_{eq}}$:

$$\Delta U_{max,Laplacian} = -\frac{\sigma_{U_{eq}}}{\sqrt{2}} \text{Ln} \left[1 - \text{Erf} \left(\frac{\Delta U_{max,Normal}}{\sqrt{2} \sigma_{U_{eq}}} \right) \right] \quad (359)$$

$$U'_{eq,Laplacian} = \langle U_{eq} \rangle + \Delta U'_{eq,Laplacian} \quad (360)$$

The maximum equivalent speed deviation expected in a Laplacian process is similar to the Gaussian case since $\Delta U_{max,Normal} / \sigma_{U_{eq}} < 3$ (see Fig. 90). In fact, the expected value computed with (359) is an approximation because the transformation (352) is not linear and the actual distribution of wind must be estimated from real data.

Fig. 95 shows the density of the Laplacian distribution. Compared to a normal with the same variance distribution,

the probability is bigger very near the average and at the tails, $\Delta U_{max} / \sigma_{U_{eq}} > 2$.

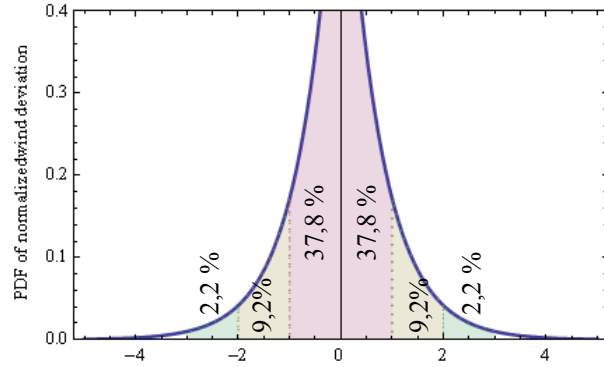


Fig. 95: Normalized PDF of the Laplacian distribution.

It should be noted that the transformation (352) is symmetric. Hence, the minimum value expected in an interval of duration T_0 is $\Delta U_{min} = -\Delta U_{max}$ for the transformed process.

C) Case III: $\pm \Delta U_{eq}^{1/2}$ is a normal process

Provided the signed squared root of the wind speed deviation $\pm \Delta U_{eq}^{1/2}(t)$ is stationary (the stochastic characteristics of $\pm \Delta U_{eq}^{1/2}(t)$ does not vary in the considered interval) and $\pm \Delta U_{eq}^{1/2}(t)$ can be considered a broadband normal process (the wind fluctuations do not present a narrow frequency band of fluctuations), then the maximum value of $\pm \Delta U_{eq}^{1/2}(t)$ expected during an interval of duration T_0 is:

$$\frac{\pm \Delta U_{max,Normal}^{1/2}}{\sigma_{\pm \Delta U_{eq}^{1/2}}} = \sqrt{2 \text{Ln} \left[\frac{T}{2\pi} \frac{\sigma_{d(\pm \Delta U_{eq}^{1/2})/dt}}{\sigma_{\pm \Delta U_{eq}^{1/2}}} \right]} \quad (361)$$

where $\sigma_{\pm \Delta U_{eq}^{1/2}}$ is the standard deviation of the signed squared root of the wind deviation, $\pm \Delta U_{eq}^{1/2}(t)$, and $\sigma_{d(\pm \Delta U_{eq}^{1/2})/dt}$ is the standard deviation of the derivative of $\pm \Delta U_{eq}^{1/2}(t)$.

These standard deviations can be computed analogously to $\sigma_{U_{eq}}$ y $\sigma_{dU_{eq}/dt}$ after generating the process $\pm \Delta U_{eq}^{1/2}(t)$ from real data and estimating its PSD:

$$\sigma_{\pm \Delta U_{eq}^{1/2}}^2 = \int_{f_{min}}^{f_{max}} PSD_{\pm \Delta U_{eq}^{1/2}}^+(f) df \quad (362)$$

$$\sigma_{d(\pm \Delta U_{eq}^{1/2})/dt}^2 = \int_{f_{min}}^{f_{max}} (2\pi f)^2 PSD_{d(\pm \Delta U_{eq}^{1/2})/dt}^+(f) df \quad (363)$$

or dividing the sampled process $\pm \Delta U_{eq}^{1/2}(t)$ in chunks of duration T_0 and using the conventional estimation of the variance of samples in the framework of an ensemble of realizations of a stochastic process.

Finally, the transformation necessary to obtain equivalent wind speed $U''_{eq}(t)$ from $\pm \Delta U_{eq}^{1/2}(t)$ is:

$$U''_{eq}(t) = \langle U_{eq} \rangle + \text{Sign}[\pm \Delta U_{eq}^{1/2}(t)] \frac{[\pm \Delta U_{eq}^{1/2}(t)]^2}{\sqrt{3} \sigma_{\pm \Delta U_{eq}^{1/2}}} \quad (364)$$

where $U''_{eq}(t)$ has been normalized by $\sqrt{3} \sigma_{\pm \Delta U_{eq}^{1/2}}$ to conserve the variance between the processes $\pm \Delta U_{eq}^{1/2}(t)$ and $U''_{eq}(t)$. Therefore, the second order statistical approximations $\sigma_{\pm \Delta U_{eq}^{1/2}} \approx \sigma_{U_{eq}}$ and $\sigma_{d(\pm \Delta U_{eq}^{1/2})/dt} \approx \sigma_{dU_{eq}/dt}$ can be used since the transformation (364) maintains the mean and variance of the equivalent wind.

Fig. 96 shows the density of the square-root-normal distribution. Compared to a normal or a Laplacian with the same variance distribution, the probability is bigger very near the average and at extreme values, $\Delta U_{\max} / \sigma_{U_{eq}} > 3$.

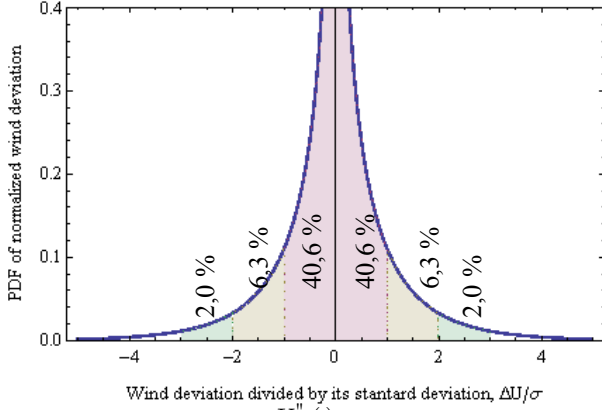


Fig. 96: Normalized PDF of $U_{eq}''(t)$ (square-root-normal distribution).

6.5. Unconditional generation of random samples

6.5.1. Notation of sampled stochastic processes

In the rest of the chapter, the continuous normal process $x(t)$ would be sampled at time $t = 0, \Delta t, 2\Delta t, \dots, (N-1)\Delta t$. In other words, the continuous process $x(t)$ is sampled evenly N times in the interval $t \in [0, (N-1)\Delta t]$ with a time step Δt and a total duration $(N-1)\Delta t$ between the first and the last sample.

For convenience, the following conventions will be used:

- The signal duration is $T_0 = N\Delta t$,
- The conventional frequency resolution is $\Delta f = 1/T_0$,
- The angular frequency resolution is $\Delta\omega = 2\pi\Delta f$
- N is even and $N \geq 4$.
- The notation of the continuous process is $x(t)$.
- The notation of the discrete process is $x[k]$ or x_k at instants $k = 0, 1, \dots, N-1$.
- Vectorial notation will be used to refer a realization of the stochastic process.

The main properties of the Gaussian or normal processes can be found on most basic bibliography on stochastic processes (e.g., chapter 8 of [260], the tutorial [261], the book [262] or chapter 13 of [263]).

The Karhunen-Loève orthogonal decomposition of a normal process is its Fourier transform. The variance of a normal process in a frequency band does not depend on the signal duration T_0 . In fact, the Fourier transform of a discrete normal process is a vector of complex points and distributed normally. The points of the Fourier transform have zero mean and variance proportional to T_0 . Thus, a factor $\sqrt{T_0}$ will be implicitly applied to the Fourier transform, denoted by \mathcal{F} , for obtaining a spectral measure whose properties independent of the duration T_0 of the sample.

The Fourier transform of a continuous stochastic signal $x(t)$ of duration T_0 , divided by $\sqrt{T_0}$, is called spectral density of the stochastic signal and its notation is $\vec{X}_{\sigma,T}(f)$:

$$\begin{aligned}\vec{X}_{\sigma,T}(f) &\equiv \frac{1}{\sqrt{T_0}} \int_0^T x(t) e^{-j2\pi f t} dt = \\ &= \frac{1}{\sqrt{T_0}} \mathcal{F}\{x(t)\} = \frac{1}{\sqrt{T_0}} \vec{X}_{\mathcal{F}}(f)\end{aligned}\quad (365)$$

$\vec{X}_{\sigma,T}(f)$ will be referred as stochastic spectral phasor density or just (stochastic) phasor for short. When the duration T of the sample is not required, the notation of the stochastic spectral density $\vec{X}_{\sigma,T}(f)$ or $\vec{X}_{\sigma,T}[k]$ will be simplified to $\vec{X}(f)$ or to $\vec{X}[k]$. The units of $\vec{X}_{\sigma,T}(f)$ are the ones of $x(t)$ per square root of Hertz (provided time t is measured in seconds).

The stochastic spectral density $\vec{X}_{\sigma,T}(f)$ has been defined in (365) so that its variance is the two-sided power spectral density of the signal, $\langle |\vec{X}_{\sigma,T}(f)|^2 \rangle = PSD_x(f)$. The power spectral density of the signal fully characterizes a normal process and it is independent of the signal duration.

The Discrete Fourier Transform of the sampled process $x[k]$ will be denoted by $DFT_x[k]$. Analogous to the discrete case (365), the $DFT_x[k]$ is scaled to match the phasor $\vec{X}_{\sigma,T}(f = k/T_0)$:

$$DFT_x[k] = \sum_{i=0}^{N-1} x[k] e^{-j\frac{2\pi}{N} k i} \quad (366)$$

$$\begin{aligned}\vec{X}_{\sigma,T}[k] &\equiv \frac{\sqrt{T_0}}{N} \sum_{i=0}^{N-1} x[k] e^{-j\frac{2\pi}{N} k i} = \frac{\sqrt{T_0}}{N} DFT\{x[k]\} = \\ &= \frac{\sqrt{T_0}}{N} DFT_x[k]\end{aligned}\quad (367)$$

$$\begin{aligned}Var[|\vec{X}_{\sigma,T}[k]|] &= \langle |\vec{X}_{\sigma,T}[k]|^2 \rangle = PSD_x(f = k/T_0) = \\ &= \frac{1}{2} PSD_x^+(f = k/T_0) \\ &\quad \forall 1 \leq k \leq N/2\end{aligned}\quad (368)$$

Thus, the discrete Fourier transform of the real vector $x[k]$ of N samples is a vector of $N/2+1$ complex random variables because $DFT_x[k]$ has Hermitian symmetry. The elements 2 to $N/2+1$ of the vector $DFT_x[k]$ are independent random variables with complex normal distributions. The mean of $DFT_x[k]$ is zero and its variance is proportional to the two-sided power spectral density of the signal, $Var[DFT_x[k]] = \langle |DFT_x[k]|^2 \rangle = N^2 T_0^{-1} PSD_x(f = k/T_0)$.

In meteorology, one-sided power density spectrums $PSD_x^+(f)$ are preferred to two-sided spectrums, $PSD_x(f)$. The variance of the Fourier transform, expressed in terms of $PSD_x^+(f)$ is:

$$\begin{aligned}Var[|DFT_x[k]|] &= \left(\frac{\sqrt{T_0}}{N} \right)^{-2} Var[|\vec{X}_{\sigma,T}[k]|] = \\ &= \frac{N^2}{2 T_0} PSD_x^+(f = k/T_0)\end{aligned}\quad (369)$$

$$\begin{aligned}Var[\text{Re}(DFT_x[k])] &= Var[\text{Re}(DFT_x[k])] = \\ &= \frac{1}{2} Var[|DFT_x[k]|] = \frac{N^2}{4 T_0} PSD_x^+(f = k/T_0)\end{aligned}\quad (370)$$

$$\forall 1 \leq k \leq N/2$$

Since the sampled signal $x[k]$ is real vector, then its Fourier transform has Hermitian symmetry:

$$\vec{X}_{\sigma,T}(-f) = \vec{X}_{\sigma,T}^*(f) \quad \forall f \quad (371)$$

The negative frequencies in the discrete Fourier transform correspond to the last $N/2-1$ elements of $DFT_{U_{eq}}[k]$. Thus, the last half elements are the conjugates of the first ones:

$$\begin{aligned} DFT_{U_{eq}}[k] &= \frac{N}{\sqrt{T_0}} \vec{X}_{\sigma,T} \left(f = \frac{N-k}{T_0} \right) = \\ &= \text{Conj} \left(DFT_{U_{eq}}[N-k] \right) \quad \forall N/2 < k < N \end{aligned} \quad (372)$$

The original sequence can be obtained back through the inverse discrete transform:

$$IDFT_{\vec{X}_{\sigma,T}}[k] = \frac{1}{N} \sum_{i=0}^{N-1} \vec{X}_{\sigma,T}[k] e^{j \frac{2\pi}{N} k i} \quad (373)$$

$$\begin{aligned} x[k] &= \frac{N}{\sqrt{T_0}} \frac{1}{N} \sum_{i=0}^{N-1} \vec{X}_{\sigma,T}[k] e^{j \frac{2\pi}{N} k i} = \\ &= \frac{N}{\sqrt{T_0}} IDFT \left\{ \vec{X}_{\sigma,T}[k] \right\} = \frac{N}{\sqrt{T_0}} IDFT_{\vec{X}_{\sigma,T}}[k] \end{aligned} \quad (374)$$

6.5.2. Foundations of the unconstrained generation of random samples

The synthesis of equivalent wind usually consists on the random generation of a signal with a desired mean level and the stochastic spectral density of a site [42, 50, 65, 153, 264]. The simplest method to generate a signal from its spectrum is, probably, the Shinozuka method [265, 266], which generates a random signal with a constant power spectrum.

However, the wind shows a variable power spectrum and the approach used in this chapter will be consistent with the approach of Wim Bierbooms, Gunner Larsen, Poul Sorensen et Al. [46, 153, 177, 75, 81, 88, 89, 103, 214, 215, 217, 220, 223, 224, 249, 264]. A simple introduction to the method is available in [177]. The main features of this method are summarized in this subsection.

The equivalent wind can be synthesized from a random spectrum that satisfies (368). Applying the Karhunen-Loève orthogonal decomposition of a normal process, the sample is generated in the frequency domain, producing $\vec{X}[k]$ randomly $\forall 1 \leq k \leq N/2$. Then, the sample is obtained in the time domain through the inverse discrete Fourier transform of $\vec{X}[k]$.

The phasors of positive frequencies, $\vec{X}[k] \quad \forall 1 \leq k \leq N/2$, are complex random variables independent and normally distributed with zero mean and variance $PSD_x(f=k/T_0)$. Since the real and imaginary part of each point $\vec{X}[k]$ are independent, they can be independently generated as real normal variables. The phasors corresponding to the negative frequencies are obtained through the Hermitian symmetry (372). Although the DC term $\vec{X}[0]$ can be sampled from a Weibull distribution, but $\vec{X}[0]$ is typically a datum because the average wind speed is usually considered a parameter.

This process has been summarized in the block diagram of Fig. 97. Since the spectral variance of the equivalent wind, $PSD_{U_{eq}}(f=k/T_0)$, depends on the wind regime and turbine, a program has been developed for estimating it. The main parameters of the wind and the turbine rotational effects are adjusted in the tab pane shown in Fig. 98.

The spectral generation is not practical for samples with many points (for example, for synthetic series of many hours with high resolution), because it implies computing and storing very long vectors. In that case, the series can be divided into portions, each portion can be generated independently in the frequency domain and they can be gathered in the time domain. Some overlap of the portions and a weighting window is required to produce a smooth joint of the signal portions, analogously to the spectrogram. A weighting with unity squared sum in the overlapped joints produces a series with uniformly distributed variance. Finally, the average wind is added to the signal. This technique only requires storing the adjacent portions and the portion duration should be longer than the slowest significant oscillations in the wind.

A more conventional approach for long samples is to design a filter bank that can be applied to white noise [42, 50] to produce a signal with the target spectral variance $PSD_x(f=k/T_0)$.

A) Estimation of the wind spectra

The wind spectra at one site and at some atmospheric conditions can be estimated from high resolution wind measurements. The standard IEC 61400-1 provides some guidelines for selecting an adequate wind spectrum for structural purposes. In fact, the wind parameters shown in Fig. 98 evolve in time and indeed they can show great dispersion according to atmospheric conditions (e.g. stable, laminar or turbulent boundary layer).

The wind smoothing due to the spatial diversity in the turbine rotor can be adjusted varying the rotor radius R and the turbulence length scale Λ_1 in Fig. 98. The rotor filter is equivalent to a low pass filter with a cut-off frequency computed from the expressions obtained in chapter 3:

- Spatial filter from Sørensen:

$$f_{cut} = \frac{\langle U_{wind} \rangle}{A R} \sqrt{0,9 - 0,0144 \frac{A^2 R^2}{\ell_{U_{wind}}^2}} \quad (375)$$

where $\ell_{U_{wind}} \approx \Lambda_1$ and the decay constant A is between 5 and 12.

- Spatial filter from Wilkie, Leithead and Anderson:

$$f_{cut} = 0,1224 \langle U_{wind} \rangle / R \quad (376)$$

- Spatial filter from the turbulence averaged along the rotor disk area:

$$f_{cut} \lesssim \langle U_{wind} \rangle / (6R) \quad (377)$$

Sørensen, Wilkie, Leithead and Anderson modelled the rotor filter as a first order low pass filter but some actual measurements have suggested that the actual order is closer to a second order in a wind turbine of the megawatt class. In fact, the model of the turbulence averaged along the rotor disk area that the rotor filter order is bigger than 1,5, depending on the wind coherence.

The rotational sampling can be included in the equivalent wind. This option is disabled by default in the program because the effect of the angle of the blades in the torque is represented more precisely with the method described in Annex A. Furthermore, this effect represents an almost cyclostationary feature that feeds mechanical vibrations, in

contrast to the bursts and wind gusts. However, the model can include spatial sampling in the equivalent wind to allow comparisons with other work because some authors have used this method to include the tower shadow and wind shear phenomenon.

B) Unconstrained sample generation module

A module for the generation of unconditional samples of equivalent wind have been integrated in the program EQWIGUST [218]. The average equivalent wind, the duration T_0 and the discretization step Δt can be selected in the tab pane shown in Fig. 99. The average wind speed can be also modified in the module of the spectral features of the equivalent wind, since the spectral variance density is usually considered proportional to the wind speed.

All modules that generate synthetic samples have a control to view a random sample from a set. This control selects different seeds in the random generator used in the random sample. Finally, this module also includes some options to modify the appearance of the graphics.

6.6. Peak type gusts

6.6.1. Gust concept

A gust of wind can be defined as a wind speed deviation out of their usual range of oscillation. The most common measure of the normal fluctuation level in the wind is the turbulence intensity, defined as the ratio of the standard deviation $\sigma_{U_{wind}}$ to the average $\langle U_{wind} \rangle$ of the wind speed. According to the IEC 61400-1 standard, the turbulence intensity usually lies between 12 % and 16 %. This standard also defines the most extreme gust during generating. However, some studies differ in shape and probability of the most extreme gust that can experience the turbine [214, 215, 220].

In this chapter, the gust concept will be extended to the equivalent wind. The turbulence intensity concept will be also extended to the coefficient of variation of the equivalent wind, $\sigma_{U_{eq}}/\langle U_{eq} \rangle$.

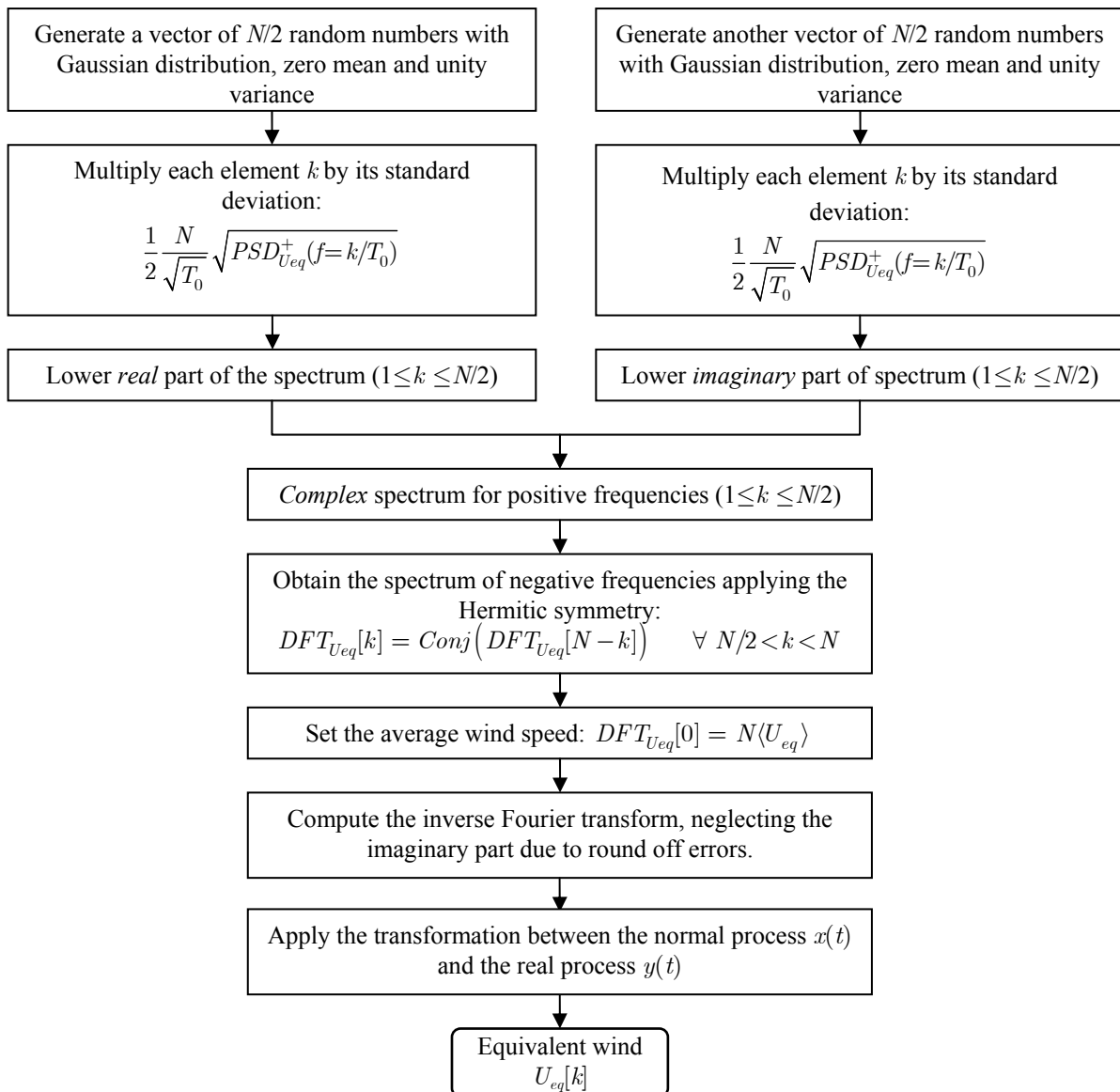


Fig. 97: Flowchart of the generation of unconditioned samples of equivalent wind.

Tipo de espectro del viento: Espectro Von Karman

Viento altura buje U_{∞} :  10

Radio del rotor R :  41

Lon Δ_1
($\Delta_1 = 47$ m según IEC 61400-1)  47

Intensity Turbulence 15 m/s, I_{15} m/s  0.14

$\frac{\sigma^2}{\text{PSD}(f_{\text{blade}})}$ due to spatial sampling:  0.5

Blade frequency ($f_{\text{blade}} = \Omega_{\text{rotor}}/3/60$):  1

Relative bandwidth of rotor oscillations at f_{blade} :  0.05

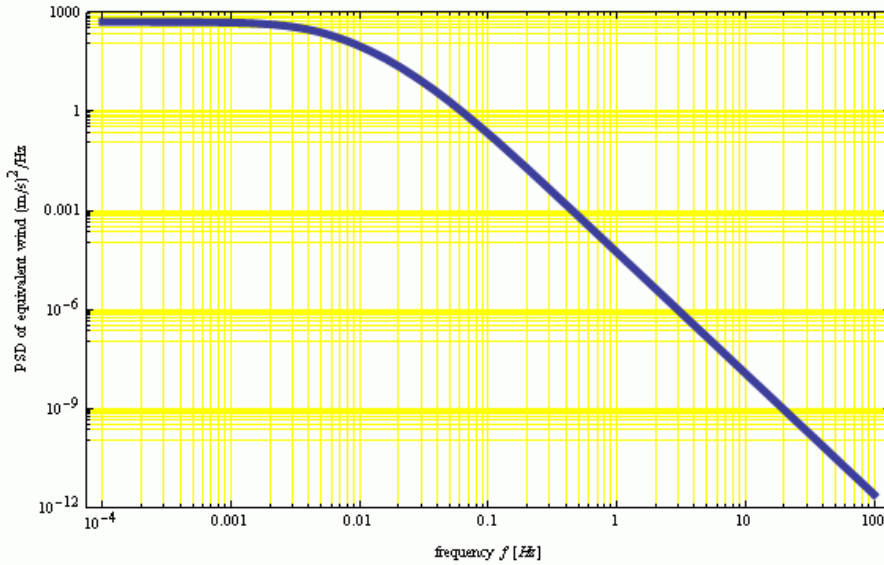
Relative RMS oscillation: $\frac{\text{Typical oscillation amplitude at } f_{\text{blade}}}{\sqrt{2} \text{ wind speed}}$  0.05

Rotor filter (first order low pass filter)

$f_{\text{cut}} = 0.1224 U_{\infty} / R = 0.0298537$ Hz

Spatial sampling
(amplification factor at f_{blade})

Spectral Density of equivalent wind (PSD)



The area beneath the f PSD(f) plot in Log–Lin axis is the variance of the equivalent wind and the height is the relative contribution at each frequency f

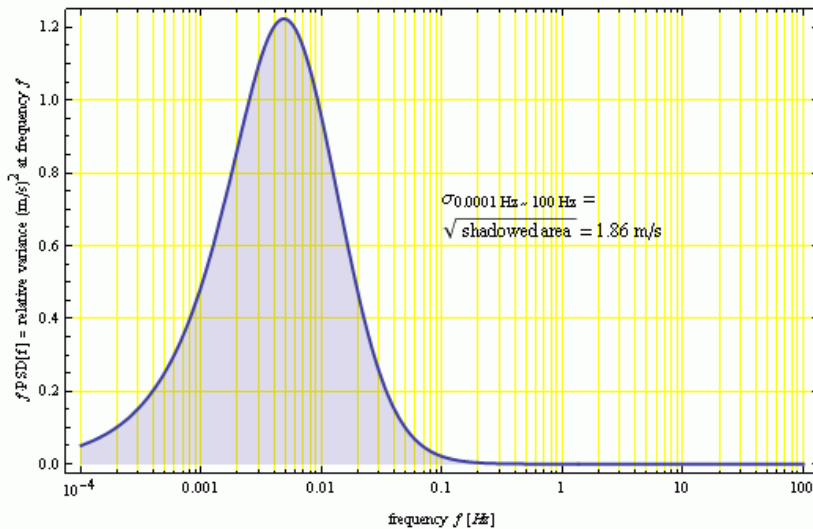


Fig. 98: Module of selection of the equivalent wind spectrum characteristics.

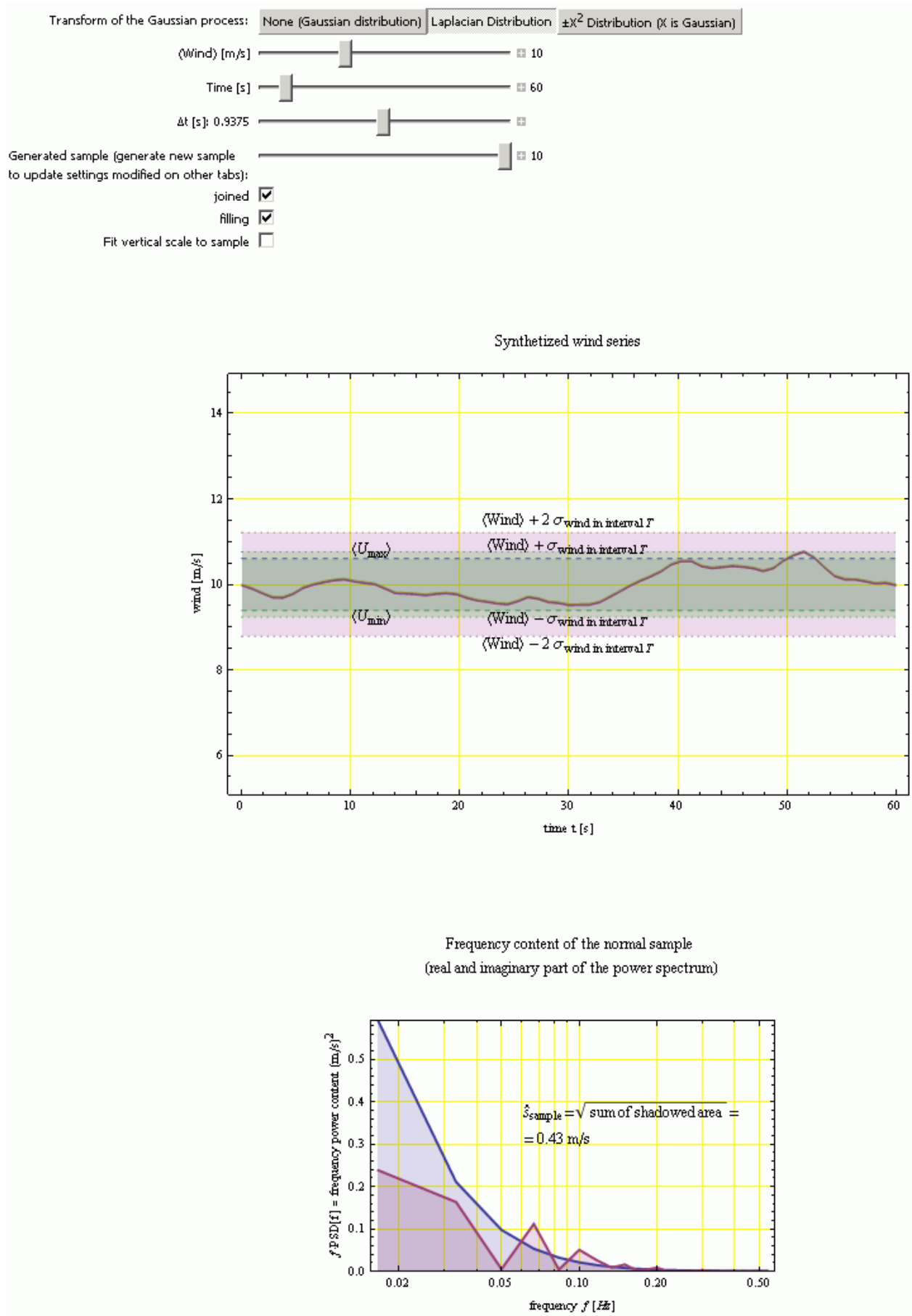


Fig. 99: Module of visualization of unconditioned samples of equivalent wind.

The equivalent wind is closely related to the power output of a turbine, wind farm or region, depending on the viewpoint. Since the power curve is typically an almost monotone function with a non-increasing region and a non-decreasing region, then a peak of the equivalent wind involves another edge of the power output. In the increasing region, a positive extreme in the equivalent wind produces a positive peak of the power output. In the decreasing region, the sign of the extremes are reversed. Therefore, the equivalent gusts produce extremes in the power output.

The gusts are basically characterized by:

- Its amplitude or the deviation from the average wind [225].
- Its shape [214, 215].
- Its characteristic time (its typical duration) [223].
- Its probability or their frequency of occurrence [258]. A similar parameter is the average time between gusts, which may be affected by episodes of gusts bursts.

It should be noted that the value of the turbulence intensity and the power spectral density of the equivalent wind are not sufficient to estimate the likelihood of the less frequent gusts.

In addition to the turbulence intensity and to the power spectral density of the equivalent wind, the distribution of the wind deviation should be also known for assessing the likelihood of the less frequent gusts. In a normal process, wind variations greater than three times the standard deviation, $\Delta U_{\max}/\sigma_U > 3$, happen only 0.3 % of the time. If a process follows a Laplacian distribution, $\Delta U_{\max}/\sigma_U > 3$ happens only 1,6 % of the time (event is 5 times more likely than in the normal case). If the signed squared transformation (364) is applied to a normal process, then $\Delta U_{\max}/\sigma_U > 3$ happens only 2,2 % of the time (event is seven times more likely than the normal case). Apart from the probability distribution of the wind deviation ΔU_{Eq} , the probability of occurring a gust during a period T_0 is influenced by the number of times the wind speed deviation and its acceleration crosses a certain threshold. The theoretical distribution of the extremes in normal processes can be found in [256, 257]. But since the wind behaviour differs from a normal process, the estimated probability of events should be considered with caution.

6.6.2. Assessment of peak type gust

The number of gusts in a time interval can be calculated by measuring:

- The maximums exceeding the threshold U_{th} .
- The number of times that ΔU_{Eq} crosses up the threshold U_{th} .

The movement of air has a "chaotic" behaviour due to the turbulence. The air is continuously accelerating and decelerating all the time (e.g., the sound is the succession of quick accelerations and decelerations of the air molecules). Moreover, the types of used Spectra (Kaimal, Karman, Davenport,...) do not take into account the dissipative processes occurring at high frequencies. This causes the wind signal to display a rough and noisy aspect, and many local maxima are present in the gusts (see Fig. 99 and Fig. 100).

Since the gust characteristic time $\langle \tau \rangle$ can be estimated from the autocorrelation function of the equivalent wind, $ACF_{U_{eq}}$, a

low pass filter can be applied to diminish the likelihood of counting several events during a burst of local maxima or a burst of threshold crossings, without significantly altering the maximum speed in the gust and without hiding short gusts. For very low threshold, two consecutive gusts can happen during one period with only one level crossing (see Fig. 100).

Therefore, a cut-off frequency f_c filter is required to avoiding counting several level crossings or several local maxima in a single gust. This is particularly required for real wind, which has very high frequency content (typically, up to the sound frequencies). The equivalent wind of a farm or a region is quite smooth and filtering high frequencies is less necessary.

Since the gust last an average time $\langle \tau \rangle$, the cut-off frequency f_c can be estimated as $f_c = k/\langle \tau \rangle$, where k is an adjustable parameter. If $k \gg 1$, the number of gusts will be overestimated but the real extent of the gust would be less affected. If $k \lesssim 1$, the number of gusts will be underestimated because quick gusts will be filtered. Thus, the optimum value of k is a small number greater than one.

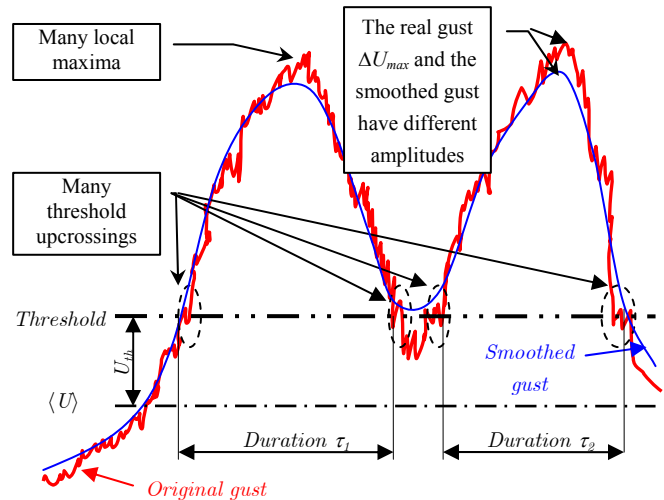


Fig. 100: Difficulties involved in the measurement of gusts.

6.6.3. Mean shape of a peak gust

This subsection deal with the shape of an equivalent gust meeting or exceeding the level ΔU_{\max} in $t=0$ respect the average equivalent wind $\langle U \rangle$ in $t \in [-T_0/2, T_0/2]$. For convenience, the time origin is in the expected gust peak. Since the process and the transformations have been assumed symmetrical, the minima have, theoretically, the analogous properties of a maxima. Thus, only maxima will be considered in this section for the sake of clarity.

The mean shape of the gust can be computed according to Bierbooms [216, 267, 268]. In [216], the gust is defined mathematically as a local extreme ($dU(t=0)/dt = 0$ y $d^2U(t=0)/dt^2 < 0$) with the value $U(t=0) = \langle U \rangle + \Delta U_{\max}$. This is equivalent to the following simultaneous conditions In the frequency domain:

$$U(t=0) = \langle U \rangle + \Delta U_{\max} \Rightarrow \frac{2}{\sqrt{T_0}} \sum_{k=1}^{N/2} \text{Re}(\vec{U}[k]) = \Delta U_{\max} \quad (378)$$

$$\frac{dU}{dt}(t=0) = 0 \Rightarrow \sum_{k=1}^{N/2} 2\pi k \Delta f \text{Im}(\vec{U}[k]) = 0 \quad (379)$$

$$\frac{d^2U}{dt^2}(t=0) < 0 \Rightarrow \sum_{k=1}^{N/2} (2\pi k \Delta f)^2 \operatorname{Re}(\vec{U}[k]) > 0 \quad (380)$$

The mean gust shape and a procedure to generate random gust can be derived from the theory of constrained stochastic simulation.

The air is continuously accelerating and decelerating all the time (e.g., the sound is the succession of quick accelerations and decelerations of the air molecules).

In the one hand, the wind is a wide spectrum process and the air is continuously accelerating and decelerating all the time at microscale level. The wind signal seems is noisy and rough and the wind presents many local maxima or minima in the surroundings of any instant. Thus, the local maximum condition in $t=0$ –equations (378), (379) and (380)– is pointless due to the fractal nature of the wind.

The equivalent wind is low pass filtered with a strength dependent on the corresponding reference (a turbine, a wind farm or a geographical area). In some cases, the equivalent wind may contain enough high frequency components to make useless the local maximum condition.

In fact, the condition $U(t=0) = \langle U \rangle + \Delta U_{\max}$ does neither imply that the global maximum of the interval $t \in [-T_0/2, T_0/2]$ happens at $t=0$ nor the global maximum is $\langle U \rangle + \Delta U_{\max}$. Thus, the gust conditioned on a local maximum at $t=0$ –equations (378), (379) and (380)– would probably have a global maximum a bit higher than ΔU_{\max} and at an instant near $t=0$. The higher is ΔU_{\max} , the global maximum is closer (in average) to $t=0$ and its value is closer (in average) to ΔU_{\max} .

On the other hand, the conditional simulation of the global maximum of the considered interval, $t \in [-T_0/2, T_0/2]$, is very complex due to the difficulties of expressing such condition in the frequency domain. The time instant where the global maximum happens is meaningless, since the sample can be centred at $t=0$ using the periodic extension of the samples.

Taking into account the uncertainties and approximations of the equivalent wind process, the constrained simulation of extreme gust can be obtained imposing $U(t=0) = \langle U \rangle + \Delta U_{\max}$ only. The algorithm used for constrained simulation is similar to the unconstrained simulation (the workflow is shown in Fig. 101). In fact, if only condition $U(t=0) = \langle U \rangle + \Delta U_{\max}$ is imposed, then the imaginary part of the spectrum is computed as in the unconstrained simulation.

However, an intermediate solution easy to implement is that the smoothed process (with an ideal cut-off frequency f_c) had a local maximum at $t=0$ while the original process fulfils $U(t=0) = \langle U \rangle + \Delta U_{\max}$. Thus, the equations (378) and (379) are transformed into:

$$U(t=0) = \langle U \rangle + \Delta U_{\max} \Rightarrow \frac{2}{\sqrt{T_0}} \sum_{k=1}^{N/2} \operatorname{Re}(\vec{U}[k]) = \Delta U_{\max} \quad (381)$$

$$\frac{dU_{\text{smooth}}}{dt}(t=0) = 0 \Rightarrow \frac{2}{\sqrt{T_0}} \sum_{k=1}^{ks} 2\pi k \Delta f \operatorname{Im}(\vec{U}[k]) = 0 \quad (382)$$

where the maximum component considered in the smoothed signal is $ks = \operatorname{Round}(f_c T_0)$. In addition, the inequation (380) –reject local minima and saddle point– can be substituted by

checking that the smoothed process has a maximum at $t=0$ before accepting the generated sample:

$$\text{Reject the sample if } \sum_{k=1}^{ks} (2\pi k \Delta f)^2 \operatorname{Re}(\vec{U}[k]) < 0 \quad (383)$$

because $\frac{d^2U_{\text{smooth}}}{dt^2}(t=0) > 0$.

If (383) fails, there is a saddle point or a local minimum in the smoothed signal and the global maximum is not exactly in $t=0$ and its value is higher than ΔU_{\max} . But even in that case, the global maximum level and its instant can be near ΔU_{\max} and $t=0$, respectively, provided $\Delta U_{\max} > 0$. Thus, the sample could even be accepted if (383) fails depending on the analysis viewpoint. In the program EQWIGUST [218], the rejection test (383) is not applied.

A thorough compilation of the mathematical properties of normal processes near a local maximum can be found in Lindgren [269]. The mean and the variances of the discrete Fourier spectrum can be obtained from the conditions (381) y (382) with the procedure shown in [216].

For convenience, the equations (381) and (382) will be expressed in matrix form using the condition vector $[\mathbf{y}]_{2 \times 1}$, the constant matrix $[\mathbf{G}]_{2 \times N}$ and the vector of real random variables $[\mathbf{x}]_{N \times 1}$ corresponding to the real and imaginary spectrum for positive frequencies. The matrix $[\mathbf{G}]_{2 \times N}$ represents the influence of each random variable (elements of $[\mathbf{x}]_{N \times 1}$) is the target conditions $[\mathbf{y}]_{2 \times 1}$:

$$[\mathbf{y}]_{2 \times 1} = [\mathbf{G}]_{2 \times N} [\mathbf{x}]_{N \times 1} \quad (384)$$

$$[\mathbf{y}]_{2 \times 1} = \begin{bmatrix} U(t=0) \\ \frac{\sqrt{T_0}}{2} \frac{dU_{\text{smooth}}}{dt}(t=0) \end{bmatrix} = \begin{bmatrix} \Delta U_{\max} \\ 0 \end{bmatrix} \quad (385)$$

$$[\mathbf{G}]_{2 \times N} = \frac{2}{\sqrt{T_0}} \cdot \left[\begin{array}{ccc|ccc} 1 & & & 1 & 0 & \dots & 0,0 & \dots & 0 \\ \dots & & & \dots & \dots & \dots & \dots & \dots & \dots \\ 0 & & & 0 & \Delta\omega \dots ks\Delta\omega & 0 & \dots & \dots & 0 \end{array} \right] \quad (386)$$

$$[\mathbf{x}]_{N \times 1} = \left[\operatorname{Re}(\vec{U}[1]) \quad \dots \quad \operatorname{Re}(\vec{U}[N/2]) \quad | \quad \operatorname{Im}(\vec{U}[1]) \quad \dots \quad \operatorname{Im}(\vec{U}[ks]), \operatorname{Im}(\vec{U}[ks+1]) \quad \dots \quad \operatorname{Im}(\vec{U}[N/2]) \right]^{\text{tr}} \quad (387)$$

The angular frequency step $\Delta\omega = 2\pi\Delta f = 2\pi/T_0$ has been used in (386) for notation compactness. The transpose of vectors and matrices is notated with the superscript tr for avoiding confusions with the sample duration, T_0 , or with the time step Δt .

The vector $[\mathbf{x}]_{N \times 1}$ defined in (387) contains first the real and after the imaginary spectrum for positive frequencies, $\vec{U}[k] \quad \forall 1 \leq k \leq N/2$. The mean value of the DC term in the spectrum is $\vec{U}[0] = \langle U \rangle / \sqrt{T_0}$ and it is a parameter of the constrained simulation. The Fourier coefficients $DFT_U[k]$, defined in (366) according to the typical convention in signal processing, has been scaled to obtain the stochastic phasor density, $\vec{U}[k] \equiv N^{-1} \sqrt{T_0} DFT_U[k]$. This density is independent of the sample duration T_0 and the time step Δt .

In a Gaussian process, each discrete spectrum component $\vec{U}[k]$ is a random variable independent of the rest of frequencies. Thus, the covariance between $\vec{U}[k]$ and $\vec{U}[l]$ is zero $\forall l \neq k, 1 \leq k \leq N/2, 1 \leq l \leq N/2$. Moreover, the

distribution of $\vec{U}[k]$ is a complex normal with zero mean. Thus, the real and imaginary parts of $\vec{U}[k]$ are independents and they have a conventional (real) normal distribution.

Therefore, the covariance matrix of the variable array $[\mathbf{x}]_{N \times 1}$ in a unconstrained simulation, notated as $[\mathbf{M}]_{N \times N}$ is a diagonal and non-singular matrix:

$$[\mathbf{M}]_{N \times N} = \text{Diag} \left[\left[\frac{1}{4} PSD_U^+ \left(\frac{1}{T_0} \right), \dots, \frac{1}{4} PSD_U^+ \left(\frac{N/2}{T_0} \right) \right] \right. \\ \left. \left| \frac{1}{4} PSD_U^+ \left(\frac{1}{T_0} \right), \dots, \frac{1}{4} PSD_U^+ \left(\frac{N/2}{T_0} \right) \right] \right] \quad (388)$$

$$[\mathbf{M}]_{N \times N} = \frac{1}{4} \begin{bmatrix} PSD_U^+ \left(\frac{1}{T_0} \right) & 0 \dots & \dots & \dots & \dots & \dots & \dots & 0 \\ 0 & \ddots & & & & & & \vdots \\ \vdots & & PSD_U^+ \left(\frac{N/2}{T_0} \right) & & & & & \vdots \\ \vdots & \dots & \dots & PSD_U^+ \left(\frac{1}{T_0} \right) & & & & \vdots \\ \vdots & & & & \ddots & & & 0 \\ 0 \dots & \dots & \dots & \dots & \dots & \dots & 0 & PSD_U^+ \left(\frac{N/2}{T_0} \right) \end{bmatrix} \quad (389)$$

The average of the random variable vector $[\mathbf{x}]_{N \times 1}$ constrained to a gust of peak value ΔU_{\max} is $[\mathbf{m}_c]_{N \times 1}$ and its value can be derived from the Sherman-Morrison-Woodbury formula, sometimes referred as the matrix inversion lemma [270, 271]:

$$[\mathbf{m}_c]_{N \times 1} = [\mathbf{M}] [\mathbf{G}]^{\text{tr}} [\mathbf{Q}]^{-1} [\mathbf{y}] = \\ = \frac{\Delta U_{\max} \sqrt{T_0}}{2 \sum_{k=1}^{N/2} PSD_U^+ \left(\frac{k}{T_0} \right)} \left[PSD_U^+ \left(\frac{1}{T_0} \right) \dots PSD_U^+ \left(\frac{N/2}{T_0} \right) \mid 0 \dots 0 \right]^{\text{tr}} \quad (390)$$

Where the covariance matrix of the condition vector $[\mathbf{y}]_{N \times 1}$ for unconstrained simulation is notated as $[\mathbf{Q}]_{2 \times 2}$ and its value is:

$$[\mathbf{Q}]_{2 \times 2} = [\mathbf{G}] [\mathbf{M}] [\mathbf{G}]^{\text{tr}} = \\ = \frac{1}{T_0} \begin{bmatrix} \sum_{k=1}^{N/2} PSD_U^+ \left(\frac{k}{T_0} \right) & 0 \\ 0 & \sum_{k=1}^{ks} (k \Delta \omega)^2 PSD_U^+ \left(\frac{k}{T_0} \right) \end{bmatrix} \quad (391)$$

The covariance matrix of the variable vector $[\mathbf{x}]_{N \times 1}$ constrained to a gust of peak value ΔU_{\max} is $[\mathbf{M}_c]_{N \times N}$:

$$[\mathbf{M}_c]_{N \times N} = [\mathbf{M}] - [\mathbf{M}] [\mathbf{G}]^{\text{tr}} [\mathbf{Q}]^{-1} [\mathbf{G}] [\mathbf{M}] \quad (392)$$

The application of the previous formula yields a quasi-diagonal matrix whose diagonal elements are the conditioned variances of a gust of peak value ΔU_{\max} and the elements outside the diagonal are the covariances. The diagonal elements in $[\mathbf{M}_c]_{N \times N}$ are the variances of the spectral components:

$$[\mathbf{M}_c]_{i,i} = \text{Var} \left(\text{Re}(\vec{U}[i]) \right) = \\ = \frac{1}{4} PSD_U^+ \left(\frac{i}{T_0} \right) \left[1 - \frac{PSD_U^+ \left(\frac{i}{T_0} \right)}{\sum_{k=1}^{N/2} PSD_U^+ \left(\frac{k}{T_0} \right)} \right] \quad \forall 1 \leq i \leq N/2 \quad (393)$$

$$[\mathbf{M}_c]_{i,i} = \text{Var} \left(\text{Im}(\vec{U}[i - N/2]) \right) = \\ = \frac{1}{4} PSD_U^+ \left(\frac{i - N/2}{T_0} \right) \left[1 - \frac{\left((i - N/2) \Delta \omega \right)^2 PSD_U^+ \left(\frac{i - N/2}{T_0} \right)}{\sum_{k=1}^{ks} (k \Delta \omega)^2 PSD_U^+ \left(\frac{k}{T_0} \right)} \right] \\ \forall N/2 < i \leq ks + N/2 \quad (394)$$

$$[\mathbf{M}_c]_{i,i} = \text{Var} \left(\text{Im}(\vec{U}[i - N/2]) \right) = \frac{1}{4} PSD_U^+ \left(\frac{i - N/2}{T_0} \right) \\ \forall ks + N/2 < i \leq N \quad (395)$$

The elements outside the diagonal of $[\mathbf{M}_c]_{N \times N}$ are the covariances of the spectral components. The covariances among the real and imaginary parts are null (that is, the real and imaginary parts of the spectrum are statistical independents). However, the real components are negatively correlated at different frequencies (the negative components shows an analogue behaviour). The covariance between the random variables $[\mathbf{x}]_i$ and $[\mathbf{x}]_j$ is notated $[\mathbf{M}_c]_{i,j}$ and its value is:

- Covariance of real coefficients.

$$[\mathbf{M}_c]_{i,j} = \text{Cov} \left(\text{Re}(\vec{U}[i]), \text{Re}(\vec{U}[j]) \right) = - \frac{PSD_U^+ \left(\frac{i}{T_0} \right) PSD_U^+ \left(\frac{j}{T_0} \right)}{4 \sum_{k=1}^{N/2} PSD_U^+ \left(\frac{k}{T_0} \right)} \\ \forall 1 \leq i \leq N/2, 1 \leq j \leq N/2, i \neq j \quad (396)$$

- Covariance of imaginary coefficients.

$$[\mathbf{M}_c]_{i,j} = \text{Cov} \left(\text{Im}(\vec{U}[i - N/2]), \text{Im}(\vec{U}[j - N/2]) \right) = \\ = - \frac{\left(i - N/2 \right) \Delta \omega \left(j - N/2 \right) \Delta \omega PSD_U^+ \left(\frac{i - N/2}{T_0} \right) PSD_U^+ \left(\frac{j - N/2}{T_0} \right)}{4 \sum_{k=1}^{ks} (k \Delta \omega)^2 PSD_U^+ \left(\frac{k}{T_0} \right)} \\ \forall N/2 < i \leq ks, N/2 < j \leq ks, i \neq j \quad (397)$$

- Null covariance between imaginary and real coefficients.

$$[\mathbf{M}_c]_{i,j} = 0 \quad \forall i \neq j \text{ elsewhere} \quad (398)$$

The covariances have small values of the magnitude of $\sigma_{U,T,N}^2/N$, that is, about N times smaller than the diagonal.

The correlation coefficient between \mathbf{x}_i and \mathbf{x}_j is $\rho_{i,j} = \mathbf{M}_{c,i,j} / \sqrt{\mathbf{M}_{c,i,i} \mathbf{M}_{c,j,j}}$. They are quite smaller in absolute value and negative (about $-1/N$ for the real components and about $-1/ks^2$ in the first ks imaginary coefficients). The ratio of the covariance to the variance product of the unconstrained components is:

- Ratio for real coefficients:

$$\frac{[\mathbf{M}_c]_{i,j}}{[\mathbf{M}_c]_{i,i} [\mathbf{M}_c]_{j,j}} \approx \frac{[\mathbf{M}_c]_{i,j}}{[\mathbf{M}]_{i,i} [\mathbf{M}]_{j,j}} = - \frac{4}{\sum_{k=1}^{N/2} PSD_U^+ \left(\frac{k}{T_0} \right)} = \\ = - \frac{4}{T_0 \sigma_{U,T,N}^2} = - \frac{1}{\sum_{k=1}^{N/2} [\mathbf{M}]_{k,k}} \\ \forall 1 \leq i \leq N/2, 1 \leq j \leq N/2, i \neq j \quad (399)$$

- Ratio for imaginary coefficients.

$$\frac{[\mathbf{M}_c]_{i,j}}{[\mathbf{M}_c]_{i,i} [\mathbf{M}_c]_{j,j}} \approx \frac{[\mathbf{M}_c]_{i,j}}{[\mathbf{M}]_{i,i} [\mathbf{M}]_{j,j}} = - \frac{4 \left(i - N/2 \right) \left(j - N/2 \right) \left(\Delta \omega \right)^2}{\sum_{k=1}^{ks} (k \Delta \omega)^2 PSD_U^+ \left(\frac{k}{T_0} \right)} = \\ = - \frac{16 \pi^2 \left(i - N/2 \right) \left(j - N/2 \right)}{T_0^3 \sigma_{dU_{smooth}/dt,T,N}^2} = - \frac{\left(i - N/2 \right) \left(j - N/2 \right)}{\sum_{k=1}^{ks} k^2 [\mathbf{M}]_{k,k}} \\ \forall N/2 < i \leq ks, N/2 < j \leq ks, i \neq j \quad (400)$$

where the variance of the equivalent wind is:

$$\sigma_{U,T,N}^2 = \sum_{k=1}^{N/2} PSD_U^+ \left(\frac{k}{T_0} \right) / T_0 \quad (401)$$

and the variance of the equivalent air acceleration is:

$$\sigma_{dU_{smooth}/dt, T, N}^2 = \sum_{k=1}^{ks} (k\Delta\omega)^2 PSD_U^+(k/T_0) / T_0 \quad (402)$$

A square root of the matrix $\sqrt{[\mathbf{M}'_c]}$ must be computed for generate the random vector $[\mathbf{x}'_c]$ (for more details, see [273] or [274]). The constrained covariance matrix $[\mathbf{M}'_c]_{N \times N}$ is symmetric and positive semidefinite, singular and its square root exist, although they are not unique. Since the conditions (381) and (382) have been imposed, the rank of the constrained covariance matrix $[\mathbf{M}'_c]_{N \times N}$ has diminished from N to $N-2$. Therefore, $[\mathbf{M}'_c]_{N \times N}$ is singular and its square root $\sqrt{[\mathbf{M}'_c]}$ can not be computed using the efficient Cholesky decomposition because $[\mathbf{M}'_c]_{N \times N}$ is non-invertible.

However, the elements with index $i=1$ and $i=1+N/2$ can be eliminated from $[\mathbf{M}'_c]_{N \times N}$ and $[\mathbf{x}'_c]_{N \times 1}$ to obtain a invertible system with a reduced set of random variables, $[\mathbf{M}'_c]_{(N-2) \times (N-2)}$ and $[\mathbf{x}'_c]_{(N-2) \times 1}$. Then, the reduced matrix $[\mathbf{M}'_c]_{(N-2) \times (N-2)}$ is invertible and strictly positive definite and its square root, $\sqrt{[\mathbf{M}'_c]}$, can be computed through the usual Cholesky decomposition.

Thus, the gust spectrum can be generated from the reduced set $[\mathbf{x}'_c]_{(N-2) \times 1}$ through the following matrix expression:

$$[\mathbf{x}'_c] = [\mathbf{m}'_c] + \sqrt{[\mathbf{M}'_c]} [\xi'] \quad (403)$$

where $[\xi']$ is a vector of $N-2$ independent random variables normally distributed of null average and unity variance. Finally, the elements $\mathbf{x}_{i=1}$ and $\mathbf{x}_{i=1+N/2}$, corresponding to the real and imaginary part of the fundamental sample component ($k=1$), can be obtained from the equations (381) and (382).

$$\begin{aligned} U(t=0) &= \langle U \rangle + \Delta U_{\max} \Rightarrow \\ \Rightarrow \text{Re}(\vec{U}[1]) &= \frac{\sqrt{T_0}}{2} \Delta U_{\max} - \sum_{k=2}^{N/2} \text{Re}(\vec{U}[k]) \end{aligned} \quad (404)$$

$$\frac{dU_{smooth}}{dt}(t=0) = 0 \Rightarrow \text{Im}(\vec{U}[1]) = -\sum_{k=2}^{ks} k \text{Im}(\vec{U}[k]) \quad (405)$$

The main computational burden is calculating $\sqrt{[\mathbf{M}'_c]}_{(N-2) \times (N-2)}$ in the formula (403). The generation of samples with a high number of points N requires the Cholesky decomposition of a big matrix. The computational burden can be divided by four if the real and the imaginary

part are generated independently because $[\mathbf{M}'_c]_{(N-2) \times (N-2)}$ is block diagonal.

Conclusions

The turbulence can be considered a stochastic process with a multiplicative behaviour and the probability of a direction change is relatively stable. Thus, the extreme wind deviations relative to the wind average have a statistical distribution more similar to a Laplacian than to a Gaussian. In fact, the real distribution of wind variations depend on the site and the time lag and some authors use families of distributions or a distribution with many parameters to adjust the measured deviation to a model.

The probability and the shape of extreme wind events heavily rely on its dynamics. The average wind shape has been estimated assuming a behaviour similar to a normal process, transformed with a memory-less conversion to obtain a Laplacian distribution of wind deviations.

The constrained generation of gust is a valuable tool to obtain random samples of wind with some features. However, the accuracy of the shape and probability of the gust can be improved. Some measurements show that the front ramp of the gust are, on average, bigger than the tail ramp, but the predicted gust shapes are symmetrical.

The physical concept of wind gust is extended to the equivalent wind of a turbine, a farm or a geographic region. The gusts of equivalent wind produce a change in the power of a turbine, farm or region. The equivalent wind model can be used to estimate structural lifetime, optimize controls or manage the grid.

A simplified model for the generation of long samples of wind is provided. The errors introduced in this simplified model is comparable with the uncertainties of the assumptions made in the wind or in the equivalent wind behaviour.

The program EQWIGUST [218] generate gusts of equivalent wind with some features and estimates their probabilities.

Chapter 7:

Variability of renewable generation in the time domain

7.1. Introduction to Markov Decision Processes

Markov Decision Processes provide optimal policies on a stochastic basis for systems whose evolution depends on its history. Markov Chains of first order only takes into account previous state, but higher order Markov Chains and Hidden Markov Models can be used for more complex history dependence. As an instance, the state of a battery or a water reservoir depends on the charge/discharge history. Network topology, transformers tap changers and voltage boosters depend on previous voltage, previous load and previous generation, whose dynamics can be stochastically characterized.

Markov Chains have been utilized in Power Systems usually as random generators in Monte Carlo Power Flows [275] or in reliability studies to account the availability of devices [276]. A new methodology to compute stochastic power flows is presented based on Markov Chain approximation [277] and fuzzy/probabilistic clustering [278]. It has the following advantages:

— A huge reduction of the number of system states allows to compute systematically all feasible states and all feasible transitions between states. Increasing the number of states reduces the error in the steady-state representation but it also increases quadratically the uncertainty of the dynamics and the computational load.

— Powerful algorithms can be used to accurately represent the interrelationship among random variables such as the load level at the different nodes. The patterns of solar and wind generation due to meteorology [279] are conveniently captured during the classification of measured data. Indeed, the non-linear relationship among variables is embedded in the classification, without requiring regression or linearization analysis

— The uncertainty of load and generation forecasts and the generation failure probability for each pattern can be accounted.

— Many state variables are continuous but these variables are discretized since the system is computed only in a small set of cases with state variables equal to the centroids of patterns. When the state variables do not coincide with a pattern centroid, the fuzzy (probabilistic) clustering process determines the membership level (the probability to belong to each pattern) and the properties of the intermediate cases are estimated using interpolation functions. In plain words, the system characteristics are computed in a reduced set of cases

and they are interpolated elsewhere according to the case similarity in the rest of cases.

— Since the number of states is small, all feasible states and transitions can be computed running regular power flows. Results are manipulated efficiently with matrix (or tensor) algebra to obtain statistics and state transitions.

— Markov processes have remarkable theoretical properties and the dynamics of the system can be formulated as stochastic differential equations. Since data is logged periodically, the analogue continuous-time system is discretized using the framework of Markov Chain approximation [255].

— The optimal control of the non-linear system can be done conveniently through a Markov Decision Process, especially when managing discrete elements such as switches and transformer tap changers (conventional linear time-invariant control theory is not intended for these devices).

Most state variables in Power Systems are continuous. The evolution of continuously and smoothly varying variables is modelled in stochastic theory as a diffusion process and the evolution of discrete variables is modelled as a jump process.

Markov Chains with continuous state space are intricate. Usually, they are discretized to use the efficient matrix algebra and the powerful properties of discrete time and discrete space Markov Chains.

The discretization of continuous system with small discretization steps can induce a lot of states, leading to matrixes of high dimension. Therefore, a discretization methodology is presented in this work where the number of states is optimized. Some guides are given to balance accuracy of the model, data requirements to estimate system parameters and computation burden.

The optimal control of a Markov system can be expressed as a policy, which gives the best decision or action to take for a given state, regardless of the prior history. Once a Markov Decision Process is combined with a policy, this fixes the action of the control for each state and the resulting combination behaves indeed like a Markov chain [280, 281]. Thus, the system is dimensioned for achieving the maximum expected outcome of the controlled system.

7.2. Formulation

7.2.1. Introduction to Markov chains

Time Markov chains are a powerful tool to cope with states and transitions between states in time domain. The probability of maintain the system state (for example, power generated

by uncontrolled renewable sources or consumer load) can be easily computed. The probability of changing to full, null or any level of production or consumption for a given horizon can be also computed very easily. The probability can take into account the forecast of renewable energy resource along its accuracy. Moreover, Markov Decision Processes can be used for optimal stochastic control (for the example, to allocate the spinning reserve needed to compensate for eventual casual bulk decreases of renewable generation or load).

The main disadvantage of Markov chains is the coarse discretization needed to make continuous systems tractable, which mask small fluctuations of the systems (for example, small variations and small cyclic oscillations of generated power). Therefore, spectral and time series approaches are complementary to Markov chains (spectral and time series represents quite well small and periodic variations for short horizons while Markov processes models better the non-linear and the long horizon behaviour of renewable generation)

An introduction to Markov models with many examples and easy to read can be found in the book of S. M. Ross [345]. Other simple books are by B. Nelson [297] and by J. R. Norris [282] (in the later, there is a valuable introduction to measure theory, needed to understand advanced books on stochastic processes). Multivariate and higher order Markov chains can be reviewed in [283]. The book by V. G. Kulkarni [284] includes some chapters for optimal design and optimal control and it has numerical examples to work with a Matlab toolbox and data form the author webpage. A more technical book by V. G. Kulkarni [335] treats also continuous time and continuous state system. Stochastic processes are a fertile field of operational research with abundant literature. However, most books are targeted to mathematicians, requiring a solid background on statistical theory.

The dynamics of a system such as a wind farm or a group of them are characterized through the transition probabilities from state i to state j , $p_{i,j}$. Transition probabilities are arranged in the transition matrix $\mathbf{P} = [p_{i,j}]$, which are estimated from actual data. The probability of staying in the same state the next interval is $p_{i,i}$. The residence time in a state (time during the system is at state i) is distributed exponentially and its characteristic value can be derived from the transition matrix.

If measures are not reliable or the state can not be determined directly from the measures, hidden Markov models can be used. An introductory tutorial can be found in [324]. A summary of multiresolution analysis with Hidden Markov Models can be reviewed in [311]. An advanced text can be found in [285]. In Hidden Markov Processes, the real state is not observable but it can be inferred from observations through Viterbi algorithm and the emission matrix which relates measured parameters and unobservable states. In this work, the complexity of hidden Markov models are avoided since the variables of interest are measured or can be computed from the measures.

7.2.2. Markov chain approximation for continuous systems

A vast number of problems in renewable energy can be formulated as continuous-time, mixed state (continuous and

discrete) stochastic control problems. This section focuses on the so-called Markov chain approximation, which is well-documented [255, 286], simple to understand and implement. Markov chain approximation can be used to efficiently solve many stochastic control problems appearing in renewable energy generation with non-controlled sources.

The basic idea of the Markov chain approximation approach is to discretize the entire control problem. The continuous-time, continuous-state state variables of the original problem are approximated by a discrete-time, discrete-state Markov chain in such a way that the value function corresponding to the Markov chain is a good approximation to the value function of the continuous-time control problem. In order to find the transition probabilities of the Markov chain, one can apply finite difference techniques related to the well-known numerical methods for linear partial differential equations.

The Markov chain approximation method is described in [255]. The algorithms are robust; they are intuitively reasonable and have physical meaning because the approximating Markov chains represent systems similar to the one being approximated. The convergence theory is purely probabilistic, using methods of stochastic control, so that the analytical difficulties are avoided [286].

A continuous stochastic variable $y(t)$ constrained to range $[y_{\min}, y_{\max}]$ can be discretized into m states, similar to the histogram calculation using m bins. To decrease the discretization error, the number of states m can be increased. In this paper, the states are interpolated with a point of view similar to fuzzy Markov Chains [287, 288] to constrain the number of states whilst reducing the classification error. The actual system state and the actual event are compared to the discrete states, estimating their similarity degree to the discrete counterparts. The similarity degrees of actual states to the discrete approximations are interpreted as the probability of classification into discrete states or discrete events [289]. Markov chain approximation shares most properties of conventional Markov chains (except some features such as the estimation of transition probabilities and the sample generation).

Markov chain approximation is based in conventional matrix algebra, instead of using the min-max matrix algebra associated with fuzzy probabilities [290]. Thus, Markov chain approximation has been selected as the optimization tool since it is numerically more efficient than Fuzzy Markov Chains.

If the random variable $y(t)$ is characterized through a first order Markov Chain of m states, the number of parameters to estimate is m^2 (the elements of the transition probability matrix). Estimating a high number of parameters with low uncertainty requires long data series (along with higher computer resources). The system can be discretized with small steps at values where the dynamics are non-linear and coarser at linear zones. In fact, this is a very successful approach already used in finite elements and in mixture distributions.

State interpolation allows reduces the required number of states and consequently, the parameters to be estimated.

The behaviour of the continuous variable $y(t)$ is modelled as the sum of some generalized functions (kernels), providing

a tractable representation of a continuous stochastic variable. After selecting the kernel, only numerical calculus with the discrete parameters are needed, reducing hugely the computational burden and increasing the accuracy of the model.

The statistical measures based on averaging remains unchanged in the discrete and in the interpolated model. Since the system expected cost/benefit is the same if the system states are mutually exclusive (only one state can actually exist at a time) or can be interpreted as a fuzzy states (intermediate states do exist because the continuous system states have been discretized).

The payoff of state interpolation approach is that the probability of non-adjacent states can represent two distinct and mutually exclusive states or the resemblance degree of the actual system to the discrete states. In the later case, the system shows features of the non-adjacent states and it behaves approximately as their interpolation.

The interpretation of the state probability relies on the model derivation and it cannot be deduced from the Markov parameters. But the derivation should be clearly stated in the derivation since it can influence the estimation of the transition matrix and the state change cost.

7.2.3. Time-Averaged vs Instantaneous Values

Most SCADA, data loggers and energy metering devices record average power and other variables in five to fifteen minute intervals. The standard time interval is 10 minutes for power curves and flicker [291, 292] and 15 minutes for reactive power billing [293] (a suitable integrating period for both task is 5 minutes and its integer fractions).

The moving average $y(t)$ can be regarded as the convolution of the instantaneous power of the wind farm $z(t)$ with a square pulse of width Δt (see Fig. 104). Afterwards, the moving average $y(t)$ is sampled $y[k]$ with the same Δt period.

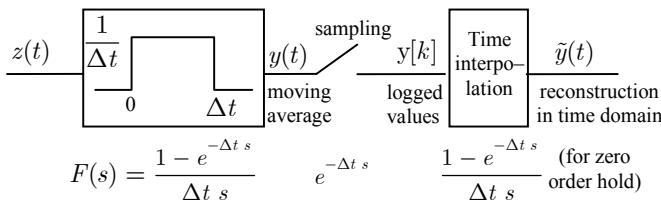


Fig. 103: Model of the data logger of the wind farm.

The continuous transfer function of the average power in an interval Δt is shown in Fig. 104, up to the logging frequency of the power analyzer, $f_{\log} = 1/\Delta t$. For a zero order hold reconstruction kernel, the frequency response $|F(f)|$ due to moving average, sampling and reconstruction is:

$$|F(f)| = \left| \frac{\hat{y}(f)}{z(f)} \right| = \left(\frac{\sin(\pi f \Delta t)}{\pi f \Delta t} \right)^2 \quad (478)$$

The average change rate between two consecutive time intervals $\langle dz(t)/dt \rangle$ can be estimated from recorded data:

$$\left\langle \frac{dz(t)}{dt} \right\rangle \approx \frac{dy(t)}{dt} \approx \frac{\Delta y[k]}{\Delta t} = \frac{y[k] - y[k-1]}{\Delta t} \quad (479)$$

In Fig. 104, the frequency response $|F(f)|$ indicate that the wattmeter behaves as a second order low pass filter of cut-off frequency $f_{cut} = 0.443/\Delta t$, a bit lower than the Nyquist frequency. The wattmeter also introduces an average time lag of $\Delta t/2$ in the measures.

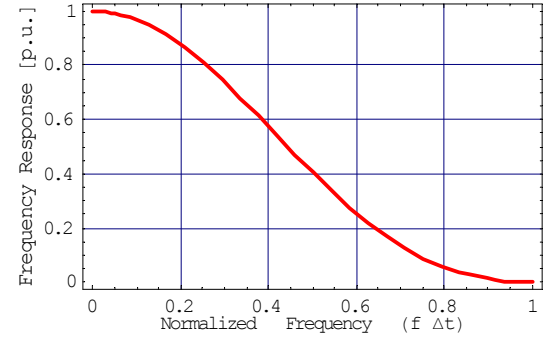


Fig. 104: Plot of frequency response of the network analyzer with a zeroth order reconstruction filter.

7.2.4. Reconstruction of continuous signal from logged values

The stochastic variable $y(t)$ is measured continuously and its average along time interval $[t-\Delta t, t]$ is logged at instant $t = k\Delta t$ as $y[k]$. The time step Δt is usually defined in standards and some usual values in renewable energy are 10 minutes, 15 minutes and 1 hour. The value $y[k]$ usually varies according to its characteristic PSD (Power Spectral Density) or ACF (Auto Correlation Function) along the time step Δt .

In this work, each state of the Discrete Markov Chain corresponds to the average level of a parameter (such as wind, solar or storage power output, load demand, etc.) during Δt time. The continuous value of the parameter can be estimated as the time interpolation of the adjacent discrete states. If the interpolation is lineal, the elementary signal is a triangular pulse of width Δt and height equal to the average value of the parameter, as in Fig. 105.

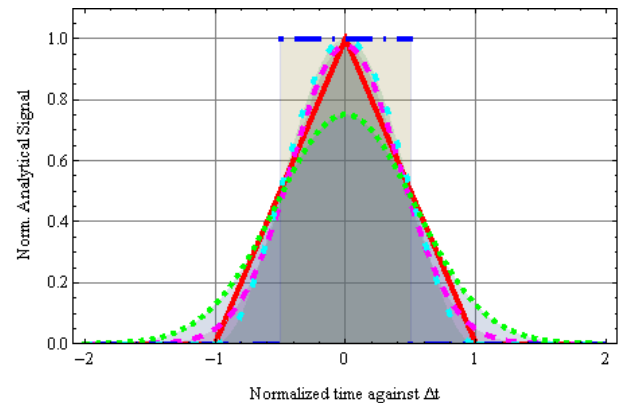


Fig. 105: Rectangular, triangular, Gaussian (minimum ripple and triangular approximation), and cosine kernels corresponding to analytical signals to interpolate discrete-time Markov Chain at $(k-1)\Delta t \leq t \leq (k+1)\Delta t$.

The analytical signals shown in Fig. 105 produce interpolations of zeroth order—the rectangular pulse in blue—, first order—the triangular pulse in red— and some smooth interpolations. The cosine kernel (in light blue in Fig. 105) is

constrained to domain $[-\Delta t, +\Delta t]$, but has the drawback that slope is always horizontal at points $t = k\Delta t$ (see Fig. 108).

Gaussian kernels provide a smooth interpolation and since they are not constrained to $[-\Delta t, +\Delta t]$, the slope at points $t = k\Delta t$ is not required to be horizontal. Gaussian kernel has a Fourier Transform with very low high frequency content and it has also very good statistical properties. The standard deviation used for Gaussian pulses is $\sigma = \Delta t / \sqrt{2\sqrt{\pi}}$ (in light grey in Fig. 105). This value has been obtained minimizing the ripple of the continuous signal when the discrete variable $y[k]$ is constant (i.e. the standard deviation is optimized for minimum ripple of the interpolated signal). Also, the use of Gaussian kernel with standard derivation $\sigma = \Delta t / \sqrt{6}$ (in pink in Fig. 105, the same standard deviation of triangular pulse) has been considered but its use has been superseded since they introduce ripple in the estimation, as can be seen in Fig. 109. Recall that even though Gaussian function formally spreads from $-\infty$ to $+\infty$, it has significant values only in central and adjacent states: $f_{\text{gauss}, k}(t) \approx 0 \quad \forall t \notin [(k-2)\Delta t, (k+2)\Delta t]$ (negligible compared to the uncertainty in the measure of $y[k]$).

$$f_{\square \text{ kernel}}(t) = \begin{cases} 1 & \left| \frac{t}{\Delta t} \right| < 1/2 \\ 0 & \left| \frac{t}{\Delta t} \right| \geq 1/2 \end{cases} \quad (480)$$

$$f_{\Delta \text{ kernel}}(t) = \begin{cases} \left(1 - \left| \frac{t}{\Delta t} \right| \right) & \left| \frac{t}{\Delta t} \right| < 1 \\ 0 & \left| \frac{t}{\Delta t} \right| \geq 1 \end{cases} \quad (481)$$

$$f_{\text{gaussian kernel}}(t) = \sqrt{\frac{3}{\pi}} e^{-3\left(\frac{t}{\Delta t}\right)^2} \quad \sigma = \Delta t / \sqrt{6} \quad (482)$$

$$f_{\text{gaussian kernel}}(t) = \pi^{-1/4} e^{-\sqrt{\pi}\left(\frac{t}{\Delta t}\right)^2} \quad \sigma = \Delta t / \sqrt{2\sqrt{\pi}} \quad (483)$$

$$f_{\text{cosine kernel}}(t) = \begin{cases} \frac{1}{2} \left\{ 1 + \cos \left[\pi \frac{t}{\Delta t} \right] \right\} & \left| \frac{t}{\Delta t} \right| < 1 \\ 0 & \left| \frac{t}{\Delta t} \right| \geq 1 \end{cases} \quad (484)$$

The integral of the kernels is Δt for correct interpolation. If $f_{\text{gauss}, k}(t)$ is constrained to $t \in [-2\Delta t, +2\Delta t]$

$$\text{Kernel Area} = \int_{-\infty}^{+\infty} f_{\text{kernel}}(t) dt = \Delta t \quad (485)$$

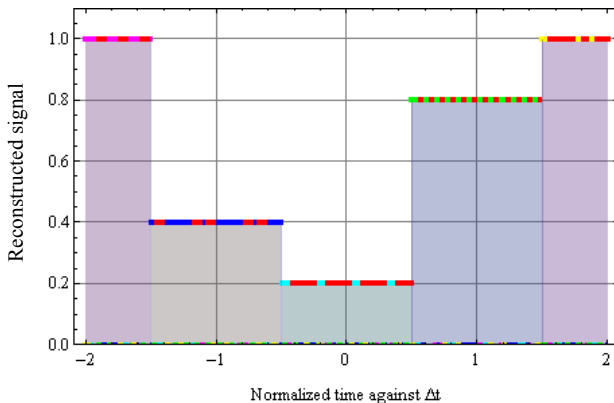


Fig. 106: Estimated continuous signal $\hat{y}(t)$ from sequence $y[k] = \{1, 0.4, 0.2, 0.8, 1\}$ using a rectangular kernel. Rectangular analytical signal is equivalent to order zero interpolation. This model is not realistic since the signals are not continuous.

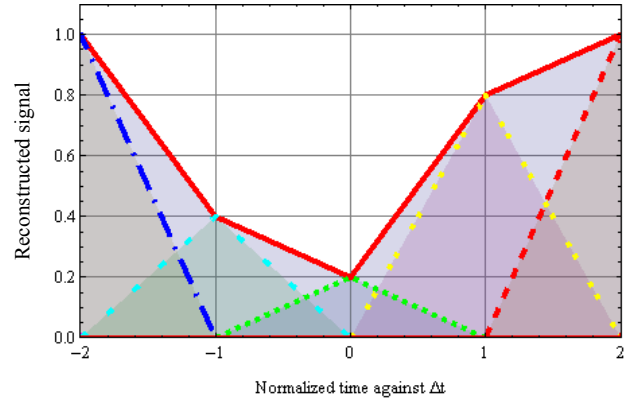


Fig. 107: Estimated continuous signal $\hat{y}(t)$ from sequence $y[k] = \{1, 0.4, 0.2, 0.8, 1\}$ using triangular kernel. Triangular analytical signal is equivalent to order one interpolation.

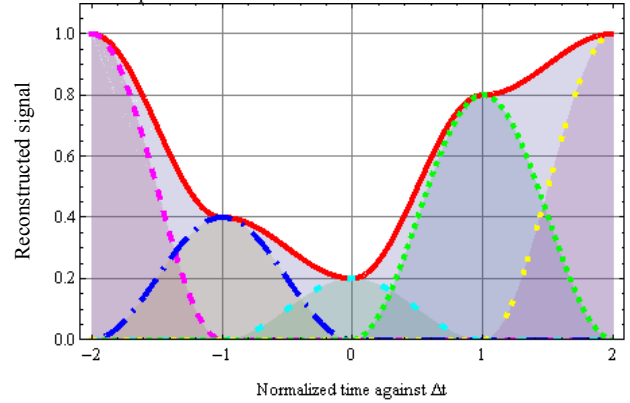


Fig. 108: Estimated continuous signal $\hat{y}(t)$ from sequence $y[k] = \{1, 0.4, 0.2, 0.8, 1\}$ using cosine kernel. The continuous signal is smooth but the interpolation is not suitable due to the flat slope at the sequence points.

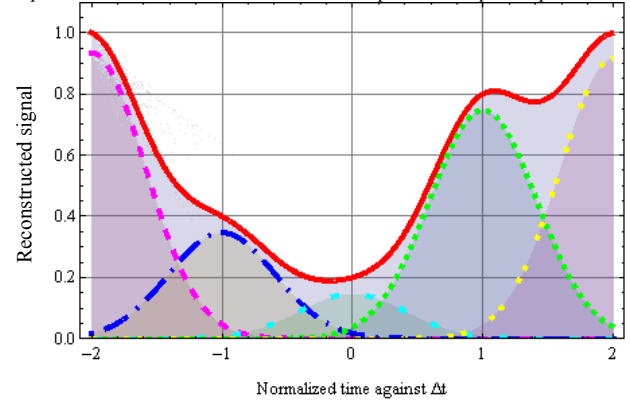


Fig. 109: Estimated continuous signal $\hat{y}(t)$ from sequence $y[k] = \{1, 0.4, 0.2, 0.8, 1\}$ using Gaussian kernel and the same standard deviation as the triangle ($\sigma = \Delta t / \sqrt{6}$). The continuous signal shows an undesirable oscillation at $1 < t < 2$.

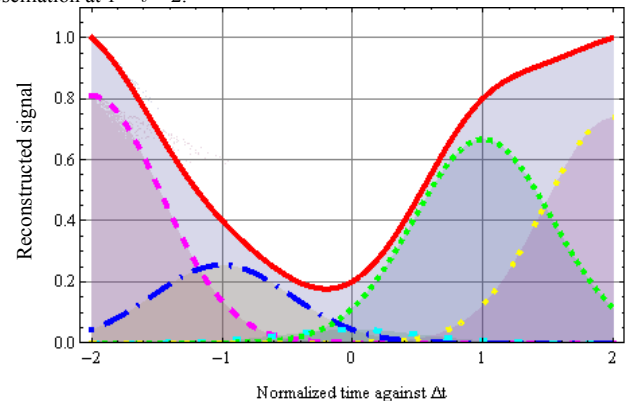


Fig. 110: Estimated continuous signal $\hat{y}(t)$ from sequence $y[k] = \{1, 0.4, 0.2, 0.8, 1\}$ using Gaussian kernel and the standard deviation of minimum ripple ($\sigma = \Delta t / \sqrt{2\sqrt{\pi}}$). This estimation is the smoothest among all analyzed and it does not show induced oscillations.

For most applications, the linear interpolation is precise enough (triangular analytical signal). If a smooth interpolation is required or the interpolated signal must be infinitely derivable, the Gaussian pulse with $\sigma = \Delta t / \sqrt{2\sqrt{\pi}}$ is more suitable. The estimated signal in the continuous time domain is:

$$\hat{y}(t) = \sum_{k=1}^l \tilde{y}[k] f_{\text{pulse}}(t - k\Delta t) \quad (486)$$

where $\tilde{y}[k]$ is the kernel scale factor.

The average lag $\Delta t / 2$ introduced by the logger measures respect to the instantaneous value $z(t)$ can be compensated modifying the former formula:

$$\tilde{z}(t) = \sum_{k=1}^l \tilde{y}[k] f_{\text{pulse}}(t - (k+1/2)\Delta t) \quad (487)$$

The kernel scale factor $\tilde{y}[k]$ are equal to $y[k]$ for signals that vanishes at $t = \pm\Delta t$ (rectangular, triangular and cosine kernels). The multipliers of the Gaussian interpolation can be easily computed from the tridiagonal system with the Thomas algorithm [294] (forward and backward sequential substitution).

$$\begin{bmatrix} a & b & & & \\ b & a & b & & \\ & b & a & b & \\ & & b & a & \ddots \\ & & & \ddots & \ddots & b \\ & & & & b & a \end{bmatrix} \begin{bmatrix} \tilde{y}[1] \\ \tilde{y}[2] \\ \tilde{y}[3] \\ \tilde{y}[4] \\ \vdots \\ \tilde{y}[l] \end{bmatrix} = \begin{bmatrix} y[1] \\ y[2] \\ y[3] \\ y[4] \\ \vdots \\ y[l] \end{bmatrix} \quad (488)$$

where $a = f_{\text{pulse}}(0)$ and $b = f_{\text{pulse}}(\Delta t)$

The continuous Fourier transform of an analytical signal is:

$$\begin{aligned} F_{\text{single pulse}}(w) &= \mathcal{F}\{f_{\text{pulse}}(t)\} = \int_{-\infty}^{\infty} f_{\text{pulse}}(t) e^{-j w t} dt = \\ &= \underset{\text{even symmetry}}{2} \int_0^{t_{\text{max}}} f_{\text{pulse}}(t) \cos(w t) dt \end{aligned} \quad (489)$$

The continuous transforms of the triangular, rectangular and Gaussian shapes are:

$$F_{\square \text{ kernel}}(f) = 2 \int_0^{\tau/2} \cos(2\pi f t) dt = \frac{1}{\pi f} \sin\left(\frac{2\pi f \Delta t}{2}\right) \quad (490)$$

$$\begin{aligned} F_{\Delta \text{ kernel}}(f) &= 2 \int_0^{\Delta t} \left(1 - \frac{t}{\Delta t}\right) \cos(2\pi f t) dt = \\ &= \frac{1 - \cos(2\pi f \Delta t)}{2\pi^2 f^2 \Delta t} \end{aligned} \quad (491)$$

$$\begin{aligned} F_{\text{gaussian}}(f) &= 2 \int_0^{\infty} \pi^{-1/4} e^{-\sqrt{\pi} \left(\frac{t}{\Delta t}\right)^2} \cos(2\pi f t) dt = \\ &= \Delta t e^{-\pi^{3/2} (f \Delta t)^2} \end{aligned} \quad (492)$$

For a non-causal Gaussian reconstruction filter with $\sigma = \Delta t / \sqrt{2\sqrt{\pi}}$ as defined in (486), the frequency response $|F(f)|$ due to moving average, sampling and reconstruction is:

$$|F(f)| = \left| \frac{\hat{y}(f)}{z(f)} \right| = \frac{|\sin(\pi f \Delta t)|}{\pi f \Delta t} e^{-\pi^{3/2} f^2 \Delta t^2} \quad (493)$$

The overall cut frequency for a Gaussian reconstructor is $f_{\text{cut Gauss}} = 0,309 / \Delta t$, as can be seen in Fig. 111. The response above the Nyquist frequency can be thought as introduced by the estimator and it is desirable for the frequency response to be as low as possible for $f > 0,5 / \Delta t$.

Recall that the PSD of $\tilde{z}(t)$ will have notably less high frequency content than the PSD of $z(t)$.

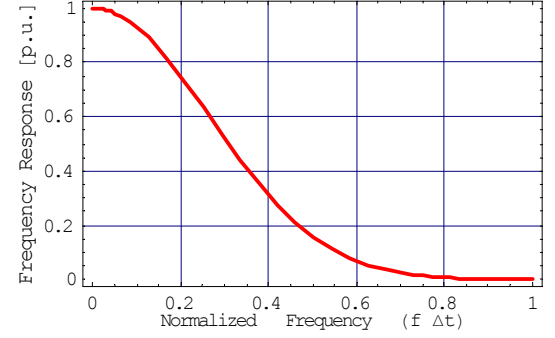


Fig. 111: Plot of frequency response of the network analyzer with a Gaussian reconstruction filter.

The frequency response above Nyquist frequency is notably higher with zeroth-order and first-order reconstruction filter than with the Gaussian filter. The cut-off frequency is a 43% higher, $f_{\text{cut rect}} = 0,443 / \Delta t$ with rectangular pulse reconstruction compared to Gaussian pulse $f_{\text{cut Gauss}} = 0,309 / \Delta t$. This indicates that Gaussian reconstruction Filter is preferably to the zeroth or first order. The first-order filter has better frequency response than zeroth-order but it does have more high frequency content than the Gaussian Filter.

During continuous operation of a wind farm, the operational point is expected not to change appreciably in a time span of minutes and the system behaviour can be considered ergodic during such lapse. Thus, the PSD of $z(t)$ for frequencies above 0.001 Hz can be characterized for each operational condition from measures with a high sampling rate [295]. The PSD for very low frequencies ($f < 0.001$ Hz) can be estimated for long data records but with a low sampling rate. Recall that results must be analyzed prudently at low frequencies since slow meteorological phenomena are not stationary (i.e., the system behaviour is history-dependent and there are analysis methods more accurate).

7.2.5. Considerations on the state discretization

Events have the inherent temporal ordering. Simple systems can be classified according to the value of a single parameter such as the generation level or the primary resource level. If the states correspond to a single numerical feature of the system, such as wind speed, solar radiation, stored energy or power output, the states have a natural order.

In real applications, the state classification depends on many system variables. In a geographical region with various wind farms, the state depends on the vector of wind farm power outputs. The state of a single wind farm can be based on many parameters: wind speed and direction at meteorological mast, power output during last 15 minutes, average power during last hour and last day...

Markov states in complex systems are not necessarily naturally structured. If states represent patterns or combinations of system parameters, the state order is not straightforward (some parameters can increase whereas other decrease, resulting in an arbitrary ordering). In such systems, the optimum interpolation and ordering depends on model purpose of the model and the interpolation weights must be

computed according to some similarity measure regardless of the state numbering.

The task of classification is to take a single observation, extract some useful features describing the observation and, based on these features, to classify the observation into one of a set of discrete classes. A probabilistic classifier gives the probability that the observation corresponds to each class; estimating the probability distribution over all classes. In multivariate systems, the fuzzy or probabilistic clustering algorithm used in the estimation of model parameters can be also used in the classification probability of the samples.

7.2.6. Need for discretization of continuous random variables

There are advances in the analytical solution of continuous state Markov Decision Processes [296], but they are quite intricate and few stochastic models are suitable for being solved analytically. Thus, this work use the more basic approach of Markov chain approximation [255]: the continuous variables are discretized, using kernels (pulse functions with normalized area and amplitude) to approximate the system to a conventional discrete time and discrete state Markov chain (MC). Discrete MC has remarkable theoretical and numerical properties and they are the basis of Markov Decision Processes, an efficient method for optimal stochastic control.

7.3. Piecewise linear interpolation of system properties

7.3.1. Triangular probability distribution of the states from observations (i.e.)

In this subsection, only the discretization of real-valued continuous random variables will be considered. Multivalued systems will not be analyzed since fuzzy or probabilistic clustering algorithms already compute the state probability.

The probability distribution of states and observations $y[k]$ are needed to perform many statistical operations (variance estimation, generation of random samples, solving MDP's, etc).

Any continuous state would be regarded as the mixture of the two adjacent discrete states. The similarity of the sample to the adjacent states would be estimated proportionally to the closeness (this procedure is analogue to the fuzzification of a crisp variable). From the mathematical theory of approximating functions, the state probability can be regarded as interpolating coefficients used to represent piecewise functions.

Most Markov Models consider that only a state is possible at each instant. For example, the Viterbi algorithm computes the most probable state from the observations in HMM.

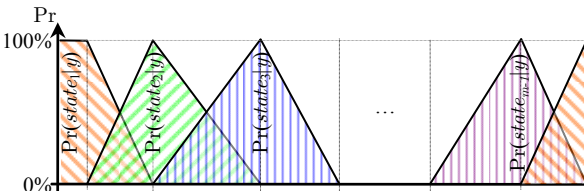


Fig. 112: Conditional probability for the Markov states given the observation y , $\Pr(state_i | y)$.

The similarity of adjacent states state depends on the discretization step and the physical dependence. The conditional probability (analogous to an interpolation function) can be fully constrained to adjacent states, $\Pr(state_i | y) = 0$ if $y \notin [\varphi_{i-1}, \varphi_{i+1}]$. Thus, any points corresponding to the mode φ_i are classified as fully pertaining to the corresponding state i . These objectives are met (see Fig. 112) with triangular distributions (494) with modes φ_i and limits φ_{i-1} and φ_{i+1} (the first and the last distributions are degenerated triangular distributions with $\varphi_0 = -\infty$ and $\varphi_{m+1} = +\infty$, respectively).

$$\Pr(state_i | y) = \begin{cases} \frac{y - \varphi_{i-1}}{\varphi_i - \varphi_{i-1}} & \varphi_{i-1} < y \leq \varphi_i \\ \frac{\varphi_{i+1} - y}{\varphi_{i+1} - \varphi_i} & \varphi_i < y < \varphi_{i+1} \\ 0 & elsewhere \end{cases} \quad (494)$$

Moreover, triangular distributions can be unsymmetrical and the expected value y is simply computed as the dot product of state probability vector $\vec{x}[k]$ by the state centroid vector $\vec{\gamma}$.

Symmetrical distributions such as the Gaussian are not straightforward applicable since discretization step is not even. Since the state ordering is (somewhat) arbitrary in complex systems and states can have very different costs and other properties, it is conservative to use narrow kernels that weight just the adjacent states. Thus, unsymmetrical narrow distributions as the triangular kernel presented in this section are preferred over wider kernels such as the Gaussians.

7.3.2. Distribution of observations from state probabilities

According to the linear discretization used here, the probability density distribution can be computed as a mixture of triangular distributions. The cumulative distribution function can be easily computed from the probability density function.

A) Conditional and marginal probability of observations

The conditional distribution of observation y conditioned to state i is:

$$pdf_{y|s_i}(y | state_i) = \frac{\Pr(state_i | y) \cdot pdf_y(y)}{\Pr(state_i)} \quad (495)$$

or, equivalently: (496)

$$pdf_{y|s_i}(y | state_i) = \begin{cases} \frac{pdf_y(y)}{\Pr(state_i)} \frac{y - \varphi_{i-1}}{\varphi_i - \varphi_{i-1}} & \varphi_{i-1} < y \leq \varphi_i \\ \frac{pdf_y(y)}{\Pr(state_i)} \frac{\varphi_{i+1} - y}{\varphi_{i+1} - \varphi_i} & \varphi_i < y < \varphi_{i+1} \\ 0 & elsewhere \end{cases}$$

The stationary state probability is (494):

$$\Pr(state_i) = \int_{\varphi_{i-1}}^{\varphi_{i+1}} \Pr(state_i | y) pdf(y) dy = \int_{\varphi_{i-1}}^{\varphi_i} \frac{y - \varphi_{i-1}}{\varphi_i - \varphi_{i-1}} pdf_y(y) dy + \int_{\varphi_i}^{\varphi_{i+1}} \frac{\varphi_{i+1} - y}{\varphi_{i+1} - \varphi_i} pdf_y(y) dy \quad (497)$$

If $pdf_y(y)$ is approximately piecewise constant, the integral can be computed approximately by:

$$\Pr(state_i) \approx \int_{\varphi_{i-1}}^{\varphi_i} \frac{y-\varphi_{i-1}}{\varphi_i-\varphi_{i-1}} \frac{cdf_y(\varphi_i) - cdf_y(\varphi_{i-1})}{\varphi_i-\varphi_{i-1}} dy + \int_{\varphi_i}^{\varphi_{i+1}} \frac{\varphi_{i+1}-y}{\varphi_{i+1}-\varphi_i} \frac{cdf_y(\varphi_{i+1}) - cdf_y(\varphi_i)}{\varphi_{i+1}-\varphi_i} dy \quad (498)$$

As a result, the state probability can be approximately computed from the cumulative distribution function:

$$\Pr(state_i) \approx \frac{cdf_y(\varphi_{i+1}) - cdf_y(\varphi_{i-1})}{2} \quad (499)$$

If $pdf_y(y)$ is approximately piecewise constant, the conditional distribution of the observation y conditioned to the state i (496) can be also simplified using the stationary state probability (499)

$$pdf_{y|s_i}(y | state_i) = \begin{cases} \frac{2}{\varphi_{i+1}-\varphi_{i-1}} \frac{y-\varphi_{i-1}}{\varphi_i-\varphi_{i-1}} & \varphi_{i-1} < y \leq \varphi_i \\ \frac{2}{\varphi_{i+1}-\varphi_{i-1}} \frac{\varphi_{i+1}-y}{\varphi_{i+1}-\varphi_i} & \varphi_i < y < \varphi_{i+1} \\ 0 & elsewhere \end{cases} \quad (500)$$

The marginal probability density function of y , $pdf_y(y)$, can be computed as the mixture of distributions of y conditioned to the states:

$$pdf_y(y) = \sum_{i=1}^m \Pr(state_i) pdf(y | state_i) \quad (501)$$

The typical use of this formula is the estimation of $pdf_y(y)$ when the state probability is known at instant k , $\Pr(state_i) = \mathbf{x}_i[k]$:

$$pdf_y(y) = \sum_{i=1}^m \mathbf{x}_i[k] pdf(y | state_i) \quad (502)$$

For the i^{th} region ($\varphi_{i-1} < y < \varphi_i$), (502) is equivalent to:

$$pdf_y(y) = \frac{2\mathbf{x}_{i-1}[k]}{\varphi_i-\varphi_{i-2}} \frac{\varphi_i - y}{\varphi_i-\varphi_{i-1}} + \frac{2\mathbf{x}_i[k]}{\varphi_{i+1}-\varphi_{i-1}} \frac{y - \varphi_{i-1}}{\varphi_i-\varphi_{i-1}} \quad (503)$$

In other words, $pdf_y(y)$ is a piecewise interpolation among points $2\mathbf{x}_i[k]/(\varphi_{i+1}-\varphi_{i-1})$, $1 \leq i \leq m$ (see Fig. 113).

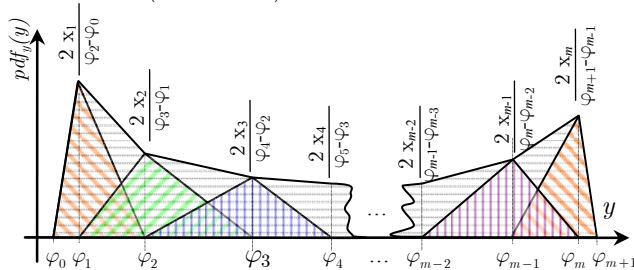


Fig. 113: $pdf_y(y)$ given the state probability, $\Pr(state_i | y)$ from (503).

B) Cumulative marginal probability

The marginal cumulative distribution function of the observation, $cdf_y(y)$, can be computed integrating $pdf_y(y)$ respect y . Since $pdf_y(y)$ is piecewise, the integration is trivial at the modes of the states $y = \varphi_i$:

$$cdf_y(\varphi_i) = \frac{\varphi_1 - \varphi_0}{2} pdf(\varphi_1) + \sum_{j=1}^i (\varphi_j - \varphi_{j-1}) \frac{pdf(\varphi_j) + pdf(\varphi_{j-1})}{2} \quad (504)$$

Thus, $cdf_y(y)$ at $y = \varphi_i$ given the state probability $\mathbf{x}[k]$ is:

$$cdf_y(\varphi_i) = \mathbf{x}_i \frac{\varphi_i - \varphi_{i-1}}{\varphi_{i+1} - \varphi_{i-1}} + \sum_{j=1}^{i-1} \mathbf{x}_j \quad (505)$$

For the i^{th} interval ($\varphi_{i-1} < y < \varphi_i$), the term of partial integration must be added:

$$cdf_y(y) = cdf_y(\varphi_{i-1}) + \frac{(y - \varphi_{i-1})}{2} \left\{ pdf_y(\varphi_{i-1}) \left[1 + \frac{\varphi_i - y}{\varphi_i - \varphi_{i-1}} \right] + pdf_y(\varphi_i) \frac{y - \varphi_{i-1}}{\varphi_i - \varphi_{i-1}} \right\} \quad (506)$$

Thus, the cumulative density function of the observation, $cdf_y(y)$, given the state probability $\mathbf{x}[k]$ can be computed:

- 1) Find the i^{th} interval where the observation is: $\varphi_{i-1} < y \leq \varphi_i$
- 2) With the value i found before, compute:

$$cdf_y(y) = \mathbf{x}_i \frac{y - \varphi_{i-1}}{\varphi_{i+1} - \varphi_{i-1}} - \mathbf{x}_{i-1} \frac{\varphi_i - y}{\varphi_i - \varphi_{i-2}} + \sum_{j=1}^{i-1} \mathbf{x}_j \quad (507)$$

7.3.3. Estimation of state centroids $\vec{\gamma}$

In general, the conditional probabilities $\Pr(state_i | y)$ are not symmetrical with respect to the mode φ_i unless the state discretization is uniform. Moreover, the state range $[\varphi_{i-1}, \varphi_{i+1}]$ can be notably wide or it can contain special features (like the full or null production) that can highlight the mode and centroid difference. Therefore, the centroid of the state γ_i can differ notably from the mode φ_i . Since most criteria to decide optimum action or policy are based on expected values, the state centroid must be computed adequately, as in (508)

$$\gamma_i = \langle y | state_i \rangle = \int_{\varphi_{i-1}}^{\varphi_{i+1}} y \frac{\Pr(state_i | y) pdf(y)}{\Pr(state_i)} dy \quad (508)$$

For the first state:

$$\gamma_1 = \frac{1}{\Pr(state_1)} \left(\int_{-\infty}^{\varphi_1} y pdf(y) dy + \int_{\varphi_1}^{\varphi_2} y \frac{\varphi_2 - y}{\varphi_2 - \varphi_1} pdf(y) dy \right) \quad (509)$$

For the last state:

$$\gamma_m = \frac{1}{\Pr(state_m)} \left(\int_{\varphi_{m-1}}^{\varphi_m} y \frac{\varphi_m - y}{\varphi_m - \varphi_{m-1}} pdf(y) dy + \int_{\varphi_m}^{\infty} y pdf(y) dy \right) \quad (510)$$

For the remaining states with triangular conditional probability ($1 < i < m$):

$$\gamma_i = \int_{\varphi_{i-1}}^{\varphi_i} y \frac{y - \varphi_{i-1}}{\varphi_i - \varphi_{i-1}} \frac{pdf(y)}{\Pr(state_i)} dy + \int_{\varphi_i}^{\varphi_{i+1}} y \frac{\varphi_{i+1} - y}{\varphi_{i+1} - \varphi_i} \frac{pdf(y)}{\Pr(state_i)} dy \quad (511)$$

If $pdf_y(y)$ is approximately piecewise constant, the centroids can be approximately computed as:

$$\gamma_i = \frac{(\varphi_{i-1} + 2\varphi_i) cdf_y(\varphi_{i-1}) + (\varphi_{i+1} - \varphi_{i-1}) cdf_y(\varphi_i) - (\varphi_{i+1} + 2\varphi_i) cdf_y(\varphi_{i+1})}{3 cdf_y(\varphi_{i-1}) - 3 cdf_y(\varphi_{i+1})} \quad (512)$$

The output of fuzzy or probabilistic clustering usually encompass the cluster centroids and includes a summary with the standard deviation of each cluster.

7.3.4. Expected observation from state probabilities

The expected value of the sample can be easily computed from state probabilities according to the next formula: (513)

$$\langle y \rangle = \sum_{i=1}^m \Pr(\text{state}_i) \langle y \mid \text{state}_i \rangle = \sum_{i=1}^m \gamma_i \Pr(\text{state}_i)$$

At the instant k , the expected observed value $y[k] = \langle y(k\Delta t) \rangle$ can be written as a dot product of state probability vector $\bar{\mathbf{x}}[k] = [\mathbf{x}_i[k]]$ and the centroid vector $\bar{\boldsymbol{\gamma}} = [\gamma_i]$:

$$y[k] = \bar{\mathbf{x}}[k] \cdot \bar{\boldsymbol{\gamma}} \quad (514)$$

For example, if state probability vector $\bar{\mathbf{x}}[k]$ is known at instant k , the expected observed value n instants later $\hat{y}[k+m]$ can be computed with the transition probability matrix.

$$\hat{y}[k+m] = \bar{\mathbf{x}}[k+m] \cdot \bar{\boldsymbol{\gamma}} = \bar{\mathbf{x}}^T[k] \mathbf{P}^m \bar{\boldsymbol{\gamma}} \quad (515)$$

7.4. Systems with multiple observations at time k

7.4.1. Estimation of \mathbf{P} from conventional clustering.

$\hat{\mathbf{P}}$ is an estimate of the transition matrix \mathbf{P} . If the output of the classification algorithm for each sample k is just the state number $s[k]$, one can find the transition occurrence F_{ij} in the sequence by counting the number of transitions from state i to state j in one step.

$$\mathbf{F} = \left[\begin{array}{c} \text{matrix of} \\ \text{observed transitions} \end{array} \right] = \begin{bmatrix} F_{11} & \cdots & \cdots & F_{1m} \\ F_{21} & \cdots & \cdots & F_{2m} \\ \vdots & \vdots & \vdots & \vdots \\ F_{m1} & \cdots & \cdots & F_{mm} \end{bmatrix} \quad (516)$$

and $F_i =$ observed occurrences of state $i = \sum_{k=1}^m F_{ki}$ (517)

Then the one-step transition matrix \mathbf{P} can be estimate as follows:

$$\hat{\mathbf{P}} = \text{estimate of } \mathbf{P} = \begin{bmatrix} \hat{p}_{11} & \cdots & \cdots & \hat{p}_{1m} \\ \hat{p}_{21} & \cdots & \cdots & \hat{p}_{2m} \\ \vdots & \vdots & \vdots & \vdots \\ \hat{p}_{m1} & \cdots & \cdots & \hat{p}_{mm} \end{bmatrix} \quad (518)$$

The elements of $\hat{\mathbf{P}} = [\hat{p}_{ij}]$ can be computed according to 6.4.2 in [297]:

$$\hat{p}_{ij} = \frac{\text{observed transitions from state } i \text{ to } j}{\text{occurrences of state } i} = \frac{F_{ij}}{F_i} \quad (519)$$

If state i is not present in the samples ($F_i = 0$), probability transition is undefined. If state is unfeasible, it should be eliminated. But the absence of occurrences can due to the combination of low probability and scarce sample data. In such cases, the more suitable assumption depends on the meaning of the state and the study aim: jump probability equal to stationary probability ($\hat{p}_{ij} \approx \pi_j$), jump to any state equally likely ($\hat{p}_{ij} \approx 1/m$) or absorbing state ($\hat{p}_{ij} \approx 1$ if $i=j$; otherwise 0).

Since states represent typical operational conditions, all states eventually occur in the sample set ($F_i > 0$).

For observed transitions ($F_{ij} > 0$), the standard error of \hat{p}_{ij} is approximately:

$$\hat{s}e = \sqrt{\frac{\hat{p}_{ij}(1 - \hat{p}_{ij})}{F_i}} \quad (520)$$

The unobserved transitions ($F_{ij} = 0$) can be due to real transition unfeasibility or to the limited available data. If $F_{ij} = 0$, the transition probability \hat{p}_{ij} is bound to $[0, 1 - (1 - \beta_{cl})^{1/F_i}]$ with confidence level β_{cl} (F_{ij} is binomially distributed). In part II of this paper, the estimation of rare events will be revised.

7.4.2. Improving state estimation

A further refinement is to quantify the similarity of real data to each cluster. For example, fuzzy classification computes the similarity of each observation with each state and the fuzzy membership degree can be interpreted as the probabilities that the measures corresponds to the states of the Markov model [298]. This approach improves the performance of the Markov Model since samples are often continuous random variables and there is not a definite division or separation between clusters.

There are powerful clustering algorithms where any real observation is classified into a group with an error that can be controlled. Since Markov Chains poses a probabilistic discretization into states and the cluster boundary is blur in wind characterization [299], fuzzy c-means clustering is a suitable clustering algorithm. In fuzzy clustering, each datum has a degree of belonging to clusters, as in fuzzy logic, rather than belonging completely to just one cluster [300]. Thus, data on the boundary of a cluster may be in the cluster to a lesser degree than points near the centroid. For each vector observation $\mathbf{y}[k] = [y_1[k], y_2[k], \dots, y_s[k]]^T$ (for example, the vector of s wind farm outputs at instant k) we have m coefficients $x_i(\mathbf{y}[k])$ giving the degree of membership to the i^{th} cluster ($1 \leq i \leq m$). Usually, the sum of those coefficients is defined to be 1, $\sum_{i=1}^m x_i(\mathbf{y}[k]) = 1$, so that $x_i(\mathbf{y}[k])$ denotes a probability of belonging to i^{th} cluster and $\mathbf{x}[k] = [x_1(\mathbf{y}[k]), x_2(\mathbf{y}[k]), \dots, x_m(\mathbf{y}[k])]^T$ is the probability vector. Since fuzzy classification is unity normalized, some authors call it probabilistic clustering.

If system is significantly influenced by external factors, those features can be included in the classification process although this increases the data requirements. In the example of the group of wind farms, each state can be classified mainly by its power output and secondary, by other parameters such as average wind direction, meteorological stability or wind prediction for a given horizon.

At a given time, the best classification of a big system into a reduced set of states can be challenging. The best procedure for estimating the system state depends of available data and aim of the analysis.

Consider the following example: near cut-off wind speeds, some turbines are stopped whereas others remain at full power. The overall situation will correspond to full generation in a portion and no generation in the rest. That intermediate situation can be represented by the probability of pertaining to full and no generation states (if the number of generating and installed turbines are known, the probability of full generation status can be interpreted as their ratio –frequentist interpretation of probability–). Using the Bayesian interpretation of statistics, the probability of full or no generation is the degree of belief that the real situation corresponds to each state. Using the interpretation of fuzzy logic, the possibility of each state is the membership grade to

a fuzzy set. From the mathematical theory of approximating functions, the state probability can be regarded as interpolating coefficients used to represent piecewise functions such as expected values and voltage or power flow profiles at some nodes.

The clusters implicitly model the relationship among random variables whereas its probability is computed from occurrence frequency of real data. If individual observations $y_i[k]$ at instant k show patterns, the number of clusters m to obtain a low classification error is proportional to s , the number of individual observations $y_i[k]$. If individual observations are statistically independent m is proportional to s^2 . Note that if observations can be classified in independent groups statistically independent, system can modelled more efficiently if it is spited into groups (for example, consumer load and wind power is very weakly related).

7.4.3. Estimation of \mathbf{P} from fuzzy clustering.

The instantaneous output can vary inside the time interval and the output of the classification process, based on averaged observations, is stochastic. If the classification of two consecutive observations is the same, the system would be regarded as “continuing” in the same state (although the actual process is more complex).

On one level, the average power at an interval can be near the classification boundary of two states and the instantaneous state could be considered as a partially corresponding to adjacent states. On another level, if the states are very similar, a fuzzy classification is required to avoid overestimating transitions due to sharp cluster boundaries. In [301, 302], conventional discretization could be the reason of the mismatch of some higher order models.

If the wind power is observed at a single location, the classification of states according can be done according to (494) and Fig. 112. But when wind power is measured at several locations or the state includes not only present observation but also average value during last 24 h, a fuzzy or probabilistic clustering algorithm is required to classify observations with similar characteristics with a minimum classification error. Additionally, The fuzzy clustering algorithm computes a similarity measure of an observation to each state or class (in fuzzy jargon, the level of state membership and in statistical jargon, the state probability). The probability of state i given the observation, $\Pr(\text{state}_i | x_i[k])$, is $x_i(\mathbf{y}[k]) = x_i[k]$.

The output of the classification algorithm is normalized, therefore:

$$\sum_{i=1}^m x_i[k] = 1 \quad (521)$$

where m is the number of states in the system. Since the membership degree totals unity, fuzzy classification is sometimes referred as probabilistic classification.

In either case, the state estimation $\mathbf{x}[k] = [x_1(\mathbf{y}[k]), x_2(\mathbf{y}[k]), \dots, x_m(\mathbf{y}[k])]$ from observation $\mathbf{y}[k]$ is equivalent to the Bayesian interpretation of probability of the occurrence of state i in observation $\mathbf{y}[k]$.

The probability of having observed a transition from state i to j at instant k is $a_{ij}[k]$, i.e. $\Pr(i \rightarrow j)$. The probability of

having observed a permanence in state i at instant k is $a_{ii}[k]$, i.e. $\Pr(i \rightarrow i)$. The estimation of transitions from state i to j is not unique. In this work, $\hat{\mathbf{P}}$ will be estimated to minimize state transitions as follows:

1) First, estimate the probability of continuing in the same state at instant k , $\Pr(i \rightarrow i)$.

$$a_{ii}[k] = \min(x_i[k], x_i[k+1]) \quad \forall 1 \leq i \leq m \quad (522)$$

2) Then, the probability of jumping to a different state at instant k is estimated as the ratio of state probability variation in contiguous instants to the probability of not continuing in the previous state:

$$a_{ij}[k] = \Pr(i \rightarrow j | i \neq j) \approx \frac{\Pr((j \neq j) \cap (i \neq i))}{\sum_{i=1}^m \Pr(i \neq i)} \quad (523)$$

Assuming that the permanence in states i and j are independent for $i \neq j$, (523) transforms into:

$$a_{ij}[k] \approx \frac{\Pr(j \neq j) \Pr(i \neq i)}{\sum_{i=1}^m \Pr(i \neq i)} \quad (524)$$

Interpreting the probabilities of not continuing in states i and j , (524) transforms into the following expression:

$$a_{ij}[k] = \begin{cases} 0 & \text{if } x_i[k] \leq x_i[k+1] \\ \text{else} & \frac{(x_j[k+1] - a_{jj}[k])(x_i[k] - a_{ii}[k])}{1 - \sum_{i=1}^m a_{ii}[k]} \end{cases} \quad (525)$$

$\forall i \neq j \wedge \forall 1 \leq i \leq m \wedge \forall 1 \leq j \leq m$

3) Finally, estimate $\hat{\mathbf{P}} = [\hat{p}_{ij}]$ from observations:

$$F_{ij} = \sum_{k=1}^{l-1} a_{ij}[k]; \quad F_i = \sum_{k=1}^m F_{ki}; \quad \hat{p}_{ij} = \frac{F_{ij}}{F_i} \quad (526)$$

If the states are not directly observable, the Viterbi algorithm should be modified to estimate the most probable hidden states based on the fuzzy classification.

7.4.4. Generation of interpolated samples

The inverse CDF technique can be used to generate continuous random observations $\mathbf{y}[k]$ from some state probability $\mathbf{x}[k] = [x_i[k]]$. This technique has been already used in [301, 302] interpolating the cumulative probability transition matrix. This technique is also valid for probabilistic clustering if (527) is computed vectorially.

Since state probability would contain several non-null states, the cumulative distribution function $cdf_y(y)$ from (505) and (507) must be used instead of the cumulative probability transition matrix. The algorithm in pseudocode is:

- 1) Generate an uniform variable u in range $[0,1]$.
- 2) Find the value i that makes $cdf_y(\varphi_{i-1}) \leq u \leq cdf_y(\varphi_i)$ from (505).
- 3) Solve y from the equation $cdf_y(y) = u$ using (507) and realizing that $\varphi_{i-1} \leq y \leq \varphi_i$. For linearly interpolated states, the solution is:

$$y = \frac{u + \frac{x_i \varphi_{i-1}}{\varphi_{i+1} - \varphi_{i-1}} + \frac{x_{i-1} \varphi_i}{\varphi_i - \varphi_{i-2}} - \sum_{j=1}^{i-1} x_j}{\frac{x_i}{\varphi_{i+1} - \varphi_{i-1}} + \frac{x_{i-1}}{\varphi_i - \varphi_{i-2}}} \quad (527)$$

- 4) Update the state probabilities from the observable value y using (494):
- $$\mathbf{x}_i[k+1] = \Pr(\text{state}_i | y) \quad \forall 1 < i < m \quad (528)$$

7.5. Autocorrelation function of Markov Chains

The ACF and the PSD of the MC are very informative, showing its main features. This is very important for selecting the suitable order of the chains to obtain a chain with approximately the same PSD or ACF characteristics as the original series.

The autocorrelation function can be computed from the transition matrix according to [303]:

$$ACF[k] = \sum_{j=1}^m \sum_{i=1}^m \gamma_i \gamma_j \Pr[\text{state}_k=j, \text{state}_0=i] \quad (529)$$

$$\begin{aligned} ACF[k] &= \sum_{j=1}^m \sum_{i=1}^m \gamma_i \gamma_j \Pr[\text{state}_k=j | \text{state}_0=i] \Pr[\text{state}_0=i] = \\ &= \sum_{i=1}^m \gamma_i \pi_i \sum_{j=1}^m \Pr[\text{state}_k=j | \text{state}_0=i] \gamma_j = \sum_{i=1}^m \gamma_i \pi_i \sum_{j=1}^m P_{ij} \gamma_j \end{aligned} \quad (530)$$

The former relation can be expressed in canonical basis of an ergodic Markov Chain:

$$\begin{aligned} ACF[k] &= \bar{\mathbf{w}}^\top \mathbf{P}^k \bar{\boldsymbol{\gamma}} = (\bar{\mathbf{w}}^\top \mathbf{V}_R^\top) \text{Diag}[\lambda^k] (\mathbf{V}_R^\top)^{-1} \bar{\boldsymbol{\gamma}} = \\ &= (\mathbf{V}_R \bar{\mathbf{w}})^\top \text{Diag}[\lambda_i^k] (\mathbf{V}_R^{-1})^\top \bar{\boldsymbol{\gamma}} = \sum_{i=1}^m a_i b_i \lambda_i^k \end{aligned} \quad (531)$$

where:

$$\bar{\mathbf{a}} = \mathbf{V}_R \bar{\mathbf{w}} = [a_1, a_2, \dots, a_m]^\top$$

$$\bar{\mathbf{b}} = (\mathbf{V}_R^{-1})^\top \bar{\boldsymbol{\gamma}} = [b_1, b_2, \dots, b_m]^\top$$

$\bar{\mathbf{w}} = [\gamma_1 \pi_1, \gamma_2 \pi_2, \dots, \gamma_m \pi_m]^\top$ is the vector of the product whose elements are the state centroids γ_i multiplied by the stationary state probability π_i .

Therefore, the ACF of regular Markov chains is monotonically decreasing, following a mixture of exponentials [304, Ch. 8]. The decrease ratio is fixed by the eigenvalues λ_i .

The normalized autocorrelation (i.e., the autocorrelation coefficient) can be computed as:

$$\rho_y[k] = \frac{ACF_y[k] - \langle \mathbf{y} \rangle^2}{ACF_y[0] - \langle \mathbf{y} \rangle^2} = \frac{\sum_{i=2}^m a_i b_i \lambda_i^k}{\sum_{i=2}^m a_i b_i} \quad (532)$$

7.5.1. Power Spectral Density of discrete Markov chains

The power spectral density (PSD) is the Fourier transform of ACF. In [305, Chapter 2], a formulation is presented for calculating the power spectral density of a generalized M-ary Markov data source, which is characterized by one of signals (referred to as elementary signals) transmitted in each Δt interval with given a priori probabilities (called stationary probabilities) and given transition probabilities, i.e., the probability that a particular elementary signal is transmitted after the occurrence of another elementary signal. This formulation was originally described in [306] and it is further explained in [307] for irreducible Markov Chains. [308] derives the formula for irreducible periodic Markov Chains.

7.5.2. Further considerations on the PSD of continuous MC

The former subsections refer to the computation of the ACF and PSD of discrete MC. Those formulas are also good approximations for the case of continuously generated samples $\hat{\mathbf{y}}[k]$. Since $\mathbf{y}[k]$ is not discretized, its PSD has more low-frequency and less high-frequency content than the discrete MC.

Due to actual computational power, it can be simpler and more precise to estimate the spectrum from Monte Carlo Markov Chain with the algorithm of continuous sample generation (527).

The elementary signals can contain the PSD of the signal $z(t)$ inside time intervals Δt , providing an effective way to construct the full PSD from quickly sampled records –high frequency spectrum– and from the PSD of low-sampled long-time historic data –low frequency spectrum–.

7.6. Addition of long-lasting memory feature

Experimentally, state transition is dependent on previous observed value $\mathbf{y}[k]$, but the wind ACF shows a noticeable peak at 24 h lag and its multiples. In [301, 302, 309], the followed approach has been using higher order Markov chains, but to reproduce the 24 h lag peak in ACF, a non-ergodic chain should be used (for example, with a periodic model that exploit diurnal wind or solar dependence).

If the hour is included in the state, there will be a transition matrix for each hour and the number of parameters to be estimated will multiply by 24, which is excessive for the limited information that the hour adds. A more efficient intraday classification will be based on the observed diurnal pattern in each location. In wind power systems, an hourly classification based on the average increase or decrease of wind power can be enough. The transition from one state to the other can be gradual and deterministic (on the hour), to account continuous change of daily weather patterns. If diurnal dependence is modeled, the eigenvalues $\lambda_i[k]$ depend on the lag k and the ACF $[k]$ can show peaks at multiples of 24 h.

A multiresolution approach with several time-scales is suitable to model the long-lasting memory and the strong and weak interactions [310, 311]. Therefore, the average value of $\mathbf{y}[k]$ during last 24 h is an important parameter to define system status. Other parameters that can be included in system status are the average rate of change during last hours. The discretization of the last 24 h average and its average change should be determined according to the supplementary information added to the model. The simplest way to choose a good classification is to use a fuzzy clustering algorithm where the classification error or the number of clusters can be selected.

Recall that only representative parameters must be considered since the number of states and estimates increases exponentially.

7.6.1. Hourly, daily, weekly and seasonal dependence

The hour, the day of the week (weekdays, Saturdays and Bank Holydays) and the season of the year can be modeled as different time states of the system. Wind and solar generation depend on the hour of the day and the season. Therefore, the transition matrix of solar and wind generation is different depending on the hour and season state (wind dependence on hour is usually small, but hourly dependence of solar radiation must be considered in any case).

Notice that time evolution is deterministic. Moreover, time n steps forward from $k = m$ can be computed easier with time equation $k = m + n$ and a calendar than with the deterministic transition matrix. An approximate stochastic model is introduced to model fuzzy time classification (even though time evolution is deterministic, system behaviour depends stochastically on the time and a stochastic model of time is sensible). A stochastic time model can speed up a discounted Markov Decision Process with infinite horizon with enough accuracy and improve the transition matrix estimation.

A) Hourly patterns

The transition diagram for hour state with time discretization step $\Delta t = 1$ h can be seen in Fig. 114.

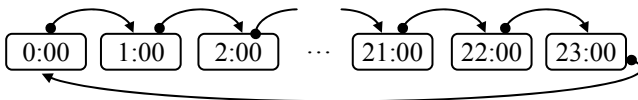


Fig. 114: Deterministic transition diagram of hour state. The behaviour is purely periodic since transitions are deterministic (probability = 100%).

The inclusion of hour state allows to use different transition rates for load and non-controllable generation each time step Δt . The transition rates for each hour can be obtained from historical data. If the model time step Δt is smaller than load and generation data or the data set is small, transition rates can be estimated hourly and then interpolated and scaled down to time step Δt . To reduce memory requirements, the number of day time steps can be decreased and interpolation can be disused.

B) Weekly patterns

Load can be forecasted with high accuracy in a big power system whereas the uncertainty is higher in small systems. Basically, load consumption depends mainly on the hour, day of the week and temperature. In a first approach, load level can be classified as high (typically, weekdays), medium (typically, Saturdays) and low (typically, Sundays and Bank Holydays). Each time the hour state jumps to 0:00, the classification of the day can change according to Fig. 115 (transition probability computed for a standard year). Take into account that a more accurate model will distinguish between full load, mid load and low load for each season instead of weekday classification.

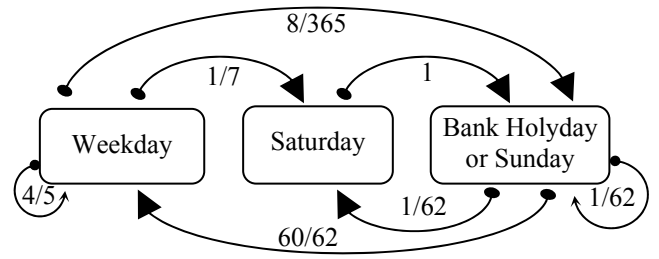


Fig. 115: Stochastic transition diagram of type of day (at the end of each day). Time transitions are stochastic (probability < 100%) except for the Saturday to Sunday/Bank Holyday transition.

Fig. 115 shows a probabilistic transition diagram. This implies that the weekday probability will evolve to the static probability in a few days (the fraction of weekdays, Saturdays and Sundays / Bank Holydays in a whole year). If the cyclic behaviour during one or several weeks is studied, the model of Fig. 116 is more suitable. Notice that the model of Fig. 116 only represents pure periodic weekly patterns and the Holydays should be modeled with this approach as yearly patterns.

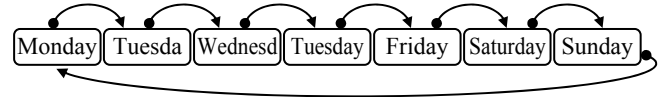


Fig. 116: Deterministic transition diagram of the week day.

C) Yearly patterns

If the horizon is longer than one season, the model should encompass the different characteristics of load, generation and reservoir dynamics along the year. Each day of the year, from January 1st to December 31st must be modelled as a state to use actually periodic Markov chain of Fig. 117. This model can account bank holydays patterns in load, but the estimation of the transition probabilities for each day of the year requires long data records and detrend the weekly patterns.

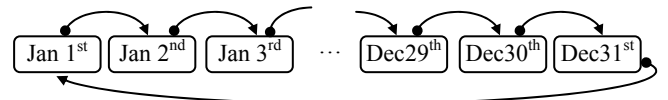


Fig. 117: Cyclic transition diagram of the year state.

A season last 91 days approximately, and the weather average characteristics vary gradually inside that period. If the scope of optimization is shorter than a whole season, each day can be classified in a state up to a certain degree (for example, March 21st can be classified as 50% winter and 50% spring). Thus, the seasonal approximated model is the stochastic transition diagram shown in Fig. 118 (note that the number of states has reduced from 365 days to 4 seasons).

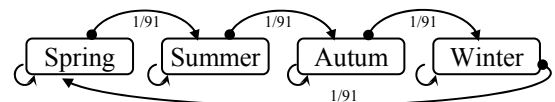


Fig. 118: Stochastic transition diagram of the approximate seasonal model. Season transitions are stochastic (probability = 1/91 a day).

7.7. Interpolation among basic periodic states

7.7.1. Introduction

Periodic chains needs to include a state for each time step, generating huge transition matrixes. On the other hand, periodic chains are deterministic and they can be handled much more effectively and naturally taking time as an input of the model and then computing with basic formulas the state of the periodic chain.

Since we are used to seasonal and daily classification of time, the stochastic model can be understood as a reduced transition matrix for each season and for each daily period, conforming the global transition matrix. Moreover, the transition matrix can be also expressed in tensor form (a reduced transition matrix for each season and for each daily period). The interpretation and analysis of the results is simpler due to the reduced dimensions of each basic transition matrix.

Even though the whole model is yearly periodic, many states are similar and they can be aggregated [312], making the model tractable. In this work, the evolution of seasons, hours... is handled by periodic interpolation. The periodic interpolation depends on time, but since time is now an input of the model, it can be estimated deterministically. Therefore, the transition matrix depends on a small subset of states (the basic periodic states and the output states), decreasing hugely the computation burden.

A full-year periodic complete model with time discretization step $\Delta t = 1$ h will include 8760 states for each of the 8760 h in a year. It is not reasonable to estimate a transition probability for each hour, since:

- It would require meteorological records from many years and available data rarely covers more than a few years, if any.
- Cyclic weather patterns show a general tendency. The seasonal weather patterns can occur with a lag of some weeks, depending on weather dynamics in each year. Therefore, a seasonal model with a bigger temporal resolution is non effective.
- There is a trade-off between temporal resolution and uncertainty in transition probability estimation, especially for short data records.
- The discounted optimum control for long horizons is less sensitive to the periodic patterns in the remote future. Thus, the stochastic transition models are more computationally efficient when calculating optimality with average or discounted average cost (or value) functions.

7.7.2. Periodic interpolation approach as a multivariate Markov chain.

The use of loose periodic patterns reduces notably the number of states and the computational burden. The advantages of estimating a transition matrix only for each combination of season, type of day and intraday period are:

- Since seasonal and hourly weather patterns are gradual tendencies, a progressive and probabilistic classification is desirable.

For example, the day of vernal equinox will be classified as winter and spring with equal probability. In other words, March 21st (the end of winter and the beginning of the spring) have climatic characteristics of winter and spring with 50% probability.

- The expected climatic parameters at an instant k are a mixture of similar seasonal, weekly and hourly patterns.
- Periodic weights and conditioned transition matrixes can be expressed as periodic Markov chains [313, Ch. 9]. If time step $\Delta t = 1$ h, the interpolation can be described as a deterministic periodic sparse transition matrix of dimension 8760×8760 . This fact can be used to derive theoretical properties of the Markov chain.
- The season, the day and the hour classification can be considered an observed state of the model (i.e., they are inputs of the model).
 - A model with 4 seasons, 3 types of day and 6 intraday periods have $4 \times 3 \times 6 = 72$ basic transition matrixes (one for each combination of season, day and intraday) instead of 8760 basic transition matrixes (one for each hour of the year).
 - Not all parameters do depend on season, day and hour (for example, wind and sun are not correlated with the day of the week). Additional economy can be obtained if intraday or seasonal resolution can be lowered (for example, wind behaviour can be classified according to half year and half day periods and two days period –four basic transition matrixes–).
 - The features of basic transition matrixes are glimpsed in density plots where each pixel has a color according to the matrix element logarithm.
- The functions $season(n_1, k)$, $weekDay(n_2, k)$ and $hourlyPeriod(n_3, k)$ will be used for simplicity to obtain the probability of each time classification, where n_1 , n_2 and n_3 are the classification periods and k is the hour from the start of the year (January 1st).
 - Season numbering: according to the order shown in Fig. 118, $n_1=1$ for spring, $n_1=2$ for summer, $n_1=3$ for autumn, $n_1=4$ for winter.
 - Day of the week numbering: according to the order shown in Fig. 115, $n_2=1$ for weekday, $n_2=2$ for Saturday, $n_2=3$ for Sunday or Bank Holiday.
 - Numbering of period of the day: according to the order shown in Fig. 114, the numbering starts from $n_3=1$ after midnight (00:00). The number of intraday classes depends on the hourly resolution required for the application:
- The division of a day into two classes can be enough for wind applications since diurnal dependence of wind is small [314, 315, 316, 317, 318]. The optimum time centroids are the periods with maximum and minimum wind average change rate

(time of the day with maximum average increase and decrease of wind, respectively).

- Solar applications need a more detailed model. Time classification can be based on clear-sky solar insolation on collector, starting from zero (night) to maximum insolation at noon. Moreover, the clear-sky power output can be computed from time if the characteristics [319] of the collector are defined (i.e., not a parameter to optimize in MDP). Thus, time can be classified according to the clear-sky power output, from zero to the maximum output.
- Hourly load profile can be classified according to the load level and the average rate of change. Since diurnal load dependence is high and quite predictable [320, 321], a clustering algorithm can be used to optimize classification given the desired number of periods. Usually, the gradual division of day into eight periods is precise enough [322].
 - If each parameter affects the system independently of rest of parameters, the joint transition matrix can be factored as:

$$p_{i,j}|_{n_1,n_2,n_3} \approx a_{i,j}|_{n_1} \cdot b_{i,j}|_{n_2} \cdot c_{i,j}|_{n_3} \quad (533)$$

Thus, only $\mathbf{A}|_{n_1}$, $\mathbf{B}|_{n_2}$ and $\mathbf{C}|_{n_3}$ matrixes must be estimated minimizing the approximation error and fixing a scale (for example, $a_{1,1}|_{n_1}=1$ and $b_{1,1}|_{n_2}=1 \forall n_1, \forall n_2$). Provided factors and joint probabilities are not null, (533) can be transformed into a linear minimization problem:

$$\ln(p_{i,j}|_{n_1,n_2,n_3}) - \ln(a_{i,j}|_{n_1}) - \ln(b_{i,j}|_{n_2}) - \ln(c_{i,j}|_{n_3}) \approx 0 \quad (534)$$

- Therefore, a factored model with $n_1 = 4$ seasons, $n_2 = 3$ types of day and $n_3 = 6$ intraday periods have $n_1 + n_2 + n_3 = 13$ basic factor matrixes: $\mathbf{A}|_{n_1=1}$, $\mathbf{A}|_{n_1=2}, \dots, \mathbf{A}|_{n_1=4}$, $\mathbf{B}|_{n_2=1}, \dots$ and $\mathbf{C}|_{n_3=6}$.

A model for multivariate Markov chains with reduced number of parameters can be found in [283]. This approach can be valuable if data is scarce or the number of states is big. However, the number of classes of the models presented here is low enough for using a conventional approach to multivariate Markov chains.

7.7.3. Comparison of linear, cosine and Gaussian periodic interpolation

This subsection compares the characteristics of periodic interpolation. Since it is an interpolation in time domain, its main features has been already discussed.

7.7.4. Periodic linear interpolation

For most applications, the linear interpolation is precise enough (triangular conditional probability). This conditional probability is analogue to the fuzzy classification of the day with triangular seasonal membership functions (see Fig. 119).

$$f_{\text{season } i|k, \Delta}(t'_i) = \begin{cases} \left(1 - \left| \frac{t'_i}{\Delta} \right| \right) & \text{if } \left| \frac{t'_i}{\Delta} \right| < 1 \\ 0 & \text{if } \left| \frac{t'_i}{\Delta} \right| \geq 1 \end{cases} \quad (535)$$

$$= \Pr(\text{Seasonal Pattern} = i | \text{hour} = k, \text{interpolation} = \text{linear})$$

$$\text{where } t'_i = \frac{2 \text{Mod}(t - \varphi_i - T/2, T) - T}{\text{Mod}(\varphi_{i+1} - \varphi_{i-1}, T)} \quad (536)$$

where Mod stands for modulo function (remainder of the first argument divided by the second).

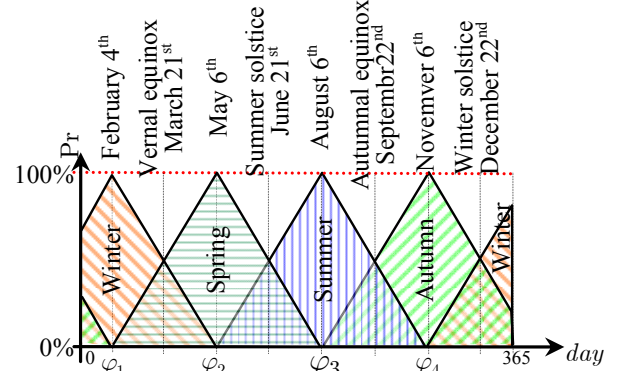


Fig. 119: Seasonal pattern Conditional probability given the day estimated using linear interpolation, $\Pr(\text{Seasonal Pattern} | \text{day})$.

Linear interpolation is piecewise linear, as can be seen in Fig. 107. Since weather patterns vary smoothly and characteristic times are big, a smoother interpolation such as Fig. 110 is more suitable to model this smooth behaviour.

A) Periodic Gaussian interpolation

If a smooth conditional probability density function is required, the Gaussian PDF is quite suitable. The standard deviation to make the sum of conditional probabilities closest to unity is $\sigma_i = \text{Mod}(\varphi_{i+1} - \varphi_{i-1}, T) / \sqrt{8\sqrt{\pi}}$. If the same transformation of (536) is applied, the PDF is (537) and the individual conditional probabilities and its sum can be viewed in Fig. 120.

$$f_{\text{season } i|k, \text{normal}}(t'_i) = \frac{e^{-\sqrt{\pi}(t'_i)^2 - 1}}{2 + e^{\sqrt{\pi}}} \quad (537)$$

$$= \Pr(\text{Seasonal Pattern} = i | \text{hour} = k, \text{interpolation} = \text{normal})$$

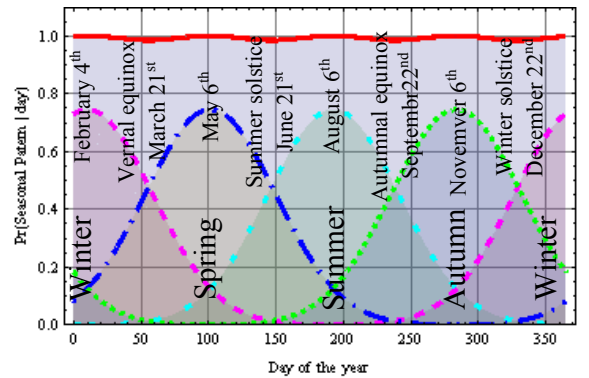


Fig. 120: Seasonal pattern Conditional probability given the day estimated using the original normal interpolation, $\Pr(\text{Seasonal Pattern} | \text{day})$.

The normal probability is not restrained to adjacent states. This conditional probability makes that an infrequent event that have happen in one season can happen in other periods with smaller probability. In most applications, this generalization is desired since long data records are not usually available (the estimation of extreme events has high uncertainty) and such infrequent events can have special consequences in the system.

The sum of normal probabilities has a maximum error of 1,5%. If (537) is scaled to sum unity, the conditional probability is:

$$f_{\text{season } i|k, \text{ normal}}(t'_i) = \frac{\pi^{-1/4} e^{-\sqrt{\pi} t'_i{}^2}}{\text{EllipticTheta}[3, -\pi t'_i, e^{-\pi^{3/2}}]} \quad (538)$$

Recall that Elliptic Theta function can be replaced by the sum of all the numerators of (538) $\forall i$. Alternatively, approximation (539) can be used if 0,15% scale error is admissible (both approximations are visually indistinguishable and they correspond to Fig. 121).

$$f_{\text{season } i|k, \text{ normal}}(t'_i) \approx \frac{0.7166}{1 + \frac{4\text{Sinh}^2(\sqrt{\pi} t'_i)}{2 + e^{-\sqrt{\pi}}}} \quad (539)$$

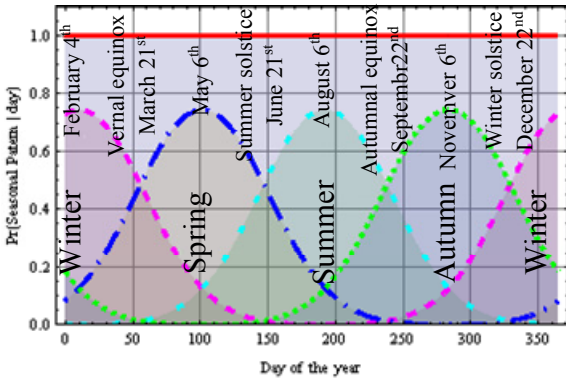


Fig. 121: Seasonal pattern Conditional probability given the day estimated using Gaussian interpolation, $\text{Pr}(\text{Seasonal Pattern} | \text{day})$.

B) Periodic Cosine interpolation

The two-state deterministic periodic system shown in Fig. 122 has the following transition matrix and rate diagram:

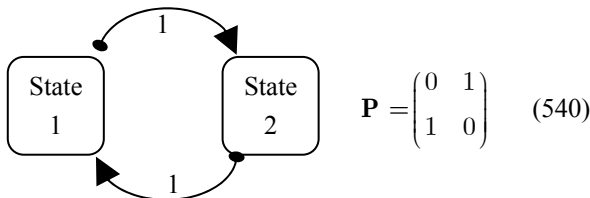


Fig. 122: Rate diagram and transition matrix of a periodic system with two states.

The evolution of state probability can be computed from Markov property:

$$\vec{x}[k] = \vec{x}[0]^T \mathbf{P}^k = \frac{1}{2} \vec{x}[0]^T \begin{bmatrix} 1+(-1)^k & 1-(-1)^k \\ 1-(-1)^k & 1+(-1)^k \end{bmatrix} \quad (541)$$

For non-integer time instant k , the probability $\vec{x}[k]$ is complex [323]. If only real part of $\vec{x}[k]$ is considered as meaningful, (541) transforms into:

$$\text{Re} \{ \vec{x}[k] \} = \frac{1}{2} \vec{x}[0]^T \begin{bmatrix} 1+\text{Cos}(\pi k) & 1-\text{Cos}(\pi k) \\ 1-\text{Cos}(\pi k) & 1+\text{Cos}(\pi k) \end{bmatrix} \quad (542)$$

Therefore, the evolution of intermediate states is trigonometric for systems with two states, as can be seen in Fig. 123. Sine and cosine functions have inherent periodic behaviour and they are the basis of frequency analysis. In many fields, periodic behaviour is represented by phasors.

Moreover, the sum of this type of conditional probability is unity (no additional factor must be included).

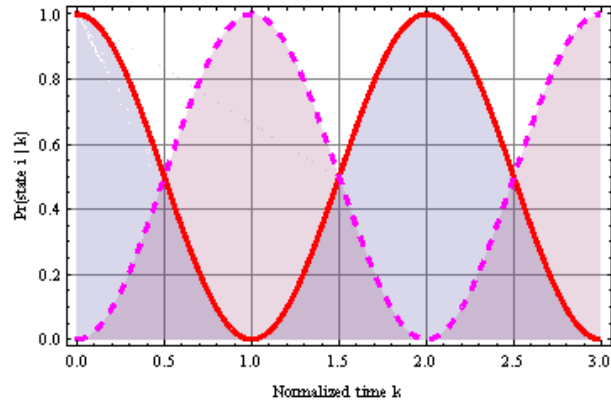


Fig. 123: Conditional probability of a two state periodic Markov chain computed using cosine formula (542).

For systems with more than two periodic states, the state probability at non-integer time instant k is not bounded to $[0,1]$ and shows complex trigonometric relations. Therefore, the former interpretation of complex probability is not longer valid. Notwithstanding this fact, the conditional probability can be defined analogously as a cosine pulse:

$$f_{\text{season } i|k, \text{ cosine}}(t'_i) = \begin{cases} \frac{1}{2} \{1 + \cos[\pi t'_i]\} & |t'_i| < 1 \\ 0 & |t'_i| \geq 1 \end{cases} \quad (543)$$

The non-null probability is constrained only to adjacent states. This can be an advantage when modelling systems with behaviour very dissimilar for different states. Gaussian interpolation (538) is very similar except the amplitude of the cosine is halved (see Fig. 124). Therefore, the behaviour is more similar at either state with normal assumption (the probability of behaving as the other state is, at least, $1/4$).

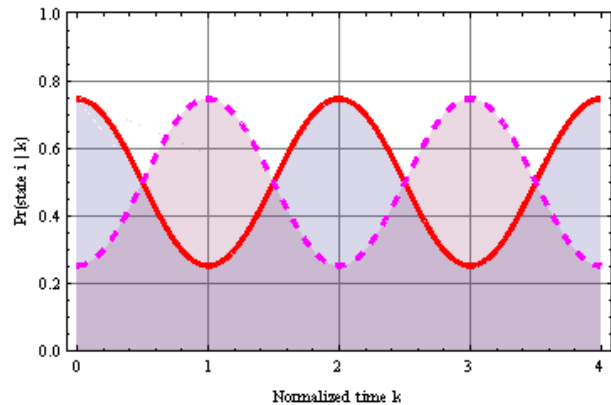


Fig. 124: Conditional probability of a two state periodic Markov chain computed using Gaussian formula (538).

The application of cosine interpolation to chains with more than two states is similar to triangular conditional probability (compare Fig. 125, Fig. 121 and Fig. 119). One disadvantage of this model is that the interpolated behaviour shows inflexion points at the state centroids, as can be seen in Fig. 108.

In sum, normal interpolation is preferred for weather systems where the behaviour at adjacent states is similar and its generalization makes less critical data scarceness.

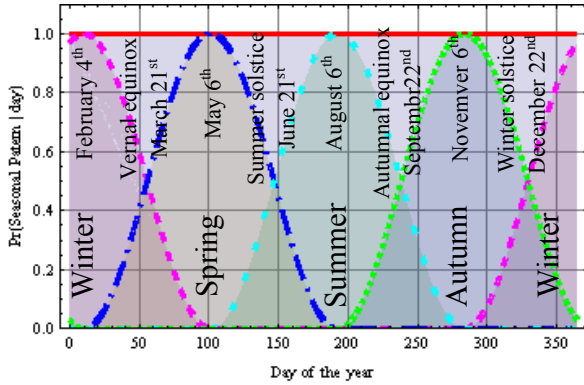


Fig. 125: Seasonal pattern Conditional probability given the day estimated using cosine interpolation, $\Pr(\text{Seasonal Pattern} | \text{day})$.

7.7.5. Benefits from discrete approximation of continuous time and state Markov models

- Continuous time and state Markov models are very difficult to solve and require algebraic manipulation, more restrictive than numerical calculus.
- Algebraic manipulations are avoided with the discrete approximation. The powerful theoretical background for Discrete Time Markov Chains can be used.
- Even though state and time interpolation can be formulated as HMM, the interpolation approach is more simple and leads to a more simple and intuitive model. The states are observable because all measures are supposed to be reliable and the states are defined by the measures. Moreover, the overhead of Forward, Viterbi, Baum-Welch algorithms [324] for HMM is avoided using regular MC.
- Regular MC have more theoretical properties than HMM and the parameters are more informative. For example, the PSD of a Markov Chain can be computed theoretically from parameters without using MCMC.
- MDP are formulated easier in MC than in HMM.

7.8. Application Example I: Characterization of wind power variability with Markov Chains

A novel technique to account wind variability is presented based on Markov Chains and classification of observations. This approach is different from the usual generation of wind series in Monte Carlo analysis through Markov Chains.

This model describes the power system status through combination of cases or “snapshots of the network” obtained from the clustering of observations and the probability (or observed occurrences) of transitions from one case to other with Markov Chains. This powerful approach is able to model not only the non-linear conventional behavior of the farms but also infrequent events that have a high impact in system reliability and stability (such as sudden disconnection of generators due to grid perturbations, swift change in wind during storms, etc).

This powerful combination just requires to run only so many power flows as states has the system. Each grid snapshot is computed using a regular power flow with a full

model of the grid (instead of linear models). Intermediate cases are interpolated using fuzzy clustering, reducing remarkably the required number of cases considered for a given accuracy.

The probability of events which can harness power system security can be derived easily and rigorously using the properties of Markov Chains. Moreover, Markov Decision Processes can be applied to optimize the regulation of spinning reserve, the reactive control and the optimal sizing of isolated systems.

To explain adequately the foundations and to show the potential applications of this approach, this work has been divided in three parts. In this part, the theoretical foundations and an overview of the method are presented. The second part shows the estimation of Markov Parameters for a system with three wind farms. The third part illustrates the stochastic power flow of the three wind farms and introduces the possible optimization through Markov Decision Processes.

7.8.1. Introduction

Wind speed fluctuations are usually analyzed through linear mathematical tools such as frequency spectrum and time series. The Van der Hoven’s wind spectra [325] show a gap between 3 minutes/cycle and 5 hours/cycle that separates fast fluctuations from slow fluctuations. Nevertheless, this division is not so clear at some locations [326, 327, 328].

On the one hand, slow fluctuations are mainly due to meteorological dynamics and they are widely correlated spatially and temporally. Slow fluctuations in power output of near farms are quite correlated and wind forecast models try to predict them to optimize power dispatch. On the other hand, fast wind speed fluctuations are mainly due to turbulence and microsite dynamics [329].

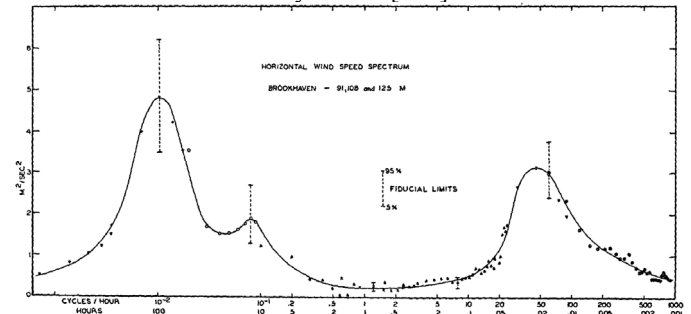


Fig. 126: Van der Hoven’s spectral model (from [78]).

7.8.2. Step changes in Power Output

Wind turbines can cause a periodic behavior if they experience repetitive connection and disconnections due to difficult operating conditions (wind speed near cut-in or cut-out, high temperatures, high turbulence, etc.). In Fig. 127, the active power output of a single turbine has extreme variations due to a combination of high ambient temperature and high wind, yielding to high temperature alarms at gearbox oil. In that situation, the power output of the farm is not so abrupt because even though this behavior was common to many turbines, the disconnection and connections of the turbines were not synchronized.

The repetitive connection and disconnection of up to two turbines is a reduced portion of the total active wind farm power output expressed in p.u. (see Fig. 128).

The sudden wind change can also cause variations in power output of the farm in minutes, as can be seen at Fig. 129. At

17:25, the power output of a farm was 0.21 p.u. and ten minutes later was 0.96 p.u. due to a storm.

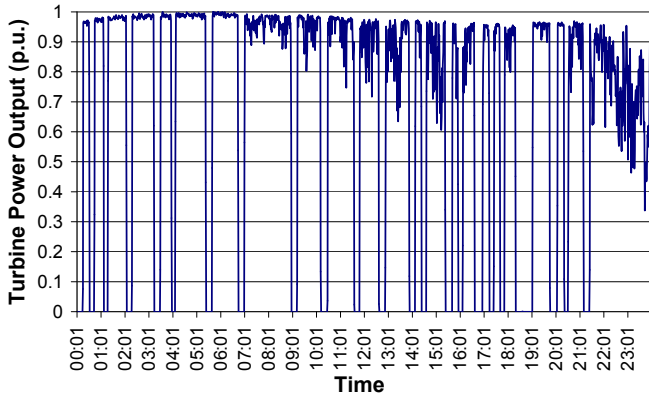


Fig. 127: Power output of a single turbine experiencing 24 repetitive stops due to over temperature in 20/07/1998 (24 h).

In general, power variations as extreme as Fig. 129 are smoothed in the total generation of a bigger area. However, even in a wide area such as Spain with 16 740 MW of wind power installed at the end of 2008 [330], a variation rate of 1000 MW/hour approximately can be seen in Fig. 130 [331].

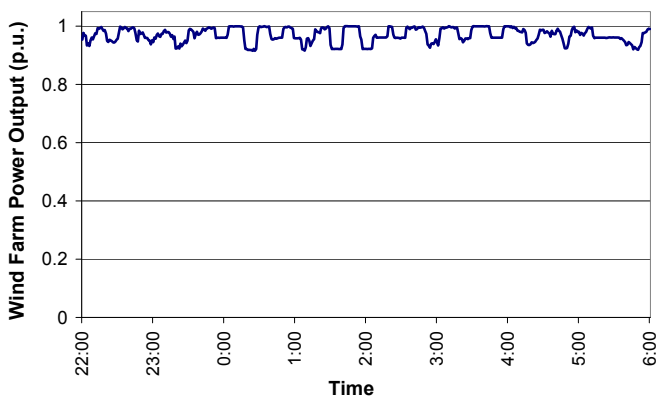


Fig. 128: Active power output of a wind farm with 26 turbines experiencing repetitive connection and disconnection of up to two turbines due to internal errors in 7/02/1999 (mean speed at meteorological mast was around 14 m/s).

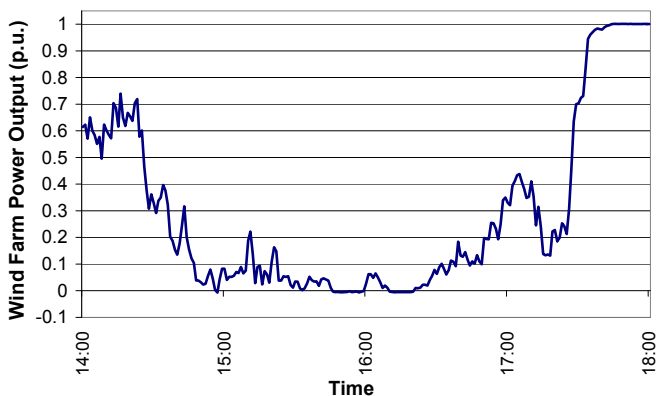


Fig. 129: Active power output of a wind farm experiencing high variability in 9/02/1999 due to a sudden change in the weather at 17:30.

The worse case is when the circuit breaker disconnects a wind farm. The Spanish Ministerial Order of 5-9-1985 [332] ordered that the protection relays of wind substations were adjusted very strictly (for example, instantaneous trip for voltages under 0,85 p.u. or over 1,1 p.u.). This caused a number of unjustified disconnection of wind farms at network

contingencies. In Fig. 131, recovering normal production from wind farm energization lasted three minutes (with Vestas Opti-Slip 600 kW turbines). Nowadays, the relays are adjusted more selectively and the turbines are rewarded for fault riding capabilities (even though [332] hasn't formally repealed, up to now).

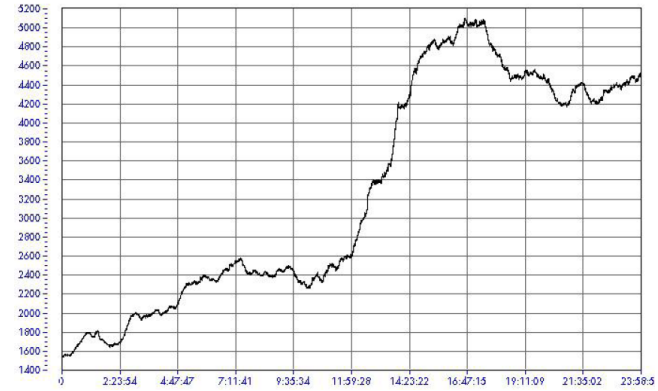


Fig. 130: Active power output (MW) of Spanish wind farms experiencing high increase in 18/01/2005 between 12:00 and 15:00.

To sum up, some events in the wind farm produce step changes in the output and they are very difficult to model using frequency or time series analysis.

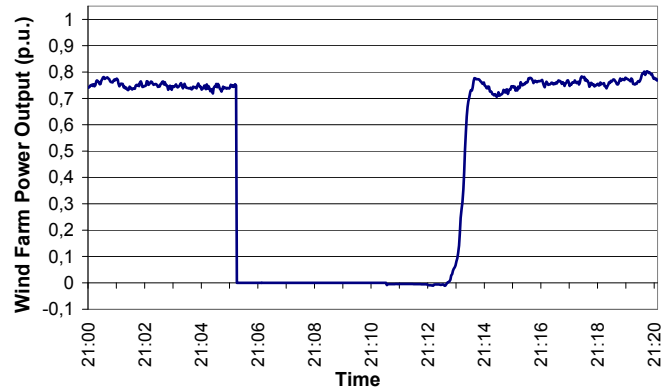


Fig. 131: Active power output of a wind farm experiencing a disconnection in 3/02/1999 due to a trip of the homopolar protection relay between 21:05:24 and 21:10:55. Three minutes later, the output reached normal values.

7.8.3. Statistical Approach to Variability

Linear stochastic tools such as time series or frequency analysis are very popular for characterizing the farm output despite casual individual turbine disconnections. However, Markov chains will be used in this work since:

- The behavior at low or high wind is very different from middle wind. Such behavior is highly non-linear.
- Some stochastic models do not model adequately that power output is constrained from zero to full generation (0 to 1 p.u.). The long run probability of the power output is bimodal, showing more steady operation at full generation or at no generation [333]. The output can vary suddenly from 0 to 100% in wind park switching events.
- Grid disturbances can trip a great amount of wind power, which can be hardly characterized with stochastic linear models based on time series or frequency analysis. Big fluctuations such as disconnection of a whole park or a group of farms are not suited for spectrum neither time

series analysis because abrupt changes involve high components in all frequencies. In contrast, the probability of a sudden change can be modelled easily with Markov Chains.

- The linearized model of an electrical system is not adequate for severe perturbations.

This work will focus in a non-linear stochastic characterization of power output through a finite number of states.

Markov chains have been chosen for this work due to its simple mathematical treatment and its superior theoretical properties for stochastic dynamics. This model is also well suited for stochastic power flows and for understanding system dynamics.

A stochastic process can be modelled by a Markov model if the evolution of the system is only dependent of the present. In other words, a Markov model implies considering the process memoryless. The utilization of regular Markov Chains imply that the permanence of the system in a state is distributed statistically exponentially (or geometrically in the case time is discretized). To override the memoryless characteristic, the tendency of the system during the last hours or the wind forecast for a given horizon can be included as another parameter of the states (at the cost of a bigger number of states).

7.8.4. Characterization of Power Variability of Wind Generation with Markov Chains

Markov chains have been used in modelling physical, biological, social, and engineering system such as population dynamics, queuing networks and manufacturing systems. One of the main advantages of using Markovian models is that they are general enough to capture the dominant factors of system uncertainty and, in the meantime, it is mathematically tractable.

Most dynamic systems in the real world such as meteorology are inevitably large and complex, mainly due to their interactions with numerous subsystems. Since exact or closed-form solutions to such large systems are difficult to obtain and they would require extensive measures, one often has to be contented with approximate solutions. Take the optimal control of a dynamic system such as spinning reserve in a power system due to wind power. Because the precise mathematical models are difficult to establish, near-optimal controls often become a viable, and sometimes the only alternative. Such near optimality requires much less computational effort and often results in more robust policy to attenuate unwanted disturbances [334].

Wind power show different prevailing dynamics when it is analyzed for a few milliseconds or for a daily horizon. It can be thought that electromechanical dynamics used different time scale from the weather evolution.

The division between fast and slow dynamics makes easier large-scale optimization of wind energy. If all the important factors are included in a Markov Model, it would lead to a large state space with many parameters to estimate and an exhaustive and extensive measuring system. To reduce the complexity, a hierarchical approach is suggested, which leads to a multi-resolution formulation. The hierarchical approach relies on decomposing the states of the Markov chains (all the possible combination of power output of wind farms) into several recurrent classes (typical patterns of generation

observed in power output of wind farms). The essence is that within each recurrent class the interactions are strong and among different recurrent classes the interactions are weak.

Traditionally, Markov chains have been applied in Electrical Engineering for the study of queues [335] and power system reliability given rate of failure and reposition times of its components. In Markov Chain Monte Carlo (MCMC) simulations, Markov Chains are employed as random number generators with particular characteristics [336], not in the way they are utilized in this paper.

7.8.5. State selection

In this proposed methodology, each Markov state can be seen as a case that characterizes a typical operational mode of the wind farm (or a group of wind farms). Full generation, no generation and partial generation are candidates for Markov states. If partial operation near cut-in wind speed is notably different from partial operation near rated wind speed, they should be considered as distinct Markov states. Fig. 132 shows this discretization and the arrows indicate a transition from a state to another one.

Fig. 132 is *a priori* arrangement, but the election of states can be optimized using a clustering algorithm which minimizes the classifying error and selects the optimum number of states [337, 338]. This is crucial when classifying data from several wind farms. Therefore, the clustering is used as a mathematical tool to transform a continuous multivariate space \mathbb{R}^s (the active power output of s wind farms) into a discrete and finite (numbered in \mathbb{N}) state space to use Discrete Time Markov Chains with convenient matrix algebra instead of functional analysis.

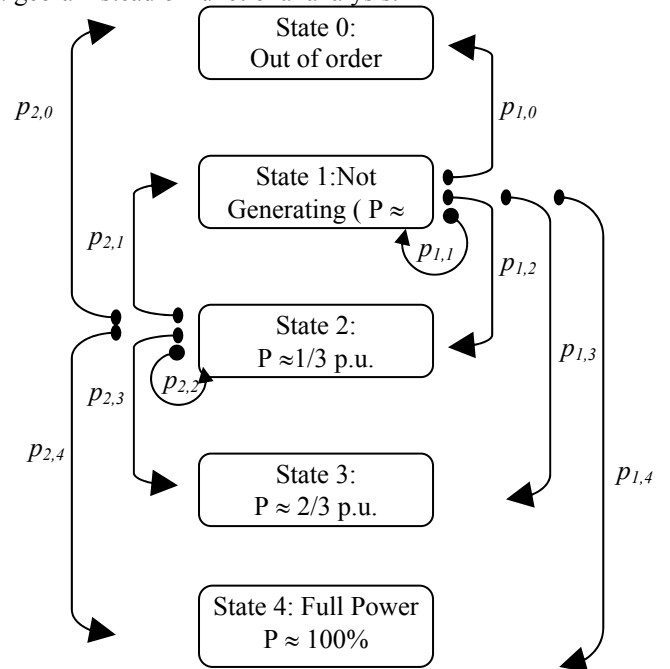


Fig. 132: Discretization of power output of one wind farm into a number of states (four in this figure). Only transitions from states 1 and 2 are shown for clarity.

The use of different states allows to use a full model of the grid (instead of the classical small-signal model) and the state weighting describe intermediate cases reducing the required number of states, m . The combination of matrix algebra and

state probability imply the (linear) interpolation between the centroids of the states for describing intermediate cases.

7.8.6. Considerations on \hat{P} .

Since the probability of state transitions is estimated from real data, this approach can handle abrupt behavior of the farms along with events that rarely happens but that they have a high impact in system reliability and stability (sudden disconnection of generators due to grid perturbations, swift change in wind during storms, etc).

The obtained Markov Chain is irreducible because starting from any state i , it is possible to enter state j in finite number of transitions. This property will be assumed in the following sections. Moreover, if all transitions \hat{p}_{ij} have non-null probability, the Markov chain is said also regular.

7.9. Experimental Validation of Case Study I

The classification of states can be based on power output, “unperturbed wind speed” and wind speed prediction, depending on available data and aim of the wind farm model. The performance matrix in Standard IEC 61400-12-3 can be used as emission matrix to relate wind and power in a wind farm using a Hidden Markov Model. The wind farm model can be used also as time interpolation between horizons of wind prediction or to account switching events such as sudden disconnection of the farm. The basic workflow to compute a stochastic power flow based in Markov Model is presented. A simplified, steady state, quadratic model of the wind farm is shown for justifying the approximation of networks to PQ nodes and the interpolation between states. This quadratic model can be used also to estimate the reactive power for steady state.

7.9.1. Markov Model Based on Wind Parameters

The consideration of wind speed and direction along with wind power output can give further insight in wind farm dynamics than using only power output. However, it is usual to have only limited data (only wind parameters or only power generation).

Power Flows require the active and reactive power of all generation and consumption nodes. This subsection discusses the modifications needed to use a Markov Model based on wind and power parameters or only wind characteristics.

If the aim of the Markov model is to work with wind forecast, the state number can be defined based on mean wind speed and direction at the wind farm. The power output can be derived from the conditional probability of power output given wind speed and direction.

Standard IEC 61400-12-3 [339] shows a detailed method to compute the wind farm power output from “unperturbed wind speed” of the wind farm. The wind farm power curve consists of performance matrix \mathbf{M} indicating the expected power output from wind speed and wind direction values. In Markov jargon, the state space can be built from wind speed and direction. The emission probability matrix can be the performance matrix \mathbf{M} if the bins of IEC 61400-12-3 are elected as Markov states.

Moreover, Hidden Markov Models (HMM) can cope with

more complex dynamics when system state is not directly observable (for example, if important information like turbine malfunctions and maintenance work are not available).

A model should be simple enough to avoid over-fitting or over-fluctuations. Even more, the use of very complex models with many parameters need big amounts of data to be adjusted and its interpretation becomes tougher.

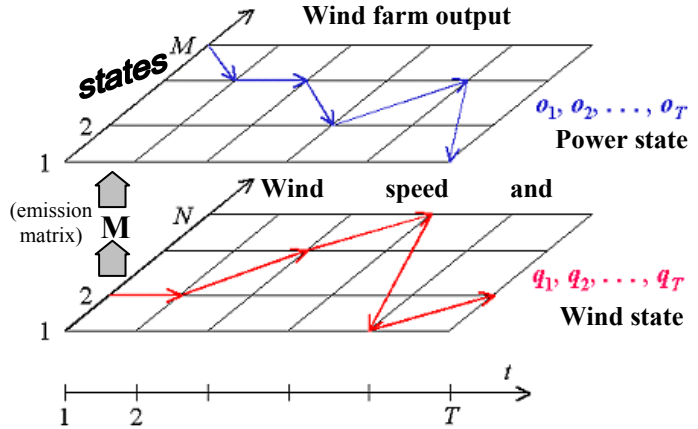


Fig. 133: Schematic relationship between measures (observations) and estimated states when they can not be derived straightforward from measures (adapted from [340]).

7.9.2. Improving Markov model with weather forecast

Weather forecast is a widespread tool to characterize wind farm power trend from 6 hours ahead. Meteorological physical models are much more precise for assessing power evolution for long horizons, whereas Markov Chains are more adequate for assessing power variability for short and medium horizons and for optimize network policy. Therefore, a model that combines weather forecast and a Markov Model is more suitable than just trying to use a more complex statistical distribution (a semi-Markov model has fewer theoretical properties, it increases model complexity and it does not account the complex weather dynamics).

The influence of meteorological dynamics can be incorporated using the weather forecast as another parameter. If weather forecast is not available, a Hidden Markov Chain (HMC) can be used for accounting the meteorological stability (an unobservable parameter). Other approach is the inclusion of the weather forecast and the farm availability in the classification process.

To sum up, if the time span of the estimation is bigger than 6 hours, weather forecast must be used to increase the accuracy of the wind power variability model.

7.9.3. Discerning switching events from continuous operation

Switching events are difficult to detect if there are no meteorological data available. Switching events can be guessed during high wind with a statistical hypothesis test based on maximum change of wind. If power has changed above the confidence level for the previous power output, the operation is not continuous up to a significance level.

Moreover, if the variability of power output during normal operation is characterized through a Hidden Markov Model, the Viterbi algorithm can be adapted to estimate the most likely sequence of states from measures.

The effect of switching events range from voltage variations to frequency drifts in small systems or tie line overloads in big systems [341]. For example, the sudden disconnection of big amounts of wind power in Spain can overload tie lines with France [342]. The sudden disconnection of such big amounts can be due only to severe network disturbances that are spread along the grid. These events are unpredictable.

The disconnection due to extreme weather is more gradual because of geographical diversity of turbines. Some wind farms will experience greater wind speeds. Inside a wind farm, the more exposed turbines would shut down first. Moreover, extreme wind can be forecasted with some accuracy and the spinning reserve can be appropriately increased [343, 344]. Sometimes, the maximum and minimum power in the interval is also measured. This extra information is very valuable to discern switching events from very fast changes in wind.

7.9.4. Stochastic time interpolation

Sometimes, wind or power forecast is given only at some time horizons and the power output should be computed at intermediate instants between actual data and forecasted value. Time interpolation can be performed using maximum a posteriori probability criterion according to a Markov Model.

The sequence of power output or wind speed and direction analyzed “as time goes by” is called the forward Markov process and it has a probability transition matrix usually denoted by \mathbf{P} and its elements p_{ij} , the transition probabilities from state i to state j . However, the sequence ordered in reverse time direction is another Markov process [335] with backward transition probability matrix $\tilde{\mathbf{P}}$ and its elements, \tilde{p}_{ij} the reverse transition probabilities from subsequent state i to the preceding state j :

$$\tilde{p}_{ij} = \pi_j p_{ji} / \pi_i \quad (544)$$

where π_i is the stationary distribution of the models and can be computed as the eigenvector for the unity eigenvalue of matrix \mathbf{P} (or $\tilde{\mathbf{P}}$) or alternatively, as any row of the limiting distribution for long time horizons, $\lim_{N \rightarrow \infty} \mathbf{P}^N$.

7.9.5. Input data

$\mathbf{x}[0] = [x_1[0], x_2[0], \dots, x_m[0]] =$ row vector of initial probabilities of all m states.

$\mathbf{x}_{forecasted}[N] = [x_1[N], x_2[N], \dots, x_m[N]] =$ forecasted probabilities of all states for time horizon N .

$\hat{\mathbf{x}}[N] =$ Expected value of $\mathbf{x}[N] = \mathbf{E}(\mathbf{x}[N]) =$ (545)

$$\begin{aligned} &= \text{Probability}(\mathbf{X}[N] \neq \mathbf{x}_{forecasted}[N]) \cdot \mathbf{x}[0] \cdot \mathbf{P}^N + \\ &+ \text{Probability}(\mathbf{X}[N] = \mathbf{x}_{forecasted}[N]) \cdot \mathbf{x}_{forecasted}[N] = \\ &= (1 - \beta) \mathbf{x}[0] \mathbf{P}^N + \beta \mathbf{x}_{forecasted}[N] \end{aligned}$$

$\beta_{cl} =$ confidence level of forecasted value $\mathbf{x}_{forecasted}[N]$

7.9.6. Estimation of the state sequence

The expected system evolution is the weighted sum of a forward and a backward Markov Process. In absence of relevant information, the weighting of the forward and

backward process at point k can be proportional to the distance to the initial and end of the time interval. Accordingly, the following formulae expressing the probability of each state ($\tilde{\mathbf{P}}$ is supposed invertible in wind power applications): (546)

$$\begin{aligned} \hat{\mathbf{x}}[k] &= \text{Expected value of } \mathbf{x}[k], 0 \leq k \leq N = \mathbf{E}(\mathbf{x}[k]) = \\ &= \text{Probability}(\mathbf{X}[k] = \mathbf{x}[0] \cdot \mathbf{P}^k) \cdot \mathbf{x}[0] \cdot \mathbf{P}^k + \\ &+ \text{Probability}(\mathbf{X}[k] = \mathbf{x}[N] \cdot \tilde{\mathbf{P}}^{N-k}) \cdot \mathbf{x}[N] \cdot \tilde{\mathbf{P}}^{N-k} \\ \hat{\mathbf{x}}[k] &= \mathbf{E}(\mathbf{x}[k]) = \frac{(N-k) \mathbf{x}[0] \mathbf{P}^k + k \hat{\mathbf{x}}[N] \tilde{\mathbf{P}}^{N-k}}{N} = \\ &= \left(1 - \beta_{cl} \frac{k}{N}\right) \mathbf{x}[0] \mathbf{P}^k + \beta_{cl} \frac{k}{N} \mathbf{x}_{forecasted}[N] \tilde{\mathbf{P}}^{N-k} = \\ &= \left(1 - k \frac{\beta_{cl}}{N}\right) \mathbf{x}[0] \mathbf{P}^k + k \frac{\beta_{cl}}{N} \mathbf{x}_{forecasted}[N] \tilde{\mathbf{P}}^N (\tilde{\mathbf{P}}^{-1})^k \end{aligned} \quad (547)$$

The latter formula can be expressed more compact as:

$$\hat{\mathbf{x}}[k] = \left[\mathbf{x}[0] + k \frac{\beta_{cl}}{N} (\mathbf{x}_{forecasted}[N] \tilde{\mathbf{P}}^N - \mathbf{x}[0]) \right] \mathbf{P}^k \quad (548)$$

If the interpolation between the measured and the forecasted values is done geometrically instead of arithmetically, a similar formula can be derived.

The probability of any sequence of generation states can be computed as in chapter 7 of [345] (for example, probability of the sequence: full generation to no generation and then to full generation in successive time intervals).

7.10. Stochastic power flows

Probabilistic power flow is a term that refers to power flow analysis methods that directly treat the uncertainty of electric load, generation and grid parameters.

Classical approaches usually rely on simplifications such as linearization and independence of random variables. In many algorithms, the loads at each bus are assumed independent and normally distributed [346], which is quite unrealistic for renewable energy and consumer loads. However, dependence of system parameters should be identified by principal component analysis and correlated random variables can be transformed into independent variables. Some authors [347, 348] proposed a linear approach with a rotational transformation to convert variables correlated into uncorrelated.

In Monte Carlo time simulation, a large number of power flows should be run to achieve a good precision. The system optimization (spinning reserve, reactive power, optimal planning,...) usually requires a lengthy iterative process.

7.10.1. Markov chains in stochastic power flow

One important contribution of this article is the use of cases for describing distributed generators with non discrete operational states. In wind or solar energy, it is not practical to take into account each single wind turbine in the simulation of a big power system. The use of cases along with its frequency of occurrence is a compact way to condense the information of turbines' operational point due to an uncontrollable primary energy, geographically related.

Markov chains are very adequate for handling transitions between states (for example, the change from available to unavailable operational state and vice versa). The main drawback of using only a reduced number of cases is that they must be chosen so that all significant operational states are included in the set. Some cases must be included because they happen very frequently (states with high probability) whereas others can be rare but they can harness system stability. Therefore, no-generation and full generation should be included as states.

Each combination of system states can be solved with a regular power flow and its probability and time variability can be obtained from the DTMC (Discrete Time Markov Chain). If the final grid state is dependent on the previous state, a continuation power flow should be run for each realizable state transition (squaring the number of required power flows).

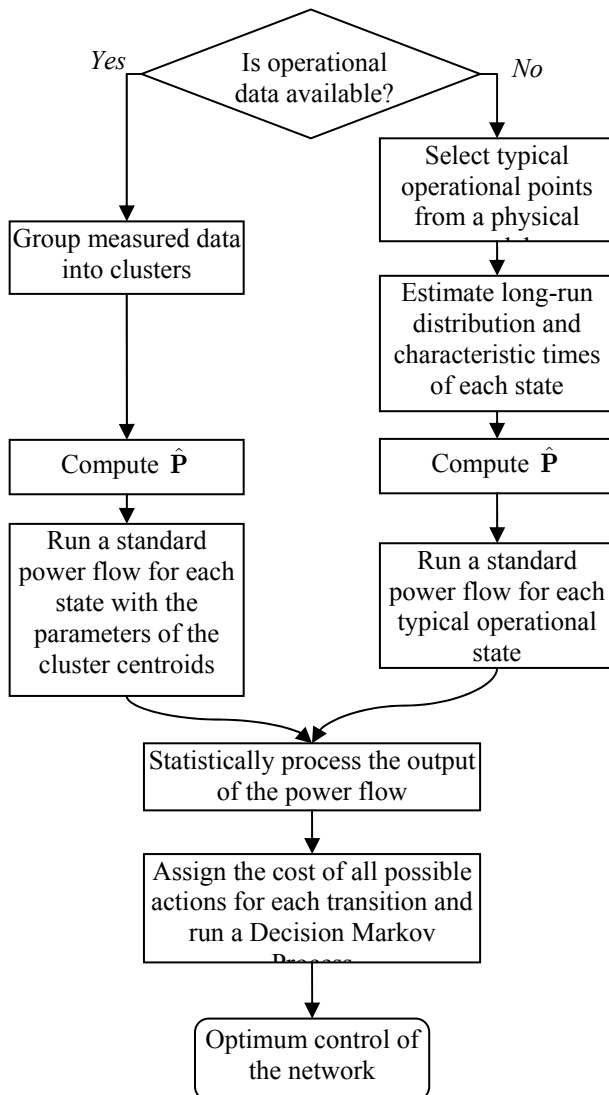


Fig. 134: Work flow for the proposed model.

The joint probability distribution of random variables is implicit in transition matrix \mathbf{P} , which is estimated from real data or from physical models. This is a desirable feature, since many statistical grid methodologies [349] suppose that random variables are not correlated (independent variables) whereas renewable generation is quite correlated in small geographic areas and loads are also quite correlated.

If each load and generator are discretized, for instance, into four states, the number of combinations are 4^n , where n is the number of stochastic variables considered. If the number of stochastic variables n is big, grouping highly related observations is necessary.

The combined use of discretization and cluster analysis allow to reduce the number of power flow runs compared to standard Monte Carlo Simulation [350]. The discretization and classification errors decrease considering more states.

Some statistical computer packages select the number of cases comparing the decrease ratio of the classification error when the number of states m are increased (i.e., including a new group in the data clustering process) [351]. Therefore, the number of states can be selected depending on the desired classification precision, the non-linear behavior of the electric grid (plausible topological changes in the grid, voltage collapse) and the data available to adjust the model parameters.

If there is enough data, the system state can encompass load and generation. Load is very weakly correlated with wind and wind generation and load can be regarded as independent random variables. The load is dependent of daylight and therefore, solar power is partially correlated to load. In the example of the following part, load and generation would be modelled as non-related Markov Chains and classified independently. The possible combinations of load and wind generation states are $N_{load} \cdot N_{wind}$ and tensor algebra can be used to compute efficiently the properties of the total system (see chapter 9 of [352]). Note that if load and generation are expressed in their respective canonical basis, the combined matrix is a diagonal with the eigenvalues of load and generation. Since $\hat{\mathbf{P}}$ is the matrix \mathbf{P} estimated from data, the probability of $\hat{\mathbf{P}}$ having two or more eigenvalues exactly the same tends to zero for increasing sets of data. Therefore, $\hat{\mathbf{P}}$ is diagonalizable in practice. Thus, the space requirements are proportional to the number of states and the matrix operations are trivial.

Since states of power generation are treated as Markov Chains, the variability of the load will be modelled with Markov States also. Therefore, the generation and consumption patterns are classified in a limited number of states, which are equivalent to transform a multidimensional continuous system into a discrete one. This makes the system tractable and it allows to obtain not only the probability density functions, but also the time variability. Therefore, it is possible to estimate the number of changes in tap changers, in capacitor banks and in the topology of the network.

To sum up, this model requires running just as many power flows as states has the system and it allows to derive easily and rigorously the probability of events. Each case can be solved with a standard power flow, considering non linear elements such as topological changes in the grid that depend on the system loads and generators.

The moments of random variables such as line power flow, generation and voltages can be computed directly from the probabilities of the cases. The continuous distribution of the network can be easily obtained from the cumulative density, adjusting an interpolating function to the case points (the probability density function is the derivative of the interpolating function).

Moreover, the allocation of spinning reserve due to wind power can be done using a Markov Decision Process. These processes can compute the optimum spinning reserve policy from the probability of wind generation variation, the cost of running the reserves and the eventual cost of insufficient reserve.

7.10.2. Simplified model of a wind farm to account active and reactive losses

The wind farm model employed in this section is based in [353, 354], where a fourth-pole equivalent representation is obtained from the electrical elements, the distributed layout of the turbines, the stochastic nature of power output and small-signal analysis of the grid.

In this section, an approximate representation with a shunt admittance and series impedance will be used to simplify the analytic expressions.

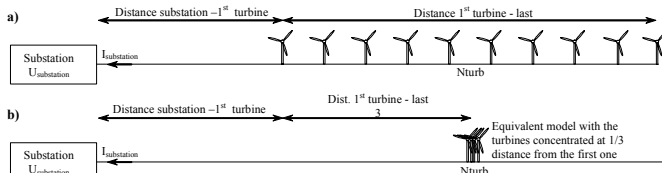


Fig. 135: Original and concentrated model of a MV circuit in a wind farm.

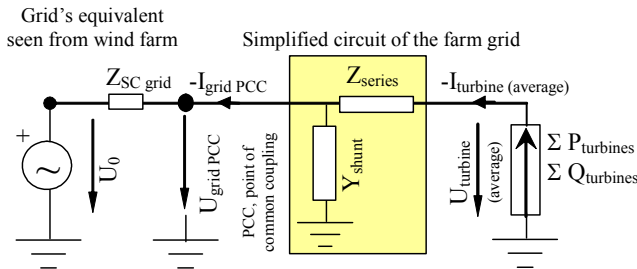


Fig. 136: Model of the farm using a fourth pole realization.

In the analyzed wind farms, the wind turbines are operated at a constant leading angle near $\varphi_0 \sim 0$ at low voltage (LV) side to increase reactive bonus. Therefore, the reactive power Q show a quadratic relationship with active power P due to series inductances and shunt stray capacitance of cables.

$$Q_{WT} \approx P_{WT} \tan(\varphi_0)$$

$$Q_{PCC} \approx -B_{shunt} U_{PCC}^2 + \Sigma Q_{WT} + X_{series} \frac{\Sigma P_{WT}^2 + \Sigma Q_{WT}^2}{U_{PCC}^2} \approx \quad (549)$$

$$\approx -B_{shunt} U_{PCC}^2 + \Sigma P_{WT} \tan(\varphi_0) + X_{series} (1 + \tan^2(\varphi_0)) \frac{\Sigma P_{WT}^2}{U_{PCC}^2}$$

$$P_{PCC} \approx \Sigma P_{WT} - R_{series} \frac{\Sigma P_{WT}^2 + \Sigma Q_{WT}^2}{U_{PCC}^2} - G_{shunt} U_{PCC}^2 \approx \quad (550)$$

$$\approx -G_{shunt} U_{PCC}^2 + \Sigma P_{WT} - R_{series} (1 + \tan^2(\varphi_0)) \frac{\Sigma P_{WT}^2}{U_{PCC}^2}$$

Where

ΣP_{WT} = sum of active power of all turbines (positive when generating)

ΣQ_{WT} = sum of active power of all turbines (positive if generators behave inductively)

P_{PCC} = Active power injected at PCC

Q_{PCC} = Reactive power injected at PCC

R_{series} and X_{series} are the real and imaginary part of Z_{series} , i.e. the resistance and reactance of the series equivalent.
 G_{shunt} and B_{shunt} are the real and imaginary part of Y_{shunt} , i.e. the shunt conductance and susceptance.

For instance, Fig. 137 shows the quadratic PQ relationship for a wind farm during one year (15 minutes measures). Its series inductance is about 16 % p.u. due to cable impedances and turbine ($U_{cc}=5,8\%$) and farm transformers ($U_{cc}=7,5\%$). The graph is scattered since U_{PCC} was variable and the value of φ_0 was adjusted at the end of each month to obtain the maximum reactive bonus according to Spanish tariff. The other two wind farms show similar relationships.

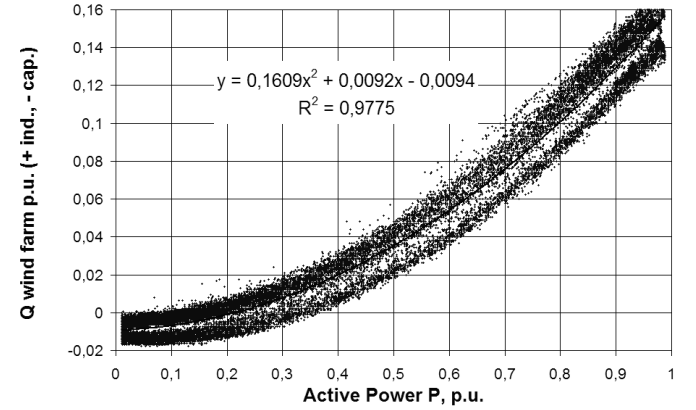


Fig. 137: PQ relationship of a wind farm at 220 kV node during one year

Even though the voltage inside the farm varies, it is expected to be near to assigned value at normal operation ($U_{turbine} \sim 1$ p.u.). This simplification is only a small source of uncertainty of the model since Z_{series} are expected small p.u. (around 0.12 p.u.) and Y_{shunt} is expected to be big (at least 20 p.u.). Standard UNE 206005 [355] assess the reactive power ability of wind farms at $U_{turbine} = 0,95, 1$ and $1,05$ p.u.

The parameters R_{series} , X_{series} , G_{shunt} and B_{shunt} of (549) and (550) can be derived from measures or from simulations at calm ($P_{WT} = 0$, $Q_{WT} = 0$) and full power with unity power ($P_{WT} = 1$ p.u., $Q_{WT} = 0$) with 1 p.u. voltage at PCC:

$$G_{shunt} = -P_{PCC} \Big|_{P_{WT}=0, Q_{WT}=0}$$

$$B_{shunt} = -Q_{PCC} \Big|_{P_{WT}=0, Q_{WT}=0} \quad (551)$$

$$R_{series} = 1 - P_{PCC} \Big|_{P_{WT}=1, Q_{WT}=0} - G_{shunt}$$

$$X_{series} = Q_{PCC} \Big|_{P_{WT}=1, Q_{WT}=0} + B_{shunt}$$

Taking into account the lines that connect the wind farms and the present unity power factor regulation at low voltage generator output, the reactive power of the three wind farms at PCC is:

$$Q_{PCC} \approx -0,008 U_{PCC}^2 + 0.0057 \Sigma P_{WT} + 0.1537 \frac{\Sigma P_{WT}^2}{U_{PCC}^2} \quad (552)$$

where ΣP_{WT} is the average per unit power of the wind turbines of the three farms. Note that (552) is estimated from nominal values of wind farm project whereas Fig. 137 (and similar graphs for the other two wind farms) are measured. The discrepancies are due to differences on real parameters compared to the values assumed, voltage at nodes of the wind farm below 1 p.u., operation of wind turbines with power factor below unity and model approximations.

Stand-by losses are smaller than the resolution of a standard power meter, making it difficult to guess from

measures. Therefore, active losses are computed from network and transformers parameters.

$$P_{PCC} \approx -P_{\text{stand-by losses}} + 0,9819 \frac{\sum P_{WT}^2}{U_{PCC}^2} \approx 0,9819 \frac{\sum P_{WT}^2}{U_{PCC}^2} \quad (553)$$

In this case, the equivalent parameters of the wind farm interior network are:

$$G_{\text{shunt}} \approx 0$$

$$B_{\text{shunt}} \approx 0,008 \text{ p.u.}$$

$$R_{\text{series}} \approx 1 - 0,9819 - 0 = 0,1781 \text{ p.u.}$$

$$X_{\text{series}} \approx 0,1537 + 0,008 = 0,1545 \text{ p.u.}$$

$$\varphi_0 \approx \text{ArcTan}(0,0057) \approx 0,0057 \text{ rad}$$

7.10.3. Essence of the new approach to probabilistic power flow

In essence, stochastic load-flow (SLF) studies assumes that the long-term nodal generation and load vector varies about an expected operating point. The SLF algorithm is easily built from existing state-estimator algorithms [356], but the drawback of the SLF is that it handles only Gaussian nodal probability density function (PDF) data for practical system sizes.

Another approach, commonly referred to as the probabilistic load-flow (PLF) algorithm, uses linear or quadratic approximations of the network behaviour. For realistic system sizes, independence of nodal power injections must be assumed in order to be able to apply convolution techniques [349].

The new approach proposed in this paper does not rely on convolution, independence of random variables or linear behavior of the power system. The new method does rely on the fact that power injections are (highly) related and some patterns can be noticed.

The parameters that affect demand curve are well established (week day or bank holyday, season, time of the day, weather temperature, type of consumers, ...). Wind generation and other types of dispersed generation show strong links due to geographical and meteorological links. Therefore, the load and the disperse generation can be classified into a (reduced) set of behaviour patterns.

Each combination of load and generation patterns represents the typical operation of the power system during some periods. Therefore, a standard (deterministic) power flow can be employed to solve each typical operation. Afterwards, a statistical analysis can be carried out to measure system performance and to optimize the control or the design of the system.

The essence of this new method is a Monte Carlo analysis where the cases are not randomly generated. First, data is classified to select the most representative cases to be simulated, giving further insight in the relationship of the players of the power system (i.e. data mining). Then, a conventional power flow is run with the values of the center of the class (if the previous state of the network is influential, a continuation power flow can be run for each pattern transition). Finally, the results of the simulation are statistically analyzed (usually, to optimize the design or the operation of the network).

Since there are very powerful classification algorithms that can handle efficiently very large amounts of data, the number of time-consuming power flow runs are highly decreased, resulting in an important reduction of computing burden compared to conventional Monte Carlo. Usually, the number of patterns is small enough for all cases to be simulated.

Other advantage of the proposed method is that electrical engineers are used to the simulation of cases (worst scenario, typical seasonal scenario,...). Therefore, this analysis is more familiar to them.

If the generation is not correlated at all, the procedure is still valid but the computing savings decrease. The number of cases to represent the operation of N generators with a given accuracy when they are not related is proportional to N^2 and the method degenerate in conventional Monte Carlo. Recall that if the random variables were independent and the system behaviour were sufficiently linear (no parameter violations, bottlenecks or topological changes in the network are expected) techniques such as convolution and two point estimates would be preferable [348].

The modelization of the system variability through Markov chains allows to obtain not only the static system performance but also its slow-dynamic behaviour (slow enough for the algebraic power flow equations to remain valid).

Markov chains, in the way they are applied in this paper, can be thought as a system of stochastic differential equations which mimics the measured evolution of loads and generators. The network response to loads and generation evolution is computed based on the power flow equations.

In fact, accounting the previous system state makes possible to include the system operator action, provided it can be specified mathematically (for example, with a set of fuzzy rules based on expert knowledge).

7.10.4. Description of the group of wind farms

A system with three wind farms will be employed to test the model described in previous subsections. The model is adjusted from one year data and some measures of the goodness of the fit are estimated. In particular, the exponential distribution of the permanence time in states is contrasted with real data. The uncertainty of the transition probabilities and the estimation of uncommon events are also studied. Some theoretical properties obtained from the model are also checked with experimental data.

Six wind farms totalling 251,3 MW are connected to a PCC at transmission level (220 kV). However, only data from 2/3 of the wind generation was available for this study. Therefore, short-circuit impedances at PCC have been scaled proportionally to account that the other farms at PCC will probably have an output similar to the measured ones (per unit short circuit impedance at PCC is computed based on installed wind power instead of measured wind power). The equivalent layout is shown in Fig. 138.

The effect of wind power variability is investigated on the voltage and the number of tap changes at the main transformer. The only available data is the active and reactive power output of the wind farm at connection buses. In case reactive power is not available or it is a parameter to be

optimized, it can be derived from a wind farm model.

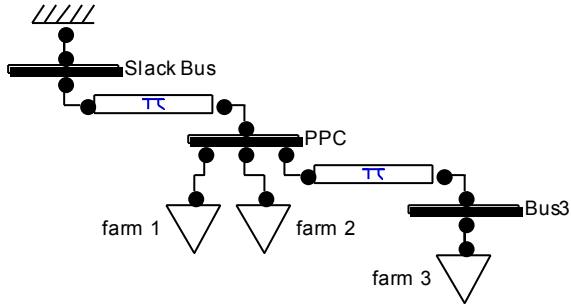


Fig. 138: PSAT model for the tree wind farms, modelled as PQ nodes connected to the PCC

7.10.5. Markov model obtained from conventional clustering

Fig. 139 shows the array of all the bivariate scatterplots between active power of the tree farms, along with a univariate histogram for each active power. The classification of each point is codified with different colors in the scatterplots. Fig. 139 show the values of the centroids of each group (i.e., their mass center). Due to the fact that the wind farm power output is highly correlated, only eight states have been used in the clustering algorithm obtaining 0.011 p.u. average classification error.

This example shows that if there is a high degree of correlation between variables, clustering can decrease notably the number of states to be considered (compare 8 to $4^3=64$ estates). In [357], an example of power classification of 14 wind farms in an area of about 100 km of diameter is shown.

The input of the clustering process can be only the active power or also the reactive power of the wind farms. Generally, the inclusion of the wind farm reactive power Q does not decrease the performance of the clustering process since P and Q are usually highly related. For a fixed power factor regulation, the reactive power Q can be computed from the active power P with acceptable precision.

If Q is controlled according to network parameters or a scheduled planning, a suitable approach is to model such relationships directly in the power flow run. Occasionally, Q can depend greatly on unmeasured parameters or unknown control policies and it must be statistically characterized. In those situations both P and Q are the inputs of the clustering process at the cost of increasing the number of groups to maintain the classification error.

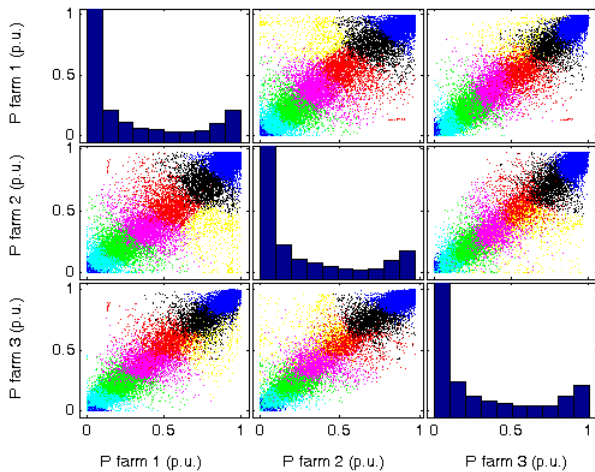


Fig. 139: Scatterplots between active farm power P and their histogram (classes are shown in blue, green, magenta, red, black and dark blue).

Table VIII is the result of a conventional clustering algorithm whose inputs are the active P and reactive Q powers measured at the billing meter of three wind farms. If only active powers are used for the clustering process, the output is very similar because P and Q are highly related in this case.

TABLE VIII: CENTROIDS OF P AND Q VALUES P.U. OF THREE WIND FARMS

#	P ₁	Q ₁	P ₂	Q ₂	P ₃	Q ₃	Freq.
1	0.0112	-0.0036	0.0119	-0.0100	0.0124	0.0009	37.9%
2	0.1092	-0.0061	0.1083	-0.0205	0.1156	0.0040	15.14%
3	0.2385	0.0024	0.2199	-0.0154	0.2402	0.0114	10.12%
4	0.4026	0.0206	0.3621	-0.0045	0.3995	0.0280	8.00%
5	0.5409	0.0435	0.5641	0.0203	0.5850	0.0587	5.97%
6	0.8152	0.1012	0.3269	-0.0035	0.6356	0.0702	1.77%
7	0.7624	0.0922	0.7238	0.0465	0.7711	0.1011	6.74%
8	0.9199	0.1354	0.8941	0.0781	0.9268	0.1437	14.37%

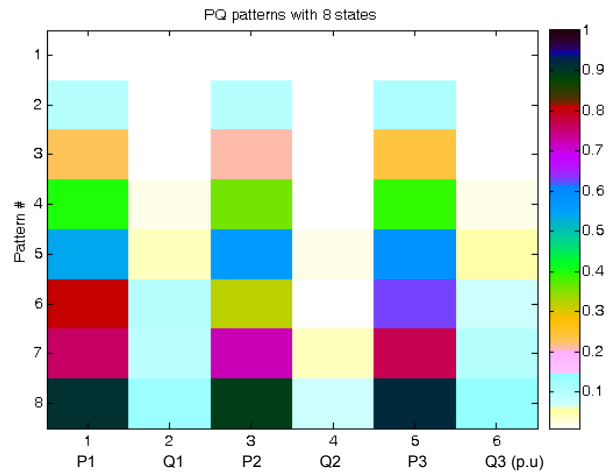


Fig. 140: Color graph of centroids of P and Q powers of table I.

Fig. 140 is a color graph representation of the centroids of the eight patterns obtained from the clustering process.

Fig. 141 is the histogram of the eight patterns obtained from the clustering process from data of a year measured every 15 minutes. The no-load and low load states are the more frequent (37.9% and 15.14%) followed by full load (14.37%). This is typical of low wind resource wind farms. The clustering algorithm has selected the pattern #6, which corresponds to high generation at the first one, low generation at the second wind farm and middle generation at the third one. The selection of this pattern decrease the total classification error, even though it represents only 1,77 % of time operation.

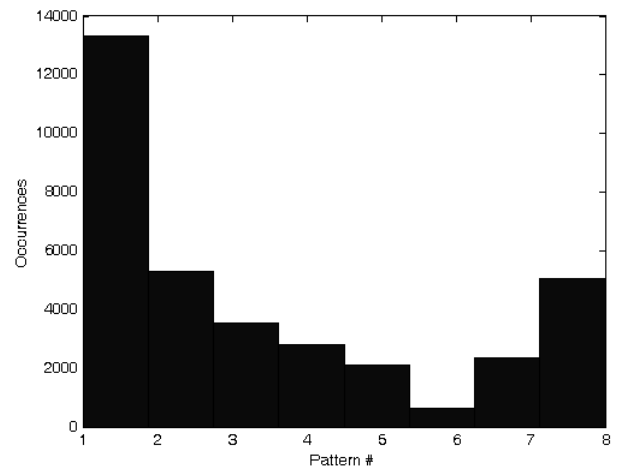


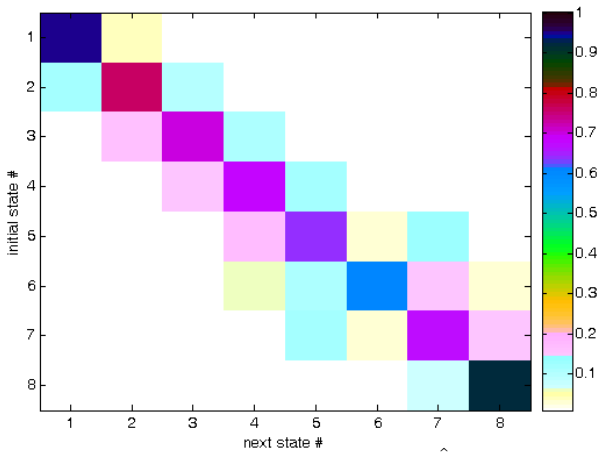
Fig. 141: Histogram of the states in data from a whole year operation.

The study of the transition rates for 15 minutes interval data reveals that the more stable states are the first and the last (full and no generation), whereas a transition to immediately upper or lower states are noticeable. However, transitions to non-adjacent states are very low except in states 6 and 7 (these states correspond to different wind directions, which are very steady in the zone).

The probability transition matrix $\hat{\mathbf{P}}$ is estimated from real data in Table IX. Fig. 142 shows that transitions with immediately upper and lower states are relatively frequent (light gray), but jumps to far states are scarcely probable (shades of white). Note that the rows correspond to the initial state and the columns correspond to the state of the next interval. Thus, the probability of going from state 5 to state 7 in one step is stored in row number 5 and column number 7.

State 6 reflects the operation of farm #2 at unusual low power (only 1,77 % of occurrences from Fig. 141). The probability transition matrix shows that jumps between states 5 and 7 states are more probable than jumping to the adjacent state 6 (unusual low power at wind farm 2 and high power at farm 1).

The unobserved transitions from state i to j of Table IX, $F_{ij} = 0$, can be due to real unfeasibility or to the limited available data (for example, infrequent transitions of sporadic states). An improved estimation can be employed if unobserved transitions are feasible even though they have not been observed because they are very rare events and data record, short.

Fig. 142: Color map representation of transition matrix $\hat{\mathbf{P}}$.TABLE IX: INITIAL PROBABILITY TRANSITION MATRIX $\hat{\mathbf{P}}$

to \ From state	1	2	3	4	5	6	7	8
1	0.9510	0.0472	0.0015	0.0001	0.0002	0	0	0
2	0.1201	0.7646	0.1074	0.0064	0.0006	0.0006	0.0004	0
3	0.0025	0.1693	0.7004	0.1156	0.0068	0.0034	0.0014	0.0006
4	0.0011	0.0057	0.1565	0.6899	0.1216	0.0181	0.0057	0.0014
5	0.0005	0.0005	0.0110	0.1760	0.6419	0.0324	0.1359	0.0019
6	0	0.0016	0.0144	0.0674	0.1124	0.6116	0.1541	0.0385
7	0	0.0017	0.0008	0.0051	0.1284	0.0363	0.6755	0.1521
8	0	0	0	0.0004	0.0010	0.0044	0.0721	0.9221

If $F_{ij} = 0$, the transition probability \hat{p}_{ij} is bound to $[0, 1 - (1 - \beta_{cl})^{1/F_i}]$ with confidence level β_{cl} (F_{ij} is binomially distributed) [297]. Thus, the null elements of \hat{p}_{ij} could be

substituted by a value in the interval $[0, 1 - (1 - \beta_{cl})^{1/F_i}]$ and the rest of the elements rearranged to make $\sum_{j=1}^m \hat{p}_{ij} = 1$. However, the use of a random point in the interval introduces bias in the estimation (usually, pessimistic overestimation of extreme variability).

The unbiased estimation of \hat{p}_{ij} is zero for unobserved transitions, but its uncertainty is inversely proportional to the number of occurrences of state F_i because their transition probability \hat{p}_{ij} is bound to $[0, 1 - (1 - \beta_{cl})^{1/F_i}] \approx [0, -F_i^{-1} \ln(1 - \beta_{cl})]$ with confidence level β_{cl} .

Characteristic times of the system (eigenvalues of $\hat{\mathbf{P}}$) and limiting distribution of states are continuous functions of matrix elements and the effect of almost zero elements are not important. But a rare transition can have very high cost associated in the optimization algorithm (for example, a sudden loss of all wind generation which can cause a blackout in an island). Therefore, a rare transition might dominate optimization.

There is a tradeoff between the number of classification states and the uncertainty of transition matrix. The use of a bigger number of states decreases classification error but increases uncertainty of infrequent transitions.

If there is a bottleneck or an important topological change when an atypical generation pattern occurs, then a big number of states is advisable because increasing the uncertainty in $\hat{\mathbf{P}}$ is acceptable. If there are no bottlenecks or violations out of the ordinary and the main purpose of the study is the effects of exceptional events (for example, assessment of contingencies, optimization of the spinning reserve allocation,...), then a reduced set of states can be enough.

The unobserved transitions are in *italics* in Table IX and Table X. Their bounds range from $\hat{p}_{16} \in [0, 2 \cdot 10^{-4}]$ to $\hat{p}_{61} \in [0, 48 \cdot 10^{-4}]$ for 95% confidence level. For a better estimation of such uncommon events, similar transitions can be joined (for example, estimate together the transition from low power –states 1 or 2– to high power –states 6, 7 or 8–). Therefore, transition probability from states $\{1, 2\}$ to $\{6, 7, 8\}$ would be assumed to be the same. The transitions which are similar can be inferred from the cluster dendrogram. Note that the numbers in italics are estimates of unobserved transitions based in available knowledge and some other elements have been adjusted for each row to sum 1.

TABLE X: PROBABILITY TRANSITION MATRIX $\hat{\mathbf{P}}$
(ADJUSTED JOINING SIMILAR INFREQUENT TRANSITIONS)

to \ From state	1	2	3	4	5	6	7	8
1	0.9510	0.0472	0.0013	0.0001	0.0001	0.0001	0.0001	0.0001
2	0.1201	0.7643	0.1074	0.0064	0.0006	0.0006	0.0003	0.0001
3	0.0025	0.1693	0.7004	0.1156	0.0068	0.0034	0.0014	0.0006
4	0.0011	0.0057	0.1565	0.6899	0.1216	0.0181	0.0057	0.0014
5	0.0005	0.0005	0.0110	0.1760	0.6418	0.0324	0.1359	0.0019
6	0.0001	0.0015	0.0144	0.0674	0.1124	0.6116	0.1541	0.0385
7	0.0003	0.0015	0.0008	0.0051	0.1284	0.0363	0.6755	0.1521
8	0.0001	0.0001	0.0001	0.0002	0.0010	0.0044	0.0720	0.9221

7.10.6. System dynamics and equivalent stochastic differential equations

The use of Discrete Time Markov Chains, (DTMC) implies that the permanence time in a state is distributed

geometrically or as an exponential random variable if the time is considered continuous (Continuous Time Markov Chains, CTMC).

For DTMC, the probability of being in state i during k measuring intervals before changing to other state is a geometric random variable with parameter $p = 1 - p_{i,i}$, where $p_{i,i}$ is the i diagonal element of the probability transition matrix \hat{P} of Table X. The number of intervals k in a time interval t is $k = t \cdot f$, where f is the frequency of the recorded data.

The probability of permanence in state i more than k measuring intervals ($k = t \cdot f$) is the complementary cumulative density function of a geometric random variable:

$$\Pr (X[j] = i, j = 0, \dots, k | X[0] = i) = p_{i,i}^k = p_{i,i}^{t \cdot f} = e^{-t/\tau_i} \quad (554)$$

$$\tau_i = \text{characteristic or decay time of state } i = \frac{-1}{f \ln(p_{i,i})}$$

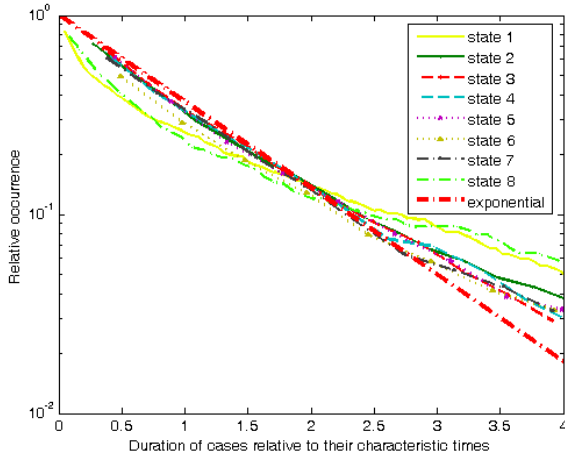


Fig. 143: Probability of permanence more than a given time in each state (complementary cumulative distribution function of permanency time) (x axis scaled to the characteristic time $\tau_i = 1/\ln(p_{i,i})$).

The average permanency time μ_i in state i can be computed using (555)

$$\begin{aligned} \mu_{i,i} &= \text{Expected Value}(\text{time staying in state } i) = \\ &= \frac{1}{f} \text{Expected Value}(k \text{ intervals staying in state } i) = \\ &= \frac{1}{f} E(k | X[k] \neq i, X[j] = i, j = 0, 1, \dots, k-1) = \frac{1}{(1 - p_{i,i})f} \quad (555) \end{aligned}$$

Wind power measures are the average value during a time interval. But if instantaneous wind power is considered, wind power and time are continuous variables. Therefore, the mean value computed with continuous time is (555)

$$\begin{aligned} \mu_{i,i} &= \text{Expected Value}(\text{time staying in state } i) = \\ &= E(T | X[T] \neq i, X[t] = i, t < T) = \int_0^\infty t \frac{1}{\tau_i} \exp(-t/\tau_i) dt = \tau_i \quad (556) \end{aligned}$$

The characteristic time τ_i can be seen as the average time spent in a state i before leaving it or, alternatively, as the time where the probability of remaining in state i at time $t = \tau_i$ is $1/e = 36,79\%$.

$$\begin{aligned} \text{Probability}(\text{staying exactly } k \text{ intervals in state } i) &= \\ = \Pr (X[k] \neq i, X[j] = i, j = 0, \dots, k-1 | X[0] = i) &= \\ = p_{i,i}^{k-1} \cdot (1 - p_{i,i}) = p_{i,i}^k \cdot (1/p_{i,i} - 1) \quad (557) \end{aligned}$$

The expression (557) can be rewritten approximately in terms of characteristic time of the state τ_i

$$\begin{aligned} \text{Probability}(\text{staying exactly } k \text{ intervals in state } i) &= \\ = p_{i,i}^k \cdot (1/p_{i,i} - 1) = \exp\left(-\frac{k}{f \tau_i}\right) \left[\exp\left(\frac{1}{f \tau_i}\right) - 1\right] &= \\ = \exp\left\{-\frac{k}{f \tau_i} + \ln\left[\exp\left(\frac{1}{f \tau_i}\right) - 1\right]\right\} \quad (558) \end{aligned}$$

Therefore, the graph of the relative occurrences of staying k intervals in state i is a straight line in a semi-logarithmic plot with slope $-1/\ln(p_{i,i})$ and intercept with vertical axis $1/p_{i,i} - 1$. In order to check the goodness of the fit, Fig. 144 shows the probability mass distribution of permanency time in each state with the horizontal axis is scaled by $-1/\ln(p_{i,i})$ and with the relative occurrence scaled by $1/p_{i,i} - 1$. In Fig. 144, the $\exp(-t)$ function (a straight dashed line) has been included to compare experimental data with theoretical distribution. Since states 1 and 8 have long characteristic times and experimental data is limited to one year, the occurrence of long periods with the same states is scarce and it shows a high variability (for example, the permanence during exactly 80 quarters of hour in state 1 can happen from 0 to 3 times in a year).

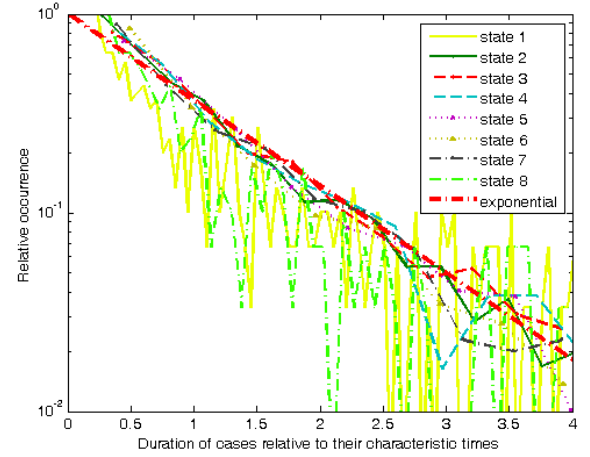


Fig. 144: Probability mass distribution of permanency time in each state (x axis scaled to $1/\ln(p_{i,i})$ and y axis scaled to $1/p_{i,i} - 1$).

\hat{P} contains much more information than just the distribution of time permanence in states. The rest of this section will look into the dynamics of the system. Note that states are not sharply defined and time is not discrete because wind farm power output is a continuous varying property.

In the discrete case, a DMTC corresponds to the forward m order difference equation (559) with the initial probability distribution $\mathbf{x}(0) = [x_1(0), x_2(0), \dots, x_m(0)]$ as initial condition. \mathbf{P} is the one-step transition probability matrix [345].

$$\mathbf{x}(k+1) = \mathbf{x}(k)\mathbf{P} \quad (559)$$

Therefore, the probability distribution k instants later can be computed as:

$$\mathbf{x}(k) = \mathbf{x}(0)\mathbf{P}^k \quad (560)$$

The stochastic matrix \mathbf{P} has a dominant eigenvalue $\lambda_1 = 1$ and it is irreducible, recurrent and acyclic in wind farm characterization. Since \hat{P} is the matrix \mathbf{P} estimated from data, the probability of \hat{P} having two or more eigenvalues exactly the same tends to zero for increasing sets of data (eigenvalues are continuous functions of matrix elements). Therefore, \hat{P} is diagonalizable in practice.

The solution (560) can be easily expressed in the coordinates specified by the left eigenvectors \mathbf{Y} of $\hat{\mathbf{P}} = \mathbf{Y}^{-1} \text{diag}(\hat{\lambda}_i) \mathbf{Y}$, where $\text{diag}(\hat{\lambda}_i)$ is the diagonal matrix containing the eigenvalues $\hat{\lambda}_i$ of $\hat{\mathbf{P}}$. The first eigenvalue is $\hat{\lambda}_1 = 1$ and the rest are smaller.

If the state probabilities are expressed in the canonical coordinates specified by basis \mathbf{Y} : $\mathbf{v}(k) = \mathbf{x}(k) \mathbf{Y}$, then the dynamics of the system are much simpler:

$$\mathbf{v}(k) = \mathbf{v}(0) [\text{diag}(\hat{\lambda}_i)]^k = [v_1(0), v_2(0), \dots, v_m(0)] \text{diag}(\hat{\lambda}_i^k) \quad (561)$$

In other words, the dynamics in these coordinates can be expressed in independent scalar equations corresponding to first order systems of characteristic time $\hat{\tau}_i$:

$$v_i(k) = v_i(0) \hat{\lambda}_i^k = v_i(0) \hat{\lambda}_i^{t/\hat{\tau}_i} = v_i(0) \cdot \exp(-t/\hat{\tau}_i) \quad (562)$$

$$\hat{\tau}_i = \frac{-1}{f \ln \hat{\lambda}_i} \quad (563)$$

The first row of \mathbf{Y} is the limiting probability, π_1 or just π (eigenvector corresponding to unity eigenvalue). When the initial probability distribution is π_1 , the distribution doesn't change in time ($\hat{\tau}_1 = 1/0 = \infty$). The rest of distributions π_i decay with characteristic time $\hat{\tau}_i$ (at $t = 3 \cdot \hat{\tau}_i$, the probability distribution π_i has faded away to 5% of the initial value).

The forward equations of a CMTC correspond to the Chapman-Kolmogorov Nth order differential equation (564). \mathbf{Q} is the generator matrix of the CMTC. \mathbf{Q} can be estimated as $\hat{\mathbf{Q}} = f \ln(\hat{\mathbf{P}}) \sim f(\hat{\mathbf{P}} - \mathbf{I})$, \ln is the matrix natural logarithm, \mathbf{I} is the identity matrix and f is the frequency of recorded data.

$$\frac{d}{dt} \mathbf{x}(t) = \mathbf{x}(t) \mathbf{Q} \quad (564)$$

Its solution is $\mathbf{x}(t) = \mathbf{x}(0) e^{\mathbf{Q}t} = \mathbf{x}(0) \mathbf{P}^{f \cdot t}$, where $e^{\mathbf{Q}t}$ is the exponential of matrix \mathbf{Q} t . If $\hat{\mathbf{P}}$ is diagonalizable, $\hat{\mathbf{Q}}$ is also diagonalizable and it has eigenvalues $f \ln \hat{\lambda}_i = 1/\hat{\tau}_i$ and the same eigenvectors than $\hat{\mathbf{P}}$. Therefore, the equations of continuous time dynamics in the canonical coordinates of $\hat{\mathbf{Q}}$ (565) are equivalent to (562), the discrete case [335].

$$v_i(t) = v_i(0) \cdot \exp(-t f \ln \hat{\lambda}_i) = v_i(0) \cdot \exp(-t/\hat{\tau}_i) \quad (565)$$

Therefore, DMTC and CMTC are equivalent. The computational burden is smaller for DMTC and discrete data is better suited for $\hat{\mathbf{P}}$ estimation. CMTC gives deeper insight on system dynamics, mimics better its continuous behavior and it can be used to derive easier some properties of the system. Moreover, CMTC approach is more familiar for control engineers.

Note that other numerical approaches (different from eigenvalue calculus) can be computational more efficient in some applications [358].

7.10.7. Permanence time in a state

The use of Markov Chains implies that the permanence time in a state is distributed geometrically if time is discretized or, equivalently, as an exponential random variable if the time is a continuous variable.

Fig. 145 confirms the assumption that a Markov Chain can approximately model the behavior of the system since the distribution of permanency time in one state approximately corresponds to a geometric random variable (for DMTC) or exponential random variable (for CMTC). This can be checked in Fig. 145, where the probabilities of remaining in the same state versus time shows an exponential relationship (i.e. distribution is approximately a straight line in a semi-log

plot whose slope corresponds to the inverse of the standard characteristic time).

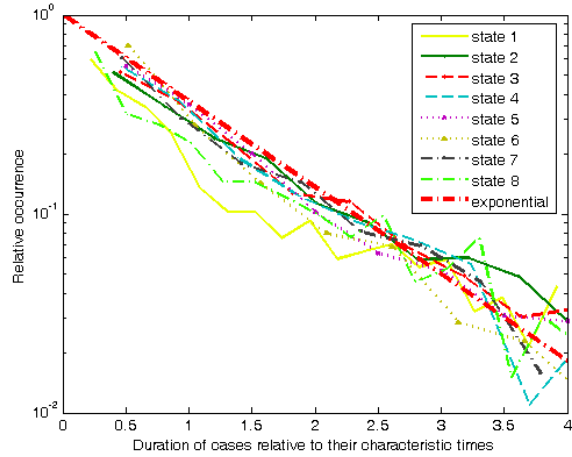


Fig. 145: Probability mass distribution of permanency time in each state (normalized scaling time by state characteristic time).

The main discrepancies are at the distribution tail in rare long-lasting periods at full or no generation (states 1 or 8) due to very stable meteorological situations. For example, period of almost 7 days in state 1 (calm) have occurred in one year data. These outliers caused states 1 (calm) and 8 (full generation) have overestimated characteristic time.

The geometrical distribution is a special case of negative binomial distribution with parameter $r = 1$. A negative binomial distribution has been adjusted and parameter r ranges from 0,5 to 3,5, depending on the state number (the 95% confidence interval did not include $r = 1$). The negative binomial distribution is an alternative to the geometric distribution when the occurrence frequency (or transition probability) varies in time.

The deviation of permanence time from geometrical distribution is due to:

- The state transition rates depend physically on meteorological conditions and on wind farm availability. For example, meteorological stable conditions at calm or high winds can eventually last long periods.
- The “hard” classification of a measurement into a solo state increases observed transitions in the state, especially if the measurement is near two cluster borders. This can explain that permanence times of states 2 to 7 decrease steeper than exponential model (r ranges from 2 to 3).
- The estimation of system characteristic times with formulas (557) to (554) is an oversimplification. In fact, the Markov Chains are “centrifugal” in the sense that when the system is at partial generation, the system tends to evolve to the first (calm) or last (full power) states. This can explain why the first and last states show a slower decrease of permanence times compared to exponential (geometrical) distribution.
- The permanence time in a state is a concept easy to visualize but it does not correspond to the physical behavior: the power output of the farms is continuously evolving. Fig. 145 shows the time that power output is bound to cluster area, but system dynamics is more complex.
- The concept of permanence time is not straightforward in fuzzy clustering. The membership level of an observation to a state can increase or decrease from an instant to the next. Therefore, the system can be thought to stay in the state with probability equal to the minimum of the pre

and post membership levels. Thus, a consistent stochastic measure of time permanence must be defined (for example, the time interval where the membership is above a threshold level can be considered the permanence time with probability equal to the mean value of the membership to that state).

- An adequate test to check if Markov Chain is a suitable model must employ full dynamics, not only the permanence in a state that is physically evolving.

TABLE XI: AVERAGE PERMANENCE IN STATES (IN HOURS)

State	Maximum likelihood estimation	Lower 95% confidence interval	Upper 95% confidence interval	Equation (555) $\frac{1}{(1-p_{ii})f}$	Equation (558)
1	5.1066	4.7362	5.5224	5.1066	5.3839
2	1.0621	1.0056	1.1235	1.0621	1.1834
3	0.8345	0.7866	0.8870	0.8345	0.9544
4	0.8065	0.7555	0.8628	0.8062	0.9276
5	0.6981	0.6507	0.7508	0.6981	0.8122
6	0.6436	0.5696	0.7331	0.6436	0.7357
7	0.7705	0.7188	0.8280	0.7705	0.8838
8	3.2029	2.9084	3.5448	3.2112	3.4453

An alternative to check model accuracy valid for “hard” clustering is to compare the theoretical and observed distribution starting from each state for various time spans (the error measure can be the mean squared difference of theoretical and observed histograms). When fuzzy clustering is used, each time the system is in a combination of states up to a certain degree and there is not possible to compute histograms in the usual way.

A measure of fit goodness that works even with fuzzy clustering is to compare the transition matrix for a time span of k measuring intervals computed from the one-step transition matrix $\hat{\mathbf{P}}$ power k times and estimating a new matrix $\hat{\mathbf{P}}_k$ based on transitions from initial states to states k intervals forward. The measure error can be $\sqrt{|\hat{\mathbf{P}}_k - (\hat{\mathbf{P}})^k| / s}$

However, the system stays occasionally long time in full or no generation due to stable meteorological conditions which are maintained for long time. Moreover, if the wind farm is unavailable for long time, it can distort the distribution of no generation. This is the reason that the actual permanence times are somewhat different from the times computed from transition matrix.

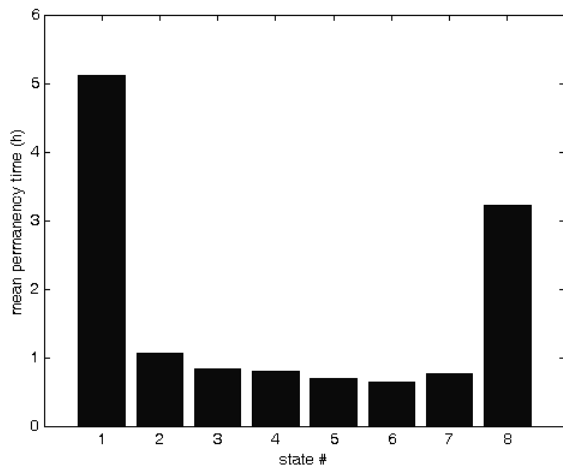


Fig. 146: Average permanency time in each state (in hours) from (555).

Fig. 146 shows the residence times, where it can be seen that zero and full generation are the most stables states. In fact, the permanency time in such estate is computed as it were a Poisson process (permanency time exponentially statistically distributed). This is characteristic of the Markov chain approach used to characterize wind variability.

Application example II: Isolated system with storage

The optimal stochastic control of load consumption of an isolated system with solar and wind generation and storage should include cost of not being able to supply demand and the ageing due to depth of discharge of batteries. The main energy sources (solar radiation and wind speed) are not controllable and some loads can be deferred or even not supplied in case of energy shortage. The control must weight the probability of not supplying critical loads; the efficiency of supplying energy from the storage and the aging of the storage system.

7.10.8. Battery State of Charge

The evolution of the battery state of charge (SOC) can be modeled with the Ah model [359]. In this model, the battery is recharged and discharged at gross powers P_{charge} and P_{disch} . The efficiency of the process is η_{charge} and η_{disch} respectively, which depend on the current. The auto-discharge is proportional to SOC at rate δ_{bat} . Thus, the differential equation of the battery dynamics is (566).

$$\frac{d}{dt}SOC = \lambda_{bat} - \delta_{bat} \cdot SOC \quad (566)$$

where the SOC variation rate due to charge or discharge is, in Ah units:

$$\lambda_{bat} = I_{charge} \eta_{charge} (I_{charge}, SOC) + \frac{I_{disch}}{\eta_{disch} (I_{disch}, SOC)} \quad (567)$$

TABLE XII: PARAMETERS OF THE BATTERY IN THE AH MODEL

Variable	Significance	Range
SOC	State Of Charge of the Battery (in Ah units)	100~2000 Ah
λ_{bat}	Instantaneous rate of variation of SOC due to charge or discharge	
δ_{bat}	Auto-discharge rate per time unit (about 3-10 % per month)	$4 \cdot 10^{-5} \sim 10^{-4}$ hour ⁻¹
P_{charge}	Gross input power into converter at AC terminals when charging the battery. Sign convention: positive.	$0 \sim \frac{SOC_{max} U_{bat}}{t_{min charge}}$
P_{charge}'	Power at battery terminals while charging. Sign convention: positive.	
P_{disch}	Gross output power from converter at AC terminals when discharging the battery. Sign convention: negative.	$0 \sim \frac{SOC_{max} U_{bat}}{t_{min discharge}}$
P_{disch}'	Power output from battery terminals while discharging. Sign convention: negative.	
$\eta_{converter}$	Efficiency of the system composed by the inverter and charge regulator.	0.9~0.95
η_{charge}	Efficiency of the battery during charge	0.7~0.9
η_{disch}	Efficiency of the battery during discharge	0.7~0.9
$U_{battery}$	Voltage at battery terminals	1.7 ~ 2.3 V per cell
I_{charge}	Current pumped into the battery while charging. Sign convention: positive.	0~1000 A
$I_{discharge}$	Current drawn from the battery at discharge. Sign convention: negative.	0~-1000 A

The electrical power at battery terminals can be computed from absorbed power of converter/charger and its efficiency:

$$P_{charge}' = P_{charge} \eta_{converter}(P_{charge}) \quad (568)$$

$$P_{disch}' = P_{disch} / \eta_{converter}(P_{disch}) \quad (569)$$

Thus, the currents at battery terminals when charging or discharging are, respectively:

$$I_{charge} = \frac{P_{charge}'}{U_{battery}(SOC, P_{charge}')} \quad (570)$$

$$I_{disch} = \frac{P_{disch}'}{U_{battery}(SOC, P_{disch}')} \quad (571)$$

Since the battery charging and discharging is relatively slow, the Ah model is accurate enough in hybrid power systems [360]. However, if the batteries are quickly charged and discharged, other models such as the Kinetic Battery Model (KiBaM) are more accurate. A very simple example of battery control with Markov Decision Process (MDP) can be found in [361].

7.10.9. Probabilistic discretized model of SOC

A stochastic model of the state of charge is suitable for the optimal control of the battery with MDP since the primary energy source is random, the battery model can have uncertainties and can suffer from aging.

In the approach of this paper, the battery status is classified in N states. Each state $i = 1$ to N is characterized by a SOC in ascending order, $soc_{i-1} < soc_i < soc_{i+1}$. The first state is the minimum battery charge without severe lifespan loss ($soc_1 = soc_{minimum\ allowed}$) and the last state corresponds to full charge ($soc_N = 1$ p.u.).

The probability that SOC is in bin soc_i is denoted by $x_i^{bat} = \Pr(SOC = soc_i)$, where $\Pr(\cdot)$ stands for probability. The row vector of probabilities of all battery states is denoted by $\mathbf{x}^{bat} = [x_1^{bat}, x_2^{bat}, \dots, x_N^{bat}]$. The derivative of the probability row vector is $\frac{d}{dt}\mathbf{x}^{bat} = [\frac{d}{dt}x_1^{bat}, \frac{d}{dt}x_2^{bat}, \dots, \frac{d}{dt}x_N^{bat}]$.

The forward equation of a continuous time Markov chain corresponds to the Chapman-Kolmogorov Nth order stochastic differential equation. In matrix notation, the dynamics of the stochastic system can be expressed in form of the generator matrix of the underlying Markov chain.

$$\frac{d}{dt}\mathbf{x}^{bat} = \mathbf{x}^{bat} \mathbf{Q}^{bat} \quad (572)$$

$\mathbf{Q}^{bat} = [q_{i,j}^{bat}]$ is the generator matrix of the CMTC and it can be inferred from system dynamics (566). To transform the deterministic formulation (566) into probabilistic formulation (573), the value of deterministic variables are substituted by the averages of the corresponding random variables, denoted by brackets $\langle \cdot \rangle$.

$$\frac{d}{dt}\langle SOC \rangle = -\lambda_{bat} \cdot 1 - \delta_{bat} \cdot \langle SOC \rangle \quad (573)$$

The sum of probabilities of all states sum unity, $\sum_{i=1}^N x_i^{bat} = 1$, and the expected value of SOC is $\langle SOC \rangle = \sum_{i=1}^N soc_i x_i^{bat}$. The fact that all state probabilities sum unity also implies:

$$\sum_{i=1}^N x_i^{bat} = 1 \Rightarrow \sum_{i=1}^N \frac{d}{dt}x_i^{bat} = 0 \quad (574)$$

Therefore, (573) expressed in function of the probabilities of all the states x_i^{bat} is (575). For convenience, the independent constant λ_{bat} is multiplied by $\sum_{i=1}^N x_i^{bat}$ to match

expression (573) in matrix form (572) and to allow λ_{bat} be dependent on soc_i .

$$\sum_{i=1}^N soc_i \frac{d}{dt}x_i^{bat} = \sum_{i=1}^N (-\lambda_{bat} - \delta_{bat} \cdot soc_i) x_i^{bat} \quad (575)$$

Since the parameters λ_{bat} and δ_{bat} can depend on SOC, the following notation will be used to remark parameter dependences on state number.

$$\sum_{i=1}^N soc_i \frac{d}{dt}x_i^{bat} = \sum_{i=1}^N (-\lambda_i^{bat} - \delta_i^{bat} \cdot soc_i) x_i^{bat} \quad (576)$$

where $\lambda_i^{bat} = \lambda_{bat}(soc_i, I_{charge}, I_{discharge})$ and $\delta_i^{bat} = \delta_{bat}(soc_i)$

The battery charges gradually and thus, SOC can only change in a infinitesimal time span from state i to the adjacent state $i - 1$ (battery discharge from state i) or $i + 1$ (battery charge from state i). Thus, the process is equivalent to a birth and death stochastic process [335]. The rate diagram of an intermediate state is shown in Fig. 147.

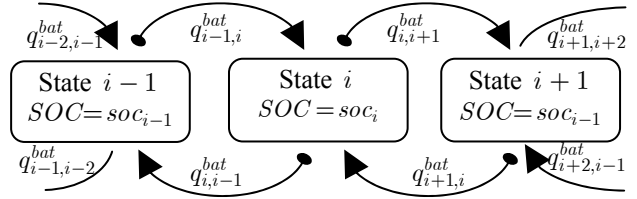


Fig. 147: Rate diagram of an intermediate state

The value of $q_{i,i-1}^{bat}$ and $q_{i,i+1}^{bat}$ can be easily obtained from (575) for the special case where $x_i^{bat} = 1$ and $x_k^{bat} = 0 \quad \forall k \neq i$.

$$soc_{i-1} \frac{d}{dt}x_{i-1}^{bat} + soc_i \frac{d}{dt}x_i^{bat} + soc_{i+1} \frac{d}{dt}x_{i+1}^{bat} = -\lambda_i^{bat} - \delta_i^{bat} \cdot soc_i \quad (577)$$

Since the state probabilities must sum unity, its derivative is null, i.e. $\frac{d}{dt}x_{i-1}^{bat} + \frac{d}{dt}x_i^{bat} + \frac{d}{dt}x_{i+1}^{bat} = 0$, (577) transforms into:

$$(soc_{i-1} - soc_i) \frac{d}{dt}x_{i-1}^{bat} + (soc_{i+1} - soc_i) \frac{d}{dt}x_{i+1}^{bat} = -\lambda_i^{bat} - \delta_i^{bat} \cdot soc_i \quad (578)$$

Since the battery can be at state i only chemically charging or discharging but not both, $q_{i,i-1}^{bat}$ or $q_{i,i+1}^{bat}$ must be zero. Thus, matrix elements of \mathbf{Q}^{bat} are:

$$q_{i,i-1}^{bat} = \text{Max} \left[0, \frac{-\lambda_i^{bat} - \delta_i^{bat} \cdot soc_i}{soc_{i-1} - soc_i} \right] \quad \forall 1 < i \leq N \quad (579)$$

$$\text{and } q_{i,i+1}^{bat} = \text{Max} \left[0, \frac{-\lambda_i^{bat} - \delta_i^{bat} \cdot soc_i}{soc_{i+1} - soc_i} \right] \quad \forall 1 \leq i < N \quad (580)$$

Notice that \mathbf{Q}^{bat} is a tridiagonal matrix, with diagonal elements $q_{i,i}^{bat} = -q_{i,i-1}^{bat} - q_{i,i+1}^{bat}$ in order to each row sum zero. Moreover, the subdiagonal elements are null if the system is charging at any state (conversely, the superdiagonal elements are null if the battery is discharging at any state) and the eigenvalues are the diagonal elements $q_{i,i}^{bat}$.

If the charging current is between the autodischarge current of a flat and a fully charged battery, the battery will charge at some states $i \leq k$ and discharge at states $i > k$. In that case, the eigenvalues are $q_{i,i}^{bat}$ for $i \neq \{k, k+1\}$, zero and $q_{k,k}^{bat} + q_{k+1,k+1}^{bat}$.

In any case, the eigenvectors can be easily and efficiently computed with Thomas algorithm –forward and backward substitution–. Therefore, the storage and computation burden for the tridiagonal matrixes are proportional to the number of states N –instead of N^2 for a regular matrix–. Special savings are achieved using the canonical basis.

Thus, the non-linear system is approximated by a system of order $N-1$ with the eigenvalues as characteristic times and the normalized eigenvectors are the distributions that decay with characteristic times, forming a canonical basis to express the system dynamics.

A) First-order battery model ($N=2$ states)

The simplest battery model is the lineal model where the accumulator charges at rate $q_{1,2}^{bat}$ and discharges at rate $q_{2,1}^{bat}$. In lead-acid batteries, the discharge is only allowed up to soc_{min} , otherwise the accumulator lifetime is seriously curtailed. Ni-Cad and Ni-MH batteries suffer from memory effect, which can be modeled increasing soc_{min} with battery partial cycles.

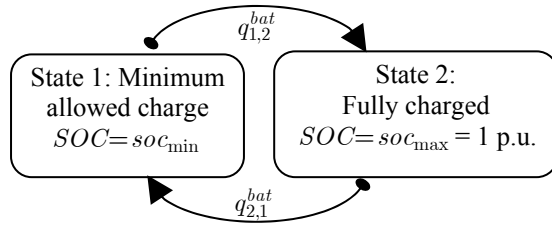


Fig. 148: Rate diagram of the model with two states (lineal model)

The infinitesimal rates of charge and discharge are:

$$q_{1,2}^{bat} = \text{Max} \left[0, \frac{\lambda_{bat}(soc_{min}, I_{charge}, I_{discharge}) + \delta_{bat}(soc_{min}) \cdot soc_{min}}{1 - soc_{min}} \right] \quad (581)$$

$$q_{2,1}^{bat} = \text{Max} \left[0, \frac{\lambda_{bat}(soc_{max}, I_{charge}, I_{discharge}) + \delta_{bat}(soc_{max}) \cdot soc_{max}}{soc_{max} - soc_{min}} \right] \quad (582)$$

Thus, the infinitesimal generator matrix is:

$$Q_{bat} = \begin{pmatrix} -q_{1,2}^{bat} & q_{1,2}^{bat} \\ q_{2,1}^{bat} & -q_{2,1}^{bat} \end{pmatrix} \quad (583)$$

Solar, wind and load data are integrating in intervals of length Δt . The model discretized for Δt time steps is shown in Fig. 149:

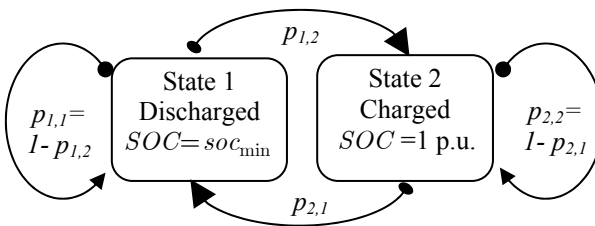


Fig. 149: Transition diagram of the model with two states (lineal model)

The transition matrix P_{bat} can be obtained from the model in continuous time:

$$P_{bat} = \text{Exp}(Q_{bat} \Delta t) = \begin{pmatrix} 1 - p_{1,2}^{bat} & p_{1,2}^{bat} \\ p_{2,1}^{bat} & 1 - p_{2,1}^{bat} \end{pmatrix} \quad (584)$$

Where
$$p_{1,2}^{bat} = \frac{q_{1,2}^{bat}}{q_{1,2}^{bat} + q_{2,1}^{bat}} \left(1 - e^{-\Delta t (q_{1,2}^{bat} + q_{2,1}^{bat})} \right) \quad (585)$$

and
$$p_{2,1}^{bat} = \frac{q_{2,1}^{bat}}{q_{1,2}^{bat} + q_{2,1}^{bat}} \left(1 - e^{-\Delta t (q_{1,2}^{bat} + q_{2,1}^{bat})} \right) \quad (586)$$

B) Higher order approximation of non-linear behaviour ($N > 2$ states)

The number of battery states can be increased to represent more accurately non linear behaviour. Moreover, cost optimization can indicate the maximum discharge depth of lead-acid batteries depending on expected cost of non-supplied load.

The memory effect of Ni-Cd batteries can be also modelled introducing a new state variable accounting for the effective loss of capacity due to shallow-cycles (and the capacity recuperation after a full discharge and full charge cycle).

7.10.10. Model of Water Reservoir Storage

The model of a reservoir with pump/turbine is analogue to the Ah battery model (566). The parameter significance for pumped storage is in Table XIII. For Markov models of pumped storage with several reservoirs, consult chapter 17 of [362].

TABLE XIII: PARAMETER EQUIVALENCE OF THE PUMPED STORAGE AND AH BATTERY MODEL.

Variable	Significance
SOC	Stored water mass in reservoir
λ_{bat}	Instantaneous rate of variation of SOC . If there is an external water injection into the reservoir or dam (such a river or rain contribution), it can be modeled as an additional term in λ_{bat} .
δ_{bat}	Relative rate of water loss (evaporation, leakage, external water consumption, etc).
P_{charge}	Gross input power at pumping facility when recharging the reservoir.
P'_{charge}	Mechanical power at pump shaft.
P_{disch}	Gross output power from turbine facility when discharging the reservoir.
P'_{disch}	Mechanical power at turbine shaft.
$\eta_{converter}$	Electrical efficiency of the system composed by the electric generator/motor which drives the turbine/pump, including consumption of auxiliary and ancillary devices.
η_{charge}	Efficiency of the system composed by the pump and the conduits from the water intake to the reservoir outlet.
η_{disch}	Efficiency of the system composed by the turbine and the conduits from the reservoir intake to the water outlet.
$U_{battery}$	Difference of gravitational potential between the reservoir and water outlet surfaces, i.e. $\rho g \Delta h_{intake-outlet}$
I_{charge}	Water mass flow (i.e. water current) at pump
$I_{discharge}$	Water mass flow (i.e. water current) at turbine

Conclusions

The variability of wind speed can be modelled during short intervals with the classical theory of stationary normal processes, which has been presented in the previous chapters. However, the weather is a non-stationary process and this cannot be neglected for horizons longer than some hours. The evolution of wind power can be described in the time domain by stochastic differential equations where the Numerical Weather Prediction (NWP) models the physics of meteorological dynamics. Wind speed is customarily transformed into generated power with a power curve or with a model output statistics (MOS).

Since the wind variations show a fairly multiplicative behaviour, the Markov Approximation Method is suitable for modelling the non-linear stochastic behaviour of the wind.

This technique is analogous to the finite difference approximation in deterministic differential equations and it is a powerful tool to optimally size and control the system, especially if numerical weather predictions are available.

Indeed, if numerical weather predictions are unattainable, the Markov chain can be used for generate a basic probabilistic forecast based on the system behaviour previously observed. In that case, the probability transition matrix among the states models the non-stationarity of wind, present in long time spans.

The optimal control of a Markov system can be expressed as a policy, which gives the best decision or action to take for a given state, regardless of the prior history. Once a Markov decision process is combined with a policy, this fixes the action of the control for each state and the resulting combination behaves indeed like a Markov chain. Thus, the system is dimensioned for achieving the maximum expected outcome of the controlled system.

The classic control theory of linear and time-invariant systems is well established. However, many devices in the grid are discrete and their control can not be linearized because unnecessary switching can produce avoidable grid disturbances or excessive wear or stress in the devices.

Markov chains can model switching or jump events such as casual generator trips, unlikely wind variations and the connection or disconnection of reactors, capacitors and other devices. The stochastic control is better suited to manage these events than the classical control of linear and time invariant systems. The optimum design and control can be achieved assigning costs or benefits to staying in the same system state or jumping to other states. In sum, the Markov Decision processes can be used to optimize the design and control of many devices which should encompass the non-linear and time-dependent variability of the wind power.

Markov chains have been typically utilized as Monte Carlo random generators in stochastic power flows due to the high dimension of their state space. To reduce the state space, a discretization methodology is presented where the number of states is remarkably reduced through careful system modelling and clustering. The state reduction condensates the significant operational condition of the system and techniques as the principal component analysis and the proper orthogonal decomposition can help to achieve an orthogonal, compact and meaningful representation of the system. This makes the Markov decision processes more tractable.

Since the system expected cost/benefit is the same if the system states are mutually exclusive (only one state can actually exist at a time) or can be interpreted as a fuzzy states (intermediate states do exist because the continuous system states have been discretized).

The classification of states can be based on power output, equivalent wind speed or wind speed prediction, depending on the available data and the aim of the wind farm model. The performance matrix in Standard IEC 61400-12-3 can be used as the emission matrix to relate wind and power in a wind farm using a Hidden Markov Model. The wind farm model can be used also as time interpolation or to guess if there is an outlier in the state (a switching event).

One application example is in probabilistic power flows. A methodology to optimize the power flow based on Markov

processes is presented. Load, generation and network topology is classified into a small set of cases represented by the centroids of the fuzzy clusters. Afterwards, regular deterministic power flows are run for each centroid and the system stochastic dynamics are derived from the transition matrix of the embedded Markov Process. Finally, the generation, the network topology and the discrete elements such as switches and transformer tap changers can be controlled conveniently by a Markov Decision Process. This approach is more advantageous for loads highly or barely interrelated and for non-controllable generators such as wind and solar. Other possible application is the design and control of reactors and capacitors in a wind farm to maximize the profit due to reactive power control. In that case, a simplified, quadratic model of the wind farm in the steady state can be used to estimate the maximum absorption and injection of reactive power at different points of the farm.

Other application is the optimal design and control of the load consumption of an isolate system with renewable generation and storage. The optimal design minimize the cost of the system infrastructure plus the expected cost of maintenance, energy losses, load deferring and not supplying regular and critical loads. The control of the optimal design manages the loads for optimize the expected profit.

Chapter 8:

Conclusions and Future Work

8.1. Conclusions

The present thesis has analyzed the main features of the variability of wind power. This thesis has been focused in providing a framework for the systematic analysis of the wind power variability in time and in space. The approach is mainly empirical, based on the data signal processing and the concept of equivalent wind.

Custom programs have been specifically implemented for processing the logged data –see for example the graphs in the Annexes. Thus, the data mining of the measured data is in the core of the thesis.

Some models of the wind structure on the space and frequency domain are extensions of some models available in the literature. The variations have been analyzed stochastically in the frequency domain and in the time domain.

The frequency representation of the wind fluctuations facilitate the estimation of the power smoothing due to the turbulence structure and cyclic features. Moreover, the orthogonal representation of a Gaussian stochastic process is its Fourier transform. However, the time domain approach is more related to the structural integrity, system control, weather evolution and forecast error and exceptional events. When possible, time and frequency approaches have been combined through the use of spectrograms.

The program WINDFREEDOM has been developed to check the approximation degree of some empirical models of the variation of the wind along the time and along the space.

The program EQWIGUST has been developed to study extreme variations of the equivalent wind. Since the wind fluctuations show a multiplicative behaviour, two simple transformations are provided to compensate the non-Gaussian behaviour of the wind.

The variability of the generated power depends mostly on turbulence and weather evolution. The weather forecast and the turbine tripping are very specific areas out of the scope of the thesis. However, the probability distribution of the forecast and the probability of a turbine trip have been accounted in the proposed Markov model of wind power variability.

Fast power fluctuations are also due to the vibration dynamics of the wind turbines and to eventual switching of wind turbines. These features have been characterized from measurements, but the results are very specific to the turbine model and the atmospheric conditions. Therefore, the analysis can be systematized but the conclusions from the measurements are difficult to generalize.

The fundamental characterization of the wind variability is presented in the second chapter. The wind fluctuations measured with an anemometer are customarily characterized

by the variance spectral density of the wind. The spatial structure of the wind fluctuations are typically described by the wind coherence, which is the correlation coefficient in the frequency-space domain.

The spatial structure of the turbulence affects to the aerodynamic torque experimented by the turbine. The torque oscillations due to turbulence can be estimated from its structure. Several models are derived and compared to the literature.

In fact, the large area swept by the blades implies that localized turbulent oscillations are significantly averaged along the area. •

In general, the spatial dimension of the wind fluctuations seems to be inversely proportional to their frequency. Therefore, a link can be established between the oscillations measured with an anemometer and the aerodynamic torque oscillations. Furthermore, the equivalent wind is defined as the one that produce the same effects that the non-uniform real wind field.

The equivalent wind speed contains a stochastic component due to the effects of turbulence, a rotational component due to the wind shear and the tower shadow and the average value of the wind in the swept area, considered stationary in short intervals. The variations of torque are estimated from blade element theory in annex C.

The comparison between the turbine measurements and the simulations is complicated by the uncertainty in the wind field. Usually the wind speed is measured at just one location which makes difficult the direct comparison between the measured and simulated turbine. However, the power density spectra of the measured and simulated processes can be compared directly because they are stationary properties of the process.

The equivalent wind can be considered a low-pass filtered version of the wind measured with an anemometer. The actual aerodynamic torque can not be reconstructed from a single point measure due to the stochastic nature of the wind and the complex vibrations of the tower, that affects the aerodynamic torque. However, the main statistical features of the torque –or the equivalent wind– can be predicted.

The concept of equivalent wind can be extended to a wind farm or even to a cluster of wind turbines. The equivalent filter of the farm respect one significant turbine can be defined from the root of the of their PSD quotient. This filter estimates the smoothing due to the spatial diversity of the turbulence across a wind farm. The equivalent cluster filter is defined analogously to the wind farm filter.

An interesting concept is the wind smoothing across an area. If many wind farms are distributed evenly enough in an area, the smoothing level can be estimated from the region dimensions and the turbulence parameters.

While slow fluctuations in the power generated by turbines are fundamentally related to the wind, fast power fluctuations are largely due to the turbine vibrations and the electric generator with its control and power interface.

Since the turbine vibrations and the electrical equipment varies notably from one model to other, the forth chapter of this thesis proposes a methodology to characterize the oscillations experimentally observed. A literature review on Power Spectral Densities (PSD) and periodograms (averaged spectrum) of wind power is presented.

There are many specific characteristics that impact notably in the power fluctuations between the first tower frequency (usually some tenths of Hertz) and the grid frequency. The realistic prediction of these power fluctuations needs a very comprehensive model of the turbine, which is usually confidential and private. Even the agreement of the measures with a full model is not trivial.

The foundations of the methodology are explained in the forth chapter and some examples are provided in annex B. One contribution of this chapter is the experimental characterization of the power fluctuations of three commercial turbines. The variations of power during the continuous operation of turbines are measured and experimentally characterized in timescales from the grid period to minutes. Some experimental measurements in the joint time-frequency domain are presented to test the mathematical model of the fluctuations.

The admittance of the wind farm is defined as the ratio of the oscillations from a wind farm compared to the fluctuations from a single turbine, representative of the operation of the turbines in the farm. Some stochastic models are derived in the frequency domain to link the overall behaviour of a large number of wind turbines from the operation of a single turbine.

The nature of turbulence and vibrations are different. The equivalent wind fluctuations due to the turbulence are broadband stochastic processes with no characteristic frequencies. However, vibrations and electrical oscillations are almost cyclostationary stochastic processes, usually with several noticeable narrowband components.

The measured power variations are the outcome of turbulence, mechanical vibrations and electrical oscillations, which are stochastic processes with different properties.

However, a wind farm typically has more than four turbines and the addition of the power variations from more than four turbines converges approximately to a Gaussian process despite of the process nature.

The partial cancellation of the variations among the turbines has been illustrated, assuming the unsynchronized rotation of the turbines. For simplicity, the turbines are assumed to experience a power dip when the blade is close to the tower. These power dips are represented as a deterministic periodic pulse, which are more severe (they converge slower to a normal process) than the actual drivetrain torque vibrations.

Since the turbine speed varies slightly from one turbine to other, the blades positions are not synchronized. Eventually, several blades can eventually cross their tower almost simultaneously. The blade crossing in front of its turbine

tower is modelled as a Poisson process. The probability of simultaneous power dips is derived from this process.

Indeed, the vibrations and electrical oscillations have almost cyclostationary nature, not deterministic and periodic features. This stochastic behaviour increases the convergence of the aggregated power to a Gaussian process in a wide frequency range. In a typical wind farm, the variance density aggregates quadratically in the range from a hundredth of Hertz to the grid frequency. Therefore, the relative amplitude of the farm power oscillations at those frequencies is inversely proportional to the number of turbines.

In the very low frequency range, the oscillations are dominated by comparatively coherent turbulence, which has a somewhat multiplicative behaviour.

The power variations of low frequency in the farm have bigger amplitudes because these oscillations have a smaller spatial variation. Moreover, they have a Laplacian distribution whereas the variations of higher frequency have a more Gaussian distribution. This Laplacian behaviour will be approximately accounted using a bijective transformation.

An approximate flickermeter model in the frequency domain is also presented in the fifth chapter to demonstrate the low relevance of the flicker emission at the farm level when the turbines are not synchronised. In the measured farms, the flicker level was very low due to the partial cancellation of the oscillations and the strength of the network at the point of common coupling.

The wind spectral density determines the stochastic behaviour of the wind, provided it can be consider a stationary Gaussian process. In the sixth chapter, this spectral density will be used to analyze the characteristics of wind variations in the time domain and to synthesize samples of equivalent wind with some features.

The mechanisms that generate turbulent wind changes are analyzed are closely related to the shape of the bursts and the distribution of the speed variations. Experimental wind differences from the mean fit approximately a Laplacian distribution, indicating there is some unknown multiplicative effect involved in the extreme deviations. A bijective transformation is defined to obtain the target distribution.

The stochastic generation of gusts is a valuable tool to obtain random samples of wind with some features. The background of the method is the constrained stochastic simulation of processes, which is based on conditional distributions. More sophisticated transformations can be used to improve the fit of the shape and the occurrence probability to experimental data. For example, some reports observed that the actual front ramp of the gust are, on average, bigger than the tail ramp, but the predicted gust shapes are symmetrical forwards and backwards.

The peak and ramp gusts are synthesized in the frequency domain using the Karhunen-Loève expansion and the theory of conditional simulation of normal processes. An approximate method is presented to avoid numerical difficulties that arise generating very long samples.

The concept of the equivalent wind gust can be extended to a geographic area and it can serve to compute the maximum variability of the power expected in a region.

The program EQWIGUST generate gusts of equivalent wind with some features that can be selected by the user and it estimates their probabilities.

The variability of wind speed can be modelled during short intervals with the classical theory of stationary normal processes, which has been presented in the previous chapters. However, the weather is a non-stationary process and this cannot be neglected for horizons longer than some hours.

Since the wind variations show a fairly multiplicative behaviour, the Markov Approximation Method is suitable for modelling the non-linear stochastic behaviour of the wind. This technique is a powerful tool to optimally control the system, especially if numerical weather predictions are available. Indeed, if numerical weather predictions are unattainable, the Markov Chain can be used for generate basic probabilistic forecasts based on the system behaviour previously observed.

Many devices in the grid are discrete and their control can not be linearized because their unnecessary switching can produce grid disturbances or excessive device wear. The optimum design and the optimum control can be achieved assigning costs to staying in the same system state or jumping to other states.

A discretization methodology is presented where the number of states is remarkably reduced through careful system modelling and clustering.

One application example is in probabilistic power flows. Other application is the optimal design and control of the load consumption of an isolate system with renewable generation and storage.

8.2. Original Contributions

Some contributions come from the experience gained designing, building, installing and analyzing a multipurpose data logger that is now commercially available. The huge work done in the development of this data logger can be seen in some articles cited in the publications section of this chapter. The development of a multipurpose power analyzer with a PC in the 1998's for the wind industry was a challenge there. Nowadays, the datalogger is rather different from the original one. However, the experience gained with the first prototypes, developed during the first years of this thesis, has been fundamental for the AIRE datalogger to become commercially available.

The third chapter estimates the equivalent wind smoothing across an area from its dimensions and the turbulence parameters. The equivalent wind has been used also in the simulation of aggregated models of wind farms. However, the estimation of the equivalent wind of a wind farm or a geographical area from the wind coherence is a contribution of this thesis.

A new methodology for characterizing the oscillations measured in the power of a wind turbine or a wind farm has been proposed in the forth chapter.

The fifth chapter shows the convergence to a Gaussian process of the aggregated oscillations due to vibration, low coherent turbulence and electrical fluctuations. This model also shows the low relevance of the flicker emission at the farm level.

The sixth chapter estimates the equivalent wind gust, that can serve to compute the maximum variability of the power expected in a region.

The seventh chapter presents the application of the Markov Approximation method to optimize the system design and control in two cases.

The annex A presents a simplified statistical model to represent a wind farm in a power flow study, taking into account the variability in the generated power from windmills and its normal operation.

The annex B shows some examples of the analysis of experimental data obtained with the multipurpose data logger. Some effects observed in the data such the measured oscillations are quite difficult to obtain from simulations.

The annex C introduces an aerodynamic model to estimate the influence of deterministic wind component (wind shear and tower shadow) from the torque coefficient and the main properties geometry of the turbine.

The distribution of wind speeds and turbulences along a wind farm is required to achieve a fair representation of a wind farm. The model included in the annex D allows testing different wakes models.

Another contribution of this thesis is the program that downloads, represents and analyzes the data from the network of meteorological weather stations, typically used by meteorological organizations for weather prediction.

An user manual of the program WINDFREEDOM with three case studies has been included to show the potential use of this program.

Another contribution of this thesis is the program that generates gust or random samples with certain features of equivalent wind.

Concisely, this thesis has attempted to provide a methodology for the study of wind power variations, based on the spatial-temporal distribution of wind and in the analysis of experimental measurements. A Markov Approximation framework has been proposed for the design and optimal control of non-linear systems affected by the wind power availability.

8.3. Perspectives and future research

Several fields for further investigation have been identified during this thesis. Ideas for future work are listed bellow:

- Further test of the proposed models. The models have been validated from available data or from literature reviews. Comparison between measurements and simulations is complex by the uncertainty in the wind field. However, the power density spectra of the measured and simulated variables can be compared because they are stationary properties of the process which can be estimated easier from measures and from simulations. The accuracy of the models proposed in this thesis depends on many factors and an extensive test of the models can retrofit and improve them.
- The blade element model of the rotor has been implemented in a turbine model in PSCAD. However, experimental measures indicate that

rotational features as the wind shear and tower shadow fuel many vibration modes of the turbine. Therefore, the relationship between rotational effects and shaft vibrations should be further studied.

- The estimation of a equivalent filter between the nacelle anemometer and the equivalent wind is very convenient. The rotor introduces many small scale (i.e., high frequency) oscillations in the nacelle anemometer. However, the frequency content of the equivalent wind at induced turbulence is quite small compared to the mechanical torque vibrations and some measures indicated a better-than-expected agreement between the equivalent wind estimated from the shaft torque and from the nacelle anemometer. However, a second order filter has been estimated from the measures while all the reviewed literature uses a first order filter. Further measuring campaigns are required to check the parameters of the equivalent filter.
- The improvement of EQWIGUST and WINDFREEDOM programs for increasing their versatility.
- A further understanding of the equivalent wind variability can be achieved if many regions are systematically characterized and critically compared. The hourly wind variability can be characterized in many regions with the program WINDFREEDOM.
- The integration of the Markov model into a probabilistic optimal flow. The workflow has been derived in the seventh chapter, but it has not been implemented yet.
- The implementation an interactive interface to the wind farm statistical electrical model. This interface could estimate the farm oscillations from the simulation of a single turbine, analogously to the method deployed for experimental measures. Other application is the centralized control of reactive power.
- A simple stochastic control of the capacitors and reactors in a wind farm has been developed in [363], using the present reactive bonus tariff in Spain and data from three wind farms. This control can be further developed to provide a centralized control of the reactive power at the turbines and at the farm substation, based on dynamic programming. An interactive interface can be implemented for optimally sizing the capacitors and reactors in a wind farm.
- For convenience, the full vibration behaviour is not included in many electrical simulations. However, the turbine models can be refined introducing the vibrations measured or obtained in structural simulations. The mechanic vibrations can be introduced in the generator shaft and the non-ideal behaviour of power electronics can be experimentally characterized and introduced as noise at the output of ideal converters.

The great variety of the contributions and the accomplishment of other duties, as the full time lecturing responsibilities from the year 2000 are, in part, the explanation of the long

time required to finish this thesis, about 12 years with varying dedication.

8.4. Publications

The research publications on wind power are ordered by chronological order. They can be accessed in the web page www.windygrid.com or from the editors web page.

Book chapter on wind power variability accepted for publishing under the working title "Wind Power", ISBN 978-953-7619-X-X.

J. Mur Amada, A.A. Bayod Rújula, "**Flicker emission of wind farms during continuous operation**", 7th International Workshop on Large-Scale Integration of Wind Power and Transmission Networks for Offshore Wind Farm. Madrid, May 2008.

J. Mur Amada, A.A. Bayod Rújula, "**Characterization of Spectral Density of Wind Farm Power Output**", 9th Conference on Electrical Power Quality and Utilisation (EPQU'2007), Barcelona, 2007.

J. Mur Amada, A.A. Bayod Rújula, "**Pace of Tower Shadow Fluctuations in a Wind Farm**", 9th Conference on Electrical Power Quality and Utilisation (EPQU'2007), Barcelona, 2007.

J. Mur Amada, A.A. Bayod Rújula, "**Wind Power Variability Model. Part I - Foundations**", 9th Conference on Electrical Power Quality and Utilisation (EPQU'2007), Barcelona, 2007.

J. Mur Amada, A.A. Bayod Rújula, "**Wind Power Variability Model. Part II - Probabilistic Power Flow**", 9th Conference on Electrical Power Quality and Utilisation (EPQU'2007), Barcelona, 2007.

J. Mur Amada, A.A. Bayod Rújula, "**Wind Power Variability Model. Part III - Validation of the model**", 9th Conference on Electrical Power Quality and Utilisation (EPQU'2007), Barcelona, 2007.

J. Mur Amada, M. P. Comech Moreno, "**Reactive Power Injection Strategies for Wind Energy Regarding its Statistical Nature**", Sixth International Workshop on Large-Scale Integration of Wind Power and Transmission Networks for Offshore Wind Farm. Delft, 2006

M.P. Comech, S. Martín, J. Mur, I. Franco, M. García-Gracia, "**Modelling of squirrel cage turbine for voltage dips studies**", Sixth International Workshop on Large-Scale Integration of Wind Power and Transmission Networks for Offshore Wind Farm. Delft, 2006

J.A. Domínguez, J.M. Yusta, A.A. Bayod, J.L. Bernal, M.J. Velilla, J. Mur, M.A. García, A. Diaz "**Optimal Location of Small Generators in Weak Networks with Optimal Operation**", ICREP '05 (Internacional Conference on Renewable Energies and Power Quality), Zaragoza 2005

Angel Antonio Bayod Rújula; Joaquín Mur Amada ; Jesús Sallán Arasanz, "**Improving the electrical value of Wind Power Plants**", EWEC '03 (European Wind Energy Conference & Exhibition). Madrid, 2003

D. García García, M.P. Comech, J. Mur, J.B. Arroyo, M. García-Gracia, "**Grid Connection of Wind Farms**", EWEC '03 (European Wind Energy Conference & Exhibition). Madrid, 2003

Joaquín Mur, Ángel A. Bayod, Jesús Sallán "**Profile of voltage in grids with wind farms**" EWEC '03 (European Wind Energy Conference & Exhibition). Madrid, 2003

Joaquín Mur, Ángel A. Bayod, Jesús Sallán "**An Experimental Study on Power Quality Wind Turbines**" EWEC '03 (European Wind Energy Conference & Exhibition). Madrid, 2003

Joaquín Mur, Jesús Sallán , Ángel A. Bayod, "**Statistical model of wind farms for power flow**" ICREP '03 (Internacional Conference on Renewable Energies and Power Quality), Vigo 2003.

Joaquín Mur, Jesús Sallán , Ángel A. Bayod, "**Power Quality Analysis of Wind Turbines. Part I - Static Análisis**", ICREP '03 (Internacional Conference on Renewable Energies and Power Quality), Vigo 2003.

Joaquín Mur, Ángel Antonio Bayod, Samuel Ortiz , Roberto Zapata "**Power Quality Analysis of Wind Turbines. Part II - Dynamic Analysis**", ICREP '03 (Internacional Conference on Renewable Energies and Power Quality), Vigo 2003.

Joaquín Mur, Ángel Antonio Bayod "**Characterization of wind farm energy production in a zone by artificial neuronal networks**", ICREP '03 (Internacional Conference on Renewable Energies and Power Quality), Vigo 2003.

Angel A. Bayod Rújula; José A. Domínguez Navarro; Joaquín Mur Amada ; Julio J. Melero Estela, "**Combined system for reactive power control in wind farms**", IEEE

Industrial Electronics Conference (IECON 2002), Sevilla 2002

Angel A. Bayod Rújula; José A. Domínguez Navarro; Joaquín Mur Amada ; Julio J. Melero Estela, "**Hybrid Configuration For Reactive Power Management In Power Systems**", Proceedings of the Second IASTED International Conference Power and Energy Systems (EuroPES 2002). Creta, 2002

Ángel Antonio Bayod Rújula , José Antonio Domínguez Navarro , Julio Melero Estela, Joaquín Mur Amada "**Configuración híbrida FC-TCR-FA para gestión de reactiva en redes eléctricas**", XII Reunión de Grupos de Investigación en Ingeniería Eléctrica, Córdoba 2002.

M. Sanz A. Llombart A. A. Bayod J. Mur, "**Power quality measurements and analysis for wind turbines**", IEEE Instrumentation and Measurement Technical Conference 2000, pp. 1167-1172. May 2000, Baltimore. (A modified version was accepted for publication in "IEEE Transaction on Instrumentation & Measurement" but, unfortunately, it did not appear finally in the special issue devoted to the conference).

M. Sanz, A. Llombart, A. A. Bayod, J. Mur, R. Sierra "**Análisis de la calidad de la energía generada en parques eólicos**" X Reunión de Grupos de Investigación en Energía Eléctrica. Santander, 2000.

M. Sanz, J. Mur, F. Gómez, R. Zapata , "**Sistema de medida de calidad de red para parques eólicos**", IX Jornadas Hispano-Lusas. Lisboa, 1998.

F.J. Martínez, L.C. Montanés, J. Mur, A. Llombart , M. García , "**Modeling lighting arresters using SPICE**", 6 th international Conference on INDUSTRIAL METROLOGY, CIMI'95. Zaragoza, 1995.

Annex A:

Simplified Electrical Model Of The Wind Farm

A.1. Introduction

The current legislation for generators included in the special regulation (mainly mini-hydraulic, wind and co-generation plants up to 50 MW) in Spain was developed in 1985 (Industry and Energy Ministry order 5/9/85). This order states that the electric plants included in this regulation must operate with unity power factor.

This characteristic was adequate when the percentage of this type of generation was small, but the great increase of co-generation and wind generation was not foreseen.

Moreover, conventional power plants must operate in accordance with procedure 7.4 (distribution network complementary voltage control service, published in BOE 18/3/2000). However, this procedure is not adapted to the characteristics of the wind farms or the grids to which they are usually connected.

Currently, AENOR is performing a review process of this regulation by means of the workgroup "Grid integration of wind generation", in particular in the group "Wind generators" AEN/CTN 206/SC88. Its goal is achieving a new regulation that allows these power plants to help grid regulation, without causing an excessive increase in cost.

According to the current regulation, reactive power compensation is performed in the plant's point of connection and it does not take into account reactive power consumption and generation in lines and transformers. This worsens the power factor in the border nodes between the distribution and transport networks.

Besides, a power plant modifies the voltage distribution in the grid. Distribution networks are usually limited, not for the maximum thermal current, but for the limits in voltage variation (specially at the end of the line). Because of that, distribution companies prefer distributed generation to be connected to higher voltage levels, where its impact in voltage distribution is very small. However, connecting to a higher voltage level increases the cost of the plant.

Traditionally, the maximum installable generation capability is calculated by using a deterministic load flow, usually based in the worse scenario of minimum load and maximum generation [364]. These studies do not take into account the probability of the different scenarios. However, the standards that establish voltage characteristics are expressed in statistic terms [365].

In addition, wind energy injection modifies the losses in the grid (losses reduction if the zone is mainly consuming and an increase if the area has a generation excess, as it happens in some wind farm concentrations).

The method proposed in this paper can help to evaluate the affection to the net, as well as to compute voltages inside the wind farm.

According to the Spanish regulation in RD 436/2004 [366], current regulation rewards the control of power factor to generators in the especial regulation (most renewable energy and cogeneration). Remunerated reactive power compensation is based on a power factor band depending on the low-load, peak or medium-load classification of the interval.

Distribution networks are usually limited, not for the maximum thermal current, but for the limits in voltage variation (especially at the end of the line) [367]. Because of that, distribution companies prefer distributed generation to be connected to higher voltage levels, where its impact in voltage distribution is very small. However, connecting to a higher voltage level increases the cost of the plant. In case the wind farm is able to control reactive power absorption or generation, voltage can be fixed, avoiding higher voltage connection [365, 368].

The new Spanish regulation is an improvement from the previous one that stated unity power factor at any time (at peak hours the farm is rewarded to be capacitive and at low-loads the farm is rewarded to be inductive). However, the reactive bonus is obtained if a power factor is accomplished. Therefore, reactive power injection depends on wind and grid support is low at low active power (i.e. low winds).

A better utilization of the infrastructure can be attained considering the availability of reactive power at low active generation or even with no active power generation (many wind turbine technologies can generate more reactive power at low active power or even, without generating active power). As the capacity factor of wind farms is usually low, this would increase the exploitation of the infrastructure.

The suitable system operation may require a set point from the control centre or measures at other points in the grid. Indeed, the power factor band regulation of RD 436/2004 may be regarded as a rough estimation of the load depending on the low-load, peak or medium-load time classification.

If online communication from control centre is not available, the set point of reactive power could be scheduled from the estimation of grid state and the forecast of near loads (based on in time of the day, day of the week, working day, weather, etc.). Moreover, the voltage at the supported node can be estimated at each turbine without the requirement of a centralised control. The wind farm model allows estimating power injection from other turbines based on its power output and its wind direction. With the estimation of power injection of the wind farm and, eventually, nearby wind farms it is

possible to compute a rough estimation of voltage at the supported node. The change of taps in transformers that connects the wind farm to the grid can be detected and included in the estimation of the supported voltage node.

Other wind farm aggregate models are available in the literature (see, for example [369]). However, the proposed model is focused on the statistical behaviour of the farm.

A.2. Simplified electrical model of the wind farm

A.2.1. Turbine power curve

The power curve relates wind at hub height and power output [370]. Turbine manufacturers provide the curve along with its uncertainty. Fig. 150 shows a power curve from a pitch controlled turbine. The uncertainty is small, except at cut-off wind speeds.

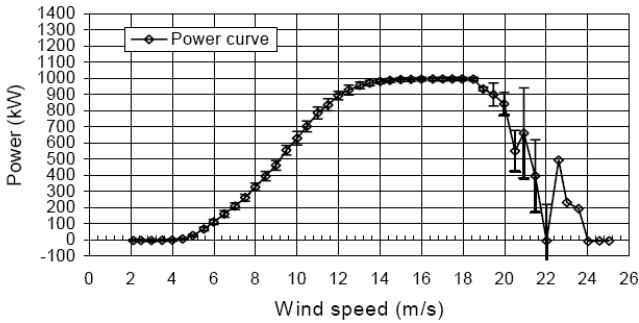


Fig. 150: Example of measured power curve (from [370]).

The paper [371] normalize power curves to ease the optimization of energy production. In this study, a simpler power curve will be employed to be able to derive analytic expressions. The power curve $P_{WT}(w_{WT})$ of (2) is characterized by cut-in, cut-off wind speeds and the wind speeds where power speed is 25% and 75% of turbine rated power. It fits well to pitch and active stall wind turbines, but it is less accurate for passive stall turbines. Those turbines can be modelled more precisely following an analogue procedure to the one shown in this work.

$$P_w(w_{WT}) = \quad (587)$$

$$\begin{cases} \frac{P_{\text{nominal}}}{2} \left(1 - \text{Tanh} \left(\frac{w_{WT} - \frac{w_{25\%} + w_{75\%}}{2}}{\frac{w_{25\%} - w_{75\%}}{\text{Ln}(3)}}} \right) \right) & w_{\text{cut in}} < w_{WT} < w_{\text{cut off}} \\ 0 & \text{elsewhere} \end{cases}$$

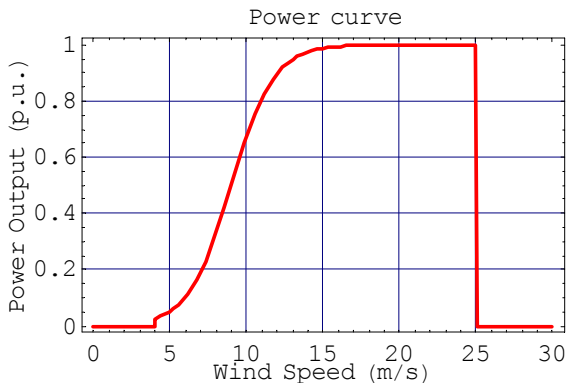


Fig. 151: Simplified power curve from (587) for example data of Annex I.

The cumulative density function is derived in (3) and it is plotted in Fig. 152 for the data shown in Annex I (a Weibull wind distribution with parameter $\text{shape} = 2$, known as Rayleigh Distribution).

$$\Pr(\text{Power} < p_{WT}) = \Pr(\text{Wind} < P_w^{-1}(p_{WT})) + \Pr(\text{Wind} > w_{\text{cut-off}}) =$$

$$= \text{CDF}_{\text{Wind}}(P_w^{-1}(p_{WT})) + 1 - \text{CDF}_{\text{Wind}}(w_{\text{cut-off}}) =$$

$$= 1 + \text{Exp} \left[- (w_{\text{cut-off}} / \text{scale})^{\text{shape}} \right] -$$

$$- \text{Exp} \left\{ - \left[\frac{w_{25\%} + w_{75\%}}{2 \text{scale}} + \frac{w_{25\%} - w_{75\%}}{\text{Ln}(3) \text{scale}} \text{ArcTanh} \left(1 - \frac{2p_{WT}}{P_{\text{nominal}}} \right) \right]^{\text{shape}} \right\}$$

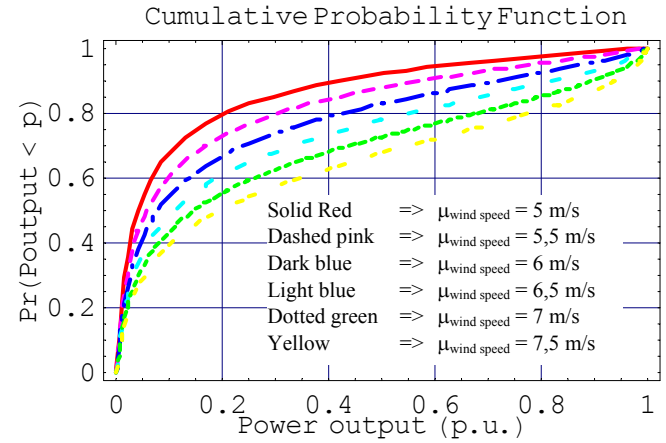


Fig. 152: Plot of $\text{CDF}_{\text{Power Output}}$ for the wind turbine of the example of Annex I.

The statistical parameters of this distribution have been derived analytically. The errors introduced in the approximations needed to achieve expressions 4 to 6 (typically 1% to 4%) are far lower than the errors due to the simplistic models of the wind and the turbine.

The median of power output can be computed using (4). The median is approximately proportional to wind scale parameter.

$$\text{median} \approx \frac{P_{\text{nominal}}}{w_{75\%} - w_{25\%}} \quad (589)$$

$$\left[0.28015 \text{scale} (0.69315^{1/\text{shape}}) - 0.51124 w_{25\%} + 0.23109 w_{75\%} \right]$$

Mean wind speed and power output of wind farms –with similar wind distributions and power curves– are linearly related to a high degree, as can be seen in Fig. 153. However, the adjusted straight line does not cross the origin ($\bar{P}_{WT} \sim a + b w_{WT}$ with $a \neq 0$).

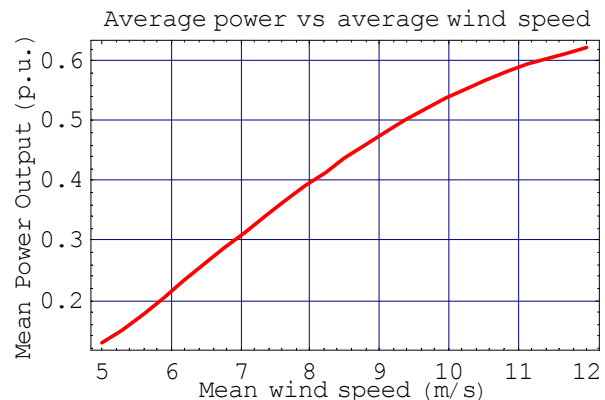


Fig. 153: Plot of average Power Output versus average wind speed at hub height of the wind farm for the example.

$$\begin{aligned}
\text{mean} \approx \frac{P_{\text{nominal}}}{360} \quad (590) \\
\left[178 \text{Exp}\left(-\left(\frac{w_{25\%}}{\text{scale}}\right)^{\text{shape}}\right) + 238 \text{Exp}\left(-\left(\frac{w_{75\%}}{\text{scale}}\right)^{\text{shape}}\right) + \right. \\
- 72 \text{Exp}\left(-\left(\frac{w_{25\%} + w_{75\%}}{2 \text{scale}}\right)^{\text{shape}}\right) + 23 \text{Exp}\left(-\left(\frac{w_{\text{cut-in}}}{\text{scale}}\right)^{\text{shape}}\right) - \\
\left. - 367 \text{Exp}\left(-\left(\frac{w_{\text{cut-off}}}{\text{scale}}\right)^{\text{shape}}\right) \right]
\end{aligned}$$

The standard deviation of power output (6) reaches the maximum at mean hub wind speeds that correspond to half the power, $w_{50\%}$, as can be seen in Fig. 154. In those cases, the probability density function (pdf) of power output is U-shaped, with two modes at the extremes, as can be seen in Fig. 155.

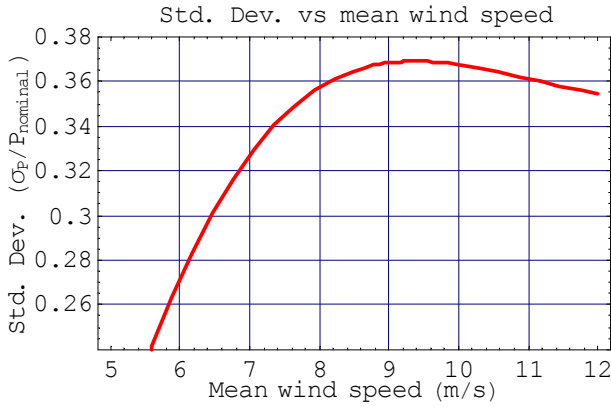


Fig. 154: Plot of $\sigma_{\text{Power Output}}$ versus average wind speed at hub height of the wind farm for the example.

$$\begin{aligned}
s^2 \approx \frac{P_{\text{nominal}}^2}{180} \\
\left[62 \text{Exp}\left(-\left(\frac{w_{25\%}}{\text{scale}}\right)^{\text{shape}}\right) + 146 \text{Exp}\left(-\left(\frac{w_{75\%}}{\text{scale}}\right)^{\text{shape}}\right) - \right. \\
- 36 \text{Exp}\left(-\left(\frac{w_{25\%} + w_{75\%}}{2 \text{scale}}\right)^{\text{shape}}\right) + 5 \text{Exp}\left(-\left(\frac{w_{\text{cut-in}}}{\text{scale}}\right)^{\text{shape}}\right) - \\
\left. - 167 \text{Exp}\left(-\left(\frac{w_{\text{cut-off}}}{\text{scale}}\right)^{\text{shape}}\right) \right] - \text{mean}^2 \quad (591)
\end{aligned}$$

The probability density function can be obtained deriving the CDF Power Output respect to power output.

$$\text{PDF}_{\text{Power Output}}(p_{\text{WT}}) = \frac{d}{dp} \text{CDF}_{\text{Power Output}}(p_{\text{WT}}) \quad (592)$$

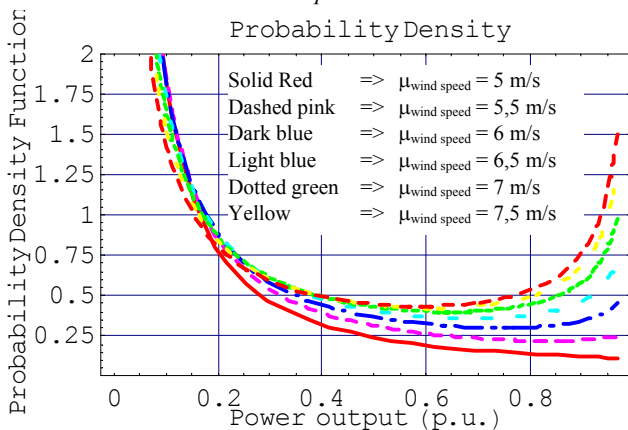


Fig. 155: Plot of PDF Power Output for example of Annex I.

The uncertainty of the power curve is bigger near cut-off and between cut-in and rated power, as can be seen in Fig. 151. The uncertainty of power curve would be considered in the wind farm power curve in the next section.

A.2.2. Wind farm power curve

The objective of this point is to get a simplified representation of the wind farm enough accurate to use it in the statistical model [372, 373].

Standard IEC 61400-123 [374] shows a detailed method to compute the wind farm power output from data of the meteorological mast. The description of the wind farm operation consists of performance matrix \mathbf{M} indicating the declared power output expected of the wind farm for pairs of wind speed and wind direction values.

In a farm, the distribution of the speed among the turbines is quite dependent of wind direction and that is why the prospective standard IEC 61400-123 utilizes a matrix dependent on wind direction.

This matrix can be expected to be produced as an integral part of the wind farm design process. The information needed to compute this matrix can consist of:

- Long-term climate information at a reference position.
- Turbine performance characteristics.
- Wind flow models for assessing topographic, land cover and turbine wake characteristics.
- Electrical data to compute losses inside the grid of the farm.

Each matrix element $m_{i,j}$ is the expected power output for the wind speed w_i and direction θ_j corresponding to the bin i, j . Therefore, the estimated power \hat{P}_{output} can be computed from the wind speed and direction bin probability, $\text{Pr}(w_i, \theta_j)$.

$$\hat{P}_{\text{output}} = \sum_j \sum_i m_{i,j} \cdot \text{Pr}(w_i, \theta_j) \quad (593)$$

The distribution of power output can be found, for example, using the relationship

$$\begin{aligned}
\text{Pr}(p_k \leq P_{\text{output}} < p_{k+1}) = \\
\sum_j \sum_i \text{if}(p_k \leq m_{i,j} < p_{k+1}, \text{Pr}(w_i, \theta_j), 0) \quad (594)
\end{aligned}$$

To be able to obtain an analytic expression, a simpler model will be employed based on the standard deviation σ_w of wind speed inside the wind farm. Therefore, the considered characteristics of the wind would be its spatial average w_{wf} and its standard deviation σ_{wf} inside the wind farm in ten minute intervals. If there is no data about the wind distribution inside the farm, σ_{wf} can be estimated from the standard deviation of turbine efficiency (from microsite optimization) or from the variance of energy output that is usually available at SCADA (average power and average wind speed show a behaviour similar).

The main effect of the wind distribution inside the farm would be:

- Decrease of wind farm w_{wf} average speed from undisturbed wind speed value w_s of the site model (section III of this paper). If performance matrix is not available and there is no more information, it is reasonable to multiply the

undisturbed value by an efficiency factor η_{WF} that would be around 90-95%, depending on the wake effects [375].

$$w_{wf} = \eta_{wf} w_s \quad (595)$$

- Smooth the power curve since each turbine experience a slightly different speed. This smoothing is evident at cut-off speed.

The power output of the wind farm would be the sum of the output of the turbines (less the grid losses that would be computed in next section).

If wind speed distribution inside the farm is known, the power output distribution of the turbines would be:

$$pdf_{Power\ output}(p_{WF}) = \frac{1}{|dp_w/dw|} pdf_{wind\ speed}(w_{WF}) \Big|_{w=P_w^{-1}(p)} \quad (596)$$

The average power output for a given mean wind speed is the cross correlation of the power curve and the wind distribution:

$$\bar{P}_{Power\ output}(w) = \int_{-3\sigma_{wf}}^{3\sigma_{wf}} pdf_{wind\ speed}(\tau) \cdot P_w(w + \tau) d\tau \quad (597)$$

The average power for a normal distribution cannot be computed analytically unless some approximations are made. However, if slope of power curve is quite steady in the interval of $w_{wf} \pm \sigma_{wf}$, the average power output can be approximated as $\bar{P}_{Power\ output}(w) \approx P(w)$. This is a good approximation except for the cut-off speeds, when the disconnection of turbines causes an abrupt change of the power curve. For such cases, the wind farm power curve can be characterized with two extra parameters that reflect how abrupt the disconnection of the turbines is:

$$P_{wf}(w_s) = \frac{P_{nominal}}{2} \left[\text{Tanh} \left(\text{Ln}(3) \frac{w_s - \frac{w_{25\%} + w_{75\%}}{2}}{w_{25\%} - w_{75\%}} \right) - \text{Tanh} \left(\text{Ln}(3) \frac{\eta_{wf} w_s - w_{cut\ off}}{\Delta w_{off}} \right) \right] \quad (598)$$

Δw_{off} is the difference between the wind speed when there is a 25 % and 75 % of disconnection of the turbine due to high wind.

$w_{cut-off}$ is the wind speed when there is a 50% probability of the turbine to shut down.

η_{wf} is the farm mean efficiency factor.

w_s is the undisturbed wind speed of the site

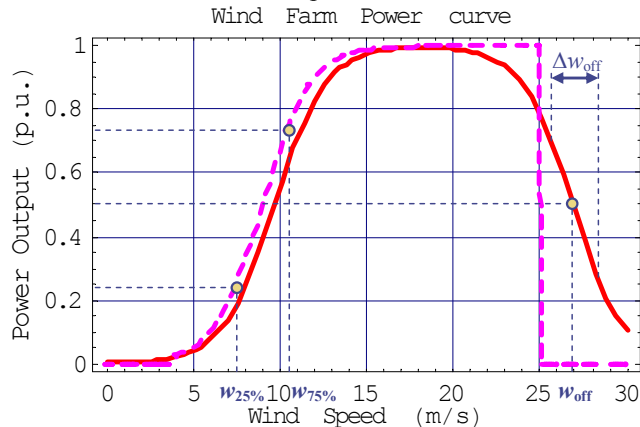


Fig. 156: Power curve of the wind farm (solid) and the turbine (dashed) for the example of annex I.

If all turbines of the wind farm are the same model, the power curve normalised “per unit” is analogous for the grid and for the turbine.

Near cut-off wind speed, the power curve is highly non linear. Also, the uncertainty of power curve is greater there. In such cases, the power show greater variability. In such wind regime, the turbines would gradually shut down starting from those more exposed.

$$\Pr(\text{Power}_{WF} < p_{WF}) = \quad (599)$$

$$= \Pr(\text{Wind}_S < P_{WF}^{-1}(p_{WF})) + \Pr(\text{Wind}_S > P_{WF}^{-1}(p_{WF})) =$$

$$= \text{CDF}_{\text{Wind}}(P_{WF}^{-1}(p_{WF})) + 1 - \text{CDF}_{\text{Wind}}(P_{WF}^{-1}(p_{WF})) =$$

$$= 1 + \text{Exp} \left\{ - \left[\frac{w_{cut\ off} + \frac{\Delta w_{off}}{\text{Ln}(3)} \text{ArcTanh} \left(1 - \frac{2p_{WF}}{P_{nominal}} \right)}{\text{scale}} \right]^{\text{shape}} \right\} -$$

$$- \text{Exp} \left\{ - \left[\frac{\frac{w_{25\%} + w_{75\%}}{2} + \frac{w_{25\%} - w_{75\%}}{\text{Ln}(3)} \text{ArcTanh} \left(1 - \frac{2p_{WF}}{P_{nominal}} \right)}{\eta_{wf} \text{scale}} \right]^{\text{shape}} \right\}$$

The uncertainty of wind at the site is σ_S (the uncertainty is the deviation of the parameter measured or estimated). The value of the combined standard uncertainty is equal to the standard deviation of the measure, that is a stochastic variable [376].

The relationship between the standard deviation of wind farm speed σ_{WF} and power output of a single turbine σ_{pof} due to wind deviation can be approximated by:

$$\sigma_{turbine\ power\ output}(p_{WF}) \approx \left| \frac{dp_{WF}}{dw_{WF}} \right|_{w=P_w^{-1}(p)} \sigma_{WF} = \frac{P_{nominal}(w_{75\%} - w_{25\%}) \sigma_{WF}}{P_{WF} \left(\frac{P_{nominal} - p_{WF}}{P_{nominal}} \right) \text{Ln}(9)} \quad (600)$$

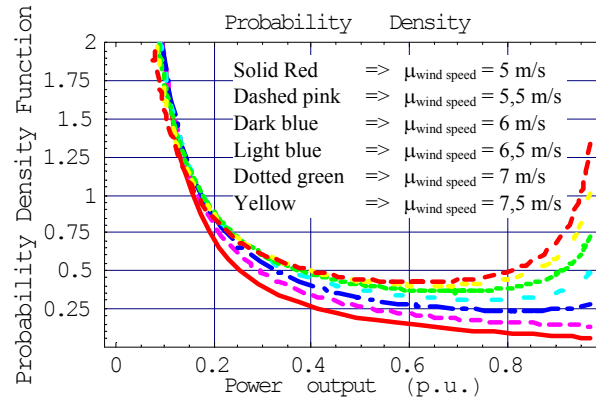


Fig. 157: Plot of PDF $P_{Power\ Output}$ for the wind farm power output of Annex I.

The deviation of the whole farm power output is not the sum of individual turbine deviations since some degree of cancellation is achieved. Unless more detailed data are available, it is reasonable to expect a normal distribution of wind speeds at the farm. If wind is distributed normally independent among n turbines of a farm, the deviation is only \sqrt{n} times the deviation of a single turbine, instead of n .

$$\sigma_{farm\ power\ output}(p_{WF}) \approx \sqrt{n} \sigma_{turbine\ power\ output}(p_{WF}) = \frac{P_{nominal}(w_{75\%} - w_{25\%}) \sigma_{WF}}{\sqrt{n} P_{WF} \left(\frac{P_{nominal} - p}{P_{nominal}} \right) \text{Ln}(9)} \quad (601)$$

The standard deviation of power output of the farm σ_{p_o} due to wind deviation at cut-off speeds can be approximated by:

$$\sigma_{farm\ power\ at\ cut-off}^{(P_{WF})} \approx \frac{P_{nominal\ farm} \Delta w_{off}}{\sqrt{n} p (P_{nominal\ farm} - P_{WF}) Ln(9)} \sigma_{wf} \quad (602)$$

The standard deviation of power output of the farm in function of the undisturbed wind speed of the site w_s is:

$$\sigma_{farm\ power}^{(w_s)} = -\frac{P_{nominal} Ln(3) \sigma_{wf}}{2 \sqrt{n}} \left[\frac{Sech \left[Ln(3) \frac{\eta_{wf} w_s - w_{cut\ off}}{\Delta w_{off}} \right]}{\Delta w_{off}} + \frac{Sech \left[Ln(3) \frac{\eta_{wf} w_s - \frac{1}{2}(w_{25\%} + w_{75\%})}{w_{25\%} - w_{75\%}} \right]}{w_{25\%} - w_{75\%}} \right] \quad (603)$$

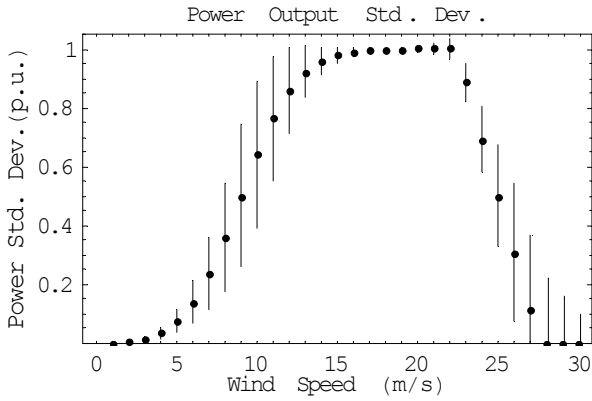


Fig. 158: Power curve of the wind farm (dots) and the uncertainty of the power for the example of annex I.

The uncertainty of power curve near cut-off usually partially accounts for this deviation since the wind varies during the 10 minute interval used for the manufacturer to compute the power curve.

A.3. Wind farm model

Within this point it is presented a new method to obtain the equivalent of a wind farm from the characteristics of its components. For the sake of simplicity, the method is applied to a farm composed by a single type of generator with the same load level.

In this model, the farm is divided into the following parts:

- substation (including the park's substation and the portion of the line that goes to the PCC)
- the medium voltage network that connects the substation to the wind turbines.
- the wind turbines (including the MV to LV transformer that usually is located into the tower)

The presented method is general and can be extended to more complex topologies using fourth-pole transformations.

A.3.1. Final representation of the Farm

A) Farm with fixed tap transformer.

The equivalent circuit for the farm, that will be obtained at the end of the modeling, will be represented by the farm's transmission matrix and the power generated by a turbine:

The basic operations required in order to obtain the transmission matrix for the park are the cascade connection of the elements (equivalent to multiplying the transmission

matrixes) and the parallel connection of circuits (equivalent to a weighted sum of the fourth-poles.

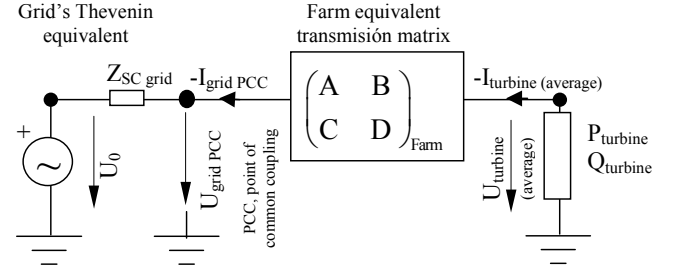


Fig. 159: Model of the farm with fixed tap transformer using its transmission matrix.

Fig. 151 shows the circuit based on the single-phase equivalent. Thus, if the per unit method is not used, power and voltages should be transformed into phase values.

In order to calculate the current injected to the grid, it is necessary to use the transmission matrix considering the network as primary side and the turbines as secondary side of the fourth-pole). (604)

$$\begin{pmatrix} U_0 \\ I_{grid\ PCC} \end{pmatrix} = \begin{pmatrix} 1 & Z_{SC\ grid} \\ 0 & 1 \end{pmatrix}_{Thév} \begin{pmatrix} A & B \\ C & D \end{pmatrix}_{Farm} \begin{pmatrix} U_{turbine} \\ I_{turbine} \end{pmatrix}$$

Two solutions are found for the PQ node. The solution of PQ node for stable operation of the turbine is given by the following equation:

$$C1 = U_0^2 + B (P - i Q) Conj [A] + A (P + i Q) Conj [B]$$

$$U_{turbine} = \sqrt{\frac{C1 + \sqrt{C1^2 - 4 (P^2 + Q^2) Abs[A]^2 Abs[B]^2}}{2 Abs[A]^2}}$$

$$I_{turbine} = \frac{-P + j Q}{U_{turbine}} \quad (605)$$

where P and Q is the power generated by the turbine (PQ node). A, B, C, D are the parameters of transmission matrix. U_0 and $U_{turbine}$ are voltage at primary and secondary side of the equivalent fourth-pole. If U_0 is voltage at infinite bus, the parameters of the transmission matrix are

$$\begin{pmatrix} A & B \\ C & D \end{pmatrix} = \begin{pmatrix} 1 & Z_{SC\ grid} \\ 0 & 1 \end{pmatrix}_{Thév} \begin{pmatrix} A & B \\ C & D \end{pmatrix}_{farm} \quad (606)$$

The static voltage collapse occurs at the following primary voltage: (607)

$$U_{o\ min} = \sqrt{\left(2 \sqrt{P^2 + Q^2} Abs[A] Abs[B] - B (P - i Q) Conj [A] - A (P + i Q) Conj [B] \right)}$$

B) Farm with tap-changing transformer

However, if the transformer allows load regulation, it is not operating at the maximum of minimum value and the voltage variation is slow, substation voltage at the MV side of the transformer is almost the commanded value.

According to that, the steady-state simplified model of a park with this type of transformer can be divided into two uncoupled parts. Thus, the grid sees the park as a PQ node. The output of the transformer, seen from the MV circuit side, as a voltage source whose absorbed or generated power

corresponds to a PQ node of the grid (power transmitted by a ideal transformer does not depend on the tap).

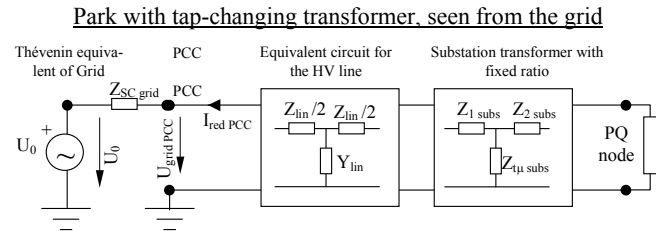


Fig. 160: Model of the farm from the utility point of view.

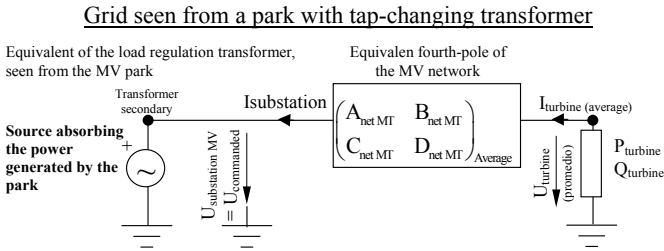


Fig. 161: Voltage uncoupled model for parks with load regulation transformer (model from the WT point of view).

C) Dependence on voltage of the power generated by a turbine

If the efficiency of a generator can be assessed as a function of voltage and the reactive power compensation policy is known, the turbine can be modeled as a node S_{turbine} = $P_{\text{turbine}} \cdot U_{\text{turbine}}^{np} + j Q_{\text{turbine}} \cdot U_{\text{turbine}}^{nq}$.

In this case, U_{turbine} can be found substituting $P = P_{\text{turbine}} \cdot U_{\text{turbine}}^{np}$ and $Q = Q_{\text{turbine}} \cdot U_{\text{turbine}}^{nq}$ in the PQ equation and numerically solving the expression. The values obtained not taking into account the voltage dependence can be used as initial value.

A.3.2. Substation modeling

Substation is connected to the grid in the point of common coupling, PCC, with a HV line. In this model, the line and the transformer are going to be represented by their transmission matrices (single-phase equivalent).

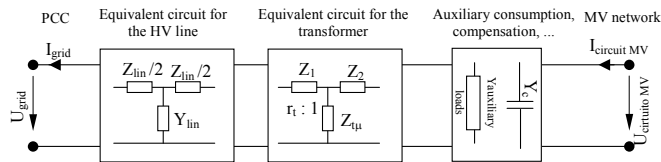


Fig. 162: Model of the substation of the farm.

A.4. Modeling of the underground MV network

Turbines are generally connected to an underground MV cable (usually 20 KV, although there are also parks with 30 kW interior network). Usual distances among turbines are around 80-300 m, they have a low consumption or generation of reactive power, and the series impedance of the cable is moderate. Under these conditions, the voltage drop between the first and last turbine is small:

$$\Delta U \approx \frac{PR + QX}{U} \quad (608)$$

The voltage drop between the substation and the closest turbine is usually small if the substation is located in the park. In some cases, the substation is away from the park because of environmental problems. In these cases the voltage drop in the cable can be a limiting factor when choosing cable and MV network voltage.

A) Added model of turbines using the moments

A simple model that provides precise results even with significant voltage drops is based in the voltage drop calculation using the method of moment.

This method is equivalent to concentrating all the generators in its load center of mass, which is at $1/3$ of the distance between the first and the last turbine, closest to the substation[†]. In the case of parks with different types of cable or different types of generators, this model can be adapted.

Considering that the current injected by the turbines varies in an almost linear way for small voltage variations, like the ones that take place between the first and the last turbine, this model gives very accurate results.

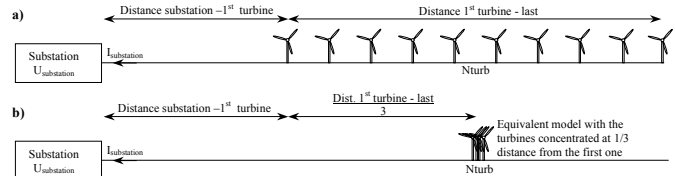


Fig. 163: Concentrated model of a MV circuit in a park.

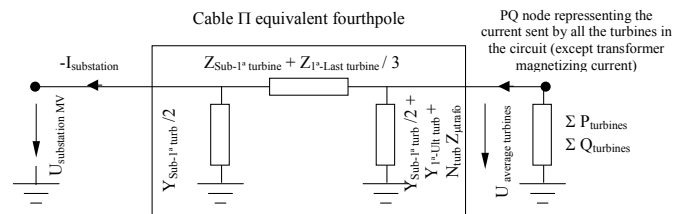


Fig. 164: Model of the MV circuit and the turbines of a park.

The power sent to the substation can be found using the parameters of the equivalent fourth-pole of the medium voltage cable.

$$\begin{pmatrix} \bar{A}_{MT} & \bar{B}_{MT} \\ \bar{C}_{MT} & \bar{D}_{MT} \end{pmatrix}_{\text{cable}} = \begin{pmatrix} 1 + Z_c Y_a & Z_c \\ Y_a + Y_b + Y_a Y_b Z_c & 1 + Z_c Y_b \end{pmatrix} \quad (609)$$

where

$$Z_c = Z_{\text{Sub-1}^{\text{st}} \text{ turbine}} + Z_{1^{\text{st}} \text{-U}^{\text{lt}} \text{ turbine}} / 3$$

$$Y_a = Y_{\text{Sub-1}^{\text{st}} \text{ turbine}} / 2 + Y_{1^{\text{st}} \text{-U}^{\text{lt}} \text{ turbine}} + N_{\text{turb}} Z_{\text{trafo}}$$

$$Y_b = Y_{\text{Sub-1}^{\text{st}} \text{ turbine}} / 2$$

N_{turb} number of turbines in the circuit

I_{turbine} average current consumed by the turbines (negative while in production)

$U_{\text{substation MV}}$ is the cable voltage in the substation terminals

[†] The centre of mass has been calculated using the criterion of equal cable power loss. If the criterion of equal average voltage in both the equivalent and the original circuits had been chosen, the turbines would be placed further, at $1/2$ of the distance between the first and the last turbine. The power criterion is more realistic since the impedance of the cable usually increases in the sections far from substation.

$Y_{1^{st}\text{-Last turb}}$ is the admittance of the part of the cable between the first and the last turbine

$Y_{\text{Sub-1}^{st}\text{ turb}}$ is the admittance of the part of the cable between the substation and the first turbine

$Z_{1^{st}\text{-Ult turb}}$ is the series impedance of the part of the conductor between the first and the last turbine.

$Z_{\text{Sub-1}^{st}\text{ turb}}$ is the series impedance of the part of the conductor between the substation and the first turbine.

$Z_{\mu\text{trafo}}$ the magnetizing inductance of the transformer inside the turbine

B) Aggregated model of the MV circuit branches

In order to solve directly, without iteration, a park with various branches on the MV circuit, they must be grouped in a single equivalent branch. The equivalent voltage of the turbines is the weighted average of the circuits and the current sent to the substation is the sum of all the circuits.

The voltage in all the branches in the MV circuit is similar if one of the following conditions takes place:

- ✓ Circuits are short and, thus, the voltage drops are small.
- ✓ Circuits are long, but all have similar length and similar number of turbines connected.

Like in the previous part, the equivalent models are based in the linearization of the behavior of the turbines around the average working voltage.

If all the turbines are the same type, it is convenient to include the number of connected turbines in the transmission matrix. By doing this, at the end of all circuits there is the same PQ power corresponding to a single turbine. Inside the matrix, the current is multiplied by the number of turbines in each circuit.

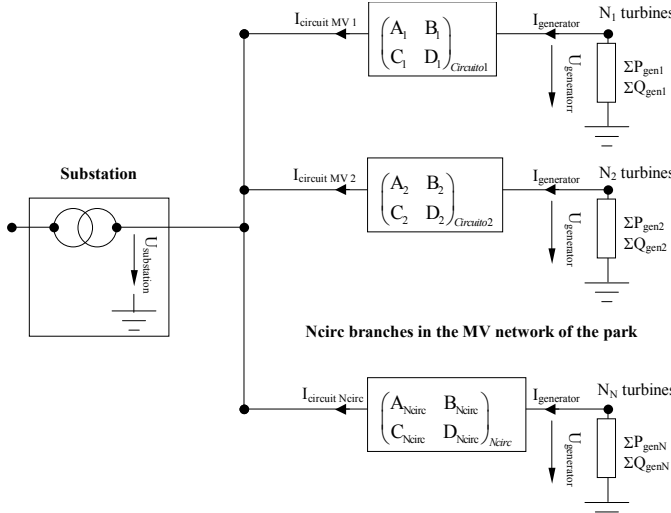


Fig. 165: Complete scheme of the medium voltage network, using the aggregated generator model.

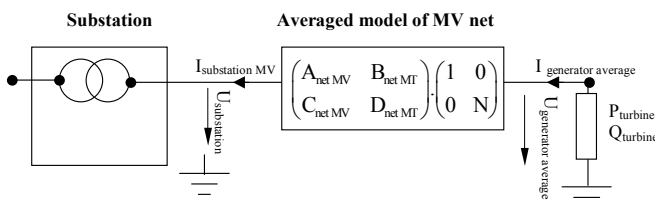


Fig. 166: Simplified scheme of the medium voltage network of the park with added generator model.

The parameters of the equivalent fourth-pole are found adding the currents and calculating the equivalent voltage as a weighted average of the voltages in each branch.

$$N = \sum_{i=1}^{N_{\text{circuits}}} N_{\text{turb}_i} \quad (610)$$

$$A_{\text{net MV}} = \frac{\sum_{i=1}^{N_{\text{circuits}}} N_{\text{turb}_i} A_{\text{circuit } i}}{N} \quad (611)$$

$$B_{\text{net MV}} = \frac{\sum_{i=1}^{N_{\text{circuits}}} N_{\text{turb}_i}^2 B_{\text{circuit } i}}{N^2} \quad (612)$$

$$C_{\text{net MV}} = \sum_{i=1}^{N_{\text{circuits}}} C_{\text{circuit } i} \quad (613)$$

$$D_{\text{net MV}} = \frac{\sum_{i=1}^{N_{\text{circuits}}} N_{\text{turb}_i} D_{\text{circuit } i}}{N} \quad (614)$$

This model can be extended to farms with turbines of different types and with complex layouts.

A.4.2. Modeling of the turbines

A) Simplified model of the low voltage circuit

In the LV side of a turbine, voltage usually is near its rated value thanks to the taps in the transformers. Small voltage changes modify lightly electrical losses and reactive power.

Losses are due to Joule effect $P_{\text{Cu}} \approx R_{\text{cc}} S^2 / U^2$ and iron losses, $P_{\text{Fe}} \approx R_{\text{Fe}} U^2$. Thus, losses depend on voltage with a function of the parameters of the generator. However, the efficiency of the generator is usually high and it does not depend greatly on voltage. Moreover, the effect of voltage fluctuations in electrical losses is small compared to the uncertainty in the power curve of the turbine.

Besides, reactive power consumed by the generator depends on the square of both voltage and current $Q_{\text{gen}} \approx (X_{\mu} - X_{\text{cap}}) U^2 + X_{\text{cc}} I^2 = (X_{\mu} - X_{\text{cap}}) U^2 + X_{\text{cc}} S^2 / U^2$. However, reactive power consumption variations are nearly compensated by the control of the capacitor sets, as long as they are sufficiently sized. In other types of generators, the control acts regulating reactive power.

The stochastic nature of wind affects the control, adding uncertainty regarding which generator (in a machine with two generators or one with different connections) or which capacitor sets are connected. On top of that, some auxiliary consumption shows an intermittent or cyclic behavior.

Because of all these reasons, the turbine can be approximated on a load flow study, in a quite realistic way, by a PQ node whose parameters are a function of the average powers at each wind speed.

It is only necessary to consider the influence of voltage in those studies focused on the behavior of the park in extreme conditions (voltages out of normal operating range, homopolar or inverse sequence voltages, ...)

The value of active power as a function of wind speed can be derived from the power curve. The value of reactive power is not usually given by the manufacturer, but it can be measured. In generators with various LV circuits in the transformer, the power in all the LV circuits must be added (A direct measure of power in MV is difficult to perform).

It is desirable to obtain the reactive power curve from the manufacturer as a function of active power or wind speed. If the turbine can control reactive power, it is necessary to know how the command is set (power factor, reactive power...) and its limitations (working PQ plane).

B) Statistical model of the turbine

When the turbines do not have the same load level, the previous equivalent circuit has some error. Active and reactive power consumed by the transformers is proportional to the square of the load level in each turbine, not to the square of the average load level. Thus, using that model underestimates the power consumed by the transformers when the load level variation is important.

However, the previous model can be adapted to turbines with different load levels using a statistical approach. The turbine works around an average working point with active and reactive powers μ_{P_i} , μ_{Q_i} and variances $\sigma_{P_i}^2$, $\sigma_{Q_i}^2$ [3]. Variance is due both to the difference in power among turbines (spatial variation), and to the time variation of the generated power.

Spatial variation can be estimated from a wind potential study of the site, when measurements are not available. In such a case, this variation can be considered deterministic.

Time variation of power can be estimated from the maximum and minimum power in a time period. Another option is to calculate the variance of the power according to the uncertainty of the power curve. The exact calculation of the joint variance requires knowing the correlation among the time power variations in the turbines. However, in most cases, it can be accepted that the time variations are independent in every turbine.

Looking at the model in Fig. 165, a fairly simple model of the circuit can be found, based in statistic parameters. The sum of the generated power by the turbines is a statistic variable whose average, for the active and reactive power, is:

$$\mu_{\Sigma P_{\text{turbines}}} = \sum_{i=1}^{N_{\text{turb}}} \mu_{P_i} \quad (615)$$

$$\frac{\xi_{Rsc}}{S_{\text{base}}} \left(\sum_{i=1}^{N_{\text{turb}}} \mu_{P_i}^2 + \sum_{i=1}^{N_{\text{turb}}} \mu_{Q_i}^2 + \sum_{i=1}^{N_{\text{turb}}} \sigma_{P_i}^2 + \sum_{i=1}^{N_{\text{turb}}} \sigma_{Q_i}^2 \right)$$

$$\mu_{\Sigma Q_{\text{turbines}}} = \sum_{i=1}^{N_{\text{turb}}} \mu_{Q_i} \quad (616)$$

$$\frac{\xi_{Xsc}}{S_{\text{base}}} \left(\sum_{i=1}^{N_{\text{turb}}} \mu_{P_i}^2 + \sum_{i=1}^{N_{\text{turb}}} \mu_{Q_i}^2 + \sum_{i=1}^{N_{\text{turb}}} \sigma_{P_i}^2 + \sum_{i=1}^{N_{\text{turb}}} \sigma_{Q_i}^2 \right)$$

In order to estimate the uncertainty of the power generated by the turbines, it is necessary to have a statistic model of the park. Some dynamic wind models can be found in the literature [4-6]. However, taking into account that the aim of this paper is to find a simple model that can be characterized by few measurements, the following hypothesis are going to be made:

Variance which appears in the previous formulae is due, on one hand to the time variation of the power in a measuring period and on the other hand to the spatial variation (along the circuit) of the power generated by the turbines [7, 8].

Spatial power variation is due mainly to fast fluctuations that can be considered independent from one machine to

another. Spatial variations are correlated. For every predominant wind speed there are machines that, in average, generate more than others. This fact is taken into account applying a coefficient C_i , that is equivalent to the efficiency of the location of each turbine, and it is obtained from the micrositting of the park.

In order to consider these effects, the power generated by every turbine is modeled as an average power

P = average power in a working point

P_i = active p. from turbine $i = C_i P + \sigma_{P \text{ spatial}} X_i + \sigma_{P \text{ temporal}} Y$

Q_i = reactive power from turbine $i =$

$$= C_i Q + \sigma_{Q \text{ spatial}} X_i + \sigma_{Q \text{ temporal}} Y$$

X, Y = normalized statistical distributions, independent between them

X_i = distribution that represents the independent fluctuations for every turbine (mainly fast variations due to turbulence, tower shadow...).

Y = distribution representing the fluctuations that affect proportionally at every turbine (mainly slow power variations)

C_i = efficiency coefficient of the location of a turbine inside the park, relative to farm average.

$$C_i = \frac{\mu_{P_i}}{P}; \quad \sigma_{\text{coefficients } C_i}^2 = \frac{\sum (C_i - 1)^2}{N}$$

$$P = \text{ExpectedValue} \left[\frac{\sum P_i}{N} \right] = E \left[\frac{\sum (C_i P + \sigma_{P \text{ spatial}} X_i + \sigma_{P \text{ temporal}} Y)}{N} \right] = \frac{\sum C_i P}{N};$$

$$E[\sum P_i^2] = N^2 P^2 (1 + \sigma_{\text{coefficients } C_i}^2) + \sigma_{P \text{ temporal}}^2 + N \sigma_{P \text{ spatial}}^2$$

The equivalent average power in the turbine, in low voltage, is the average power of all turbines minus the average power consumption in the transformers. Performing the same analysis for the reactive power results in:

$$P_{\text{equiv turbine}} = P - \frac{\xi_{RCC}}{S_{\text{base}}} \sigma_{S \text{ turbine}}^2; \quad Q_{\text{equiv turbine}} = Q - \frac{\xi_{XCC}}{S_{\text{base}}} \sigma_{S \text{ turbine}}^2$$

$$\sigma_{S \text{ turbine}}^2 = (P^2 + Q^2) \sigma_{\text{coefficients } C_i}^2 + \sigma_{P \text{ temporal}}^2 + \sigma_{Q \text{ temporal}}^2 + \frac{\sigma_{P \text{ spatial}}^2 + \sigma_{Q \text{ spatial}}^2}{N} \quad (617)$$

It is important to know the variance of $P_{\text{equiv turbine}}$ y $Q_{\text{equiv turbine}}$, because it is going to be the main contribution to the uncertainty on the power generated by the park

$$\sigma_{P \text{ equiv turbine}}^2 \approx \sigma_{P \text{ temporal}}^2 + \frac{\sigma_{P \text{ spatial}}^2}{N} \quad (618)$$

$$\sigma_{Q \text{ equiv turbine}}^2 \approx \sigma_{Q \text{ temporal}}^2 + \frac{\sigma_{Q \text{ spatial}}^2}{N}$$

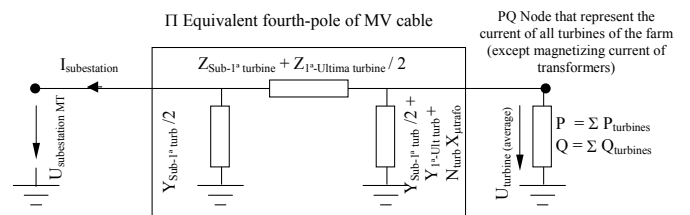


Fig. 167: Joint model of the MV circuit and the turbines of a park.

In order to have into account the consumption of active and reactive power when the load level is not the same in all the turbines, it is necessary to decrement the average power

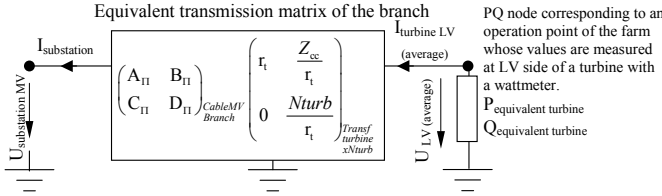


Fig. 168: Compact model, compensated for the variability of the power injected by the turbines.

The parameter $\sigma_{\text{coefficients } C_i}$ can be found from the study of the micro-siting of the park, or from the correlation of the active and reactive power of each turbine with the average in the park.

The parameter σ_{spatial} can be determined from an operating park, through the remote measurement system, with the correlation matrix. For a farm that is not operating yet, the order can be estimated from, at least two wind measurements and the active and reactive power curves.

The parameter σ_{temporal} can be found measuring the standard deviation of active and reactive power in one turbine whose turbulence is on the same order as the one of the park. It can also be estimated from the maximum and minimum power in the time period, although this method has less precision.

C) Electronically controlled generators.

Models for generators controlled by power converters can be found in the literature. The more frequent configuration is the doubly-fed induction generator, because of the lower cost of the power stages. However, it is becoming more common to find squirrel cage induction generators or synchronous generators connected to the grid through converters, in order to achieve variable speed.

The main problem when trying to model this type of generators is that there is no precise information about the control of the machine. In general, it is useless to try to find a precise model of the machine in a power flow study when the control strategies have to be “guessed” and whose parameters vary in each farm in order to achieve maximum efficiency at every location.

Taking into account that the efficiency of the generator is high, that the voltage is within a narrow range, that usually the information about the control is insufficient and that the power curve has a uncertainty from 3% to 5%, it is acceptable to approximate the group generator + electronics + auxiliary consumption by a PQ model.

Because of that, unless there is in-deep information about the generator (usually available only for the manufacturer), the model to be used is the simplified one.

D) Specific model for induction generators, directly connected to the grid.

The typical induction generator can be modeled as the cascade connection of the fourth-pole corresponding to the equivalent circuit of the generator, power factor correction capacitors and transformer. The variable resistor on the left represents the mechanical power in the generator.

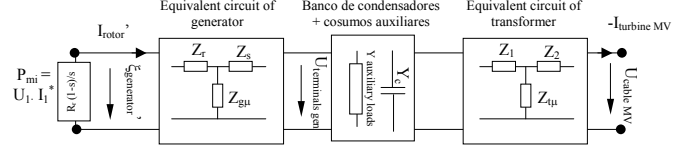


Fig. 169: Equivalent circuit of a turbine with a directly connected induction generator.

The transmission matrix is the cascade composition of the transmission matrix of the equivalent circuit of the generator (without the variable resistor), the capacitors and the transformer, ($\xi_{\text{generator}}$ is the e.m.f. of the generator in the rotor, referred to the stator).

If it is assumed that all the generators in the circuit work at the same point, the inverse transmission matrix can be found by cascade multiplying all the corresponding fourth-poles.

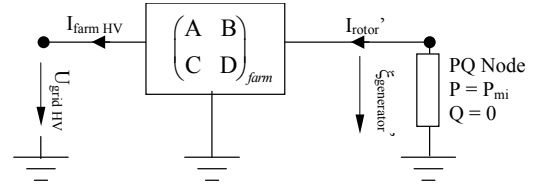


Fig. 170: Complete model of a park with directly-connected induction generators, valid when the number of capacitors and the auxiliary consumption can be estimated.

The slip of the generator depends on the terminal voltage. However, induction generators operate with at low slip (around 1% at full load) and it can be considered that blade speed is almost constant and thus, P_{mi} does not depend on voltage.

If the number of capacitor banks and the auxiliary consumption can be estimated, the influence of voltage in active and reactive power can be approximated by a power of voltage. In order to obtain the optimum power, the following equation can be solved with the rated values of the turbine.

$$\frac{\partial (P_{\text{turbina}}[U_{MT}, P_{mi}] U_{MT}^{-n_p})}{\partial U_{MT}} = 0 \implies \quad (619)$$

$$P_{\text{turbina}}[U_{MT}, P_{mi}] \approx P_{\text{turbina}}[U_{\text{nominal}}, P_{mi}] \cdot \left(\frac{U_{MT}}{U_{\text{nominal}}} \right)^{n_p}$$

$$\frac{\partial (Q_{\text{turbina}}[U_{MT}, P_{mi}] U_{MT}^{-n_q})}{\partial U_{MT}} = 0 \implies \quad (620)$$

$$Q_{\text{turbina}}[U_{MT}, P_{mi}] \approx Q_{\text{turbina}}[U_{\text{nominal}}, P_{mi}] \cdot \left(\frac{U_{MT}}{U_{\text{nominal}}} \right)^{n_q}$$

Coefficients n_p y n_q can be calculated analytically as a function of the inverse transmission coefficients. For simplicity, the quotes have been omitted from A' , B' , C' y D' :

$$C1 = \text{Cos} \left[\text{Arg} \left[\sqrt{\frac{(BC - AD)^2 + 4BD P_{mi}}{B^2 D^2}} \right] \right] \quad (621)$$

$$C2 = BD (BC + AD) \sqrt{\frac{(BC - AD)^2 + 4BD P_{mi}}{B^2 D^2}}$$

$$n_p = \text{Re} \left[-1 - \frac{C1 (BC - AD)^2 - C2}{C1 ((BC - AD)^2 + 4BD P_{mi}) - C2} \right] \quad (622)$$

$$n_q = \text{Re} \left[-1 - \frac{(BC - AD)^2 + 8BD P_{mi}}{(BC - AD)^2 + 4BD P_{mi}} \right] \quad (623)$$

For a 600 kW turbine, the following curves have been obtained.

$$P_{\text{turbina}}[U_{\text{MT}}, P_{\text{mi}}] \approx P_{\text{turbina}}[U_{\text{nominal}}, P_{\text{mi}}] \cdot U_{\text{MT}}^{0.19}$$

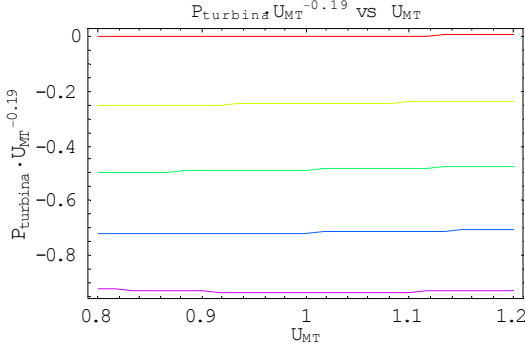


Fig. 171: Influence of voltage on real power.

$$Q_{\text{turbina}}[U_{\text{MT}}, P_{\text{mi}}] \approx Q_{\text{turbina}}[U_{\text{nominal}}, P_{\text{mi}}] \cdot U_{\text{MT}}^{-1.6}$$

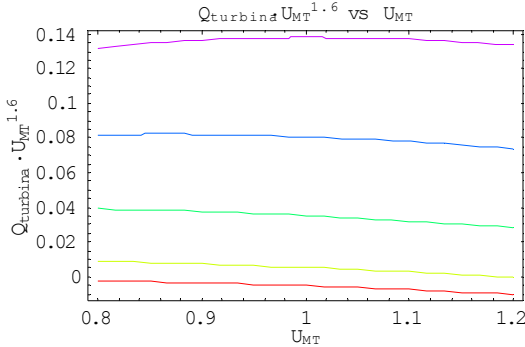


Fig. 172: Influence of voltage on reactive power.

Powers n_p or n_Q near zero show little influence of voltage. In the previous example, it can be seen that the influence of voltage in P and Q is small because the machine operates with power factor near unity and the resistance in the system is small.

The previous expressions have been obtained with a fixed number of capacitors connected (without power factor regulation with voltage).

The generator emf referred to the stator, $\xi_{\text{generator}}$, can be calculated from the voltage at the PCC, solving the PQ node. Then, the generator terminal voltage can be easily calculated using the impedances of the generator equivalent circuit.

$$U_{\text{terminal generator}} = \xi_{\text{generator}} \cdot \left(1 + \frac{Z_r}{Z_{gu}}\right) - \left(\frac{P_{\text{mi}}}{\xi_{\text{generator}}}\right) \cdot \left(Z_r Z_s + \frac{Z_r Z_s}{Z_{gu}}\right) \quad (624)$$

A.4.3. Uncertainty of the model

The uncertainty of the power injected to the grid by the wind farm can be divided in two parts, depending on its origin. One part is due to the stochastic behavior of the wind, and the other is due to the electric model [9].

A) Uncertainty due to the stochastic behavior of the park.

The main source of uncertainty is originated by the variability of the primary source of energy, the wind. This affects directly both P_{turbine} and Q_{turbine} .

In the part dedicated to the stochastic modeling of the turbines, a very simplified model has been used. In practice, wind will interactuate with aerodynamics and the control system. The uncertainties can be found from data measured in a park.

$$u_P \text{ due to the wind} \approx P_{\text{farm}} \sqrt{\frac{\sigma_{P \text{ temporal}}^2 + \frac{\sigma_{P \text{ spatial}}^2}{N}}{N}} \quad (625)$$

$$u_Q \text{ due to the wind} \approx Q_{\text{farm}} \sqrt{\frac{\sigma_{Q \text{ temporal}}^2 + \frac{\sigma_{Q \text{ spatial}}^2}{N}}{N}}$$

Uncertainty due to the stochastic operation can be around 5%, although depends greatly on the measuring period and the power sampling speed. If uncertainty is calculated from field data, these will include the effect of outage of the turbines.

B) Uncertainty due to the simplified model of the park.

In general, the uncertainties introduced by the park model will be much lower than the ones introduced by the wind, because in normal operation $\Delta V < 3\%$.

The uncertainty due to the approximate solving of the circuit of the park depends on the voltage difference among turbines. The model is based in the assumption that all the turbines work at the average voltage. In practice, errors are introduced because the behavior is not linear. The uncertainty associated to the voltage distribution is, as a function of the impedances of the circuit in p.u.

$$\Delta V_{\text{turb}} = \frac{V_{\text{max turbine}} - V_{\text{min turbine}}}{2}; \quad (626)$$

$$S_{Z_{\text{serie}}} \approx \left(\frac{Z_{\text{Cable First-Last turbine}}}{3} + \frac{Z_{\text{turbine trafo}}}{N_{\text{turbines}}} \right) \frac{|S_{\text{branch}}|^2}{V^2}$$

$$\frac{\partial S_{Z_{\text{serie}}}}{\partial V_{\text{turb}}} \approx 2 \left(\frac{Z_{\text{Cable First-Last turbine}}}{3} + \frac{Z_{\text{turbine trafo}}}{N_{\text{turbines}}} \right) \frac{|S_{\text{circuito}}|^2}{V^3} \quad (627)$$

$$u_P \text{ due to } \Delta V \text{ among turbines} = \left(\frac{\partial P}{\partial V} \right) \frac{\Delta V_{\text{turb}}}{\sqrt{3}} \approx \quad (628)$$

$$\approx \sum_{N \text{ branches}} \frac{-2}{\sqrt{3}} \Delta V_{\text{turb}} \left(\frac{R_{\text{Cable First-Last turbine}}}{2} + \frac{R_{\text{trafo turbine}}}{N_{\text{turbines}}} \right) \frac{|S_{\text{branch}}|^2}{V^3}$$

$$u_Q \text{ due to } \Delta V \text{ among turbines} = \left(\frac{\partial Q}{\partial V} \right) \frac{\Delta V_{\text{turb}}}{\sqrt{3}} \approx \quad (629)$$

$$\approx \sum_{N \text{ branches}} \frac{-2}{\sqrt{3}} \Delta V_{\text{turb}} \left(\frac{X_{\text{Cable First-Last turbine}}}{2} + \frac{X_{\text{trafo turbine}}}{N_{\text{turbines}}} \right) \frac{|S_{\text{branch}}|^2}{V^3}$$

There are other sources of uncertainty, like the dependence of generated power with voltage. However, the behavior of the turbine is highly dependent on the technology used and on the parameters of the machine, so it would be necessary to measure or simulate it precisely.

Using these data, the turbine can be represented by a node $S_{\text{turbine}} = P_{\text{turbine}} \cdot V_{\text{p.u.}}^{np} + j Q_{\text{turbine}} \cdot V_{\text{p.u.}}^{nq}$, where the parameters n_p y n_q show the influence of voltage. Uncertainty from these parameters is:

$$S_{\text{turbine}} = P_{\text{turbine}} \cdot \left(\frac{V_{\text{turbine}}}{V_{\text{no min al}}} \right)^{np} + j Q_{\text{turbine}} \cdot \left(\frac{V_{\text{turbine}}}{V_{\text{no min al}}} \right)^{nq} \quad (631)$$

$$u_P \text{ due to } V \text{ different from nominal} \approx \frac{n_p P_{farm}}{\sqrt{3}} \left(\frac{V_{turbine}}{V_{nominal}} \right)^{np-1} \left| 1 - \frac{V_{turbine}}{V_{nominal}} \right| \quad (633)$$

$$u_Q \text{ due to } V \text{ different from nominal} \approx \frac{n_q Q_{farm}}{\sqrt{3}} \left(\frac{V_{turbine}}{V_{nominal}} \right)^{nq-1} \left| 1 - \frac{V_{turbine}}{V_{nominal}} \right| \quad (634)$$

C) Uncertainty due to grid voltage

In the model it has been assumed an infinite bus voltage U_0 corresponding to the Thevenin equivalent. This voltage varies in parks connected to distribution networks, lines with highly variable consumption... The uncertainty associated to voltage variations in the grid is:

$$\Delta V_{grid} = \frac{V_{\max \text{ grid PCC}} - V_{\min \text{ grid PCC}}}{2} \quad (635)$$

$$\frac{\partial S_{farm}}{\partial V_{grid}} = 2 I_{grid \text{ PCC}}^* + \frac{S_{farm}}{\sqrt{B'D'S_{farm}^* + \frac{V_{grid}^2}{4}(A'D - B'C')}} \quad (636)$$

$$u_P \text{ due to } \Delta V \text{ in the grid} = \operatorname{Re} \left(\frac{\partial S_{farm}}{\partial V_{grid}} \right) \frac{\Delta V_{grid}}{\sqrt{3}} \quad (637)$$

$$u_Q \text{ due to } \Delta V \text{ in the grid} = \operatorname{Im} \left(\frac{\partial S_{farm}}{\partial V_{grid}} \right) \frac{\Delta V_{grid}}{\sqrt{3}} \quad (638)$$

D) Total uncertainty

In order to calculate the total uncertainty of the power injected to the utility, due to all the factors previously mentioned, the square addition law must be used. In general, it is normal to use the total extended uncertainty $k=2$ (interval where power is the 95% of the time, for a given set of operating conditions).

$$u_P = 2 \sqrt{u_{P \text{ wind}}^2 + u_{P \Delta V_{grid}}^2 + u_{P \Delta V_{turbines}}^2 + u_{P V \neq \text{nominal}}^2} \quad (639)$$

$$u_Q = 2 \sqrt{u_{Q \text{ viento}}^2 + u_{Q \Delta V_{grid}}^2 + u_{Q \Delta V_{turbines}}^2 + u_{Q V \neq \text{nominal}}^2} \quad (640)$$

A.4.4. Model of the electrical grid of the farm

The approach followed in this section is based in [377], where a simplified model of the wind farm is derived based on the fourth-pole equivalent representation of the electrical elements, the distributed layout of the turbines, the stochastic nature of power output and small-signal analysis of the grid. The uncertainties of the approximations made in the model are also assessed there. The overall system uncertainty is barely affected by this representation since it is precise enough and the grid behaviour is much more deterministic than the wind and power curves.

The approximate method of the moments is widely accepted in electrical engineering. Using that approach, the turbines can be concentrated in some points, as it is pictured in Fig. 159. Due to the fact that the turbines inside a wind farm have similar power output and voltage, a “concentrated

model” can be used for accounting power losses in shunt admittances and series inductances.

The behaviour of turbines resemble PQ nodes because its efficiency is high, voltage is near nominal value for usual operation and because reactive control tries to reach control target (usually certain power factor).

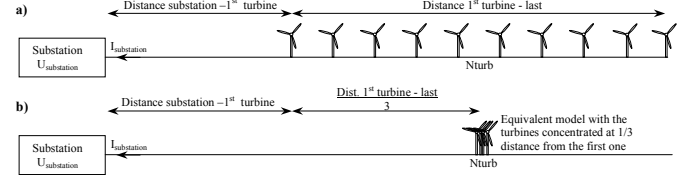


Fig. 173: Original and concentrated model of a MV circuit in a park.

Paper [204] computes the model parameters from resistance, capacity and reactance of each element, obtaining the farm equivalent transmission matrix shown in the Fig. 158. However, it is more convenient to estimate the parameters from power flow solutions.

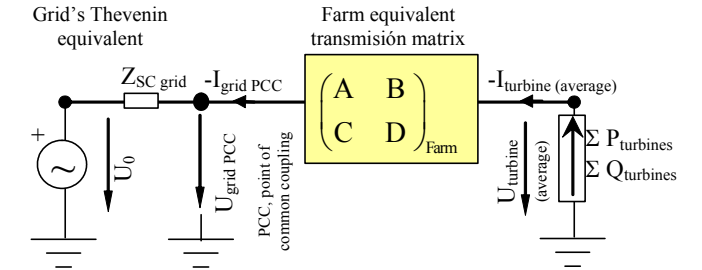


Fig. 174: Model of the farm using its transmission matrix.

The farm equivalent can be regarded as Π or T equivalent. However, an approximate representation with a shunt admittance and series impedance will be used to simplify the analytic expressions. If a more precise model of the farm is needed, a full Π or T fourth pole equivalent can be used (another simulation case would be needed to estimate the extra parameter).

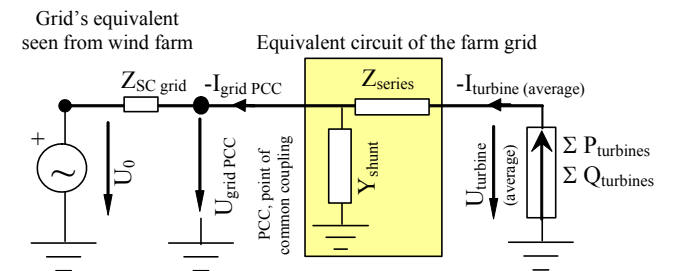


Fig. 175: Model of the farm using a fourth pole realization.

(632)

In this article, the electrical parameters of the farm will be expressed in per unit using the nominal power of the wind farm as base.

The relation of power flow at turbines and at point of common coupling PCC can be easily derived.

$$P_{PCC} = P_{WT} - R_{series} \frac{P_{WT}^2 + Q_{WT}^2}{U_{PCC}^2} - G_{shunt} U_{PCC}^2 \quad (641)$$

$$Q_{PCC} = Q_{WT} - X_{series} \frac{P_{WT}^2 + Q_{WT}^2}{U_{PCC}^2} + B_{shunt} U_{PCC}^2 \quad (642)$$

Where

$$P_{WT} = \sum P_{turbines} = \text{sum of active power of all turbines}$$

$Q_{WT} = \Sigma Q_{turbines}$ = sum of active power of all turbines

P_{PCC} = Active power injected at PCC

P_{PCC} = Reactive power injected at PCC

R_{series} and X_{series} are the real and imaginary part of Z_{series} , i.e. the resistance and reactance of the series equivalent.

G_{shunt} and B_{shunt} are the real and imaginary part of Y_{shunt} , i.e. the shunt conductance and susceptance.

In case of fixed capacitors that are always connected, it is more precise to compute them in B_{shunt} . Also, if the maximum supply or drain of reactive power is being studied, all the capacitors and inductances shunt connected should be included in B_{shunt} . In other cases, the automatic reactive compensation must be included in Q_{WT} .

Even though the voltage inside the farm varies, it is expected to be near to assigned value on normal operation ($U_{turbine} \sim 1$ p.u.). This simplification is only a small source of uncertainty of the model since Z_{series} are expected small p.u. (around 0.12 p.u.) and Y_{shunt} is expected to be big (at least 20 p.u.). Standard UNE 206005 [378] assess the reactive power ability of wind farms at $U_{turbine} = 0,95$ p.u., 1 p.u. and 1,05 p.u. This standard states a method to compute farm power losses that is equivalent to the one presented in this section.

The new method to obtain the farm equivalent consists on simulate the wind farm with a power flow program at two power levels and to solve the parameters R_{series} , X_{series} , G_{shunt} and B_{shunt} from equations (641) and (642). For 1 p.u. voltage at PCC and power simulations at calm ($P_{WT} = 0$, $Q_{WT} = 0$) and full power with unity power ($P_{WT} = 1$ p.u., $Q_{WT} = 0$), the parameters are:

$$\begin{aligned} G_{shunt} &= -P_{PCC} \Big|_{P_{WT}=0, Q_{WT}=0} \\ B_{shunt} &= Q_{PCC} \Big|_{P_{WT}=0, Q_{WT}=0} \\ R_{series} &= 1 - P_{PCC} \Big|_{P_{WT}=1, Q_{WT}=0} - G_{shunt} \\ X_{series} &= -Q_{PCC} \Big|_{P_{WT}=1, Q_{WT}=0} + Y_{series} \end{aligned} \quad (643)$$

A.4.5. Model of nearby wind farms

The influence of near wind farms should be taken into account because their active power output are quite correlated (they show a similar behaviour).

A simple linear correlation can be enough precise for grid studies of near wind farms. Far away wind farms show generally complex relationships and have low correlation coefficients. But those farms are expected to interact less with the studied wind farm. Therefore, a linear correlation of the farms is enough in most cases (the more influencing wind farms are better modelled).

If grid parameters vary linearly with the power output of the analyzed wind farm, the average effect of other wind farms would be approximately computed using average power for the given selected power level of the studied farm (a linear function, applied to a stochastic variable, also transform linearly the expected value and standard deviation of that variable). For example, voltage deviations and power flows are related mainly linearly with power (except near a voltage collapse or very high wind share).

The linear regression of the power predicted in wind farm “j” based on the power of the reference farm “i” is given by:

$$P_j = \bar{P}_j + b_j (P_i - \bar{P}_i) \quad (644)$$

$$b_j = r_{ij} \frac{s_j}{s_i} \quad (645)$$

where \bar{P}_j and \bar{P}_i are the average power output in park “j” (estimated farm) and “i” (reference farm);

r_{ij} is the experimental correlation coefficient;
 s_i and s_j are the standard deviation of power in farms i and j.

The interaction between reactive power of wind farms must be also taken into account. If the control is a fixed power factor, $Q = P \tan \varphi$, a linear correlation is also advisable for compute reactive power injection of other wind farms (note that unity power factor is a special case where $\varphi = 0$).

In case of Automatic Voltage Support or other control strategies, the reactive power of the wind farms must be estimated accordingly.

A precise model of interaction can be needed in some studies (topology changes and congestion typically show a non-linear behaviour). In such cases, a Monte Carlo simulation is advisable, where wind power and load are stochastically modelled. This type of study is beyond the scope of this article.

A.5. Reactive power control

A.5.1. Limits on reactive power

The maximum amount of reactive power that can be injected or absorbed are given by:

- Limits provided by the turbine manufacturer. Second edition of IEC 61400-21 will include a section devoted to the reactive power capability and the ability to participate in an automatic voltage control scheme.
- Allowable voltage limits at the turbines. The wind turbine that is electrically farer from PCC will suffer the greatest voltage deviations of the wind farm.
- Allowable current in series elements (electronic converters, lines, transformers, etc).

Turbines inside a wind farm operate at similar power levels and voltage drops are small enough to use the linear relationship:

$$\begin{aligned} U_{WT} &\approx U_0 + \frac{(R_{sc \text{ at PCC}} + R_{series}) P_{WT} + (X_{sc \text{ at PCC}} + X_{series}) Q_{WT}}{U_0} \\ \Delta U_{turbine}^{worse} &= R_{eff} P_{WT} + X_{eff} Q_{WT} \end{aligned} \quad (646)$$

where the parameters R_{eff} y X_{eff} can be adjusted from a simulated power flow with $P_{WT} = 1$ p.u., $Q_{WT} = 0$ and with $P_{WT} = 0$, $Q_{WT} = 1/3$ p.u. (a simulation with $Q_{WT} = 1$ p.u. can lead to voltage out of range in many cases and the linear approximation is not valid near voltage collapse).

$$\begin{aligned} R_{eff} &= \frac{R_{sc} + R_{series}}{U_0} = U_{turbine}^{worse} \Big|_{P_{WT}=1 \text{ p.u.}, Q_{WT}=0} - U_0 \\ X_{eff} &= \frac{X_{sc} + X_{series}}{U_0} = \frac{1}{3} U_{turbine}^{worse} \Big|_{P_{WT}=0, Q_{WT}=1/3 \text{ p.u.}} - U_0 \end{aligned} \quad (647)$$

The limit of voltage rise or drop leads to a band of allowed power in the P,Q plane (p.u.).

$$U_{\min} < U_0 + \Delta U_{\text{turbine}} < U_{\max}$$

$$\Delta U_{\min} = U_{\min} - U_0 < \Delta U_{\text{turbine}} < U_{\max} - U_0 = \Delta U_{\max}$$

$$\Delta U_{\min} < R_{\text{eff}} P_{\text{WT}} + Q_{\text{eff}} P_{\text{WT}} < \Delta U_{\max}$$

Upper voltage limit : (648)

$$R_{\text{eff}} P_{\text{WT}} + Q_{\text{eff}} P_{\text{WT}} = \Delta U_{\max}$$

Lower voltage limit :

$$R_{\text{eff}} P_{\text{WT}} + Q_{\text{eff}} P_{\text{WT}} = \Delta U_{\min}$$

The locus of excessive current is determined by a circumference of radius $S_{\max} = U_{\text{turbine}} I_{\max}$ (p.u.)

$$\frac{P_{\text{WT}}^2 + Q_{\text{WT}}^2}{U_{\text{turbine}}^2} < I_{\max}^2 \xrightarrow[U_{\text{turbine}} \sim 1 \text{ p.u.}]{} P_{\text{WT}}^2 + Q_{\text{WT}}^2 < I_{\max}^2 \text{ (p.u.)} \quad (649)$$

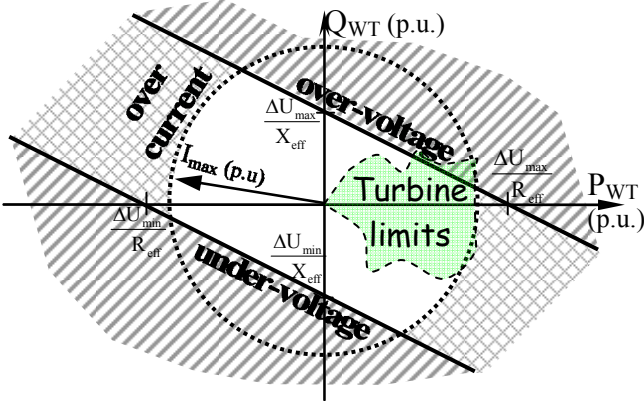


Fig. 176: Operational limits of turbine reactive power Q_{WT} due to excessive voltage deviations and over current at the wind turbine.

The quadratic equations (550) and (642) transforms the P, Q limits of Fig. 160 (at turbine) to the P, Q values that are achievable at PCC. Therefore the straight lines bend a little and the circle is slightly smashed when the power limits are calculated at PCC

A.5.2. Reactive Power Policy

Nowadays, most turbines use unity power factor regulation [379]. However, the reactive power injection can achieve some goals:

- Minimize voltage variations at a point in the grid due to the wind farm. This control would lead to a power factor near unity at wind turbines (slightly inductive).
- Stabilize voltage at a nearby point of the network. This control would need to measure the actual voltage at the reference node or, alternatively, an algorithm to estimate voltage there from voltage measured at wind farm.
- Try to compensate reactive needs in the surrounding grid. In fact, this would also minimize power losses in the grid. This strategy would be typically managed by a control centre that measures nearby load consumption, line flows and grid constrains.

A.5.3. Constant power factor regulation

The voltage variations due to a wind farm with constant power factor would be proportional to active power.

$$\Delta U_{\text{WT}} = \frac{R_{\text{eff}} + X_{\text{eff}} \tan \varphi_{\text{WT}}}{U_0'} P_{\text{WT}} = K_{\varphi} P_{\text{WT}}$$

$$R_{\text{eff}} + jX_{\text{eff}} = \frac{Z_{\text{SC}}}{1 + Y_{\text{shunt}} Z_{\text{SC}}} + Z_{\text{series}} \quad (650)$$

$$U_0' = U_0 \frac{1 + Y_{\text{shunt}} Z_{\text{series}}}{1 + Y_{\text{shunt}} Z_{\text{SC}}}$$

The voltage influence of the farm can be cancelled at the wind turbines ($\Delta U_{\text{WT}} \approx 0$) or at the PCC ($\Delta U_{\text{PCC}} \approx 0$).

If the target is not to influence voltage at a point, the wind farm will behave inductively, that in many scenarios is not a desired scenario.

$$\Delta U_{\text{WT}} \approx 0 \Rightarrow K_{\varphi} = 0 \Rightarrow \tan \varphi = -R_{\text{eff}} / X_{\text{eff}} \quad (651)$$

If the target is $\Delta U_{\text{PCC}} \approx 0$ then the power factor is determined by the short circuit impedance at the PCC, $\tan \varphi_{\text{PCC}} = -R_{\text{SC at PCC}} / X_{\text{SC at PCC}}$

If the target is a fixed power factor at PCC, then the value of turbine reactive power Q_{WT} can be determined solving the quadratic equations (550) and (642). For unity power factor at PCC, there must be injection of reactive power at the wind farm that is not proportional to P_{WT} .

$$Q_{\text{PCC}} = \frac{U_{\text{PCC}} - \sqrt{U_{\text{PCC}}^2 + 4 B_{\text{shunt}} X_{\text{series}} U_{\text{PCC}}^3 - 4 P_{\text{WT}}^2 X_{\text{series}}^2}}{2 X_{\text{series}}} \quad (652)$$

The effect of a power factor in the voltage profile can be computed taking into account that the voltage deviation due to the farm is proportional to the active power output, $\Delta U_{\text{WT}} = K_{\varphi} P_{\text{WT}}$. Therefore, the voltage distribution and the power have the same shape as (see Fig. apparent and complex power) and the scale factor is K_{φ} .

A.5.4. Automatic voltage control

The voltage control is difficult to achieve without communication with a control centre. If neither the detection of voltage regulators is made nor there is connection to a monitoring centre, the estimation of voltage at PCC from farm voltage can be fooled. Think in an under voltage scenario, where tap or a topological change in the grid push up the voltage at the wind farm. Then, the automatic voltage regulator (AVR) can make the wind farm to restrain the reactive power injection (or even, to start behaving inductively), increasing the deficit of reactive power in the grid.

Even if there are other loads connected between the wind farm and the reference node (usually, PCC), the state of tap changing transformers or voltage boosters in the line can be accounted. If tap changing transformers are close to the wind farm, the sudden voltage or angle jump can be detected and identified. However, the voltage or angle jump must be significantly bigger than voltage variations due to nearby sudden load variation or connection of nearby farms.

A Bayesian decision tree can be used to detect tap changes. Voltage deviations due to nearby loads can be estimated from statistical data of consumers, even though these data can be difficult to obtain in a de-regulated market (for example, the loads can be estimated from working day classification, month and hour)

One way to compute Q_{WT} to support voltage at a net node is to compute $\partial U_{node} / \partial Q_{WT}$ through network simulation at two power levels.

$$\frac{\partial U_{node}}{\partial Q_{WT}} \approx \frac{\Delta U_{node}}{\Delta Q_{WT}} = \frac{U_{node}|_{Q_{WT}=Q_{MAX}} - U_{node}|_{Q_{WT}=0}}{Q_{MAX} - 0} \quad (653)$$

$$Q_{WT} = K_{Q_{WT}} \frac{\Delta U_{measured \text{ or } estimated \text{ at node}}}{\frac{\partial U_{node}}{\partial Q_{WT}}} \quad (654)$$

The weighting factor $0 < K_{Q_{WT}} < 1$ accounts for the fact that more generators and devices are performing voltage support. This factor must be small if the supported node is electrically far from the wind farm. Otherwise, the turbines would operate very often at maximum reactive power absorption or injection.

A.5.5. Scheduled reactive control

If communication with the system operator (S.O.) is not possible, a schedule of reactive power at PCC based on load is possible. In fact, Spanish regulation RD 436/2004 [366] rewards certain power factor depending on the time of the day and the Spanish region. This is an improvement from past regulation (unity power factor) since there is more correlation between system reactive needs and reactive generation.

However, actual Spanish regulation is based in type 3 classification of the tariff established in OM 12/1/1995 [380]. *A clear improvement would be to establish the bonus based on type 5 schedule*, where the type of the day (labour, weekend, bank holiday) and the season would be also considered. The improvement would be due to higher correlation between system reactive needs and reactive generation. The increase of control complexity with type 5 schedule is very small since all SCADA have a built in calendar.

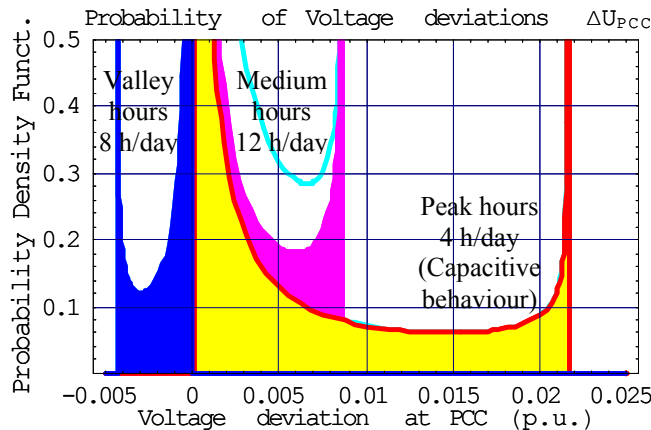


Fig. 177: Distribution of voltage deviations at PCC due to the wind farm of Annex I (data corresponding to P.F. at wind turbine 0,95 inductive in blue; 0,95 capacitive in yellow and unity in magenta).

One drawback of power factor discount is that, as active power is random, voltage and reactive power support would be also. Calm and low wind are the more likely states at wind farms, as can be seen from Fig. 6. In such states, the grid support and the use of available infrastructure is low.

Moreover, the reactive power capability of most wind farms is bigger at low active power: many technologies and compensating devices can inject or absorb reactive power when the generator is not connected.

Therefore, other clear improvement is to compute the reactive bonus on reactive power, not on power factor.

Voltage at PCC for several power factors

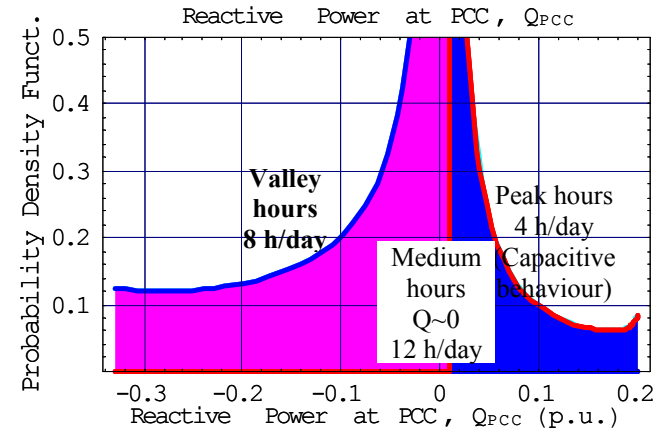


Fig. 178: Reactive power injected at PCC by the wind farm of Annex I.

A.5.6. Reactive power under centralized control

The optimum policy for reactive power control must support voltage and try to maintain power losses at low level, avoiding network congestion.

The cost of voltage support, power losses and net congestion can be derived from voltage deviation penalty at border nodes, mean power tariff and costs derived from congestions. An optimum power flow could attain a global optimum considering these factors [381].

Reactive power pricing must be adjusted carefully for the optimum control to be performed.

The availability of reactive power injection is a random variable because it depends on wind. It must be assessed depending on the technology of wind turbines, ancillary reactive devices and wind potential at the site. Even though active and reactive power are related, existing technology allow some level of control freedom.

For example, Fig. 15 show the realizable power at a turbine equipped with a full rated converter. The limits on the converter displayed are due to maximum current and maximum voltage at turbine. Other constrains can appear due to internal features of the converter, but they are not considered here (for example, the choke coils can decrease the capacitive capability of the converter, but here is not considered).

The probability of being able to inject more than Q reactive power at the PCC can be computed through the cumulative distribution of power.

$$\Pr(q_{WT} < \text{Maximum } Q) = \Pr(\text{Power} < Q_{WT \text{ MAX}}^{-1}(q_{WT})) \quad (655)$$

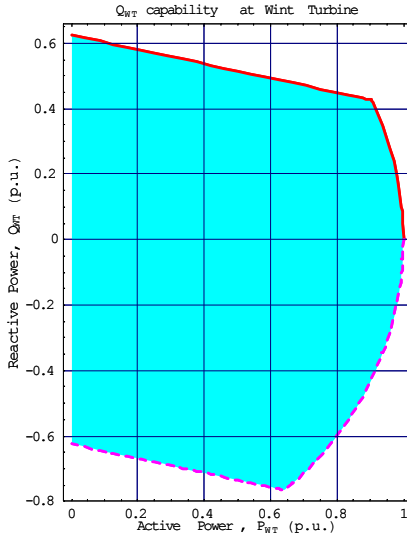


Fig. 179: Realizable reactive power at the wind turbine for the example of Annex I.

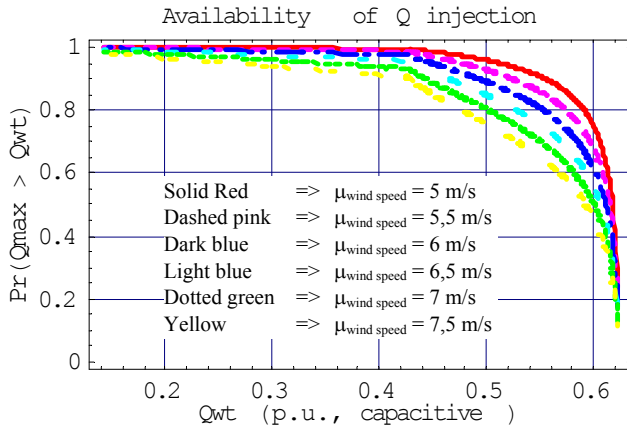


Fig. 180: Availability of reactive power injection (capacitive behaviour of the WT) by the wind farm of Annex I.

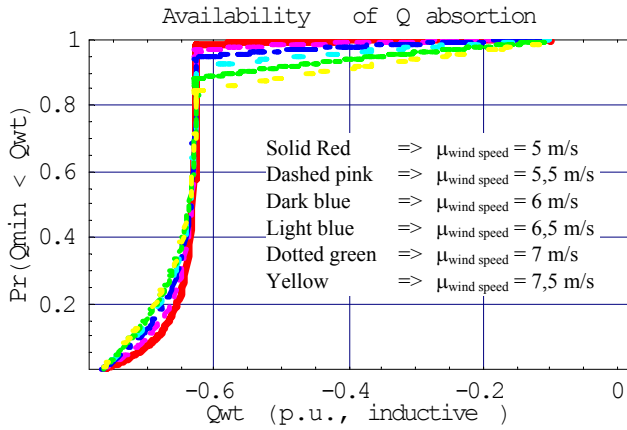


Fig. 181: Availability of reactive power absorption (inductive behaviour of the WT) by the wind farm of Annex I.

The calculus of availability is quite straightforward from CDF of the wind farms.

$$\Pr(\text{Minimum } Q < q_{WT}) = \Pr(\text{Power} < \sqrt{S_{max}^2 - q_{WT}^2}) - \Pr\left(\text{Minimum } Q_{|P_{WT}=0} < q_{WT} ; \Pr\left(\text{Power} < P_{\text{undervoltage operating region}}^{-1}(q_{WT})\right)\right) \quad (656)$$

The optimum reactive power Q_{WT} , from voltage point of view, can be computed taking into account several node voltages, each one with its weighting factor.

$$Q_{WT} = \sum_{i=1}^n K_{Q_{WT,i}} \frac{\Delta U_{\text{measured or estimated at node } i}}{\frac{\partial U_{\text{node } i}}{\partial Q_{WT}}} \quad (657)$$

A.5.7. Effect on power losses

The farm power output influence elements active and reactive power network losses. Power in shunt elements is voltage dependent in a non-linear way. Since the farm affects voltage only at nearby nodes and the main losses are in series elements, the influence of the farm in shunt losses will not be considered in this simplified approach.

Let's consider power losses $P_{\text{losses}, i}$ in a series element i that carry an apparent power $S_{\text{element}, i}$. The power injected by the farm would spread along the grid. Active and reactive power flows are quite decoupled and the farm power is approximately linearly distributed between parallel elements. Therefore, it is reasonable to use the following simplified model for the power loss in a grid element:

$$P_{\text{loss}, i} = \frac{R_i}{U_i} S_i^2; \quad (658)$$

$$S_i^2 \approx (P_{0,i} + k_{p,i} P_{WT})^2 + (Q_{0,i} + k_{Q,i} Q_{WT})^2$$

$P_{0,i}$ and $Q_{0,i}$ are the power flow at the elements when the turbines are disconnected. Approximate factors $k_{p,i}$ and $k_{Q,i}$ can be estimated simulating the network at maximum active and reactive power and computing the power flow difference at the element. The overall power loss with the aforementioned approximations would lead to a quadratic behaviour of net losses.

$$P_{\text{loss}} = \sum_i P_{\text{losses}, i} = P_{\text{loss}}|_{P_{WT}=0, Q_{WT}=0} + a_p P_{WT} + b_p P_{WT}^2 + a_Q Q_{WT} + b_Q Q_{WT}^2 \quad (659)$$

The five coefficients of (659) can be adjusted from the power flow losses in 5 different combinations of active P_{WT} and reactive Q_{WT} wind power.

If the network losses due to wind power are allocated mainly in elements electrically close to the wind farm, b_p and b_Q will have greater values. Thus, the relationship would be mainly quadratic with P_{WT} and Q_{WT} .

If wind power influence losses in elements mainly electrically far from the wind farm to vary, a_p and a_Q will have greater values. Thus, the relationship would be mainly linear with P_{WT} and Q_{WT} .

If network configuration or flows can change notably on high, medium and low load, the coefficients must be computed for those cases. Therefore, the reactive control of the wind farm might take into account the load classification at each time (a different control policy must be used depending on a scheduled load classification).

Reactive power losses also show an analogue relationship with P_{WT} and Q_{WT} .

A.5.8. Uncertainty analysis

The uncertainty in the farm power output is due to:

- Adjustment of wind resource to a Weibull distribution.

- The uncertainty of the power curve.
- Simplistic model of the power curve with only two or four parameters.
- The wind farm speed characteristics are usually not well known and they depend on wind speed and direction. More over, the “undisturbed wind speed” should be estimated once the wind farm is in operation.
- Approximations done in the model of the grid (for example, considering U_0 constant).
- Availability of turbines and network.

The main source of uncertainty comes from the wind and the power curve. In case the performance matrix of the farm is available, the uncertainty can be notably decreased. The grid influence in power output is low since characteristics are usually well known and it is designed for high efficiency.

The availability of turbines is high due to scheduled maintenance and high reliability (the availability of the electrical network is even higher). However, the effect of events such as nearby short-circuits in some situations can trip many wind power stations. This is an example of very infrequent event but that can affect power quality because it concerns system stability in grids with high wind share.

The estimation of uncertainty is not easy. Apart from the ISO guide of uncertainty, GUM [382], all the power curve standards ISO 61400-12-1 [370], 61400-12-2 [383] and 61400-12-3 [339] include some annexes to help in uncertainty assessment.

The general procedure is to estimate the uncertainty of each component (i.e. power curve, wind distribution, etc). The sensitivity coefficients of individual uncertainty in the overall power output must be derived. Also, a model of propagation between uncertainties must be supposed. Should the uncertainties be uncorrelated, they partially cancels and the rooted sum of squares law should applied instead of the arithmetic sum of uncertainties. Sometimes, it is not clear which type of assumption is more adequate. In those cases, the assumptions can be classified as “conservative” or “optimistic”. At the end, the uncertainty computed for several scenarios (optimistic, conservative, etc.) can be weighted by its likelihood or by an expert to obtain the expected uncertainty.

The uncertainty of the power output can be reduced using more detailed data. The process is roughly the same that has been presented here except that the majority of the computations must be done numerically. Moreover, the Monte Carlo method can be used to cope with detailed models. However, the increase of accuracy comes at the cost of a not so easy analysis of parameter sensitivity as in the analytic case.

Even though there is a small correlation of renewable energy and consumer load through the weather, this effect can be neglected in energy sources as wind and non-storage hydroelectric [384].

Conclusions

The annex shows a statistical model of the farm that can be used in power flow studies, and a methodology for adjusting its parameters to the available data (if it is already operating) or using data from micrositting and power curve of wind turbine (if it is under project state).

The model is fairly simple and reflects the normal operation of the farm. Moreover, the minimum voltage for stable operation is assessed in farms with asynchronous generators.

The uncertainty of the model is also estimated. The sources of uncertainty are stochastic operation of wind farm, employ of a simplified model and grid voltage.

This work shows a statistical model of wind farms and a methodology for adjusting its parameters. This model has been used to assess the grid impact of a wind farm reactive power during normal operation. Several reactive power control strategies are analyzed.

The uncertainty of the final data due to the approximations made is studied. The accuracy can be increased if non-parametric models of farm power curve and wind resource is employed.

Annex: Example Data

A) Power curve shown in figures:

$$w_{25\%} = 7,5 \text{ m/s}; \quad w_{75\%} = 10,5 \text{ m/s}; \quad w_{\text{cut-in}} = 4 \text{ m/s}; \\ w_{\text{cut-off}} = 25 \text{ m/s}; \quad P_{\text{nominal}} = 1 \text{ p.u.}; \quad \sigma_{\text{wf}} = 1,5 \text{ m/s}$$

B) Parameters of wind speed distribution:

$$\text{scale} = 2 \mu_{\text{wind}} / \sqrt{\pi}; \quad \text{shape} = 2$$

C) Parameters of the wind farm:

$$\eta_{\text{wf}} = 0,93; \quad \Delta w_{\text{off}} = 2 \text{ m/s}; \quad w_{\text{cut-off}} = 25 \text{ m/s}; \quad \sigma_{\text{wf}} = 1,5 \text{ m/s} \\ R_{\text{series}} = 0.03 \text{ p.u.}; \quad X_{\text{series}} = 0,12 \text{ p.u.}; \quad G_{\text{shunt}} = 0.005 \text{ p.u.}; \\ B_{\text{shunt}} = 0.01 \text{ p.u.}; \quad R_{\text{sc}} = 0.02 \text{ p.u.}; \quad X_{\text{sc}} = 0,18 \text{ p.u.}; \\ \mu_{\text{wind}} \text{ is assumed to be } 7 \text{ m/s if it is not stated.}$$

D) Limits of reactive power generation:

$$S_{\text{max}} = 1 \text{ p.u.}; \quad \Delta U_{\text{max}} = 0.10 \text{ p.u. at turbine converter.}$$

Annex B: Analysis of wind power variability from measured data

B.1. Fixed speed, stall regulated turbine of 750 kW

This subsection studies the power fluctuations of a 750 kW wind turbine from TAIM-NEG MICON (Nordtank squirrel cage induction generator and stall regulation) measured at Valdecuadros wind farm (Spain) [52]. For the sake of clarity, most plots show either 10 s or 20 s of typical turbine operation. The measured amplitude is around $1/30^{\text{th}}$ of the nominal power and the shape varies continuously and it is quite random. This behaviour has been found in other wind turbines with different frequencies and amplitudes of the fluctuations.

Almost periodic behaviour can be characterized as a sinusoidal fluctuation at the blade frequency with random amplitude. However, the shape and the amplitude vary and they are quite random. The amplitude modulation can be decomposed into oscillations of close frequency. To test this, the power spectrum density (PSD) of power during 5 minutes have been calculated in Fig. 187, showing several overlapping peaks spread around $f_{blade} \approx 1,06$ Hz, $\frac{3}{4}f_{blade} \approx 0,77$ Hz and $\frac{1}{2}f_{blade} \approx 0,51$ Hz. The harmonics of tower shadow are very sharp and thus, their power content is much lower than the fundamental component and its $\frac{3}{4}$ and $\frac{1}{2}$ sub-harmonics. Therefore, tower shadow harmonics can have structural concerns but their influence in the variance of power is small.

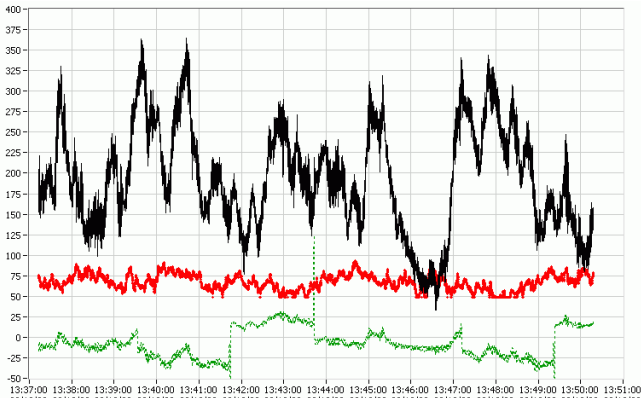


Fig. 182: Operation of a SCIG 750 kW wind turbine for wind speeds around 6,5 m/s during 14 minutes. From top to bottom, time series of the real power P [kW] (in black), wind speed U_{wind} [m/s] at 40 m in the met mast (in red, with a magnification factor $\times 10$ respect the vertical axis) and reactive power Q [kVAr] (in dashed green).

B.1.1. Record of 20/10/00, 13:37-13:50 (low winds)

The record analyzed here corresponds to date 20/10/00 and time 13:37-13:50 (about 13 minutes). The average blade frequency in the interval was $f_{blade} \approx 1,12$ Hz. The wind, measured in a meteorological mast at 40 m above the surface with a cup anemometer, was $U_{wind} = 6.7$ m/s $\pm 1,86$ m/s

(expanded uncertainty, aka $k = 2$ or twice the standard deviation, is used to indicate range variation of stochastic magnitudes unless otherwise is stated). The main features of this record are summarized in the following table and Fig. 182.

TABLE XIV: PARAMETERS OF THE 750 kW SCIG TURBINE, SERIES 20/10/00, 13:37-13:50 ($f_{BLADE} \approx 1,12$ Hz)

	U_{wind} [m/s]	P [kW]	Q [kVAr]
Mean	6,7 m/s	192,83 kW	-7,70 kVAr
Variance	0,93 m/s	63,48 kW	18,01kVA
Ratio Std. Dev./mean	71,5 %	4,0 %	3,0%
Mean \pm uncertainty	6.7 $\pm 1,86$ m/s	192,83 $\pm 126,96$ kW	-7,70 $\pm 36,02$ kVAr
r^2	$\sim 0,85$	$\sim 1,35$	$\sim 0,88$
$P_1' \approx PSD^+(1)$	0,0152 (m/s) ² /Hz	1,02 kW ² /Hz	2 kW ² /Hz
f_1	$\leq 0,008$ Hz	$\leq 0,013$ Hz	$\leq 0,004$ Hz
f_2	∞	12 Hz	∞

B.1.2. Analysis of real power output

In the graph of the full time series, Fig. 182, the oscillations due to rotor position cannot be seen clearly. In the following magnified graphs, one oscillation per 0.9 second are noticeable in turbine power output.



Fig. 183: Real power of a SCIG 750 kW wind turbine for wind speeds around 6,5 m/s during one minute.

For simplicity, tower shadow of Fig. 183 can be characterized as a sinusoidal fluctuation at the blade frequency with random amplitude (i.e. an amplitude modulated signal) [385]. In fact, the modulation can be due to the sum of fluctuations at frequency f_{blade} dependent on rotor position and tower resonance frequency f_{tower} (the modulation

happens when two oscillations of similar amplitude and frequency are close). There are also a higher frequency oscillation (possibly due to oscillation modes of the mechanic system of frequency around 6 Hz). A similar behaviour (but with lower 6 Hz oscillation) is shown in [186].

However, when the coupling of generator and turbine rotor is stiffer, high frequency vibrations are transferred more directly to the generator [48]. In those cases, generator fluctuations have a wider frequency spectrum and more complex shapes.

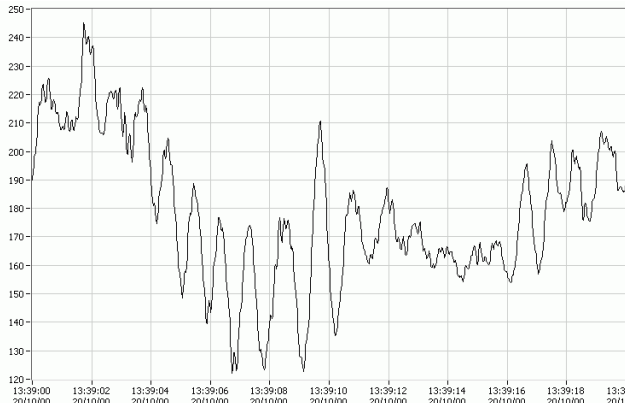


Fig. 184: Real power of a SCIG 750 kW wind turbine for wind speeds around 6,7 m/s during 20 s.

Fig. 185 shows a rich dynamic behaviour of the real power output, where the modulation and high frequency oscillations are superimposed to the fundamental oscillation.

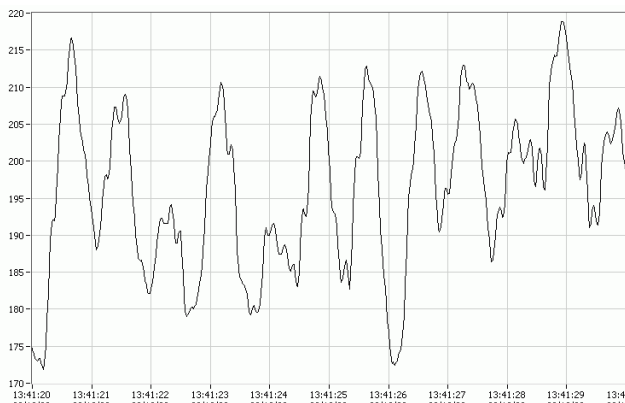


Fig. 185: Real power of a SCIG 750 kW wind turbine for wind speeds around 6,7 m/s during 10s.

The previous images are comparable to other time series found in the literature. For example, Fig. 186 shows modulation and high-frequency oscillations superimposed to the fundamental oscillation.

Fig. 187 indicates that power spectrum is quite constant for frequencies bellow 0,02 Hz. The wide peak between 0,8 to 1,12 Hz is due to the rotational effects, which excites tower vibration modes. In fact, the peak at 0,5 Hz is the 1/2 subharmonic of the fundamental oscillation at blade frequency. Other narrow peaks corresponding to harmonics of fundamental oscillation can be clearly seen in Fig. 187.

Fig. 188 shows the contribution of each frequency to the variance of power $\sigma_{P,T,f}^2$ –the area bellow $f \cdot PSD_P^+(f)$ in a semi-logarithmic plot is the signal variance according to (10).

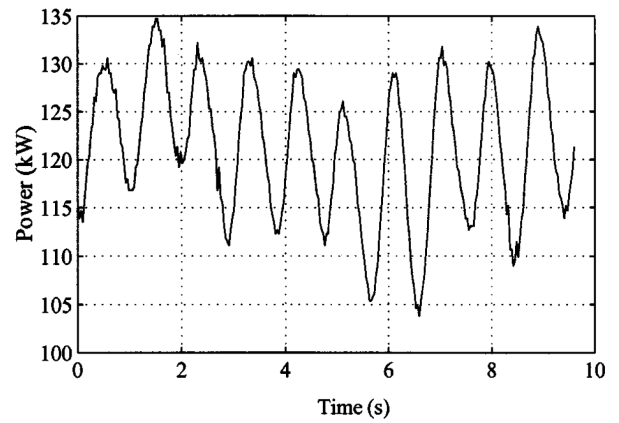


Fig. 186: Power from a fixed speed stall-regulated wind turbine at 10 m/s (from [186]).

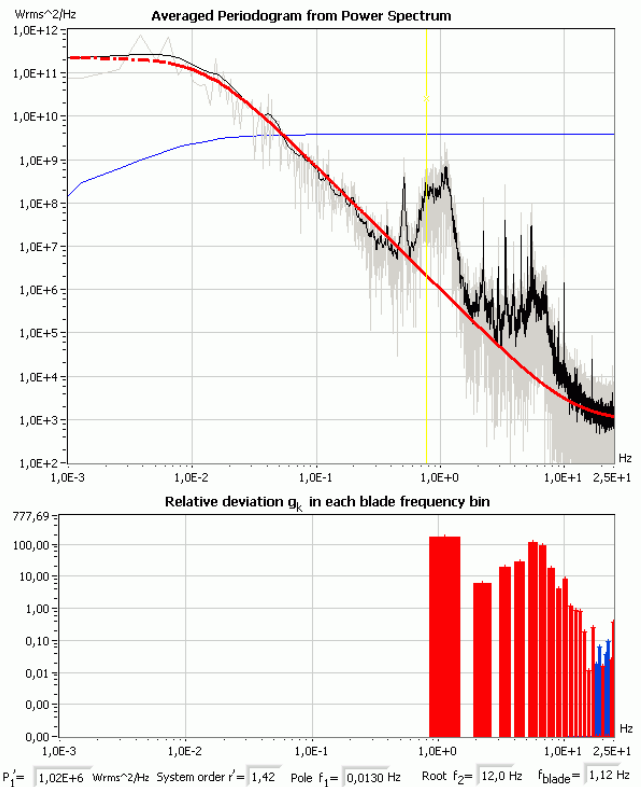


Fig. 187: $PSD_P^+(f)$ parameterization of real power of a SCIG 750 kW wind turbine for wind speeds around 6,7 m/s (average power 190 kW) computed from 13 minute data.

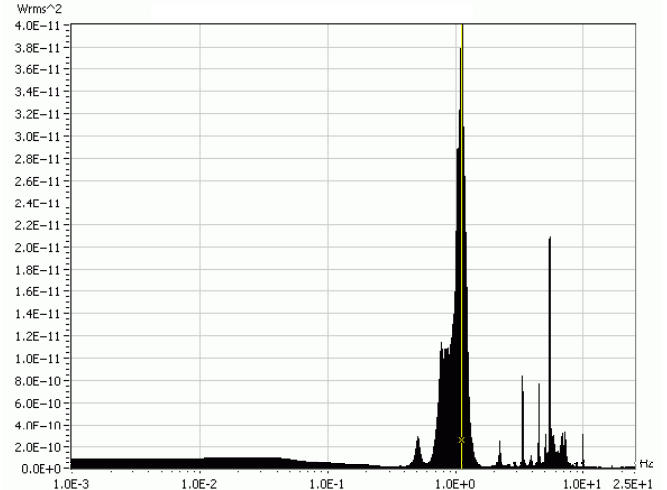


Fig. 188: Contribution of each frequency to the variance of power corresponding to Fig. 187 (the area bellow $f \cdot PSD_P^+(f)$ is the variance of power).

The main contributions to power variability are:

- Low frequencies due to wind variation ($f < 0.1$ Hz).
- Blade and tower fluctuations ($0.5 \text{ Hz} < f < 1.5$ Hz).
- Minor contributions in $5 \text{ Hz} < f < 7$ Hz, due mainly to drive train, generator and blade frequency harmonics.

B.1.3. Analysis of reactive power output

The main features of reactive power are the capacitor switching and the variations of reactive power due to variations of generator slip and power. The capacitor bank switching is seen in Fig. 189 as jumps of 50 kVAR in the reactive power. The control can be further optimized since there are 3 switches in 13 minutes.

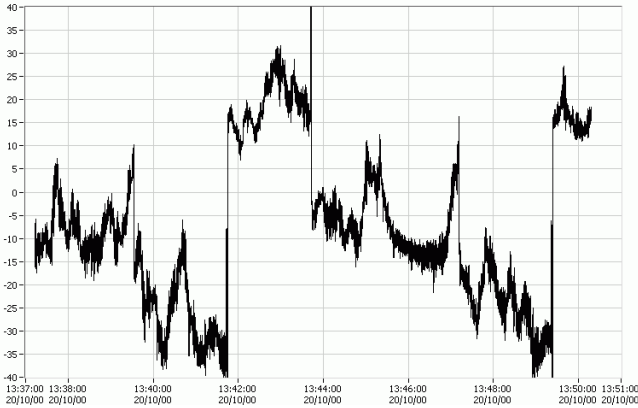


Fig. 189: Reactive power of a SCIG 750 kW wind turbine corresponding to Fig. 183.

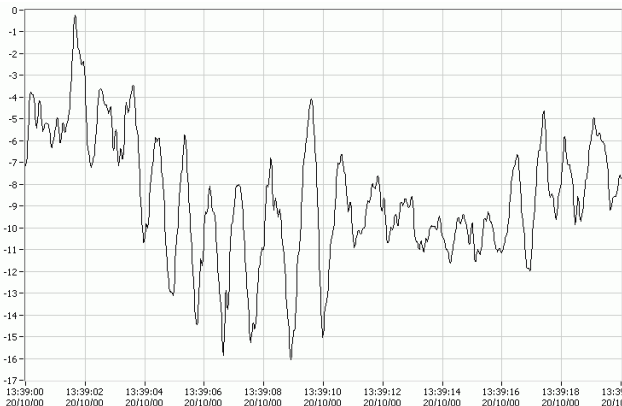


Fig. 190: Reactive power Q [kVAR] of a SCIG 750 kW wind turbine corresponding to the real power of Fig. 184.

At frequencies below 0,02 Hz, the PSD of reactive power in Fig. 191 is similar to the PSD of real power in Fig. 187 since the static relationship between P and Q holds valid. Between 0,2 Hz and 0,6 Hz, the spectrum remains quite constant due to generator dynamics. Oscillations at blade frequency and its harmonics and sub harmonics are much smaller in the reactive power than in the real power. Beyond 8 Hz, the frequency content of the signal drops sharply. The system order for the reactive power is similar to the wind and to the voltage, indicating that the behaviour of reactive power could be influenced by voltage, which, in turn, is influenced by wind since there are many turbines connected nearby.

The system order r^* of Q is 0,88 –quite similar to wind and voltage order– while the system order r^* of P is significantly different, $r^* \approx 1,35$. This discrepancy can be due to the poor fitting of the reactive power in Fig. 191 and the great

influence of voltage in Q . Conversely, real power is less related to the line voltage and more related to the angle between rotor and stator magnetic moments.

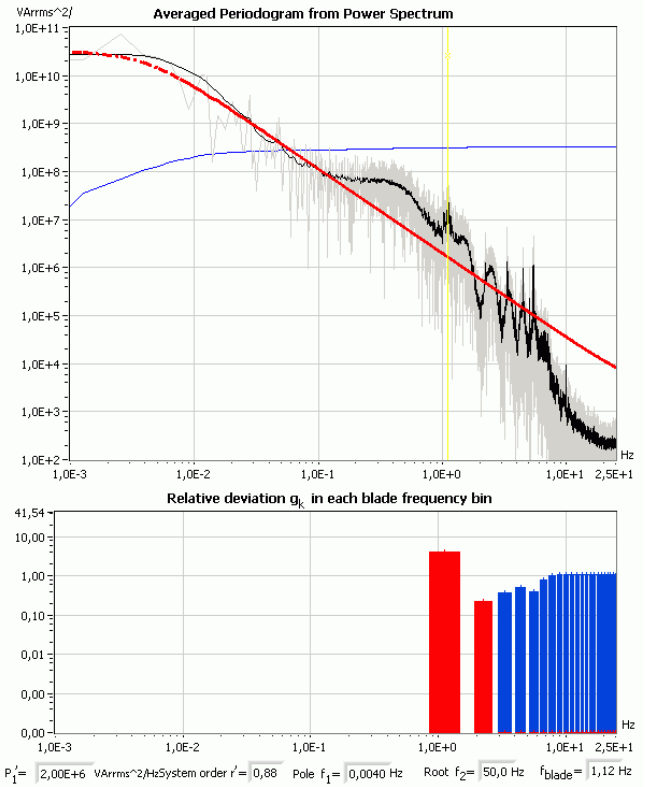


Fig. 191: $PSD_Q^+(f)$ of the reactive power corresponding to Fig. 187.

B.1.4. Analysis of wind measured at the meteorological mast 40 m above surface level

The $PSD_{U_{wind}}^+(f)$, estimated during the same interval that $PSD_P^+(f)$ in Fig. 187, is shown in Fig. 192. Due to the anemometer inertia, it behaves as a low-pass filter of cut-off frequency around $U_{wind} / 10 \text{ m} \sim 0,67$ Hz (from such cut-off frequency, the recorded wind speed shows an additional drop corresponding to a low-pass 1st order system). Beyond 3 Hz, some artifacts appear related to the measuring procedure. At higher frequencies, the system introduces errors in the wind measure.

Up to anemometer cut-off frequency, the slope is smooth and it fits well the model (184) (black and red lines in Fig. 192 are almost superimposed up to 0,67 Hz). The system order is $r^* \approx 0,85$ (agrees approximately with the order $r^* = 5/6 = 0,833$ corresponding to the Kaimal (11), Harris (13) and Von Karman (14) spectra).

Taking into account the measuring system limitations, the real frequency content in the wind is expected to be quite close to the adjusted model (184) –in thick solid red in Fig. 192– and to the Kaimal Spectra.

The pole is $f_i \lesssim 0,008$ Hz, corresponding to an integral length scale of the turbulence $\ell_{U_{wind}} \gtrsim \langle U_{wind} \rangle / (6 a f_i) \approx 82$ m, assuming $a = 1,7$ according to the draft Eurocode ENV 1991-2-4 and (11). Low values such as the previous one are possible in unstable atmospheric conditions in complex sites. However, the analysis of longer duration meteorological records indicates that the turbulence length scale is usually in

the order of 1 km and the actual length scale in this sample is believed to be significantly greater than 82 m.

The scale parameter is $P_1' \approx PSD_{U_{wind}}^+(f=1 \text{ Hz}) \approx 0,00153 \text{ (m/s)}^2/\text{Hz}$. The value of the wind variance is $\sigma_{wind} = 0,93 \text{ m/s}$, corresponding to a turbulence intensity $I = \sigma_{wind} / \langle U_{wind} \rangle = (0,93 \text{ m/s}) / (6,7 \text{ m/s}) = 13,8 \%$ –high since the turbine was in a hill top and surrounded by other turbines.

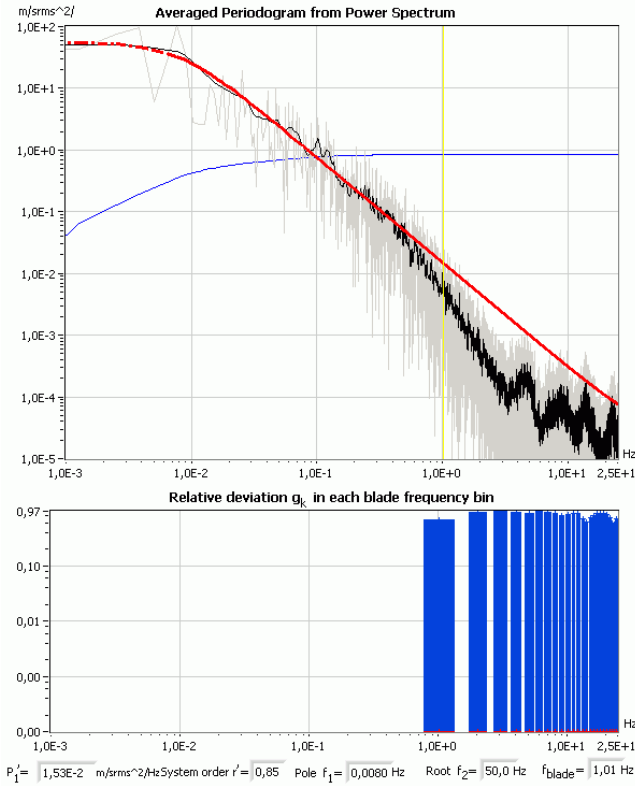


Fig. 192: $PSD_{U_{wind}}^+(f)$ of the wind corresponding to Fig. 187 ($U_{wind} = 6.71 \text{ m/s} \pm 1,86 \text{ m/s}$ at 40 m height). Beyond 0,67 Hz, some artifices appear due to measuring limitations.

B.1.5. Analysis of phase-to-phase voltage

$PSD_{V_{rs}}^+(f)$ of the low voltage phase to phase corresponding to Fig. 187 is shown in Fig. 193. The voltage during the series is quite variable for a period of 13 minutes, $691,2 \pm 2,06 \text{ V}$ (extended uncertainty). The $PSD_{V_{rs}}^+(f)$ corresponds to a first order system, approximately (the slope of the voltage spectrum is $r' \approx 0,9-1,1$). The influence of nearby generators and loads are similar to the contribution of the analyzed turbine, $\Delta V_{RS} \sim (R_{eff} \Delta P + X_{eff} \Delta Q) / \langle V_{RS} \rangle$. The individual effect of the analyzed turbine in the voltage is difficult to distinguish from external influences without extensive measurements.

A L-R circuit behaves as a first-order filter with cut-off frequency $f_1 \approx R_{eff} / (2\pi L_{eff})$. Considering only the external loads and generators, a L-R network fed by random loads and generators with constant $PSD_p^+(f)$, also referred as a “white noise” loads or generators, would experience a voltage with $r' \approx 1$. In such case, the cut-off frequency f_1 would be determined from the effective resistance R_{eff} and reactance L_{eff} shared by the white noise loads/generators and the analyzed turbine (R_{eff} and L_{eff} can be computed from a small-signal model of the grid).

Despite L_{eff} (equivalent grid shared inductance) and R_{eff} (equivalent grid shared resistance) could not be computed, the

cut-off frequency $f_1 \approx 0,0025 \text{ Hz}$ would correspond to a ratio $R_{eff} / X_{Leff} \approx f_1 / 50 \approx 5 \cdot 10^{-5}$ for a 50 Hz grid.

Usual ratios R_{eff} / X_{Leff} are in the range of a few units to some tenths. Table XV, taken from [386], shows typical values of resistance and reactance per kilometer depending on the voltage level.

TABLE XV: TYPICAL LINE PARAMETERS [386]

Type of line	R' [Ω/km]	X' [Ω/km]	I_N [A]	R'/X'
low voltage line	0,642	0,083	142	7,7
medium voltage line	0,161	0,190	396	0,85
high voltage line	0,06	0,191	580	0,31

Since generators and loads are connected by medium and high voltage networks, the cut-off frequencies inherent to the RL tie lines are in the range of 15,5-42,5 Hz (the filtering effect of the reactances of the grid is negligible at frequencies far bellow $50 \cdot R_{eff} / X_{Leff}$). The expected ratios $50 \cdot R_{eff} / X_{Leff}$ are much higher than the cut-off frequencies f_1 observed in voltage spectrums. Thus, the hypothesis of the “white noise” loads and generators should be rejected.

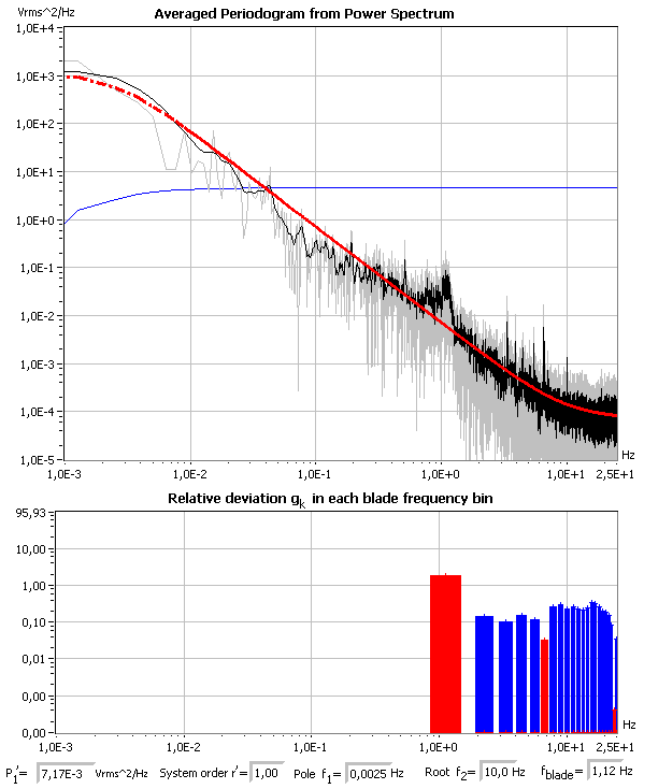


Fig. 193: $PSD_{V_{rs}}^+(f)$ of the low voltage phase to phase corresponding to Fig. 187.

The observed voltage frequency response would be due, in great extent, to nearby generators and loads behaving as colored (not white) noise. Nearby wind turbines introduces small voltage fluctuations somewhat proportional to wind variations ($r' \approx 0,88 \sim 1$), adding colored noise in the voltage instead of white noise and this is the expected cause of the drop in $PSD_{V_{rs}}^+(f)$. Due to the spatial spreading of the turbines, the cut-off frequency f_1 in the voltage can be much lower than the f_1 corresponding to the power of a single turbine.

The voltage drop in the line up to the main transformer (a 690 V line of 300 m) is (quite approximately) linearly related to the reactive and real power. Hence, the PSD of the voltage

drop should be similar to a combination of Fig. 191 and Fig. 187. The small peak near the blade frequency is due to the oscillation due to rotor angle. However, the amplitude of the fundamental peak of voltage is noticeably smaller than in Fig. 191 and Fig. 187. The rest of harmonics cannot be distinguished in Fig. 193, indicating that the background voltage fluctuation in the network is, in general terms, bigger than the voltage drop due to the varying reactive and real power. In fact, this background oscillation can be considered a “noise source” in the odd Bode plot of reactive power respect real power in Fig. 195.

B.1.6. Bode magnitude plots

The turbine can be assumed to be a system whose primary input is wind and its main output is real power. Even though considering the real turbine a linear single-input single-output system is an obvious oversimplification, it allows to derive a small signal model for accounting wind variations in power.

The transfer function has been estimated as the smoothed ratio of the Fourier transforms of the input and output magnitudes. Since the system has actually many inputs, the gain includes cross-effects due to relationship among input variables (the transfer function matrix might be estimated for a more rigorous analysis of MIMO –multiple input, multiple output– systems). For example, the Bode plot of voltage vs. power will be influenced by the turbine where the voltage is being measured but also by the nearby turbines.

When the transfer function is above the average gain (indicated with a horizontal red line for convenience), the oscillations of these frequencies in the input are amplified in the output above the average. When the transfer function is below the average gain, these frequencies are attenuated or damped respect the average.

The ratio of the spectrum of real power P to the spectrum of wind U_{wind} is the frequency response of the real power respect to the wind at the met mast in Fig. 194. Wind is measured at the met mast with a cup anemometer (its frequency response is only $\sim 0,67$ Hz). At frequencies higher than 0,7 Hz, the measuring system introduces error in the wind measure and thus the transfer function is not reliable.

In Fig. 194, the peaks due to rotor position and turbine vibration modes in real power do not appear in wind, and hence correspond to gain peaks at 0.7-1.4 Hz and 5-7 Hz frequencies in the transfer function. Conversely, 0,02~0,5 Hz fluctuations are damped by the aerodynamic stall and its gain is below the static gain.

Near blade frequency, $f \sim f_{blade}$, the ratio of wind to power fluctuation presents a peak but this is due to the tower shadow effect, which is not proportional to the fluctuation of the wind in such range. Thus, fluctuation of power at blade frequencies and its sub-harmonics and harmonics should be regarded as an additive factor (almost) insensitive to wind turbulence.

Fig. 195 shows the bode plot of the reactive power Q respect to the spectrum of wind, U_{winds} at the met mast. Between 0,02-0,2 Hz, the transfer function shows a small dip and then outreaches the static gain in the 0,2-0,7 Hz range.

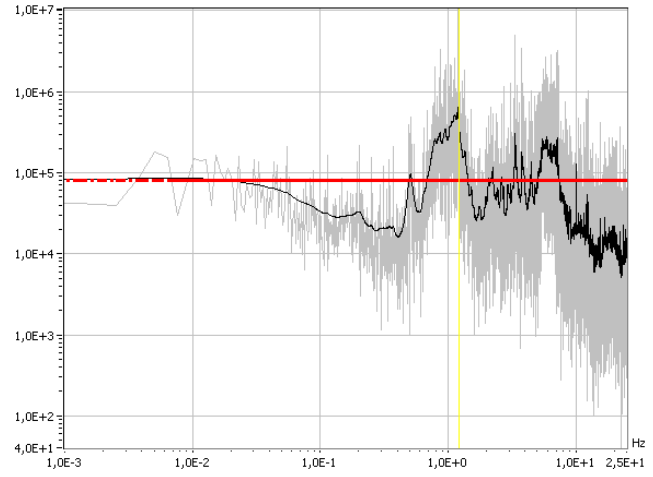


Fig. 194: Bode magnitude plot of real power P [W] respect wind U_{wind} [m/s] (beyond 0,7 Hz, the transfer function is underestimated due to limitations in the wind measure).

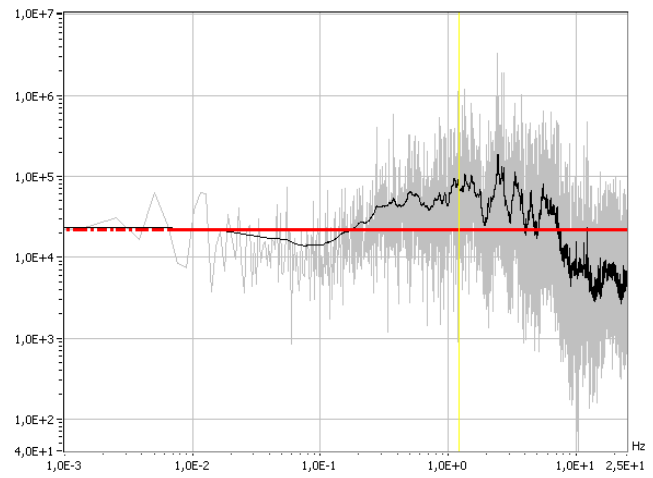


Fig. 195: Bode magnitude plot of reactive power Q [VAr] respect wind U_{wind} [m/s] (beyond 0,7 Hz, the transfer function is underestimated due to limitations in the wind measure).

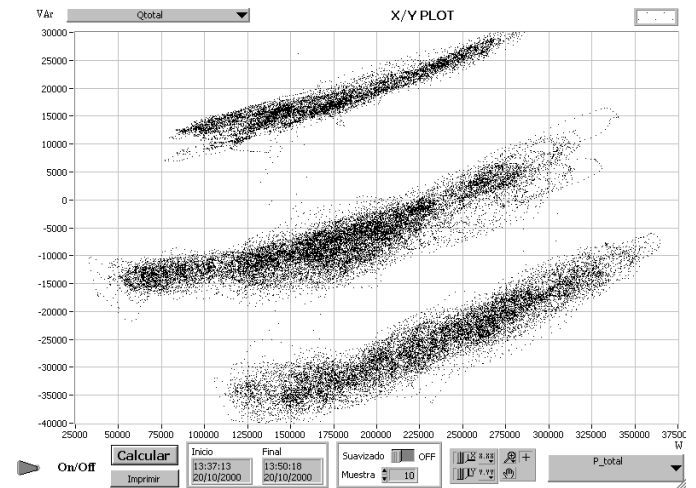


Fig. 196: Reactive power Q [VAr] versus real power P [W] in the 750 kW SCIG turbine (25 kVAr capacitor banks).

Fig. 197 shows the bode plot of the reactive power Q respect to the real power P . There is a quasi-static quadratic relation among real and reactive power in a SCIG generator [160] provided the voltage and the number of connected capacitor banks are constant (see Fig. 196).

Regardless the number of capacitor banks connected, the slope of the X/Y graphs is roughly the same: $\Delta Q \sim 0,3\Delta P$.

Thus, the linearized small signal model can be valid if real power excursion is small and voltage is fairly constant. This could explain why the horizontal line of constant gain 0,3 is a simple fit of the bode plot in Fig. 197.

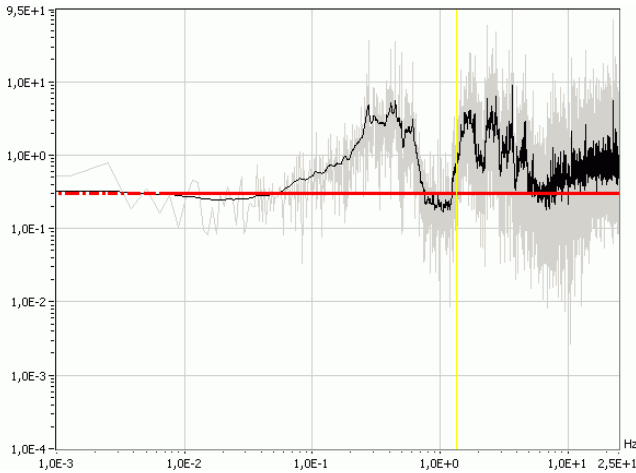


Fig. 197: Bode magnitude plot of reactive power Q [VAr] respect real power P [W].

Since the rated slip of induction generator is as low as 1%, the rotor current have noticeably slower dynamics than the stator current. The frequency response of Q respect P in Fig. 197 reveals that real power fluctuations in the ranges 0,3-0,6 Hz and 1,5-5 Hz have stronger impact in the reactive power. Fluctuation at blade frequency and its subharmonics are damped in the reactive power.

The influences of real P and reactive Q power on line voltage (V_{RS}) are shown in Fig. 198 and Fig. 199. Since the real and reactive powers are closely related, both plots are cross-related. The small-signal lineal model for voltage is $\Delta V_{RS} \sim (R_{eff} \Delta P + X_{eff} \Delta Q) / \langle V_{RS} \rangle$, where R_{eff} and X_{eff} are the effective Thévenin resistance and reactance seen from the voltage point of measure. However, the presence of other independent loads and generators electrically near, makes the values of R_{eff} and X_{eff} depend on the frequency.

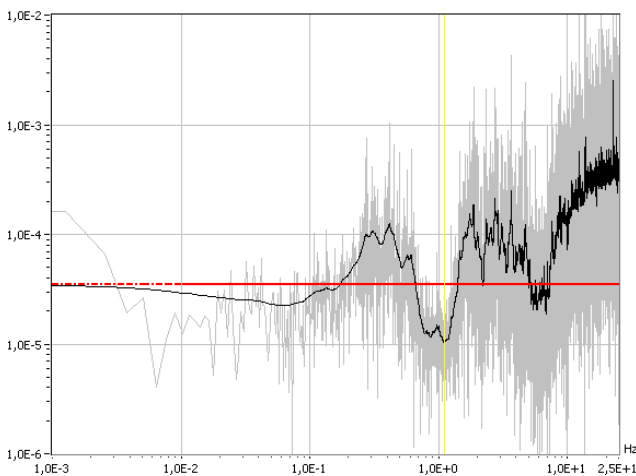


Fig. 198: Bode magnitude plot of line voltage V_{RS} [V] respect real power P [W].

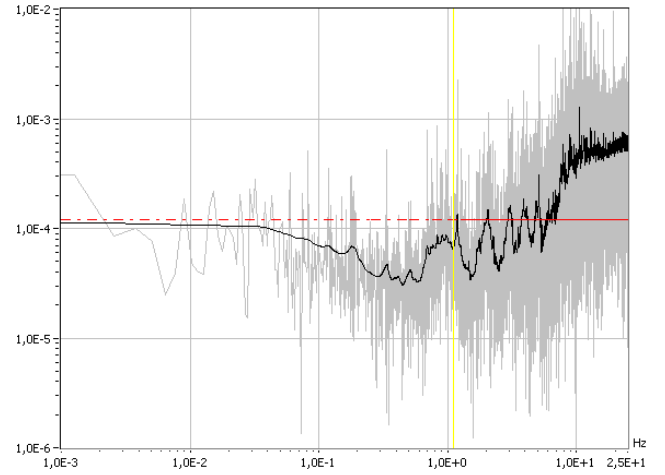


Fig. 199: Bode magnitude plot of line voltage V_{RS} [V] respect reactive power Q [VAr].

B.2. Fixed speed, stall regulated turbine of 600 kW

This subsection studies the power fluctuations of a 600 kW wind turbine from TAIM-NEG MICON (Nordtank squirrel cage induction generator and stall regulation) measured at Valdecuadros wind farm (Spain) [52].

B.2.1. Record of 28/7/00, 13:48 to 13:52 and 13:36 to 13:41 (medium winds)

The time series analyzed in this subseries corresponds to date 28/7/00. Some starting and stopping test were done, and data considered in this test corresponds to the portion of time the turbine is in continuous operation, after all the switching transients have faded away. After discarding the transients, there are two series since there is a turbine stop and a start in between. The time series #1 last 5:30 minutes (from 13:36:10 to 13:41:40) and the time series #2 lasts 3:30 minutes (from 13:48:30 to 13:52:00).

The wind, measured in a meteorological mast at 40 m above the surface with a cup anemometer, was $U_{wind} = 9,5$ m/s $\pm 2,8$ m/s and $U_{wind} = 9,8$ m/s $\pm 2,8$ m/s in the first and second series (expanded uncertainty).



Fig. 200: Operation of a SCIG 600 kW wind turbine for wind speeds around 9,5 m/s during 5:30 minutes (series #1). From top to bottom, time series of the real power P [kW] (in black), wind speed U_{wind} [m/s] at 40 m in the met mast (in red, with a magnification factor $\times 10$ respect the vertical axis) and reactive power Q [kVAr] (in dashed green).

The main features of the time series from 13:36:10 to 13:41:40 (5:30 minutes of duration) are summarized in the following table and Fig. 200.

TABLE XVI: PARAMETERS OF THE 600 kW SCIG TURBINE SERIES #1, (DATE 28/7/00, FROM 13:36:10 TO 13:41:40, $F_{BLADE} \approx 1,35$ Hz)

	U_{wind} [m/s]	P [kW]	Q [kVAr]
Mean	9,50 m/s	322,7 kW	40,7 kVAr
Variance	1,42 m/s	80,7 kW	13,9 kVA
Ratio Std. Dev./mean	7,3 %	2,6 %	4,7%
Mean \pm uncertainty	9,50 \pm 2,84 m/s	322,7 \pm 161,4 kW	40,7 \pm 27,8 kVAr
r^2	$\sim 1,1$	$\sim 1,3$	$\sim 1,35$
$P_1' \approx PSD^+(1)$	0,02 (m/s) ² /Hz	10 kW ² /Hz	0,27 kW ² /Hz
f_1	$\lesssim 0,025$ Hz	$\lesssim 0,020$ Hz	$\lesssim 0,020$ Hz
f_2	∞	∞	∞

The second series (from 13:48:30 to 13:52:00, 3:30 minutes of duration) is quite similar (see Table XVII and Fig. 200).

The differences in the order r^2 between the runs depend greatly on the weighting of the error at different frequencies. Even though the wind speed in the 750 kW and 600 kW SCIG turbines is measured in the same meteorological tower, the series presented at the 750 kW and 600 kW sections corresponds to different atmospheric conditions. In the data from 750 kW, the system order matched well the Kaimal spectrum. But in the data of the 600 kW series, the order is a bit beyond unity, indicating a worse fit. The study of the wind spectra requires complete atmospheric information and systematic measure of meteorological magnitudes. Thus, no conclusions can be drawn except that experimental wind spectra can differ notably from Kaimal, von Karman or Davenport models.



Fig. 201: Operation of a SCIG 600 kW wind turbine for wind speeds around 9,8 m/s during 3:30 minutes (series #2).

In the analyzed data, the estimated parameter f_1 is only 4 to 9 times the inverse of the time series duration, $1/T$. Therefore, the estimate of the pole frequency f_1 is severely influenced by the limited data duration and actual estimate is, in fact, an

upper bound limit of f_1 . In other words, f_1 should be estimated using longer data series.

No significant spectrum noise floor has been observed in the 600 kW series. Thus, the root frequency f_2 is beyond the maximum frequency of the measuring system and, consequently, f_2 has been considered ∞ in all measurements from the 600 kW turbine (i.e., negligible).

TABLE XVII: PARAMETERS OF THE 600 kW SCIG TURBINE, SERIES #2, (DATE 28/7/00, FROM 13:48:30 TO 13:52:00, $F_{BLADE} \approx 1,35$ Hz)

	U_{wind} [m/s]	P [kW]	Q [kVAr]
Mean	9,8 m/s	338,2 kW	43,4 kVAr
Variance	1,43 m/s	81,5 kW	13,95 kVAr
Ratio Std. Dev./mean	25,9 %	2,5 %	23,0%
Mean \pm uncertainty	9,8 \pm 2,86 m/s	338,2 \pm 162 kW	43,4 \pm 27,9 kVAr
r^2	$\sim 1,04$	$\sim 1,373$	$\sim 1,45$
$P_1' \approx PSD^+(1)$	0,0309 (m/s) ² /Hz	17,7 kW ² /Hz	0,258 kW ² /Hz
f_1	$\lesssim 0,025$ Hz	$\lesssim 0,025$ Hz	$\lesssim 0,025$ Hz
f_2	∞	∞	∞

B.2.2. Analysis of real power output

In the full graph of the time series, Fig. 200 and Fig. 201, the oscillations due to rotor position cannot be seen clearly. In the following magnified graphs, approximately one oscillation per 0,8 second is noticeable in turbine power output.

The oscillation pattern in the 600 kW is complex since subharmonics $1/3$, $1/2$ and $2/3$ of the blade frequency f_{blade} have similar energy content to the fundamental component. The presence of subharmonic $1/3$ is very likely bound to misalignments in the blades or in the rotor. Thus, the turbine experience a mixture of oscillation modes resulting in a more complex signal than an amplitude modulated single tone.

Harmonic content in the 600 kW turbine is lower than in the 750 kW turbine and only harmonics 4 and 5 have significant energy content (harmonics 2 and 3 are noticeable but small). This is due to lower stiffness and higher damping in the mechanic drive train of the 600 kW turbine respect 750 kW case.

The 600 kW data corresponds to near rate wind ($U_{wind} \sim 9,8 \pm 2,86$ m/s) whereas the 750 kW data corresponds to smaller wind speeds ($U_{wind} \sim 6,7 \pm 1,86$ m/s). Free stream turbulence intensity in both cases is similar (14,6 % for 600 kW and 13,9 % for 750 kW), but the 600 kW turbine is operating near the rated speed and blades are more likely to stall, producing separation of the boundary layer and unsteady flow. Unsteady flow increases fast power fluctuations, such as subharmonics $1/3$, $1/2$ and $2/3$. Conversely, stall limits overall power excursion and the ratio of the power variance to the power mean is lower for greater wind speeds since the slope of the power

curve is smaller. In plain words, the aerodynamic stall limits the signal excursion decreasing very low frequency content and widening the spectrum peaks (narrow peaks are related to high amplitude tones in the time domain).



Fig. 202: Detail of real power of a SCIG 600 kW wind turbine for wind speeds around 9,5 m/s during 1 minute in series #1.



Fig. 203: Detail of real power of a SCIG 600 kW wind turbine for wind speeds around 7 m/s during one minute in series #1.

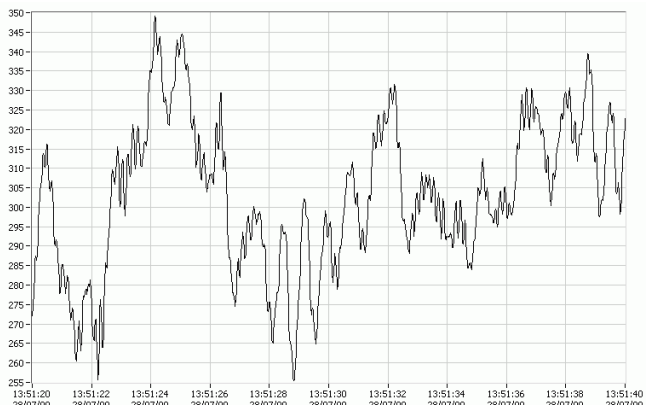


Fig. 204: Detail of real power of a SCIG 600 kW wind turbine for wind speeds around 9,5 m/s during 20 seconds in series #2.

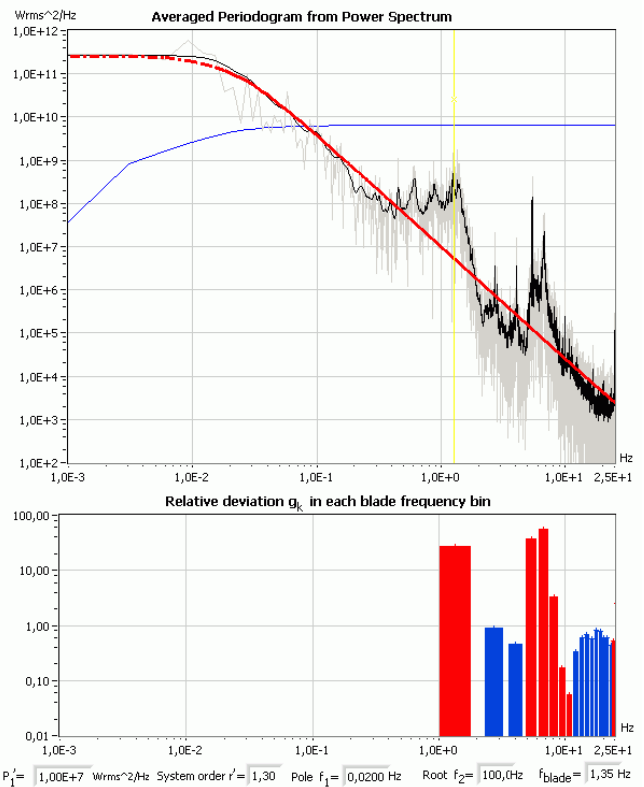


Fig. 205: $PSD_{P^+}(f)$ parameterization of real power of a SCIG 600 kW wind turbine for time series #1.

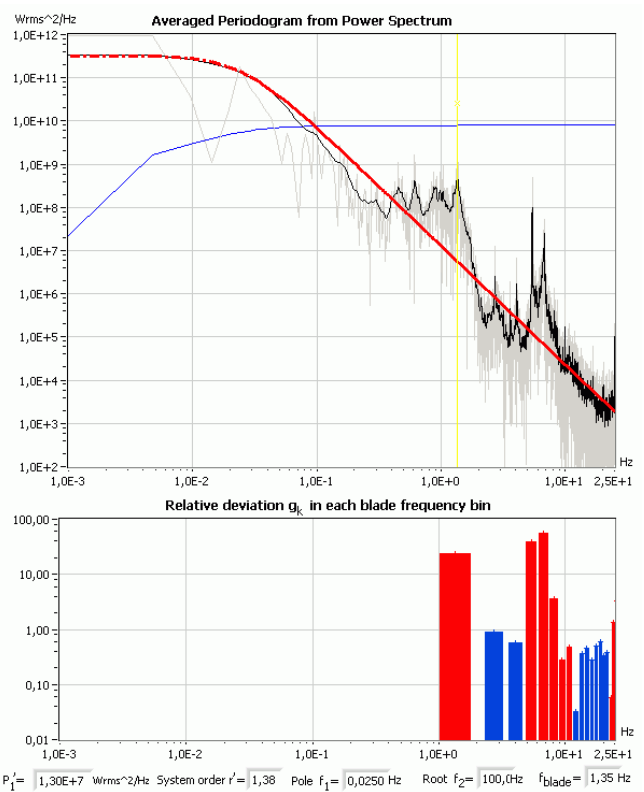


Fig. 206: $PSD_{P^+}(f)$ parameterization of real power of a SCIG 600 kW wind turbine for time series #2.

B.2.3. Analysis of reactive power output

The main features of reactive power are the capacitor switching and the variations of reactive power due to variations of generator power. In this model, all the capacitor banks are connected just after the generator coupling and they

are not disconnected until a bit earlier than the generator uncoupling.

Therefore, a static relationship can be used to relate real and reactive power. Fig. 207 shows the measured reactive power (in solid black) and its estimation from real power with a least square linear relationship with red dots ($Q \approx 0,1702P - 14,524$).

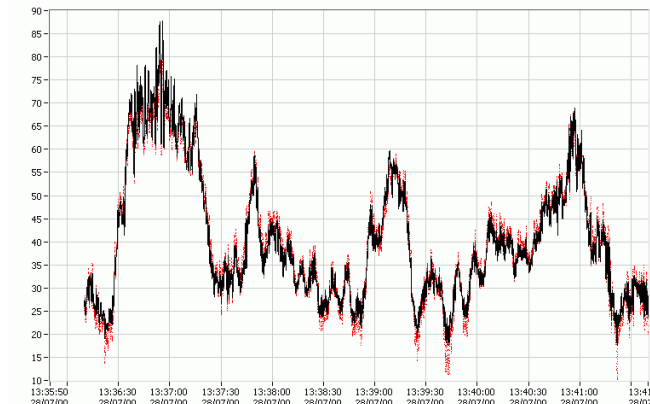


Fig. 207: Rective power Q [kVAr] (in solid black line) of a SCIG 600 kW wind turbine for series #1, corresponding to Fig. 200, and its linear estimation from real power.

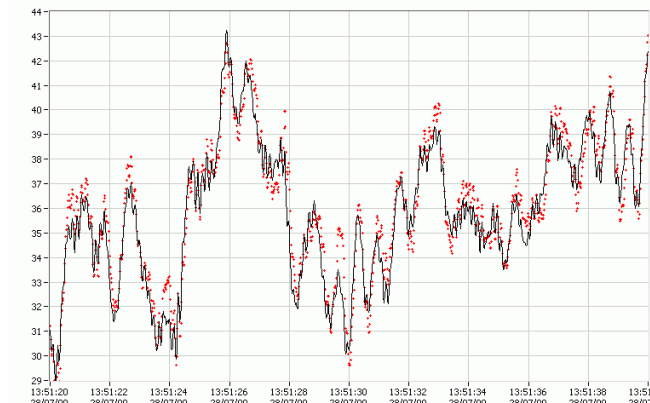


Fig. 208: Detail corresponding to the reactive power of Fig. 204 (in solid black line) and its linear estimation from real power (red dots).

In fact, the scatter plots of real and reactive powers (Fig. 209 and Fig. 210) shows that the relationship is quadratic since reactive consumption of the generator is approximately proportional to the squared current and real power is proportional to current provided grid voltage is held constant. In fact, part of the error in the quadratic fit can be due to the variability in grid voltage.

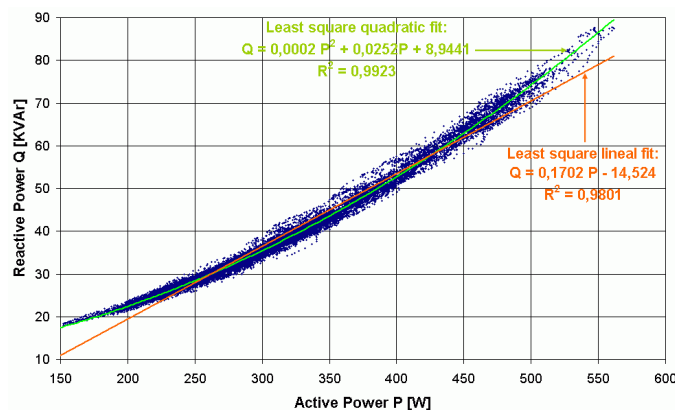


Fig. 209: Reactive vs. real power scatter plot of series #1 of a SCIG 600 kW wind turbine.

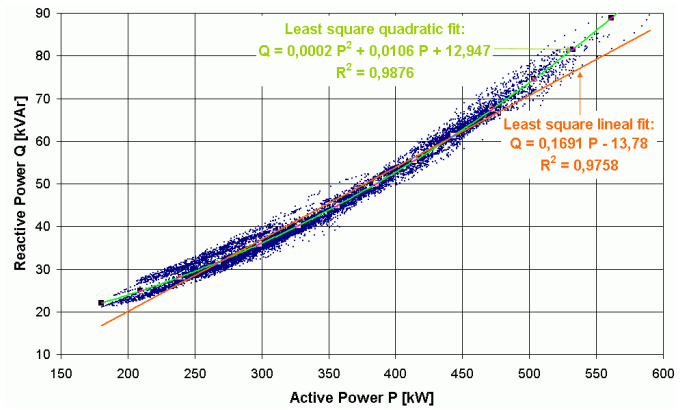


Fig. 210: Reactive vs. real power scatter plot of series #2 of a SCIG 600 kW wind turbine.

Due to the almost linear relationship between the real and reactive power, both PSD are very similar (see, for example, Fig. 205 and Fig. 211). However, the discrepancy is greater when the power excursions are bigger and a quadratic fit outperforms a simple lineal relationship. The system order r' of real P and reactive Q power are quite close, as it can be seen in Table XVI and Table XVII (differences have the same order of magnitude than the uncertainty of r'). The better agreement of real and reactive power, compared to the 750 kW data, can be partly due to greater stability of grid voltage during the measuring campaign in the 600 kW turbine.

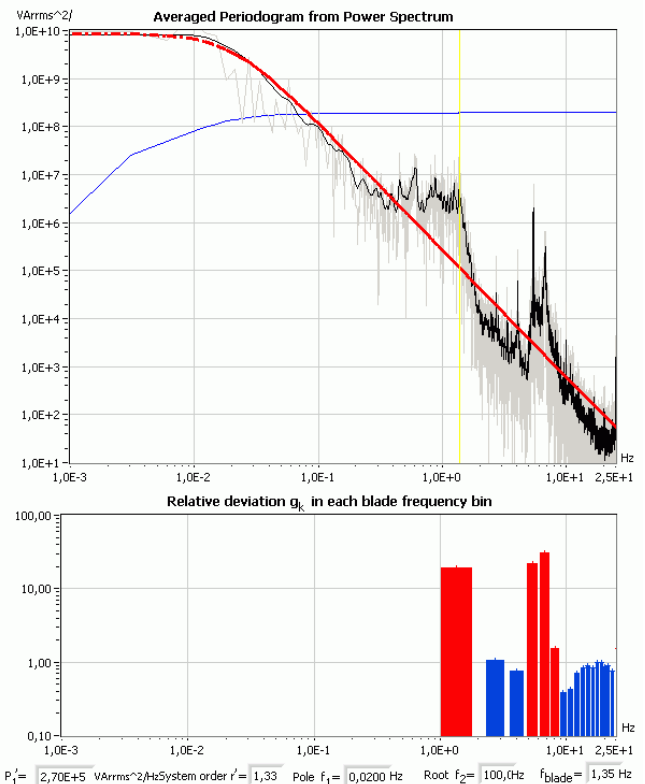


Fig. 211: $PSD_Q^+(f)$ of the reactive power corresponding to Fig. 207.

B.2.4. Analysis of wind measured at the meteorological mast 40 m above surface level

The $PSD_{U_{wind}}^+(f)$ estimated in series #1 and #2 are shown in Fig. 212 and Fig. 213, respectively. The cup anemometer behaves as a low-pass filter of cut-off frequency around $U_{wind} / 10 \text{ m} \sim 1 \text{ Hz}$. The recorded wind speed show an additional drop corresponding to a low-pass 1st order system from 1 Hz and some artifices due to the digital treatment of the signal appear beyond 3 Hz.

Up to anemometer cut-off frequency, the slope is smooth and it fits well the model (184) (black and red lines in Fig. 212 and Fig. 213 are almost superimposed up to 0,67 Hz). The system order is $r' \approx 0,97 \sim 1,1$ (higher than the usual order $5/6 = 0,833$ corresponding to the Kaimal (11), Harris (13) and Von Karman (14) spectra). Taking into account the measuring system limitations, the real frequency content in the wind is expected to be quite close to the adjusted model (184) –in thick solid red in Fig. 192–, which can be thought as a generalization of the Kaimal Spectra.

The pole is $f_i \lesssim 0,020 \sim 0,025 \text{ Hz}$, corresponding to an integral length scale of the turbulence $\ell_{U_{wind}} \gtrsim \langle U_{wind} \rangle / (6 a f_i) \approx 37 \sim 46 \text{ m}$, assuming $a = 1,7$ according to the draft Eurocode ENV 1991-2-4 and (11). Since the turbulence length scale of this site is usually in the order of 1 km, the actual length scale in this sample is believed to be significantly greater than 46 m.

The scale parameter is $P_1' \approx PSD_{U_{wind}}^+(f = 1 \text{ Hz}) \approx 0,020 \sim 0,037 \text{ (m/s)}^2/\text{Hz}$. The value of the wind variance is $\sigma_{wind} = 1,42 \text{ m/s}$, corresponding to a turbulence intensity $I = \sigma_{wind} / \langle U_{wind} \rangle = (1,42 \text{ m/s}) / (9,65 \text{ m/s}) = 14,7 \%$ –high since the turbine was in a hill top and surrounded by other turbines.

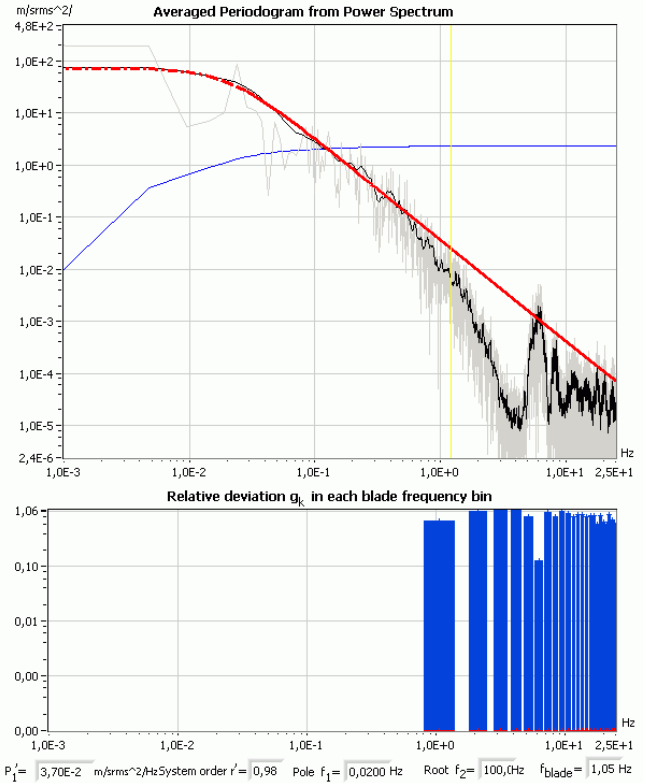


Fig. 213: $PSD_{U_{wind}}^+(f)$ of the wind corresponding to series #2. Beyond 1 Hz, some artifices appear due to measuring limitations.

B.2.5. Analysis of phase-to-phase voltage

$PSD_{V_{rs}}^+(f)$ of the low voltage phase to phase corresponding to Fig. 187 is shown in Fig. 193. The voltage is $684,2 \pm 0,48 \text{ V}$. Voltage at series #1 and #2 is significantly more stable than the series for the 750 kW turbine and this is the likely cause of the better agreement of the real and reactive.

The slope of the voltage corresponds to a first order system ($r' \approx 1$), similar to the wind spectra ($r' \approx 0,97 \sim 1,1$). Small voltage fluctuations are somewhat proportional to wind variations (partly due to the turbine analyzed and partly due to the other turbines electrically close).

The voltage drop in the line up to the main transformer (a 690 V line of 500 m) is (quite approximately) linearly related to the reactive and real power. Hence, the PSD of the voltage drop should be similar to a combination of Fig. 206 and Fig. 211.

The small peak near the blade frequency is due to the oscillation due to turbine angle. However, the amplitude of the fundamental peak of voltage is noticeably smaller than in Fig. 205 and Fig. 211, indicating that external influence is strong. On one hand, the voltage oscillation around 0,08 Hz is not related to the turbine and thus, its origin is assumed to be outside the turbine. On the other hand, the power fluctuations of the turbine in the 5-8 Hz range have a limited effect on the voltage (likely, because other nearby turbines are not experiencing these oscillations).

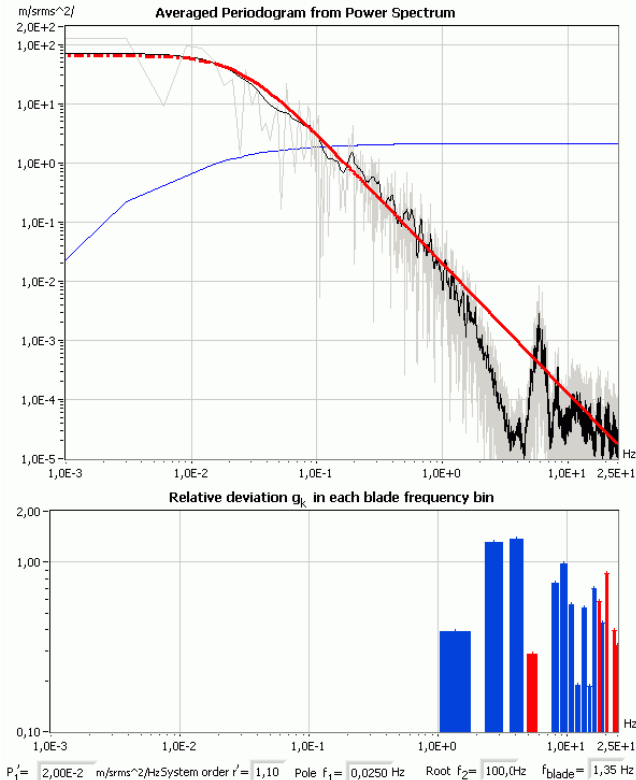


Fig. 212: $PSD_{U_{wind}}^+(f)$ of the wind corresponding to series #1. Beyond 1 Hz, some artifices appear due to measuring limitations.

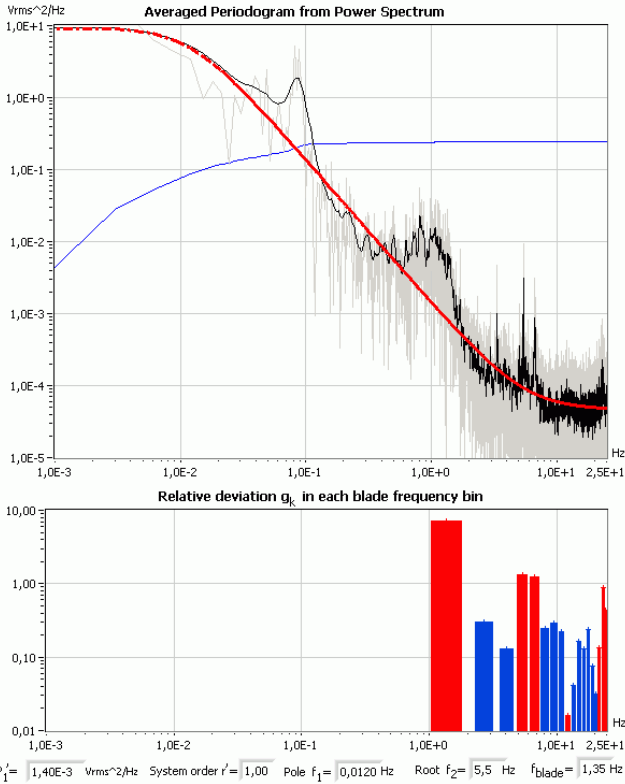


Fig. 214: $PSD_{V_{rs}^+}(f)$ of the low voltage phase R to phase S corresponding to series #1.

B.2.6. Bode magnitude plots

The ratio of the spectrum of real power P to the spectrum of wind U_{wind} is the frequency response of the real power respect to the wind at the meteorological mast in Fig. 215. Wind is measured at the met mast with a cup anemometer (its frequency response at 10 m/s is only ~ 1 Hz).

In Fig. 215, the peaks at subharmonics $1/3$, $1/2$ and $2/3$ and harmonics 3, 4 and 5 frequencies correspond to rotational effects. They appear as gain peaks at fundamental frequency since rotor position and turbine vibration modes are not present in wind. Thus, they should be considered as additive factors quite insensitive to wind turbulence.

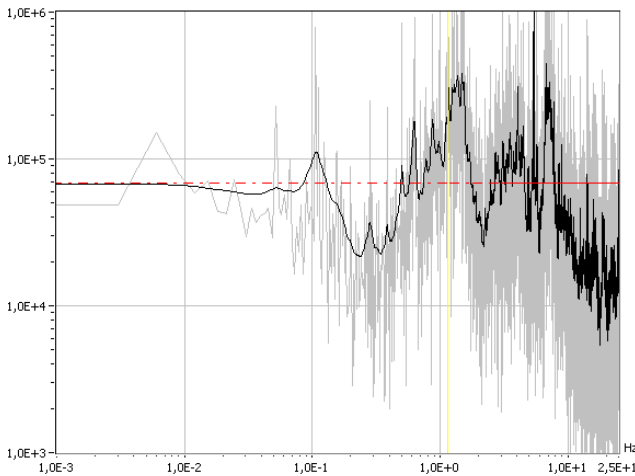


Fig. 215: Bode magnitude plot of real power P [W] respect wind U_{wind} [m/s] for series #1 (beyond 1 Hz, the transfer function is underestimated due to limitations in the wind measure).

There is also a small peak at 0,12 Hz and a damping in the 0,2-0,5 Hz range. The quasi-static approximation $\Delta P \sim$

$68000\Delta U_{wind}$ can be valid for simplistic calculations, i.e. the static gain is 68 kW/(m/s).

Fig. 216 shows the bode plot of the reactive power Q respect to the spectrum of wind at the met mast U_{wind} . The behaviour is similar to the frequency response of real power P respect to U_{wind} . The quasi-static approximation $\Delta Q \sim 11200\Delta U_{wind}$ can be valid for simplistic calculations.

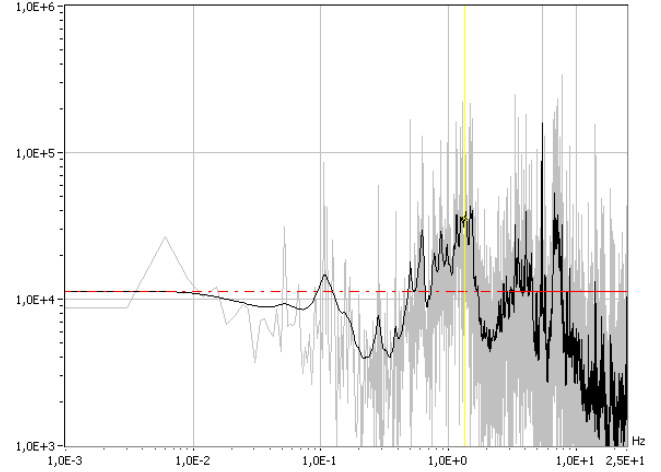


Fig. 216: Bode magnitude plot of reactive power Q [VAR] respect wind U_{wind} [m/s] for series #1 (beyond 15 Hz, the transfer function is underestimated due to limitations in the wind measure).

Fig. 217 shows the bode plot of the reactive power Q respect to the real power P and the reference quasi-static approximation $\Delta Q \sim 0,157\Delta P$.

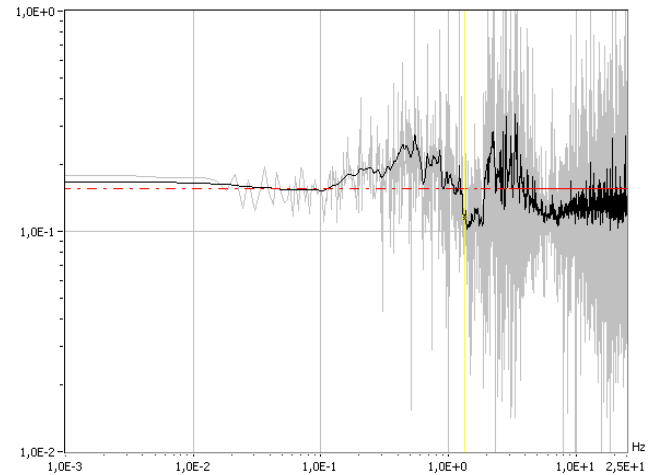


Fig. 217: Bode magnitude plot of reactive power Q [VAR] respect real power P [W] for series #1.

The influences of real P and reactive Q power on line voltage (V_{RS}) is shown in Fig. 218 and Fig. 219. Since the real and reactive powers are closely related, both plots are cross-related. The small-signal lineal model for voltage is $\Delta V_{RS} \sim (R_{eff}\Delta P + X_{eff}\Delta Q) / \langle V_{RS} \rangle$, where R_{eff} and X_{eff} are the effective Thévenin resistance and reactance seen from the voltage point of measure. However, the frequency response beyond 0,7 Hz increases at a pace of a system of order $1/2$.

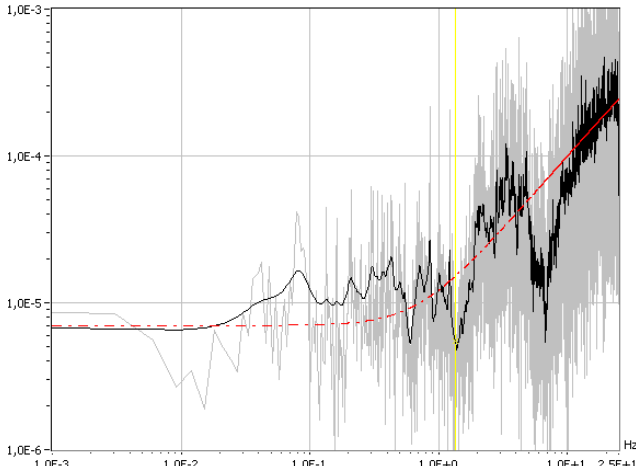


Fig. 218: Bode magnitude plot of line voltage V_{RS} [V] respect real power P [W] for series #1.

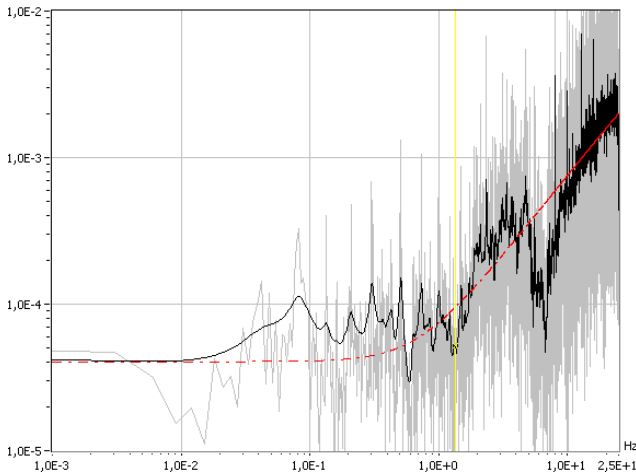


Fig. 219: Bode magnitude plot of line voltage V_{RS} [V] respect reactive power Q [VAr] for series #1.

B.3. VRIG wind farm

This subsection studies the power fluctuations of Borja wind farm (Spain) a wind farm composed by 26 wind turbines of 600 kW with variable resistance induction generator (VRIG) [52] with “opti-slip” control from VESTAS. The datalogger recorded signals either at a single turbine or at the substation. In either case, wind speed from the meteorological mast of the wind farm was also recorded.

One-second or two-second averages were customarily stored. The low frequency spectrum band could have been compared on the basis of these data sets at the turbine and at the substation. The comparison of magnitudes at a single turbine and at the wind farm can lead to experimental estimation of the coherence of the fluctuations in the low frequency band. Due to the magnitude of this chapter, this work line has not been considered here.

Waveforms of the substation were only occasionally kept stored. Only a data sequence corresponding to wind farm waveforms analyzed at grid frequency will be considered in this subsection.

B.3.1. Record of 26/2/99, 13:52:53-14:07:30 (low winds)

The record analyzed in this subsection corresponds to date 26/2/99 and time 13:52:53-14:07:30 (about 14:37 minutes). The average blade frequency in the turbines was $f_{blade} \approx 1,48 \pm 0,03$ Hz during the interval. The wind, measured in a meteorological mast at 40 m above the surface with a propeller anemometer, was $U_{wind} = 7,6$ m/s $\pm 2,0$ m/s (expanded uncertainty). The main features of this time series are summarized in the following table and plot.

TABLE XVIII: PARAMETERS OF THE VRIG WIND FARM, SERIES 26/2/99, 13:52:53-14:07:30 ($F_{BLADE} \approx 1,48$ Hz)

	U_{wind} [m/s]	P [kW]	Q [kVAr]
Mean	7,59 m/s	3614 kW	524 kVAr
Variance	1,0 m/s	466 kW	79 kVA
Ratio Std. Dev./mean	0,2 %	1,3 %	1,5%
Mean \pm uncertainty	7,6 $\pm 2,0$ m/s	3614 ± 932 kW	-524 ± 158 kVAr
r^2	$\sim 1,341$	$\sim 1,253$	$\sim 1,15$
$P_1' \approx PSD^+(1)$	0,00325 (m/s) ² /Hz	129 kW ² /Hz	8 kW ² /Hz
f_1	$\leq 0,03$ Hz	$\leq 0,008$ Hz	$\leq 0,008$ Hz
f_2	∞	11 Hz	∞

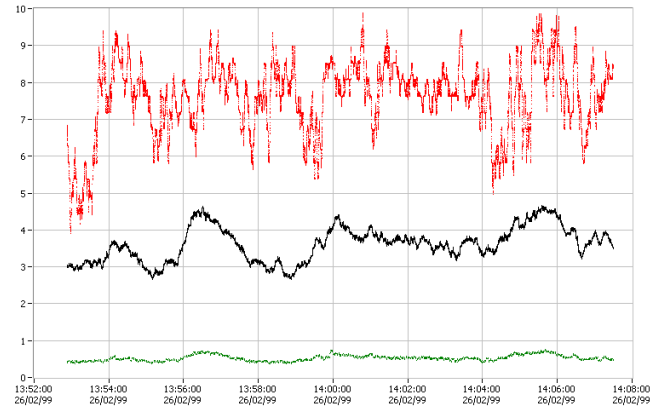


Fig. 220: Operation of VRIG wind farm with wind speeds around $7,6 \pm 2,0$ m/s during 14,6 minutes. From top to bottom, time series of the real power P [MW] (in black), wind speed U_{wind} [m/s] at 40 m in the met mast (in red) and reactive power Q [MVar] (in dashed green).

B.3.2. Analysis of real power output

In the graph of the full time series, Fig. 221, the oscillations due to rotor position are not evident since the total power is the sum of the power from 26 unsynchronized wind turbines minus losses in the farm network.

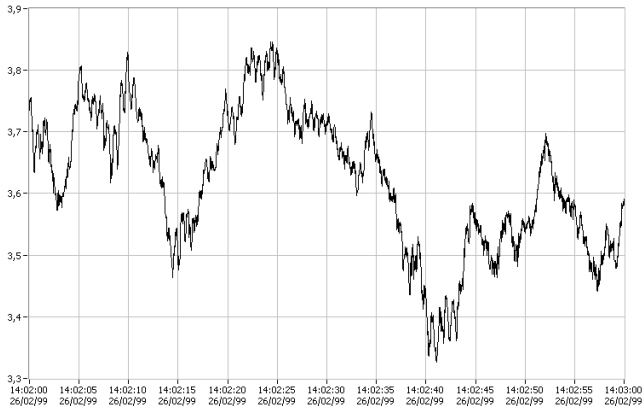


Fig. 221: Real power of a VRIG wind farm for wind speeds around 7,6 m/s during one minute.

Fig. 221 and Fig. 222 shows a rich dynamic behaviour of the real power output, where the modulation and high frequency oscillations are superimposed to the fundamental oscillation.

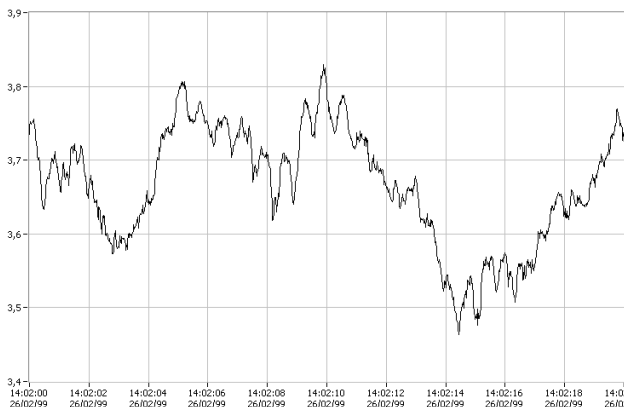


Fig. 222: Real power of a VRIG wind farm for wind speeds around 6,7 m/s during 20 s.

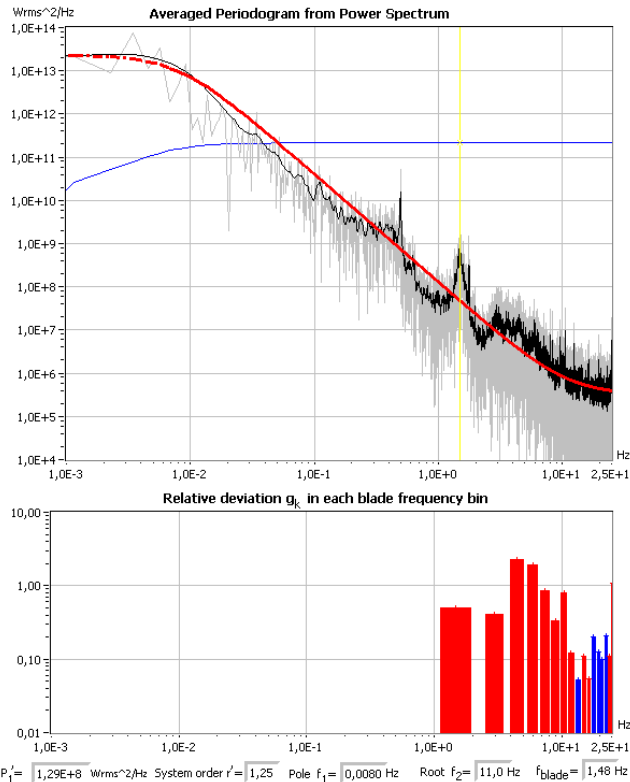


Fig. 223: $PSD_{P^+}(f)$ parameterization of real power of a VRIG wind farm for wind speeds around 7,6 m/s (average power 3,6 MW) computed from Fig. 220.

Fig. 223 indicates that power spectrum is quite constant for frequencies smaller than 0,013 Hz. The peak at blade frequency $f_{blade} \approx 1,48$ Hz and its $1/3$ subharmonic are noticeable (subharmonic $1/3$ is due to misalignments in the rotor). Other narrow peaks corresponding to harmonics of fundamental oscillation are very low in Fig. 223.

Fig. 224 shows the contribution of each frequency to the variance of power $\sigma_{P,T,f}^2$ –the area bellow $f \cdot PSD_{P^+}(f)$ in a semi-logarithmic plot is the signal variance according to (10). The main contributions to power variability are:

- Low frequencies due to wind variation ($f < 0,3$ Hz).
- Blade ($\sim 1,5$ Hz) and rotor frequencies ($\sim 0,5$ Hz).
- Contributions at $f > 3$ Hz due mainly to drive train, generator and blade frequency harmonics.

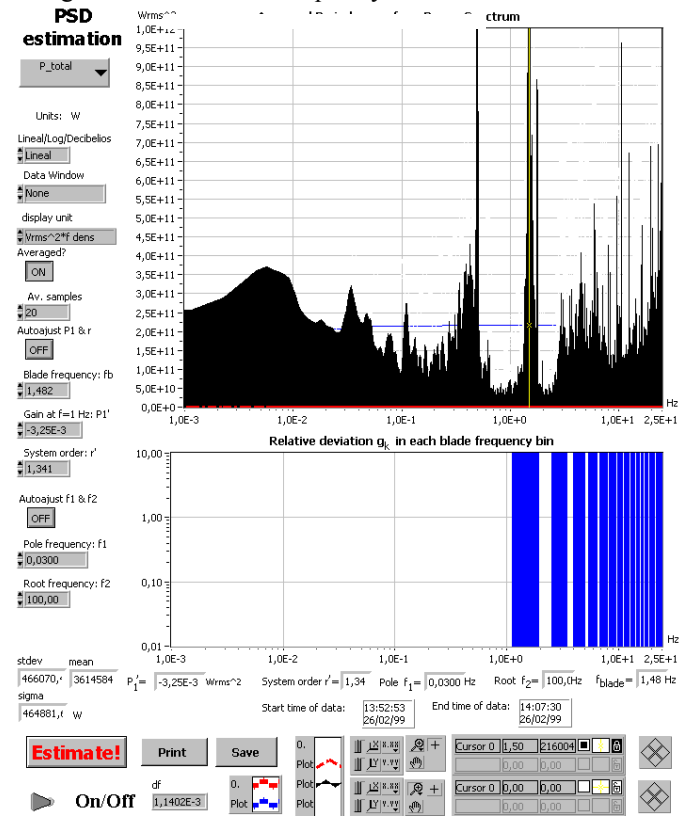


Fig. 224: Contribution of each frequency to the variance of power computed from Fig. 220 (the area bellow $f \cdot PSD_{P^+}(f)$ is the variance of power).

B.3.3. Analysis of reactive power output

The reactive power shows significant fluctuations at $f \gtrsim 0,5$ Hz, as it can be seen in Fig. 225 and Fig. 226. Although reactive power fluctuations are, in absolute value, smaller than real power fluctuations, reactive power fluctuates at higher frequency than real power. In fact, reactive power fluctuations are significant up to 6 Hz due to VRIG generator dynamics. Beyond 8 Hz, $PSD_{Q^+}(f)$ decreases sharply but the frequency content of the reactive power is still noticeable.

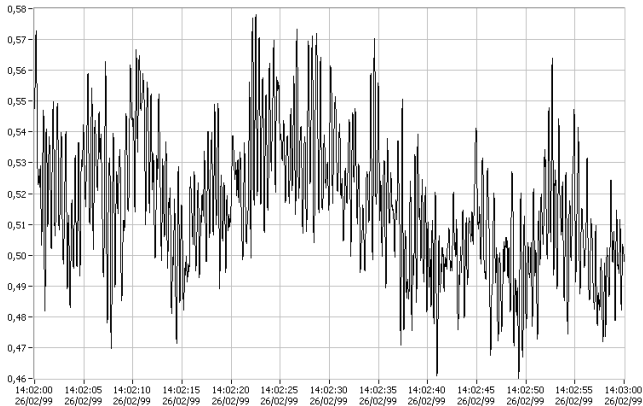


Fig. 225: Reactive power Q [MVar] of a VRIG wind farm corresponding to real power P shown in Fig. 221.

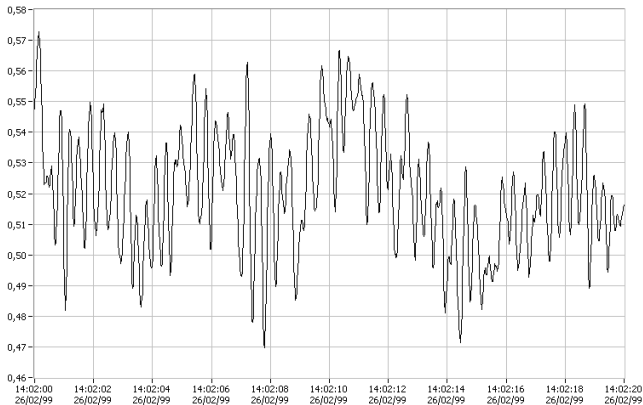


Fig. 226: Reactive power Q [MVar] of a VRIG wind farm corresponding to the real power of Fig. 222.

The static relationship between P and Q can be seen in Fig. 226. It can be inferred from this image that $\Delta Q \sim 0,164 \Delta P$, approximately.

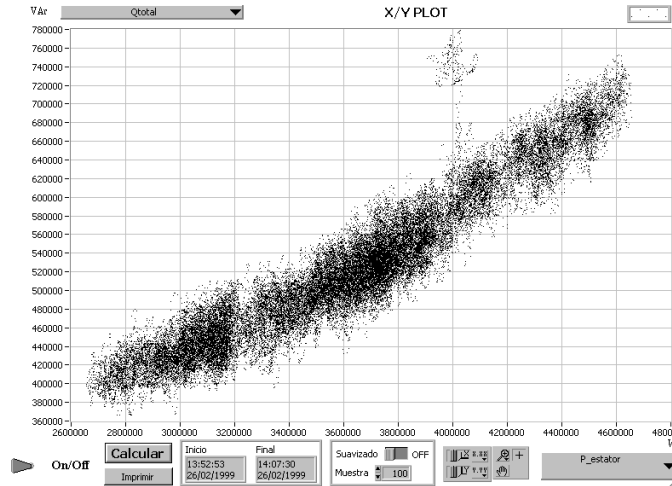


Fig. 227: Reactive power Q [VAr] versus real power P [W] computed from Fig. 220.

The PSD of reactive power in Fig. 228 is comparable to the PSD of real power in Fig. 223 except in the 1-6 Hz range. This deviation is likely due to the dynamics of rotor current. Real and reactive power order is similar, but reactive power descends slower.

The system order for the reactive power is $r^2 \approx 1,15$, a value between the voltage order ($r^2 \approx 0,81$) and the real power order ($r^2 \approx 1,25$). This discrepancy can be due to the poor fitting of the reactive power in Fig. 228 and the great influence of

voltage in Q . Conversely, the behaviour of voltage is influenced by wind since there was other wind farms connected nearby.

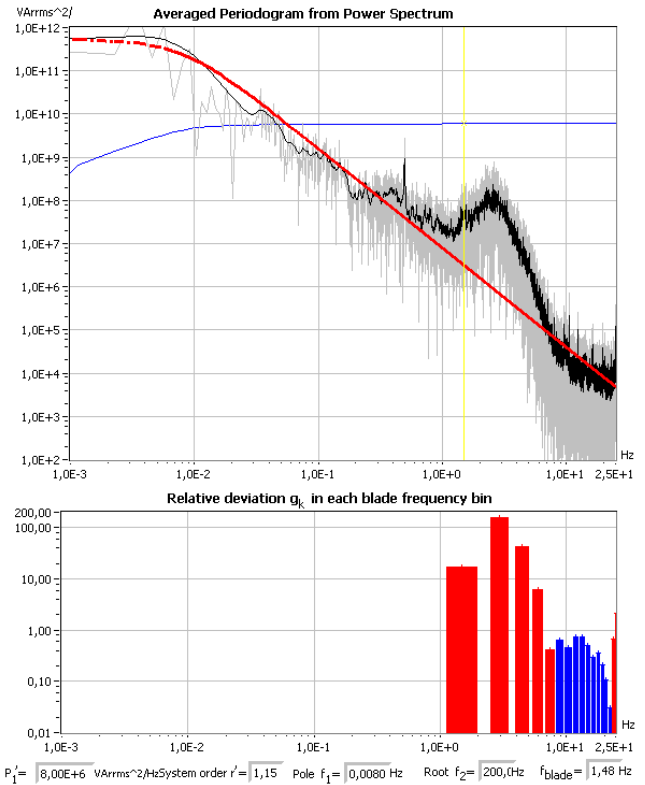


Fig. 228: $PSD_{Q^+}(f)$ of the wind computed from Fig. 220.

B.3.4. Analysis of wind measured at the meteorological mast 40 m above surface level

The $PSD_{U_{wind}^+}(f)$ is shown in Fig. 229. Due to the anemometer inertia, it behaves as a low-pass filter of cut-off frequency around $U_{wind} / 1 \text{ m} \sim 7,6 \text{ Hz}$ (beyond such frequency, some artifices appear). Notice that the length constant of the propeller anemometer used here ($\sim 1 \text{ m}$) is significantly smaller than the cup anemometer length constant used in the previous subsections ($\sim 10 \text{ m}$).

Up to anemometer cut-off frequency, the slope is smooth and it fits well the model (184) (black and red lines in Fig. 229 are almost superimposed up to 6 Hz). The system order is $r^2 \approx 1,34$, significantly bigger than the order $r^2 = 5/6 = 0,833$ corresponding to the Kaimal (11), Harris (13) and Von Karman (14) spectra.

The pole is $f_1 \lesssim 0,03 \text{ Hz}$, corresponding to an integral length scale of the turbulence $\ell_{U_{wind}} \gtrsim \langle U_{wind} \rangle / (6 a f_1) \approx 24 \text{ m}$, assuming $a = 1,7$ according to the draft Eurocode ENV 1991-2-4 and (11). This very low value indicates that the anemometer is affected by wakes.

The scale parameter is $P_1' \approx PSD_{U_{wind}^+}(f = 1 \text{ Hz}) \approx 0,00325 \text{ (m/s)}^2/\text{Hz}$. The value of the wind variance is $\sigma_{wind} = 1,0 \text{ m/s}$, corresponding to a turbulence intensity $I = \sigma_{wind} / \langle U_{wind} \rangle = (1,0 \text{ m/s}) / (7,6 \text{ m/s}) = 13,1 \%$ –high since the wind farm was in a hill top and the met mast is surrounded by turbines.

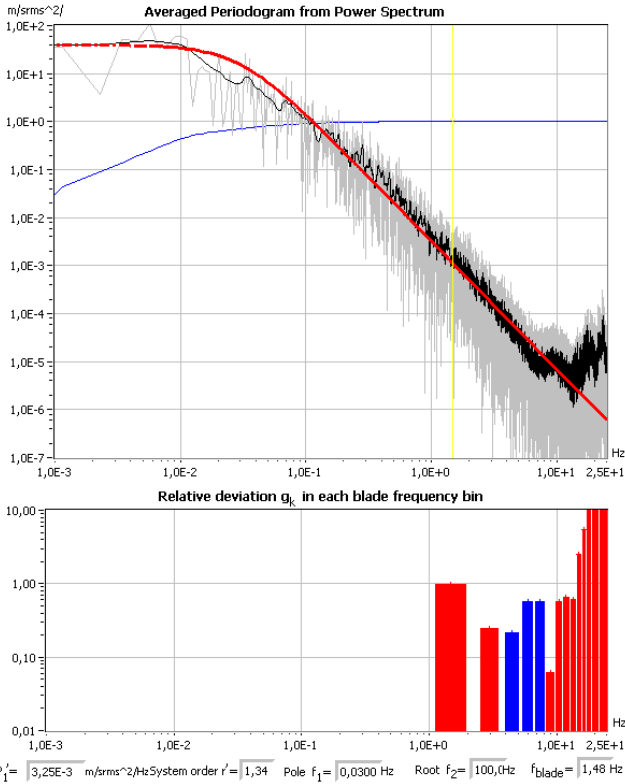


Fig. 229: $PSD_{U_{wind}}(f)$ of the wind computed from Fig. 220. Beyond 6 Hz, some artifices appear due to measuring limitations.

B.3.5. Analysis of phase-to-phase voltage

$PSD_{V_{RS}}(f)$ of the phase to phase high voltage is shown in Fig. 230. The voltage during the series is quite variable for a period of 14:37 minutes, $67,98 \pm 0,2$ kV (extended uncertainty). The $PSD_{V_{RS}}(f)$ corresponds to a system of order $r' \approx 0,81$, approximately. The influence of nearby generators and loads are similar to the contribution of the analyzed turbine, $\Delta V_{RS} \sim (R_{eff} \Delta P + X_{eff} \Delta Q) / \langle V_{RS} \rangle$. The individual effect of the analyzed wind farm in the voltage is difficult to distinguish from external influences (for example, the peak at 0,1 Hz is not related to the wind farm)

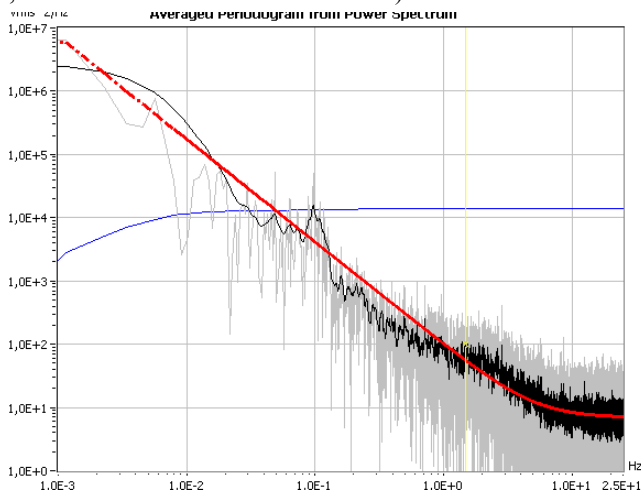


Fig. 230: $PSD_{V_{RS}}(f)$ of the low voltage phase to phase computed from Fig. 220.

B.3.6. Bode magnitude plots

The turbine can be assumed to be a system whose primary input is wind and its main output is real power. Even though considering the real turbine a linear single-input single-output

system is an obvious oversimplification, it allows to derive a small signal model for accounting wind variations in power.

When the transfer function is above the static gain (indicated with a horizontal red line for convenience), the oscillations of these frequencies in the input are considered amplified in the output. When the transfer function is below the static gain, these frequencies are considered attenuated or damped.

The ratio of the spectrum of real power P to the spectrum of wind U_{wind} is the frequency response of the real power respect to the wind at the met mast in Fig. 231. Wind is measured at the met mast with a propeller anemometer.

Fig. 231 shows that wind oscillations in the 0,004 ~ 3 Hz range –excluding blade frequency– are damped in the real power output, P . At frequencies higher than 6 Hz, the measuring system introduces error in the wind measure and the transfer function in Fig. 231 is underestimated (at $f > 6$ Hz, the sensitivity of P to U_{wind} may be close to the static gain).

Near blade frequency, $f \sim f_{blade}$, the ratio of wind to power fluctuation presents a peak but this is due to the tower shadow effect, which is not proportional to the fluctuation of the wind in such range. Thus, fluctuation of power at blade frequencies and its sub-harmonics and harmonics should be regarded as an additive factor (almost) insensitive to wind turbulence.

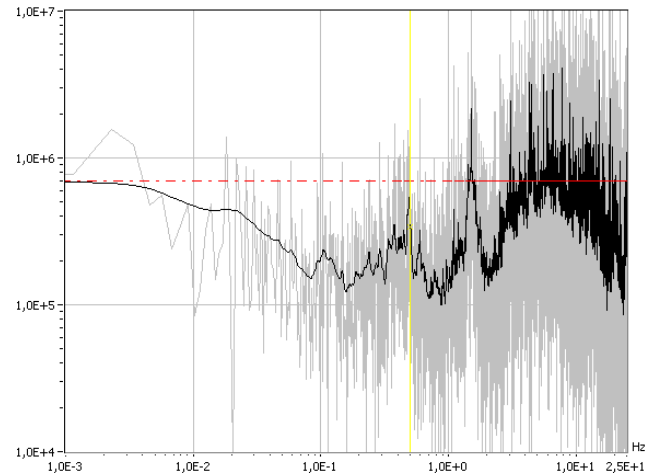


Fig. 231: Bode magnitude plot of real power P [W] respect wind U_{wind} [m/s] (beyond 6 Hz, the transfer function is underestimated due to limitations in the wind measure).

Fig. 232 shows the bode plot of the reactive power Q respect to the spectrum of wind, U_{winds} at the met mast. Wind oscillations in the 0,004 ~ 0.4 Hz range are damped in the reactive power output, Q . However, wind fluctuations in 1-10 Hz are amplified due to rotor current dynamics. Notice that tower shadow has a small effect on reactive power, specially compared to real power. At $f > 10$, the gain is thought to be not far from the static coefficient.

Fig. 233 shows the bode plot of the reactive power Q respect to the real power P . There is a quasi-static quadratic relation among real and reactive power in a SCIG generator [160] provided the voltage and the number of connected capacitor banks are constant (see Fig. 227). Regardless the number of capacitor banks connected, the slope of the X/Y graphs is $\Delta Q \sim 0,164 \Delta P$. Thus, the linearized small signal model can be valid if real power excursion is small and

voltage is fairly constant. According to the bode plot in Fig. 233, the dynamic gain is different to the static gain (0,164) in the frequency range 0,03 ~ 7 Hz, where rotor dynamics are significant. Notice that the reactive power gain decreases at blade frequency and its $1/3$ subharmonic respect to nearby frequencies.

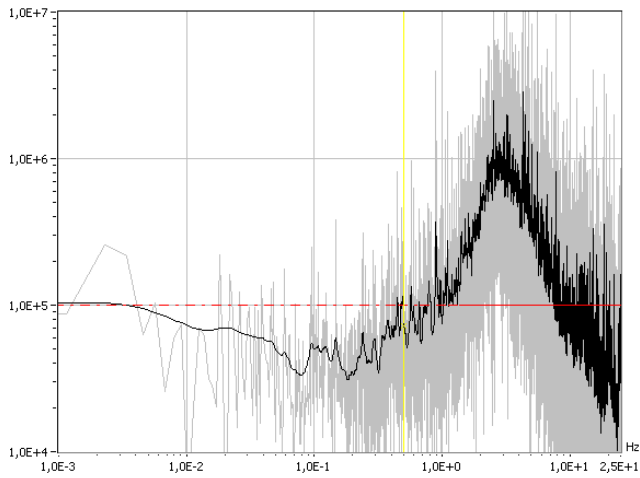


Fig. 232: Bode magnitude plot of reactive power Q [VAr] respect wind U_{wind} [m/s] (beyond 6 Hz, the transfer function is underestimated due to limitations in the wind measure).

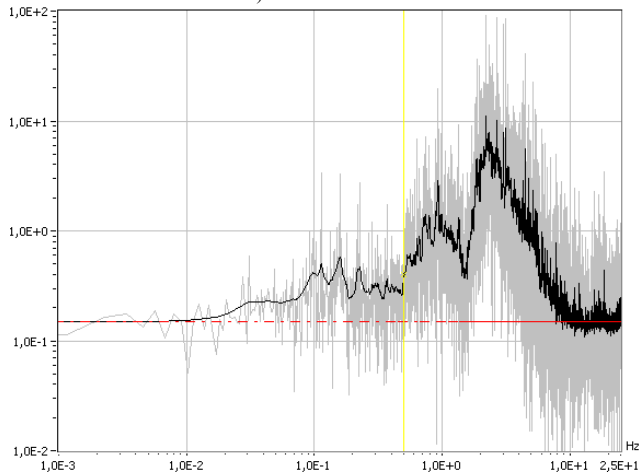


Fig. 233: Bode magnitude plot of reactive power Q [VAr] respect real power P [W].

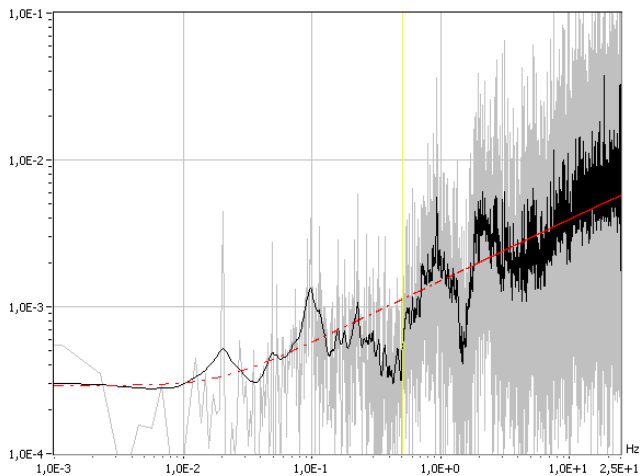


Fig. 234: Bode magnitude plot of line voltage V_{RS} [V] respect real power P [W].

The influences of real P and reactive Q power on line voltage (V_{RS}) are shown in Fig. 234 and Fig. 235, respectively. Since the real and reactive powers are closely related, both plots are cross-related. The small-signal lineal

model for voltage is $\Delta V_{RS} \sim (R_{eff} \Delta P + X_{eff} \Delta Q) / \langle V_{RS} \rangle$, where R_{eff} and X_{eff} are the effective Thévenin resistance and reactance seen from the voltage point of measure.

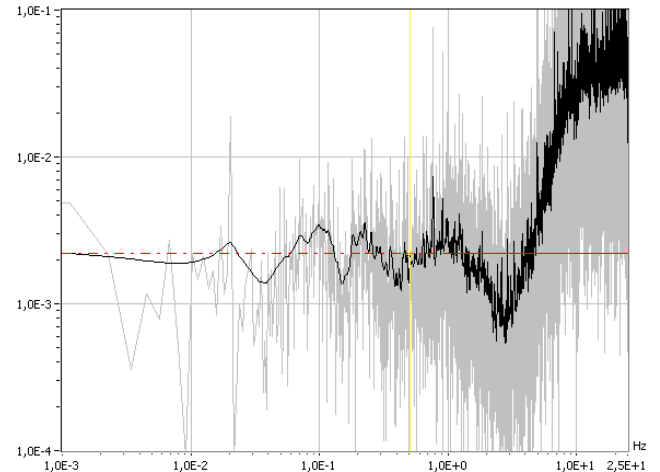


Fig. 235: Bode magnitude plot of line voltage V_{RS} [V] respect reactive power Q [VAr].

B.4. DFIG wind turbines

This subsection studies the power fluctuations of Remolinos wind farm (Spain). Remolinos wind farm is in a cliff top (wind regime is specially turbulent [387]) and it has doubly fed induction generators (DFIG) from Gamesa, with generator speed ranging from 1220 to 1620 rpm. It is composed by 15 turbines of 648 kW (model G42 from Gamesa with 42 m rotor diameter) and 3 turbines of 660 kW named G47 (model G47 from Gamesa with 47 m rotor diameter), both of them with variable pitch [52]. The datalogger recorded signals either at a single turbine or at the substation. In either case, wind speed from the meteorological mast of the wind farm was also recorded.

One-second or two-second averages were customarily stored. The low frequency spectrum band could have been compared on the basis of these data sets at the turbine and at the substation. The comparison of magnitudes at a single turbine and at the wind farm can lead to experimental estimation of the coherence of the fluctuations in the low frequency band.

Unfortunately, waveforms at the turbine and at the substation were only once kept stored at grid frequency. These data, divided in two series will be analyzed and compared between the turbine and at the substation.

B.4.1. Notes on the estimation of model parameters

In the analyzed data, the estimated parameter f_i is only 4 to 30 times the inverse of the time series duration, $1/T$. Therefore, the estimate of the pole frequency f_i is severely influenced by the limited data duration. Thus, the actual estimate is, in fact, an upper bound limit of f_i . In plain words, f_i should be estimated using longer data series.

The differences in the order r^2 between each subseries depend greatly on the weighting of the error at different frequencies. Thus, the uncertainty of the parameters is high when using only two short data runs. The differences found between the first and the second subseries measured at the

same point (either at the turbine or at the substation) are not noteworthy in general.

However, when the data at the turbine and at the substation is compared, they are significant differences. The main differences between the power at a single turbine or at the substation consist on the partial cancellation of fluctuations among turbines.

The oscillation cancellation is bigger on reactive power since they have more oscillations of higher frequency which are less related among turbines.

The cancellation is smaller on active power oscillations since its variance is determined mainly by fluctuations under 0,05 Hz. These low fluctuations are considerably correlated and the fact that wind turbine layout is perpendicular to the wind does not help to increase cancellation.

Voltage at the turbine transformer secondary presents higher variability and a noticeable 0,27 Hz oscillation when compared to the voltage at the primary of the farm substation. The rotor electronic converter affects voltage at the turbine, but due to the partial cancellation and the filtering effect of transformers, this effects is highly attenuated at the substation.

B.4.2. Wind turbine at medium winds, 12/3/99, 9:52 to 10:07 and 10:07 to 10:14

The time series analyzed in this subseries corresponds to date 12/3/99. Some starting and stopping test were done, and data considered in this test corresponds to the portion of time the turbine is in continuous operation, after all the switching transients have faded away. After discarding the transients, there are two series since there is a turbine stop and a start in between. The time series #1 last 10:37 minutes (from 9:52:00 to 10:02:37) and the time series #2 lasts 7:25 minutes (from 10:07:10 to 10:14:35).

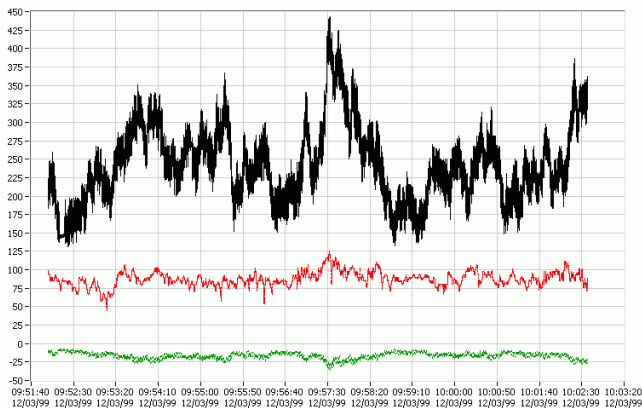


Fig. 236: Operation of a DFIG 648 kW wind turbine for wind speeds around 8,75 m/s during 10:37 minutes (series #1). From top to bottom, time series of the real power P [kW] (in black), wind speed U_{wind} [m/s] at 30 m in the met mast (in red, with a magnification factor x 10 respect the vertical axis) and reactive power Q [kVAr] (in dashed green).

The wind, measured in a meteorological mast at 30 m above the surface with a propeller anemometer, was $U_{wind} = 8,75 \text{ m/s} \pm 1,94 \text{ m/s}$ and $U_{wind} = 8,7 \text{ m/s} \pm 1,48 \text{ m/s}$ in the first and second series (expanded uncertainty).

The main features of the time series from 9:52:00 to 10:02:37 (10:37 minutes of duration) are summarized in the following table and plot (see Table XIX and Fig. 236).

TABLE XIX: PARAMETERS OF THE 648 kW DFIG TURBINE SERIES #1, (DATE 12/3/99, FROM 9:52:00 TO 10:02:37, $F_{BLADE} \approx 1,54 \text{ Hz}$)

	U_{wind} [m/s]	P [kW]	Q [kVAr]
Mean	8,75 m/s	242,2 kW	-16,41 kVAr
Variance	0,97 m/s	51,2 kW	4,22 kVA
Ratio Std. Dev./mean	11,7 %	2,2 %	10,4%
Mean \pm uncertainty	8,75 \pm 1,94 m/s	242,2 \pm 102,4 kW	-16,41 \pm 8,44 kVAr
r^2	$\sim 5/3$	$\sim 1,5$	$\sim 1,1$
$P_1' \approx PSD^+(1)$	0,007 (m/s) ² /Hz	1,2 kW ² /Hz	0,05 kW ² /Hz
f_1	$\lesssim 0,075 \text{ Hz}$	$\lesssim 0,021 \text{ Hz}$	$\lesssim 0,012 \text{ Hz}$
f_2	∞	0,65 Hz	1,40

The second series (from 10:07:10 to 10:14:35, see Table XX and Fig. 237) is quite similar to the first one.

TABLE XX: PARAMETERS OF THE 648 kW DFIG TURBINE, SERIES #2, (DATE 12/3/99, FROM 13:48:30 TO 13:52:00, $F_{BLADE} \approx 1,54 \text{ Hz}$)

	U_{wind} [m/s]	P [kW]	Q [kVAr]
Mean	8,7 m/s	225,3 kW	-15,52 kVAr
Variance	0,74 m/s	52,0 kW	4,57 kVAr
Ratio Std. Dev./mean	49,3 %	2,3 %	16,5%
Mean \pm uncertainty	8,7 \pm 1,48 m/s	225,3 \pm 104 kW	-15,52 \pm 9,14 kVAr
r^2	$\sim 5/3$	$\sim 1,5$	$\sim 1,1$
$P_1' \approx PSD^+(1)$	0,005 (m/s) ² /Hz	0,6 kW ² /Hz	0,05 kW ² /Hz
f_1	$\lesssim 0,082 \text{ Hz}$	$\lesssim 0,014 \text{ Hz}$	$\lesssim 0,009 \text{ Hz}$
f_2	∞	0,54 Hz	1,40 Hz

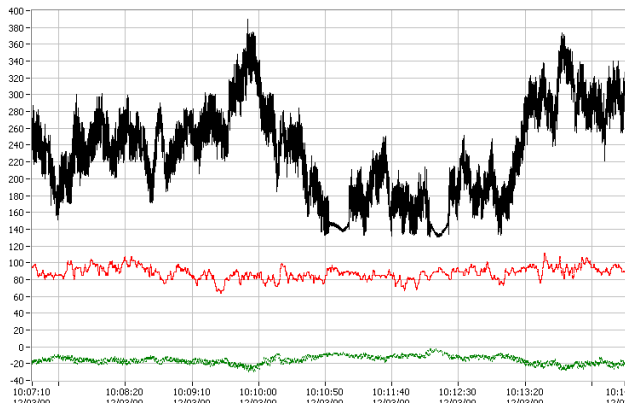


Fig. 237: Operation of a DFIG 648 kW wind turbine for wind speeds around 8,7 m/s during 7:27 minutes (series #2).

B.4.3. Analysis of real power output

In the full graph of the time series, Fig. 236 and Fig. 237, the oscillations due to rotor position cannot be seen clearly.

In Fig. 239, the oscillation pattern is complex since subharmonics $\frac{1}{3}$ and $\frac{1}{2}$ of the blade frequency f_{blade} are present. The presence of subharmonic $\frac{1}{3}$ is very likely bound to misalignments in the blades or in the rotor.

Moreover, Fig. 239 shows some characteristic levels in the turbine power. This suggests that that power is discretized into a number of levels due to the generator control (the generator is controlled through its rotor with a multilevel PWM inverter).



Fig. 238: Detail of real power of a DFIG 648 kW wind turbine for wind speeds around 8,75 m/s during 1 minute in series #1.

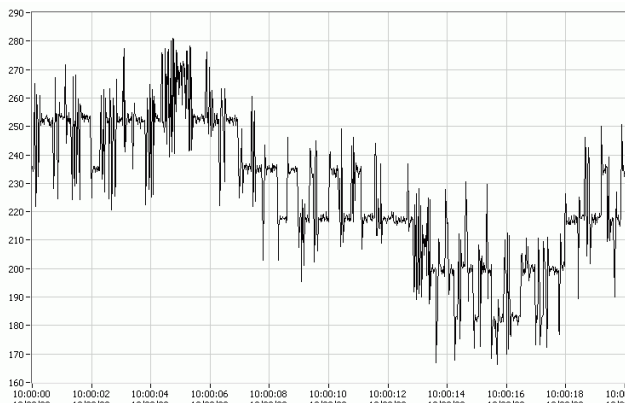


Fig. 239: Detail of real power of a DFIG 648 kW wind turbine for wind speeds around 8,75 m/s during 20 seconds in series #1.

The variability in power is similar to other turbines up to the blade frequency, reaching its minimum at 2,1 Hz. On the contrary, variability at frequencies higher than 3 Hz is high and considerably constant (around 2-6 kW²/Hz), probably due to the discrete control of the power in each grid cycle. In other words, the power level discretization turn out into a sort of high frequency noise in the signal of power.

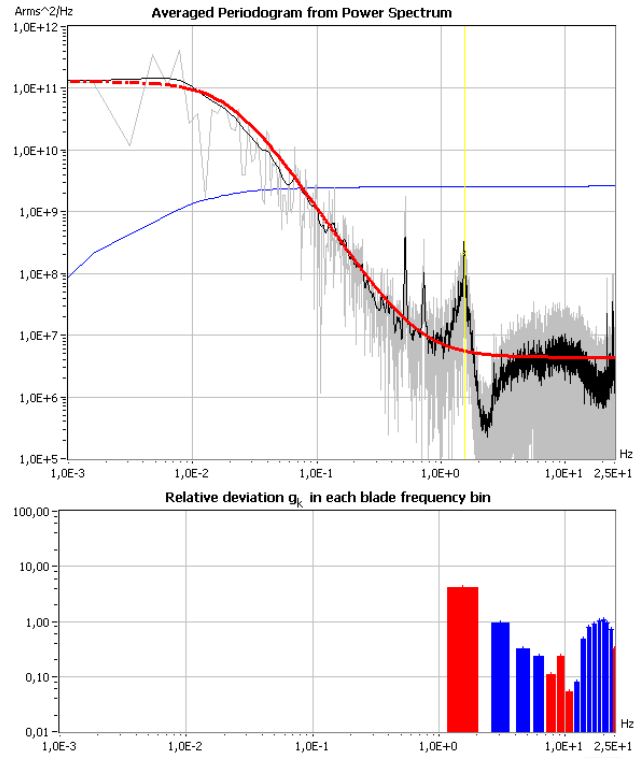


Fig. 240: $PSD_{p^+}(f)$ parameterization of real power of a DFIG 648 kW wind turbine for time series #1.

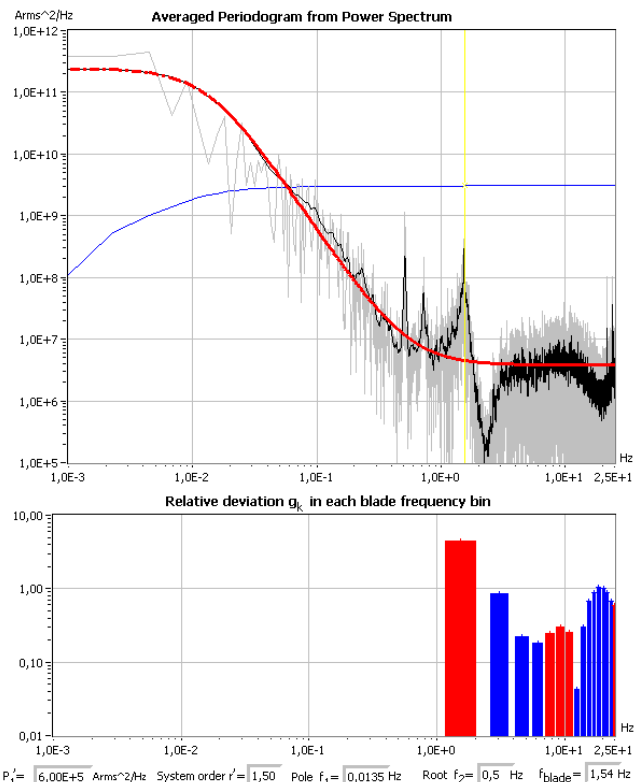


Fig. 241: $PSD_{p^+}(f)$ parameterization of real power of a DFIG 648 kW wind turbine for time series #2.

B.4.4. Analysis of reactive power output

In fact, the scatter plots of reactive vs. real powers (Fig. 242 and Fig. 243) show that the relationship is lineal since the control try to achieve a given power factor. Since unity power factor is desired at the power meter at the wind farm substation, the power factor has been power set to 0,997 capacitive to compensate the reactive consumption of the transformer.

Fig. 242 shows the original one grid cycle values of real and reactive powers. It is quite notorious the discretization of the real power. Moreover, the one-second averaged values shown in Fig. 243 removes the discretization, resulting into a good fit to the linear model ($Q \approx 2,395 - 0,0776 P$).

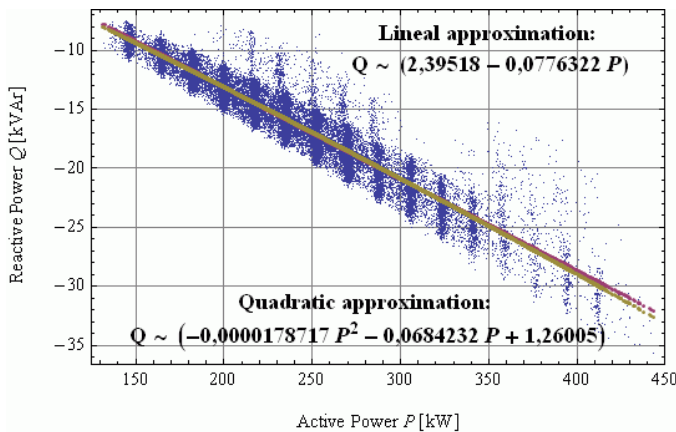


Fig. 242: Reactive vs. real powers of a DFIG 648 kW wind turbine for series #1, based on the original one grid cycle values.

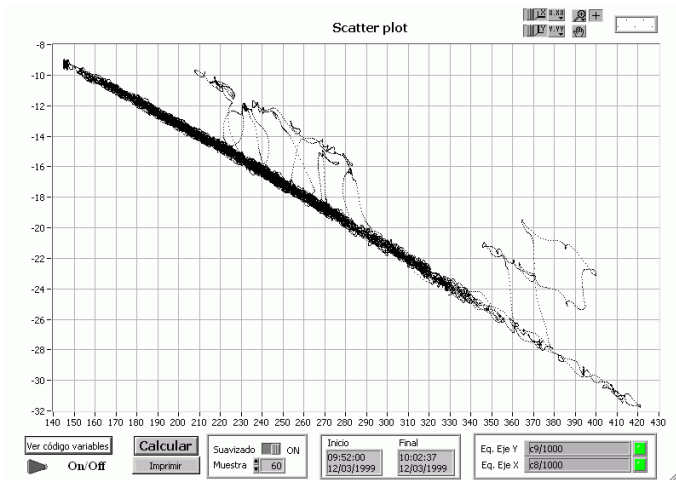


Fig. 243: Previous figure, but based on averaged one-second values instead of the original one grid cycle values.

Due to the almost linear relationship between the real and reactive power, both PSD are expected to be very similar. Real and reactive power shows similar behaviour at low frequencies, but the differences are obvious at frequencies higher than the blade rate (especially between 2 Hz to 5 Hz). Moreover, the system order r^s of real P and reactive Q power are 1,5 and 1,1 respectively (see Table XIX and Table XX).

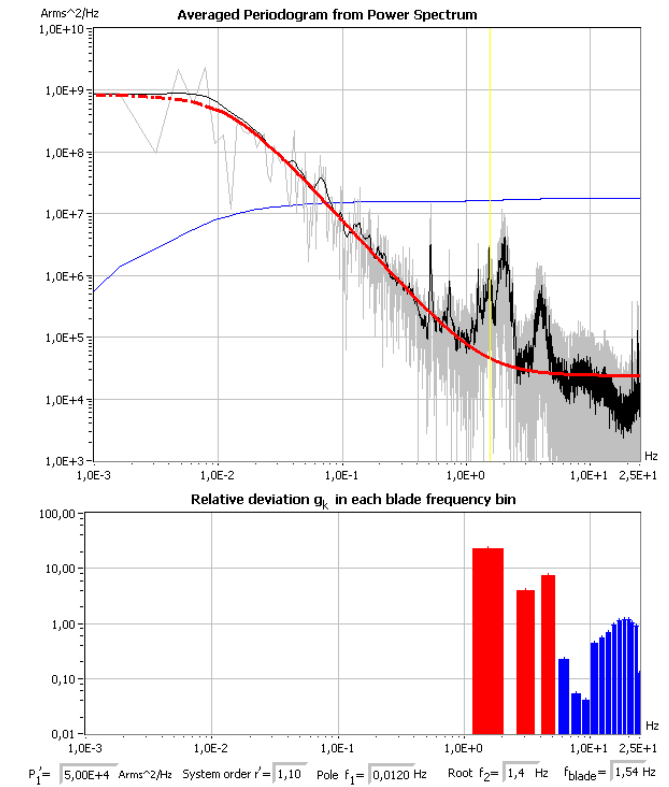


Fig. 244: $PSD_Q^+(f)$ of the reactive power in series #1.

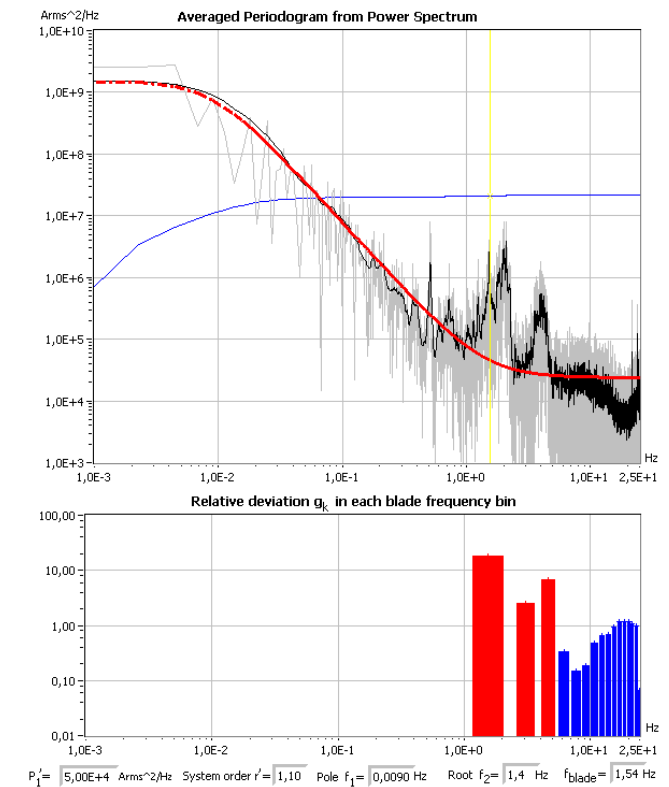


Fig. 245: $PSD_Q^+(f)$ of the reactive power in series #2.

B.4.5. Analysis of wind measured at the meteorological mast 30 m above surface level

The $PSD_{U_{wind}}^+(f)$ estimated in series #1 and #2 are shown in Fig. 246 and Fig. 247, respectively. The propeller anemometer behaves as a low-pass filter of cut-off frequency around $U_{wind} / 1 \text{ m} \sim 0,1 \text{ Hz}$. The recorded wind speed show

an additional drop corresponding to a low-pass 1st order system from 1 Hz. Moreover, some artifices due to the digital treatment of the signal appear beyond 15 Hz.

Up to anemometer cut-off frequency, the slope is smooth and it fits well the model (184) (black and red lines in Fig. 246 and Fig. 247 are quite close from 0,1 to 15 Hz). The system order is $r' \approx 1,67$ (twice the usual Kaimal order, 5/6), possibly due to the increased turbulence at the top of a crest where the wind farm is settled.

The pole is $f_1 \lesssim 0,048\sim 0,056$ Hz, but the transition is significantly slower than the model. The corresponding integral length scale of the turbulence is $\ell_{U_{wind}} \gtrsim \langle U_{wind} \rangle / (6 a f_1) \approx 15\sim 18$ m, assuming $a = 1,7$ according to the draft Eurocode ENV 1991-2-4 and (11). Since the turbulence length scale of this site is significantly smaller than the expected value and the transition at f_1 is slower than the model (184), it is believed that the limited duration of the records influenced the estimated value of f_1 .

The scale parameter is $P_1' \approx PSD_{U_{wind}}(f=1 \text{ Hz}) \approx 0,00485 \text{ (m/s)}^2/\text{Hz}$. The value of the wind variance is $\sigma_{wind} = 0,74\sim 0,97$ m/s, corresponding to a turbulence intensity $I = \sigma_{wind} / \langle U_{wind} \rangle = 8,5\sim 11,1$ % –low since the series corresponds to periods of fairly constant wind.

frequency spectrum is significantly influenced by weather evolution.

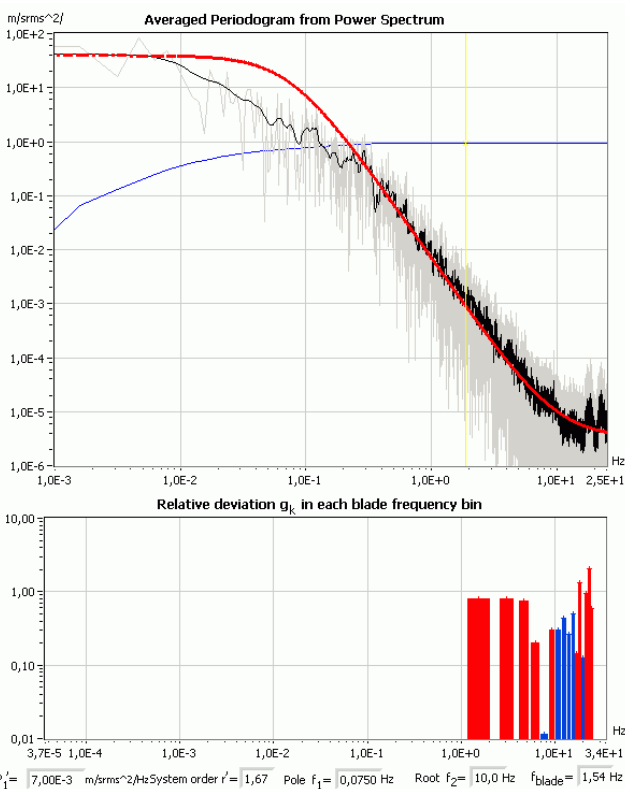


Fig. 246: $PSD_{U_{wind}}(f)$ of the wind corresponding to series #1. Beyond 15 Hz, some artifices appear due to measuring limitations.

Since wind is hardly affected by the stops and starts of the wind turbines, the full record (series #1 and #2 plus the time in between) can be used to decrease the uncertainty of $PSD_{U_{wind}}(f)$ in the low frequency range. Since wind was stable around 8,7 m/s during the records, the wind variances at series #1 and at the full record are approximately the same, despite the record duration has tripled.

The model (184) is not able to represent the mild decrease of the slope in between 0,004 Hz to 0,2 Hz. Moreover, even longer records would be necessary to test the slope trend at frequencies smaller than 0,004 Hz. Recall that the very low

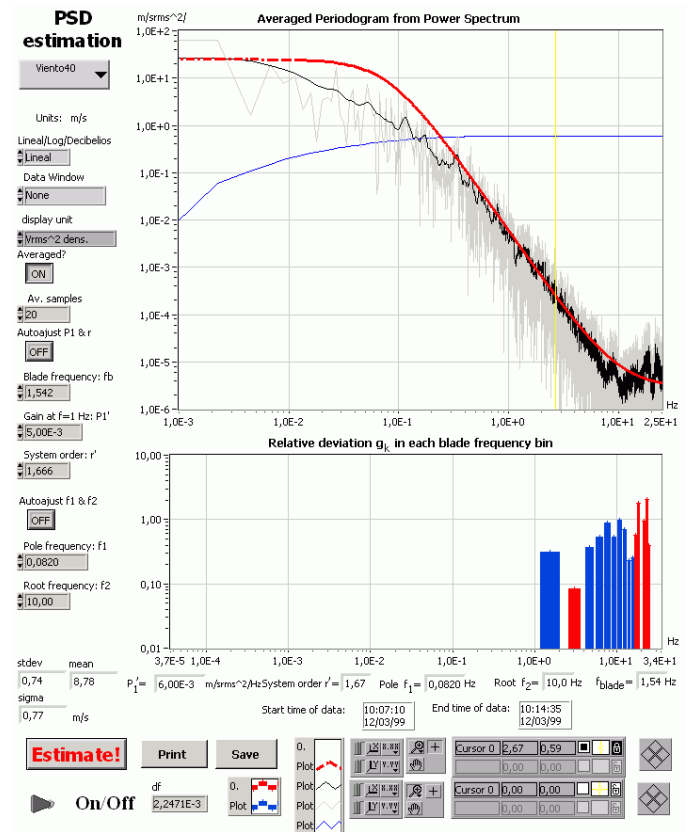


Fig. 247: $PSD_{U_{wind}}(f)$ of the wind corresponding to series #2. Beyond 15 Hz, some artifices appear due to measuring limitations.

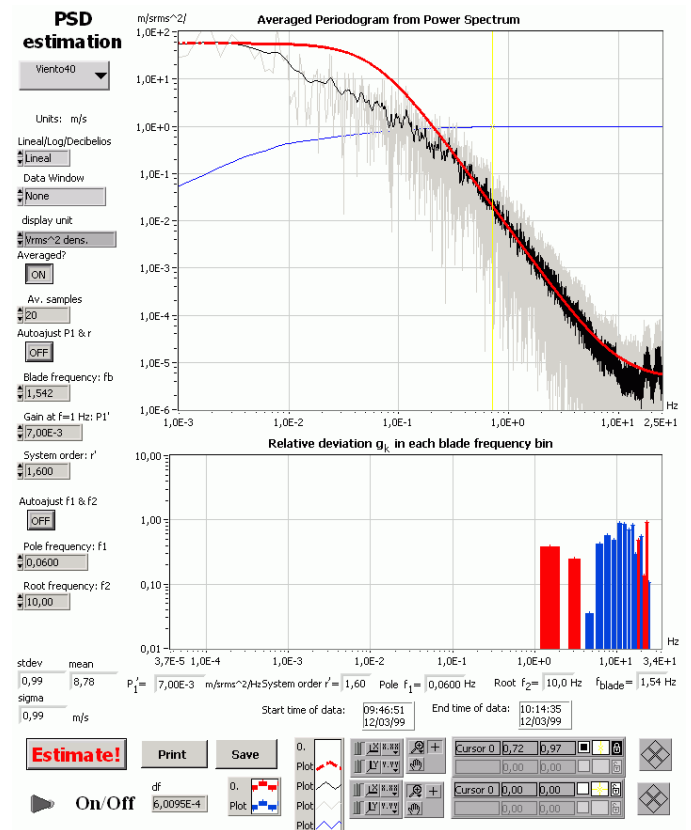


Fig. 248: $PSD_{U_{wind}}(f)$ of the wind corresponding to the full record (28:44 minutes). Notice that spectrum show a slower droop at low frequency due to the longer record.

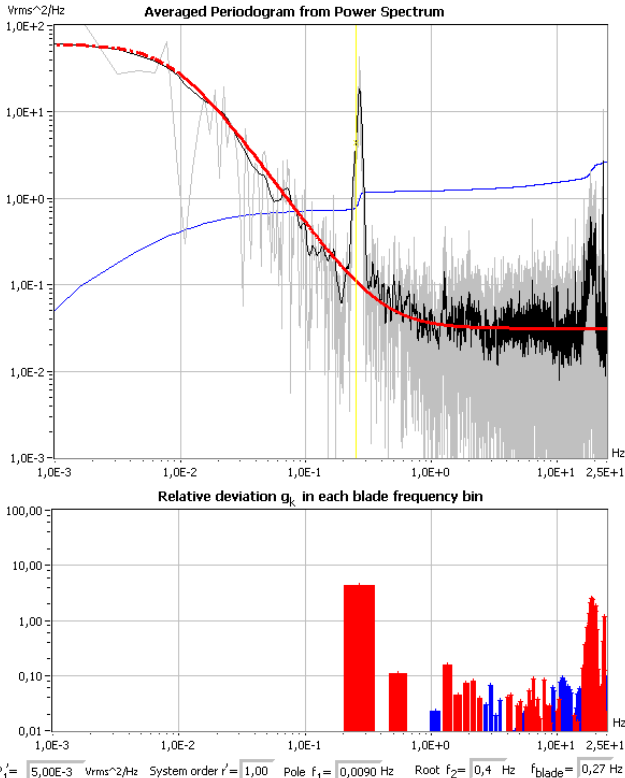


Fig. 249: $PSD_{V_{rs}^+}(f)$ of the low voltage phase R to phase S corresponding to series #1.

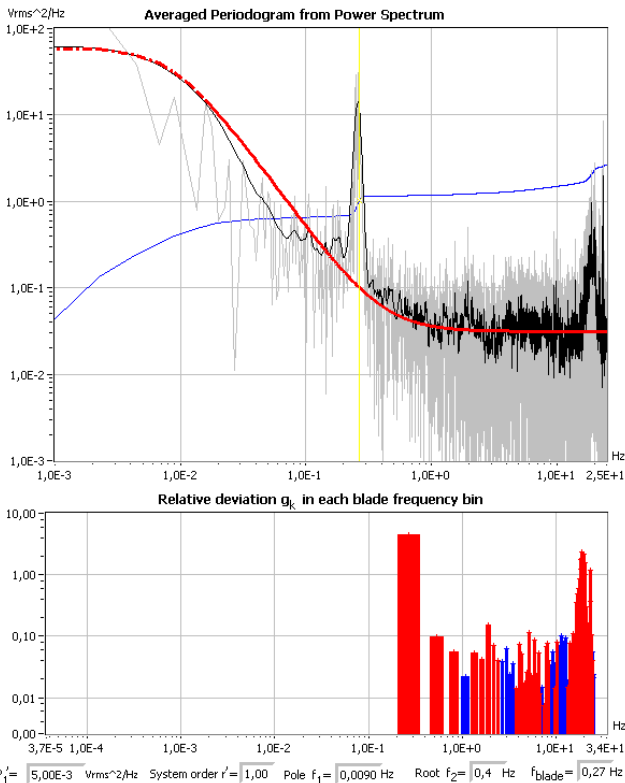


Fig. 250: $PSD_{V_{rs}^+}(f)$ of the low voltage phase R to phase S corresponding to series #2.

B.4.6. Analysis of line voltage

$PSD_{V_{rs}^+}(f)$ of the low voltage phase to phase of series #1 and #2 are shown in Fig. 249 and Fig. 250. The voltage is $704,24 \pm 3,22$ V. The slope of the voltage corresponds to a first order system ($r' \approx 1$) up to 0,2 Hz. The voltage contains significant fluctuations around 0,27 Hz and the slope of the

voltage does not decrease at frequencies higher than 0,1 Hz due to the influence of the electronic converter. The electronic converter is also expected the cause of the voltage fluctuations around 22 Hz.

B.4.7. Bode magnitude plots

Fig. 251 shows the estimated frequency response of the real power respect to the wind. It is the averaged ratio of the spectrum of real power P to the spectrum of wind U_{wind} (measured with a propeller anemometer at the meteorological mast). Notice that the response above 15 Hz should not be considered due to the limitations in the wind measurement.

According to Fig. 251, the static gain (i.e., gain at frequencies smaller than 0,09 Hz) is $k_{\Delta P/\Delta U} \approx 58$ kW/(m/s). Wind fluctuations in the range $0,09 \text{ Hz} < f < 1,1 \text{ Hz}$ are attenuated in the real power respect the static gain ($\Delta P \sim k_{\Delta P/\Delta U} \Delta U_{wind}$).

Near blade frequency, $f \sim f_{blade}$, the ratio of wind to power fluctuation is noticeably bigger than the static gain but this is due to the tower shadow effect, which is not proportional to the fluctuation of the wind in such range. Thus, fluctuation of power at blade frequencies and its $1/3$, $1/2$ and $2/3$ sub-harmonics should be regarded as an additive factor quite insensitive to wind turbulence.

Wind fluctuations at $f > 2$ Hz are intensified in the power output. The origin of these power fluctuations are expected to be not only the turbulence, but also the discrete control of power. Since high frequency fluctuations are greatly influenced by the generator control which, in turn, is influenced by turbine dynamics, it cannot be stated which portion of the high frequency fluctuations are due to the generator control or to the wind turbulence.

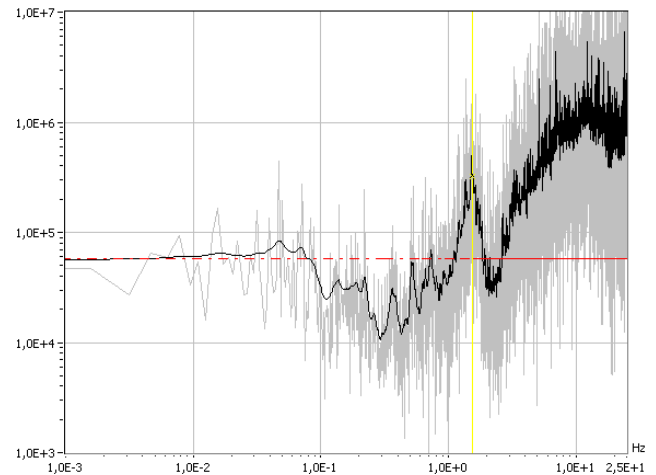


Fig. 251: Bode magnitude plot of real power P [W] respect wind U_{wind} [m/s] for series #1.

Fig. 252 shows the bode plot of the reactive power Q respect to the spectrum of wind at the met mast U_{wind} . The quasi-static approximation $\Delta Q \sim k_{\Delta Q/\Delta U} \Delta U_{wind}$ –with the static gain $k_{\Delta Q/\Delta U} \approx 4,5$ kVAR/(m/s)– is valid at $f < 0,04$ Hz. Wind fluctuations in the range $0,09 \text{ Hz} < f < 1,0 \text{ Hz}$ are slightly attenuated in the reactive power respect the static gain. But at $f > 1,0$ Hz, the reactive power fluctuations present a considerable increase due, in great extent, to the generator control. Thus, the influences of turbulence, generator control and turbine dynamics in power oscillations

are cross-related in Fig. 252 and the frequency response of Q respect to U_{wind} should be considered with caution.

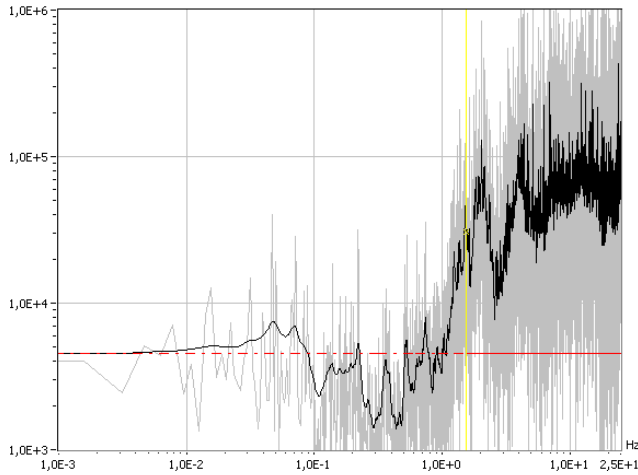


Fig. 252: Bode magnitude plot of reactive power Q [VAr] respect wind U_{wind} [m/s] for series #1 (beyond 1 Hz, the transfer function is underestimated due to limitations in the wind measure).

Fig. 253 shows the bode plot of the reactive power Q respect to the real power P and the reference quasi-static approximation $\Delta Q \sim 0,08\Delta P$.

The influences of real P and reactive Q power on line voltage (V_{RS}) is shown in Fig. 254 and Fig. 255. Since the real and reactive powers are closely related, both plots are cross-related.

The small-signal lineal model for voltage is $\Delta V_{RS} \sim (R_{eff}\Delta P + X_{eff}\Delta Q) / \langle V_{RS} \rangle$, where R_{eff} and X_{eff} are the effective Thévenin resistance and reactance seen from the voltage point of measure. The quasi-static gains (at $f < 0,2$ Hz) are $k_{\Delta V_{RS}/\Delta P} \approx 0,022$ V/kW and $k_{\Delta V_{RS}/\Delta Q} \approx 0,27$ V/kVAr of the real and reactive power, respectively. Thus, a very rough estimation of the effective impedances at $\langle V_{RS} \rangle \approx 704$ V are $R_{eff} \sim k_{\Delta V_{RS}/\Delta P} \langle V_{RS} \rangle \approx 15$ m Ω and $X_{eff} \sim k_{\Delta V_{RS}/\Delta Q} \langle V_{RS} \rangle \approx 190$ m Ω (including the cross-effect of nearby turbines).

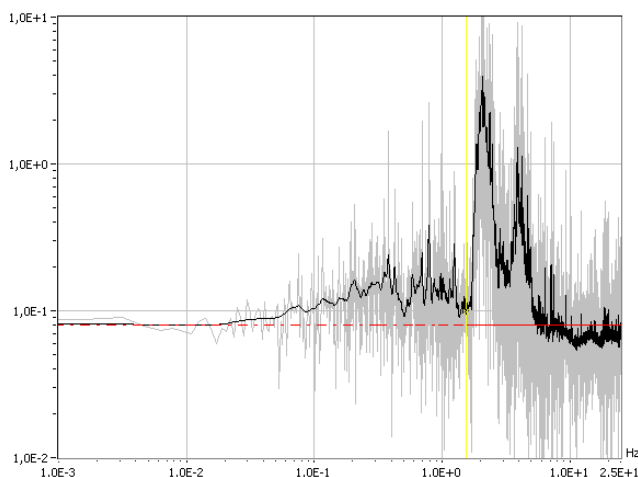


Fig. 253: Bode magnitude plot of reactive power Q [VAr] respect real power P [W] for series #1.

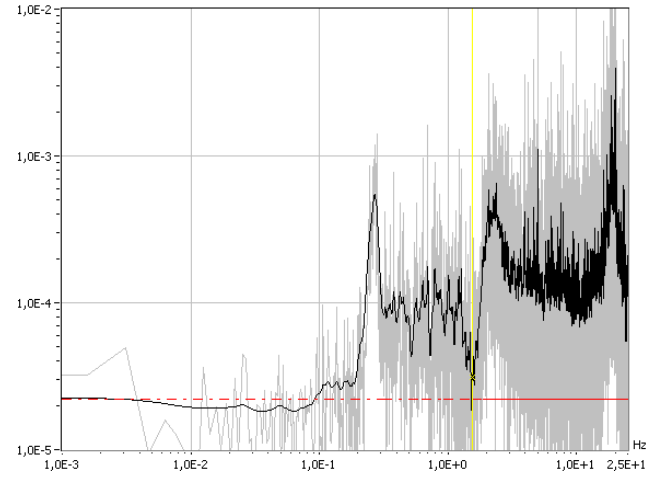


Fig. 254: Bode magnitude plot of line voltage V_{RS} [V] respect real power P [W] for series #1.

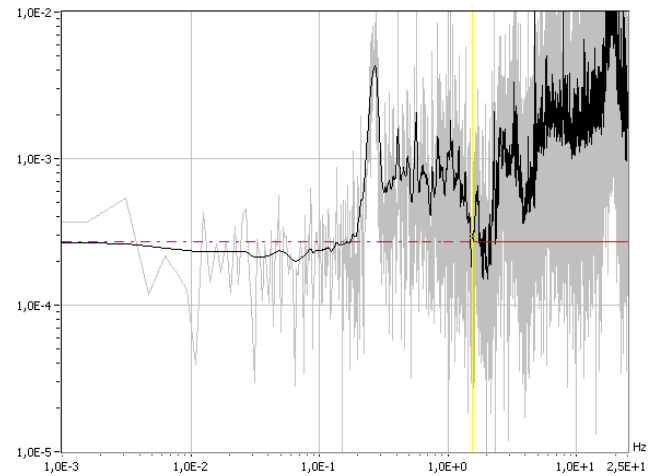


Fig. 255: Bode magnitude plot of line voltage V_{RS} [V] respect reactive power Q [VAr] for series #1.

At $f > 0,2$ Hz, the gain increases considerably. For example, the notably presence of voltage fluctuations at $f \sim 0,27$ Hz cannot be explained from power oscillations.

Since active and reactive oscillation at f_{blade} is bigger, its influence in voltage is supposed to be notably bigger than other external sources. In other words, the gain at $f \sim f_{blade}$ is supposed to have less uncertainty than at other frequencies. Since the gain at f_{blade} and at very low frequencies (quasi-static gain) are similar, the estimates of $k_{\Delta V_{RS}/\Delta P}$ and $k_{\Delta V_{RS}/\Delta Q}$ are supposed to be valid. Since the gain at $f \sim f_{blade}$ is similar to the quasi-static gain, voltage fluctuations at other frequencies can be due to external factors and to the electronic converter, in great extent.

B.5. Wind farm at medium winds, 12/3/99, 9:48 to 10:01 and 10:09 to 10:19

The time series analyzed in this sub-section corresponds to a wind farm composed by 15 x G42 and 3 x G47 turbines from Gamesa in 12/3/99 (simultaneously with the previous analysis of one of its turbines). The nominal output of the wind farm is 15 x 648 kW + 3 x 660 kW = 11,7 MW. Some starting and stopping test were done, and data considered in this test corresponds to the portion of time the turbines are in continuous operation, after all the switching transients have

faded away. After discarding the transients, there are two series since there are a turbine stops and a starts in between. The time series #1 last 12:51 minutes (from 9:48:09 to 10:01:00) and the time series #2 lasts 10:27 minutes (from 10:09:00 to 10:19:27).

The main features of the time series from 9:48:09 to 10:01:00 (12:51 minutes of duration) are summarized in the following table and plot (see Table XXI and Fig. 256).

TABLE XXI: PARAMETERS OF A DFIG WIND FARM, SERIES #1, (DATE 12/3/99, FROM 9:48:09 TO 10:01:00, $F_{BLADE} \approx 1,54$ Hz)

	U_{wind} [m/s]	P [kW]	Q [kVAr]
Mean	8,85 m/s	3432 kW	-47,9 kVAr
Variance	0,95 m/s	224 kW	18,0 kVA
Ratio Std. Dev./mean	10,2 %	0,7 %	-4,7%
Mean \pm uncertainty	8,85 \pm 1,90 m/s	3432 \pm 448 kW	-47,9 \pm 36 kVAr
r^2	$\sim 1,6$	$\sim 1,5$	$\sim 1,0$
$P_1' \approx PSD^+(1)$	0,007 (m/s) ² /Hz	10 kW ² /Hz	1 kW ² /Hz
f_1	$\lesssim 0,075$ Hz	$\lesssim 0,0125$ Hz	$\lesssim 0,0048$ Hz
f_2	∞	0,55 Hz	10

The second series (from 10:09:00 to 10:19:27, see Table XXII and Fig. 257) is quite similar to the first one.

TABLE XXII: PARAMETERS OF A DFIG WIND FARM, SERIES #2, (DATE 12/3/99, FROM 10:09:00 TO 10:19:27, $F_{BLADE} \approx 1,54$ Hz)

	U_{wind} [m/s]	P [kW]	Q [kVAr]
Mean	8,65 m/s	2935 kW	-24,3 kVAr
Variance	0,79 m/s	273 kW	12,4 kVAr
Ratio Std. Dev./mean	10,8 %	0,9 %	-7,6%
Mean \pm uncertainty	8,65 \pm 1,68 m/s	2935 \pm 446 kW	-24,3 \pm 24,8 kVAr
r^2	$\sim 1,6$	$\sim 1,3$	$\sim 1,0$
$P_1' \approx PSD^+(1)$	0,007 (m/s) ² /Hz	50 kW ² /Hz	1 kW ² /Hz
f_1	$\lesssim 0,082$ Hz	$\lesssim 0,0125$ Hz	$\lesssim 0,0125$ Hz
f_2	∞	1,1 Hz	20 Hz

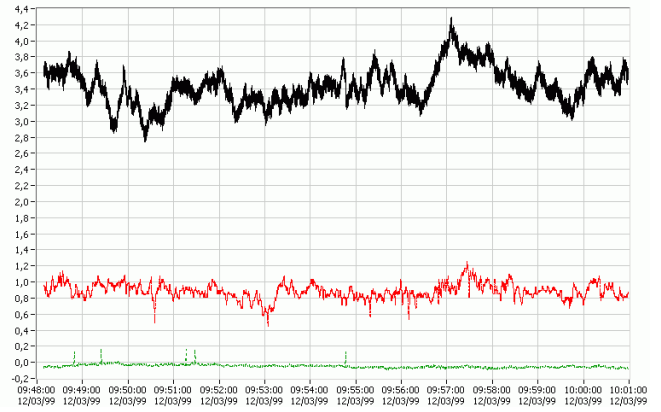


Fig. 256: Operation of a DFIG wind farm for wind speeds around 8,75 m/s during 12:51 minutes (series #1). From top to bottom, time series of the real power P [MW] (in black), wind speed U_{wind} [m/s] at 30 m in the met mast (in red, with a attenuation factor $\times 0,1$ respect the vertical axis) and reactive power Q [MVar] (in dashed green).



Fig. 257: Operation of a DFIG wind farm for wind speeds around 8,7 m/s during 10:27 minutes (series #2). From top to bottom, time series of the real power P [MW] (in black), wind speed U_{wind} [m/s] at 30 m in the met mast (in red, with a attenuation factor $\times 0,1$ respect the vertical axis) and reactive power Q [MVar] (in dashed green).

B.5.1. Analysis of real power output

In the full graph of the time series, Fig. 258 and Fig. 259, the oscillations due to rotor position cannot be seen clearly. In Fig. 259, three oscillations each two seconds can be spotted in the turbine power output.

The oscillation pattern is complex since subharmonics $1/3$ and $1/2$ of the blade frequency f_{blade} are present. The presence of subharmonic $1/3$ is very likely bound to misalignments in the blades or in the rotor.

The typical magnitude of spikes in power has increased from 30 kW to 90 kW in the turbine and in the farm output, respectively (compare Fig. 239 and Fig. 259). These spikes are 4,63 % and 0,85 % of the assigned power, in the turbine and wind farm, respectively. More than three net spikes in the wind farm simultaneously are low probable. The power of a single V42 DFIG turbine can be characterized basically by three levels –normal, positive spike and negative spike– and thus, the statistical distribution of their sum is multinomial.

Thus, the characteristic levels of the turbine power are masked in the total wind farm output by its overall trend and the amplitude of the spikes decrease in relative terms at the total farm output.

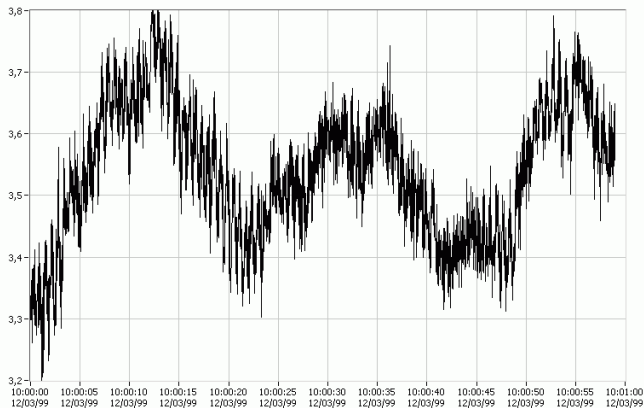


Fig. 258: Detail of real power (in MW) of a DFIG wind farm during 1 minute in series #1.

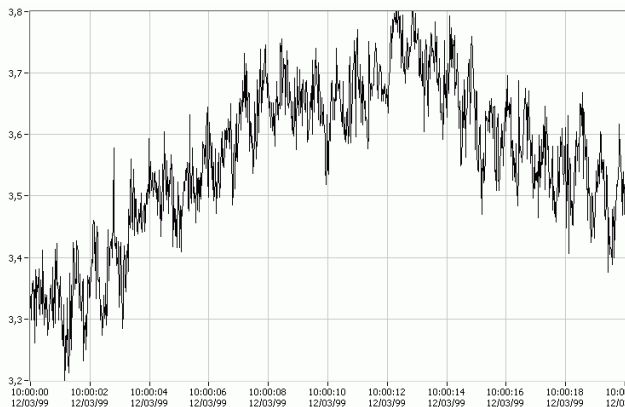


Fig. 259: Detail of real power (in MW) of a DFIG wind farm during 20 seconds in series #2.

fluctuations are due to wind evolution and they affect in a more evenly way to all the turbines in the wind farm.

The standard deviation of the wind farm real power is between 4 to 5 times the one of the single turbine (compare Table XIX and Table XX to Table XXI and Table XXII). The square root of the number of turbines in the farm is $\sqrt{18} \approx 4,24$, suggesting that the \sqrt{N} law for the standard deviation of the sum of uncorrelated random variables could be applied in the real power for time spans up to a few minutes.

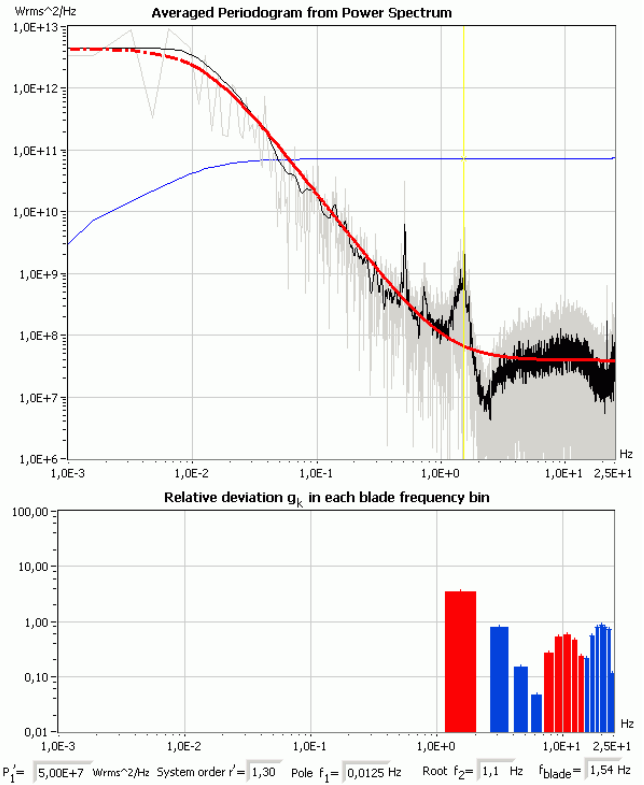


Fig. 261: $PSD_{P^+}(f)$ parameterization of the real power of the DFIG wind farm during time series #2.

B.5.2. Analysis of reactive power output

Fig. 243 showed a good fit of a linear model between real and reactive power for a single turbine. However, Fig. 262 shows a much worse fit between reactive power and real power at the wind farm output. This is probably be due to the influence of voltage on reactive power.

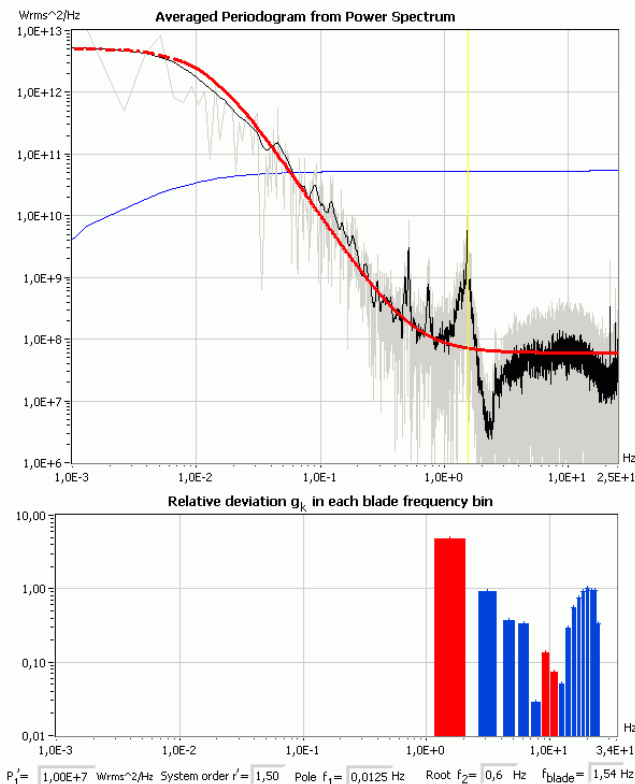


Fig. 260: $PSD_{P^+}(f)$ parameterization of the real power of the DFIG wind farm during time series #1.

As more turbines are aggregated, high frequency oscillations are damped in relative terms whereas slower

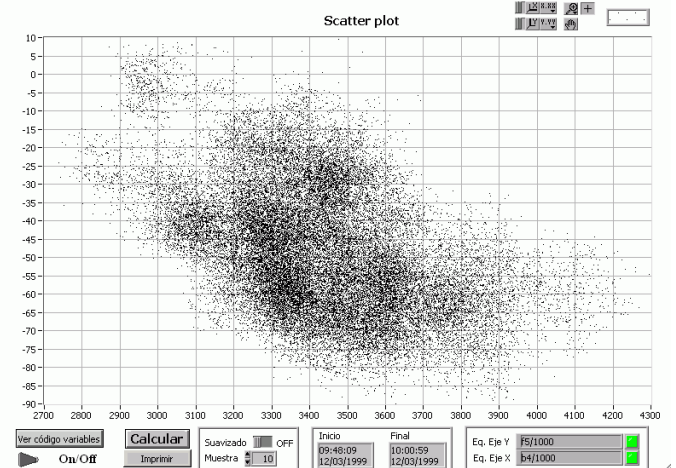


Fig. 262: Reactive vs. real powers of the DFIG wind farm during time series #1, based o the original one grid cycle values.

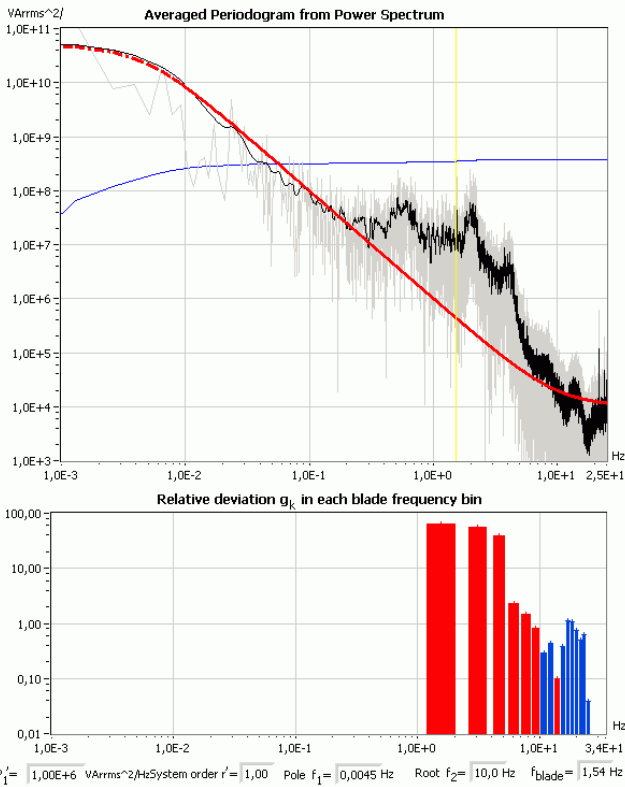


Fig. 263: $PSD_{Q^+}(f)$ of the reactive power in series #1.

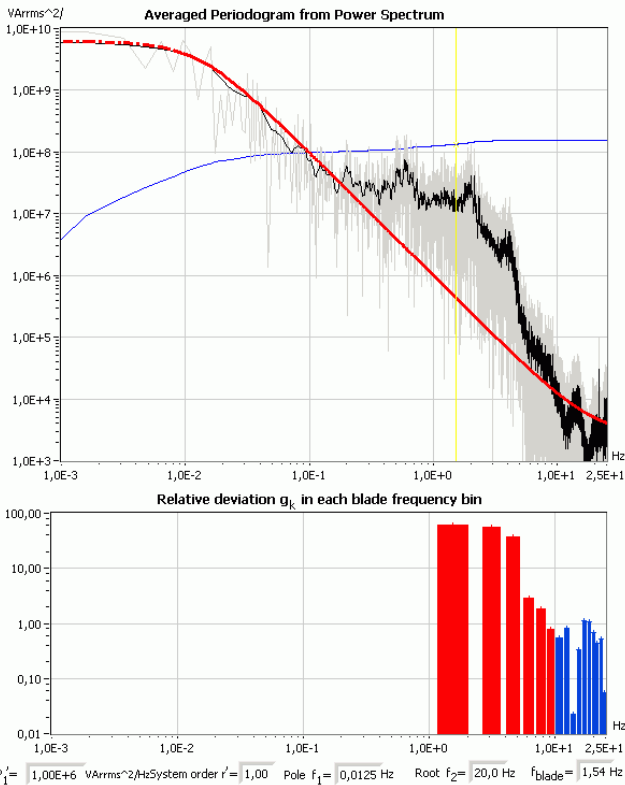


Fig. 264: $PSD_{Q^+}(f)$ of the reactive power in series #2.

The PSD of reactive power at the turbine and at the farm substation were expected to be very similar, but the differences came about remarkably. The noise floor is remarkably lower in the wind farm, partly due to the cancelation of fast fluctuation and partly due to the less noisy voltage measure (the voltage measure at the secondary of the turbine is greatly influenced by its electronic converter). This results in f_2 being around 10 times bigger at the substation than at the turbine. Other difference is that the peaks of the

single turbine appear less marked at the wind farm, especially from 0,4 Hz to 5 Hz.

The standard deviation of the wind farm reactive power is between 3 to 4 times the one of the single turbine, suggesting that the \sqrt{N} law could be also applied in the reactive power for time spans up to a few minutes.

B.5.3. Analysis of wind measured at the meteorological mast 30 m above surface level

The wind in both substation and turbine records is measured at the meteorological tower. Thus, its characteristics have been already estimated in Fig. 246 to Fig. 248.

B.5.4. Analysis of phase-to-phase voltage

$PSD_{Vrs^+}(f)$ of the low voltage phase to phase of series #1 and #2 are shown in Fig. 265 and Fig. 266. The voltage is $48,3 \pm 0,1$ kV. The slope of the voltage corresponds to a system of fractional order $r' \approx 0,7$ in the range from 1 mHz up to 8 Hz. Neither the 0,27 Hz and 22 Hz components nor the noise floor at $f > 0,4$ Hz, previously seen at the low-voltage side of the turbine, are present at the substation voltage. These phenomena are thought to be closely related to the turbine electronic converter and they are effectively filtered at the substation. Moreover, since farm power is at least 20 times smaller than the short circuit power at the substation, the substation voltage is influenced by the surrounding network more than the wind farm itself.

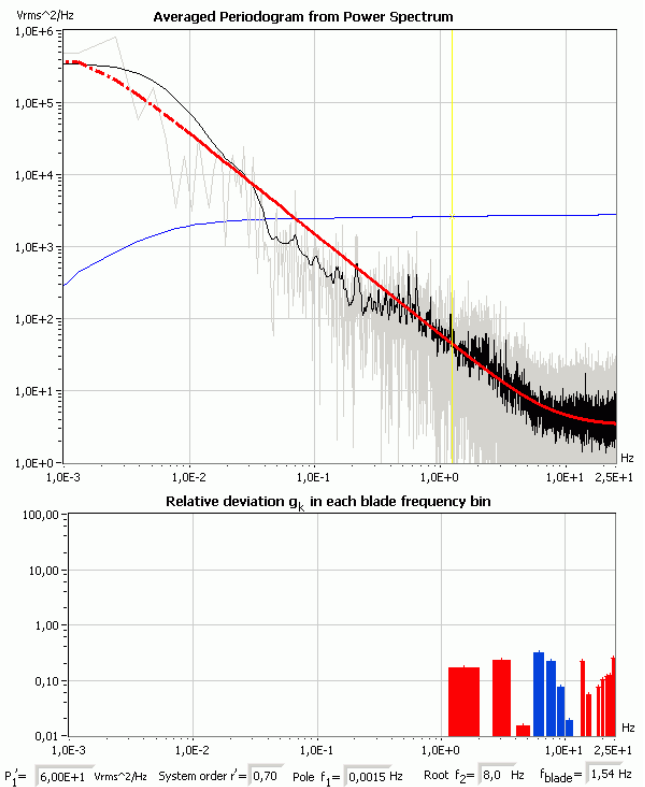


Fig. 265: $PSD_{Vrs^+}(f)$ of the phase R to phase S substation voltage corresponding to series #1.

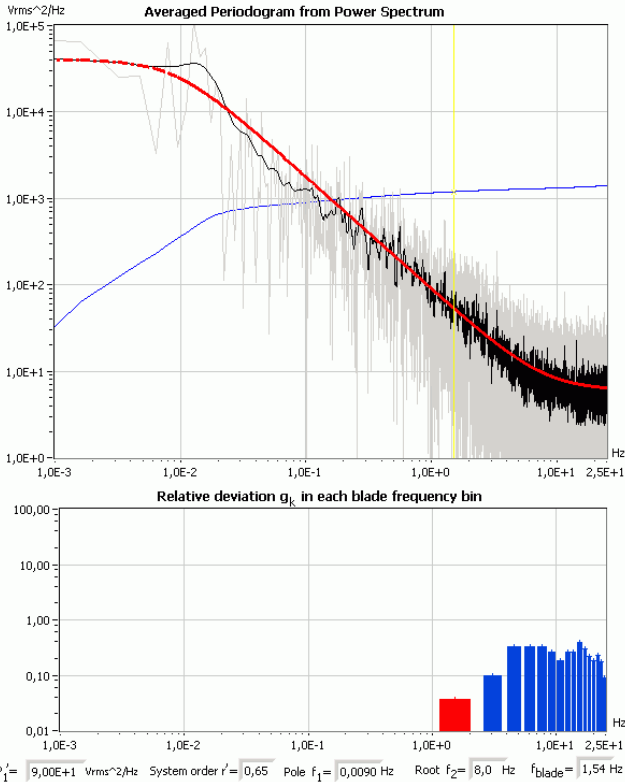


Fig. 266: $PSD_{Vrs}^+(f)$ of the phase R to phase S substation voltage corresponding to series #2.

B.5.5. Bode magnitude plots

The observations made to cyclic oscillations due to wind shear and tower shadow in the turbine are typically valid also for the wind farm. Even though fluctuations are bigger in absolute value at the farm substation; fluctuations tend to be smaller in relative terms since some degree of cancellation happens among turbines.

Fig. 267 shows the estimated frequency response of the real power respect to the wind. It is the averaged ratio of the spectrum of real power P to the spectrum of wind U_{wind} (measured with a propeller anemometer at the meteorological mast at 30 m above the surface level). Notice that the response above 15 Hz should not be considered due to the limitations in the wind measurement.

According to Fig. 267, the static gain (i.e., gain at frequencies smaller than 0,02 Hz) is $k_{\Delta P/\Delta U} \approx 0,32 \text{ MW}/(\text{m/s})$. Wind fluctuations in the range $0,03 \text{ Hz} < f < 1,1 \text{ Hz}$ and $2 \text{ Hz} < f < 3 \text{ Hz}$ are attenuated in the real power respect the static gain ($\Delta P \lesssim k_{\Delta P/\Delta U} \Delta U_{wind}$). The ratio of static gain at the substation respect the substation is slightly bigger than the square root of the number of wind turbines in the farm:

$$\frac{k_{\Delta P/\Delta U, Farm}}{k_{\Delta P/\Delta U, Turbine}} \approx \frac{320 \text{ kW}/(\text{m/s})}{58 \text{ kW}/(\text{m/s})} \approx 5,51 \lesssim \sqrt{18} = 4,24 \quad (660)$$

In the time span of up to some minutes, the fluctuations of power in the turbines of a farm are not coherent. The turbines experience power oscillations with some time lag and with some local variations. Thus, the individual oscillations are partially cancelled in the total for short horizons. The outcome is not very different from considering the power fluctuations independent among turbines for medium size wind farms during time spans shorter than a few minutes (this

appreciation is based on a 11,7 MW wind farm with 18 turbines aligned along a cliff top).

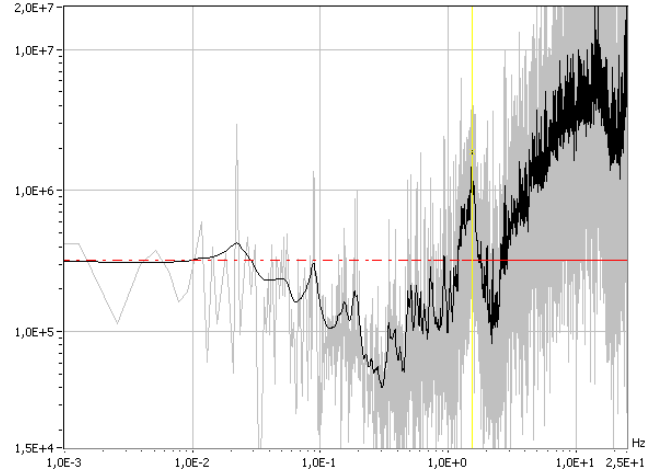


Fig. 267: Bode magnitude plot of real power P [W] respect wind U_{wind} [m/s] for series #1.

Fig. 268 shows the bode plot of the reactive power Q respect to the spectrum of wind at the met mast U_{wind} . The quasi-static approximation $\Delta Q \sim k_{\Delta Q/\Delta U} \Delta U_{wind}$ —with the static gain $k_{\Delta Q/\Delta U} \approx 21 \text{ kVAR}/(\text{m/s})$ —is roughly valid for $f < 0,5 \text{ Hz}$. Wind fluctuations in the range $0,003 \text{ Hz} < f < 0,3 \text{ Hz}$ are slightly attenuated in the reactive power respect the static gain. But at $f > 0,5 \text{ Hz}$, the reactive power fluctuations present a considerable increase due, in great extent, to the generator control. Thus, the influences of turbulence, generator control and turbine dynamics in power oscillations are cross-related and the frequency response of Q respect to U_{wind} should be considered with caution.

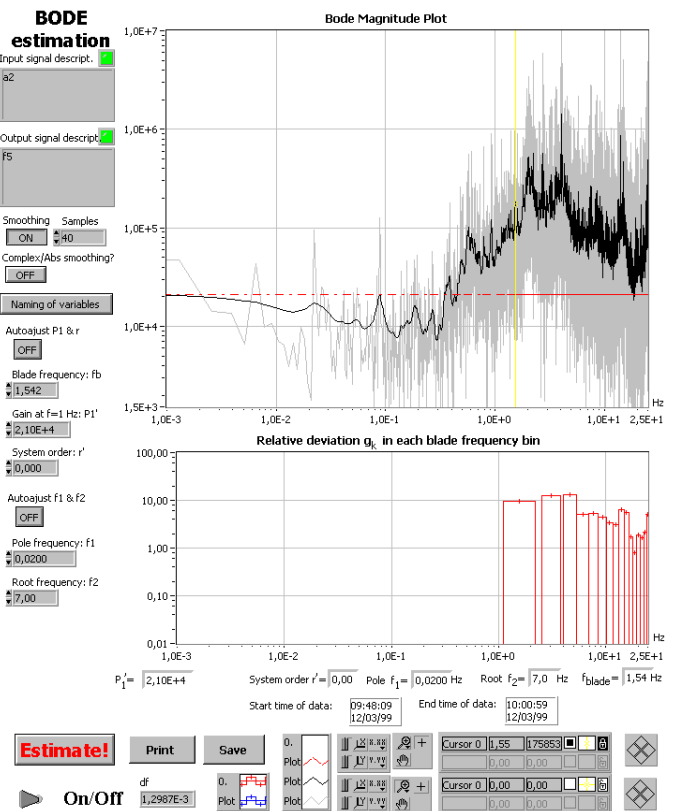


Fig. 268: Bode magnitude plot of reactive power Q [VAR] respect wind U_{wind} [m/s] for series #1 (beyond 15 Hz, the transfer function is underestimated due to limitations in the wind measure).

Fig. 269 shows the bode plot of the reactive power Q respect to the real power P and the quasi-static approximation $\Delta Q \sim k_{\Delta Q/\Delta P} \Delta P$ with $k_{\Delta Q/\Delta P} \approx 0,075$ for reference. The reactive power surpasses the quasi-static approximation in the range $0,2 \text{ Hz} < f < 5 \text{ Hz}$ and the reactive power is bellow the quasi-static approximation at high frequencies ($f > 5 \text{ Hz}$). If Fig. 269 is compared to Fig. 253, the gain at $0,2 \text{ Hz} < f < f_{blade}/2$ has increased at the substation and the gain has decreased at $f > 5 \text{ Hz}$.

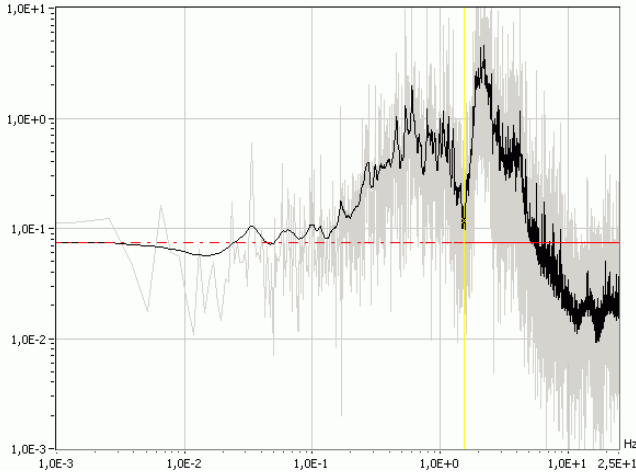


Fig. 269: Bode magnitude plot of reactive power Q [VAr] respect real power P [W] for series #1.

The influences of real P and reactive Q power on line voltage (V_{RS}) are shown in Fig. 270 and Fig. 271. Since the real and reactive powers are closely related, both plots are cross-related.

The small-signal lineal model for voltage is $\Delta V_{RS} \sim (R_{eff}\Delta P + X_{eff} \Delta Q) / \langle V_{RS} \rangle \sim (R_{eff} k_{\Delta P/\Delta U} + X_{eff} k_{\Delta Q/\Delta U}) \Delta U_{wind} / \langle V_{RS} \rangle$, where R_{eff} and X_{eff} are the effective Thévenin resistance and reactance seen from the voltage point of measure. The quasi-static gains (at $f < 0,2 \text{ Hz}$) are $k_{\Delta V_{RS}/\Delta P} \approx 0,3 \text{ kV/MW}$ and $k_{\Delta V_{RS}/\Delta Q} \approx 0,48 \text{ kV/MVAr}$ of the real and reactive power, respectively. Thus, a very rough estimation of the effective impedances at $\langle V_{RS} \rangle \approx 48305 \pm 103 \text{ V}$ are $R_{eff} \sim k_{\Delta V_{RS}/\Delta P} \cdot \langle V_{RS} \rangle \approx 14,5 \Omega$ and $X_{eff} \sim k_{\Delta V_{RS}/\Delta Q} \cdot \langle V_{RS} \rangle \approx 23 \Omega$ (including the cross-effect of nearby turbines).

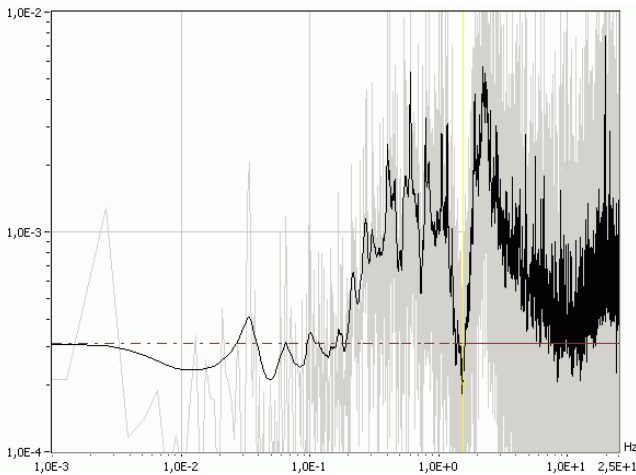


Fig. 270: Bode magnitude plot of line voltage V_{RS} [V] respect real power P [W] for series #1.

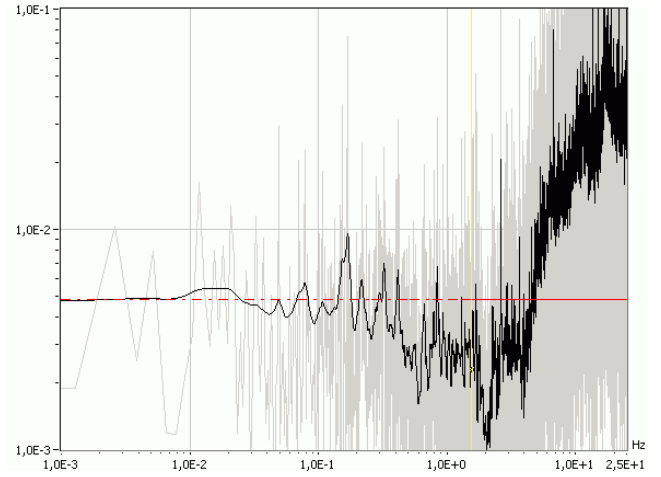


Fig. 271: Bode magnitude plot of line voltage V_{RS} [V] respect reactive power Q [VAr] for series #1.

Since active and reactive oscillation at f_{blade} is bigger, its influence in voltage is supposed to be notably bigger than other external sources. In other words, the gain at $f \sim f_{blade}$ is supposed to have less uncertainty than at other frequencies. Since the gain at f_{blade} and at very low frequencies (quasi-static gain) are similar, the estimates of $k_{\Delta V_{RS}/\Delta P}$ and $k_{\Delta V_{RS}/\Delta Q}$ are supposed to be valid.

B.6. Comparison of PSD of a wind farm with respect to one of its turbines, 12/3/99, 9:48 to 10:01 and 10:09 to 10:19

B.6.1. Real power

The similarity of the PSD at one turbine and at the overall output of the wind farm of 18 turbines has been tested. If the fluctuations at every turbine are independent (i.e. the turbines behaves independently one from another), then the PSD of the wind farm is the sum of the PSD of each turbine –see (168).

Each turbine experiment different turbulence levels and wind averages, so a representative turbine should be selected. The position of the turbine inside the farm affects also at the time lag the wind experience fluctuations respect the wind farm overall. Since wind fluctuations are usually considered independent from time (for example, they don't have characteristic shapes) and weather evolution is not considered in this study, the phase information has been discarded (the phase of an ergodic stochastic processes don't contain statistical information).

If the turbines behaves independently one from another and they are similar, then the PSD of the wind farm is the PSD of one turbine times the number of turbines in the farm. To test this hypothesis, the PSD of the single turbine are factored by the number of the turbines in the wind farm (18) and represented with PSD of the wind farm. In Fig. 272, the farm PSD is in solid black and the turbine PSD times 18 is in dashed green.

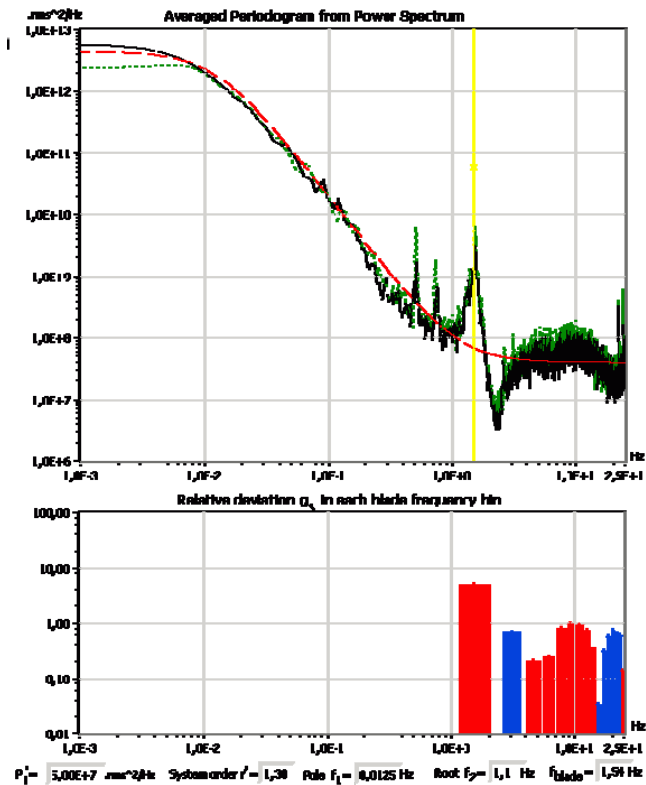


Fig. 272: $PSD_{p^+}(f)$ of a wind farm (in solid black) and $PSD_{p^+}(f)$ of one of its DFIG 648 kW turbines times 18 (in dashed green), for time series #1. Both the farm $PSD_{p^+}(f)$ and the scaled turbine $PSD_{p^+}(f)$ agree notably.

Fig. 272 shows that Eq. (167) is fairly valid. However, the wind farm PSD is a bit lower than 18 times the turbine PSD , specially at the peaks and at $f > 2f_{blade}$. On the one hand, this turbine experiences more cyclic oscillations, partly due to a misalignment of the rotor worse than the farm average. On the other hand, this turbine produced an average of the $1/14^{th}$ of the wind farm power on the series #1 (see Fig. 273). This explain that PSD at $f > 2f_{blade}$ is primarily proportional to power output ratio (the farm PSD is 14 times the turbine PSD).

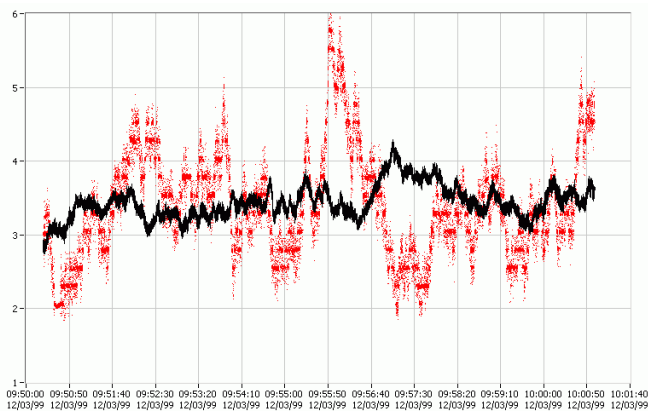


Fig. 273: Power output of the wind farm (in solid black) and the power of the turbine times 14.

The real power admittance is shown in Fig. 274. The admittance is the ratio of the farm spectrum to the turbine spectrum of real power and it can be estimated as the square root of the PSD ratios. The level $\sqrt{18}$ has been added in dash-dotted red line to validate easier the Eq. (168).

In general terms, Eq. (168) is valid: the admittance is approximately $\sqrt{18}$, the square root of the number of turbines

in the farm. At $f > 2f_{blade}$, the admittance is more similar to $\sqrt{14}$ (the square root of the farm power divided by the turbine power). At $f < 0,02$ Hz, the admittance starts drifting from $\sqrt{18}$, indicating that oscillations at very low frequency are somewhat correlated. The peak at $2 \text{ Hz} < f < 2,5 \text{ Hz}$ indicates that the analyzed turbine has comparative less fluctuations in such range than the other turbines in the farm.

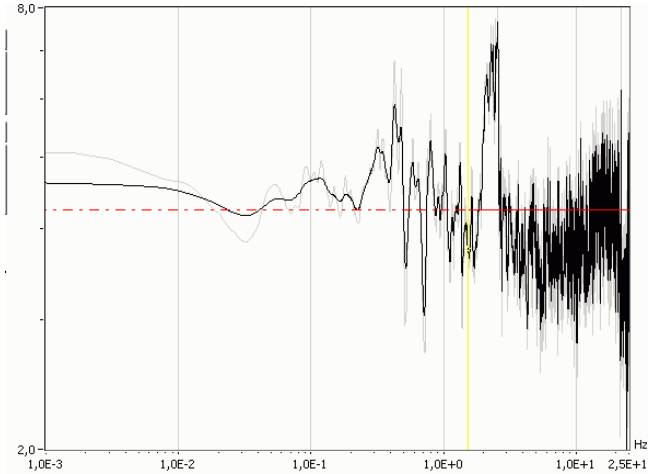


Fig. 274: Admittance of the real power (ratio of the farm PSD to the turbine PSD).

In short, the real power oscillations quicker than one minute can be considered independent among turbines of a wind farm. The PSD due to rotational effects scale proportionally to the number of the turbines. The PSD at $f > 2f_{blade}$ scale proportionally to the turbine power output ratio.

B.6.2. Reactive power

The average admittance of the reactive power is $\sqrt{9} = 3$, smaller than the value of active power, $\sqrt{18}$. This indicates that there may be a negative correlation among reactive power fluctuations of the turbines. This extent cannot be confirmed and it could be due to some interaction with voltage and network reactive losses (the manufacturer did not inform of any special farm control to compensate fluctuations in some turbines with the others).

In fact, the accurate measurement of reactive power at the turbine is complex: voltage and current waveforms are polluted with harmonics and other distortions, and voltage at rotor is not measured directly (it is estimated from stator voltage). This can explain why the admittance at $f > 5\text{Hz}$ drops notably (probably, the reactive power at the wind turbine is overestimated and the impedances damps harmonics and fluctuations of frequencies near the grid frequency).

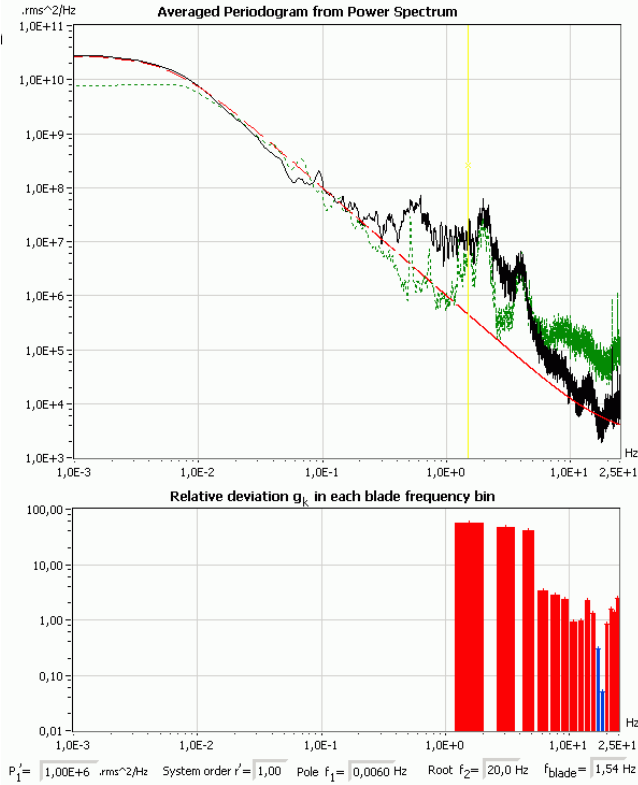


Fig. 275: $PSD_{Q^+}(f)$ of a wind farm (in solid black) and $PSD_{Q^+}(f)$ of one of its DFIG 648 kW turbines times 9 (in dashed green), for time series #1. Eventhough both the farm $PSD_{Q^+}(f)$ and the scaled turbine $PSD_{Q^+}(f)$ agree in general terms for reactive power, the fit is significantly worse than for real power.

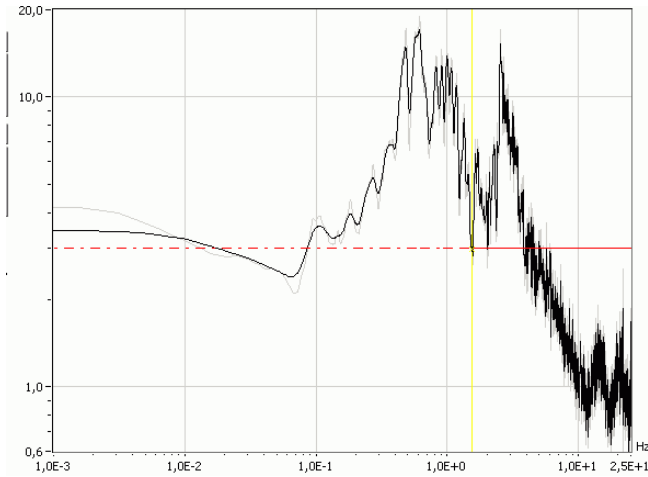


Fig. 276: Admittance of the reactive power (ratio of the farm PSD to the turbine PSD). Notice that reactive power admittance deviates from the average more than the real power in Fig. 274.

B.7. Spectrogram

This subsection is focused on the oscillations between 0.1 and 25 Hz, which are the most influential in the flicker level. This range covers the fluctuations due to the blade passing the tower and its frequency multiples, the fast wind gusts and possible resonances in the machine (with mechanical or aerodynamical origin).

The upper frequency limit is set because the RMS power values for every grid cycle or semi cycle are taken as input data, and the sample rate is therefore 50 or 100 Hz, respectively. In order to carry out a study of the high

frequency fluctuations, instantaneous power should be taken as an input data. Fluctuations of higher frequency than the grid generate grid harmonics and inter-harmonics. The impact in the grid of the harmonics ($f > f_{grid}$) and the sub-harmonics ($f < f_{grid}$) is very different. The main disadvantage of using the instantaneous power instead of one or $\frac{1}{2}$ grid cycle is that the CPU time and the memory requirements increase notably.

The standard IEC 61400-21 establishes a procedure to calculate the flicker produced by a wind turbine in power grid, from real data, during continuous and switching operation.

During switching operations (the connection and disconnection of the generator or capacitors), the system experiments transients similar to the response to a step input. These transients are non-stationary signals with eventual spread frequency components which gradually vanish after the transient.

The PSD in the FOT probabilistic framework is the long term average of power spectrum and it characterizes the behaviour of stochastically stationary systems.

In contrast, the spectrogram allows to study the spectrum evolution to test the stationarity of signals. Every spectrogram column can be thought as the power spectrum of a small signal sample. Therefore, the PSD in the classical stochastic framework is the ensemble average of the power spectrums. For stationary systems, both approaches are equivalent.

The analysis of the evolution of fluctuations between 0.1 and 25 Hz has been performed using the spectrogram of the real and reactive power variables.

Apart from the Short FFT (SFFT), other methods with higher frequency resolution have been tested for the calculation of the spectrogram, as the Wigner-Ville distribution (WVD) and the S-method (SM) [388]. Since the analyzed signals present wide frequency content, the SFFT method is the most reliable and the amplitudes of the fluctuations are less affected by cross-terms.

The WVD is the best way to observe the frequency of fast fluctuations, as the frequency resolution is higher. The main drawback of this method in this application is that the fluctuations are severely overestimated (i.e. for a fixed frequency, the measured fluctuation is higher than the real one due to cross frequency replicas). Therefore, the WVD values are only comparable with those of other different frequencies. Due to lack of memory, the original signal has been divided in 8192 samples with a 75% overlapping, in order to apply the WVD and then discarding the overlapping edges.

The S-method has been discarded since it is severely affected in the analyzed signals by noise problems due to the presence of cross-terms.

In a time-frequency analysis of a turbine, shown in Fig. 277, we could see that maximum fluctuations occur at connexion of the generator and in second place, at connexion of capacitor banks (steep changes generate a broad spectrum of frequency components) [389].

The best spectrogram estimation have been obtained with SFFT with Hanning windows of 128, 256 or 512 samples (approximate window gap of 2.5, 5 or 10 s, respectively) and a 50% overlapping. The 256 samples window provides

enough frequency resolution for our aims and it has a fast enough response in the time domain. The 50% overlapping has been used to increase the time axis resolution and to improve the estimation of the PSD module average, which has been obtained with the mean value of the spectrogram. Hanning window has been used because of its good properties for general purposes (other windows were tested, but results were similar except for the rectangular one, where the result was clearly worse due to spectral leakage).

The program to compute the spectrogram can be viewed in Fig. 277 through Fig. 280. Even though the legends are in Spanish, the use is quite intuitive. The central density chart represents the actual spectrogram. On the right, a bar indicates the colour scale of the spectrogram. On the left, the average of the spectrogram is plotted (the average of the spectrogram is the PSD in stationary systems). Below the spectrogram, the temporal series is represented, where the connection can be noticed a bit after 14:04. The rest of the controls adjust the method for estimating the spectrogram.

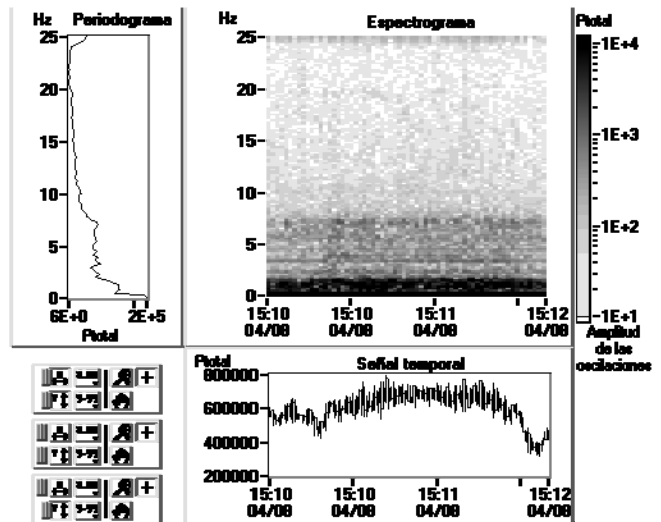


Fig. 279: Spectrogram of output power at SCIG of 750 kW during normal operation operating at $\approx 9,5$ m/s?

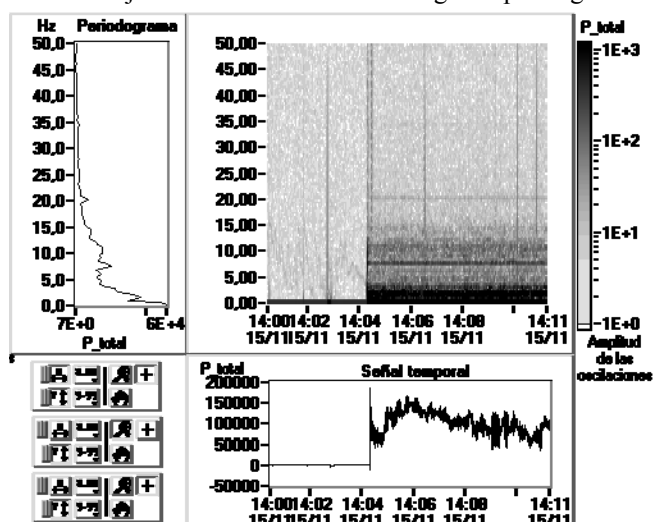


Fig. 277: Spectrogram of total power at SCIG (Squirrel Cage Induction Generator) of 750 kW turbine start-up.

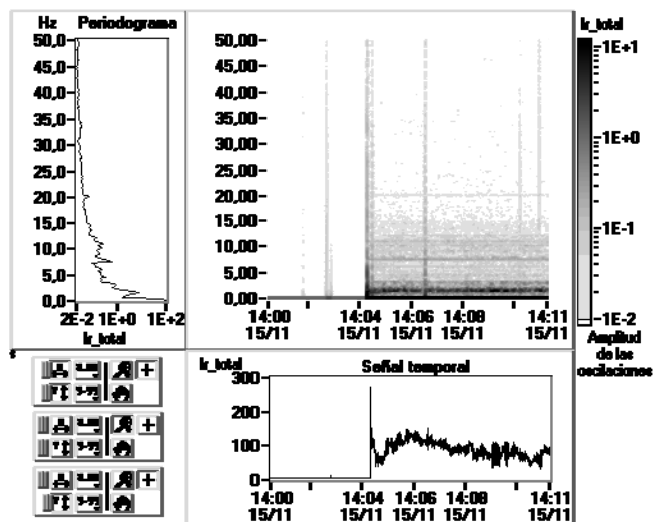


Fig. 280: Spectrogram of total current at SCIG of 750 kW turbine start-up.

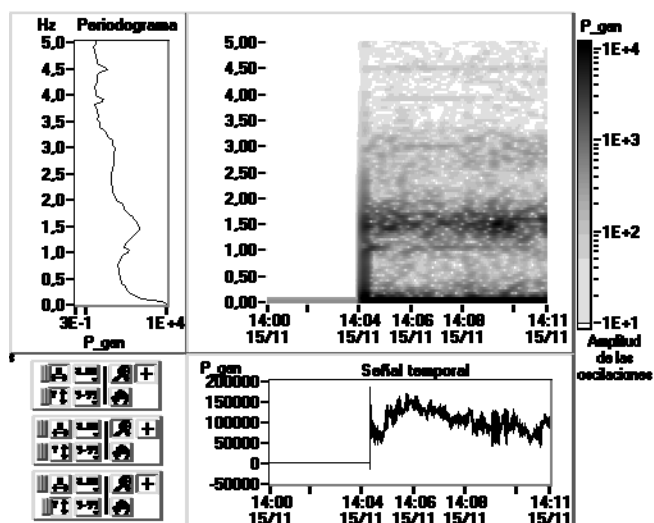


Fig. 278: Spectrogram of total power at SCIG of 750 kW turbine start-up. Detail of tower shadow frequencies.

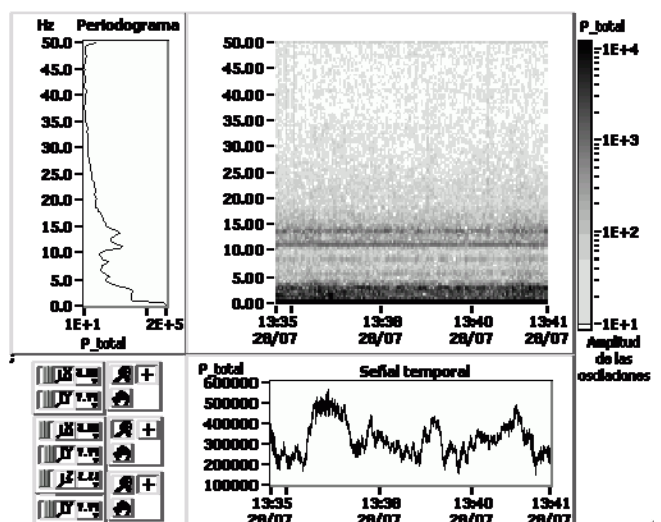


Fig. 281: Spectrogram of real power of a SCIG 600 kW wind turbine for wind speeds around 9,5 m/s corresponding to Fig. 200.

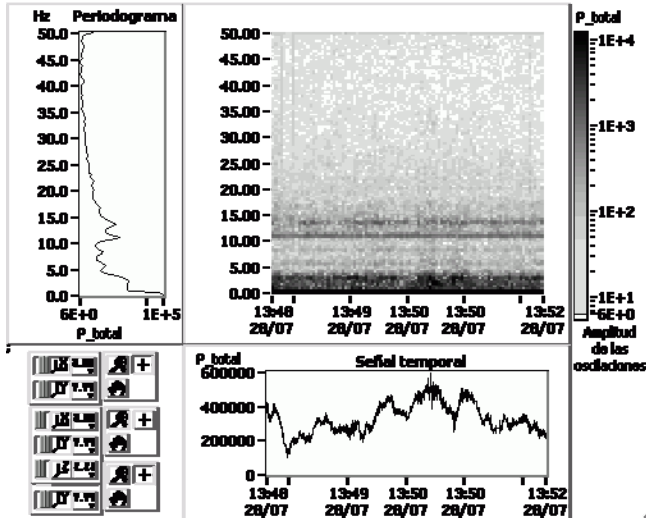


Fig. 282: Spectrogram of real power of a SCIG 600 kW wind turbine for wind speeds around 9,5 m/s corresponding to Fig. 201.

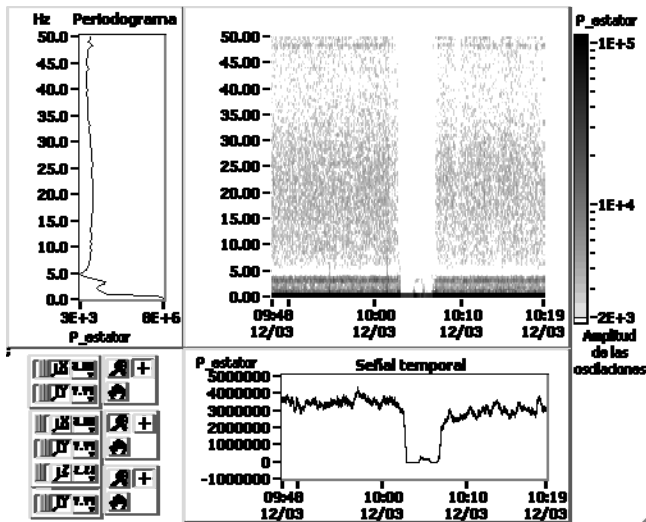


Fig. 283: Spectrogram of a VRIG pitch regulated wind farm operating at low winds in a stop and re-start time series.

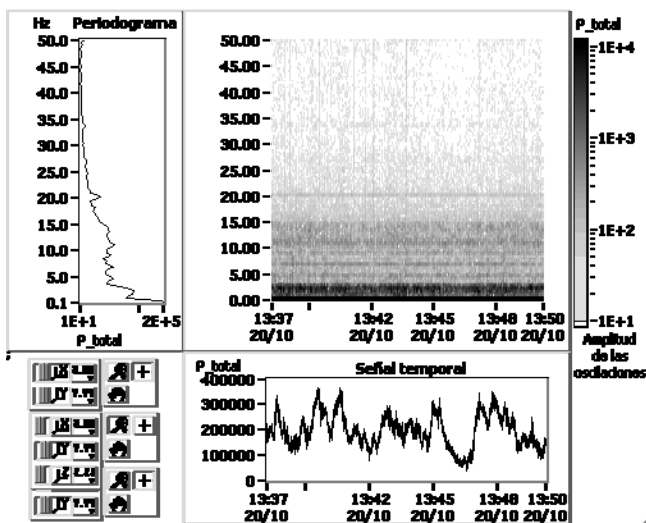


Fig. 284: Spectrogram of a 750 kW induction generator, stall regulation WT operating at 6,5 m/s.

Conclusions

The models developed in this thesis are based in the personal experience gained designing, installing and analyzing the records of a multipurpose data logger for wind turbines and wind farms. The first prototypes have been developed further and now it is commercially available under the name AIRE (Analizador Integral de Recursos Energéticos).

This annex shows some examples of data analysis. The contributions of this examples are the analysis methodology and the conclusions gained from the analysis of the measurements shown in the annex. In fact, some effects observed in the data such the measured oscillations are quite difficult to obtain from simulations.

The measurement system was installed in several wind farms between 1998 and 2000 owned by CEASA (now NEO Energía) and TAIM-NEG-MICON (now VESTAS).

Borja wind farm had 27 Vestas' turbines with variable pitch and wound rotor induction generators with a variable resistor connected to their rotor, VRIG (generator speed vary from 1500 to 1560 rpm).

Remolinos wind farm is in a cliff top and it has doubly fed induction generators (DFIG) from Gamesa, with generator speed ranging from 1220 to 1620 rpm. There are 15 x G42 wind turbines of 648 kW (42 m rotor diameter) and 3 turbines G47 of 660 kW (47 m rotor diameter), both of them with variable pitch.

It was also installed in Valdecuadros, a wind farm with two 600 kW wind turbines and one 750 kW turbine and with fixed pitch (stall control). The utilized generators are squirrel cage induction generators (SCIG), fixed speed, directly connected to the network. The 600 kW WT has a solo generator, with one fixed speed (1500 to 1514 rpm). The 750 kW wind turbine has a secondary 200 kW generator to increase production at low wind by reducing rotor speed (1000-1006 rpm versus 1500-1510 rpm).

Annex C: Torque estimation from blade element theory

C.1. Blade element theory fundamentals

The aerodynamic torque can be accurately estimated with specific software such as ADAMS/WT, ALCYONE, BLADED, DUWECS, FAST (AeroDyn), FLEX, FLEXLAST, GAST, HAWC, PHATAS, TWISTER, VIDYN and YAWDIN (see Hansen [390], Peeters [391] or Ahlström [392] for details). Full details of the blade and rotor geometry are required to compute aerodynamics with these programs.

Sometimes, comprehensive rotor details are not available or the integration of full aerodynamic models in electrical simulation programs is not convenient. Even in those situations, the effect of tower shadow and shear can be estimated roughly provided the power coefficient is known.

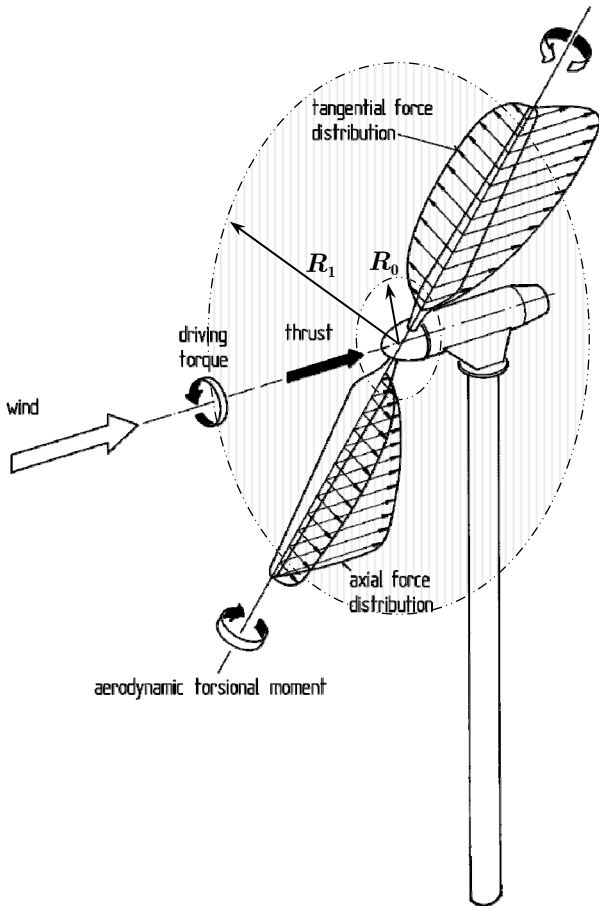


Fig. 285: Distribution of tangential and axial aerodynamic forces over the blade length. Modified from Hau [394].

In this section, a model based on blade element theory and uniform tangential load distribution over the blade length is derived (see tangential force distribution in Fig. 286). The blades are designed to operate at maximum efficiency below rated wind speed and this implies that the rotor tangential force per unit length is fairly constant along the blade. This assumption holds except at the root blade and at the blade

tip due to structural limitations and vortex generation, respectively (see aerodynamic tangential force distribution at 9 m/s and 12 m/s in Fig. 286).

The basics of blade element theory can be revised in the books of Manwell [393], Hau [394], Burton [90] or in Lanzafame [395]. For convenience, a simple sketch is presented here. The forces on the blades of a wind turbine can be expressed as a function of lift and drag coefficients and the angle of attack. The blade is assumed to be divided into sections (or elements) of radial length Δr .

For low and moderate winds, the tangential force (projections of the lift and drag forces on the rotor disk) can be assumed to be fairly constant along the blade. The nose, the blade root and tip must be discounted to compute effective swept area since the tangential force in those blade areas is small (see Fig. 286). In Fig. 287, the considered effective area ranges from $r=R_0$, a small distance (around 20% or turbine radius) from the rotor axis, to a bit before the tip blade, $r=R_1$ (around 95% or turbine radius).

Stall usually begins at blade tip (see aerodynamic tangential force distribution at 24 m/s in Fig. 286). Thus, the approximation derived is poor at high winds unless R_0 and R_1 is adjusted to account partial stall. Pitch regulated turbines also show non-uniform loading at high winds due to blade twist and R_0 and R_1 might be adjusted to maintain the accuracy.

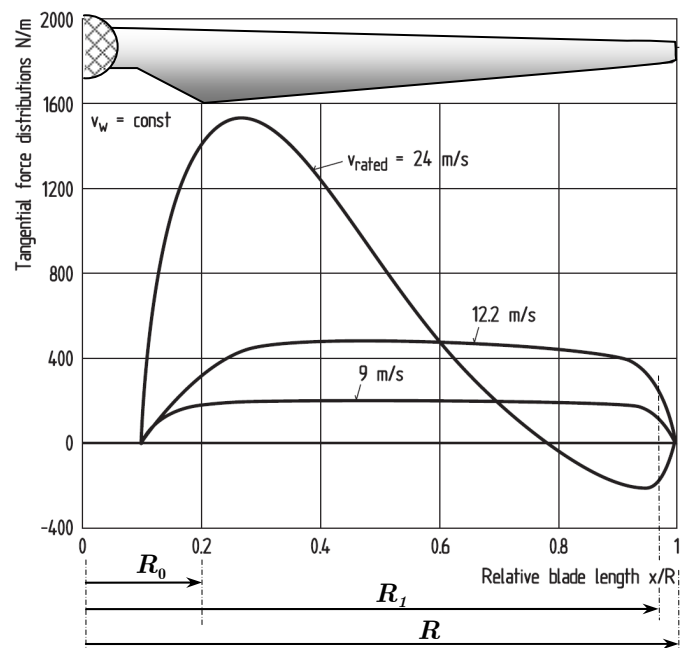


Fig. 286: Tangential load distribution over the blade length of the experimental WKA-60 wind turbine. Modified from Hau [394].

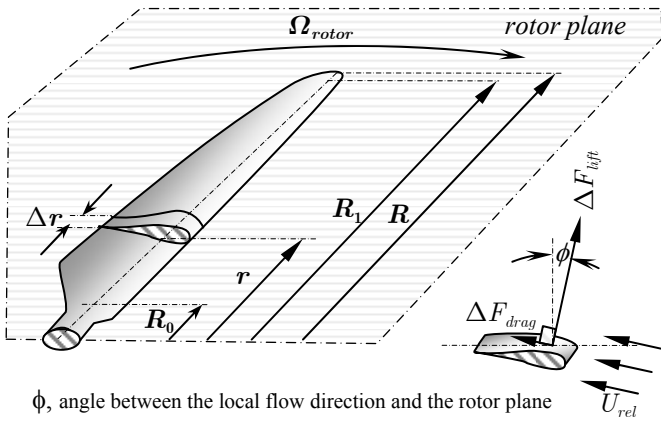


Fig. 287: Schematic of blade elements: r , location of the element of Δr depth; R , rotor radius; Ω_{rotor} , angular velocity of rotor.

The following assumptions are made along this section:

- There is no aerodynamic interaction between elements since the radial speed of the air is small in the swept area, the solidity of the blades is low and the decrease of longitudinal wind speed through the swept area is relative small.
- The forces on the blades are determined solely by the lift and drag characteristics of the airfoil shape of the blades.
- The wind speed upstream the rotor is notated U_{wind} (i.e., the unperturbed wind speed). The wind speed in axial direction just close the rotor blades is $U_{wind, rtptr}$ somewhat lower than U_{wind} . Then the axial induction factor a is defined as the relative loss of axial wind speed across the rotor, $a = (U_{wind} - U_{wind, rtptr}) / U_{wind}$.
- The wind relative to the element U_{rel} is the air speed measured in a reference moving attached to the blade. When the incident wind only has longitudinal direction, the longitudinal component of U_{rel} is $(1-a)U_{wind}$ and its tangential component is $(1+a')\Omega_{rotor}r$, where a' is the tangential induction factor (see Fig. 292 for details).
- To be able to compute the torque with only the power or torque coefficient, it will be eventually assumed that the efficiency of the rotor is the same between $r=R_0$ and $r=R_1$.

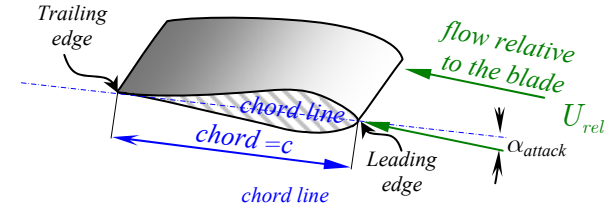
Also, the usual definitions in aerodynamics are followed in this section:

- Lift F_{lift} and drag F_{drag} forces are defined perpendicular and parallel, respectively, to an effective, or relative, wind (see Fig. 289 for details).
- A blade element of depth Δr in the radial direction experience the following lift ΔF_{lift} and drag ΔF_{drag} forces. Thus, the 2-D lift C_l and drag C_d coefficients are defined as the force perpendicular or parallel to direction of the oncoming airflow, respectively, per unit span.

$$C_l = \frac{\text{Lift force}}{\text{Dynamic force}} = \frac{\Delta F_{lift} / \Delta r}{\frac{1}{2} \rho_{air} U_{rel}^2 c} \quad (661)$$

$$C_d = \frac{\text{Drag force}}{\text{Dynamic force}} = \frac{\Delta F_{drag} / \Delta r}{\frac{1}{2} \rho_{air} U_{rel}^2 c} \quad (662)$$

where c is the chord of the blade at the section considered (the distance from the leading edge to the trailing edge).



α_{attack} = attack angle

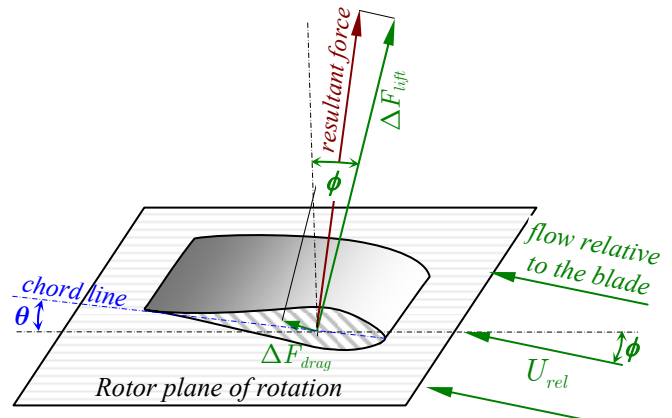
= angle between flow relative to the blade and its chord

Fig. 288: Detail of airfoil nomenclature.

- The tangential force ΔF_T on a section of depth Δr at a distance r from the hub axis center is the vectorial sum of drag and lift forces, projected on the rotor plane:

$$\Delta F_{tangential} = \frac{1}{2} \rho_{air} U_{rel}^2(r) (C_l \sin \phi + C_d \cos \phi) c \Delta r \quad (663)$$

where ϕ is the angle between the local flow direction and the rotor plane,



(far away the blade, wind is perpendicular to rotor plane in a stationary reference)

θ = blade pitch angle = angle between the chord and the rotor rotation plane

ϕ = angle between the local flow direction and the rotor plane of rotation

α_{attack} = attack angle = angle between flow relative to the blade and its

chord = $\phi - \theta$

Fig. 289: Flow velocities and aerodynamic forces at the airfoil cross-section of a blade element.

The torque per blade of an element placed at a distance r from the rotor shaft is $\Delta T_{element} = r \Delta F_{tangential}$.

In a rotor with N_{blades} blades, the overall shaft torque can be computed using differential elements dr instead of finite elements Δr :

$$T_{rotor} = \sum_{i=1}^{N_{blades}} \int_{R_0}^{R_1} \frac{1}{2} \rho_{air} U_{rel,i}^2(r) (C_l \sin \phi + C_d \cos \phi) c r dr \quad (664)$$

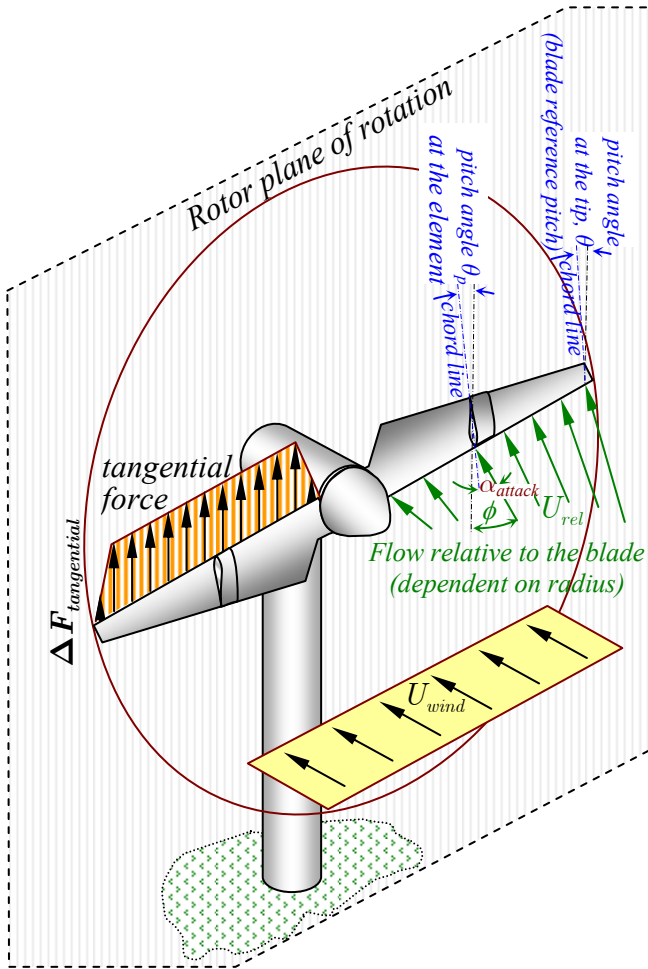


Fig. 290: Sketch of the angles and forces along the blades used to compute the rotor torque.

The power in a differential blade element at radius r is $dP_{element} = \Omega_{rotor} dT_{element}$, where $dT_{element} = dF_{Tangential} r$ is the blade element torque respect the rotor axis. The tangential force on the blade element can be derived from (663) assuming differential elements. Thus, the mechanical power due to blade element at radius r is:

$$dP_{element} = \frac{1}{2} \rho_{air} \Omega_{rotor} U_{rel}^2(r) (C_l \sin \phi + C_d \cos \phi) c r dr \quad (665)$$

The incoming flow power of the area swept by the blade element, divided by the number of blades, is, for Fig. 291:

$$dP_{flow, per element} = \frac{\frac{1}{2} \rho_{air} U_{wind, long}^3 2\pi r dr}{N_{blades}} \quad (666)$$

where $U_{wind, long}$ is the longitudinal component in the wind (just in case the rotor is not aligned or the wind direction varies along the rotor disk).

The efficiency of the element (ratio of transferred mechanical power to inflow power) is the power coefficient of the blade element, $C_P(\lambda'', \theta, r)$, but referred to an element of the blade instead of the whole blade:

$$\begin{aligned} \eta_{element} &= C_P(\lambda'', \theta, r) = \frac{dP_{element}}{dP_{flow, per element}} = \\ &= \frac{\Omega_{rotor} \frac{1}{2} \rho_{air} U_{rel}^2(r) (C_l \sin \phi + C_d \cos \phi) c r dr}{\frac{1}{2} \rho_{air} U_{wind, long}^3 2\pi r dr / N_{blades}} = \\ &= \frac{N_{blades} \Omega_{rotor}}{2\pi} \frac{U_{rel}^2(r)}{U_{wind, long}^3} (C_l \sin \phi + C_d \cos \phi) c \end{aligned} \quad (667)$$

The frequency of a blade passing through the tower is:

$$f_{blade} = N_{blades} \Omega_{rotor} / 2\pi. \quad (668)$$

and the torque contribution of the blade element is:

$$dT_{element} = \frac{dP_{element}}{\Omega_{rotor}} = \frac{1}{2} \rho_{air} \frac{U_{wind, long}^3}{f_{blade}} C_P(\lambda'', \theta, r) r dr \quad (669)$$

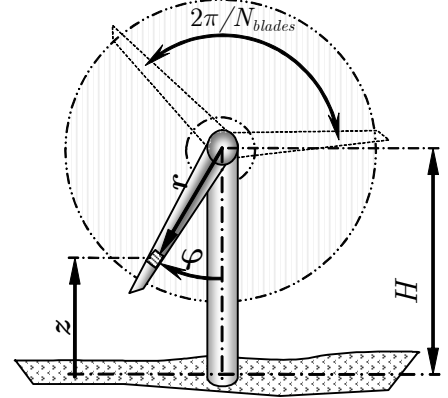


Fig. 291: Geometric position of the blade element in the rotor disk.

The power coefficient of the blade element, $C_P(\lambda'', \theta, r)$, can be simplified assuming that the upstream wind is perpendicular to the swept area (see Fig. 292 for details). (670)

$$\begin{aligned} C_P(\lambda'', \theta, r) &= f_{blade} \frac{U_{rel}^2(r)}{U_{wind, long}^3} (C_l \sin \phi + C_d \cos \phi) c \approx \\ &\approx f_{blade} \frac{U_{wind, long}^2 (1-a)^2 + r^2 \Omega_{rotor}^2 (1+a)^2}{U_{wind, long}^3} (C_l \sin \phi + C_d \cos \phi) c \end{aligned}$$

where a is the axial induction factor and a' the tangential (or angular) induction factor (for details, see Hansen [390] or Ahlström [392]). Note that the assumption that wind is orthogonal to the swept area is not correct near the tower and it will be refined later.

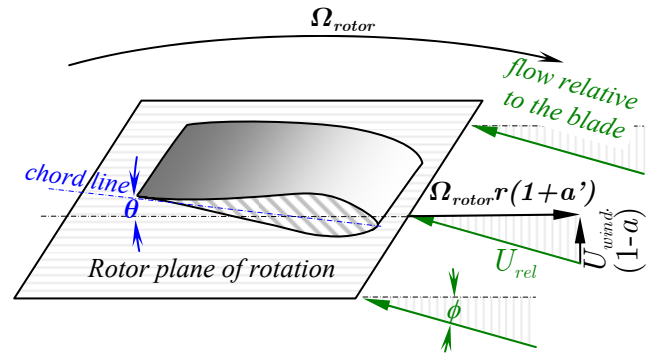


Fig. 292: Velocities at the rotor plane with upstream wind perpendicular to the rotor plane.

$C_P(\lambda'', \theta, r)$ can be refined using the element speed $\lambda''(r)$. The element speed ratio $\lambda''(r)$ is the cotangent of the relative flow angle $\phi'(r)$. When the wind is perpendicular to the swept area, $\lambda''(r)$ is:

$$\lambda''(r) = \cot(\phi'(r)) = \frac{r \Omega_{rotor} (1+a')}{(1-a) U_{wind, long}(r)} \quad (671)$$

The power coefficient of the blade element expressed in terms of the element speed ratio, the drag and lift coefficients and the axial induction factor is:

$$C_P(\lambda'', \theta, r) \approx f_{blade} \frac{(1-a)^2}{U_{wind, long}} (1+\lambda''^2) (C_l \sin \phi + C_d \cos \phi) c \quad (672)$$

The blades of big wind turbines are twisted so that the attack angle is somewhat constant along the blade. The blade twist angle, θ_T , is defined relative to the blade tip (it could be defined otherwise). Therefore $\theta_p = \theta_T + \theta$, where θ is the blade pitch angle at the tip. Thus, the angle of the relative wind is the sum of the element pitch angle θ_p and the angle of attack, $\phi = \theta_p + \alpha_{attack}$ (see Fig. 290 and Fig. 292 for blade geometry). If the blades torsional elasticity is negligible, the twist angle θ_T depends only on the blade geometry. Then, the element pitch angle θ_p only changes if the angle of the blade measured at its tip, θ , is changed by pitch actuators and, since the blades can be considered rigid, the element power coefficient $C_P(\lambda'', \theta, r)$ can be defined relative to the blade tip pitch angle θ for convenience.

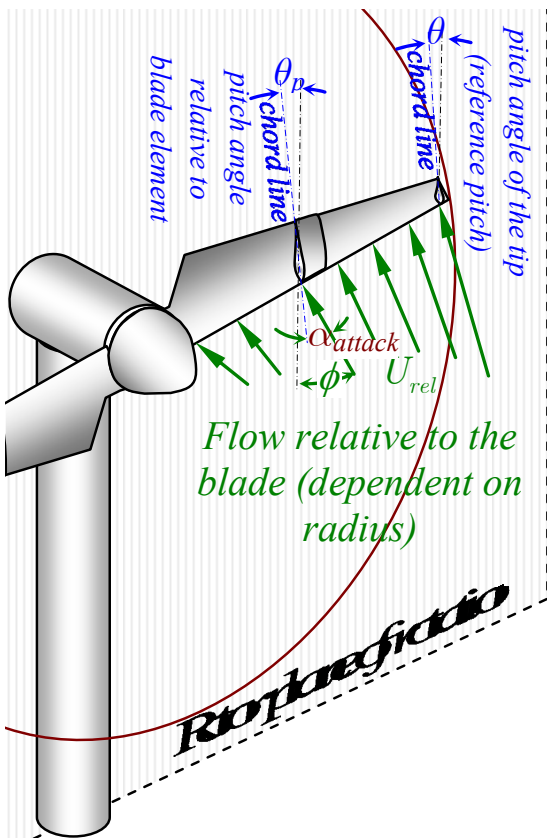


Fig. 293: The pitch angle can be measured respect the element chord θ_p , or respect the blade tip chord θ .

Full details of the blade and rotor geometry and wind field are required to compute aerodynamics. The efficiency of the element $C_P(\lambda'', \theta, r)$ depends on r since structural and mechanical features impose limitations on the airfoil shape. The root of the blade has thicker chamber to increase its rigidity. Thus, the nose and the blade root and tip must be discounted from the effective area. Moreover, vortexes are formed at the tip of the blade due to pressure difference between intrados and extrados.

However, the element power coefficient $C_P(\lambda'', \theta, r)$ can be assumed to be fairly constant along the effective portion of the blades. For simplicity, the efficiency is considered constant in the region $R_0 \leq r \leq R_1$ and null in the rest of the blade (the effective blade section starts at $r=R_0$, a small distance from the shaft axis, and it finishes at $r=R_1$, a bit shorter than the geometric radius of the blade R ,—see Fig. 286).

Under the previous assumption (named *uniform blade loading*), the element power coefficient $C_P(\lambda'', \theta, r)$ can be estimated from the turbine power coefficient $C_P(\lambda, \theta)$, expressed in conventional blade tip speed ratio and pitch angle at the tip. Thus, the element power coefficient is, under the assumption of uniform blade loading and (671):

$$C_P(\lambda'', \theta, r) \approx \frac{R^2}{(R_1^2 - R_0^2)} C_P \left(\frac{R}{r} \frac{1-a}{1+a'}, \lambda'', \theta \right) \quad (673)$$

Now, the torque at the element can be roughly estimated assuming uniform blade loading.

$$\begin{aligned} dT_{element} &\approx \\ & \text{uniform loading} \\ & \approx \frac{1}{2} \rho_{air} \frac{U_{wind, long}^3}{f_{blade}} C_P \left(\frac{R}{r} \frac{1-a}{1+a'}, \lambda'', \theta \right) \frac{R^2}{(R_1^2 - R_0^2)} r dr \end{aligned} \quad (674)$$

Due to the presence of the tower, the flow diverts slightly from the axial in an angle ϕ_{wind} along the blade. Moreover, due to wind shear, the wind is not uniform and it varies for each element. The unperturbed (or upstream) wind varies in modulo and direction along the blade i and its value at radius r is $U_{wind, i}(r)$. The element speed ratio $\lambda_i''(r)$ is estimated in (675) as the cotangent of the flow angle $\phi_i'(r)$ between the relative flow speed and the swept area (see Fig. 294 for details).

$$\begin{aligned} \lambda_i''(r) &= \cot[\phi_i'(r)] = \frac{r \Omega_{rotor} (1+a') + U_{wind, angular, i}(r)}{(1-a) U_{wind, long, i}(r)} = \\ &= \frac{r \Omega_{rotor} (1+a') + (1-a) U_{wind, i}(r) \sin[\phi_{wind, i}(r)]}{(1-a) U_{wind, i}(r) \cos[\phi_{wind, i}(r)]} = \\ &= \frac{1+a'}{1-a} \frac{r \Omega_{rotor}}{U_{wind, i}(r) \cos[\phi_{wind, i}(r)]} + \tan[\phi_{wind, i}(r)] \end{aligned} \quad (675)$$

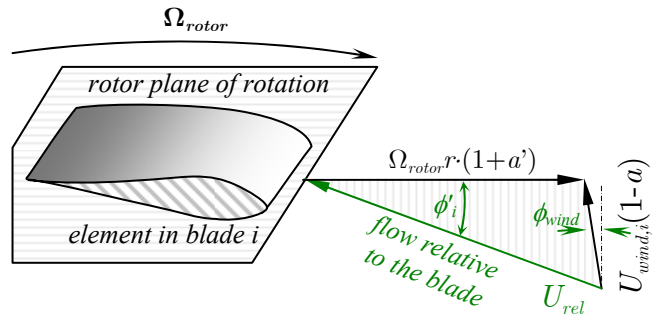


Fig. 294: Detail of velocities at the rotor plane with wind oblique to the rotor plane.

In wind turbines, the power and torque coefficients are referred to the blade tip speed ratio. For convenience, an effective blade tip speed ratio $\lambda_i'(r)$ will be defined from the element speed ratio $\lambda_i''(r)$ as:

$$\lambda_i'(r) = \frac{R}{r} \frac{1-a}{1+a'} \lambda_i''(r) \quad (676)$$

The effective blade tip speed ratio $\lambda_i'(r)$ is the tip speed ratio of the turbine in case the longitudinal component and the angular speed of the wind along the rotor were the same as in the considered blade i element. It can be expressed in terms of wind speed, induction factors and geometry: (677)

$$\lambda'_i(r) = \frac{R\Omega_{rotor}}{U_{wind,i}(r) \cos[\phi_{wind,i}(r)]} + \frac{R}{r} \frac{1-a(r)}{1+a'(r)} \tan[\phi_{wind,i}(r)]$$

Induction factors a and a' depends on many features. However, *induction* factors are *close to zero* since the solidity of the turbine rotors are small. In (678), they are neglected to obtain a closed formula for big wind deviations.

$$\lambda'_i(r) \cong \frac{R\Omega_{rotor}}{U_{wind,i}(r) \cos[\phi_{wind,i}(r)]} + \frac{R}{r} \tan[\phi_{wind,i}(r)] \quad (678)$$

$\forall a \sim 0 \text{ and } a' \sim 0$

When the turbine is oriented against the airflow, the wind diverts from longitudinal direction in the rotor disk only near the tower, where the deflection angle ϕ_{wind} is about some degrees (see Fig. 305). Realize that if upstream wind is perpendicular to rotor area ($\phi_{wind} \approx 0$), the effective blade tip speed ratio $\lambda'_i(r)$ simplifies to the usual tip speed ratio:

$$\lambda'_i(r) \approx \frac{R\Omega_{rotor}}{U_{wind,i}(r)} \quad \forall \phi_{wind,i} \sim 0 \quad (679)$$

If wind conditions vary along the blade i , the effective tip speed ratio $\lambda'_i(r)$ referred to the element of blade i at radius r is not longer constant and (674) transforms into (680) from (668) and (679).

$$\begin{aligned} dT_{element,i} &\approx \frac{1}{2} \rho_{air} \frac{U_{wind,i}^3(r)}{f_{blade}} C_P(\lambda'_i(r), \theta) \frac{R^2}{R_1^2 - R_0^2} r dr = \\ &= \frac{1}{2} \rho_{air} \frac{2\pi R^3 \Omega_{rotor}^2}{N_{blades} \lambda_i^2(r)} \frac{R^2}{R_1^2 - R_0^2} \frac{C_P(\lambda'_i(r), \theta)}{\lambda'_i(r)} r dr \end{aligned} \quad (680)$$

The former expression transforms, through the power and torque coefficient relationship $C_P(\lambda, \theta) = C_q(\lambda, \theta)/\lambda$, into:

$$dT_{element} \approx U_{wind}^2 \frac{\rho_{air} \pi}{N_{blades}} \frac{R^3}{(R_1^2 - R_0^2)} \frac{C_q(\lambda'_i(r), \theta)}{\lambda_i^2(r)} r dr \quad (681)$$

Thus, the rotor torque can be computed integrating the contribution of the effective elements along all the blades:

$$\begin{aligned} T_{rotor} &= \sum_{i=1}^{N_{blades}} \int_{R_0}^{R_1} dT_{element,i} = \\ &= \sum_{i=1}^{N_{blades}} \int_{R_0}^{R_1} \rho_{air} \frac{\pi R^3 \Omega_{rotor}^2}{N_{blades}} \frac{R^2}{R_1^2 - R_0^2} \frac{C_q(\lambda'_i(r), \theta)}{\lambda_i^2(r)} r dr \end{aligned} \quad (682)$$

Finally, the rotor torque can be conveniently computed integrating the torque coefficient:

$$T_{rotor} = \frac{1}{2} \rho_{air} \pi R^5 \Omega_{rotor}^2 \sum_{i=1}^{N_{blades}} \int_{R_0}^{R_1} \frac{2}{R_1^2 - R_0^2} \frac{C_q(\lambda'_i(r), \theta)}{N_{blades} \lambda_i^2(r)} r dr \quad (683)$$

Applying the first mean value theorem for integration, the proposed method is *similar to computing the rotor torque for the average operational conditions along the blades* – compare (683) with the usual formula (684).

Under constant longitudinal and angular wind speed along the rotor, $\lambda'_i(r)$ is constant and the rotor torque (683) transforms into the usual formula (684).

$$T_{rotor} = \frac{1}{2} \rho_{air} \pi R^5 \Omega_{rotor}^2 \frac{C_q(\lambda, \theta)}{\lambda^2} = \frac{1}{2} \rho_{air} \pi R^3 U_{wind}^2 C_q(\lambda, \theta) \quad (684)$$

The first order small-signal approximation on λ' in $C_q(\lambda, \theta)/\lambda^2$, the rotor torque due to differences in wind along the rotor is:

$$\begin{aligned} \frac{C_q(\lambda'_i, \theta)}{\lambda_i^2} &\approx \frac{C_q(\langle \lambda' \rangle, \theta)}{\langle \lambda' \rangle^2} + \\ &+ \left[\frac{2}{\langle \lambda' \rangle} C_q(\langle \lambda' \rangle, \theta) - \frac{\partial C_q(\langle \lambda' \rangle, \theta)}{\partial \lambda} \right] \left[\frac{1}{\lambda'_i} - \frac{1}{\langle \lambda' \rangle} \right] \end{aligned} \quad (685)$$

With the previous approximation, the integral in (683) can be estimated as:

$$\sum_{i=1}^{N_{blades}} \int_{R_0}^{R_1} \frac{2}{R_1^2 - R_0^2} \frac{C_q(\lambda'_i(r), \theta)}{N_{blades} \lambda_i^2(r)} r dr = \frac{C_q(\langle \lambda' \rangle, \theta)}{\langle \lambda' \rangle^2} \quad (686)$$

provided $\langle \lambda' \rangle$ is the weighted average of the tip speed ratio computed as:

$$\frac{1}{\langle \lambda' \rangle} = \frac{2}{N_{blades} (R_1^2 - R_0^2)} \sum_{i=1}^{N_{blades}} \int_{R_0}^{R_1} \frac{1}{\lambda'_i(r)} r dr \quad (687)$$

Notice that $1/\langle \lambda' \rangle$ is proportional to $U_{eq}(\varphi)$ and therefore, (687) is a model linearized on wind speed. Finally, the rotor torque in terms of average tip speed ratio (687) is:

$$T_{rotor} = \frac{1}{2} \rho_{air} \pi R^5 \Omega_{rotor}^2 \frac{C_q(\langle \lambda' \rangle, \theta)}{\langle \lambda' \rangle^2} \quad (688)$$

If wind speed variations are considerable, a better approximation can be obtained if the first order small-signal approximation is based on $1/\lambda'^2$ instead of on λ' . This will give a model on squared wind speed since $\langle \lambda'^{-2} \rangle$ is proportional to $U_{eq}^2(\varphi)$. In such case, the estimations are:

$$\begin{aligned} \frac{C_q(\lambda'_i, \theta)}{\lambda_i^2} &\approx \langle \lambda'^{-2} \rangle C_q \left(\frac{1}{\sqrt{\langle \lambda'^{-2} \rangle}}, \theta \right) + \\ &+ \left[C_q \left(\frac{1}{\sqrt{\langle \lambda'^{-2} \rangle}}, \theta \right) - \frac{\partial C_q \left(\frac{1}{\sqrt{\langle \lambda'^{-2} \rangle}}, \theta \right)}{\partial \lambda} \frac{1}{2\sqrt{\langle \lambda'^{-2} \rangle}} \right] \left[\frac{1}{\lambda_i^2} - \langle \lambda'^{-2} \rangle \right] \end{aligned} \quad (689)$$

where the average squared inverse of the blade tip speed ratio is:

$$\langle \lambda'^{-2} \rangle = \frac{2}{N_{blades} (R_1^2 - R_0^2)} \sum_{i=1}^{N_{blades}} \int_{R_0}^{R_1} \frac{1}{\lambda_i^2(r)} r dr \quad (690)$$

and the aerodynamic torque in the turbine is:

$$T_{rotor} = \frac{1}{2} \rho_{air} \pi R^5 \Omega_{rotor}^2 \langle \lambda'^{-2} \rangle C_q \left(\frac{1}{\sqrt{\langle \lambda'^{-2} \rangle}}, \theta \right) \quad (691)$$

In short, the influence of variable conditions along the rotor can be computed averaging the effective speed tip ratio along each blade proportionally to its torque contribution. In order to account lateral/vertical flow, the angular wind speed is subtracted or added to the angular speed of the blade. The radial flux is not considered, but its influence in the turbine torque is tiny.

The model proposed in this section does not account blade vibrations and elasticity. Neither blade added twist nor bending due to varying loads is analysed. Thus, the pitch of the blade θ is assumed to be not affected by wind variations.

C.2. Alternative torque calculation by Sørensen

A similar method to compute the torque has been developed by Sørensen [153]. The main difference with the previous model is that Sørensen linearized the wind influence on torque employing a sensitivity function $\psi(r)$ of wind in torque. For clarity and completeness, Sørensen's approach is briefly outlined in this section. The aerodynamic torque produced by a three bladed wind turbine immersed in a wind field in polar coordinates $U_{wind}(r, \varphi)$ is given as:

$$T_{rotor}(\varphi) = N_{blades} M(\langle U_{wind} \rangle) + \sum_{i=1}^{N_{blades}} \int_{R_0}^{R_1} \psi(r) [U_{wind}(r, \varphi + 2\pi i/N_{blades}) - \langle U_{wind} \rangle] dr \quad (692)$$

where

$T_{rotor}(\varphi)$ = aerodynamic torque for rotor angle φ ,
 $M(\langle U_{wind} \rangle)$ = steady state blade root moment resulting from spatial mean wind speed $\langle U_{wind} \rangle$,
 R_1 = radius of the rotor disk,
 R_0 = radius at which blade profile begins and
 $\psi(r)$ = influence coefficient of wind on blade root moment.

This equation has been determined through linearization of individual blade torque dependence on wind speed. The equivalent wind speed at rotor angle φ , $U_{eq}(\varphi)$, would give the same aerodynamic torque as the actual wind field:

$$T_{rotor}(\varphi) = N_{blades} \int_{R_0}^{R_1} \psi(r) U_{eq}(\varphi + 2\pi i/N_{blades}) dr \quad (693)$$

The equivalent wind speed $U_{eq}(\varphi)$ is a representation of the actual spatially varying wind speed that is defined such that it will give the same aerodynamic torque $T_{rotor}(\varphi)$. Equating (692) and (693), Sørensen determined the expression for equivalent wind speed $U_{eq}(\varphi)$ as a weighted average across the blades:

$$U_{eq}(\varphi) = \frac{1}{N_{blades}} \frac{\sum_{i=1}^{N_{blades}} \int_{R_0}^{R_1} \psi(r) U_{wind}(r, \varphi + 2\pi i/N_{blades}) dr}{\int_{R_0}^{R_1} \psi(r) dr} \quad (694)$$

Sørensen approach and the method proposed in this thesis are approximations based on linearizing simplifications. Since flux hysteresis is not accounted, flux transitions are not accurately represented.

Since torque is related to squared wind speed, the method from Sørensen can be optimized for torque. Therefore, the torque function is:

$$T_{rotor}(\varphi) = N_{blades} \int_{R_0}^{R_1} \psi(r) U_{eq}^2(\varphi + 2\pi i/N_{blades}) dr \quad (695)$$

where $\psi(r)$ is the influence coefficient of aerodynamic load on blade root moment. Assuming uniform loading from R_0 to R_1 and average tip speed ratio $\langle \lambda \rangle$, $\psi(r)$ can be estimated as:

$$\psi(r) = \frac{\rho_{air} \pi R^3 C_q(\langle \lambda \rangle, \theta)}{N_{blades} (R^2 - r_0^2)} r \quad (696)$$

Finally, the equivalent squared wind speed $U_{eq}^2(\varphi)$ can be estimated as:

$$U_{eq}^2(\varphi) = \frac{1}{N_{blades}} \frac{\sum_{i=1}^{N_{blades}} \int_{R_0}^{R_1} \psi(r) U_{wind}^2(r, \varphi + 2\pi i/N_{blades}) dr}{\int_{R_0}^{R_1} \psi(r) dr} = \frac{\sum_{i=1}^{N_{blades}} \int_{R_0}^{R_1} \psi(r) U_{wind}^2(r, \varphi + 2\pi i/N_{blades}) dr}{\frac{1}{2} \rho_{air} \pi R^3 C_q(\langle \lambda \rangle, \theta)}$$

which is independent of $\langle \lambda \rangle$ and θ since the factor $C_q(\langle \lambda \rangle, \theta)$ appears in the denominator and in the numerator –inside $\psi(r)$.

The main advantages of the proposed method from the Sørensen approach are:

- Since uniform blade loading is assumed, non additional sensitivity function is required. Only the power coefficient (or alternatively, the torque coefficient) and dimensions of the turbine are required.
- The average of the squared inverse of the blade tip speed ratio $\langle \lambda^{-2} \rangle$ is straightforward related to power and torque coefficients. Moreover, $\langle \lambda^{-2} \rangle$ is proportional to the torque.
- The effect of tower shear has not been thoroughly reported in the Sørensen approach. In contrast, the numerical calculation (752) of is a good tradeoff of accuracy and simplicity, including tower shadow and non-linearities in torque with a low footprint in simulation time.
- Formulation has been carefully optimized to be easily included in simulations of turbine control and electrical power systems without noteworthy footprint in simulation times.
- Turbine vibration modes are not considered in neither model. However, a method to add eventual ad-hoc vibrations is provided in this work.

C.3. Modulation of torque due to wind shear

The approximation (691) allows to estimate the wind shear from torque coefficient. The equivalent tip speed ratio can be estimated from wind shear model (52):

$$\langle \lambda^{-2} \rangle = \frac{N_{blades} (R_1^2 - R_0^2)}{2 \sum_{i=1}^{N_{blades}} \int_{R_0}^{R_1} \frac{1}{\lambda_i^2(r)} r dr} = \frac{N_{blades} (R_1^2 - R_0^2)}{2 \sum_{i=1}^{N_{blades}} \int_{R_0}^{R_1} \left[\frac{U_{wind}(z)}{R \Omega_{rotor}} \right]^2 r dr} \quad (698)$$

According to Fig. 295, the ground elevation is $z = H - r \cos(\varphi + 2\pi i/N_{blades})$ for blade $i = 1$ to N_{blades} and the former integral can be estimated for rotor angle φ as: (699)

$$\langle \lambda'^2 \rangle_\varphi = \frac{N_{blades} R \Omega_{rotor} (R_1^2 - R_0^2)}{2 \sum_{i=1}^{N_{blades}} \int_{R_0}^{R_1} U_{wind}^2(H) \left(\frac{H-r \cos(\varphi + 2\pi i/N_{blades})}{H} \right)^{2\alpha_z} r dr}$$

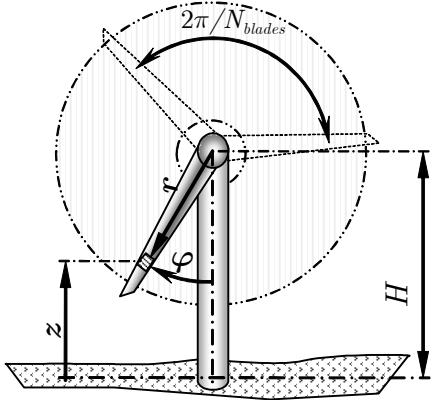


Fig. 295: Computation of equivalent tip speed ratio in blade element.

For convenience, the equivalent tip speed ratio in function of rotor angle $\langle \lambda' \rangle_{\varphi, N_{blades}}$ will be abbreviately notated as $\lambda_{N_{blades}}(\varphi)$ or even $\lambda(\varphi)$ if there is no confusion risk. The integral in (699) can be computed analytically and this expression can be compactly expressed as:

$$\langle \lambda'^{-2} \rangle_\varphi \equiv \lambda^{-2}(\varphi) = \frac{\sum_{i=1}^{N_{blades}} f_2(\varphi + 2\pi i/N_{blades})}{k_{shear}} \quad (700)$$

where the following functions are used to obtain a compact notation:

$$k_{shear} = N_{blades} \lambda_H^2 (R_1^2 - R_0^2) (1 + 2\alpha_z)(1 + \alpha_z) \quad (701)$$

$$f_0(x) = H / \cos(x) \quad (702)$$

$$f_1(x, y) = [1 - y/f_0(x)]^{2\alpha_z} [y - f_0(x)][y(1 + 2\alpha_z) + f_0(x)] \quad (703)$$

$$f_2(x) = f_1(x, R_1) - f_1(x, R_0) \quad (704)$$

where the nominal tip speed ratio is $\lambda_H = \frac{\Omega_{rotor} R}{U_{wind}(H)}$ (705)

Thus, the effective wind at a blade at angle φ can be defined as:

$$U_{wind, blade}(\varphi) = R \Omega_{rotor} \sqrt{\frac{N_{blades} f_2(\varphi)}{k_{shear}}} \quad (706)$$

And the overall equivalent wind at angle φ along the rotor is:

$$U_{eq}(\varphi) = R \Omega_{rotor} \sqrt{\frac{\sum_{i=1}^{N_{blades}} f_2(\varphi + 2\pi i/N_{blades})}{k_{shear}}} \quad (707)$$

For the usual parameter values, the inverse of the squared equivalent tip speed ratio, $\lambda^{-2}(\varphi)$, can be accurately approximated by the constant term and the fundamental oscillation (limits are used to indicate that the points $\varphi = 0$ or $\varphi = 2\pi/N_{blades}$ can be singular points):

$$\lambda^{-2}(\varphi) \approx \lambda_H^{-2} [\mu_{shear} + A_{shear} \cos(N_{blades} \varphi)] \quad (708)$$

where the normalized torque average and modulation due to shear are defined, respectively, as:

$$\mu_{shear} = \frac{\lim_{\varphi \rightarrow 0} \lambda^{-2}(\varphi) + \lim_{\varphi \rightarrow \pi/N_{blades}} \lambda^{-2}(\varphi)}{2\lambda_H^{-2}} \quad (709)$$

$$A_{shear} = \frac{\lim_{\varphi \rightarrow 0} \lambda^{-2}(\varphi) - \lim_{\varphi \rightarrow \pi/N_{blades}} \lambda^{-2}(\varphi)}{2\lambda_H^{-2}} \quad (710)$$

In accordance with (691), A_{shear}/μ_{shear} is the torque relative modulation and torque can be approximated to a signal with a constant value and a superimposed sinusoidal oscillation:

$$T_{rotor}(\varphi) \approx \quad (711)$$

$$\approx \frac{\frac{1}{2} \rho_{air} \pi R^5 \Omega_{rotor}^2 C_q \left(\langle \theta' \rangle, \frac{\lambda_H}{\sqrt{\mu_{shear}}} \right)}{\lambda_H^2 / \mu_{shear}} \left[1 + \frac{A_{shear}}{\mu_{shear}} \cos(N_{blades} \varphi) \right]$$

C.3.1. Two-bladed turbine

In a two-bladed turbine, the equivalent tip speed ratio in function of rotor angle is notated as $\langle \lambda' \rangle_{\varphi, N_{blades}=2}$ or just $\lambda_2(\varphi)$ for short:

$$\langle \lambda' \rangle_{\varphi, 2} = \lambda_2(\varphi) = \sqrt{\frac{k_{shear}}{f_2(\varphi) + f_2(\varphi + \pi)}} \quad (N_{blades}=2) \quad (712)$$

The average and amplitude of $\lambda_2(\varphi)$ are shown in Fig. 296 and in Fig. 297, respectively. These values have been computed for a turbine with effective blade root $R_0 = 0.20R$ and effective maximum span $R_1 = 0.95R$. Due to symmetry

When the blades of a two bladed turbine are horizontal, they experience the wind at hub height and thus $A_{shear} + \mu_{shear} = 1$, as can be deduced of Fig. 296 and Fig. 297. In Fig. 297, negative amplitudes occurs for $\alpha_z < 1/2$, indicating that the maximum occurs when the blades are horizontal. For $\alpha_z > 1/2$, the amplitudes are positive, indicating that the maximum occurs when the blades are vertical.

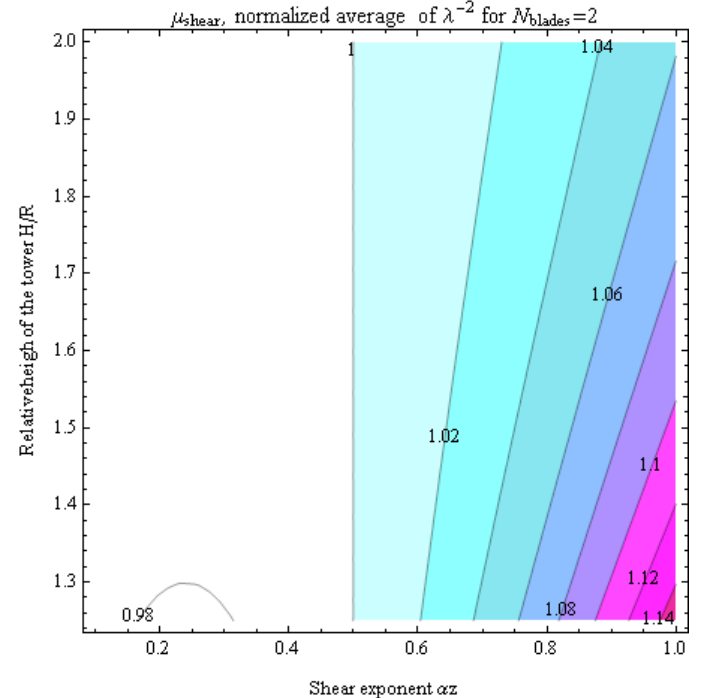
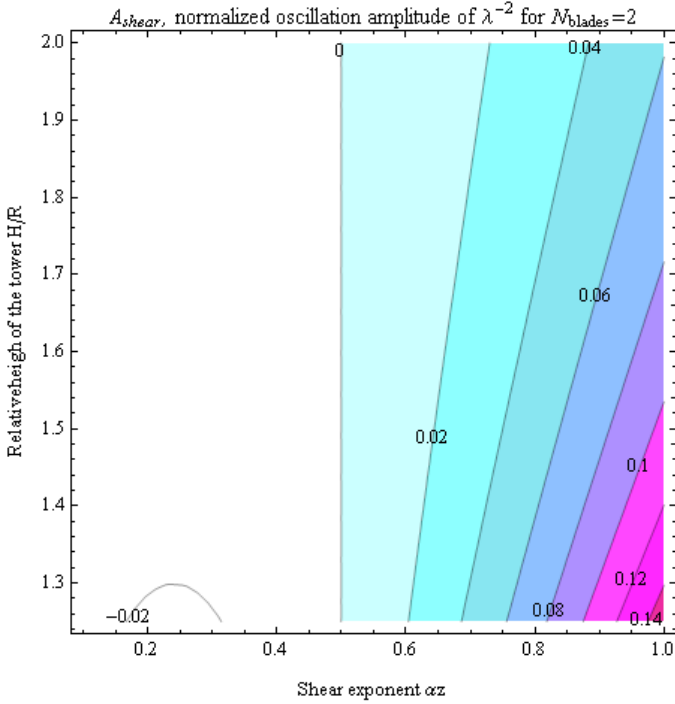


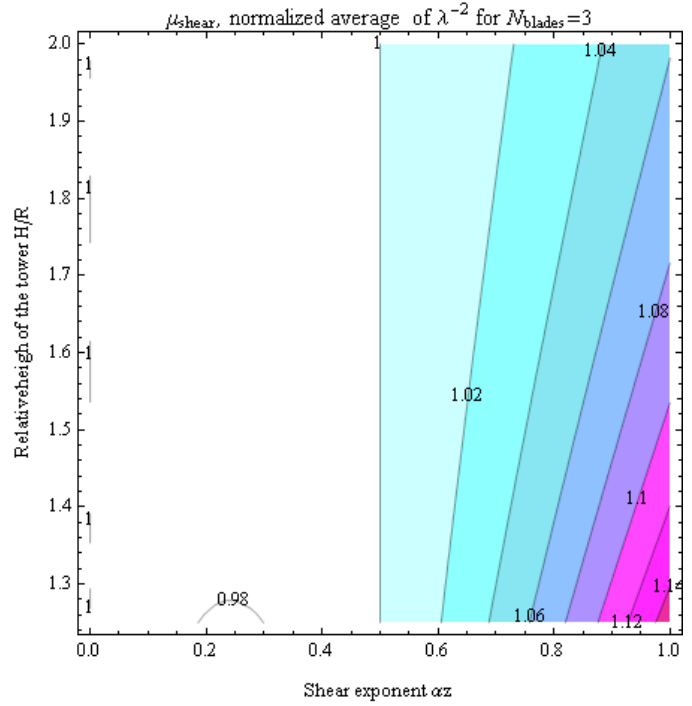
Fig. 296: Normalized average of λ^{-2} , μ_{shear} in a two-bladed turbine.Fig. 297: Normalized modulation amplitude of λ^{-2} , A_{shear} in a two-bladed turbine. Negative amplitudes indicate that a torque minimum occurs instead of a maximum when the blade is aligned with the tower.

C.3.2. Three-bladed turbine

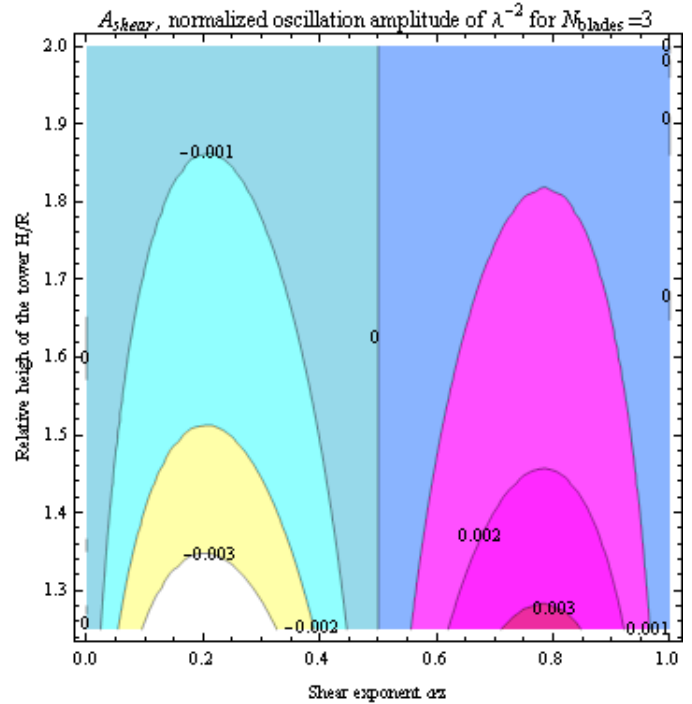
In a three-bladed turbine, the equivalent tip speed ratio is:

$$\lambda_3(\varphi) = \sqrt{\frac{k_{shear}}{f_2(\varphi - \frac{2}{3}\pi) + f_2(\varphi) + f_2(\varphi + \frac{2}{3}\pi)}} \quad (N_{blades}=3) \quad (713)$$

The average and amplitude of $\lambda_3(\varphi)$ are shown in Fig. 298 and in Fig. 299, respectively. These values have been computed for a turbine with effective blade root $R_0 = 0.20R$ and effective maximum span $R_1 = 0.95R$. Realize that in a three-bladed turbine the shear modulation is approximately one tenth of the two-bladed turbine with rigid rotors. In practical implementations of two-bladed turbines, teetered hub and other solutions [394, 90, 109] are used to diminish force modulation compared to a rigid rotor (as shown in Fig. 296 and Fig. 297). Even with these solutions, tower and drivetrain loads have smaller modulations in a three-bladed turbine, experiencing less fatigue and it is one of the reasons of its actual preference among manufacturers.

Fig. 298: Normalized average of λ^{-2} , μ_{shear} in a three-bladed turbine.

In Fig. 299, negative amplitudes occur for $\alpha_z < 1/2$, indicating that the maximum occurs when a blade is aligned with the tower ($\varphi = 0$). For $\alpha_z > 1/2$, the amplitudes are positive, indicating that the maximum occurs at $\varphi = 0$.

Fig. 299: Normalized modulation amplitude of λ^{-2} , A_{shear} in a three-bladed turbine. Negative amplitudes indicate that a torque minimum occurs instead of a maximum when the blade is aligned with the tower.

C.3.3. Effect of rotor tilt and coning in the equivalent tip speed ratio

A commercial turbine presents a tilt and a cone angle. Despite tilt angle can be considered constant, the coning depends on wind speed through the flapwise blade elasticity and pitch angle [396]. In fact, vibration of blades can introduce a stochastic behaviour in the torque.

The methodology presented in the former subsection can be easily modified to take into account tilt and coning. Tilt and coning effect on shear modulation is usually small. They can be accounted modifying the relative speed that experiences each blade element.

Fig. 300 shows a sketch of the geometric model of wind turbine. A model based on four coordinate systems can be found, for example, in [390].

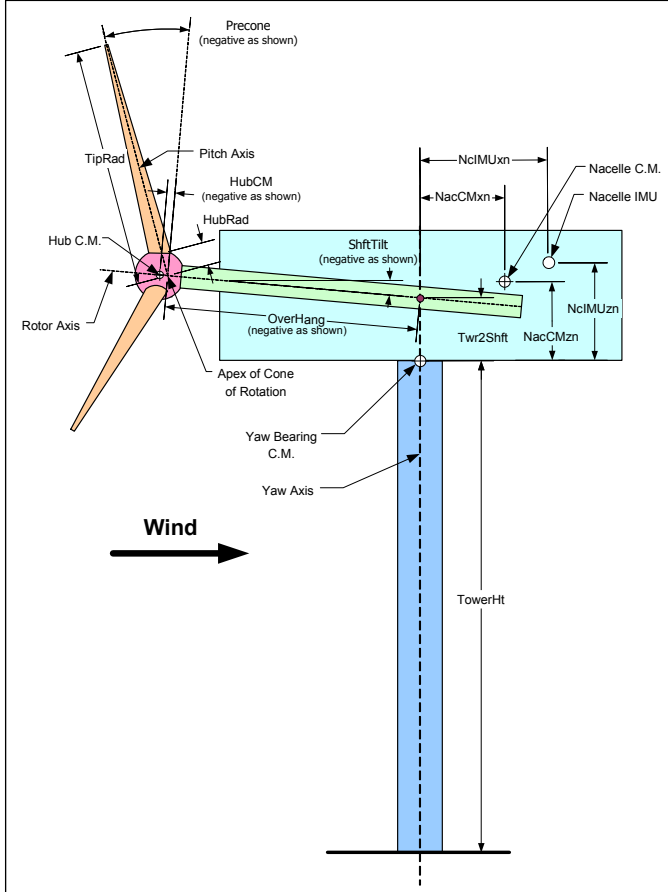


Fig. 300: Wind turbine geometry described by four coordinate systems. Reproduced from [396].

Notice that the coning angle can be significantly different of the precone angle due to blade elasticity. For the calculus of tower shadow effect, a simplified model will be used where the effective inclination angle γ respect the vertical when the blade is close to the tower is $\alpha_{tilt} + \alpha_{cone}$ (see Fig. 301 for geometric details). Due to precone, γ is positive for low wind speeds (corresponding to upstream coning as shown in Fig. 301) and γ can be negative (downstream coning) at high wind speeds due to the flapwise bending of the blades. Therefore, the tower shadow effect is more appreciable at full generation since the blade of the tip is closer to the tower and the torque is more dependable on the attack angle.

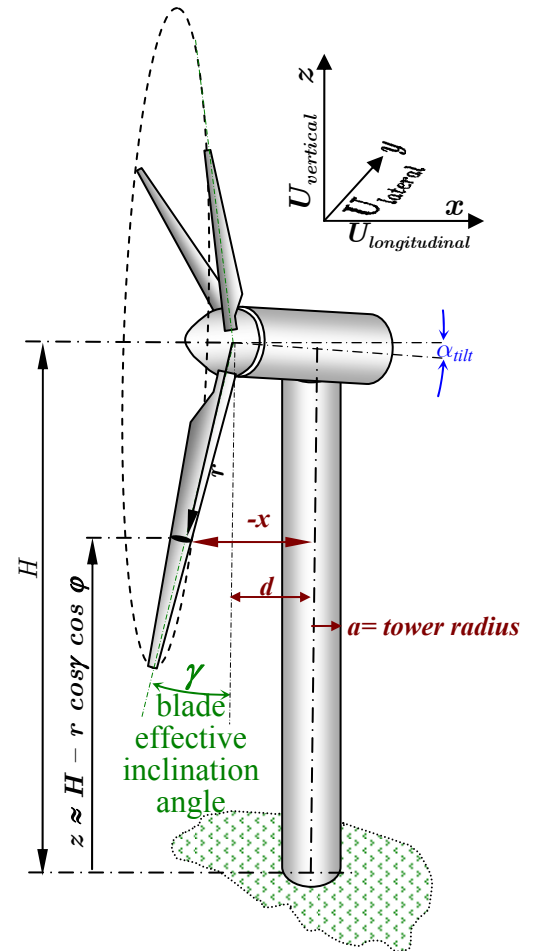


Fig. 301: Simplified turbine geometry to compute blade element distance to tower axis, ρ .

C.4. Tower shadow effect

The tubular tower diverts wind flow producing a local change of wind speed modulus and direction. Its main effect is a swift change of the attack angle α_{attack} and the relative wind speed U_{rel} at the blade elements. The 2D potential flow is a suitable model of tower disturbance for upwind rotors and it has been previously used (see Sørensen et Al. [153]). For downwards rotors a turbulent wake model is required (see [397] for example).

Details of application of potential flow to the stream disturbance around a cylinder can be found in many fluid mechanic books (see White [398] for example). Flow around a cylinder can be approached by an air sink and a source very close to the cylinder axis, superposed to the uniform flow corresponding to the unperturbed upstream wind.

Using the cartesian coordinates with origin in the tower axis, as shown in Fig. 302, the stream function ψ for this problem is:

$$\psi = y U_{wind}(z) \text{Sin} \left(1 - \frac{a^2}{x^2 + y^2} \right) \quad (714)$$

The longitudinal component of wind is straightforward from the stream function ψ :

$$U_x(z) = -\frac{\partial \psi}{\partial y} = U_{wind}(z) \left(1 + \frac{a^2(-x^2 + y^2)}{(x^2 + y^2)^2} \right) \quad (715)$$

and the lateral component of wind is:

$$U_y(z) = -\frac{\partial\psi}{\partial x} = U_{wind}(z) \frac{-2xya^2}{(x^2 + y^2)^2} \quad (716)$$

The wind field is shown in Fig. 302 and Fig. 303, where the stream lines (ψ constant) are plotted and the contours of constant speed modulo are coloured. The numbers in the contour lines correspond to the wind speed module relative to the unperturbed wind speed far away the cylinder.

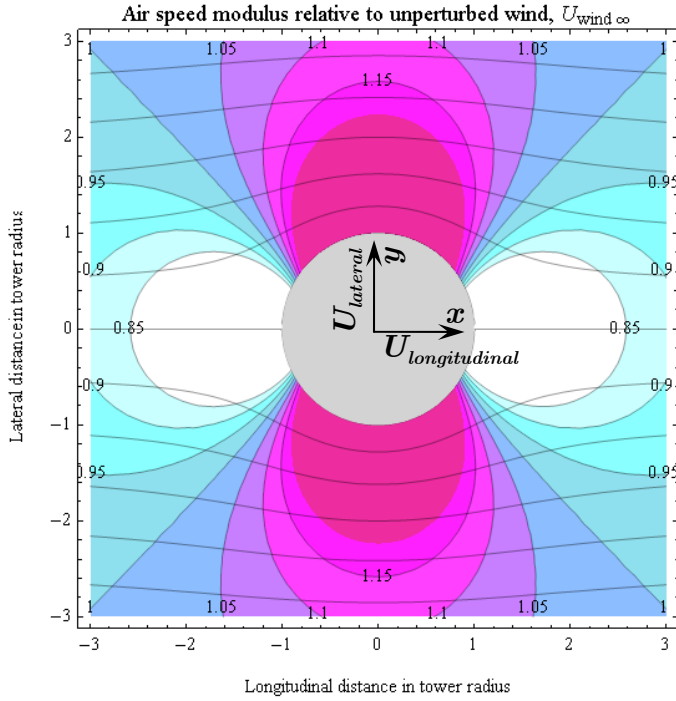


Fig. 302: Flow around a cylinder computed by potential flow (the streamlines, the lines of equal wind modulus and the cartesian coordinates are plotted).

Using the reference frames shown in Fig. 301 or Fig. 302, the coordinate transformation from tower to blade reference is:

$$x = -d - r \sin(\gamma) \quad (717)$$

$$y = r \cos(\gamma) \sin(\varphi) \quad (718)$$

$$z = H - r \cos(\gamma) \cos(\varphi) \quad (719)$$

The squared modulus of wind speed below the nacelle can be obtained in blade coordinates applying the former transformations:

$$U_{wind,i=0}^2(r, \varphi) = \left| \vec{U}_{wind,i=0}(r, \varphi) \right|^2 = U_x^2(r, \varphi) + U_y^2(r, \varphi) \approx (720)$$

$$\approx U_{wind}^2(H) \frac{(a^2 - d^2)^2 + 2(a^2 + d^2)r^2 \sin^2[\varphi] + r^4 \sin^4[\varphi]}{(d^2 + r^2 \sin^2[\varphi])^2 \left\{ 1 - r \cos[\varphi] / H \right\}^{-2\alpha_z}}$$

$$\forall -\pi/N_{blades} < \varphi \leq +\pi/N_{blades}$$

where $U_{wind}^2(H)$ is the wind speed at hub height, α_z is the shear exponent in (52), a is the tower radius and \bar{d} is the weighted average of the distance of the blade to the tower axis when they are aligned:

$$\bar{d} = \frac{-2}{R_1^2 - R_0^2} \int_{R_0}^{R_1} x(r) r dr = \bar{d} + \frac{2(R_0^2 + R_0 R_1 + R_1^2) \sin[\gamma]}{3(R_0 + R_1)} \quad (721)$$

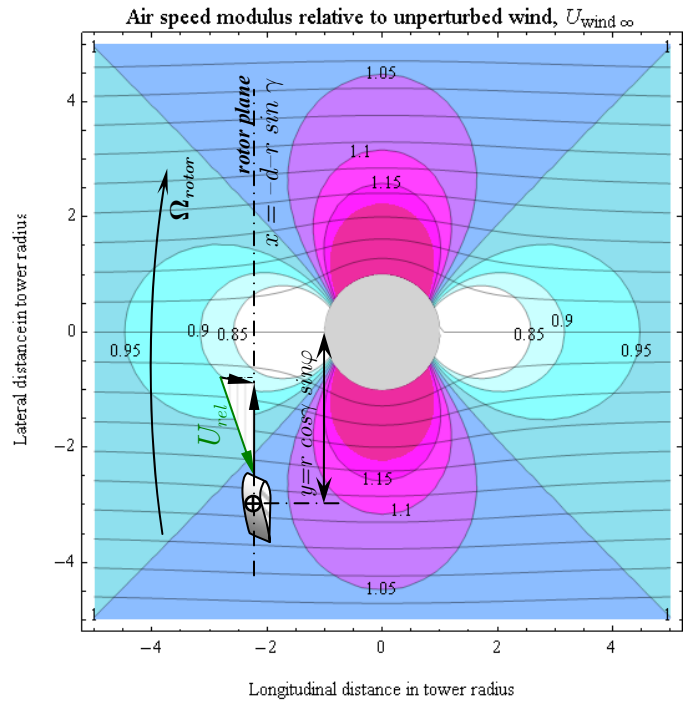


Fig. 303: Position of blade element near the tower. For details on relative wind speed composition, see Fig. 292.

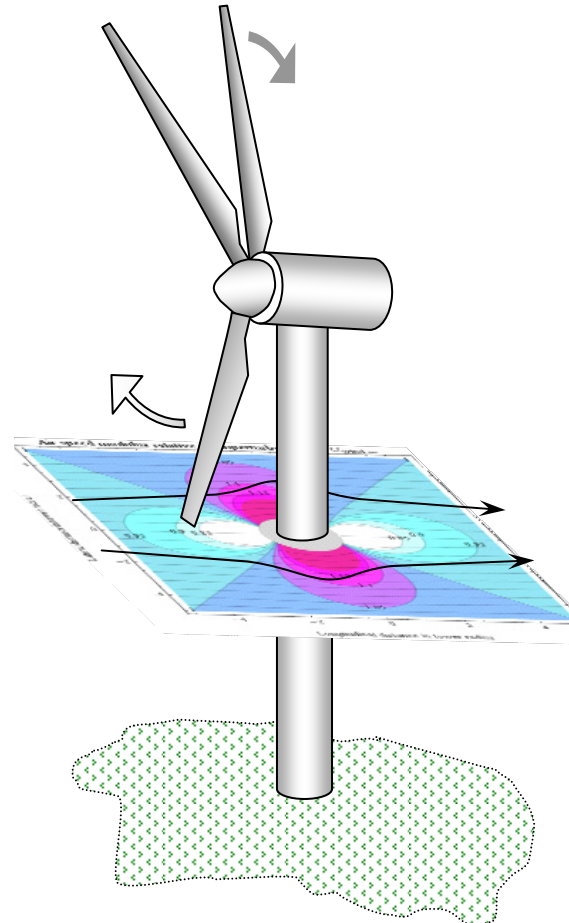


Fig. 304: 3-D representation of the wind field section.

In fact, (720) is a simplistic estimation of the wind field since the blade chord dimension is comparable with the tower radius, producing interactions between the tower and the blade.

C.4.1. Relative flow angle variation $\Delta\phi(\varphi)$ on the blade near the tower

The tower shadow effect only appears in the blade that is closer to the tower, which will be zero numbered for convenience (therefore, the rest of blades are numbered from 1 to $N_{blades}-1$). In this blade, the wind diverts slightly from the longitudinal direction in an angle $\phi_{wind} = \text{ArcTan}[U_y(z)/U_x(z)]$:

$$\phi_{wind}(x, y) = \text{ArcTan}\left(\frac{U_y(z)}{U_x(z)}\right) = \text{ArcTan}\left(\frac{2xy}{x^2 - \frac{(x^2+y^2)^2}{a^2} - y^2}\right) \quad (722)$$

The expression of the wind deflection in polar coordinates is straightforward applying the coordinate transformation in (717) to (719):

$$\phi_{wind}(\varphi, r) = \phi_{wind}(x = d - r \sin(\gamma), y = r \cos(\gamma) \sin(\varphi)) \quad (723)$$

The wind is not uniform and it varies for each element in modulo and direction. The weighted average of the wind deviation angle along the lowest blade at rotor position φ is

$$\langle \phi_{wind}(\varphi) \rangle = \frac{2}{R_1^2 - R_0^2} \int_{R_0}^{R_1} \phi_{wind}(\varphi, r) r dr \quad (724)$$

The integral in $\langle \phi_{wind}(\varphi) \rangle$ is not analytical (or at least, too complex to resolve for a generic case). It can be easily computed numerically –since the integrand is well behaved, simple numerical integration formulas such as the 3/8 Simpson's Rule are usually accurate enough, specially if integration errors are compared to errors introduced by assumptions made in this section–.

If a closed form is required, the wind angle deviation can be estimated using an average distance of the blade to the tower d' and the approximation $\text{ArcTan}(x) \approx x/(1+x^2) \approx x$ for small deviations and: (see Fig. 305 for accuracy comparison)

$$\langle \phi_{wind}(\varphi) \rangle \approx \frac{2ad' [f_3(b, \varphi) - f_3(c, \varphi)]}{\text{Sin}^2(\varphi) (R_1^2 - R_0^2) \sqrt{a^2 + 8d'^2}} \quad (725)$$

where:

$$f_3(x, \varphi) = x \left[\text{ArcTan}\left[\frac{2R_1 \text{Sin}(\varphi)}{x}\right] - \text{ArcTan}\left[\frac{2R_0 \text{Sin}(\varphi)}{x}\right] \right] \quad (726)$$

$$b = \sqrt{2(a^2 + 2d'^2) - 2a\sqrt{(a^2 + 8d'^2)}} \quad (727)$$

$$c = \sqrt{2(a^2 + 2d'^2) + 2a\sqrt{(a^2 + 8d'^2)}} \quad (728)$$

The original expression (724) –in solid red– and its approximation (725) –in solid lighter pink– are almost superposed in Fig. 305, indicating very good agreement of the approximation of $\phi_{wind}(\varphi)$. Thus, the approximation is a valid choice since its error is small comparing to the approximations made in aerodynamics.

The relative flow angles ϕ and ϕ' (with and without tower shadow) are depicted in Fig. 292 and Fig. 294. For clarity, both velocity triangles are compared in Fig. 306.

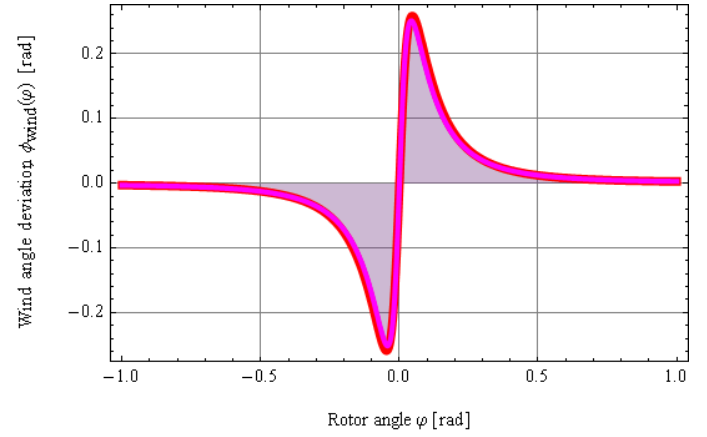
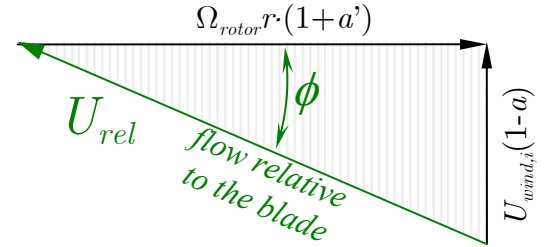


Fig. 305: Average wind angle deviation $\phi_{wind}(\varphi)$ at the blade crossing the tower computed with exact expression (724) and approximation (725) in a turbine with $R_0/R = 0.2$, $R_1/R = 0.95$, $a/R = 2/50$, $d/R = 4/50$, $\gamma = -0.02$ radians.

a) Flow relative to the blade without tower shadow.



b) Flow relative to the blade with tower shadow.

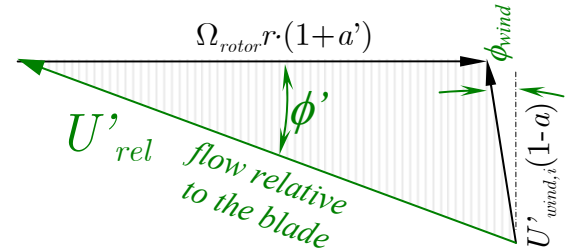


Fig. 306: Detail of velocities at the rotor plane with and without rotor shadow.

The difference in flow angle due to the presence of the tower can be estimated as:

$$\begin{aligned} \Delta\phi &= \phi' - \phi = \\ &= \text{ArcTan}\left(\frac{U'_{wind} \cos(\phi_{wind})(1-a)}{\Omega_{rotor} r (1+a') + U'_{wind} \sin(\phi_{wind})(1-a)}\right) - \\ &\quad - \text{ArcTan}\left(\frac{U_{wind}(1-a)}{\Omega_{rotor} r (1+a')}\right) \end{aligned} \quad (729)$$

The relative flow angles ϕ and ϕ' depends on axial and tangential induction factors, a and a' respectively, but they are close to zero. Thus, the difference in flow angle $\Delta\phi$ due to the presence of the tower can be estimated as:

$$\Delta\phi \approx \text{ArcCot}\left(\lambda''_{with\ tower}\right) - \text{ArcCot}\left(\lambda''_{without\ tower}\right) \quad (730)$$

where λ'' is the element speed ratio computed considering – formula (675)– or without considering –formula (671)– the wind flow deviation near the tower, ϕ_{wind} .

Then, the relative flow angle at element at radius r in blade $i=0$ (the blade near the tower) is $\phi'_{i=0} = \phi + \Delta\phi$. The rest of the blades has the conventional flow angle $\phi'_{i \neq 0}(r) = \phi = \text{ArcTan}(1/\lambda')$ computed from (671). Thus, the influence of tower shadow can be computed averaging the relative flow angle and speed tip ratio proportionally to the element position r and individual blade conditions for the blade that is closer to the tower. The average relative flow angle of the turbine $\langle \phi' \rangle$ is the average angle $\langle \phi \rangle$ plus the average equivalent deviation $\langle \Delta\phi(\varphi) \rangle$ on the blade near the tower:

$$\langle \phi' \rangle = \frac{2/N_{blades}}{R_1^2 - R_0^2} \sum_{i=0}^{N_{blades}-1} \int_{R_0}^{R_1} \phi'_i(r) r dr = \langle \phi \rangle + \frac{\langle \Delta\phi(\varphi) \rangle}{N_{blades}} \quad (731)$$

The effective attack angle deviation is $\Delta\alpha_{attack} \approx \Delta\phi$, the variation of the relative flow angle due to the presence of the tower. If the blades are stiff enough, the pitch θ (defined as the angle of the chord respect the rotor plane in Fig. 289) is constant independently of the relative flow angle ϕ . As can be seen in Fig. 306, the attack angle near the tower can be computed as the arc cotangent of λ' minus the pitch angle $\theta(r)$.

For a megawatt class turbine operating near the rated speed, the relative flow angle deviation, averaged along the rotor, is usually under a few degrees, as can be seen in Fig. 307.

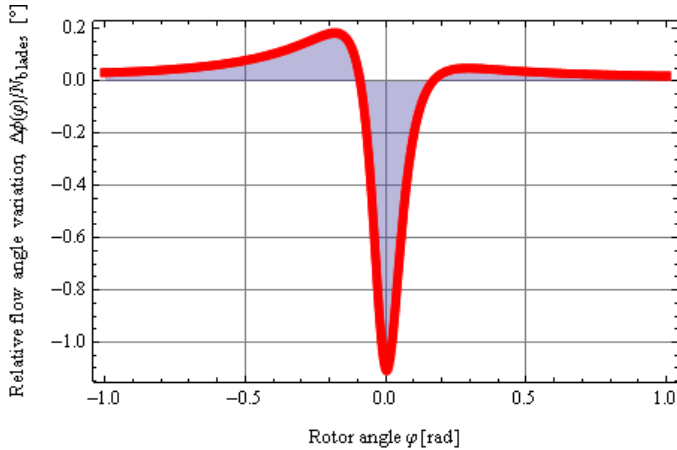


Fig. 307: Rotor-averaged relative flow angle variation $\Delta\phi(\varphi)$ in degrees computed from (729) for the operational conditions of Fig. 308.

C.4.2. Equivalent average squared inverse tip speed ratio $\langle \lambda_i'^2 \rangle$

The rotor torque in terms of average squared inverse tip speed ratio has been derived in (691)

$$T_{rotor} = \frac{1}{2} \rho_{air} \pi R^5 \Omega_{rotor}^2 \langle \lambda'^{-2} \rangle C_q \left(\frac{1}{\sqrt{\langle \lambda'^{-2} \rangle}}, \theta \right) \quad (732)$$

where $\langle \lambda'^{-2} \rangle$ is the arithmetic average among the blades.

$$\langle \lambda'^{-2} \rangle = \frac{1}{N_{blades}} \sum_{i=1}^{N_{blades}} \langle \lambda_i'^{-2} \rangle \quad (733)$$

Each blade i can be considered operating at an average squared inverse tip speed ratio $\langle \lambda_i'^2 \rangle$.

$$\langle \lambda_i'^{-2} \rangle = \frac{2}{(R_1^2 - R_0^2)} \int_{R_0}^{R_1} \frac{1}{\lambda_i'^2(r, \varphi)} r dr \quad (734)$$

where the effective tip speed ratio $\lambda_i'^2(r)$ has a specific formula in the blade in the lower position since it is affected by tower shadow

C.4.3. Equivalent average squared inverse tip speed ratio $\langle \lambda_i'^2 \rangle$ on the blades not affected by tower shadow

The effective tip speed ratio has been calculated before for the blades not affected by the tower shadow in (679):

$$\lambda_{i \neq 0}'(r, \varphi) = \frac{R \Omega_{rotor}}{U_{wind}(r, \varphi)} \quad (735)$$

The average of the squared inverse tip speed ratio for the blades not affected by the tower shadow $\langle \lambda_{i \neq 0}'^{-2} \rangle$ has been computed previously in (700) as:

$$\langle \lambda_{i \neq 0}'^{-2} \rangle = N_{blades} \frac{f_2(\varphi + 2\pi i/N_{blades})}{k_{shear}} \quad (736)$$

C.4.4. Equivalent average squared inverse tip speed ratio $\langle \lambda_i'^2 \rangle$ on the lowest blade

The effective tip speed ratio $\lambda_{i=0}'(r, \varphi)$ can be estimated analogously to (675) in the lowest blade (numbered as $i=0$) and as the conventional tip speed ratio (679) for the rest of the blades. Neglecting the induction factors in (677), $\lambda_{i=0}'(r, \varphi)$ is:

$$\begin{aligned} \lambda_{i=0}'(r, \varphi) &= R \frac{\Omega_{rotor} + U_{wind}(r, \varphi) \sin[\phi_{wind}(r, \varphi)]/r}{U_{wind}(r, \varphi) \cos[\phi_{wind}(r, \varphi)]} = \\ &= \frac{R \Omega_{rotor}}{U_x(r, \varphi)} + \frac{R}{r} \text{Tan}[\phi_{wind}(r, \varphi)] \quad \forall -\pi/2 < \varphi < \pi/2 \end{aligned} \quad (737)$$

where $U_x(r, \varphi)$ can be computed from (715) and (719) and $\text{Tan}[\phi_{wind}(r, \varphi)]$ can be estimated from (722).

The torque contribution in the lowest blade can be computed analogously to (674) and (682):

$$\begin{aligned} dT_{element} \approx \frac{1}{2} \rho_{air} \frac{2\pi R^5 \Omega_{rotor}^2 C_q(\lambda_{i=0}'(r, \varphi), \theta)}{N_{blades} (R_1^2 - R_0^2) \lambda_{i=0}'^2(r, \varphi)} r dr = \\ = \frac{1}{2} \rho_{air} \pi R^5 \Omega_{rotor}^2 \frac{2 C_q(\lambda_{i=0}'(r, \varphi), \theta)}{N_{blades} (R_1^2 - R_0^2)} f_4(r, \varphi) dr \end{aligned} \quad (738)$$

$$\text{where} \quad f_4(r, \varphi) = r \lambda_{i=0}'^{-2}(r, \varphi) \quad (739)$$

The average squared inverse tip speed ratio in the lowest blade is:

$$\langle \lambda_{i=0}'^{-2} \rangle = \frac{2}{(R_1^2 - R_0^2)} \int_{R_0}^{R_1} f_4(r, \varphi) dr \quad (740)$$

The integration of the function $f_4(r, \varphi)$ have not been obtained analytically and thus, the exact value of $\langle \lambda_{i=0}'^{-2} \rangle$ has not a closed form.

Since analytical approximations that have been tried produced lengthy expressions and may introduce errors, the numerical integration of $f_4(r)$ and the fit of a function with rotor angle is a suitable alternative to compute the torque

dependence on rotor angle. However, $\langle \lambda_{i=0}^{\prime-2} \rangle$ can be estimated with enough accuracy using a simple 3/8 Simpson's Rule since $f_4(r, \varphi)$ is a smooth function on r :

$$\langle \lambda_{i=0}^{\prime-2} \rangle \approx \quad (741)$$

$$\approx \frac{f_4(R_0, \varphi) + 3f_4\left(\frac{2R_0+R_1}{3}, \varphi\right) + 3f_4\left(\frac{R_0+2R_1}{3}, \varphi\right) + f_4(R_1, \varphi)}{4(R_1 + R_0)}$$

Since the wind deflection angle $\phi_{wind}(r, \varphi)$ is relatively small at usual blade positions, $\phi_{wind}(r, \varphi) \sim \langle \phi_{wind}(\varphi) \rangle$. The lateral component of the wind can be negligible compared to the blade element speed, specially far from the blade root, $r \Omega_{rotor} \gg U_{wind}(r, \varphi) \sin[\phi_{wind,i}(r, \varphi)]$ for $r > R_0$. Under these assumptions, the effective tip speed ratio $\lambda'_i(r)$ is somewhat proportional to the conventional tip speed ratio $\lambda_i(r)$:

$$\lambda'_{i=0}(r, \varphi) \approx \frac{R \Omega_{rotor} + \langle U_{wind}(\varphi) \rangle \sin[\langle \phi_{wind}(\varphi) \rangle]}{U_{wind}(r, \varphi) \cos[\langle \phi_{wind}(\varphi) \rangle]} \quad (742)$$

Provided $\phi_{wind}(\varphi, r) \approx \langle \phi_{wind}(\varphi) \rangle$, the integral in $\langle \lambda_{i=0}^{\prime-2} \rangle$ can be computed analytically:

$$\langle \lambda_{i=0}^{\prime-2} \rangle = \frac{2}{(R_1^2 - R_0^2)} \int_{R_0}^{R_1} f_4(r) dr \approx \quad (743)$$

$$\approx \frac{N_{blades} f_2(\varphi)}{k_{shear} \cos[\langle \phi_{wind}(\varphi) \rangle]} \left\{ 1 + \frac{\langle U_{wind,i}(\varphi) \rangle \sin[\langle \phi_{wind}(\varphi) \rangle]}{\Omega_{rotor} R} \right\}^{-2} \cdot \left\{ 1 + \frac{2a^2(a^2 - 4d^2)}{d^2(R_0^2 - R_1^2)} [f_5(R_0) - f_5(R_1)] + \frac{2a^2 \text{Csc}^2(\varphi)}{(R_0^2 - R_1^2)} L_n \left[\frac{R_0^2 f_5(R_1)}{R_1^2 f_5(R_0)} \right] \right\}$$

$$\text{where } f_5(x) = \frac{1}{1 - \text{Cos}[2\varphi] + 2d^2/x^2} \quad \forall -\pi/2 < \varphi < \pi/2 \quad (744)$$

Thus, $\langle \lambda_{i=0}^{\prime-2} \rangle$ can be estimated as $\langle \lambda_{i \neq 0}^{\prime-2} \rangle$ in (736) multiplied by a correcting factor –to account tower shadow– which depends on average wind angle and average wind speed at blade angle φ :

$$\langle \lambda_{i=0}^{\prime-2} \rangle \sim \quad (745)$$

$$\sim \langle \lambda_{i \neq 0}^{\prime-2} \rangle \cos^2[\langle \phi_{wind}(\varphi) \rangle] \left\{ 1 + \frac{\langle U_{wind}(\varphi) \rangle \sin[\langle \phi_{wind}(\varphi) \rangle]}{\Omega_{rotor} R} \right\}^{-2}$$

C.4.5. Comparison of the accuracy of the approximate analytical formulas

The computation of $\langle \lambda^{\prime-2} \rangle$ is shown in Fig. 308 for the original numerical integral (734) and its analytical approximations. The approximation with the Simpson's 3/8 rule (741) is completely superimposed in dotted pink and it cannot be distinguished from the original numerical integral in solid red. The approximation considering the wind flow angle constant along the blade in (743), i.e. $\phi_{wind}(\varphi, r) \approx \langle \phi_{wind}(\varphi) \rangle$, shows some deviation just exiting the tower influence (dashed deep blue line in Fig. 308).

In sum, the Simpson's 3/8 rule (741) is an accurate approximation that makes unnecessary the application of

more complex numerical integration in (740). In control schemes, uncoupling wind deviation $\phi_{wind}(\varphi)$ and the tip speed ratio can be quite convenient. In such cases, the approximation (743) can be valuable.

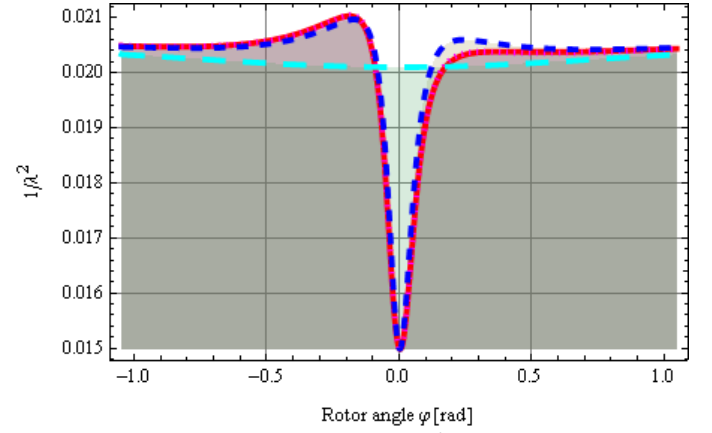


Fig. 308: Inverse squared blade tip ratio $\lambda^2(\varphi)$ computed with exact expression (734) and its analytical approximations: (741) –completely superimposed in dotted pink– and (743) –in dashed blue–. In light blue is λ^2 without considering tower shadow (700). Turbine with $U_{wind}(H) = 10$ m/s, $R = 50$ m, $H/R = 2$, $R_0/R = 0.2$, $R_1/R = 0.95$, $d/R = 2/50$, $d/R = 4/50$, $\gamma = -0.02$ rad, $N_{blades} = 3$, $\alpha_z = 0.2$, $\lambda_H = 7$.

C.4.6. Comparison of the aerodynamic torque accuracy from the approximate models

Using the Simpson 3/8 model presented in previous section and (691), the torque in the slow shaft of a 1500 kW wind turbine with blades LM 40.3 has been computed in Fig. 309. The torque has been computed according to (732) with $\rho_{air} = 1.2$ kg/m³, pitch $\theta = 0^\circ$ and the same conditions than in Fig. 308.

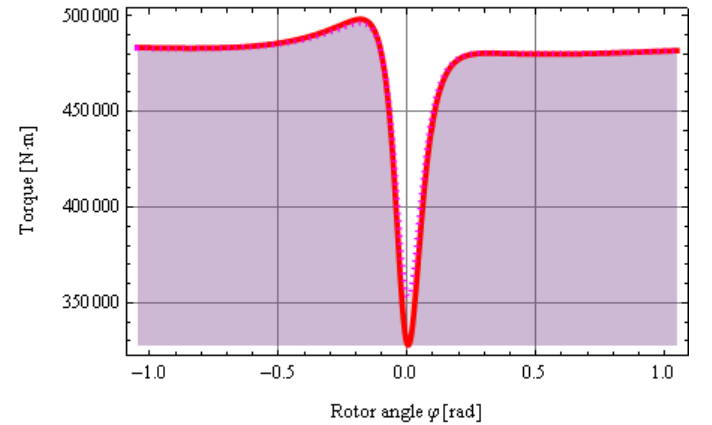


Fig. 309: Aerodynamic torque in a 1500 kW wind turbine corresponding to the parameters of Fig. 308 (near rated wind speed: $U_{wind}(H) = 10$ m/s, $\lambda_H = 7$ and pitch $\theta = 0^\circ$). The dashed line, $\lambda^2(\varphi)$ multiplied by a factor, has been added to show that fluctuations are mostly proportional below rated wind speed.

At partial load, $C_q(\theta, \lambda)$ varies moderately and torque fluctuations are mainly proportional to $\langle \lambda^{\prime-2} \rangle$ (compare Fig. 308 and Fig. 309). At full load, torque coefficient is more sensible to the attack angle and the variations of $\lambda^2(\varphi)$ are amplified in torque (see Fig. 310).

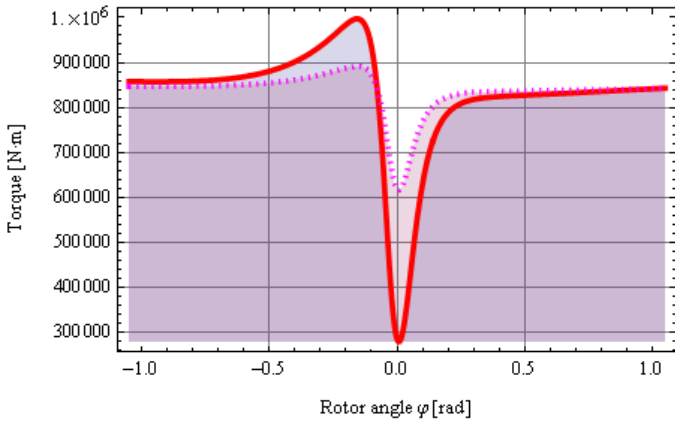


Fig. 310: Aerodynamic torque in a 1500 kW wind turbine corresponding to the parameters of Fig. 308 but near cut-off speed: $U_{wind}(H) = 20$ m/s, $\lambda_H = 3,58$ and pitch $\theta = 19,5^\circ$. The dashed line is $\lambda^2(\varphi)$ multiplied by a factor to show that torque fluctuations are not proportional to $\lambda^2(\varphi)$ at full load.

The greatest torque variations happen at high winds since the torque coefficient is quite sensitive to tip speed ratio λ variations at that operational conditions (see Fig. 301).

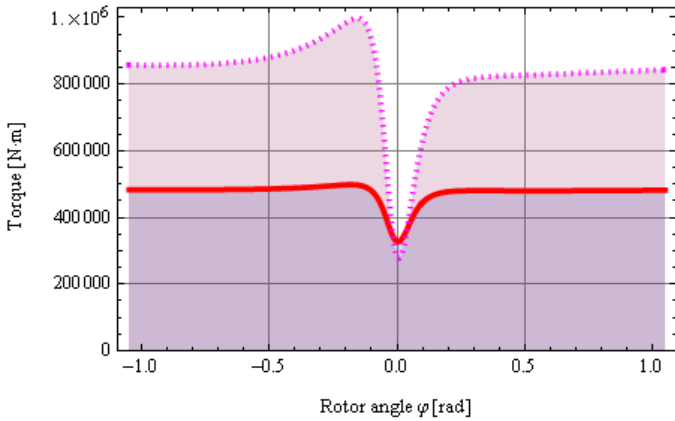


Fig. 311: Aerodynamic torque in a 1500 kW wind turbine corresponding to the parameters of Fig. 308 computed near rated wind speed (solid line: $U_{wind}(H) = 10$ m/s, $\lambda_H = 7$ and pitch $\theta = 0^\circ$ corresponding to Fig. 309) and at cut-off wind speed (dashed line: $U_{wind}(H) = 20$ m/s, $\lambda_H = 3,58$ and pitch $\theta = 19,5^\circ$ corresponding to Fig. 310).

C.5. Tower lateral and longitudinal bending oscillations

The combination of the structural flexibility of the tower and blades, tower shadow, wind shear and the stochastic character of the wind can lead to the excitation of the turbine vibration modes (see Fig. 312). The estimation of the magnitude of these oscillations is out of the scope of this work.

In general, these vibrations do not show a significant angular dependence on rotor angle. The first vibrational mode of the turbine corresponds to tower bending. These oscillations can be important, especially in floating offshore wind turbines.

C.5.1. Tower longitudinal bending

The backwards and forwards displacement of the nacelle produce a modulation of the equivalent lateral wind $\Delta U_{wind, longitudinal bending}$ of rms value σ_{\leftrightarrow} . If the nacelle

experience a displacement of typical amplitude Δx and typical tower resonance frequency f_{\leftrightarrow} (for usual values see table 12.25 in [88] –in the range of a fraction of the blade frequency f_{blade} –), then the equivalent wind speed modulation can be characterized by its rms value σ_{\leftrightarrow} , its average frequency f_{\leftrightarrow} and its frequency bandwidth BW_{\leftrightarrow} .

$$\sigma_{\leftrightarrow} = \frac{2\pi f_{\leftrightarrow} \Delta x}{\sqrt{2}} \quad (746)$$

Tower bending can be included as an additional contribution to the equivalent wind:

$$\Delta PSD_{\leftrightarrow}[f, \sigma_{\leftrightarrow}, f_{\leftrightarrow}, BW_{\leftrightarrow}] = \frac{2 BW_{\leftrightarrow} f^2 \sigma_{\leftrightarrow}^2 / \pi}{BW_{\leftrightarrow}^2 f^2 + (f^2 - f_{\leftrightarrow}^2)^2} \quad (747)$$

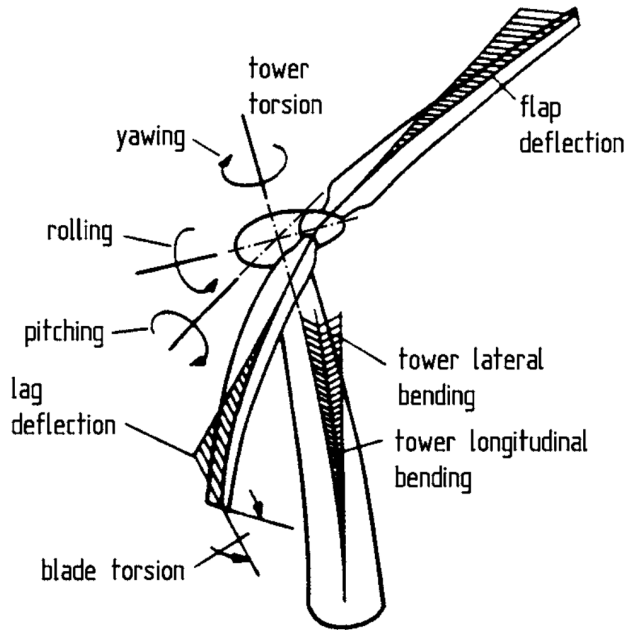


Fig. 312: Exciting forces and degrees of vibrational freedom of a wind turbine. From F. Kießling [399], page 24.

C.5.2. Tower lateral bending

Thiringer [186] studied the sideways movement of the nacelle in the turbines of the Alsvik offshore wind farm. He obtained a good agreement between the angular deflection of the cantilevered beam and the power modulation. This correlation depends on the generator torque characteristics and Thiringer assumed that it is due to the angular movement of the stator. Since the housing of the generator is solidly attached to the nacelle, the angular deflection can be accounted as a noise added to the generator rotor angle, referred to the stator.

Notice that these vibrations also affects to the wind speed that experience the blade elements and thus, rotor torque. Lateral bending can be included in expression (747), eventhough their interaction nature and the sensitivity of the torque to tower oscillations depends on the direction. Thus, the totalized effective oscillation value $\sigma'_{\leftrightarrow}$ and bandwidth BW'_{\leftrightarrow} must be estimated accordingly.

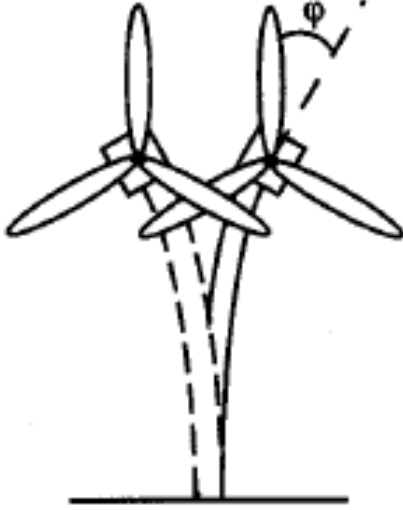


Fig. 313: Sideways oscillation of the tower. Reproduced from Thiringer [186].

C.6. Numerical integration of rotor torque

C.6.1. Turbine aligned with the wind

In previous section, a detailed parametric model has been derived based on the effective blade tip speed ratio λ' . This model is aimed to study general properties, assuming power or torque coefficients are smooth enough for the range of variation of λ' . But if the turbine is operating at a point where $C_q(\lambda, \theta)$ varies abruptly, the assumption (689) introduces a small error.

Despite λ'_i is near its nominal value λ_H (705) in the blades not affected by tower shadow ($i \neq 0$), it can differ notably in a blade crossing the tower (blade numbered as $i = 0$). Since λ'_i can vary significantly from blade to blade or the blades can be slightly misaligned (i.e., pitch θ is not exactly the same for all blades), the torque can be computed individually for each blade i in order to decrease the error introduced by the nonlinearities in $C_q(\lambda, \theta)$. Thus, the torque in the blade i can be estimated as:

$$T_i \approx \frac{1}{2} \rho_{air} \pi R^5 \Omega_{rotor}^2 \frac{\langle \lambda_i'^{-2} \rangle}{N_{blades}} C_q \left(\frac{1}{\sqrt{\langle \lambda_i'^{-2} \rangle}}, \theta \right) \quad (748)$$

where $\langle \lambda_{i=0}'^{-2} \rangle$ is computed from (741) for the lowest blade and $\langle \lambda_{i \neq 0}'^{-2} \rangle$ is computed from (736) for the blades not affected by tower shadow.

The torque accuracy can be increased furthermore integrating directly the blade element torque (summing the contributions along the effective blade span):

$$T_i \approx \int_{R_0}^{R_1} dT_{element} \underset{\text{uniform loading}}{=} \frac{1}{2} \rho_{air} \pi R^5 \Omega_{rotor}^2 \int_{R_0}^{R_1} f_6(r, \varphi) dr \quad (749)$$

If φ is the angle of the lowest blade ($i = 0$), then $\lambda'_{i=0}(r, \varphi)$ should be computed from (737) to take into account tower shadow:

$$f_{6,i=0}(r, \varphi) = \frac{2r}{N_{blades}(R_1^2 - R_0^2)} \frac{C_q(\lambda'_{i=0}(r, \varphi), \theta)}{\lambda'_{i=0}(r, \varphi)} \quad (750)$$

The rest of the blades ($i \neq 0$) do not experience tower shadow and $\lambda'_{i=0}(r, \varphi)$ is substituted in (750) for $\lambda'_{i \neq 0}(r, \varphi + 2\pi i / N_{blades})$ computed from (735) in f_6 :

$$f_{6,i \neq 0}(r, \varphi) = \frac{2r}{N_{blades}(R_1^2 - R_0^2)} \frac{C_q \left[\lambda'_{i \neq 0}(r, \varphi + \frac{2\pi i}{N_{blades}}), \theta \right]}{\lambda'_{i \neq 0}(r, \varphi + \frac{2\pi i}{N_{blades}})} \quad (751)$$

Since $C_q(\lambda, \theta)$ do not have a simple analytical form, the integral (749) cannot be computed analytically. However, the integral (749) is well behaved and it can be computed numerically with simple methods such as the 3/8 Simpson's Rule:

$$T_i \approx \frac{1}{2} \rho_{air} \pi R^5 \Omega_{rotor}^2 \quad (752)$$

$$\frac{f_6(R_0, \varphi) + 3f_6\left(\frac{2R_0 + R_1}{3}, \varphi\right) + 3f_6\left(\frac{R_0 + 2R_1}{3}, \varphi\right) + f_6(R_1, \varphi)}{8 / (R_1 - R_0)}$$

The numerical calculation of the torque in (752) is a good tradeoff of accuracy and simplicity, allowing the consideration of tower shadow and blade misalignment in simulations with a low footprint in simulation time. The integration error is small compared to errors introduced by assumptions made in this section and compared to the uncertainty of torque (or power) coefficient.

Finally, the rotor torque is the sum of the contribution of each blade plus the vibrations which have not been accounted previously ($T_{vibrations}$ are due mainly to tower, blade and drivetrain vibrations and it can be estimated from measurements or structural simulations):

$$T_{rotor} = T_{vibrations} + \sum_{i=0}^{N_{blades}-1} T_i \quad (753)$$

The shear and tower shadow effects in pitch regulated turbines increases at full generation due to the bigger torque coefficient sensitivity and the blade flap-wise bending. Fig. 314 shows an example of the influence of tower shadow on the rotor torque at two wind speeds.

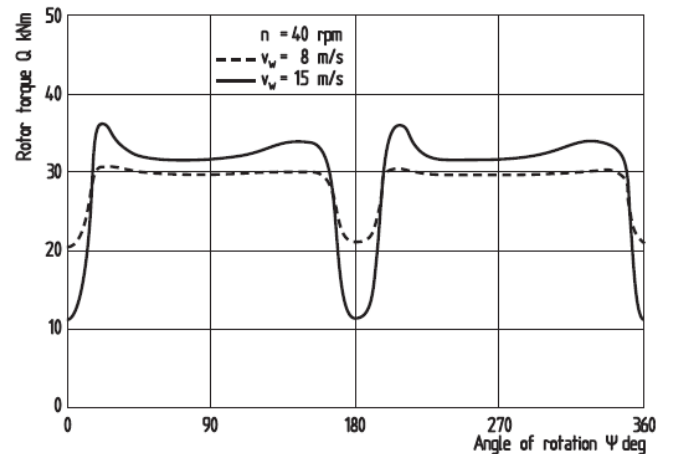


Fig. 314: Influence of tower shadow on the rotor torque at the example of the experimental MOD-0 two-bladed wind turbine. Taken from Hau [88] (originally from [400]).

C.6.2. Turbine misaligned with respect average wind direction

The effective blade tip speed ratio $\lambda'_{i=0}(r, \varphi)$ can be estimated analogously to (675) in the lower blade ($i=0$) and

with the conventional expression (679) in the rest of the blades. Neglecting the induction factors in the (677), $\lambda'_{i=0}(r, \varphi)$ can be estimated as:

$$\begin{aligned} \lambda'_{i=0}(r, \varphi) &= \\ &= \frac{R r \Omega_{rotor} + U_{wind}(r, \varphi) \sin[\phi_{wind}(r, \varphi) + \phi_{misalign}] \cos[\varphi]}{r U_{wind}(r, \varphi) \cos[\phi_{wind}(r, \varphi) + \phi_{misalign}]} = \\ &= \frac{R \Omega_{rotor}}{U_{wind}(r, \varphi)} \sec[\phi_{wind}(r, \varphi) + \phi_{misalign}] + \\ &\quad + \frac{R}{r} \tan[\phi_{wind}(r, \varphi) + \phi_{misalign}] \cos[\varphi] \quad (754) \\ &\quad \forall -\pi/2 < \varphi < \pi/2 \end{aligned}$$

The longitudinal component of the wind $U_{wind}(r, \varphi)$ can be computed from (715) and (719). The incident flow angle due to tower shadow $\phi_{wind}(r, \varphi)$ can be estimated from (722). $\phi_{misalign}$ is the yaw orientation error of the turbine and φ is the blade angle respect the tower axis.

The unperturbed effective blade tip speed ratio has been computed previously in (679):

$$\lambda'_{i=0}(r, \varphi) = \frac{R \Omega_{rotor}}{U_{wind}(r, \varphi)} \sec[\phi_{misalign}] + \frac{R}{r} \tan[\phi_{misalign}] \cos[\varphi] \quad (755)$$

Conclusions

This annex has introduced an aerodynamic model to estimate the influence of deterministic wind component (wind shear and tower shadow) from the torque coefficient and the main properties geometry of the turbine. The model has been

derived using blade element theory, potential flow upstream the tower and uniform blade loading.

The model presented in this annex is based on blade element theory with constant tangent force distribution, also known as uniform blade loading. The tangential force distribution is approximately constant in the main body of the blade when the turbine operates at partial load (maximum turbine efficiency), but may introduce errors when the tip of the blades stalls. However, the starting of the blade stall is intricate and a more complex model is needed to take into account the hysteresis of the separation of the boundary layer in the blades. Since pitch controlled turbine is unusually operating with attached flux and the proposed method is valid for pitch controlled turbines.

The aim of this model is to compute the aerodynamic torque at the low-speed shaft, simply enough to be included in the generator control or for simulating a cluster of turbines, and requiring only basic features such as the aerodynamic torque coefficient and the main constructive parameters of the turbine. This model can also be used to study the effect of mismatches in the blades (pitch errors in each blade) and errors in orientation of the turbine.

Besides its computational efficiency, another advantage of this method is that only requires the torque coefficient and the main dimensions of the turbine (it does not need to know the airfoil section along blades).

Annex D: Wake estimation in an offshore wind farm

D.1. Introduction

The wake is estimated in this document using a kinematic model. Kinematic models are based on self-similar velocity deficit profiles obtained from experimental and theoretical work on co-flowing jets.

A very good overview on turbine wakes can be found in [401]. The wake kinematic model can be revised in [402]. The Risø report [403] summarize the experience in Horns Rev and Nysted offshore wind farms. The impact of wakes in turbine power output is analyzed in [404] and [405]. A friendly outline of the effect of turbulence and wakes in the farm output can be found in [406].

The wake expansion rate depends greatly on atmospheric conditions (stable, neutral or unstable atmosphere and turbulence) and the expansion rate is an input of the program. The factors influencing the expansion are not considered in this work and the user is expected to vary expansion rates to simulate different atmospheric conditions. Default values of the expansion rates are estimated from Horns Rev and Nysted offshore wind farms.

D.2. Momentum deficit in a wake

The wind deficit in a wake can be estimate from the longitudinal force experienced by the turbine, called thrust force F_T . There is a momentum transfer F_T from the wind flow to the turbine (see Fig. 315). The thrust force F_T that experiment a wind turbine may be expressed as:

$$F_T = \frac{1}{2} \rho_{air} \pi R^2 U_{wind}^2 C_T \quad (756)$$

where ρ_{air} is the density of air, πR^2 is the total area swept by the rotor, U_{wind} is the original upstream wind speed and C_T is the trust force coefficient.

The initial wind speed reduction ΔU_{wind} from U_{wind} to V , when passing the rotor plane, is related to C_T by: $(1 - C_T) = (V/U_{wind})^2$.

The momentum deficit in the control volume equals the momentum loss. However, when the wake is well developed, the speed deficit ΔU_{wind} varies smoothly downwards due to

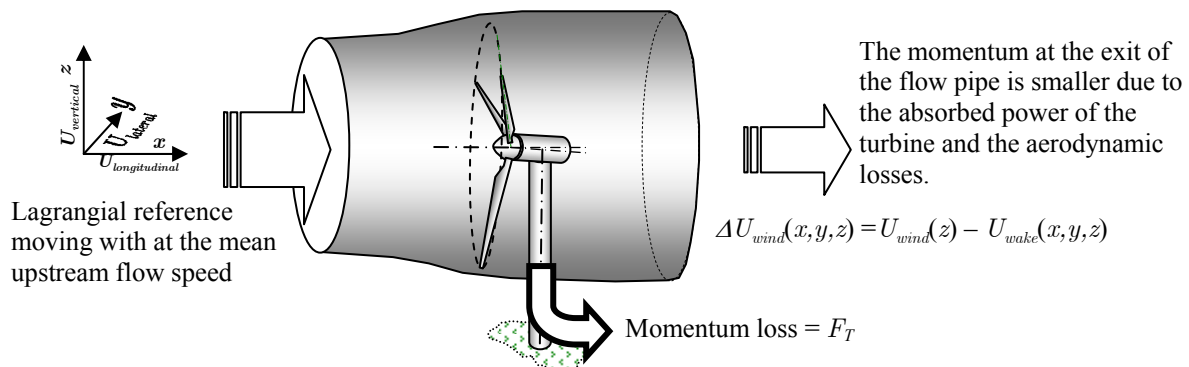


Fig. 315: Momentum balance in a flow tube of the disk actuator.

turbulence mixing and diffusion processes (see [407] for more details). In the far wake, the control volume can be extended in the lateral and vertical dimensions. Fig. 320 shows the axis reference used in this document.

The following relations can be obtained from the actuator disk model (Fig. 316), where a is the axial induction factor of the disk actuator:

$$C_{thrust} = \frac{ThrustForce}{DynamicForce} = \frac{\frac{1}{2} \rho \pi R^2 U_{\infty}^2 [4a(1-a)]}{\frac{1}{2} \rho \pi R^2 U_{\infty}^2} \quad (757)$$

$$C_{thrust} = 4a(1-a) \quad (758)$$

$$C_{power} = \frac{TurbinePower}{CineticPower} = \frac{TurbinePower}{\frac{1}{2} \rho \pi R^2 U_{\infty}^3} = 4a(1-a)^2 \quad (759)$$

$$\frac{C_{power}}{C_{thrust}} = 1 - a \quad (760)$$

Maximum turbine efficiency is achieved with $a = 1/3$

$$C_{thrust} \sim \frac{2}{3} C_{power} = \frac{TurbinePower}{3 \rho \pi R^2 U_{\infty}^3 \eta_{turbine}} = 1 - a \quad (761)$$

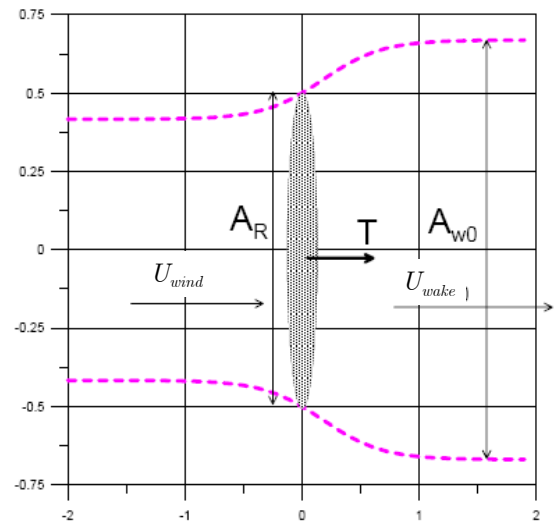


Fig. 316: Near field flow around a turbine rotor modelled as an actuator disk.

The thrust force coefficient depends on the control strategy

for the wind turbine. The control strategy for wind velocities below the rated wind speed is to control the rotational speed of the rotor in order to achieve maximum power, while the control strategy above the rated wind speed is to achieve constant power. The latter is usually obtained by rotor blade pitch control.

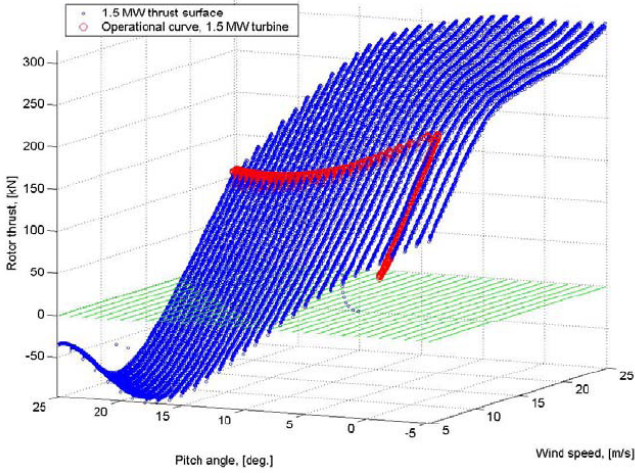


Fig. 317: Thrust development of a 1.5 MW rotor depending on wind speed and pitch angle, rotational velocity 1.93 rad/s (blue), deterministic winds. Normal turbine operation is shown as red line. Taken from A. Knauer [408].

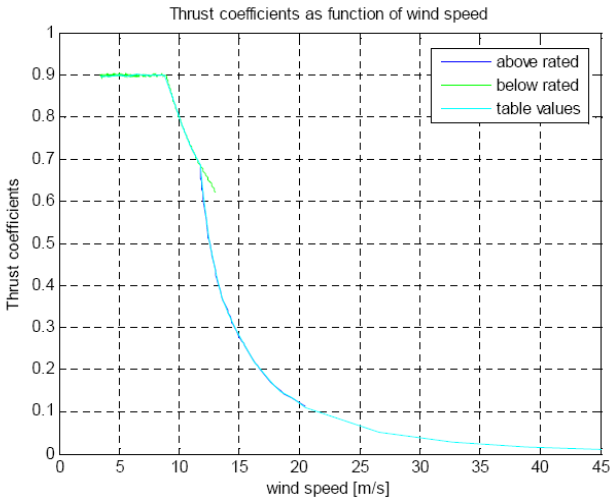


Fig. 318: Plot of a thrust force coefficient lookup table. Taken from Knauer [408].

The velocity dependent thrust coefficient C_T is based on the thrust force relations such as shown in Fig. 317 (taken from [408]). Typical tabulated thrust force coefficients are shown in Fig. 318. The table lookup may be based on the

instantaneous relative wind speed.

The wind shear introduces a momentum transfer from the flow to the sea. This effect is usually accounted separately in the wind vertical profile.

The real wind flow is approximated in this program as the superposition of the unperturbed flow and the wake deficit. The wake deficit can be estimated computing the momentum transfer in the flow tube of the disk actuator moving in longitudinal direction at speed U_{wind} .

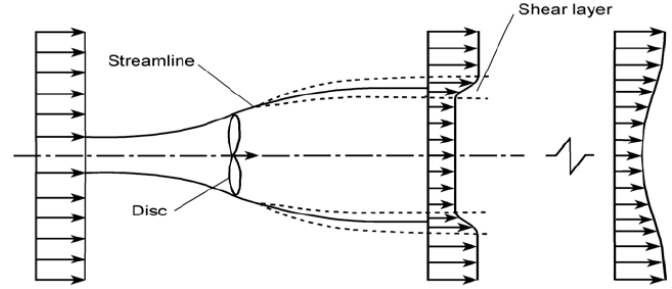


Fig. 319: Simplified representation of the wind turbine wake. Taken from A. Jiménez [407].

If the shape of the wake is known, the speed deficit can be estimated applying the momentum balance to a control volume limited by two transversal semi planes (upstream and downstream planes) and the sea. Since the control volume is moving at a constant speed U_{wind} the momentum change is due to the mass flow rate in the downstream semi plane.

$$\begin{aligned} \text{Momentum deficit} &= F_T = \\ &= \int_{\text{upstream}} U_{wind} d(\text{mass}) - \int_{\text{downstream}} U_{wake} d(\text{mass}') \end{aligned} \quad (762)$$

If the area integrals are expressed in Cartesian coordinates, the following relation is obtained:

$$F_T \approx \rho_{air} \int_{-\infty < y < +\infty} \int_{0 < z < +\infty}^{x=\text{constant}} [U_{wind}^2(z) - U_{wake}^2(x, y, z)] dy dz \quad (763)$$

If the vertical profile of the unperturbed wind is neglected, $U_{wind}(z) \approx U_{wind}(H) = \text{constant}$, the following relation is obtained:

$$\frac{1}{2} \pi R^2 C_T \approx \int_{-\infty < y < +\infty} \int_{0 < z < +\infty}^{x=\text{constant}} \left[1 - \frac{U_{wake}^2(x, y, z)}{U_{wind}^2(z)} \right] dy dz \quad (764)$$

If the shape of the wake deficit can be guessed from measured or from fluid mechanic models, then the relative momentum deficit $\delta(x, y, z)$ can be expressed as the shape

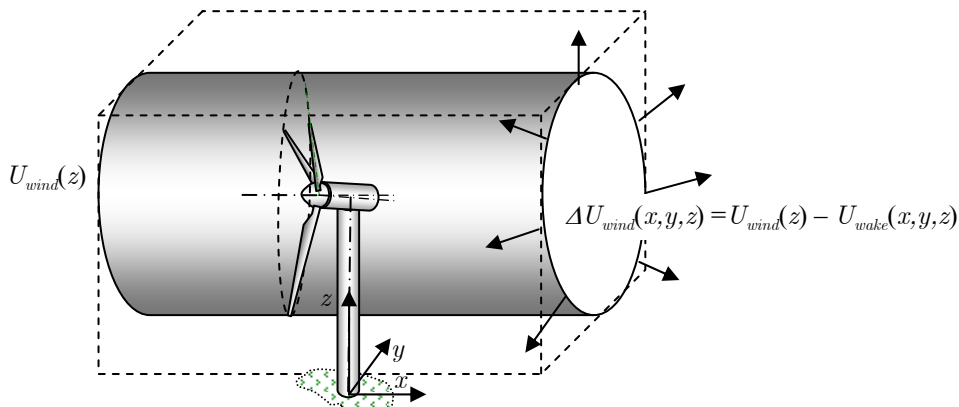


Fig. 320: Expansion of the control volume up to two vertical semi-planes.

function $\phi(x, y, z)$ multiplied by the magnitude factor $k_{\Delta U_{wind}}$:

$$\delta(x, y, z) \equiv 1 - \frac{U_{wake}^2(x, y, z)}{U_{wind}^2(z)} = k_{\Delta U_{wind}} \phi(x, y, z) \quad (765)$$

If the shape function is chosen with unitary weight in any vertical plane, $\int_{-\infty < y < +\infty} \int_{0 < z < +\infty} \phi(x, y, z) dy dz = 1$, then the magnitude factor is:

$$k_{\Delta U_{wind}} = \frac{\pi R^2 C_T / 2}{\int_{-\infty < y < +\infty} \int_{0 < z < +\infty} \phi(x, y, z) dy dz} = \frac{1}{2} \pi R^2 C_T \quad (766)$$

Two key parameters of the wake cross section shape are the mean position and its extent. For example, $\phi(x, y, z)$ can be any bivariate probability density function in the y and z variables, where the wake center and extent is the distribution mean and standard deviation.

Laboratory test show that shape of the far wakes is a smooth perturbation (see [401] for example) and they can be approximated by bivariate Gaussians [402, 409]. Since the bivariate normal is curtailed to positive heights y (heights above the sea surface), the scale function is:

$$\phi(x, y, z) = \begin{cases} \frac{e^{-\frac{y^2}{2\sigma_y^2} - \frac{(H-z)^2}{2\sigma_z^2}}}{\pi\sigma_y\sigma_z \left(1 + \operatorname{Erf}\left[\frac{H}{\sqrt{2}\sigma_z}\right]\right)} & \forall x > 0 \text{ (turbine downstream)} \\ 0 & \forall x \leq 0 \text{ (turbine upstream)} \end{cases} \quad (767)$$

where H is the height of the maximum wind deficit (it can be approximately considered the mean height of the wake). The lateral extent of the wake cross section is parameterized by the horizontal standard deviation σ_y and the vertical extent of the wake is σ_z . The parameters of the wake cross section depend on the distance x from the turbine. For downstream points far away the wake ($y \gg \sigma_y$ or $H - z \gg \sigma_z$), the bivariate can be considered null to speed up the calculi.

The height of the wake H increases very slightly far away the turbine due to the sea surface (see Fig. 38, 41 and 42 in [401]). Therefore, H can be considered constant and equal to the hub height. If wind speed is only computed at hub height, the calculi can be speeded further up.

The horizontal extent σ_y is expected to be bigger than the vertical extent σ_z , specially in highly stratified atmospheric flow and low turbulence conditions. In absence of detailed

data or other evidence, the wake is customarily considered with rotational symmetry ($\sigma_y \approx \sigma_z$). Moreover, the wake extent will be considered proportional to the distance to the turbine in laminar flow, or equivalently, when diffusion is controlled by a constant ambient turbulent diffusivity.

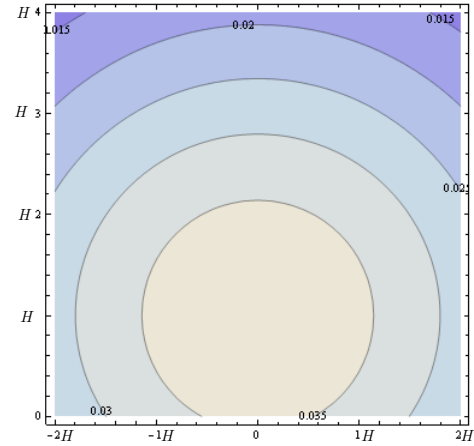


Fig. 321: Wake cross section shape $\phi(x, y, z)$ for $\sigma_y = \sigma_z = 2,5 H$.

The former assumptions are consistent with the computer program WAsP [410], where wakes are considered as truncated cones. The recommended expansion rate in WAsP for offshore applications is $tg(\alpha) = 0.04$, almost half the usual value for on land farms.

The wake cross section (767) presents a smooth transition instead a sharp transition. In the absence of more details, the mean quadratic radius $\langle r^2 \rangle$ of the rotor disk and the wake is expected to match at the turbine ($x = 0$):

$$\begin{aligned} \langle r_{rotor\ disk}^2 \rangle &= \int_0^R r^2 \frac{2\pi r}{\pi R^2} d\rho = \frac{R^2}{2} \\ \langle r_{wake, x=0}^2 \rangle &= \int_{-\infty < y < +\infty} \int_{0 < z < +\infty} [y^2 + (z - H)^2] \phi(x, y, z) dy dz = 2\sigma^2 \end{aligned} \quad (768)$$

Note: This criterion yields the same mass moment of inertia respect the wake axis for the disk and the wake.

Therefore the extent parameter is $\sigma(x=0) = R/2$ at the turbine and then, it increases linearly downstream:

$$\sigma(x) = R/2 + x tg(\alpha) \quad (769)$$

When there are many turbines in a line, it has been observed experimentally that while the first turbine produces full power, there is a significant decrease of power in the second turbine, with practically no further loss in successive machines [401, 403]. The wake expansion rate depends on inflow turbulence, being significantly bigger in the successive

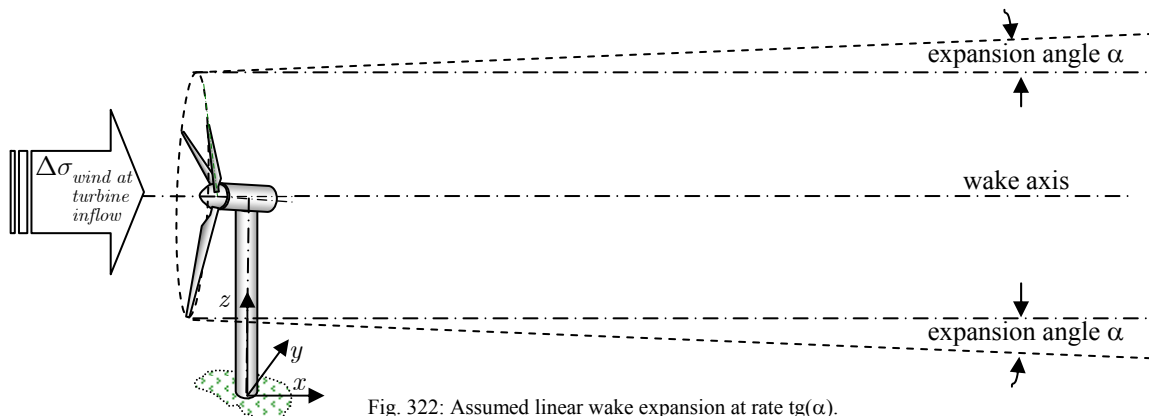


Fig. 322: Assumed linear wake expansion at rate $tg(\alpha)$.

turbines. This can be accounted adding a sensitivity factor in the extent parameter:

$$(770)$$

$$\sigma'(x) = R/2 + x \left[tg(\alpha) + \beta (TurbInt_{wind \text{ at turbine}} - TurbInt_{unperturbed \text{ wind}}) \right]$$

where $TurbInt_{wind \text{ at turbine}} - TurbInt_{unperturbed \text{ wind}}$ is the added turbulence intensity at the turbine inflow and β is the sensitivity factor of the expansion rate respect the turbulence at the inflow.

D.2.1. Model fit to experimental measures

The wake behaviour is complex and it has subjected to many experimental tests (a summary of them can be read in [401]). The wakes at the sea show some distinctive behaviour since the atmosphere shows often lower turbulence and higher stability than inland locations. The UPWIND project [403] studied the offshore wakes in the Horns Rev and Nysed wind farms.

The offshore wind farm at Horns Rev is characterized with low turbulence (<8 %) and many operational hours in near neutral stability [411], implying very small expansion rates (long and narrow wakes). The turbines operating in full wake at 7 diameters distance from upwind turbines experience about 40% power loss at low winds. The major findings are an almost constant deficit at low winds in turbines operating in cascaded wakes. This can be due to an extra expansion when a wake crosses another turbine rotor due to the near-field stream-line expansion occurring here. However, these refinements are not considered in the program.

The Vindeby wind farm is modelled in [412] in the framework of the ENDOW project [413]. The turbulence intensity usually lies between 6% and 8% in the free flow.

Actual wake deficit measures can be transformed into wake extent σ evolution downstream. The wake expansion at very low turbulence typical of offshore farms is still a topic of research and $tg(\alpha)$ has been left as an input parameter so the user can analyze its impact on farm efficiency.

In general, it is easier to estimate the relative momentum deficit $\delta(x, y, z)$ from the wind measured unperturbed and at a wake:

$$\delta(x, y, z) = \frac{R^2 C_T}{2\sigma_y \sigma_z \left(1 + \text{Erf} \left[\frac{H}{\sqrt{2}\sigma_z} \right] \right)} e^{-\frac{y^2}{2\sigma_y^2} - \frac{(H-z)^2}{2\sigma_z^2}} \quad (771)$$

Assuming rotational symmetry ($\sigma_y \approx \sigma_z$) in the wake, the extent of the wake cross section radius σ can be estimated from the wind speed deficit solving (771).

According to [401], the velocity deficit at the axis of the far wake is usually fitted to a power law formula:

$$\frac{U_{wake}(x, 0, H)}{U_{wind}(z)} \approx 1 - A \left(\frac{D}{x} \right)^n \quad (772)$$

where x is the downstream distance, D is the rotor diameter and $1 < A < 3$ and $0,75 < n < 1,25$ are constants. For the case of a turbulent wake that is diffusing with zero ambient turbulence, $n = 2/3$ and for a laminar wake, or equivalently, when

diffusion is controlled by a constant ambient turbulent diffusivity, $n = 1$.

$$(773)$$

$$\delta(x, 0, H) \approx 1 - \left[1 - A \left(\frac{D}{x} \right)^n \right]^2 = A \left(\frac{\text{Diam}}{x} \right)^n \left[2 - A \left(\frac{\text{Diam}}{x} \right)^n \right]$$

The dependence of wake radius σ with distance x from the turbine is obtained equating (771) and (773) and solving for wake radius σ :

$$\frac{R^2 C_T}{2\sigma^2 \left(1 + \text{Erf} \left[\frac{H}{\sqrt{2}\sigma} \right] \right)} \approx A \left(\frac{\text{Diam}}{x} \right)^n \left[2 - A \left(\frac{\text{Diam}}{x} \right)^n \right] \quad (774)$$

The wake radius σ obtained solving (774) is loosely linearly related to the distance to the turbine. An analytical expression of the wake radius σ can be obtained if the error function is approximated, for example, to its Taylor series of second order around $2/3$:

$$(775)$$

$$\text{Erf} \left[\frac{H}{\sqrt{2}\sigma} \right] \approx -0,0424771 + 1,3666 \frac{H}{\sqrt{2}\sigma} - 0,48233 \left(\frac{H}{\sqrt{2}\sigma} \right)^2$$

D.2.2. Upstream/downstream ordering of turbines

It is assumed that turbines are only affected by upstream turbines. Therefore, the turbines are sorted according to the stream flow and wakes are computed starting by the first turbine (where a flat wave arrives first) and sequentially iterate in order only considering the upstream turbines.

The arrival time of the wind can be computed from the distance to a vertical plane transversal to the wind. In an aerial 2D view, the transversal plane is transformed into a line perpendicular to the wind vector \vec{U}_{wind} .

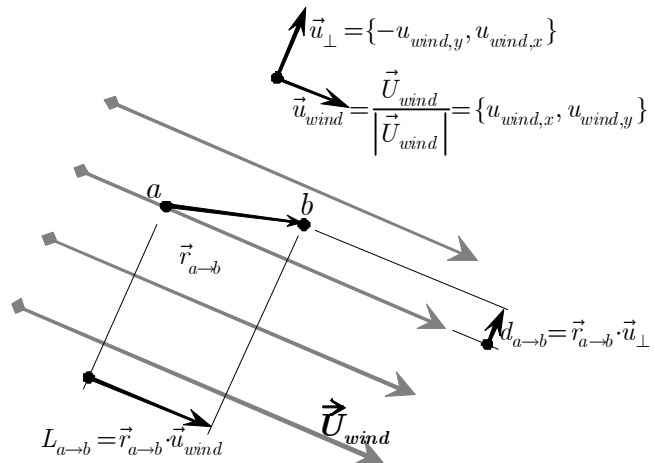


Fig. 323: Downstream distance of turbine b respect turbine a in Lagrangian coordinates

The downstream distance of turbine b respect turbine a is $L_{a \rightarrow b} = \vec{r}_{a \rightarrow b} \cdot \vec{u}_{wind}$, where $\vec{r}_{a \rightarrow b}$ is the distance vector starting from a and ending in b , \vec{u}_{wind} is the wind vector normalized to unity modulo and the dot \cdot represent the scalar product of wind and separation vectors. The turbine b is downstream the turbine a if $L_{a \rightarrow b} > 0$.

D.2.3. Cascade estimation of the wind field

The wind speed is computed sequentially since it is assumed that a point is only affected by upstream turbines, but not by downstream obstacles. The wind speed is assumed to be variable due to upstream wakes, but its direction is considered constant along the wind farm.

The first turbine is assumed to experience the unperturbed wind of magnitude $U_{wind,0}(z)$, a parameter of the simulation. Then, the squared wind modulo only considering the first turbine (the turbine most upstream) is the following field:

$$U_{wind,1}^2(x, y, z) = U_{wind,0}^2(z) [1 - \delta(x, y, z)] \quad (776)$$

The squared wind only considering the first and second turbine (the two turbines most upstream) is:

$$U_{wind,2}^2(x, y, z) = U_{wind,1}^2(x, y, z) - U_{wind,1}^2(x_2, y_2, z) \delta(x, y, z) \quad (777)$$

where $\{x_2, y_2, H\}$ are the coordinates of the second turbine hub.

The squared wind only considering the three turbines most upstream) is:

$$U_{wind,3}^2(x, y, z) = U_{wind,2}^2(x, y, z) - U_{wind,2}^2(x_3, y_3, z) \delta(x, y, z)$$

where $\{x_3, y_3, H\}$ are the coordinates of the third turbine hub.

This procedure is iterated up to the most downstream turbine, numbered n . Then $U_{wind,n}(x, y, z)$ is the estimated wind field accounting all turbines. Thus, this model is the superposition of the squared speed deficits.

D.3. Added turbulence in a wake

The turbulence in the wakes is needed since the expansion rate increases in wakes by a sensitivity factor β respect original turbulence in free flow (see Fig. 324). Thus, the procedure used in wind speed estimation can be used also for turbulence since turbulence at one turbine is influenced only by upstream turbines.

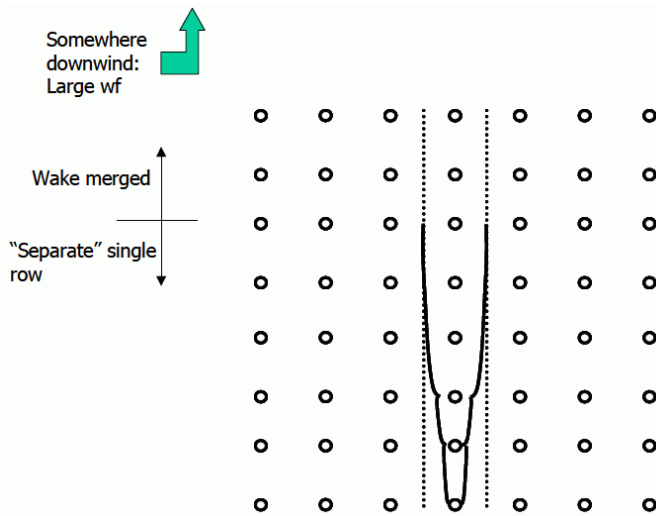


Fig. 324: Expansion of cascaded wakes due to the increased turbulence downstream, respect the more upstream turbines in the wind farm. Reproduced from Risø report 1615 [403].

The turbulence intensity, $TurbInt$, is defined as the ratio of the standard deviation of the wind velocity in the average wind direction σ_{wind} divided by the average wind velocity

U_{wind} The turbulence intensity in the axis of the wake, referred to the inflow wind speed is, according to Crespo and Hernandez [401]:

$$\Delta TurbInt(x) = \begin{cases} 0.73a^{0.83} TurbInt_{inflow}^{-0.0325} (2R/x)^{0.32} & \forall x > 0 \text{ (downstream)} \\ 0 & \forall x < 0 \text{ (upstream)} \end{cases} \quad (779)$$

where a is the induction factor of the turbine, $TurbInt_{inflow}$ is the turbulence intensity upstream the turbine and $\Delta TurbInt$ is the added turbulence intensity downstream. Crespo and Hernandez [401] point out that the decay of the turbulence intensity downstream, $\Delta TurbInt$, is slower than the decay of the velocity deficit.

The induction factor can be computed from the thrust coefficient C_t of the turbine at the inflow wind $U_{inflow\ wind}$, considering only the upstream turbines:

$$a \approx \frac{1 - \sqrt{1 - C_t(U_{inflow\ wind})}}{2} \quad (780)$$

However, (779) only informs of the turbulence of the axis of the wake. The square of the turbulence can be considered the turbulent kinetic energy of the flow. If the energy associated to the chaotic movement of the flow is considered fairly constant downstream, then the variance of the wind speed is held fairly constant in transversal downstream wake sections. The turbulence is the outcome of many perturbations. If the main interactions in the wake are due to momentum transfers and they can be considered stochastically independent in some extent, then the wind speed variance is fairly constant downstream

Thus, the bivariate Gaussian will be used for expressing the fading of the added turbulence (surplus variance of the downstream wind) from the wake axis.

$$\sigma_{wind,downstream}^2(x, y, z) = \sigma_{wind,upstream}^2 + \frac{y^2}{2\sigma_y^2(x)} \frac{(H-z)^2}{2\sigma_z^2(x)} + U_{wind,upstream}^2 \Delta TurbInt^2(x) e \quad (781)$$

This leads to a linear model on wind variance and, hence, the total variance is the sum of the variance of the upstream turbines.

$$\Delta \sigma_{wind,downstream}^2(x, y, z) = U_{wind,upstream}^2 \Delta TurbInt^2(x) e \frac{y^2}{2\sigma_y^2(x)} \frac{(H-z)^2}{2\sigma_z^2(x)} \quad (782)$$

D.3.1. Cascade estimation of the squared turbulence

The wind speed average and its variance are computed sequentially since it is assumed that a point is only affected by upstream turbines, but not by downstream obstacles. Both average wind speed and turbulence should be computed jointly since the wake expansion is dependent of the turbulence level.

The first turbine is assumed to experience the unperturbed turbulence of the free flow, $\sigma_{wind,0}(z) = U_{wind,0}(z) TurbInt_{free}$, a parameter of the simulation. Then, the squared turbulence only considering the first turbine (the turbine most upstream) is the following field:

$$\sigma_{wind,1}^2(x, y, z) = \sigma_{wind,0}^2(z) + U_{wind,0}^2(z) \Delta TurbInt^2(x) e^{-\frac{y^2}{2\sigma_y^2(x)} - \frac{(H-z)^2}{2\sigma_z^2(x)}} \quad (783)$$

The squared turbulence only considering the first and second turbine (the two turbines most upstream) is:

$$\sigma_{wind,2}^2(x, y, z) = \sigma_{wind,1}^2(x, y, z) + U_{wind,1}^2(x_2, y_2, z) \Delta TurbInt^2(x) e^{-\frac{y^2}{2\sigma_y^2(x)} - \frac{(H-z)^2}{2\sigma_z^2(x)}} \quad (784)$$

where $\{x_2, y_2, H\}$ are the coordinates of the second turbine hub.

The squared turbulence only considering the three turbines most upstream is:

$$\sigma_{wind,3}^2(x, y, z) = \sigma_{wind,2}^2(x, y, z) + U_{wind,2}^2(x_3, y_3, z) \Delta TurbInt^2(x) e^{-\frac{y^2}{2\sigma_y^2(x)} - \frac{(H-z)^2}{2\sigma_z^2(x)}} \quad (785)$$

where $\{x_3, y_3, H\}$ are the coordinates of the third turbine hub.

This procedure is iterated up to the most downstream turbine, numbered n . Then $\sigma_{wind,n}^2(x, y, z)/U_{wind,n}^2(x, y, z)$ is the estimated turbulence intensity accounting all turbines.

D.3.2. Definition of the speed deficit and the turbulence excess in the source code

One contribution of the interactive program is the easy test of wake models. In the absence of orography features, the perturbation depends on the distance to the wake axis, the distance downstream the turbine and the cross section of the wake.

For example, the portion of the source code where the shape function and the increment of turbulence are defined is shown in Fig. 325. These definitions can be changed to test other wake models.

D.4. Conclusions

An efficient procedure has been proposed for interactively compute final wind field in a symbolic mathematic program. The principle of momentum balance has been used to derive the spatial shape of the wind deficit in the wake. The conservation of turbulent energy has lead to the same spatial shape of the energy.

For convenience, very far wakes in transversal direction are neglected and only wind speed at hub height is presented.

The use of an iterative procedure makes it easy to derive and test different wake models. This procedure has been implemented in a Mathematica Player™ notebook to compute interactively the power curve of offshore wind farms.

```
(*****
(* Scale function of the momentum deficit, corresponding to a *)
(* Bivariate normal statistical distribution *)
(* Parameters: *)
(* ρ = distance to the wake axis *)
(* L = downstream distance to the rotor plane *)
(* σ = cross section radius of the wake, measured as the *)
(* standard deviation of the momentum deficit distribution *)
(* Hhub = heigh of the wake axis, that is assumed do be, *)
(* approximately, the hub height*)
φ[ρ_, L_, σ_, Hhub_] =

If[ (ρ > -3 σ) && (ρ < 3 σ) && (L > 0.01) ,  $\frac{e^{-\frac{\rho^2}{2\sigma^2}}}{\pi \sigma^2 \left(1 + \text{Erf}\left[\frac{Hhub}{\sqrt{2}\sigma}\right]\right)}$ , 0];

(*****
(* Turbulence Intensity increment in the wake respect the *)
(* ambient turbulence according to Crespo and Hernandez *)
(* See Vermer, Sorensen and Crespo, 'Wind Turbine Wake *)
(* Aerodynamics', 2003 for more details *)
(* L = downstream distance to the rotor plane *)
(* R = turbine radius *)
(* TurbInt∞ = √ TurbInt2∞ = upstream turbulence intensity *)
(* a = induction factor of the turbine =  $\frac{1 - \sqrt{1 - Cthrust[v0]}}{2}$  *)
(* Cthrust[v0] = thrust coef. for the upstream wind speed *)
AverageΔTurbIntInWake[L_, v0_] =

( 0.73  $\left(\frac{1 - \sqrt{1 - Cthrust[v0]}}{2}\right)^{0.83} \sqrt{\text{TurbInt2∞}^{-0.0325}} (2 R / L)^{0.32}$  );

(* AverageΔTurbIntInWake is multiplied by  $\text{Exp}\left[-\frac{r^2}{2\sigma^2}\right]$  because
the expression AverageTurbIntInWake is the turbulence in the
wake axis. It is assumed that the square of the turbulence
distributes as the momentum deficit, with a Gaussian shape.
In the wake axis, the turbulence intensity increment is the
100% of AverageΔTurbIntInWake, decreasing to zero in the far
turbine axis (ρ → ∞). The cinetic energy associated to
the caotic turbulent movement is assumed constant. This
energy is proportional to Turbulencia2 = wind variance, and
hence the turbulence excess diminishes with a similar law
than the speed deficit *)
ΔTurbInt2[TurbInt2∞_, ρ_, L_, σ_, R_, v0_] =

If[(0.01 < L (* < 35 . R*)) && (r < 3 σ) && (-r < 3 σ), Evaluate[

Exp[- $\frac{\rho^2}{2\sigma^2}$ ] AverageΔTurbIntInWake[L, v0]2

]];

```

Fig. 325: Portion of source code where the shape function and the increment of turbulence, $\Delta TurbInt(x)$ are defined.

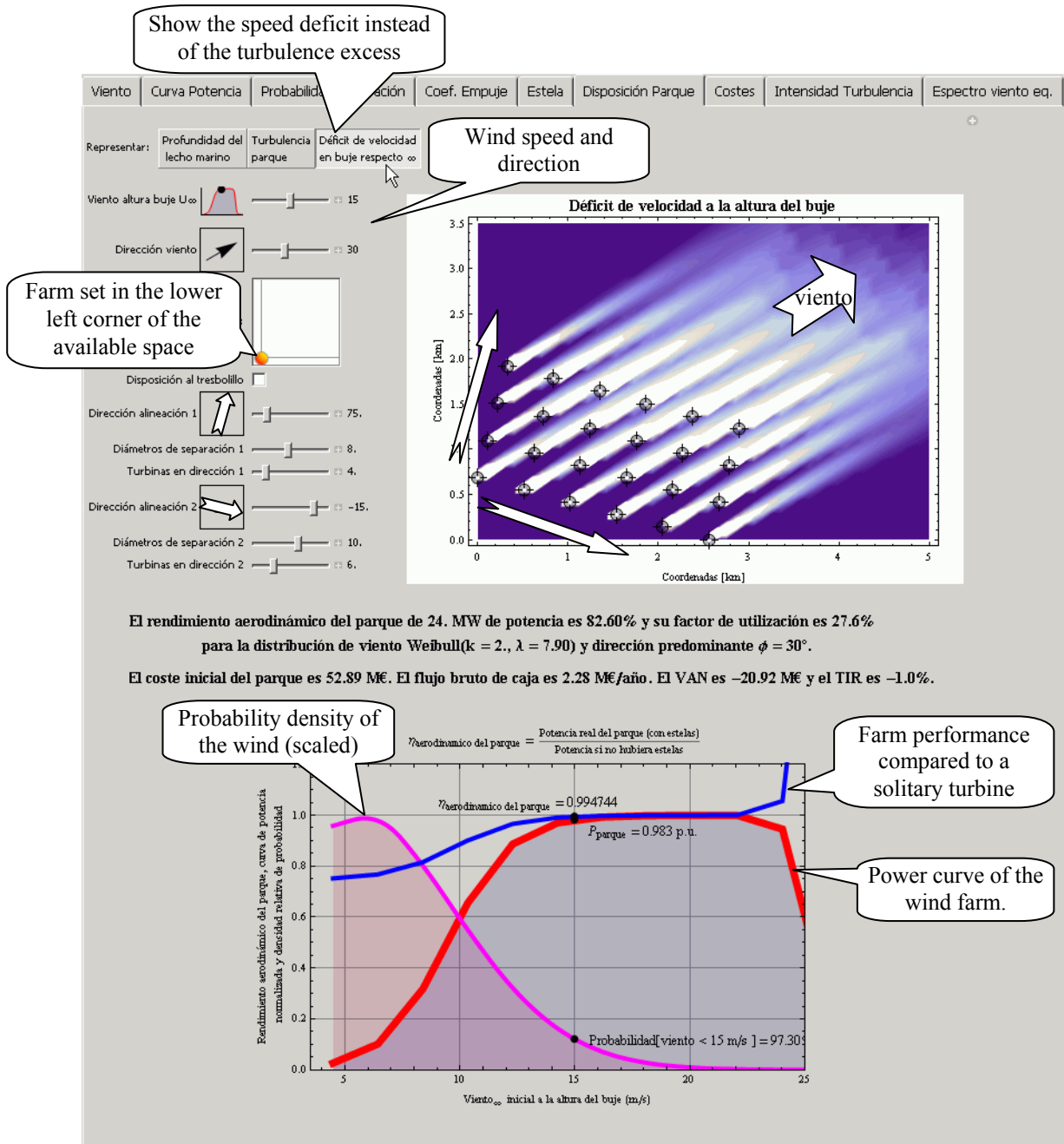


Fig. 326: Example of calculation of wind farm wakes with the model of this annex.

Annex E: Manual of the program

WINDFREDOM

El programa WINDFREDOM visualiza los datos de estaciones meteorológicas mundiales y compara las variaciones de los datos entre dos estaciones. Por conveniencia, se ha implementado como un cuaderno en el programa de cálculo Mathematica™. De esta forma, se simplifica la realización de algunos cálculos y la interacción con el usuario.

Para poder utilizar el programa interactivo para visualizar datos de estaciones meteorológicas mundiales, es necesario tener instalado en el ordenador el visor gratuito Mathematica Player™ o bien la versión 7 del programa de pago Mathematica™.

A continuación se explica el proceso para instalar el visor gratuito Mathematica Player™.

E.1. Instalación del programa “Mathematica Player”

Para poder utilizar el programa interactivo, es necesario instalar el visor de los ficheros compilados con Mathematica™. Este visor se puede descargar gratuitamente desde la página web del fabricante de Mathematica™, <http://www.wolfram.com/products/player/download.cgi>

Para instalar el programa, basta con pulsar dos veces el icono siguiente:



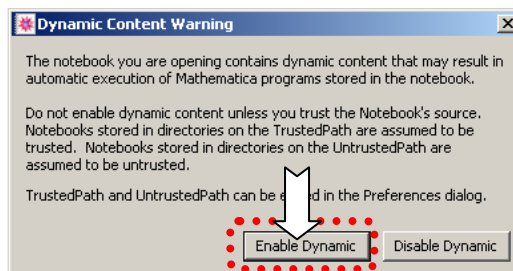
La instalación es un proceso muy sencillo y tarda unos 4 minutos. Al principio, el instalador permite instalar un buscador de documentos de Mathematica™, que es opcional y no es necesario para ejecutar los cálculos.

E.2. Apertura del fichero de cálculos

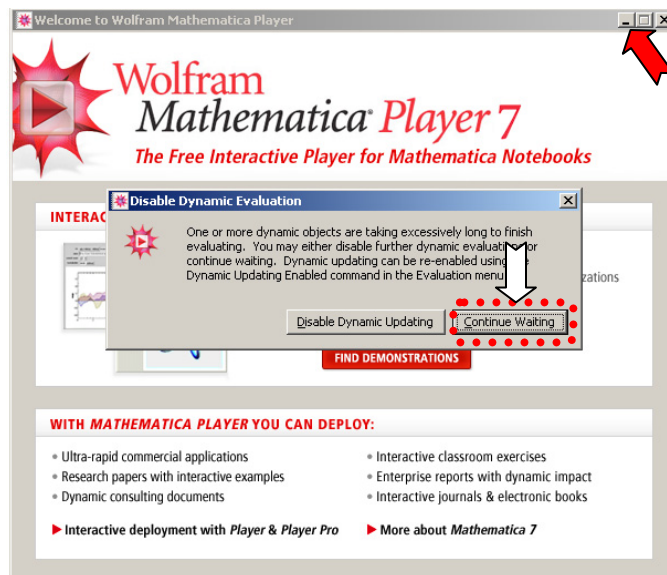
Los algoritmos de cálculo se encuentran en el siguiente fichero:



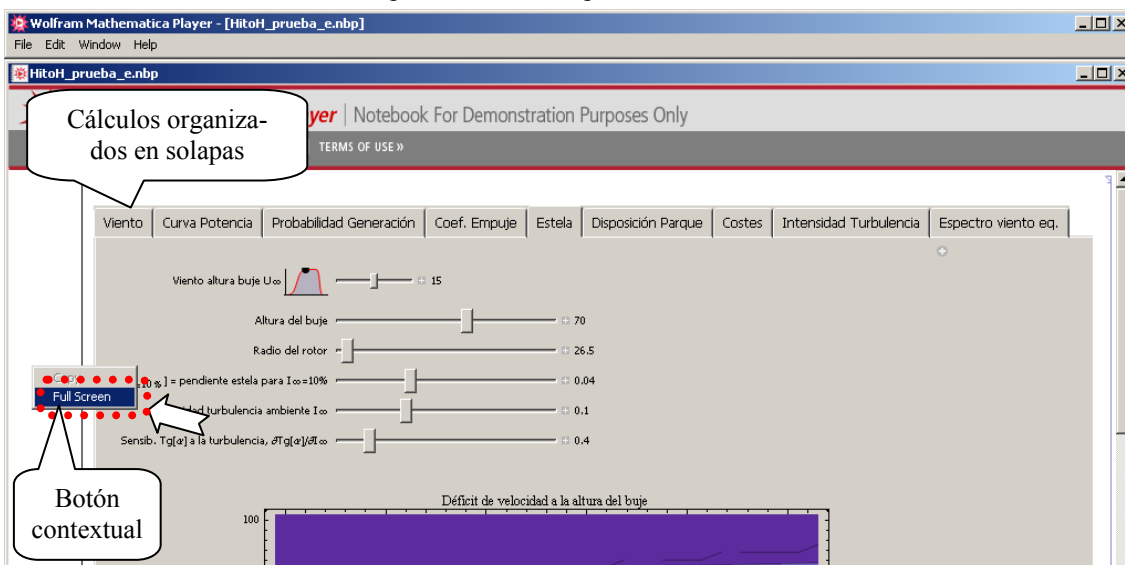
Al pulsar dos veces sobre el icono se abre el visor de Mathematica™ y nos advierte que estamos abriendo un fichero que contiene cálculos dinámicos. Para poder utilizar los cálculos, debemos habilitar dichos cálculos dinámicos pulsando el botón “Enable Dynamic”.



El visor de Mathematica™ puede avisarnos eventualmente si queremos cancelar los cálculos cuando éstos se ralentizan más de un minuto. Esto puede suceder en ordenadores antiguos y es suficiente con responder que continúe calculando. También debemos cerrar el cuadro de diálogo de bienvenida al visor de Mathematica™ que aparece las primeras veces que utilizamos el visor.



Para trabajar con los cálculos, se recomienda trabajar a *pantalla completa* pulsando la tecla de función “F12” o con el botón contextual sobre una parte blanca de la pantalla:



E.3. Datos disponibles de estaciones meteorológicas mundiales

El programa que se presenta a continuación está diseñado para estudiar la evolución del viento en emplazamientos cercanos y es parte de una tesis doctoral [414]. Para ello, el programa descarga automáticamente datos de las estaciones meteorológicas seleccionadas a través de Internet. Por ello, el ordenador en el que se utiliza debe estar conectado a Internet. Los datos utilizados se toman de organizaciones meteorológicas gubernamentales a través de los servidores de Wolfram Research.

En general, los datos de las estaciones meteorológicas institucionales deben ser considerados con precaución, ya que no se dispone de información precisa de su emplazamiento y pueden presentar fallos de mantenimiento y técnicos. Además, las series de datos pueden presentar huecos y datos perdidos, lo que limita su tratamiento automático.

A pesar de estas deficiencias, lógicas en una amplia red de estaciones diseñadas para la predicción del tiempo y muchas veces mantenidas a través de instituciones con presupuestos limitados, estos datos son valiosos para el desarrollo de la energía eólica.

Las estaciones a las que se pueden acceder normalmente están situadas en emplazamientos sin calibrar y cuyas condiciones concretas no se suelen conocer. Muchas veces se encuentran en zonas semi-urbanas, con obstáculos cercanos y a alturas variadas.

El valor de estas estaciones en la energía eólica es debido a la disponibilidad de largas series temporales de datos en una amplia red mundial. Estas series pueden ayudar a corregir variaciones estacionales e interanuales del recurso eólico.

Las estaciones meteorológicas instaladas en aeropuertos proporcionan datos relativamente fiables y habitualmente se disponen de datos cada 30 minutos. Las estaciones de institutos meteorológicos estatales también pueden ser una fuente útil de datos, aunque su disponibilidad suele ser más reducida y la velocidad del viento no suele estar tan bien monitorizada. En los estudios que necesitan registros de datos sin huecos, los valores no disponibles se sustituyen por la interpolación entre los datos más próximos. El programa, en la versión actual, no incluye ningún filtro para compensar errores en las medidas ni realiza ninguna comprobación adicional excepto interpolar los datos no disponibles.

Este programa permite el análisis interactivo de las variaciones del viento en el rango de 10 días hasta las variaciones horarias. Las oscilaciones del viento que duran más de 10 días (por ejemplo, las estacionales) se pueden estudiar con las mismas herramientas, pero precisa series muy largas de datos cuya calidad es conveniente contrastar antes de obtener conclusiones.

Para poder utilizar el visor gratuito de Mathematica™, se ha eliminado la opción de grabar los datos en el programa. No obstante, si se dispone de una licencia del programa Mathematica™ 7, los datos que se muestran en el programa se pueden almacenar en un fichero de texto separado por tabuladores tecleando el comando `Export["fichero1.txt", availabledata, "TSV"]` para la estación meteorológica de referencia y `Export["fichero2.txt", availabledata2, "TSV"]` para la estación comparada.

A día de hoy, el programa está en fase beta y, eventualmente, puede fallar si la base de datos no dispone de datos requeridos de la estación meteorológica o estos son erróneos (puede haber varios datos para el mismo instante, datos aberrantes, velocidades de viento negativas en vez de calmas, etc.). Estos fallos en los datos pueden generar errores numéricos que, en algunos casos, bloquean el programa. En el peor caso, este problema se resuelve cerrando el programa “Mathematica Player” y/o MathKernel y realizando otro análisis, seleccionando otras fechas u otra estación meteorológica cuyos datos no contengan errores. Puede contribuir al desarrollo del programa enviando un correo a joaquin.mur@unizar.es indicando la estación meteorológica, la variable y el periodo que ha generado un error en el programa. Estos correos ayudarán a diseñar un filtro inicial que evite los errores numéricos asociados a datos erróneos.

E.4. Solapas del programa

El programa se ha organizado por solapas para poder acceder a la información rápidamente. El funcionamiento de las solapas es análogo al comportamiento de las solapas de otros programas como navegadores, editores de textos, etc.

Cada solapa muestra una pantalla con información relacionada estrechamente. Las solapas actualmente disponibles son:

Map	Station availability	Station #1	Station #2	Spect. Ratio	Coherence phase	Coherence module	Fit of coherence models
-----	----------------------	------------	------------	--------------	-----------------	------------------	-------------------------

Las solapas de la izquierda se utilizan para seleccionar las estaciones meteorológicas y los datos que se quieren comparar. Las solapas de la derecha contienen las gráficas de la comparación.

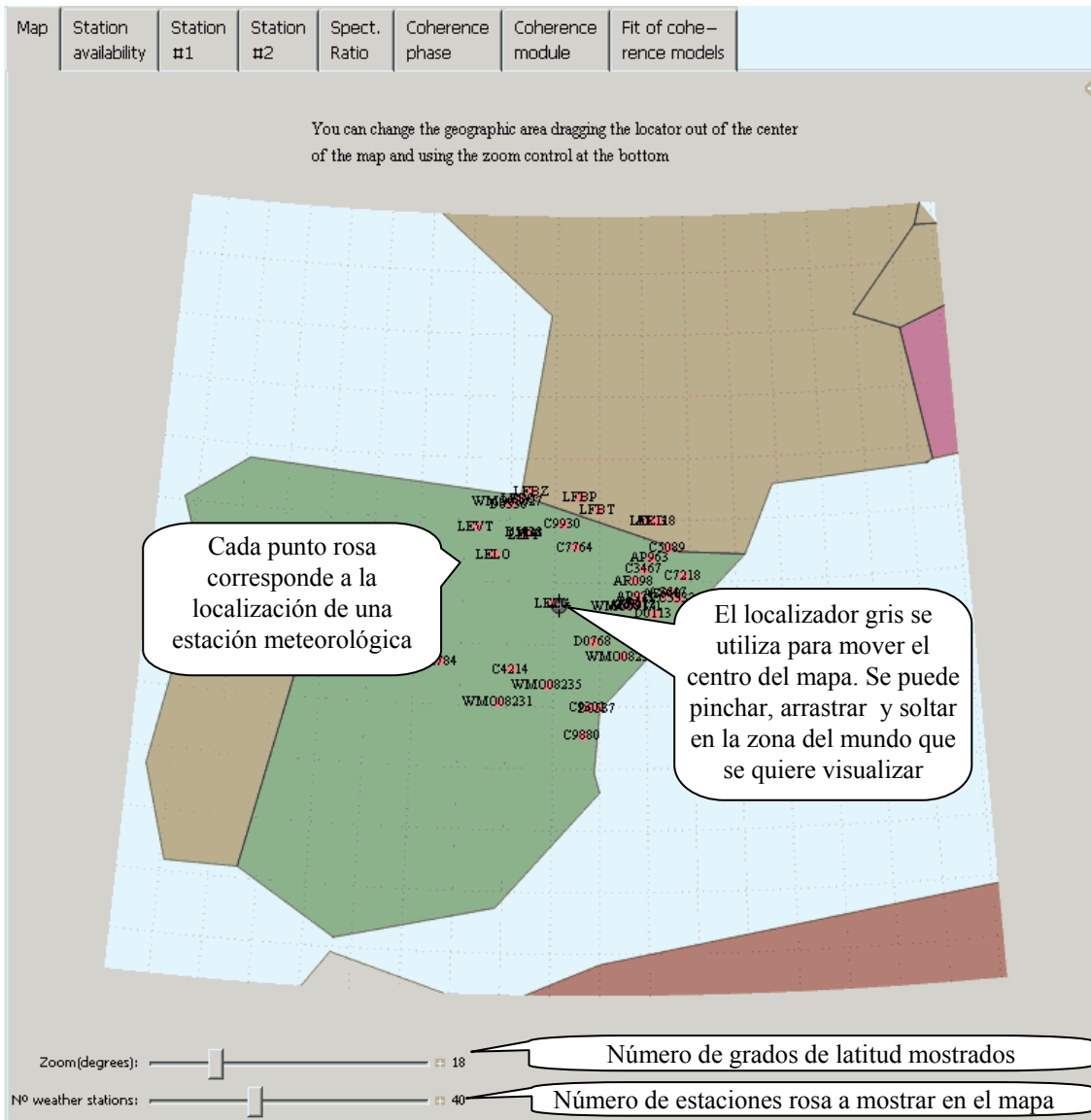
A continuación se muestra una breve guía gráfica de la utilización más habitual del programa.

E.4.1. Mapa de las estaciones meteorológicas cercanas

Al abrir el fichero “EstacionesMeteorologicas.nbp”, el programa se inicializa y muestra la solapa “Map” con un mapa esquemático centrado en el lugar de utilización. En el centro del mapa aparece un localizador gris. El localizador está inicialmente en la ubicación más probable del ordenador en que se ejecuta el programa. Para cambiar la zona geográfica mostrada, basta con pinchar, arrastrar y soltar el localizador gris a la zona que se desea visualizar.

El programa dispone de un control del número de estaciones a mostrar. Un valor muy alto de estaciones ralentiza la presentación de algunos resultados porque requiere descargar datos de más estaciones. Además, cuando movemos el centro del plano, debe esperar a recibir de internet los datos del número de estaciones más cercanas al localizador del centro.

También se dispone de un control para ajustar la escala del mapa. El valor del Zoom es el número de grados de latitud que se muestran en pantalla.



E.4.2. Disponibilidad de las estaciones meteorológicas

La solapa “Station availability” contiene una lista con la posición geográfica de las estaciones, la velocidad media del viento, la distancia al localizador del mapa y el rango de fechas disponibles. La velocidad del viento suele ser más fiable en aquellas estaciones con mayor disponibilidad de fechas, que tengan mayor velocidad media $\langle \text{Wind} \rangle$ [m/s] o que correspondan a Aeropuertos.

La velocidad del viento $\langle \text{Wind} \rangle$ [m/s] que se muestra en la tabla corresponde a la media de la estación, sin corregir su valor por la altura del anemómetro o por los obstáculos cercanos. Las estaciones facilitan a la organización mundial de predicción la velocidad del viento en las unidades km/h y se convierten a m/s dividiendo por el factor 3,6. Muchas estaciones proporcionan los datos semi-horarios de velocidad sin cifras decimales o con errores significativos de discretización.

El entorno alrededor de cada estación se puede observar pulsando un botón. Entonces, el programa abre en Google maps la imagen del satélite. La estación puede estar a unos metros del centro de la imagen del satélite mostrada ya que no se suelen conocer las coordenadas de las estaciones con más de 3 decimales.

Las estaciones de los aeropuertos españoles empiezan con las siglas LE y luego siguen las siglas de la ciudad. Por ejemplo, LEZG corresponde al aeropuerto Español de Zaragoza, LEPP corresponde al aeropuerto Español de Pamplona y LEVT corresponde al aeropuerto Español de Vitoria, LFBZ corresponde al aeropuerto Francés de Biarritz, etc.

Las estaciones asociadas a la organización meteorológica mundial empiezan por WMO (correspondiente a Weather Meteorological Organization).

Map	Station availability	Station #1	Station #2	Spect. Ratio	Coherence phase	Coherence module	Fit of coherence models	
		Latitude	Longitude	Elevation [m]	(Wind) [m/s]	Date availability	Distance [km]	
	LEZG	41.667	-1.	258.	8.94	1 Jan 1973 → 4 Sep 2009	10.81	
	D0768	41.052	-0.128	320.	1.17	24 Jun 2008 → 11 Aug 2008	89.9	
	C7764	See D0768 weather station in google maps						
	WMO08171	41.633	0.6	199.	1.78	1 Jan 1973 → 4 Sep 2009	123.3	
	AR097	41.651	0.69	188.	3.11	14 Mar 2008 → 23 Aug 2009	130.8	
	AR112	41.673	0.818	210.	2.72	1 Mar 2008 → 29 Aug 2008	141.5	
	LEPP	42.77	-1.646	459.	6.25	13 Mar 1973 → 4 Sep 2009	141.6	
	AP971	41.789	0.817	240.	3.89	1 Mar 2008 → 25 Nov 2008	142.3	
	WMO08235	40.35	-1.117	902.	2.22	1 Jan 1973 → 4 Sep 2009	143.5	
	C4214	40.594	-1.907	1187.	---	1 Mar 2008 → 14 Oct 2008	143.8	
	AR098	42.04	0.787	1670.	---	1 Mar 2008 → 4 Sep 2009	145.8	
	D1438	42.807	-1.662	448.	3.11	13 Oct 2008 → 4 Sep 2009	145.8	
	C5711	42.815	-1.644	452.	---	1 Mar 2008 → 4 Sep 2009	146.	
	WMO08238	40.817	0.5	50.	2.69	1 Jan 1973 → 4 Sep 2009	146.8	
	C9930	42.952	-0.803	1550.	1.17	18 Mar 2008 → 13 May 2008	147.	
	LELO	42.45	-2.333	363.	2.69	1 Jan 1973 → 4 Sep 2009	150.9	
	C3467	42.225	0.99	650.	---	1 Mar 2008 → 20 Aug 2009	168.6	
	D0113	41.504	1.187	781.	3.11	31 Mar 2008 → 19 Jul 2008	173.	
	LERS	41.147	1.167	76.	3.14	1 Jan 1973 → 4 Sep 2009	179.4	
	LFBT	43.179	-0.006	363.	6.69	1 Jan 1973 → 4 Sep 2009	186.5	
	AP963	42.409	1.133	711.	---	1 Mar 2008 → 10 May 2008	187.8	
	C9301	39.994	-0.241	227.	2.72	1 Mar 2008 → 4 Sep 2009	189.5	
	AS648	41.812	1.407	439.	1.17	1 Mar 2008 → 23 Jan 2009	191.4	
	D0537	39.985	-0.027	0.	---	14 May 2008 → 16 May 2008	196.3	
	LFBP	43.38	-0.419	183.	6.25	15 Jun 1936 → 4 Sep 2009	198.1	
	AS647	41.837	1.537	930.	---	1 Mar 2008 → 4 Sep 2009	202.4	
	WMO08231	40.067	-2.133	946.	0.89	1 Jan 1973 → 4 Sep 2009	203.2	
	D0336	43.269	-2.019	55.	1.94	15 Apr 2008 → 4 Sep 2009	204.8	
	LEVT	42.883	-2.724	510.	4.92	1 Jan 1973 → 4 Sep 2009	206.2	
	LESO	43.357	-1.791	8.	1.33	1 Jan 1973 → 4 Sep 2009	205.9	
	WMO08027	43.3	-2.033	259.	4.92	1 Jan 1973 → 4 Sep 2009	208.3	
	LFBZ	43.468	-1.523	71.	4.47	1 Aug 1929 → 4 Sep 2009	210.9	
	C5532	41.743	1.713	400.	1.94	1 Mar 2008 → 4 Sep 2009	216.2	
	LFCG	43.008	1.103	412.	3.58	1 Jan 1973 → 4 Sep 2009	223.9	
	C5089	42.562	1.53	1320.	---	4 Sep 2009 → 4 Sep 2009	224.6	
	AS763	41.26	1.771	100.	---	4 Sep 2009 → 4 Sep 2009	225.3	
	C7218	42.099	1.846	704.	0.78	1 Mar 2008 → 4 Sep 2009	232.2	
	AR118	42.993	1.287	522.	0.39	1 Mar 2008 → 3 Sep 2009	234.2	
	C9880	39.539	-0.35	45.	---	29 Mar 2008 → 9 Oct 2008	236.5	
	C1784	40.699	-3.449	752.	---	1 Mar 2008 → 20 Jul 2009	239.1	

E.4.3. Selección de la estación meteorológica de referencia

En esta solapa se puede visualizar un análisis de los datos facilitados por una estación meteorológica. Para ello, hay que elegir una estación de una lista desplegable, que corresponde al mapa y tabla mostrados anteriormente. Con el control "Period center" se selecciona la fecha del centro del periodo que se va a estudiar. Si el control deslizante está a la izquierda, se utilizarán los primeros datos disponibles y si está a la derecha (opción por defecto), se utilizarán los últimos datos disponibles (el último dato disponible suele corresponder a unas dos horas antes de la hora actual). Por tanto, los datos se podrían utilizar incluso para predicción de generación eólica en las próximas horas.

Map	Station availability	Station #1	Station #2	Spect. Ratio	Coherence phase	Coherence module	Fit of coherence models
-----	----------------------	------------	------------	--------------	-----------------	------------------	-------------------------

Select weather station:

Period center:

Days: 1

Analysis:

Select variable:

Averaging period: Year Month Week Day All

Instructions:

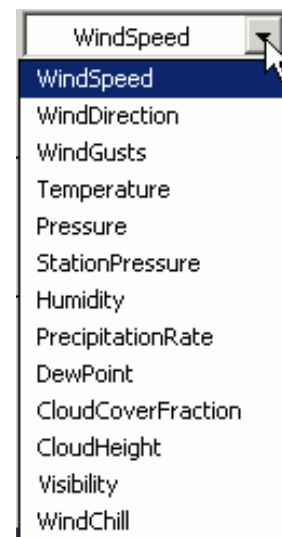
- 1.- Choose a reference weather station, a time period and push a button corresponding to the type of analysis in [Station #1] tab.
- 2.- After that, select the second weather station in [Station #2] tab to compare with the first one.
- 3.- Finally, select the tab [Coherence] to compare their dynamics.

Con el control “Days” se selecciona la duración del periodo bajo estudio. Los periodos muy largos requieren más tiempo para descargar los datos y es más probable que contengan algún dato aberrante.

Por defecto, los análisis se realizan con los valores de mayor frecuencia guardados en la base de datos. Si los datos originales contienen errores o producen gráficos con excesiva variabilidad, se pueden utilizar los promedios diario, semanal, mensual o anual con sólo pulsar los botones de radio “Day”, “Week”, “Month” o “Year” respectivamente. Los promedios se encuentran están procesados en la base de datos de la organización mundial meteorológica y contienen menos errores que los originales.

La variable a estudiar se selecciona en la lista desplegable “Select a variable”. Las variables que se pueden demandar a la base de datos son:

- Velocidad del viento en km/h (*WindSpeed*).
- Dirección del viento en grados sexagesimales (*WindDirection*).
- Racha de viento máxima en km/h (*WindGusts*).
- Temperatura en grados Celsius (*Temperature*).
- Presión milibárica, corregida a la altura del mar (*Pressure*).
- Presión milibárica sin corregir por la altura (*StationPressure*).
- Humedad relativa, de 0 a 1 (*Humidity*).
- Tasa de precipitación en cm/hora (*PrecipitationRate*).
- Temperatura del punto de rocío en grados Celsius (*DewPoint*).
- Fracción de cielo cubierto por nubes, de 0 a 1 (*CloudCoverFraction*).
- Altura en metros de las nubes estimada en 5/8 del oscurecimiento de la nube (*CloudHeight*).
- Visibilidad en kilómetros (*Visibility*).
- Sensación térmica de temperatura (*WindChill*).

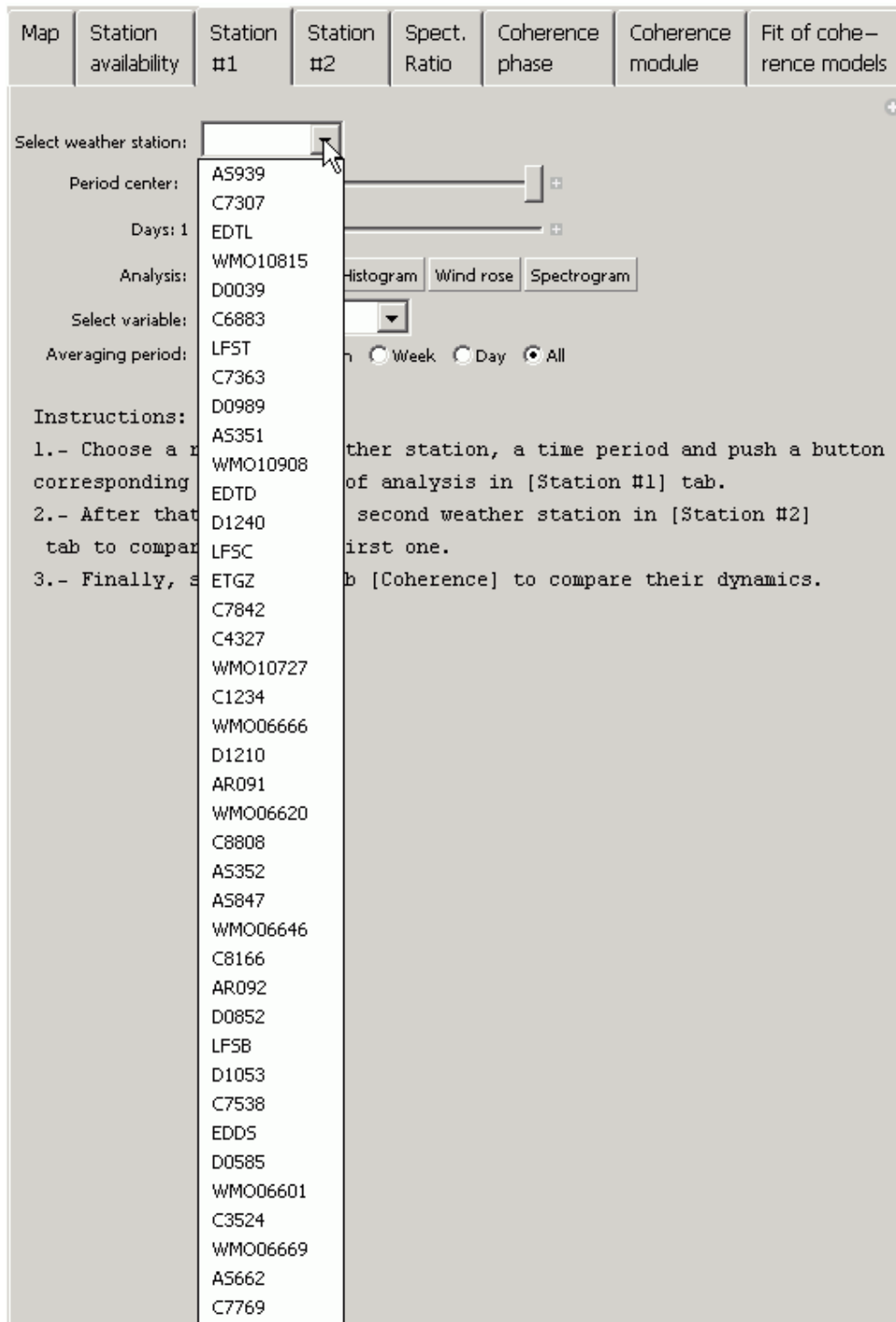


Muchas de estas variables no están disponibles en las estaciones meteorológicas. En general, cuando el programa no tiene más de 10 datos válidos, informa al usuario de este problema.

Los tipos de análisis disponibles son:

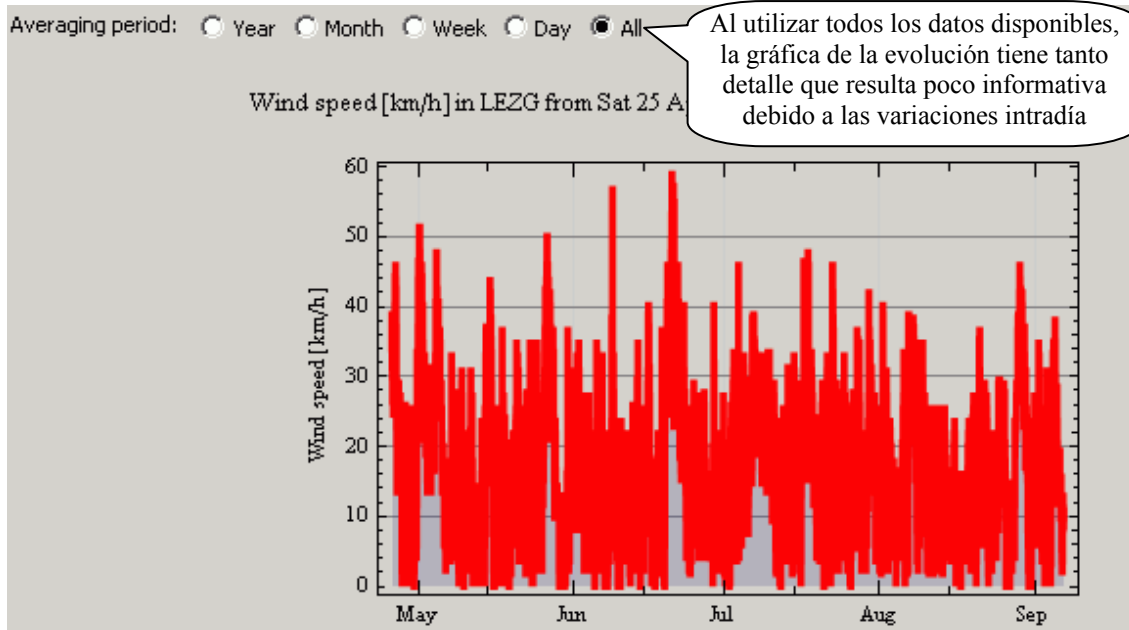


- Gráfico de la evolución de la variable en el tiempo (*Time series plot*).
- Histograma (*Histogram*) con la frecuencia de observación de la variable meteorológica, comparado con la distribución estadística normal y Weibull ajustada a partir de la media y varianza de los datos.
- Rosa de vientos (*Wind rose*), mostrada como un histograma del vector de viento. La velocidad se descompone en componentes Norte-Sur y Este-Oeste y la frecuencia de observación es dibujada en una cuadrícula.
- Espectrograma (*Spectrogram*), que muestra la evolución del contenido frecuencial de la señal con el tiempo. Al pulsar el tipo de análisis, se actualiza el número de días y el centro del intervalo de análisis.

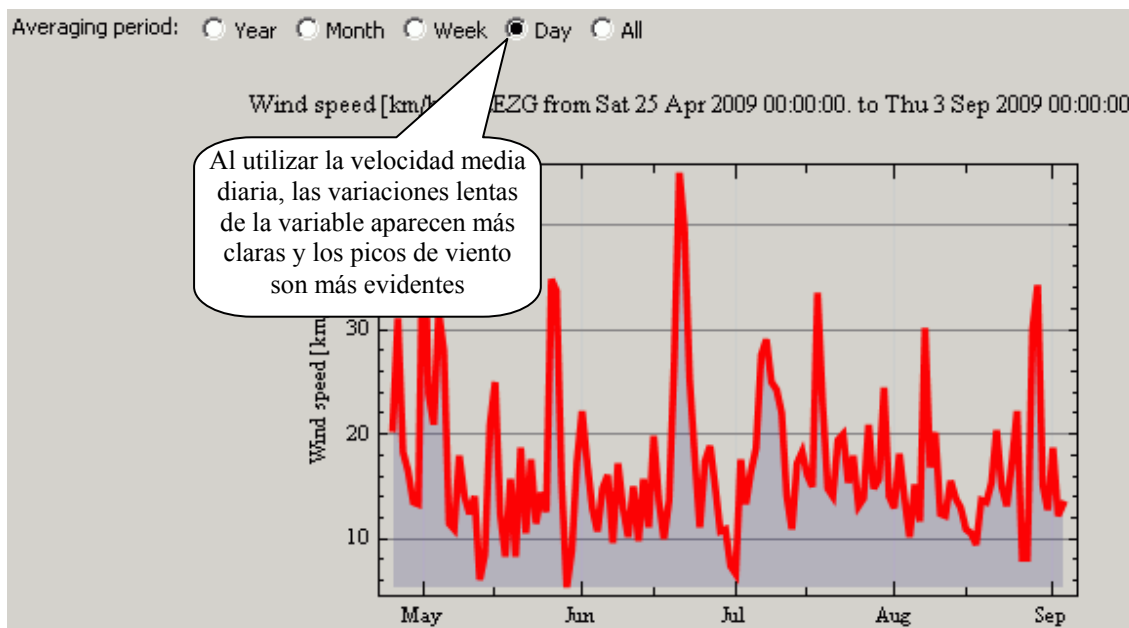


E) Evolución de la variable en el tiempo (*Time series plot*)

El primer paso en un estudio de datos meteorológicos es visualizarlos para detectar posibles anomalías en la serie. Esto lo podemos realizar pulsando el botón “*Time series plot*”.



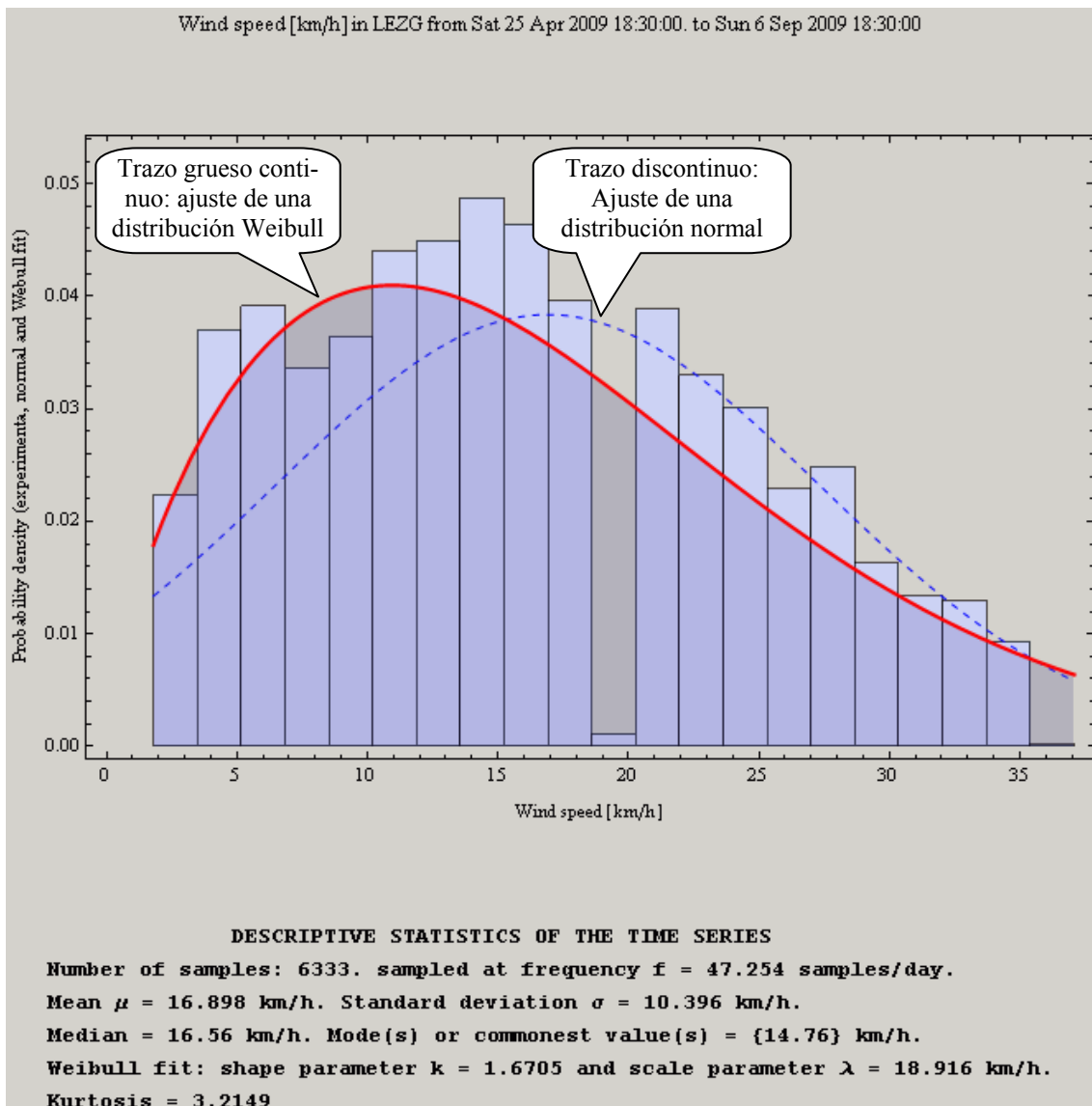
Por defecto, se muestran todos los datos disponibles. Las gráficas de más de una semana resultan poco informativas debido a las variaciones intradía. Dependiendo del periodo de estudio, es recomendable utilizar los datos diarios (que ocultan las variaciones intradías) o incluso las variaciones semanales, mensuales o anuales (que ocultan las variaciones estacionales).



F) Histograma (*Histogram*)

Para estudiar la variación estática del viento o el potencial eólico de un emplazamiento, se utiliza la frecuencia de ocurrencia del viento. En bastantes emplazamientos, la distribución estadística medida se puede aproximar a una distribución Weibull. El histograma también se puede realizar a otras variables meteorológicas, aunque en esos casos, la distribución normal puede ajustarse mejor a las observaciones.

Al igual que el dibujo de la serie temporal, el histograma se puede basar en todos los datos disponibles (habitualmente, valores cada media hora y horarios) o en los datos diarios.

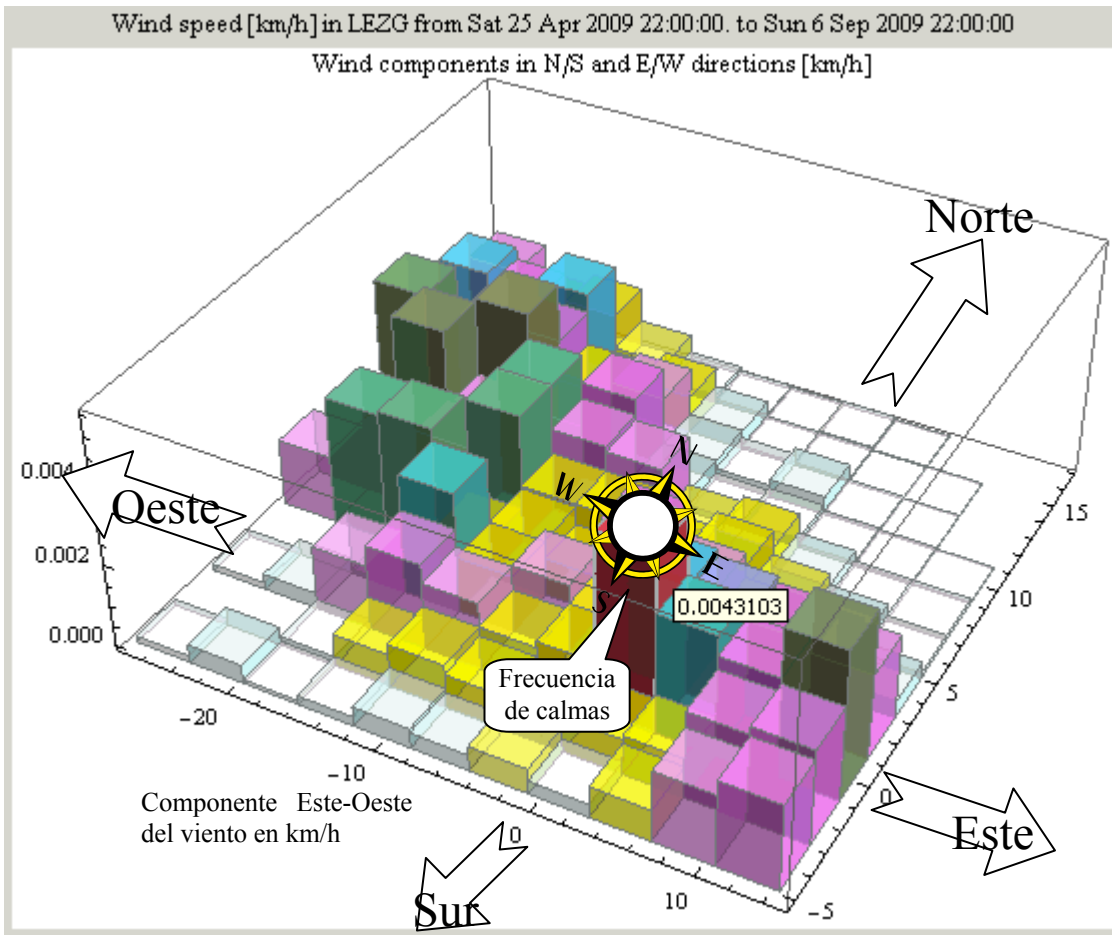


G) Rosa de vientos (*Wind rose*)

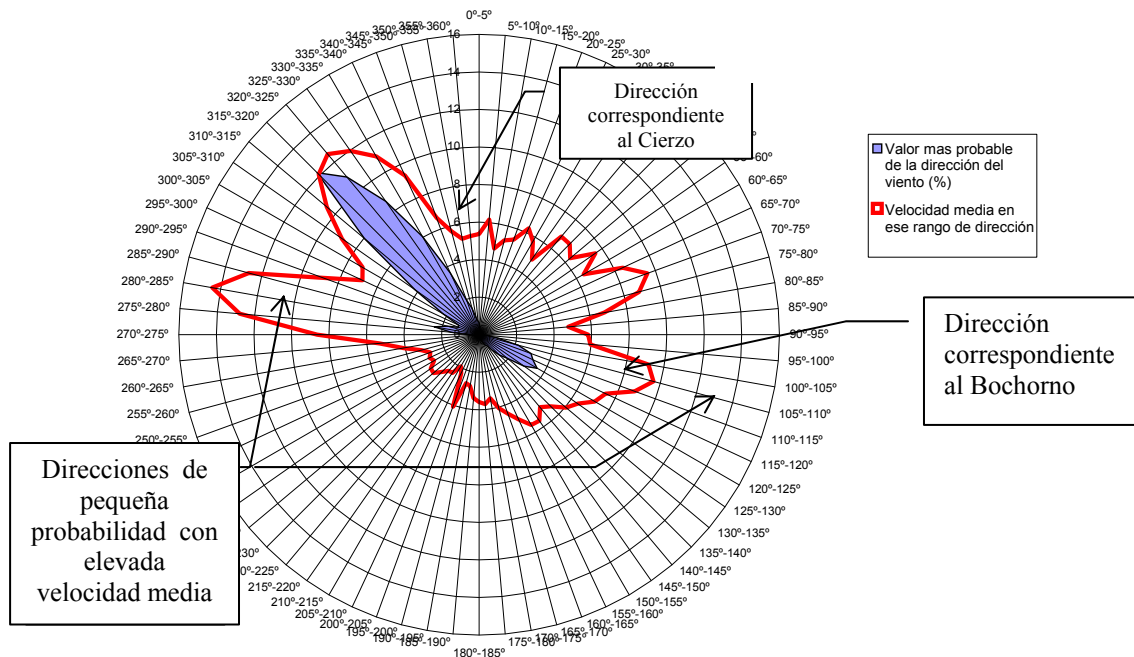
La rosa de viento se calcula en este programa como el histograma del vector de viento. La velocidad se descompone en componentes Norte-Sur y Este-Oeste y la frecuencia de observación en cada rango de la cuadrícula se dibuja en forma de altura de la barra.

Aunque este formato es menos habitual que la representación polar del viento, permite una detección más rápida del rango habitual del viento en cada dirección y de la frecuencia de las calmas. Habitualmente, la barra de mayor altura corresponde a la cuadrícula con componentes del viento nulos (calmas).

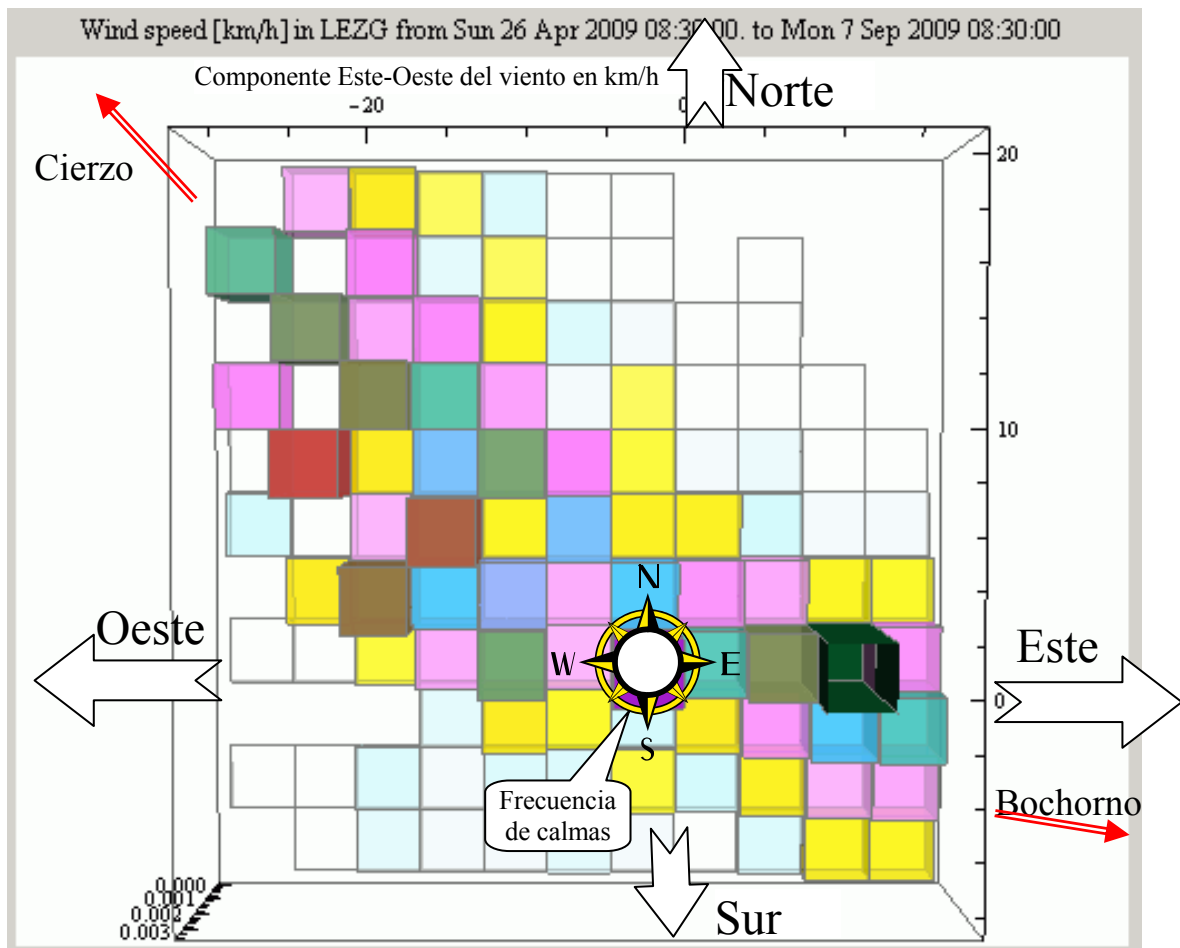
El histograma tridimensional puede girarse pulsando sobre él y arrastrando el ratón. A veces es útil la vista de pájaro para visualizar mejor la orientación del viento, ya que la frecuencia de ocurrencia de cada cuadrícula está codificado por colores cuya luminosidad es proporcional a su frecuencia.



La representación más habitual de la rosa de vientos en coordenadas polares. Puede verse que ambas son equivalentes.



La vista de pájaro del histograma tridimensional proporciona una visualización similar a la representación polar de la rosa de vientos.



H) Espectrograma (*Spectrogram*)

Las fluctuaciones de una magnitud aleatoria estacionaria (cuyas propiedades no varían en el tiempo) se puede realizar calculando la densidad espectral de varianza o PSD (del inglés “*Power Spectral Density*”). La densidad espectral de varianza indica en qué frecuencias se reparte la varianza de la señal. Esto permite cuantificar que porción de la varianza de la magnitud se debe a las oscilaciones diurnas, semidiurnas y de unos cuantos días.

En la práctica, las propiedades del viento y de otras variables meteorológicas cambian en función de la situación atmosférica. Por ello, es conveniente dividir series largas de tiempo en porciones de unos pocos días y observar la distribución de la varianza en la frecuencia. Esto permite constatar si se producen patrones diferentes a lo largo del tiempo.

El espectrograma consiste en una representación del contenido frecuencial de la señal en función del tiempo. Se suele estimar aplicando la transformada de Fourier a pequeñas porciones de la serie temporal. Esto permite estudiar señales en el dominio del tiempo y de la frecuencia conjuntamente. Se emplea habitualmente en audio y en tratamiento de señales de frecuencia variable. Su uso para la energía eólica es novedoso.

La disposición que se ha elegido para en esta aplicación consiste en:

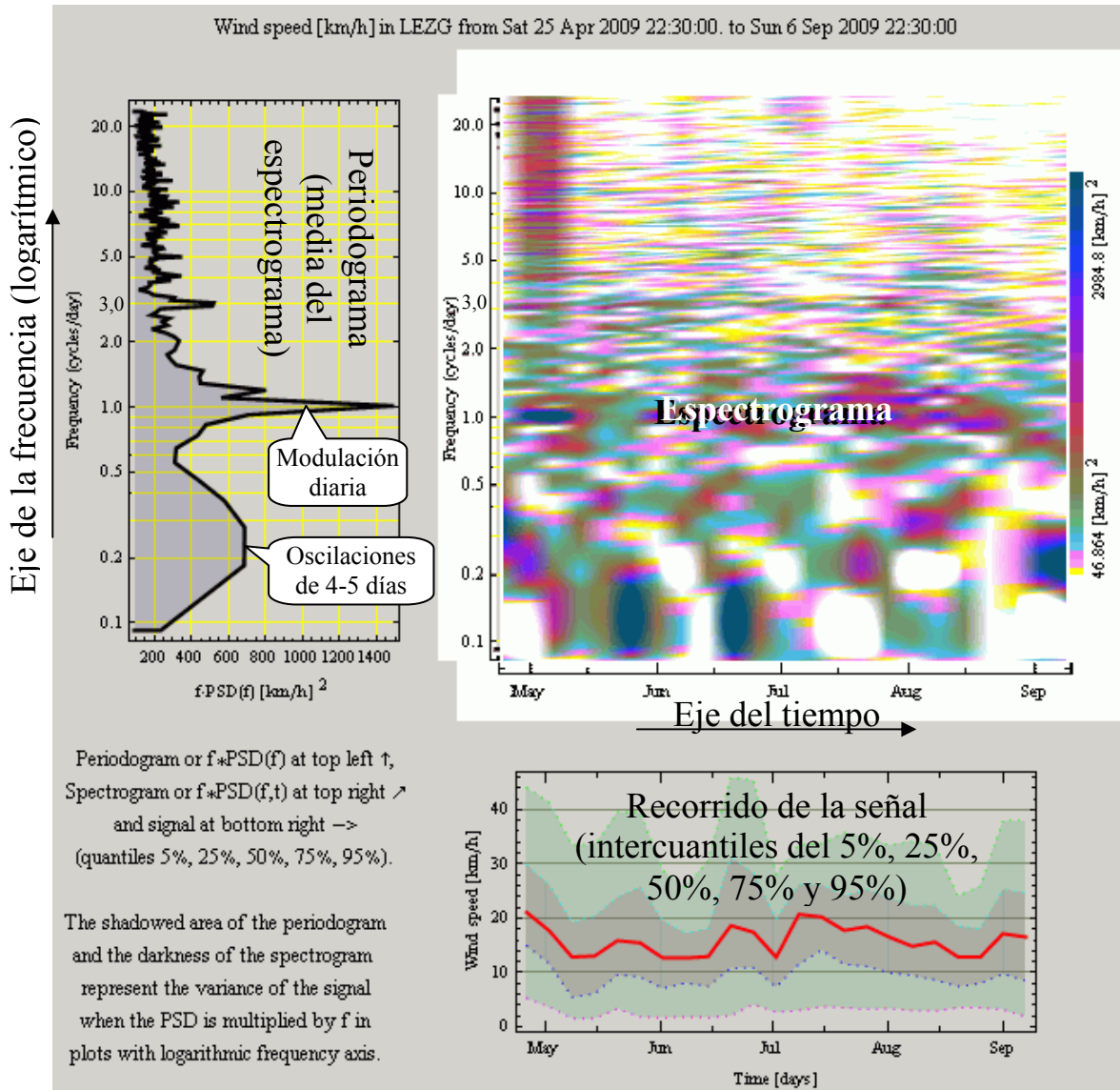
- el periodograma en la esquina superior derecha;
- el recorrido intercuartil junto con la media y el cuantil 5% y 95% en la esquina inferior derecha;
- el espectrograma, propiamente dicho, en la esquina superior derecha..

El espectrograma muestra las oscilaciones que contiene una señal a lo largo del tiempo. El promedio del espectrograma, es decir, el promedio de las oscilaciones de la señal es el periodograma. En la página siguiente se muestra como ejemplo la gráfica del aeropuerto de Zaragoza.

Se ha utilizado la escala logarítmica para la frecuencia porque se observan mejor las oscilaciones de baja frecuencia en las variables meteorológicas. Cuando se utiliza la escala logarítmica en la frecuencia, se suele representar la densidad espectral de la varianza multiplicada por la frecuencia, $f \cdot PSD$, ya que así el área sombreada del periodograma y la oscuridad en el espectrograma representan la varianza de la señal. Es decir, los

puntos más oscuros del espectrograma indican que se ha producido una oscilación en el tiempo y frecuencia correspondiente. Las zonas blancas del espectrograma indican ausencias de la frecuencia correspondiente al eje vertical en el instante de tiempo indicado por el eje horizontal.

Por ejemplo, los emplazamientos cercanos al mar suelen mostrar oscilaciones semi-diurnas (frecuencia $f = 2$ ciclos/día, con 2 picos de viento y 2 periodos de menor viento por día) mientras que en la zona del valle del Ebro las oscilaciones intradía más habituales son de frecuencia $f = 3$ ciclos/día (3 picos locales de viento y 3 periodos de menor viento por día).



E.4.4. Selección de la estación meteorológica a comparar

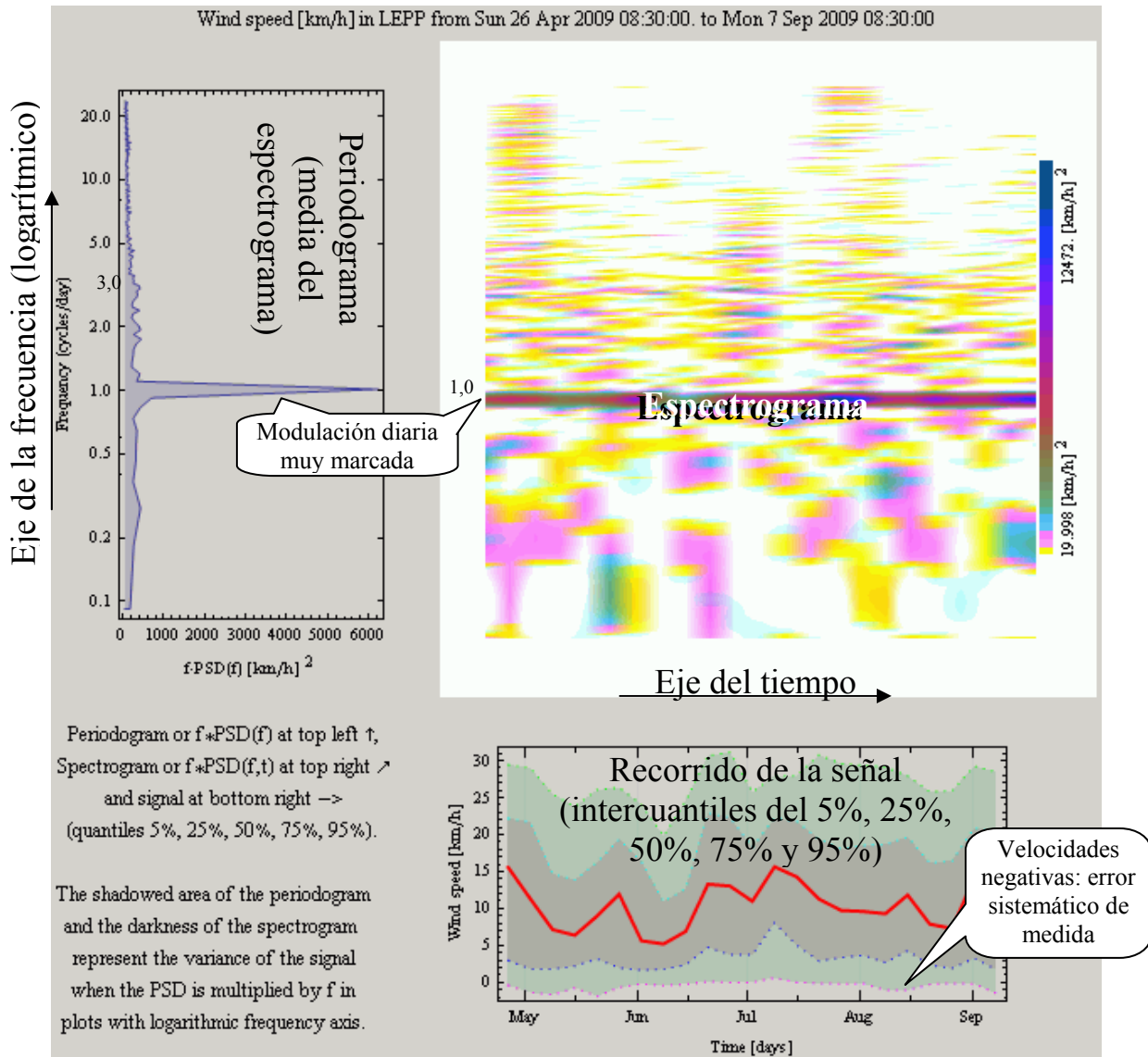
Uno de los objetivos del programa es comparar las oscilaciones entre dos estaciones. La estación de referencia (*Station #1*) se compara con una segunda estación (*Station #2*) en el dominio tiempo-frecuencia utilizando el ratio de los espectrogramas.

La solapa de la segunda estación es análoga a la primera, salvo que en la segunda estación (*Station #2*) se utiliza el intervalo de tiempo de análisis ajustado en la solapa en la estación de referencia (*Station #1*).

La gráfica siguiente muestra el espectrograma del viento en el aeropuerto de Pamplona como variable que se comparará posteriormente con el viento en el aeropuerto de Zaragoza. Lo primero que salta a la vista es el pico tan marcado que aparece en la frecuencia unidad (oscilación diaria). En el periodograma aparece como un pico mientras que en el espectrograma aparece como una franja horizontal oscura mientras que el resto es más claro. Esto indica que, en todos los subperiodos analizados, las oscilaciones diarias han predominado.

Si nos fijamos en la escala de las gráficas, vemos que las oscilaciones del resto de frecuencias tienen un valor comparable en Pamplona y Zaragoza. Esto se observará mejor en la solapa de ratio de espectrogramas.

El cuantil del 5% es negativo en algunos periodos, indicando un error de medida sistemático que no se puede corregir al no tener más información de la estación.

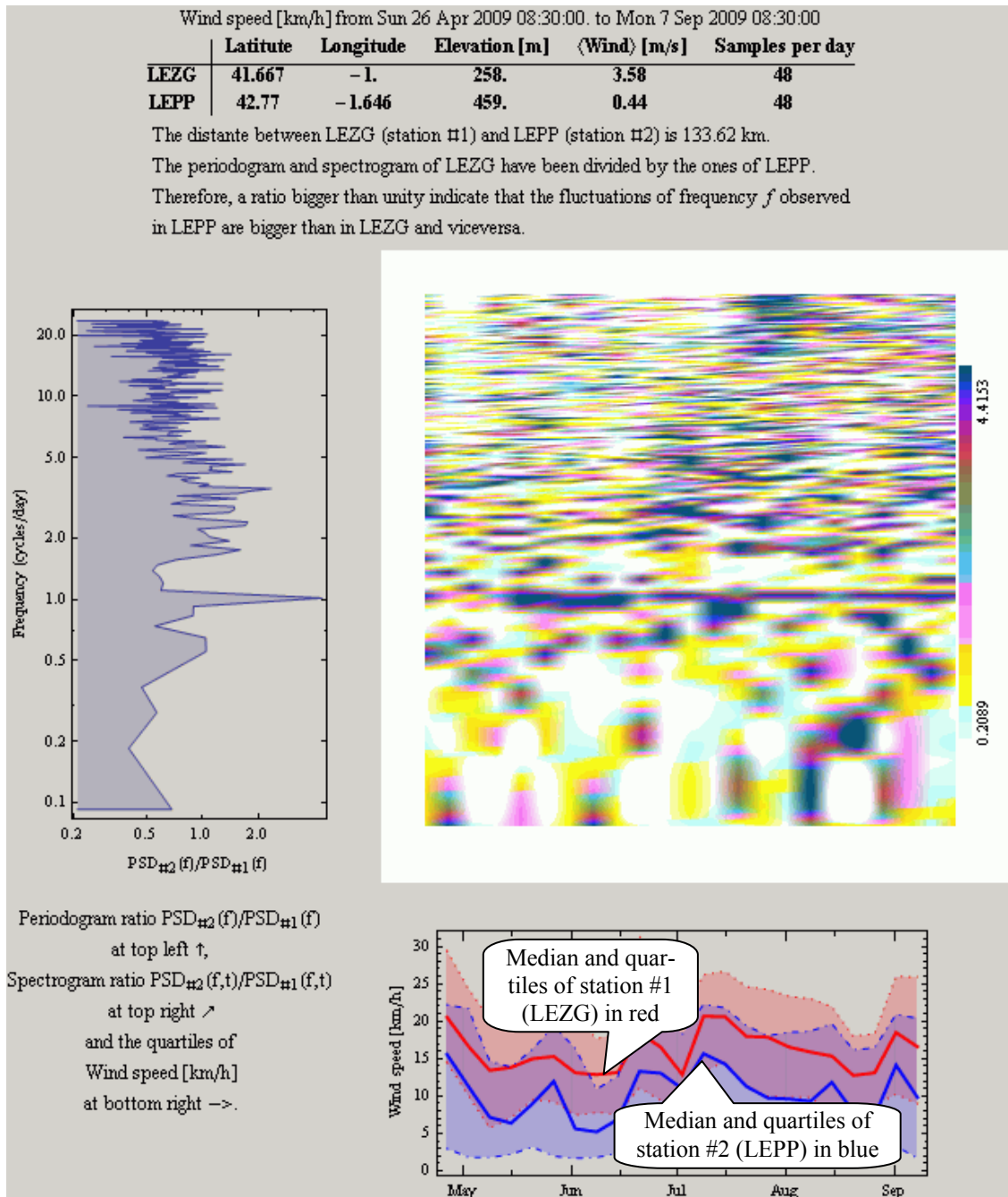


E.4.5. Periodograma y ratio entre espectrogramas

Para señales determinísticas, se suele calcular la función de transferencia entre las dos magnitudes dividiendo el espectro de las señales. Utilizando la teoría clásica de sistemas lineales invariantes en el tiempo, las variables meteorológicas se podrían aproximar, a lo sumo, a un sistema multidimensional donde, en vez de utilizar una función de transferencia, habría que utilizar una matriz de funciones de transferencia y en donde las incertidumbres de modelado y medida se considerarían ruido.

Un primer paso sería calcular el ratio de los espectros de la señal de salida (magnitud seleccionada en la segunda estación) respecto a la señal de entrada (magnitud seleccionada en la estación principal). En la práctica, este ratio es variable tanto en módulo como en fase y se representa en una gráfica de intensidad análoga a la utilizada para el espectrograma.

El programa permite seleccionar variables distintas para cada estación meteorológica, e incluso se puede seleccionar la misma estación en la solapa *Station #1* y *Station #2* para comparar las oscilaciones de distintas variables meteorológicas en una misma estación.



En la gráfica anterior, se puede ver que las estaciones están separadas 133 km y que la velocidad media del viento en la estación de Pamplona es mucho menor que en Zaragoza (0,44 m/s respecto 3.58 m/s). Esto también se observa en la gráfica temporal de la señal (la línea roja, correspondiente a la mediana de la velocidad en Zaragoza, estación #1 o de referencia, está por encima de la mediana de la velocidad en Pamplona, estación #2 o secundaria). Se han añadido los recorridos intercuartiles (cuantiles 25% y 75%) a la gráfica temporal del viento.

El hecho de que las velocidades de viento de Pamplona sean negativas durante las calmas hace que los resultados de la comparación deban tomarse con prudencia. Al no disponer de más datos sobre las estaciones, no se conoce si el anemómetro de Pamplona está en una posición relativamente más protegida del viento que el de Zaragoza. No obstante, el aeropuerto de Pamplona está rodeado de montañas y es lógico que la velocidad media sea menor allí.

Las oscilaciones por debajo de la unidad o con colores claros indican que las oscilaciones tienen mayor magnitud en la estación #1 o de referencia, mientras que las oscilaciones por encima de 1 o colores oscuros indican que las oscilaciones han sido más acusadas en la estación #2 o secundaria. En la gráfica anterior se puede observar que las oscilaciones diarias son mayores en la estación2 (zona oscura horizontal correspondiente a frecuencia $f=1$ ciclo/día). El resto de frecuencias muestra alternancias en sentido horizontal entre zonas claras y oscuras, indicando que el ratio entre la magnitud de las oscilaciones es relativamente variable.

E.4.6. Coherencia entre dos series temporales

En el caso hipotético que la serie temporal medida en una estación fuese igual a la medida en la otra estación multiplicada por una constante y sumada una desviación constante, el coeficiente de correlación sería la unidad. Si el valor instantáneo medido en una estación fuese independiente del medido en la otra estación, entonces el coeficiente de correlación sería nulo.

En la práctica, las oscilaciones que se observan en una estación se reflejan parcialmente y con un cierto retraso o adelanto en la otra. Como hay una relación temporal entre las señales, es preferible utilizar la función de correlación normalizada entre las dos señales, en vez del simple coeficiente de correlación.

Una de las técnicas más utilizadas para señales estacionarias es la coherencia, que muestra el coeficiente de correlación entre las oscilaciones de una cierta frecuencia entre las dos señales. Es de esperar que las fluctuaciones lentas sean bastante coherentes puesto que los cambios meteorológicos afectan amplias zonas geográficas. Por otra parte, las variaciones diurnas y semidiurnas están relacionadas en amplias zonas debido a la relación que existe con la radiación solar. Dado que las oscilaciones tienen magnitud y fase, la coherencia $\tilde{\gamma}_{\#1,\#2}$ es una magnitud compleja que tiene un módulo entre 0 y 1 y un desfase, que representa el retraso (ángulos positivos) o el adelanto (ángulos negativos) de las oscilaciones en la segunda magnitud respecto la de referencia. Se puede demostrar que la coherencia es la transformada de Fourier de la función de correlación entre las señales normalizada.

La coherencia a una determinada frecuencia f es nula si las señales presentan oscilaciones a la frecuencia f de magnitud independiente entre sí o con un desfase totalmente aleatorio, o bien con una relación totalmente no lineal entre los fasores. El argumento de la coherencia corresponde al desfase promedio ϕ entre las oscilaciones de frecuencia f (el retraso o adelanto promedio τ se obtiene dividiendo el desfase ϕ en radianes por la frecuencia angular $\omega = 2\pi f$).

I) Relación entre la fase y módulo de la coherencia

Existen dos diferencias principales entre el ratio entre espectrogramas y el módulo de la coherencia:

- El módulo de la coherencia está normalizado entre 0 y 1.
- Ambas magnitudes pueden exhibir oscilaciones de una cierta frecuencia f pero en donde el retraso o adelanto entre ellas no sea constante. En ese caso, el ratio entre espectrogramas mostraría la relación entre las magnitud promedio de las oscilaciones, pero la coherencia sería nula. Esta discrepancia entre ratio de espectrograma y módulo de la coherencia es típica de la relación no lineal y compleja de la atmósfera.

Si las perturbaciones que se observan en una estación, se experimentan con un cierto retraso o adelanto $\tau = \phi / (2\pi f)$ constante en el tiempo (el periodo que cuesta viajar la perturbación). Esta hipótesis de turbulencia congelada o de Taylor implica que la fase de la coherencia sea $\phi = 2\pi f \tau$. Bajo esta hipótesis, el desfase es un valor determinístico y proporcional a la frecuencia y , por tanto, la coherencia será la unidad.

En la práctica, las perturbaciones evolucionan mientras se transmiten en la atmósfera y por ello la coherencia de las señales es menor de la unidad.

E.4.7. Fase de la coherencia entre dos estaciones (desfase entre los espectros)

La fase de la coherencia indica el retraso medio τ entre las oscilaciones de cada serie temporal de frecuencia f . La fase se suele plegar al rango $[-\pi, +\pi]$ o $[0, 2\pi]$ por conveniencia, pero el retraso o adelanto entre las oscilaciones pueden exceder un periodo de oscilación ($\tau > 1/f$).

En tal caso, la fase puede exceder del rango $[-\pi, +\pi]$ o $[0, 2\pi]$ y es importante desplegar la frecuencia para obtener una estimación real del retraso entre oscilaciones utilizando la fórmula $\tau = \phi / (2\pi f)$. Los algoritmos básicos detectan saltos entre dos líneas espectrales de más de π radianes, pero en presencia de ruido y fenómenos no lineales es conveniente utilizar métodos más robustos. Para estimar la fase real del espectrograma se pueden utilizar algoritmos 2-D como los que se utilizan en tratamiento de imágenes (ver [415]).

La gráfica siguiente muestra el desfase entre los espectros estimado a la derecha y la fase de la coherencia a la izquierda. Por conveniencia se ha añadido los cuartiles de las dos señales en la parte inferior.

La estimación de la fase a bajas frecuencias no presenta problemas de estabilidad, ya que las señales muestran retrasos menores que el periodo de la oscilación. Estas oscilaciones lentas se observan con una diferencia de tiempo aproximadamente constante entre estaciones y para dichas oscilaciones la hipótesis de Taylor es aproximadamente válida.

Las oscilaciones intradía sí presentan retrasos significativamente mayores al periodo de la oscilación y la fase está muy replegada. Por tanto, es difícil estimar con precisión el número de pliegues de la fase para frecuencias mayores a 2 ciclos/día (oscilaciones más rápidas que las semidiurnas). El gráfico de intensidad muestra la elevada variabilidad de la fase de las oscilaciones intradía. Esta variabilidad indica que las fluctuaciones rápidas pueden ocurrir antes en cualquiera de las dos estaciones, sin una relación temporal simple. Para dichas oscilaciones rápidas, la hipótesis de Taylor no es válida y estas fluctuaciones se pueden considerar locales y esencialmente independientes entre las dos estaciones.

Wind speed [km/h] from Sun 26 Apr 2009 08:30:00. to Mon 7 Sep 2009 08:30:00

	Latitude	Longitude	Elevation [m]	⟨Wind⟩ [m/s]	Samples per day
LEZG	41.667	-1.	258.	3.58	48
LEPP	42.77	-1.646	459.	0.44	48

The distance between LEZG (station #1) and LEPP (station #2) is 133.62 km.

The phase difference between the spectrum of LEZG and LEPP is computed to estimate the lag between the oscillations in both stations.

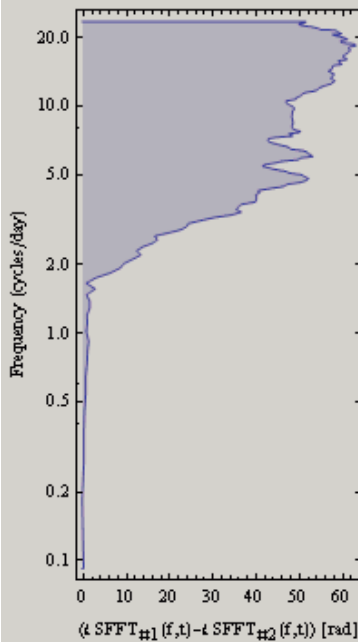
* A phase positive indicate that the fluctuations of f frequency observed (in average) first in LEZG and then in LEPP and viceversa.

* The average time lag can be computed as $lag \approx phase / (2\pi \cdot f)$ when the phase is expressed in radians.

=> In general, slow fluctuations show a phase proportional to frequency indicating that the slow fluctuations are observed with a constant time delay between stations.

* A random phase indicates that the fluctuations happen first indifferently in any station without a simple temporal link.

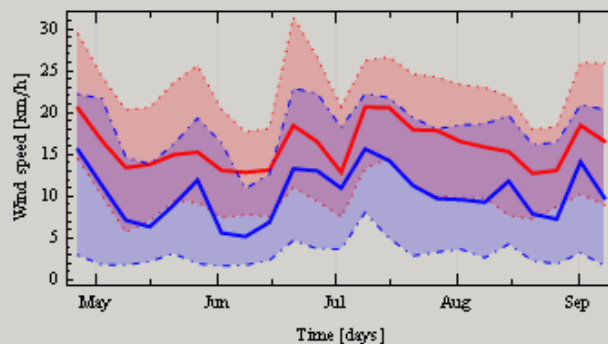
=> In general, fast fluctuations show a chaotic phase indicating that fast fluctuations are local or that their durations are smaller than the time delay.



Average spectrum phase difference between stations #1 and #2 at top left ↑
 $\langle \Delta SFFT_{\#1}(f,t) - \Delta SFFT_{\#2}(f,t) \rangle$

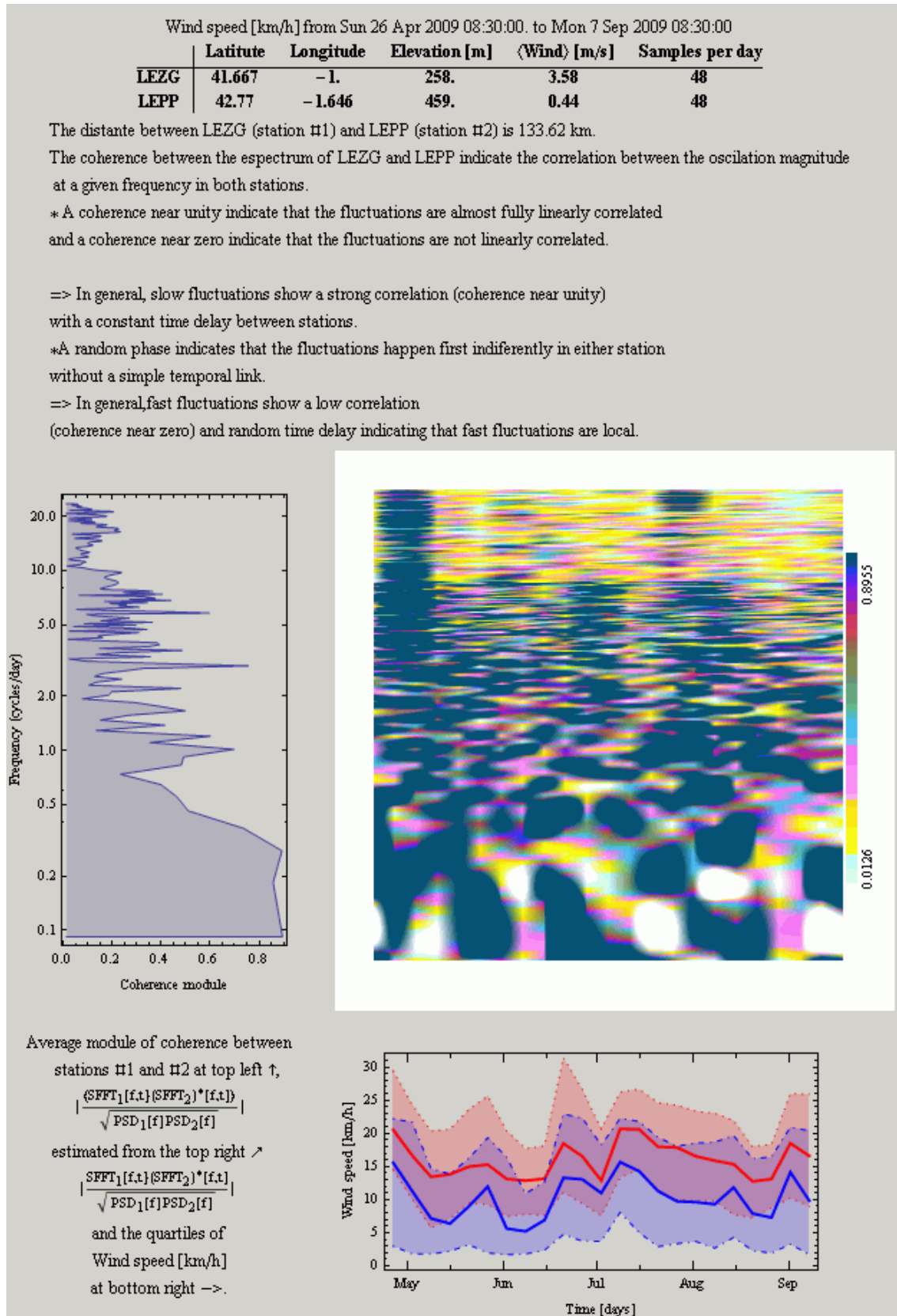
Spectrum phase difference at top right ↗
 $\Delta SFFT_{\#1}(f,t) - \Delta SFFT_{\#2}(f,t)$

and the quartiles of Wind speed [km/h] at bottom right →.



E.4.8. Módulo de la coherencia entre dos estaciones

El módulo de la coherencia es muy informativo. La coherencia a la frecuencia f de las señales no es constante en el tiempo. En el gráfico de la página siguiente se puede ver zonas oscuras, que indican que se ha observado en ambas estaciones fluctuaciones significativas en el instante y frecuencia correspondiente. Las zonas blancas indican que no se han observado fluctuaciones significativas de las características correspondientes a las coordenadas en los ejes tiempo-frecuencia en, al menos, una de las dos estaciones.



Un ejemplo de la información que se puede obtener del módulo de la coherencia es la gráfica de la siguiente página. La gráfica muestra que las fluctuaciones lentas muestran una fuerte correlación (coherencia cerca de la

unidad) hasta una frecuencia cerca de 0,3 ciclos/día entre los aeropuertos de Zaragoza y Pamplona. Entre 0,3 ciclos/día y 0,7 ciclos día, la coherencia disminuye hasta un valor de 0,2. Sin embargo, aumenta súbitamente para fluctuaciones diarias ($f = 1$ ciclo/día) debido a que la dinámica atmosférica y el calentamiento debido a la radiación solar relaciona las oscilaciones diarias entre emplazamientos lejanos. Este fenómeno también ocurre con las oscilaciones de frecuencia $f = 3$ ciclos/día (3 picos locales de viento y 3 periodos de menor viento por día) y otras frecuencias armónicas debido a que la modulación diaria del viento no es totalmente senoidal.

Exceptuando las frecuencias armónicas, las oscilaciones intradía están poco correladas y esto se puede deber a que las oscilaciones rápidas tienen una extensión geográfica significativamente menor que la distancia entre las estaciones meteorológicas (133 km).

E.5. Resumen de la comparación entre las estaciones

La gráfica de la página siguiente muestra un resumen de la coherencia entre las estaciones y lapso promedio entre las fluctuaciones. En las estaciones de Pamplona y Zaragoza, separadas 133 km, el módulo de la coherencia, salvo la frecuencia diurna y sus armónicos, se puede aproximar por un modelo fraccionario que decae con orden $0,81 \approx 5/6$. Es decir, la tendencia de la coherencia se comporta de forma parecida a los espectros habituales del viento (Kaimal, Von Karman,...), que decaen con orden $5/6$.

La tendencia de la coherencia se reduce a la mitad cerca de la frecuencia diaria, lo que indica que al agregar la generación eólica de los alrededores de Pamplona y de Zaragoza se produce, en promedio, un filtrado de las oscilaciones de frecuencias intradiarias no armónicas, con orden 0,81 (un filtrado menor que el que se esperaría de un filtro paso bajo de primer orden). No obstante, el comportamiento real se aleja significativamente del promedio en instantes concretos, tal como se ha visto en el análisis tiempo-frecuencia del viento.

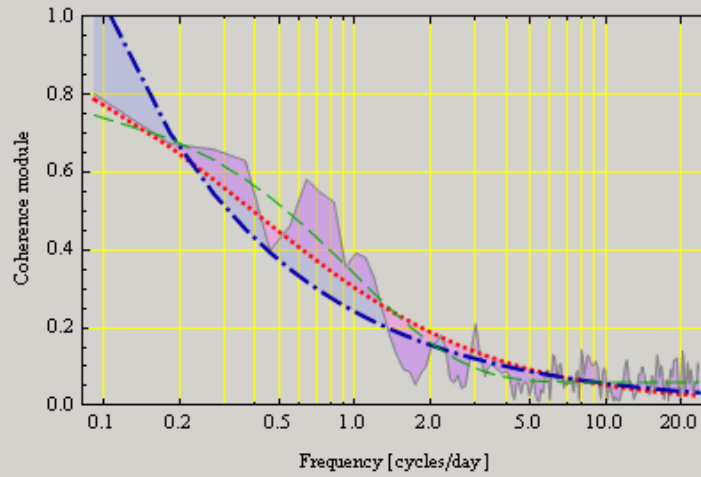
El retraso entre la observación de una fluctuación en una estación y otra no es constante. Esto es una pequeña muestra de la complejidad de la predicción meteorológica. El retraso entre las observaciones depende grandemente de la dirección del viento, que no se ha considerado en esta comparación. Las estaciones meteorológicas se encuentran alineadas, en gran medida, con las dos direcciones de viento predominante (cierzo y bochorno). Por tanto, las conclusiones que se obtienen del retraso deben tomarse como valores medios, representativos de la dirección del viento más habitual (cierzo). Con bochorno, la diferencia de tiempo puede ser a la inversa, ya que los dos vientos predominantes tienen direcciones prácticamente opuestas.

Las oscilaciones que duran varios días se suelen presentar con un día de retraso (oscilaciones de 5 días de periodo o $f \sim 0,2$ ciclos/día) o con un día de antelación (rango de frecuencias $0,3 < f < 1,5$ ciclos/día).

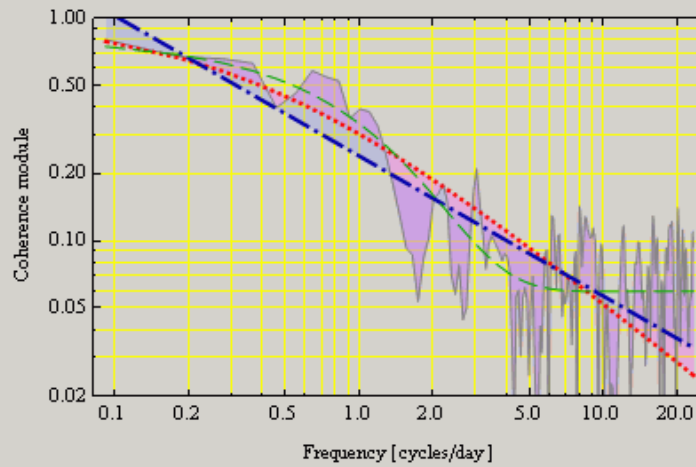
A partir de 1,5 ciclos/día (fluctuaciones intradiarias), el módulo de la coherencia tiene un valor alrededor de 0,3 o menor y, debido a la baja coherencia, la estimación de la fase tiene mucha incertidumbre, dependiendo en exceso del algoritmo utilizado y de los datos suministrados. En todo caso, retraso de hasta 10 días para fluctuaciones intradiarias no son verosímiles y no se puede concluir ningún patrón temporal con las herramientas utilizadas.

	Module of coherence [f]	Appearance
Measured coherence	$\frac{ \langle SFFT_1[f,t] \cdot (SFFT_2)^*[f,t] \rangle }{\sqrt{PSD_1[f] PSD_2[f]}}$	thin, grey solid line
Fractional model	$\frac{0.658044}{0.658044 + 1.51965 f^{0.897815}}$	thick, dotted red line
Power law model	$\frac{0.241025}{f^{0.629593}}$	dot-dashed blue line
Exponential model	$0.0592189 + 0.7532 e^{-0.997879 f}$	thin, dashed green line

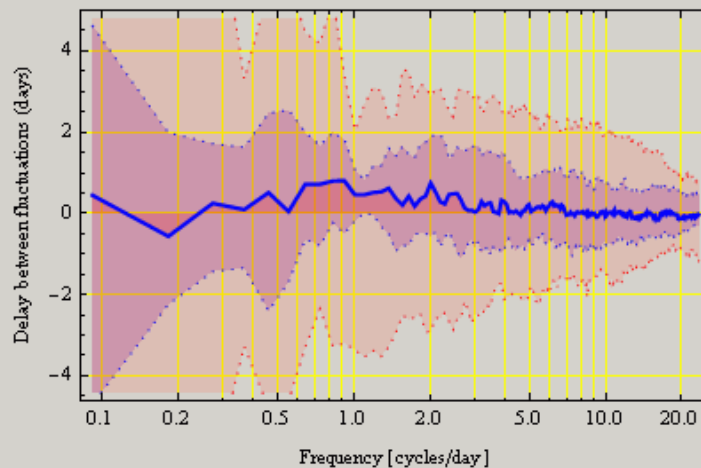
Comparison of the models in semi-logarithmic plot:



Comparison of the models in double-logarithmic plot:



Quantiles 5%, 25%, 50%, 75% and 95% of the estimated time delay (in days) between the fluctuations in LEZG respect the fluctuations in LEPP of the same frequency. (They are fairly constant provided Taylor hypothesis is applicable).



Annex F: Manual of the program

EQWIGUST

El programa EQWIGUST genera rachas de viento equivalente a partir del espectro de ese proceso. El programa tiene varias solapas en las cuales se seleccionan los parámetros del viento que se quiere analizar. A continuación se presentan las secciones del programa.

Para poder utilizar el programa interactivo para visualizar datos de estaciones meteorológicas mundiales, es necesario tener instalado en el ordenador el visor gratuito Mathematica Player™ o bien la versión 7 del programa de pago Mathematica™. El proceso para instalar el visor gratuito Mathematica Player™ se puede consultar en el anexo B

F.1. Espectro del viento equivalente

En esta pestaña se caracteriza el viento en el emplazamiento a estudiar. Un proceso normal está caracterizado totalmente por el espectro, por lo que este apartado consiste en fijar el tipo de espectro a utilizar (Kaimal, Karman, Davenport,...) y sus parámetros asociados. En general, los parámetros originales de cada espectro se han convertido a la nomenclatura utilizada en la norma IEC 61400-1. En vez de las longitudes de escala utilizadas en los espectros de Kaimal, Karman, Davenport,... se ha utilizado la escala espacial de la turbulencia Λ_1 . La turbulencia se obtiene multiplicando el viento a la altura de la turbina por la intensidad de turbulencia.

Selección del tipo de espectro según las características del emplazamiento

Wind spectrum type: Comparing Von Karman, Kaimal & IEC 61400

Wind at hub height U_{∞} : 10

Intensity Turbulence at 15 m/s, $I_{15 \text{ m/s}}$: 0.14

Length Λ_1 ($\Lambda_1 = 42 \text{ m}$ in IEC 61400-1): 42

Rotor Filter Utilizar viento equivalente

Rotor radius R: 41

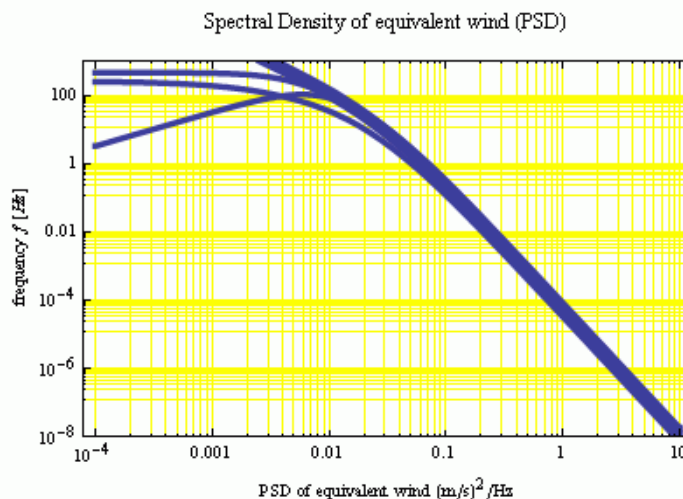
Velocidad U_{∞} aguas arriba del parque eólico

Intensidad de turbulencia $I_{15 \text{ m/s}}$ según IEC 61400-1

Escala espacial de la turbulencia Λ_1

Radio de la turbina

Rotor filter => first order low pass filter with $f_{\text{cut}} = 0.1224 U_{\infty} / R = 0.0298537 \text{ Hz}$.



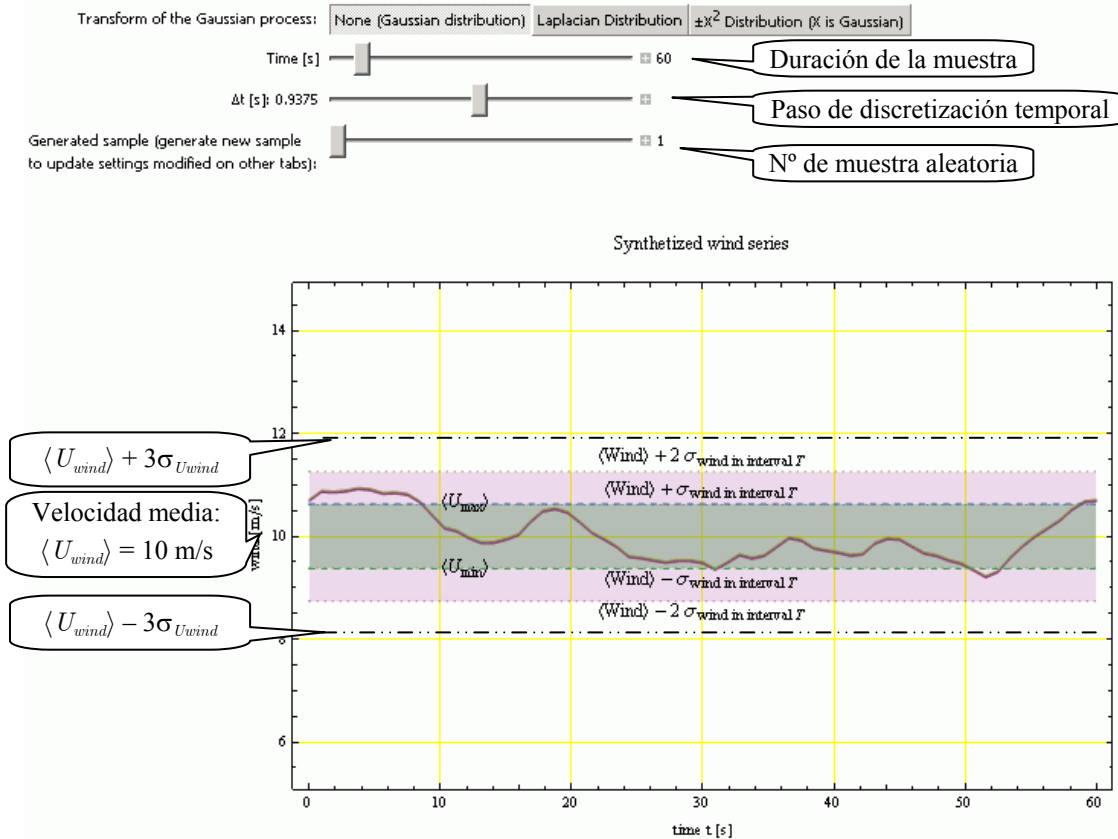
Cuando en el programa se escoge aplicar el filtro rotórico, el espectro del viento se filtra para representar la diversidad espacial en el área rotórica. Actualmente, el programa aplica un filtro paso-bajo de primer orden, pero en un futuro próximo se habilitará la selección de un filtro de primer (el referido por la literatura y que implica

un promediado a lo largo de las palas) o de segundo orden (más de acuerdo con los datos experimentales obtenidos y que representaría un filtrado a lo ancho del área barrida).

F.2. Generación de serie aleatoria de viento equivalente

En esta pestaña se sintetizan rachas de viento equivalente sin imponer ninguna condición especial. Es decir, correspondería a un intervalo cualquiera de los que se miden con un anemómetro.

Los controles sirven para ajustar la transformación del proceso normal, la duración de la muestra sintetizada, el paso de discretización temporal. El control del número de muestra aleatoria sirve para generar rachas distintas.



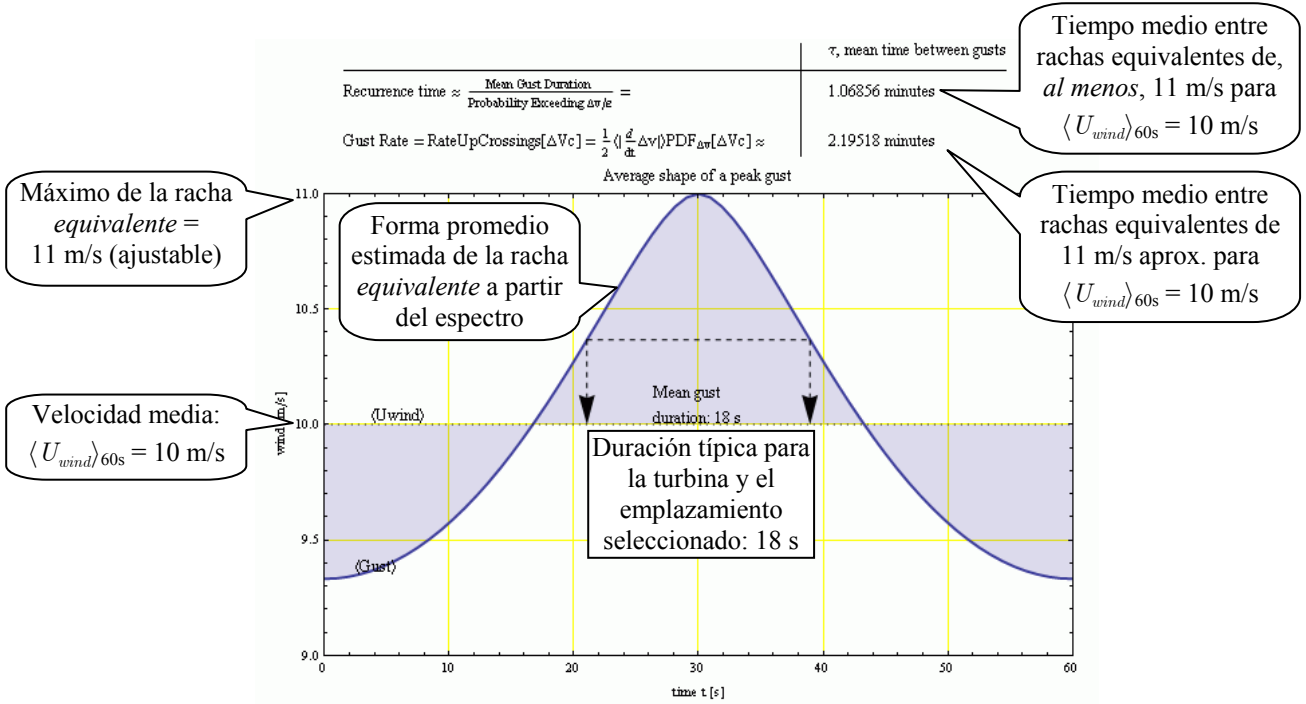
F.3. Forma promedio de racha tipo pico

La forma de una racha pico, en un proceso normal, no depende de su amplitud. Por ello resulta interesante analizar dicha racha y sus parámetros (duración típica, rampa de subida y bajada, energía contenida en la racha,...).

La solapa de la forma media de la racha pico indica no sólo cómo es la racha, sino que da la frecuencia estimada de ocurrencia. Esta frecuencia es bastante fiable para rachas convencionales, pero puede presentar errores importantes para rachas extremas, las que se producen menos de una vez a la semana. Además, el proceso es simétrico en el tiempo (la racha tiene la misma forma si se visualiza cámara adelante o atrás). Sin embargo, medidas experimentales indican que la rampa de subida es más pronunciada y la de bajada es más tendida.

Una característica interesante a citar es que la racha de viento equivalente tiene una forma bastante menos picuda que la del viento convencional. Si no se hubiera elegido aplicar el filtro rotórico, la racha correspondería a viento convencional y su forma sería considerablemente más impulsiva. Esto se debe a que el espectro del viento equivalente tiene un menor contenido de frecuencias altas (la frecuencia de corte en una turbina multimegawatio es del orden de algunas centésimas de hercio).

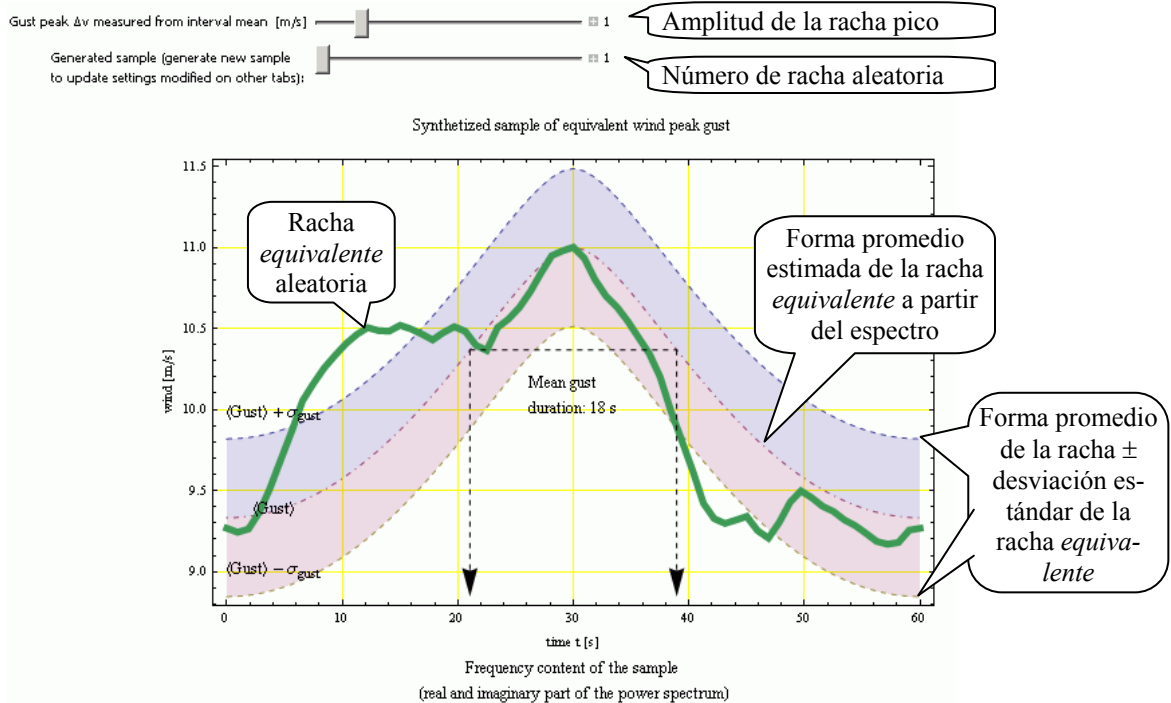
La norma IEC 61400-1, sobre la seguridad estructural de las turbinas, recomienda utilizar una racha tipo pico que se parece bastante a la racha de viento equivalente mostrada en la figura anterior. Las rachas medidas en campo son más impulsivas, pero la norma utiliza implícitamente una racha de viento equivalente para analizar la seguridad estructural de la máquina.



F.4. Generación de racha tipo pico aleatoria

En esta solapa se muestra una muestra aleatoria de una ráfaga pico, superpuesta a la forma promedio más/menos la desviación estándar del viento. El control del número de muestra aleatoria sirve para generar rachas distintas. De esta forma se puede comprobar la variabilidad en la forma de las rachas.

En la figura siguiente se puede observar que aunque la amplitud de la racha es de 1 m/s respecto la media de la racha (10 m/s), el recorrido del viento es de 1,7 m/s. Esto se debe a que el periodo utilizado para generar la racha es de solo tres veces la duración media de la misma.



F.5. Generación de racha tipo rampa aleatoria

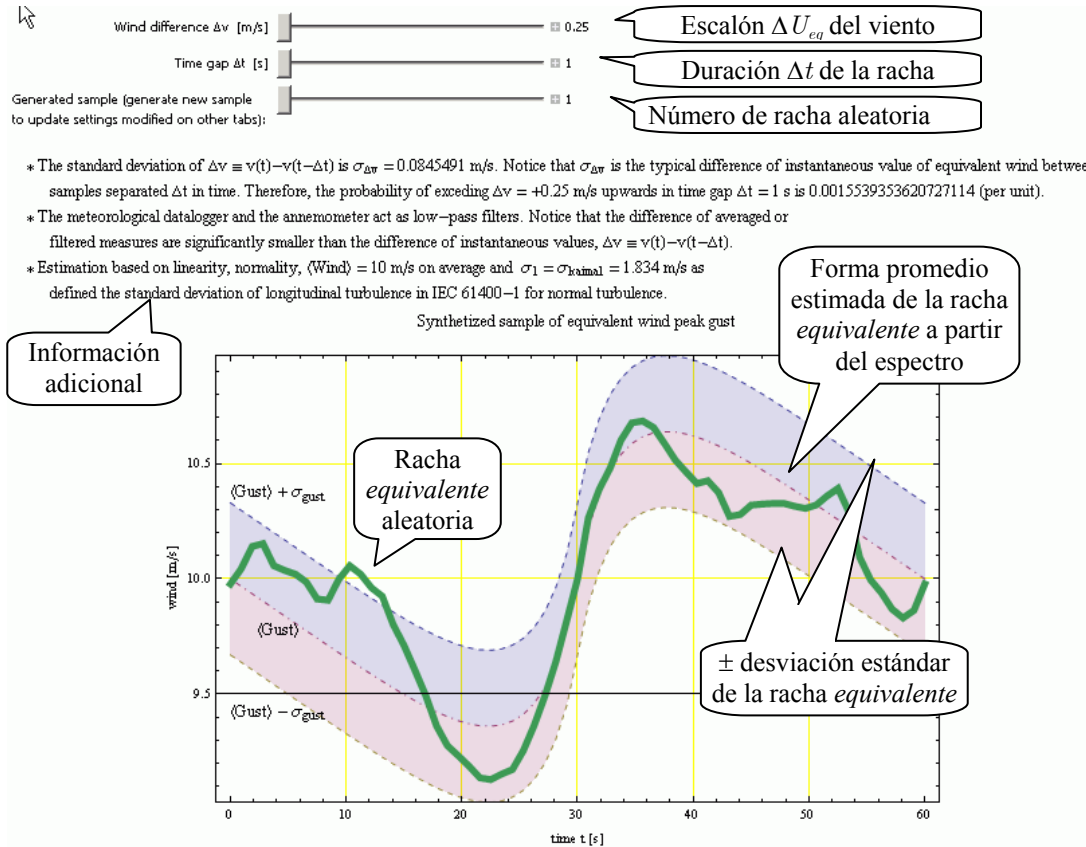
En esta solapa se muestra una muestra aleatoria de una ráfaga tipo rampa, superpuesta a la forma promedio más/menos la desviación estándar del viento. La rampa de la racha se define por un intervalo de tiempo Δt y el salto de velocidad, Δv .

La forma de la racha depende de la rampa de la racha, $\Delta v/\Delta t$. Es decir, la racha tiene una duración típica para cada rampa. Además, la solapa da información adicional sobre la misma

El control del número de muestra aleatoria sirve para generar rachas distintas. De esta forma se puede comprobar la variabilidad en la forma de las rachas.

En la figura siguiente se puede observar que aunque se ha seleccionado una rampa de duración $\Delta t = 1$ s y amplitud $\Delta v = 0,25$ m/s, la duración típica es del orden de unos 10 s.

la amplitud de la racha es de 1 m/s respecto la media de la racha (10 m/s), el recorrido del viento es de 1,7 m/s. Esto se debe a que el periodo utilizado para generar la racha es de solo tres veces la duración media de la misma.



Annex G: Symbols and Nomenclature

G.1. Frequently Used Symbols and Abbreviations

G.1.1. General Acronyms

ACF = Auto correlation function (of a random signal)
ACVF = Auto covariance function (of a random signal)
CCF = Cross correlation function (of two random signals)
CDF = Cumulative Density Function (of a random signal)
CN(μ, σ) = Complex Normal Distribution of mean μ and standard deviation σ .
CPSD = Cross Power Spectral Density (of two random signals)
CRV = Complex Random Variable
CTMC = Continuous Time Markov Chain
DAQ = Digital Acquisition Board
DFIG = Doubly Fed Induction Generator
DFT = Discrete Fourier Transform
DTMC = Discrete Time Markov Chain
FFT = Fast Fourier Transform
FMC = Fuzzy Markov Chain
FOT = Fraction-Of-Time probability framework
HMM = Hidden Markov Chain
IDFT = Inverse Discrete Fourier Transform
LV = Low Voltage
MC = Markov Chain
MCA = Markov Chain approximation
MCMC = Monte Carlo Markov Chain
MCS = Monte Carlo Simulation
MDP = Markov Decision Process
MV = Medium Voltage
PCC = Point of Common Coupling
PDE = Partial Differential Equation
PDF = Probability Density Function
PMF = Probability Mass Function
PSD = Power Spectral Density (of a random signal)
P_{st} = Short Time Flicker Emission Level
RMS = Root Mean Squared (value of a signal)
RV = Random Variable
SDE = Stochastic Differential Equation
SCR = The short circuit ratio is the ratio of the short circuit power at the point of common coupling of the grid, $S_{k,PCC}$, to the installed wind power, $N S_n$ in a cluster of N turbines
SCIG = Squirrel Cage Induction Generator
S_n = Assigned power of a wind turbine
SOC = State Of Charge (of a battery)
VRIG = Variable Resistance Induction Generator
WF = Wind Farm
WMO = World Meteorological Organization
WT = Wind Turbine

G.1.2. Aerodynamic variables and functions

a = axial induction factor at the blade element.
 a' = the tangential (or angular) induction factor at the blade element.

$C_p(\lambda, \theta)$ = turbine power coefficient.
 $C_q(\lambda, \theta)$ = turbine torque coefficient = $C_p(\lambda, \theta) / \lambda$
 $\ell_{U_{wind}}$ = integral length scale of the turbulence.
 $\lambda = R \Omega_{rotor} / U_{eq}$ = blade tip speed ratio (dimensionless blade speed).
 $\lambda_i''(\tau)$ = element speed ratio = cotangent of the relative flow angle at the blade element (see Fig. 294 for details).
 $\lambda_i'(\tau)$ = effective blade tip speed ratio.
 $\langle \lambda' \rangle$ = mean equivalent blade tip speed ratio.
 $\langle \lambda'^2 \rangle$ = mean equivalent squared inverse of blade tip speed ratio.
 N_{blades} = number of blades in the turbine.
 θ = blade pitch angle.
 Ω_{rotor} = is the rotor angular speed in rad/s.
 $PSD_{U_{eq}}^+(f)$ = dimensionless one-sided power spectral density of equivalent wind U_{eq}
 ρ_{air} = air density in kg/m³.
 T_{rotor} = turbine torque in N·m.
 ΔT_{rotor} = turbine torque deviation from its mean in N·m.
 τ_{fzc} = lag of the first zero-crossing of $ACF(\tau)$.
 $T_{U_{wind}}$ = integral time scale of the turbulence.
 $U_{wind} = U_{longitudinal}$ = longitudinal component of the wind measured in m/s with an ideal anemometer at hub height and unperturbed by the presence of any wind turbines.
 $U_{vertical}$ = vertical component of the wind in m/s.
 $U_{lateral}$ = lateral component of the wind in m/s.
 $U_{eq} = \sqrt{\frac{2 T_{rotor}}{\rho_{air} \pi R^3 C_q(\theta, \lambda)}}$ = equivalent wind in m/s.
 $\Delta U_{eq} = U_{eq} - \langle U_{eq} \rangle$ = equivalent turbulence in m/s.
 $\Delta(U_{eq}^2) = U_{eq}^2 - \langle U_{eq}^2 \rangle$ = effective quadratic turbulence in m²/s².
 $\dot{U}_{wind}(t) \equiv dU_{wind}(t)/dt$ = Instantaneous air acceleration

G.1.3. Power output variables and functions

The main variables and parameters are listed bellow in order of appearance.

$P_{farm}(t)$ = real power output of wind farm at time t .
 $Q_{farm}(t)$ = reactive power output of wind farm at time t .
 f = frequency in Hertz.
 $j = \sqrt{-1}$ = the imaginary unit.
 $w = 2\pi f$ = angular frequency in rad/s.
 R = rotor radius in m.
 $\vec{P}_{farm}(f)$ = phasor component of wind farm power output at frequency f .
 $\vec{P}_{turbine\ i}(f)$ = phasor component of wind turbine number i at frequency f .
 $\vec{P}_1(f)$ = phasor component of power output at frequency f from one turbine.
 $\vec{P}_N(f)$ = phasor component of power output at frequency f from a turbine cluster with N turbines.
 $\langle |\vec{P}_{farm}(f)|^2 \rangle = \langle P_{farm}^2(f) \rangle$ = PSD of the farm power output at frequency f .

$\langle |\tilde{P}_{turbine\ i}(f)|^2 \rangle = \langle P_{turbine\ i}^2(f) \rangle$ = PSD of the turbine number i at frequency f
 $J(f) = \sqrt{\langle P_{farm}^2(f) \rangle / \langle P_{turbine}^2(f) \rangle}$ = admittance at frequency f of the wind farm power.
 $\varphi_{i,j}/3$ = angle difference between blades of turbines i and j (in a three bladed rotor).

G.1.4. Model parameters

r = system order of the considered signal (i.e., half the slope trend of PSD in a double logarithmic plot).
 $\frac{P_1}{P_n^2}$ = overall fluctuation level of the turbine (i.e., the PSD trend line at 1 Hz) in p.u. units.
 P_0 = squared average of tower shadow power oscillation relative to P_1 .
 f_0 = mean tower shadow frequency.
 P_2 = squared noise level on power output relative to P_1 .
 P_n = nominal power of the turbine.
 N = number of equivalent turbines in the farm.
 f_1 = cut-off PSD frequency or frequency where PSD starts dropping with slope $2r$ in a double logarithmic plot ($f_1 \leq 0,02$ Hz).
 $f_2 = 1/\tau_2$ = high pass PSD frequency or minimum frequency where PSD remains approximately constant ($f_2 \geq 10$ Hz).
 f_{blade} = frequency of blade crossing the tower (in a three bladed turbine $f_{blade} = 3 \Omega_{rotor} / 2\pi$ and for megawatt turbines, $0,5 \text{ Hz} \leq f_{blade} \leq 2 \text{ Hz}$).
 σ_{blade}^2 = contribution of wind shear and tower shadow to power variance.
 $\tau_1 = 1/f_1$ = characteristic time associated with the PSD cut-off frequency = zero of the transfer function modeling the power output of wind farms or turbines (without sign).
 $\tau_2 = 1/f_2$ = characteristic time associated with PSD noise floor = root of rational transfer function modeling the power output of wind farms or turbines (without sign).

G.1.5. Markov Decision Processes

$a_{ij}[k]$ = probability of having observed a transition from state i to j at instant k .
 β_{cl} = confidence level.
 β_{sun} = altitude angle of the sun
 γ_i = Centroid of state i .
 $\vec{\gamma} = [\gamma_1, \gamma_2, \dots, \gamma_m]^T$ is the vector of the state centroids.
 $\boldsymbol{\pi} = [\pi_1, \pi_2, \dots, \pi_m]^T$ = the stationary distribution of the Markov chain.
 φ_i = Mode of $\Pr(\text{state}_i | \mathbf{x}[k])$
 λ_i = eigenvalue of \mathbf{P} , numbered in decreasing absolute order ($|\lambda_i| \geq |\lambda_{i+1}|$) starting from $\lambda_1 = 1$.
 F_i = observed occurrences of state i
 F_{ij} = observed transitions from state i to j
 l = number of observed samples of $y[k]$.
 m = number of states of the Markov chain.
 $\mathbf{P} = [p_{ij}]_{s \times s}$ = transition matrix of a ergodic Markov chain.
 $\mathbf{P}[k] = \sum_{n_1} \sum_{n_2} \sum_{n_3} \Pr(n_1|k)\Pr(n_2|k)\Pr(n_3|k)\mathbf{P}|_{n_1, n_2, n_3}$ = basic transition matrix at instant k .
 p_{ij} = forward transition probabilities from state i to state j of the Markov chain.
 $\tilde{\mathbf{P}} = [\tilde{p}_{ij}]_{s \times s}$ = backward transition probabilities.
 $\hat{\mathbf{P}} = [\hat{p}_{ij}]_{s \times s}$ = estimate of transition probability of the Markov chain.

$\mathbf{P}|_{n_1, n_2, n_3}$ = basic transition matrix given the season n_1 , type of day n_2 and hour period n_3 .
 $season(n_1, k) = \Pr(\text{Seasonal Pattern} = n_1 | k)$ = Probability that the behaviour of the system corresponds to the seasonal pattern numbered as n_1 at instant k .
 $hourlyPeriod(n_3, k) = \Pr(\text{hour classification} = n_3 | k)$ = Probability that the behaviour of the system corresponds to the intraday pattern numbered as n_3 at instant k .
 $weekDay(n_2, k) = \Pr(\text{Type of day} = n_2 | k)$ = Probability that the behaviour of the system corresponds to the weekly pattern numbered as n_2 at instant k .
 $s[k]$ = number of the most likely state of the Markov chain at instant k .
 $\boldsymbol{\Lambda}$ = the diagonal matrix whose diagonal elements are the corresponding eigenvalues (i.e. $\Lambda_{ii} = \lambda_i$).
 \mathbf{V}_L = the square ($m \times m$) matrix whose i^{th} row is the basis of the left eigenvector \vec{v}_i^L of \mathbf{P} , normalized with unity sum of vector components: $\mathbf{P} = \mathbf{V}_L^{-1} \boldsymbol{\Lambda} \mathbf{V}_L^T$.
 \mathbf{V}_R = the square ($m \times m$) matrix whose i^{th} column is the basis of the right eigenvector \vec{v}_i^R of \mathbf{P} : $\mathbf{P} = \mathbf{V}_R \boldsymbol{\Lambda} (\mathbf{V}_R^T)^{-1}$.
 $\vec{v}[k] = [v_1[k], v_2[k], \dots, v_m[k]]$ = vector of wind farm power output in the canonical basis of left eigenvectors of $\hat{\mathbf{P}}$ at instant k .
 $y(t)$ = observed variable in the continuous time domain. Recall that $y(t=k\Delta t) = y[k]$
 $y[k]$ = observation at instant k (for instance, the moving average computed during Δt period of the wind or solar power output).
 $\langle y \rangle$ = mean of observations $y[k]$.
 $\hat{y}[k]$ = estimated observation at instant k .
 $\hat{y}(t)$ = estimation of the periodically observed variable $y[k]$ in the continuous time domain. Recall that $\hat{y}(t=k\Delta t) = y[k]$
 $\tilde{y}[k]$ = kernel scale factor used to estimate $\hat{y}(t)$.
 $\vec{x}[t] = \mathbf{x}(t) = [x_1(t), x_2(t), \dots, x_m(t)]$ = vector of estimated probability (or membership degree) of Markov state in continuous time domain. Recall that $\mathbf{x}(t=k\Delta t) = \mathbf{x}[k]$.
 $\vec{x}[k] = \mathbf{x}[k] = [x_1[k], x_2[k], \dots, x_m[k]]$ = vector of probability (or membership degree) of each state of the Markov chain at instant k .
 $z(t)$ = instantaneous wind farm power output in continuous time domain. Recall that $y(t) = \int_{t-\Delta t}^t z(t) dt / \Delta t$
 $u[k]$ = most likely state for the observation $y[k]$.
 $\mathbf{z}[k] = [z_1[\mathbf{x}[k]], z_2[\mathbf{x}[k]], \dots, z_m[\mathbf{x}[k]]]$ = output of the fuzzy classification representing the state probability at instant k .

G.2. Nomenclature

G.2.1. General conventions

The utility of a mathematical notation is proportional to the amount of information it condenses. Thus, notation has been intended to be as simple, uniform and consistent with specialized literature conventions as possible, with the aim of making this thesis to be as easy to read as possible.

Lower-case symbols normally denote instantaneous values, sampled random variables, Fourier series coefficients and vectors. Upper-case symbols normally denote phasors, spectral phasor densities, statistical distributions and matrixes.

Vector, as \mathbf{x} , and matrices, as \mathbf{M} , are denoted in bold face whereas their elements are in italic lowercase with indexes

subscripted, as m_{ij} or x_i . When confusion among the whole vector/matrix and its elements can arise, the vector/matrix has been eventually remarked with an arrow on top.

Complex variables and phasors have been remarked with an arrow on top, as in \vec{S} , and their modulus is indicated with single vertical bars, as in $|\vec{S}|$. Arrows have been used to emphasize the vectorial meaning of phasors, which condense in a complex number the amplitude and lag from the time reference of an almost cyclostationary process. Special care has been taken to notice complex stochastic variables to avoid applying definitions or properties which are valid only for real random variables, instead of the extended generalized versions valid also for complex random variables.

$\text{Re}(\cdot)$ and $\text{Im}(\cdot)$ state for the real and imaginary part of a complex number. When Re is eventually used to refer to the Reynolds number of a flow, it is clearly stated in the text.

Probability is denoted by $\text{Pr}(\cdot)$ to avoid confusion with real power, P . Average values are denoted by angle brackets $\langle \cdot \rangle$ and estimated elements are stressed with the circumflex accent, as $\hat{\sigma}$, when it is necessary to distinguish real and estimated parameters, as σ .

G.2.2. Nomenclature in frequency domain

In the literature, apparent and complex power and power spectral density, both are denoted by the letter S . Since this thesis is focused on the grid, S and \vec{S} stand for apparent and complex power respectively unless otherwise stated in the text. Hence, power spectral density is referred as $PSD(f)$.

When the context is sufficiently clear and there is no misleading risk, indexes or explicit functional dependences have been dropped to clarify expressions. Moreover, the phasor modulus is also notated removing the simple vertical bars and the top arrow, $|\vec{S}| \equiv S$, for the sake of simplicity when there is no confusion risk.

a) General Fourier Conventions

The usual conventions in signal theory and stochastic processes have been used for Fourier Transforms.

On the one hand, complex Fourier coefficients and two-sided spectrums are preferred in signal processing theory and its algorithms because the notation and computer codes are simpler. In brief, two-sided spectrums are best suited for calculus. Spectral calculus are based on two-sided spectrums, complex Fourier coefficients and regular frequency f measured in Hertz, which are the default convention in this work.

On the other hand, negative frequencies can be valid mathematically, but not physically. Peak (i.e. amplitude) or rms phasors are used for analyzing data. Phasors in peak – when $x(t)$ is an instantaneous value– or rms units –when $x(t)$ is an rms value– are employed. The charts only show positive frequencies to be crisper since Fourier transform of a real signal has Hermitian symmetry. Since no negative frequencies are shown at those graphs, one-sided magnitudes are represented unless otherwise stated. In brief, one-sided spectrums are used for visualizing data.

One-sided spectrums are used just only in plots and in a few more convenient cases. To avoid ambiguities, whichever

a one-side value is used, it is noticed with a plus exponent, as in $\vec{X}^+(f)$, indicating that only non-negative frequencies must be considered. Even though using two-sided spectrums in definitions and calculations and using one-sided spectrums in plots might seem a notational inconsistency, this decision is quite pragmatic since only the positive frequencies are customarily represented in Electrical Engineering and Meteorology.

The two-sided magnitudes considered in this work are hermitic since all the signals are real. The two-sided $\vec{X}(f)$ and one-sided $\vec{X}^+(f)$ magnitudes have been defined so that its integral in the corresponding (one or two sided) frequency domain is the same. This notation agrees with usual conventions for Fourier coefficients and power spectral densities since most signals in this work are either stochastic or periodic. This convention implies that a 2 factor is applied to plot the one-sided magnitudes from the two-sided variables:

$$\vec{X}^+(f) \equiv 2\vec{X}(f) \quad \forall f > 0 \quad (786)$$

$$\vec{X}^+(0) \equiv \vec{X}(0) \quad (\text{DC term or } \langle x(t) \rangle) \quad (787)$$

$$\vec{X}^+(f) \equiv 0 \quad \forall f < 0 \quad (788)$$

The former definitions (786) to (788) has the advantage that the same formulas are valid for one and two sided variables. Notice that in some areas of signal theory the 2 factor is not applied and congruently, factors which depends on the considered frequency domain (one or two side) must be included in the calculus.

In practice, the continuous signals are discretized to be measured and they have finite duration, usually from time origin up to time T . Although the general theoretic treatment is continuous, special care has been taken so that final expressions can be applied straightforward to real measurements, just replacing continuous Fourier transforms and integrals by their discrete counterparts. Integrals must be interpreted as sums with an eventual factor due to the sum step. Infinite integrating limits must be limited to the data boundaries. Notice also that anti-aliasing filtering, window tapering and padding are customarily applied to real data for adjusting leakage (or picket fence effect), spectral resolution and uncertainty of the estimates, although it might be eventually omitted in the text.

b) Scaling Fourier Transforms to obtain spectral measures not dependent on data length

The Fourier transform of a periodic signal is proportional to the number of cycles considered in the transform. Hence, the Fourier coefficients, which are basically the Fourier transform of the discretized signal divided by signal length, are customarily used because they are the component amplitudes, irrespective of the number of cycles considered.

In a stochastic signal, the Fourier transform is customarily divided by \sqrt{T} since its squared absolute value is, in average, the $PSD(f)$ independently of signal duration – $PSD(f)$ is a measure of signal variance at frequency f –.

In signals which vanish to zero except in a limited domain, it is customary to use the Fourier transform without scaling since its squared absolute value is considered to be its energy at frequency f .

Notice that the type of signal (energy-bounded pulse, periodic signal or stochastic process) should be stated (using a subscript or in the text) to know which scaling factor applied to the Fourier transform. If nothing is stated, then $\vec{X}(f)$ should be interpreted just as the Fourier transform of the signal divided by \sqrt{T} as in (791).

c) Conventions for pulses.

If $x(t)$ is a signal of finite energy defined in $0 \leq t \leq T$, then its frequencial content is characterized through its Fourier transform, denoted by \mathcal{F} :

$$\vec{X}_{\mathcal{F}}(f) = \int_0^T x(t) e^{-j2\pi f t} dt = \mathcal{F}\{x(t)\} \quad (789)$$

Whenever the sample duration T of the original time series should be noticed, the notation $\vec{X}_{\mathcal{F}}(f)$ may be replaced by $\vec{X}_{\mathcal{F},T}(f)$.

The units of $\vec{X}_{\mathcal{F}}(f)$ are the same than the ones of $x(t)$ per Hertz. If the signal is padded with zeroes at its domain extremes, $\vec{X}_{\mathcal{F}}(f)$ does not vary. If the pulse is symmetric respect time origin, then the Fourier transform is real.

d) Conventions for periodic signals

If $x(t)$ is a periodic signal of period T , its Fourier transform is a modulated Dirac comb. The complex Fourier coefficient of order k , \vec{X}_k , is the conventional Fourier transform of the signal during one or several periods, scaled by the sample duration, at harmonic frequency $f = k/T$:

$$\vec{X}_k = \frac{1}{T} \int_0^T x(t) e^{-j2\pi k t/T} dt = \frac{1}{T} \mathcal{F}\{x(t)\} = \frac{1}{T} \vec{X}_{\mathcal{F}}(f=k/T) \quad (790)$$

The units of \vec{X}_k is the same than $x(t)$. The Fourier coefficients are notated with the k subscript to distinguish them from the Fourier transform of stochastic signals or bounded-energy pulses. The amplitude of the fluctuation of harmonic k is $|\vec{X}_k + \vec{X}_{-k}^*| = 2|\vec{X}_k|$ in peak values and its initial phase is $\text{Arg}[\vec{X}_k]$, independently of signal period T .

The complex Fourier coefficient \vec{X}_k can include signal duration in the subscript, as in $\vec{X}_{k/T}$, to indicate the sample duration T from where the Fourier coefficients has been estimated.

e) Conventions for stochastic processes

The power of a stochastic signal in any frequency band does no statistically depend on signal duration T . But its Fourier coefficients corresponding to a given frequency $f = k/T$ decreases inversely proportionally to \sqrt{T} (for a Gaussian signal). Thus, a \sqrt{T} factor is preferred in stochastic processes to obtain a spectral measure whose mean does not depend on signal duration T .

The Fourier transform of a stochastic signal in time domain $x(t)$ of length T , divided by \sqrt{T} is notated as $\vec{X}_{\sigma}(f)$:

$$\vec{X}_{\sigma}(f) \equiv \frac{1}{\sqrt{T}} \int_0^T x(t) e^{-j2\pi f t} dt = \frac{1}{\sqrt{T}} \mathcal{F}\{x(t)\} = \frac{1}{\sqrt{T}} \vec{X}_{\mathcal{F}}(f) \quad (791)$$

Fortunately, the definition (791) has the advantage that the variance of $\vec{X}_{\sigma}(f)$ is the two-sided power spectral density, $\langle |\vec{X}_{\sigma,T}(f)|^2 \rangle = PSD_x(f)$, which is independent of the sample length and it characterizes the process [416].

$\vec{X}_{\sigma}(f)$ will be referred as stochastic spectral phasor density or just (stochastic) phasor for short. The units of $\vec{X}_{\sigma}(f)$ are the same than the ones of $x(t)$ per square root of Hertz.

The scale factor of $\vec{X}_{\sigma,T}(f)$ is between the conventional Fourier transform, used for pulses and signals of bounded energy, and the Fourier coefficients, used for pure periodic signals.

f) Power spectral density $PSD_x(f)$, cross power spectral density $CPSD_{xy}(f)$ and squared complex coherence $\vec{\gamma}_{xy}^2(f)$

The power spectral density $PSD_x(f)$ and the cross power spectral density $CPSD_{xy}(f)$ of stochastic processes $x(t)$ and $y(t)$ are formally defined in the *fraction-of-time (FOT)* probability framework [417] as the limiting average of power density for long data sets.

$$\begin{aligned} |\vec{X}_{\sigma,\infty}(f)| &\equiv \lim_{T \rightarrow \infty} |\vec{X}_{\sigma,T}(f)| = \lim_{T \rightarrow \infty} \frac{1}{\sqrt{T}} \left| \int_0^T x(t) e^{-j2\pi f t} dt \right| \\ PSD_x(f) &\equiv \lim_{T \rightarrow \infty} \frac{1}{T} \left| \int_0^T x(t) e^{-j2\pi f t} dt \right|^2 = \lim_{T \rightarrow \infty} |\vec{X}_{\sigma,T}(f)|^2 \quad (793) \end{aligned}$$

$$\begin{aligned} \overline{CPSD}_{xy}(f) &\equiv \\ &\equiv \lim_{T \rightarrow \infty} \frac{1}{T} \left(\int_0^T x(t) e^{-j2\pi f t} dt \right) \left(\int_0^T y(t) e^{-j2\pi f t} dt \right)^* \quad (794) \end{aligned}$$

In fact, the use of very long samples for the estimation of spectral measures would encompass inevitably very complex and non-stationary meteorological phenomena. For the processes to be tractable, they are assumed to be wide-sense stationary. Thus, the weather characteristics and the wind turbine operational points should remain fairly constant in each data series. Hence, this limits the applicable time horizon of this approach, making impractical the former definitions.

Fortunately, they can be alternatively defined as the ensemble average estimates from data sets of finite duration [418, 419] according to the classical stochastic-process framework.

$$|\vec{X}_{\sigma,\infty}(f)| = \langle |\vec{X}_{\sigma,T}(f)| \rangle \quad (795)$$

$$PSD_x(f) = \langle |\vec{X}_{\sigma,T}(f)|^2 \rangle \quad (796)$$

$$\overline{CPSD}_{xy}(f) = \langle \vec{X}_{\sigma,T}(f) \vec{Y}_{\sigma,T}^*(f) \rangle \quad (797)$$

The previous definitions stresses the meaning of $PSD_x(f)$ as the average of many experimental power spectrums, $\langle |\vec{X}_{\sigma}(f)|^2 \rangle$, and $\overline{CPSD}_{xy}(f)$ as the average of many experimental cross spectrums, $\langle \vec{X}_{\sigma}(f) \vec{Y}_{\sigma}^*(f) \rangle$ for some operational conditions. They are applicable in wind energy providing the spectral averages are computed while the system behaviour do not change significantly. In fact, $\langle |\vec{X}_{\sigma,T}(f)| \rangle$, $\langle |\vec{X}_{\sigma,T}(f)|^2 \rangle$ and $\langle \vec{X}_{\sigma,T}(f) \vec{Y}_{\sigma,T}^*(f) \rangle$ should be estimated for each significantly different operational mode of the system. The determination of the operational conditions to be considered for a given representation precision is out of the scope of this thesis and it is a future line of work [46].

To avoid confusions, the one-sided power spectral density is denoted by $PSD_x^+(f)$ to distinguish from the two-sided

power spectral density, $PSD_x(f)$, and their units are the same than $x^2(t)$ per Hertz.

If $x(t)$ is a normal process, then $\vec{X}_\sigma(f)$ is a complex Gaussian variable [420] of zero mean and variance $PSD_x(f)$. Moreover, the modulus of $\vec{X}_{\sigma,T}(f)$ is a Rayleigh random variable of mean:

$$\langle |\vec{X}_\sigma(f)| \rangle = \sqrt{\pi/4} \sqrt{PSD_x(f)} = 0,886 \sqrt{PSD_x(f)} \quad (798)$$

The modulus of $\overline{CPSD}_{xy}(f)$ is the spectral analogue of the absolute value of the covariance and its phase is the average angle lag between signals $x(t)$ and $y(t)$ at frequency f . For instance, if input current and voltage in a circuit are stochastic signals, the $\overline{CPSD}_{vi}(f)$ is just the average complex power at frequency f .

The cross power spectral density is also referred as ‘‘cross-spectral density’’. The terms ‘‘cross-power spectrum’’ or ‘‘cross-spectrum’’ are eluded to avoid ambiguities in the normalizing factors. Unlike the variance spectrum, $\overline{CPSD}_{xy}(f)$ has both real and imaginary parts, which are called respectively the cospectrum, $\text{Re}[\overline{CPSD}_{xy}(f)]$, and the quadrature spectrum, $\text{Im}[\overline{CPSD}_{xy}(f)]$.

For a wide-sense stationary process and according to the Wiener-Khinchine theorem, the Fourier transform of the autocorrelation function $ACF_x(\tau)$ and the cross-correlation function $CCF_{xy}(\tau)$ are $PSD_x(f)$ and $\overline{CPSD}_{xy}(f)$, respectively.

The complex coherence $\vec{\gamma}_{xy}(f)$ is the $\overline{CPSD}_{xy}(f)$ normalized by the root of the PSD of signals $x(t)$ and $y(t)$ and it is the spectral analogue to the regression correlation coefficient. The modulus of the coherence, $|\vec{\gamma}_{xy}(f)| \equiv \gamma_{xy}(f)$, is a number between 0 and 1 that indicates the correlation of amplitudes in the signals $x(t)$ and $y(t)$ at frequency f . Unity coherence indicates perfect correlation of amplitudes at frequency f and zero indicates that the amplitudes at frequency f are independent random variables.

The argument of $\vec{\gamma}_{xy}(f)$ gives information of the phase delay of the signal $y(t)$ respect $x(t)$ at frequency f . Usually, the squared complex coherence $\vec{\gamma}_{xy}^2(f)$ is preferred to the ‘‘root’’ coherence $\vec{\gamma}_{xy}(f)$ since its properties are determined easier. The squared complex coherence $\vec{\gamma}_{xy}^2(f)$ can be computed as:

$$\vec{\gamma}_{xy}^2(f) = \frac{\langle \vec{X}_\sigma(f) \vec{Y}_\sigma^*(f) \rangle \langle \vec{Y}_\sigma(f) \vec{X}_\sigma^*(f) \rangle^*}{\langle |\vec{X}_\sigma(f)|^2 \rangle \langle |\vec{Y}_\sigma(f)|^2 \rangle} = \frac{\overline{CPSD}_{xy}(f)^2}{PSD_x(f) PSD_y(f)} \quad (799)$$

$$\text{since } \overline{CPSD}_{xy}(f) = \langle \vec{X}_\sigma(f) \vec{Y}_\sigma^*(f) \rangle = \langle \vec{Y}_\sigma(f) \vec{X}_\sigma^*(f) \rangle^* = \overline{CPSD}_{yx}^*(f)$$

The coherence $\vec{\gamma}_{xy}(f)$ is undefined at frequencies where the PSD are null. In general, the estimates of $\overline{CPSD}_{xy}(f)$ have lower relative uncertainty than the estimates of $\vec{\gamma}_{xy}(f)$, specially if $PSD_x(f)$ or $PSD_y(f)$ is close to zero.

G.2.3. Convention for indicating the typical range of magnitudes

The expanded uncertainty, aka $k = 2$ or twice the standard deviation, is used to indicate range variation of stochastic magnitudes unless otherwise is stated. For example, the value $U_{wind} = 6.7 \text{ m/s} \pm 1,86 \text{ m/s}$ indicates a fluctuating wind speed of mean $\langle U_{wind} \rangle = 6.7 \text{ m/s}$ and standard deviation $\sigma_{U_{wind}} = (1,86 \text{ m/s})/2 = 0,93 \text{ m/s}$.

G.2.4. Nomenclature in Markov Decision Processes

When a variable is discretized, values in continuous time are noted in italics to distinguish from their discretized counterparts. In general, temporal sequences of values are indicated as instant dependent, as $\mathbf{P}[k]$, just to avoid confusing with vector or matrix element indexing (in fact, $\mathbf{P}[k]$ can be interpreted formally as a tensor with indexes i, j and k). Arguments of functions are indicated by parentheses (\cdot) while square brackets $[\cdot]$ are preferred for indicating index number. Square brackets $[\cdot]$ are also used to indicate a vector, matrix or tensor composed by the inner elements. Probability is denoted by $\text{Pr}(\cdot)$ to avoid confusion with transition probability matrix. Average values are denoted by angle brackets $\langle \cdot \rangle$ and estimated elements are stressed with the circumflex accent, as $\hat{\mathbf{P}}$.

When the context is sufficiently clear and there is no risk of misleading, indexes or explicit functional dependences have been dropped to clarify expressions.

G.2.5. Convention for indicating the typical range of magnitudes

The expanded uncertainty, aka $k = 2$ or twice the standard deviation, is used to indicate range variation of stochastic magnitudes unless otherwise is stated. For example, the value $U_{wind} = 6.7 \text{ m/s} \pm 1,86 \text{ m/s}$ indicates a fluctuating wind speed of mean $\langle U_{wind} \rangle = 6.7 \text{ m/s}$ and standard deviation $\sigma_{U_{wind}} = (1,86 \text{ m/s})/2 = 0,93 \text{ m/s}$.

References

-
- [1] Directive 2009/28/EC of the European Parliament and of the Council of 23 April 2009 on the promotion of the use of energy from renewable sources and amending and subsequently repealing Directives 2001/77/EC and 2003/30/EC
- [2] "Report finds US is world's top wind producer". The Guardian. 2008-07-30. <http://www.guardian.co.uk/environment/2008/jul/30/windpower.energy>. Retrieved 2008-08-24.
- [3] EnerNex Corporation, "Final Report – 2006 Minnesota Wind Integration Study Volume 1," Nov. 30, 2006, Available: http://www.puc.state.mn.us/docs/windrpt_vol%201.pdf
- [4] U.S. Department of Energy, "20% Wind Energy by 2030. Increasing Wind Energy's Contribution to U.S. Electricity Supply", July 2008
- [5] J. F. DeCarolis, D.W. Keith, "The Costs of Wind's Variability: Is There a Threshold?", *The Electricity Journal*, Volume 18, Issue 1, pp. 69-77, 2005
- [6] U.S. Department of Energy, "Wind Energy Myths", Wind Powering America Fact Sheet Series, May 2005
- [7] Stacy Feldman, "The Wind Power Variability Myth Gets Debunked, Again", SolveClimate, Jul 17th, 2009. Retrieved on 20
- [8] Pöyry PLC, "Impact of intermittency. How wind intermittency could shape the electricity markets?". Available at <http://www.ilxenergy.com/>
- [9] International Energy Agency, "Variability Of Wind Power And Other Renewables. Management options and strategies", 2005. Available: <http://www.iea.org/textbase/papers/2005/variability.pdf>
- [10] B. K. Sovacool, "The intermittency of wind, solar, and renewable electricity generators: Technical barrier or rhetorical excuse?", *Utilities Policy* 17 (2009), 288–296
- [11] R. Piwko, G. Boukarikm, K. Clark, G. Haringa, G. Jordan, N. Miller, Y. Zhou, J. Zimberlin, (2004, Feb.). The Effects of Integrating Wind Power on Transmission System Planning, Reliability, and Operations. GE Power Systems Energy Consulting, Schenectady, NY. Available: http://www.nyserda.org/publications/wind_integration_report.pdf
- [12] C. Lindsay Anderson, Judith B. Cardell, "Reducing the Variability of Wind Power Generation for Participation in Day Ahead Electricity Markets", Proceedings of the 41st Hawaii International Conference on System Sciences – 2008.
- [13] G. Boyle "Renewable Electricity and the Grid. The Challenge of Variability", September 2007, Earthscan
- [14] E.M. Constantinescu, V.M. Zavala, M. Rocklin, S. Lee, M. Anitescu, "Unit Commitment with Wind Power Generation: Integrating Wind Forecast Uncertainty and Stochastic Programming", Argonne National Laboratory, September 2009
- [15] M. Milligan, "Modelling Utility-Scale Wind Power Plants. Part 2: Capacity Credit", *Wind Energy*, Volume 3, Issue 4, pp. 167-206, 2001
- [16] B. Parsons, Y. Wan, B. Kirby, "Wind Farm Power Fluctuations, Ancillary Services, and System Operating Impact Analysis Activities in the United States", *National Renewable Energy Laboratory*, 2001
- [17] B. Parson, M. Milligan, B. Zavadil, D. Brooks, B. Kirby, K. Dragoon, J. Caldwell, "Grid Impacts of Wind Power: A summary of recent studies in the United States," *Wind Energy*, vol. 7, Apr./Jun. 2004, pp 87-108.
- [18] Julija Matevosyan, "Wind power integration in power systems with transmission bottlenecks", KTH, Stockholm, 2006.
- [19] H. Holttinen, B. Lemström, P. Meibom, H. Bindner, A. Orth, F. van Hulle, C. Ensslin, A. Tiedemann, L. Hofmann, W. Winter, A. Tuohy, M. O'Malley, P. Smith, J. Pierik, J. Olav Tande, A. Estanqueiro, J. Ricardo, E. Gomez, L. Söder, G. Strbac, A. Shakoob, J. C. Smith, B. Parsons, M. Milligan, Y. H. Wan, "Design and Operation of Power Systems with Large Amounts of Wind Power. State-of-the-art report", VTT Technical Research Centre of Finland, 2007.
- [20] I. Martí, G. Kariniotakis, P. Pinson, I. Sanchez, T. S. Nielsen, H. Madsen, G. Giebel, J. Usaola, A.M. Palomares, R. Brownsword, J. Tambke, U. Focken, M. Lange, G. Sideratos, G. Descombes, "Evaluation of Advanced Wind Power Forecasting Models – Results of the Anemos Project", EWEC 2006, Athens.
- [21] Ignacio J Ramirez-Rosado, L. Alfredo Fernandez-Jimenez, Cláudio Monteiro, João Sousa, Ricardo Bessa, "Comparison of two new short-term wind-power forecasting systems", *Renewable Energy* (2009)
- [22] J. Juban, L. Fugon, G. Kariniotakis, "Uncertainty Estimation of Wind Power Forecasts", EWEC 2008, Brussels, Belgium.
- [23] Y. Wan, D. Bucaneg, "Short-term power fluctuations of large wind power plants", *Journal of Solar Energy Engineering*, Volume 124, pp. 427-431, 2002
- [24] J. Apt, "The spectrum of power from wind turbines", *Journal of Power Sources* 169 (2007) 369–374
- [25] P. Cappers, C. Goldman, D. Kathan "Demand response in U.S. electricity markets: Empirical evidence", *Energy* (2009).
- [26] K. Porter, D. Yen-Nakafuji and B. Morgenstern, "A Review of the International Experience with Integrating Wind Energy Generation", *The Electricity Journal*, Volume 20, Issue 8, October 2007, Pages 48-59.

- [27] A D. Lamont, “Assessing the long-term system value of intermittent electric generation technologies”, *Energy Economics* 30 (2008) 1208–1231
- [28] M. A. Matos, R. Bessa, “Operating Reserve Adequacy Evaluation using Uncertainties of Wind Power Forecast”, IEEE Bucharest PowerTech Conference, June 28th 2009.
- [29] H. Holttinen, “Estimating the impacts of wind power on power systems—summary of IEA Wind collaboration”, *Environ. Res. Lett.* 3 (2008)
- [30] E. Hirst, J. Hild, “The Value of Wind Energy as a Function of Wind Capacity”, *The Electricity Journal*, Volume 17, Issue 6, pp. 11-20, 2004.
- [31] D. Milborrow, “Managing Variability”, A report to WWF-UK, RSPB, Greenpeace UK and Friends of the Earth EWNI, 24 June 2009.
- [32] D. Snieckus, “Myth of wind variability problems debunked”, *Recharge News*, July 9 2009.
- [33] Operating the Electricity Transmission Networks in 2020. Initial Consultation. UK's National Grid, June 2009.
- [34] IEA Wind Energy Annual Report 2006, July 2006
- [35] M. Sanz A. Llombart A. A. Bayod J. Mur, "Power quality measurements and analisis for wind turbines", IEEE Instrumentation and Measurement Technical Conference 2000, pp. 1167-1172. May 2000, Baltimore.
- [36] J. Mur Amada, A.A. Bayod Rújula, "Characterization of Spectral Density of Wind Farm Power Output", 9th Conference on Electrical Power Quality and Utilisation (EPQU'2007), Barcelona, 2007. ISBN 978-84-690-9441-9.
- [37] W. Schlez, D. Infield, “Horizontal, two point coherence for separations greater than the measurement height”, *Boundary-Layer Meteor.* 87 (1998), 459-480.
- [38] Poul Sørensen, Nicolaos A. Cutululis, Antonio Viguera-Rodríguez, Henrik Madsen, Pierre Pinson, Leo E. Jensen, Jesper Hjerrild and Martin Donovan, “Modelling of Power Fluctuations from Large Offshore Wind Farms”, *WIND ENERGY* 2008 (to be published)
- [39] António P. Martins, Paulo C. Costa Adriano, S. Carvalho, “Coherence and wakes in wind models for electromechanical and power systems standard simulations”, *EWEC* 2006, Athens.
- [40] G. Papaefthymiou and Bernd Klöckl “MCMC for Wind Power Simulation”, *IEEE Trans. Energy Conv.*, 2008 (to be published).
- [41] G. Papaefthymiou, “Integration of Stochastic Generation in Power Systems”, Ph.D. Dissertation, Delf University, Neetherlands, 2007.
- [42] Cristian Nichita, Dragos Luca, Brayima Dakyo, and Emil Ceanga, “Large Band Simulation of the Wind Speed for Real Time Wind Turbine Simulators”, *IEEE Transactions On Energy Conversion*, Vol. 17, No. 4, December 2002.
- [43] T. Petru and T. Thiringer, “Modeling of Wind Turbines for Power System Studies”, *IEEE Trans. On Power Systems*, Vol. 17, No. 4, Nov. 2002, pp. 1132 - 1139
- [44] P. Rosas, “Dynamic influences of wind power on the power system”, Ph. D Thesis, Ørsted•DTU, March 2003, ISBN: 87-91184-16-9. Available at www.risoe.dk/rispubl/VEA/veapdf/ris-r-1408.pdf
- [45] W. Schlez, D. Infield, “Horizontal, two point coherence for separations greater than the measurement height”, *Boundary-Layer Meteor.* 87 (1998), 459-480.
- [46] P. Sørensen, N. A. Cutululis, A. Viguera-Rodríguez, H. Madsen, P. Pinson, L. E. Jensen, J. Hjerrild, M. Donovan, “Modelling of Power Fluctuations from Large Offshore Wind Farms”, *Wind Energy*, Oct 2007.
- [47] E. Welfonder, R. Neifer and M. Spaimer, “Development And Experimental Identification Of Dynamic Models For Wind Turbines”, *Control Eng. Practice*, Vol. 5, No. 1, pp. 63-73, 1997.
- [48] J. Gordon Leishman “Challenges in Modeling the Unsteady Aerodynamics of Wind Turbines”, 21st ASME Wind Energy Symposium, Reno, NV, Jan. 14–17, 2002.
- [49] D. S. L. Dolan and P. W. Lehn “Real-Time Wind Turbine Emulator Suitable for Power Quality and Dynamic Control Studies” International Conference on Power Systems Transients (IPST'05) in Montreal, Canada on June 19-23, 2005.
- [50] D. S. L. Dolan and P. W. Lehn, “Simulation Model of Wind Turbine 3p Torque Oscillations due to Wind Shear and Tower Shadow”, *IEEE Trans. Energy Conversion*, Sept. 2006, Vol. 21, N. 3, pp. 717-724.
- [51] J. Cidrás, A.E. Feijóo, C. Carrillo González, “Synchronization of Asynchronous Wind Turbines” *IEEE Trans, on Energy Conv.*, Vol. 17, No 4, Nov. 2002, pp 1162-1169
- [52] J. Mur, A.A. Bayod, S. Ortiz, R. Zapata, “Power Quality Analysis of Wind Turbines. Part II – Dynamic Analysis”, *ICREP* 2003, Vigo. Available at : www.joaquinmur.eu
- [53] M. Sanz, A. Llombart, Á. A. Bayod, J. Mur, “Power Quality Measurements and Analysis for Wind Turbines” *IEEE Instrumentation and Measurement Technical Conference, IMTC* 2000, pp. 1167-1172.
- [54] J. Mur, “WINDFREEDOM, WIND variability in the FREquency DOMain”, 2009. Program under the GNU General Program License, available freely at <http://www.windygrid.org/software>.
- [55] Benoit Cushman-Roisin, “Environmental Fluid Mechanics”, John Wiley & Sons, 2007.
- [56] Simon Watson, “Introduction to the Atmospheric Boundary Layer”, *CREST MSc Flexible & Distance Learning Series. Wind Power Fundamentals*. Crest, Loughborough University, 2003.
- [57] Kolmogorov, A. N., 1941. Dissipation of energy in locally isotropic turbulence. *Dokl. Akad. Nauk SSSR*, 32, 19–21 [in Russian].
- [58] Y. Tamura, A. Karrem, G. Solari, K. C. S.Kwok, J. D. Holmes. Report from IAWE Working Group WGE-Dynamic Response. 2003.

- [59] K. R. Sreenivasan, A. J. Chambers, and R. A. Antonia, "Accuracy of moments of velocity and scalar fluctuations in the atmospheric surface layer." *Boundary-Layer Meteorology*, 14, 341–359, (1978).
- [60] Kaimal, J. and J. Finnigan, 1994: "Atmospheric Boundary Layer Flows; Their Structure and Measurements". Oxford University Press, New York, USA.
- [61] M. Metzger and H. Holmes "Time Scales in the Unstable Atmospheric Surface Layer", *Boundary-Layer Meteorology*, Vol. 126, No. 1, January 2008.
- [62] Stijn de Waele, A. van Dijk, P. Broersen, and P. G. Duynkerke, "Estimation of the integral time scale with time series models", 15th Conference on Boundary Layer and Turbulence, Wageningen, The Netherlands, 2002.
- [63] E. L. Petersen, N. G. Mortensen, L. Landberg, J. Højstrup and H. P. Frank, "Wind Power Meteorology", Risø National Laboratory, Roskilde, Denmark, December 1997. Riso-I-1206(EN).
- [64] S. E. Larsen, H. R. Olesen and J. Højstrup, 'Parameterization of the low frequency part of spectra of horizontal velocity components in the stable surface boundary layer', *Turbulence and Diffusion in Stable Environments*, ed. J. C. R. Hunt, Clarendon Press, Oxford 1985, pp. 181-204.
- [65] J. Højstrup, S. E. Larsen and P. H. Madsen, 'Power spectra of horizontal wind components in the neutral atmospheric surface boundary layer', *AMS 9th Symposium on Turbulence and Diffusion*, Roskilde, Denmark 1990, pp. 305-308.
- [66] A. A. Townsend, "The structure of turbulent shear flows", 2nd ed., Cambridge University Press, 1976.
- [67] S. B. Pope, "Turbulent Flows", Cambridge University Press (2000)
- [68] S. Frandsen (Ed.), L. Chacon, A. Crespo, P. Enevoldsen, R. Gomez-Elvira, J. Hernandez, J. Højstrup, F. Manuel, K. Thomsen, and P. Sørensen., "Measurements on and Modelling of Offshore Wind Farms", Risø National Laboratory, Roskilde, Denmark 1996.
- [69] Antebi, J., Zarghamee, M. S., & Kan, F. W. 1997, *Wind Characterization and Beam Pointing Error – Large Millimeter Telescope*, SGH Report to LMT Project
- [70] J. C. Kaimal, J. C. Wyngaard, Y. Izumi, and O. R. Cote, "Spectral Characteristics of Surface Layer Turbulence". *Quarterly Journal of the Royal Meteorological Society*, vol. 98, 1972.
- [71] Davenport, A. G. 1961, *Quart. J. Royal Meteorol. Soc.*, 87, 194
- [72] T. von Karman, "Progress in the statistical theory of turbulence". *Proceedings of the National Academy of Sciences of the United States of America*. 1948; 34: 530–539.
- [73] Morfiadakis EE, Glinou GL, Koulouvari MJ., "The Suitability of the von Karman Spectrum for the Structure of Turbulence in a Complex Terrain Wind Farm". *Journal of Wind Engineering and Industrial Aerodynamics*, vol. 62, 1996, 237-257.
- [74] Shiau B-S, Chen Y-B. "Observation on Wind Turbulence Characteristics and Velocity Spectra near the Ground at the Coastal Region". *Journal of Wind Engineering and Industrial Aerodynamics*, vol. 90, 2002, 1671–1681.
- [75] Frandsen S. "Turbulence and Turbulence-Generated Structural Loading in Wind Turbine Clusters". Risø-R-1188(EN), Roskilde, 2007. Available online: <http://www.risoe.dk/rispubl/VEA/reapdf/ris-r-1188.pdf>
- [76] K. E. Kaasen, "Time Domain Model Representations of Standard Wind Gust Spectra", 9th Int. Offshore and Polar Engineering Conference, Brest, France, 1999.
- [77] P. Teigen, A. Naess, "Extreme Response of Floating Structures in Combined Wind and Waves", *Journal of Offshore Mechanics and Arctic Engineering*, Vol. 125, pp. 87-93, May 2003
- [78] Isaac Van der Hoven, "Power Spectrum Of Horizontal Wind Speed In The Frequency Range From 0.0007 To 900 Cycles Per Hour", *Journal of the Atmospheric Sciences*, Vol. 14, Issue 2, pp. 160–164
- [79] F. Fiedler and H. A. Panofsky, "Atmospheric Scales and Spectral Gaps", *Bulletin of the American Meteorological Society*, Vol. 51, Issue 12 (Dec. 1970).
- [80] T. Heggem, R. Lende and J. Løvseth, "Analysis of Long Time Series of Coastal Wind", *Journal of the Atmospheric Sciences*, Volume 55, Issue 18, pp. 2907–2917 (September 1998)
- [81] P. Sørensen, N. A. Cutululis, J. Hjerrild, L. Jensen, M. Donovan, L. E. A. Christensen, H. Madsen, A. Viguera-Rodríguez, "Power Fluctuations from Large Offshore Wind Farms", *Nordic Wind Power Conference*, 22-23 May, 2006, Espoo, Finland.
- [82] K. Saranyasoontorn, L. Manuel, P. S. Veers, "A Comparison of Standard Coherence Models from Inflow Turbulence With Estimates from Field Measurements", *Journal of Solar Energy Engineering*, Vol. 126 (2004), Issue 4, pp. 1069-1082
- [83] D. Baldocchi, E. Falgea and K. Wilsonc, "A spectral analysis of biosphere-atmosphere trace gas flux densities and meteorological variables across hour to multi-year time scales", *Agricultural and Forest Meteorology*, Vol. 107, Issue 1, 1 March 2001, Pages 1-27.
- [84] M. Courtney, I. Troen. "Wind speed spectrum from one year of continuous 8 Hz measurements". In: 9. Symposium on turbulence and diffusion. 9. Symposium on turbulence and diffusion, Roskilde, 30 Apr - 3 May 1990. Jensen, N.O.; Kristensen, L.; Larsen, S.E. (eds.), (American Meteorological Society, Boston, MA, 1990) p. 301-304
- [85] P. Sørensen and N. Cutululis, A. Viguera-Rodríguez, H. Madsen, P. Pinson, L. E. Jensen, J. Hjerrild, M. Donovan, "Modelling of Power Fluctuations from Large Offshore Wind Farms", *Wind Energy* Vol. 11 (2008), pp. 29-43.
- [86] S. Frandsen, H.E. Jørgensen, J.D. Sørensen, "Relevant criteria for testing the quality of turbulence models", 2007 European Wind Energy Conference and Exhibition, Milan (IT), 7-10 May 2007. (2007) p. 128-132.

- [87] K. Saranyasoontorn, L. Manuel, P. S. Veers, “On estimation of coherence in inflow turbulence based on field measurements”, *Proceedings of the 2004 ASME Wind Energy Symposium*, pp. 424-434, Reno, Nevada, January 2004.
- [88] A. D. Hansen, C. Jauch, P. Sørensen, F. Iov, F. Blaabjerg “Dynamic wind turbine models in power system simulation tool DIgSILENT” Risø National Laboratory, Roskilde, December 2003, Risø-R-1400(EN).
- [89] A. D. Hansen, F. Iov, P. Sørensen, N. Cutululis, C. Jauch, F. Blaabjerg, “Dynamic wind turbine models in power system simulation tool DIgSILENT”, Risø National Laboratory, Roskilde, Denmark August 2007, Risø-R-1400(ed.2)(EN).
- [90] Burton T, Sharpe D, Jenkins N, Bossanyi E., “Wind Energy Handbook”. John Wiley & Sons Ltd, England, 2001.
- [91] Veers PS. “Three-Dimensional Wind Simulation”. Sandia Report, SAND88-0152 UC-261, 1988.
- [92] S.Heier “Grid Integration of Wind Energy Conversion Systems”. John Wiley & Sons, New York 2006 (2nd edition).
- [93] T. F. Pedersen, J.-Å. Dahlberg, A. Cuerva, F. Mouzakis, P. Busche, P. Eecen A. Sanz-Andres, S Franchini, S. M. Petersen, “ACCUWIND -Accurate Wind Speed Measurements in Wind Energy” Risø National Laboratory, Roskilde, Denmark, July 2006.
- [94] Mann J. “Wind Field Simulation”. *Probabilistic Engineering Mechanics*, vol. 13, n° 4, 1998, 269-282.
- [95] Ioannis Antoniou et al. “Influence of wind characteristics on turbine performance” Risø National Laboratory, Denmark
- [96] T.G. van Engelen, “Control design based on aero-hydro-servo-elastic linear models from TURBU (ECN)”, *EWEC 2007*.
- [97] IEC 61400-1, “Wind Turbines—Part 1: Design Requirements, Int. Std.”, 3rd Ed. 2005-2008.
- [98] L. Kristensen, “Power spectra and cross-spectra as seen from the moving blade of a wind turbine”, *J. Wind Eng. Ind. Aerodyn.*, 12, 245-250 (1983).
- [99] A. G. Davenport, ‘The spectrum of horizontal gustiness near the ground in high winds’, *Q. J. R. Meteorol. Soc.*, 87, 194-211 (1961).
- [100] J. Højstrup, “Spectral coherence in wind turbine wakes”, *J. Wind. Eng. Ind. Aerodyn.*, 80, 137-146 (1999).
- [101] L. Kristensen and N. O. Jensen, “Lateral coherence in isotropic turbulence and in the natural wind”, *Boundary-Layer Meteorol.*, 17, 353-373 (1979).
- [102] L. J. Vermeer, J.N. Sørensen, A. Crespo, “Wind turbine wake aerodynamics”, *Progress in Aerospace Sciences* 39 (2003) 467-510.
- [103] S. Frandsen, R. Barthelmie, O. Rathmann, H. E. Jørgensen, J. Badger, K. Hansen, S. Ott, P. E. Rethore, S. E. Larsen, L. E. Jensen, “Summary report: The shadow effect of large wind farms: measurements, data analysis and modelling”, Risø National Laboratory, Roskilde, Denmark. October 2007, Risø-R- 1615 (EN)
- [104] S. Frandsen, H.E. Jørgensen, J.D. Sørensen, “Relevant criteria for testing the quality of turbulence models”, 2007 European Wind Energy Conference and Exhibition, Milan (IT), 7-10 May 2007. (2007) p. 128-132.
- [105] P. Sørensen. Frequency domain modelling of wind turbine structures. Risø-R-749. Roskilde 1994.
- [106] Wilkie J, Leithead WE, Anderson C, “Modelling of Wind Turbines by Simple Models”. *Wind Engineering*, Vol. 14, n° 4, 1990.
- [107] I. Troen and E. L. Petersen, “European Wind Atlas”, Riso, 1989.
- [108] J. Tambke, J.A.T. Bye, B. Lange and J.-O. Wolff , “Wind Speed Profiles above the North Sea”, *Wind Energy - Proceedings of the Euromech Colloquium*, Springer, Berlin 2007, p. 27 - 32
- [109] D. A. Spera, “Wind Turbine Technology”, ASME Press, New York, 1994.
- [110] B. H. Bailey and S. L. McDonald, “Wind resource assessment handbook”, AWS Scientific, Inc., www.awsscientific.com, April 1997
- [111] A. J. Eggers, Jr., R. Digumarthi, K. Chaney “Wind Shear and Turbulence Effects on Rotor Fatigue and Loads Control”, *Transactions of the ASME*, Vol. 125, Nov. 2003.
- [112] Kelley, Neil, Shirazi, Mari, Hand, Maureen, and Jager, David, “Low-Level Jet Turbulence Field Test,” NREL/NWTC, 2002 DOE Wind Program Review Meeting, May 7-9.
- [113] S. REHMAN; N. M. AL-ABBADI “Wind shear coefficients and their effect on energy production”, *Energy conversion and management*, 2005, vol. 46, n 15-16, pp. 2578-2591
- [114] Engström S, Ganander H, Lindström R. “Short Term Power Variations in the Output of Wind Turbines”. *DEWI Magazin*, n° 19, 2001.
- [115] S. Hier, “Grid Integration of Wind Energy Conversion Systems”, Wiley, 1998.
- [116] J. Sallán-Arasanz, “Estudio y desarrollo de nuevos sistemas de generación y conexión a red para máquinas asíncronas de rotor en cortocircuito impulsadas por turbinas eólicas para su funcionamiento a velocidad variable”, Ph.D. Thesis, Universidad de Zaragoza, June 2002 (in Spanish).
- [117] J. F. Sanz Osorio, “Optimización de sistemas integrados de energías renovables para el abastecimiento de núcleos aislados.”, Ph.D. Thesis, Universidad de Zaragoza, June 2007 (in Spanish).
- [118] Sørensen P., Hansen A.D., Janosi L., Bech J., Bak-Jensen B. “Simulation of interaction between wind farm and power system”. Risø National Laboratory, 2001. Risø-R-1281,
- [119] B. Stoevesandt, J. Peinke, A. Shishkin and C. Wagner, “Numerical simulation of dynamic stall using spectral/hp method”, *Wind Energy - Proceedings of the Euromech Colloquium*, Springer, Berlin 2007, p. 241 - 244

- [120] M.P. Comech-Moreno, "Análisis y ensayo de sistemas eólicos ante huecos de tensión", Ph.D. Thesis, Universidad de Zaragoza, Octubre de 2007 (in Spanish).
- [121] V. Akhmatov, "Analysis of Dynamic Behaviour of Electrical Power Systems with Large Amount of Wind Power", Ørsted-DTU, April 2003.
- [122] F. D. Bianchi, H. De Battista, and R. J. Mantz, "Wind Turbine Control Systems. Principles, Modelling and Gain Scheduling Design", Springer, 2006.
- [123] Chee-Mun Ong "Dynamic simulation of electric machinery using Matlab/Simulink", Prentice Hall, 1998.
- [124] B.C. Lesieutre, P.W. Sauer, M.A. Pai, "Development and comparative study of induction machine based dynamic P, Q load models", IEEE Transactions on Power Systems, Vol. 10, No. 1. February 1995.
- [125] G.K. Singh, "Self-excited induction generator research—a survey", Electric Power Systems Research 69 (2004) 107–114.
- [126] J.A.A. Melkebeek, D.W. Novotny, "Small signal dynamic analysis of regeneration and self-excitation in induction machines", Electric Machines Power Syst. 8 (1983) 259–280.
- [127] Y. Uçtug, M. Demirekler, "Modelling, analysis and control of a wind-turbine driven self-excited induction generator", IEE Proceedings, Vol. 135, Pt. C, No. 4, July 1988
- [128] F. Wu, X.P. Zhang, K. Godfrey and P. Ju, "Modeling and Control of Wind Turbine with Doubly Fed Induction Generator", PSCE 2006 conference.
- [129] D. Nagaria, G. N. Pillai, H. O. Gupta, "Small signal stability analysis of variable speed wind energy conversion system equipped with DFIG" International Journal of Distributed Energy Resources, Volume 4 Number 3 (2008) Pages 233 - 251
- [130] R. Erickson, S. Angkititrakul, and K. Almazeedi, "A New Family of Multilevel Matrix Converters for Wind Power Applications: Final Report". NREL Subcontract Report NREL/SR-500-40051, December 2006.
- [131] S. Masoud Barakati, "Modeling and Controller Design of a Wind Energy Conversion System Including a Matrix Converter", Ph. D. Thesis, University of Waterloo, Ontario, Canada, 2008.
- [132] V. Akhmatov, H. Knudsen, "An aggregate model of a grid-connected, large scale, offshore wind farm for power stability investigations-importance of windmill mechanical system", Electrical Power Systems 24 (2002) 709-717.
- [133] Kazachkov, S. Stapleton, "Modeling wind farms for power system stability studies", Power Technology Newsletter Issue 95, April 2004
- [134] L.M. Fernandez, J.R. Saenz, F. Jurado, "Dynamic models of wind farms with fixed speed wind turbines", Renewable Energy, 31 (8), pp.1203-1230, Jul 2006.
- [135] R. Arens, "Complex Processes for Envelopes of Normal Noise", IRE Transactions on Information Theory, September 1958, pp.204-207.
- [136] N. S. Pannu, A. J. McCoy and R. J. Read, "Application of the complex multivariate normal distribution to crystallographic methods with insights into multiple isomorphous replacement phasing", Acta Cryst. (2003), D59, 1801-1808.
- [137] M. Sanz, J. Mur, F. Gómez, R. Zapata, "Sistema de medida de calidad de red para parques eólicos", IX Jornadas Hispano-Lusas. Lisboa, 1998.
- [138] M. Sanz, A. Llombart, A. A. Bayod, J. Mur, R. Sierra "Análisis de la calidad de la energía generada en parques eólicos" X Reunión de Grupos de Investigación en Energía Eléctrica. Santander, 2000.
- [139] M. Sanz A. Llombart A. A. Bayod J. Mur, "Power quality measurements and analysis for wind turbines", IEEE Instrumentation and Measurement Technical Conference 2000, pp. 1167-1172. May 2000, Baltimore.
- [140] Joaquín Mur, Ángel A. Bayod, Jesús Sallán "An Experimental Study on Power Quality Wind Turbines" EWEC '03 (European Wind Energy Conference & Exhibition). Madrid, 2003.
- [141] Joaquín Mur, Ángel A. Bayod, Jesús Sallán "Profile of voltage in grids with wind farms" EWEC '03 (European Wind Energy Conference & Exhibition). Madrid, 2003.
- [142] M. Sanz, A. Llombart, J. Mur, R. Sierra, "Análisis de la calidad de la energía eléctrica entregada a la red de los parques eólicos de puntaza de Remolinos". Zaragoza University, April 1999.
- [143] M. Sanz, A. Llombart, J. Mur, I. Palacios, "Análisis de la calidad de la energía eléctrica entregada a la red de los parques eólicos de puntaza de Borja", Zaragoza University, September 1999.
- [144] M. Sanz, A. Llombart, J. Mur, F. Gómez, "Análisis de la calidad de la energía eléctrica entregada a la red de los parques eólicos de puntaza de Pola", Zaragoza University, December 1999.
- [145] M. Sanz, A. Llombart, J. Mur, R. Zapata, D. Romanos, S. Ortiz, "Análisis de la calidad de la energía eléctrica entregada a la red de los parques eólicos de Valdecuadros", Zaragoza University, August 2000.
- [146] "Manual de los programas realizados para los estudios en parques eólicos de Compañía Eólica Aragonesa S.A.", Zaragoza University, December 21st 1999.
- [147] J. Mur, "Parque eólico de VALDECUADROS. Manual de los programas realizados en VISUAL C++", Zaragoza University, March 9th 2000
- [148] Joaquín Mur, Ángel Antonio Bayod, Samuel Ortiz, Roberto Zapata "Power Quality Analysis of Wind Turbines. Part II - Dynamic Analysis", ICREP '03 (Internacional Conference on Renewable Energies and Power Quality), Vigo 2003.
- [149] CIRCE Foundation, "AIRE- Análisis Integral de Recursos Energéticos", web page teide.cps.unizar.es: 8080/pub/info.nsf/paginas/diveleaire accessed in October 13rd 2009.
- [150] Inycom T&M, "AIRE. Analizador Integral De Recursos Energéticos". Available at www.inycom.es. Accessed in October 13rd 2009.

- [151] Sami H. Karaki, Bassel A. Salim, and Riad B. Chedid, "Probabilistic Model of a Two-Site Wind Energy Conversion System", IEEE Transactions On Energy Conversion, Vol. 17, No. 4, December 2002
- [152] C. Vilar Moreno, "Voltage fluctuation due to constant speed wind generators" Ph.D. dissertation at Carlos III University, Leganés, Spain, 2003.
- [153] P. Sorensen, A. D. Hansen, P.A. Carvalho Rosas "Wind models for simulation of power fluctuations from wind farms", Journal of Wind Engineering and Ind. Aerodynamics 90 (2002), pp. 1381-1402
- [154] T. Thiringer, T. Petru, and S. Lundberg "Flicker Contribution From Wind Turbine Installations" IEEE Trans, on Energy Conv., Vol. 19, No 1, March 2004, pp 157-163
- [155] H. Amarís, J. Usaola. Evaluación en el dominio de la frecuencia de las fluctuaciones de tensión producidas por los generadores eólicos. V Jornadas Hispano-Lusas de Ingeniería Eléctrica. 1997.
- [156] W. Wangdee, R. Billinton "Considering Load-Carrying Capability and Wind Speed Correlation of WECS in Generation Adequacy Assessment", IEEE Trans, on Energy Conv., Vol. 21, No 3, Sept. 06, pp 734-741
- [157] I. Sánchez, "Short-term prediction of wind energy production," International Journal of Forecasting, 22, 43-56.
- [158] W. A. Gardner, "Cyclostationarity in Communications and Signal Processing", IEEE press, 1994.
- [159] J. Cidrás, A.E. Feijóo, C. Carrillo González, "Synchronization of Asynchronous Wind Turbines" IEEE Trans, on Energy Conv., Vol. 17, No 4, Nov. 2002, pp 1162-1169
- [160] J. Mur, M.P. Comech, "Reactive Power Injection Strategies for Wind Energy Regarding its Statistical Nature", Sixth International Workshop on Large-Scale Integration of Wind Power and Transmission Networks for Offshore Wind Farm. Delft, 2006.
- [161] P. (Prabha) Kundur, Neal J. Balu, Mark G. Lauby, "Power System Stability and Control", McGraw-Hill, 1994.
- [162] Chun-Lien Su, "Probabilistic Load-Flow Computation Using Point Estimate Method", IEEE Trans. Power Systems, Vol. 20, No. 4, November 2005, pp. 1843-1851.
- [163] G. Stefopoulos, A. P. Meliopoulos and G. J. Cokkinides, "Advanced Probabilistic Power Flow Methodology", 15th PSCC, Liege, 22-26 August 2005
- [164] H. Hurd, "Notes on the Periodogram", <http://www.stat.unc.edu/faculty/hurd.html> (accessed on May 16, 2008).
- [165] H. Bodén, "Signal Analysis", The Marcus Wallenberg Laboratory for Sound and Vibration Research. <http://www.ave.kth.se/education/msce/TSOVM/course/sSD2130/> (accessed on May 16, 2008).
- [166] D. M. Meko, "Applied Time Series Analysis", Ch. 6, University of Arizona, Spring 2007, <http://www.ltrr.arizona.edu/~dmeko/geos585a.html> (accessed on May 16, 2008).
- [167] H. Stark and J. Woods, "Probability and Random Processes with Applications to Signal Processing", Third Edition, Prentice Hall, 2002.
- [168] Oppenheim, A. V., R. W. Schaffer, and J. R. Buck. "Discrete-Time Signal Processing", 2nd ed. Upper Saddle River, NJ: Prentice Hall, 1999.
- [169] Timothy M. Hollis, "Power Spectral Density (PSD) Estimation", 2004, www.et.byu.edu/~tmh27/PSD.pdf (accessed January 14, 2008).
- [170] J.K. Cavers, *Mobile Channel Characteristics*, 2nd ed., Shady Island Press, 2003
- [171] J. K. Cavers, "*Mobile Channel Characteristics*", 2nd Ed., Shady Island Press, 2003..
- [172] A. Abdi, H. Hashemi, and S. Nader-Esfahani, "On the PDF of the Sum of Random Vectors", IEEE Trans. on Communications. Vol. 48, No.1, January 2000, pp 7-12.
- [173] Y. Baghzouz, R. F. Burch et al "Time-Varying Harmonics: Part II—Harmonic Summation and Propagation", IEEE Trans. On Power Systems, Vol. 17, No. 1, January 2002, pp. 279-285.
- [174] S. T. Tentzerakis and S. A. Papathanassiou, "An Investigation of the Harmonic Emissions of Wind Turbines", IEEE Trans, on Energy Conv., Vol. 22, No 1, March. 07, pp 150-158.
- [175] M.-S. Alouini, A. Abdi, M. Kaveh, "Sum of Gamma Variates and Performance of Wireless Communication Systems Over Nakagami-Fading Channels", IEEE Trans. On Vehicular Technology, Vol. 50, No. 6, pp. 1471-1480.
- [176] J.C. Kaimal, "Horizontal Velocity Spectra in an Unstable Surface Layer" Journal of the Atmospheric Sciences, Vol. 35, Issue 1, pp. 18–24
- [177] António Martins, Paulo C. Costa, Adriano S. Carvalho, "Coherence And Wakes In Wind Models For Electromechanical And Power Systems Standard Simulations", European Wind Energy Conferences EWEC 2006.
- [178] P. Li, H. Banakar, P. K. Keung, H.G. Far, and B.T. Ooi, "Macromodel of Spatial Smoothing in Wind Farms", IEEE Trans, on Energy Conv., Vol. 22, No 1, March. 07, pp 119-128.
- [179] M. Schwab, P. Noll, and T. Sikora, "Noise robust relative transfer function estimation", XIV European Signal Processing Conference, September 4 - 8, 2006, Florence, Italy.
- [180] P. Norgaard, H. Holtinen, "A Multi-turbine Power Curve Approach", in Proc. 2002 Nordic Wind Power Conference.
- [181] IEC 61400-4-15, Electromagnetic compatibility (EMC). Part 4: Testing and measurement techniques. Section 15: Flickermeter. Functional and design specifications.
- [182] Kurt S. Hansen, Gunner Chr. Larsen, "De-trending of turbulence measurements", EWEC 2007, Milan
- [183] T. Thiringer, T. Petru, and C. Liljegren "Power Quality Impact of a Sea Located Hybrid Wind Park", IEEE Transactions On Energy Conversion, Vol. 16, No. 2, June 2001 pp. 123-127

- [184] T. Petru, T. Thiringer "Active flicker reduction from a sea-based 2.5 MW wind park connected to a weak grid", 2000 Nordic Workshop on Power and Industrial Electronics (NORpie 2000), Aalborg, Denmark, June 13-16, 2000.
- [185] T. Thiringer "Power Quality Measurements Performed on a Low-Voltage Grid Equipped with Two Wind Turbines", IEEE Trans. Energy Conversion, Vol. 11, No. 3, September 1996
- [186] T. Thiringer, J.-Å. Dahlberg, "Periodic Pulsations from a Three-Bladed Wind Turbine", IEEE Trans Energy Conversion, Vol. 16, No. 2, June 2001
- [187] T. Thiringer, "Frequency Scanning for Power System Property Determination—Applied to a Wind Power Grid" IEEE Trans. on Power Systems, Vol. 21, No. 2, MAY 2006
- [188] Nayeem Rahmat Ulla, "Topic 9.1: Power Quality Evaluation of a Sea Based Wind Farm", Nordic PhD course on Wind Power. Available at www.elkraft.ntnu.no/smola2005
- [189] S. A. Papathanassiou and Fritz Santjer, "Power Quality Measurements in an Autonomous Island Grid with High Wind Penetration", IEEE Transactions on Power Delivery, Vol 21, No 1, Jan. 2006, pp 218 - 224
- [190] T. Petru "Modeling of wind turbines for Power System Studies", Ph. Disertation, Chalmers University of Technology, Goteborg, Sweden 2003
- [191] P. Sørensen, A. D. Hansena and P. A. Carvalho Rosas, "Wind models for simulation of power fluctuations from wind farms", Journal of Wind Engineering and Industrial Aerodynamics, Vol. 90, No. 12-15, Dec. 2002, pp. 1381-1402.
- [192] P. Sørensen, A. Hansen, L. Janosi, J. Bech and B. Bak-Jensen, "Simulation of Interaction between Wind Farm and Power System", Risø National Laboratory, Roskilde, December 2001. Available at www.risoe.dk/rispubl/VEA/veapdf/ris-r-1281.pdf
- [193] A. D. Hansen, P. Sørensen, F. Blaabjerg and John Becho "Dynamic modelling of wind farm grid interaction", Wind Engineering Vol. 26, No. 4 , 2002, pp. 191–208
- [194] W. E. Leithead and S. Domínguez, "Coordinated Control Design for Wind Turbine Control Systems", EWEC 2006, Athens
- [195] H. Bindner, P. Nørgård, "11kW Gaia Wind Turbine Connected to a Diesel Grid", Risø-I-nr2035(EN), Risø National Laboratory, Roskilde. Available at www.gaia-wind.com.
- [196] Stefan Marko, Ivan Darul'a, Stanislav Vlcek, "Development Of Wind Farm Models For Power System Studies", Journal of Electrical Engineering, VOL. 56, NO. 5-6, 2005, pp. 165–168.
- [197] K. Johnsen and B. Eliasson, "SIMULINK® Implementation of Wind Farm Model for use in Power System Studies", Nordic Wind Power Conference, 1-2 March, 2004, Chalmers University Of Technology.
- [198] J. Pierik, J. Morren, T. Engelen., S. Haan, Jan Bozelie "Development and validation of wind farm models for power system studies. Alsvik wind farm results", EWEC 2006, Athens.
- [199] J. Soens, J. Driesen, R. Belmans, "Equivalent Transfer Function for a Variable-speed Wind Turbine in Power System Dynamic Simulations", International Journal of Distributed Energy Resources, Volume 1 Number 2, April-June, 2005; pp. 111-133.
- [200] S. M. Ross, "Introduction to Probability Models", Academic Press (Elsevier), 2006.
- [201] L.N. Thibos, "Fourier Analysis for Beginners", Indiana University, <http://research.opt.indiana.edu/Library/FourierBook/toc.html> (accessed on May 16, 2008).
- [202] F. D. Neeser, J. L. Massey, "Proper Complex Random Processes with Applications to Information Theory", IEEE Transactions on Information Theory, Vol. 39, No. 4, July 1993, pp. 1293-1302.
- [203] B. Picinbono, "On Circularity", IEEE Trans. On Signal Processing, Vol. 42, No 12, Dec. 1994., pp. 3473-3482
- [204] J. Mur, J. Sallán, A.A. Bayod, "Statistical model of wind farms for power flow", ICREP 2003, Vigo. Available at : www.joaquinmur.eu
- [205] Wind Turbine Generator Systems—Part 21: Measurement and assessment of power quality characteristics of grid connected wind turbines, IEC61400-21.
- [206] N. Visbøll, A. L. Pinegin, T. Fischer, J. Bugge. "Analysis of Advantages of the Double Supply Machine With Variable Rotation Speed Application in Wind Energy Converters". DEWI Magazin Nr. 11, August 1997.
- [207] A. Feijoo, J. Cidras. "Analysis of mechanical power fluctuations in asynchronous WECS". IEEE Transactions on Energy Conversion, Vol. 14, No. 3, pp. 284-291. Sept. 1999.
- [208] E. Bossanyi, Z. Saad-Saoud and N. Jenkins. Prediction of Flicker Produced by Wind Turbines. Wind Energy 1, pp 35-51. 1998.
- [209] IEC 61400-4-15, Electromagnetic compatibility (EMC). Part 4: Testing and measurement techniques. Section 15: Flickermeter. Functional and design specifications.
- [210] CEI IEC 1000-3-7, Electromagnetic compatibility (EMC). Part 3: Limits – Section 7: Assessment of emission limits for fluctuating loads in MV and HV power systems – Basic EMC publication.
- [211] Ministerio de Industria y Energía, "Orden de 5 de Septiembre de 1985", BOE número 219, año 1985.
- [212] Joris Soens, "Impact Of Wind Energy In A Future Power Grid", Ph.D. Dissertation, Katholieke Universiteit Leuven, December 2005.
- [213] Z. Lubosny, "Wind Turbine Operation in Electric Power Systems", Ed. Springer 2003.
- [214] G. C. Larsen, W. Bierbooms and K. S. Hansen, "Mean Gust Shapes", Risø National Laboratory, Roskilde, Denmark.. December 2003, Risø-R-1133(EN)
- [215] W. Bierbooms, "Specific gust shapes leading to extreme response of pitch regulated wind turbines", The Science Of Making Torque From Wind, 28–31 August 2007, Technical University of Denmark

- [216] Bierbooms, WAAM (2005). Constrained stochastic simulation - generation of time series around some specific event in a normal process. *Extremes*, 8(3), 207-224.
- [217] P. S. Veers, Three dimensional wind simulation, Sandia National Laboratories, SAND88-0152, 1988.
- [218] J. Mur, "EQWIGUST, EQuivalent WInd GUST", 2009.
- [219] E. Bertin, M. Clusell, "Generalised extreme value statistics and sum of correlated variables", *J. Phys. A: Math. Gen.* 39, 7607 (2006)
- [220] G. C. Larsen, K. S. Hansen, "Statistical Model of Extreme Shear", *Journal of Solar Energy Engineering*, November 2005, Vol. 127, No. 4, pp. 444-455.
- [221] G. C. Larsen, "An asymptotic closed form solution for the distribution of combined wind speed and wind direction extremes", *The Science of Making Torque*, 2007. Technical University of Denmark
- [222] Z. Warhaft, "Passive scalars in turbulent flows", *Annu. Rev. Fluid Mech.* 2000. 32:203-240.
- [223] M. Nielsen, G. C. Larsen, J. Mann, S. Ott, K. S. Hansen, and B. J. Pedersen, "Wind Simulation for Extreme and Fatigue Loads", Risø National Laboratory, Roskilde, Denmark. January 2004, Risø-R-1437 (EN).
- [224] J. Gottschall and J. Peinke, "Stochastic modelling of a wind turbine's power output with special respect to turbulent dynamics", *The Science Of Making Torque From Wind*, 28-31 August 2007, Technical University of Denmark.
- [225] M. Wächter, A. Rettenmeier, M. Kühn and J. Peinke, "Wind velocity measurements using a pulsed LIDAR system: first results", *IOP Conf. Series: Earth and Environmental Science* 1 (2008).
- [226] F. Böttcher, S. Barth and J. Peinke, "2007 Stoch Environ Res Ris Assess", 21 299-308
- [227] J.A. Molina, G.G. Farias, R.M. Dagnino, "A practical procedure to estimate the shape parameter in the generalized Gaussian distribution", Technical Report, Centro de Investigación en Matemáticas, Guanajuato University, Mexico, 2001.
- [228] B. Fox, D. Flynn, L. Bryans, N. Jenkins, D. Milborrow, M. O'Malley, R. Watson, O. Anaya-Lara, "Wind Power Integration: Connection and System Operational Aspects", Willey, 2007
- [229] S. Rizzo and .A. Rapisarda, "Application of superstatistics to atmospheric turbulence", *International Conference Complexity, Metastability and Nonextensivity*, Erice (Sicily) July 20-26 2004.
- [230] S. Rizzo and .A. Rapisarda, "Environmental atmospheric turbulence at Florence airport", 8th Experimental Chaos Conference, 14-17 June 2004, Florence, ITALY, AIP Conference proceedings Vol. 742, p.176.
- [231] F. Böttcher, St. Barth, and J. Peinke, "Small and Large Scale Fluctuations in Atmospheric Wind Speeds", *Stochastic Environmental Research and Risk Assessment (SERRA)* 21, 299 (2007)
- [232] St. Barth, F. Böttcher and J. Peinke, "Superposition model for atmospheric turbulence", *Wind Energy - Proceedings of the Euromech Colloquium*, Springer, Berlin 2007, p. 115 -118
- [233] A. Wessel, J. Peinke and B. Lange, "Modelling turbulence intensities inside wind farms", *Wind Energy - Proceedings of the Euromech Colloquium*, Springer, Berlin 2007, p. 253 - 256
- [234] J. F. Price, "Lagrangian and Eulerian Representations of Fluid Flow: Kinematics and the Equations of Motion", 2006
- [235] P. Tabeling, "Two-dimensional turbulence: a physicist approach", *Physics Reports*, Volume 362, Issue 1, May 2002, Pages 1-62,
- [236] A.E. Gill, "Atmosphere-ocean Dynamics". Academic Press, NY. 1982.
- [237] M., Hossain, "Reduction of the dimensionality of turbulence due to a strong rotation". *Phys. Fluids* 6 (4), 1077-1080. 1994.
- [238] W.D. McComb, "The Physics of Fluid Turbulence". Clarendon Press, Oxford. 1992.
- [239] Y. Zhou, "A phenomenological treatment of rotating turbulence". *Phys. Fluids*, 7 (8), 2092-2094. 1995.
- [240] P. Constantin "Energy spectrum of quasigeostrophic turbulence". *Phys. Rev. Lett.* 89 (18), 184501-184504. 2002.
- [241] S. Rizzo and .A. Rapisarda, "Application of superstatistics to atmospheric turbulence", *International Conference Complexity, Metastability and Nonextensivity*, Erice (Sicily) July 20-26 2004.
- [242] S. Rizzo and .A. Rapisarda, "Environmental atmospheric turbulence at Florence airport", 8th Experimental Chaos Conference, 14-17 June 2004, Florence, ITALY, AIP Conference proceedings Vol. 742, p.176.
- [243] F. Böttcher, St. Barth, and J. Peinke, "Small and Large Scale Fluctuations in Atmospheric Wind Speeds", *Stochastic Environmental Research and Risk Assessment (SERRA)* 21, 299 (2007)
- [244] St. Barth, F. Böttcher and J. Peinke, "Superposition model for atmospheric turbulence", *Wind Energy - Proceedings of the Euromech Colloquium*, Springer, Berlin 2007, p. 115 -118
- [245] A. Wessel, J. Peinke and B. Lange, "Modelling turbulence intensities inside wind farms", *Wind Energy - Proceedings of the Euromech Colloquium*, Springer, Berlin 2007, p. 253 - 256
- [246] M. Wächter, A. Rettenmeier, M. Kühn and J. Peinke, "Wind velocity measurements using a pulsed LIDAR system: first results", *IOP Conf. Series: Earth and Environmental Science* 1 (2008).
- [247] J. Peinke, E. Anahua, St. Barth, H. Gontier, A.P. Schaffarczyk, D. Kleinhaus, R. Friedrich, "Turbulence: a Challenging Issue for the Wind Energy Conversion", *EWEC 2008 Proceedings*.
- [248] N. Barberis Negra, O. Holmström, B. Bak-Jensen, P. Sørensen, "Model of a synthetic wind speed time series generator", *Wind Energy*. 2008 ; vol. 11, nr. 2, September.

- [249] M Nielsen, G C Larsen, K S Hansen, "Simulation of inhomogeneous, non-stationary and non-Gaussian turbulent winds", *The Science of Making Torque from Wind*, IOP Publishing, Journal of Physics: Conference Series 75 (2007)
- [250] J. Eggers, Z. J. Wang, "Crossover behavior in turbulent velocity fluctuations", *Physical Review E*, Vol. 57, No. 4, April 1998
- [251] K. Gurley, M. Tognarelli, and A. Kareem, "Analysis and Simulation Tools for Wind Engineering", *Probabilistic Engineering Mechanics*, 12(1), pp. 9-31, 1997.
- [252] M. Grigoriu, "Non-Gaussian models for stochastic mechanics", *Prob. Engn. Mech.*, 15, 15–23. (2000).
- [253] St. Lück1, Ch. Renner, J. Peinke and R. Friedrich, "The Markov- Einstein coherence length - a new meaning for the Taylor length in Turbulence", *Physics letters. A*, 2006, vol. 359, no5, pp. 335-338
- [254] H.J. Kushner and G. Yin. "Stochastic Approximation Algorithms and Applications". Springer-Verlag, 1997. Revised second edition, 2003.
- [255] Kushner, H. J. and P. G. Dupuis. "Numerical Methods for Stochastic Control Problems in Continuous Time", Springer; 2nd Rev. Edition (Jan 2001)
- [256] S. O. Rice, "Mathematical analysis of random noise," *Bell Syst. Tech. J.*, vol. 23, pp. 282-332, July 1944; vol. 24, pp. 46-156, Jan. 1945. Reprinted in N. Wax (ed.), *Selected papers on noise and stochastic processes*, Dover Publ.
- [257] D.E. Cartwright, and M. S. Longuet-Higgins, "The statistical distribution of the maxima of a random function", *Proc. Royal Soc. London Ser. A* 237, 212-232. (1956).
- [258] G. C. Larsen, W. Bierbooms, K. S. Larsen, "Statistics of Local Extremes", December 2003, Risø-R-1220(EN), Roskilde, Denmark.
- [259] "Database on Wind Characteristics", Available at <http://www.winddata.com>
- [260] P. Prandoni and M. Vetterli, "Signal Processing for Communications", EPFL press, 2008. Available at <http://www.sp4comm.org/webversion.html>
- [261] M. Ebden, "Gaussian Processes for Regression: A Quick Introduction", Oxford University, August 2008. Available at <http://www.robots.ox.ac.uk/~mebden/reports/GPtutorial.pdf>
- [262] C. E. Rasmussen, C. K. I. Williams, "Gaussian Processes for Machine Learning", MIT Press, 2006. Available at <http://www.gaussianprocess.org/gpml>
- [263] O. Kallenberg, "Foundations on Modern Probability", Spinger, 2nd Ed., 2002.
- [264] W. Bierbooms, "Simulation of stochastic wind fields which encompass measured wind speed series", *Proceedings of the EWEC 2004*, (pp. 1-12). Brussel: EWEA.
- [265] M. Shinozuka, C. M. Jan. "Digital simulation of random processes and its applications", *Journal of Sound and Vibration*, 25, N° 1, 111-128, 1972.
- [266] Shinozuka, M.: Simulation of multivariate and multidimensional random processes. *J. Acoust. Soc. America*. 357–368 (1971)
- [267] W. Bierbooms, Po-Wen Cheng; G. Larsen, B. J. Pedersen, "Modelling of Extreme Gusts for Design Calculations – NewGust", The European commission, contract JOULE III JOR3-CT98-0239, Final Report. TU Delft, 2001, 25 p
- [268] W.A.A.M Bierbooms, "Constrained Stochastic Simulation Of Wind Gusts For Wind Turbine Design", DUWIND Delft University Wind Energy Research Institute, March 2009.
- [269] G. Lindgren, "Some properties of a normal process near a local maximum", *Ann. Math. Stat.* 41, 1870-1883 (1970).
- [270] C.R. Rao, "Linear Statistical Inference and its Applications", Wiley, 1965.
- [271] R.E. Mortensen, "Random Signals and Systems", Wiley, New York, 1987.
- [272] G. Moe, J. M. Niedzwecki, "Frequency of maxima of non-narrow banded stochastic processes", *Applied Ocean Research*, Vol. 27, Issue 6, Dec. 2005, pp. 265-272.
- [273] S. L. Miller, D. G. Childers "Probability and Random Processes: With Applications to Signal Processing and Communications", 2nd Ed., Academic Press, 2004.
- [274] S. Kotz, N. Lloyd Johnson, N. Balakrishnan, "Continuous Multivariate Distributions: Models and Applications", 2nd Ed., John Wiley and Sons, 2000.
- [275] M. R. Milligan, "Modeling Utility-Scale Wind Power Plants. Part 2: Capacity Credit". NREL/TP-500-29701. March 2002.
- [276] R. Billinton, W. Li, "Reliability Assessment of Electric Power Systems Using Monte Carlo Methods", Plenum Press, NY, pp. 351, 1994.
- [277] Kushner, H. J. and P. G. Dupuis. "Numerical Methods for Stochastic Control Problems in Continuous Time", Springer; 2nd Rev. Edition (Jan 2001)
- [278] Sato-Ilic, Mika, Jain, Lakhmi C., "Innovations in Fuzzy Clustering. Theory and Applications", Springer 2006.
- [279] Scott Beaver and Ahmet Palazoglu, "Cluster Analysis of Hourly Wind Measurements to Reveal Synoptic Regimes Affecting Air Quality", *Journal of Applied Meteorology*, vol. 45 (2006), No 12, pp. 1710-1726.
- [280] J. Filar, K. Vrieze, "Competitive Markov Decision Processes", 1997, Springer.
- [281] M.L. Putterman, "Markov Decision Processes. Discrete Stochastic Dynamic Programming", John Willey, New York, 1994.
- [282] J. R. Norris, "Markov Chains", Cambridge University Press, 1996
- [283] Wai-Ki Ching, Michael K. Ng, "Markov Chains. Models, Algorithms and Applications", Springer 2006.
- [284] V. G. Kulkarni, "Modeling, Analysis, Design, and Control of Stochastic Systems", Springer 1999.
- [285] O. Cappé, E. Moulines, T. Rydén, "Inference in Hidden Markov Models", Springer, 2005.

- [286] Munk, C. “Numerical Methods for Continuous-Time, Continuous-State Stochastic Control Problems”. Publications from Department of Management 11, Odense University, 1997
- [287] Avrachenkov, K., Sanchez, E. “Fuzzy chains and decision-making”. *Fuzzy Optim. Decis. Making* 1 (2), 143–159, 2002.
- [288] J.J. Buckley and E. Eslami, “Fuzzy Markov Chains: Uncertain Probabilities”, *Mathware and Soft Computing*, 9(1):33–41, 2002.
- [289] F. Salzenstein, C. Collet, S. Lecam and M. Hatt “Non-stationary fuzzy Markov chain”, *Pattern Recognition Letters* 28 (2007) 2201–2208.
- [290] J.J. Buckley, “Fuzzy Probabilities. New Approach and Applications”, Springer, 2005.
- [291] IEC 61400-12-1, Wind Turbines – Part 12: Power performance measurements of electricity producing wind turbines. 2007.
- [292] IEC 61400-21, Wind Turbines – Part 21: Measurement and assessment of power quality characteristics of grid connected wind turbines. 1st Edition, 2001.
- [293] Royal Degree 436/2004, Boletín Oficial del Estado. Publishing date: 27th March 2004. Available: <http://www.boe.es/boe/dias/2004-03-27/pdfs/A13217-13238.pdf>
- [294] John H. Mathews and Kurtis Fink, “Numerical Methods using Matlab”, 4th edition, 2004.
- [295] J. Mur Amada, A.A. Bayod Rújula, "Characterization of Spectral Density of Wind Farm Power Output", 9th Conference on Electrical Power Quality and Utilisation (EPQU'2007), Barcelona, 2007. ISBN 978-84-690-9441-9.
- [296] Janusz Marecki, Sven Koenig, Milind Tambe "A Fast Analytical Algorithm for Solving Markov Decision Processes with Continuous Resources" In Proceedings of the 20th International Joint Conference on Artificial Intelligence (IJCAI), 2007
- [297] Barry L. Nelson, “Stochastic Modeling (Analysis & Simulation)”, Mac Graw-Hill, New York, 1995.
- [298] A.K. Jain, M.N. Murty, P.J. Flynn, “Data Clustering: A Review”, *ACM Computing Surveys*, Vol. 31, No. 3, September 1999
- [299] J. Mur, A. A. Bayod "Characterization of wind farm energy production in a zone by artificial neuronal networks", ICREP '03 (Internacional Conference on Renewable Energies and Power Quality), Vigo 2003.
- [300] Sato-Ilic, Mika, Jain, Lakhmi C., “Innovations in Fuzzy Clustering. Theory and Applications”, Springer 2006.
- [301] Shaning AD, Sen Z. “First-order Markov chain approach to wind speed modeling”. *J. Wind. Engineering Ind. Aerodynamics* 2001, 89: 263-9.
- [302] A. Shamshad, M.A. Bawadi, W.M.A. Wand Hussing, T.A. Majid, S.A.M. Sanusi, “First and second order Markov chain models for synthetic generation of wind speed time series”, *Energy* 30, 693-708, 2005.
- [303] Christopher C. Tan, Norman C. Beaulieu, “On First-Order Markov Modeling for the Rayleigh Fading Channel”, *IEEE Trans. Communications*, Vol. 48, No. 12, Dec 2000.
- [304] C.P. Robert, “Discretization and MCMC Convergence Assessment”, Springer, 1998
- [305] M. K. Simon, S. M. Hinedi, and W. C. Lindsey, *Digital Communication Techniques: Signal Design and Detection*. Englewood Cliffs, NJ: Prentice-Hall, 1994.
- [306] R. C. Titsworth and L. R. Welch, “Power spectra of signal modulated by random and pseudorandom sequences,” *Jet Propulsion Lab., Pasadena, CA, Tech. Rep. 32-140*, Oct. 1961.
- [307] D. F. Bishop, S. Million, T. M. Nguyen, and M. K. Simon, “Power Spectrum of Unbalanced NRZ and Biphasic Signals in the Presence of Data Asymmetry”, *IEEE Trans. Electromagnetic Compatibility*, Vol. 40, No. 1, February 1998
- [308] Y. Yang, “General method for computing the power spectrum density of irreducible periodic Markov chains” *IEEE GLOBECOM 98*, Vol. 6, pp. 3320-3325, 8-12 Nov. 1998.
- [309] Papaefthymiou G, Klöckl B., “MCMC for Wind Power Simulation” *IEEE Trans. Energy Conversion*,
- [310] G. George Yin, Quing Zhang, “Discrete-Time Markov Chains. Two-Time-Scale Methods and Applications”, Springer, 2005.
- [311] Alan S. WillSky, “Multiresolution Markov Models for Signal and Image Processing”, *Proceedings IEEE*, Vol. 90, No. 8, August 2002.
- [312] Anne Benoit, L. Brenner, P. Fernandes, B. Plateau, “Aggregation of stochastic automata networks with replicas”, *Linear Algebra and its Applications* 386 (2004) 111–136.
- [313] William J. Stewart, “Introduction to the Numerical Solution of Markov Chains”, Princeton University Press, 1994.
- [314] Per Nørgård, Gregor Giebel, Hannele Holttinen, Lennart Söder, Astrid Petterteig, “Fluctuations and predictability of wind and hydropower”, *Risø National Laboratory, Roskilde, Denmark*, June 2004
- [315] Report of the Research Project “Análisis de la Energía entregada a la red de distribución eléctrica por las Centrales Eólicas - Compañía Eólica Aragonesa S.A.”, Zaragoza University, January 1999.
- [316] Report of the Research Project “Análisis de la Energía entregada a la red de distribución eléctrica por las Centrales Eólicas - Neg-Micon Eólica S.A.”, Zaragoza University, November 2000.
- [317] Hannele Holttinen, “Hourly Wind Power Variations in the Nordic Countries”, *Wind Energy*, vol. 8 (2005), Issue 2, pp.173-195.
- [318] K. Altaii, R.N. Farrugia, “Wind characteristics on the Caribbean island of Puerto Rico”, *Renewable Energy* 28 (2003) pp. 1701–1710.
- [319] Gilbert M. Masters, “Renewable and Efficient Electric Power Systems”, Wiley 2004.
- [320] G. Papaefthymiou, “Integration of Stochastic Generation in Power Systems”, Ph.D Thesis, Delft 2006

- [321] Holttinen, H.; Lemström, B.; Meibom, P.; Bindner, H.; Orths, A. et al. "Design and operation of power systems with large amounts of wind power", 2007. VTT Working Papers : 82, Espoo. 119 p. + app. 25 p.
- [322] B. Parsons, M. Milligan, B. Zavadil, D. Brooks, B. Kirby, K. Dragoon, J. Caldwell, "Grid Impacts of Wind Power: A Summary of Recent Studies in the United States", EWEC 2003.
- [323] B. Bidabad, B. Bidabad, "Complex Probability and Markov Stochastic Process". Proceeding of the 1st Iranian Statistics Conference, Isfahan University of Technology, 1992.
- [324] Lawrence R. Rabiner, "A Tutorial on Hidden Markov Models and Selected Applications in Speech Recognition", Proceedings of the IEEE, Vol. 77, No. 2, February 1989
- [325] Isaac Van der Hoven, "Power Spectrum Of Horizontal Wind Speed In The Frequency Range From 0.0007 To 900 Cycles Per Hour", Journal of the Atmospheric Sciences, Vol. 14, Issue 2, pp. 160–164
- [326] Tore Heggem, Rune Lende, And Jørgen Løvseth, "Analysis of Long Time Series of Coastal Wind", Journal of the Atmospheric Sciences, Volume 55, Issue 18, pp. 2907–2917
- [327] P. Sørensen, N. A. Cutululis, J. Hjerrild, L. Jensen, M. Donovan, L. E. A. Christensen, H. Madsen, A. Viguera-Rodríguez, "Power Fluctuations from Large Offshore Wind Farms", Nordic Wind Power Conference, 22-23 May, 2006, Espoo, Finland.
- [328] K. Saranyasontorn, L. Manuel, Paul S. Veers, "A Comparison of Standard Coherence Models form Inflow Turbulence With Estimates from Field Measurements", Journal of Solar Energy Engineering, Vol. 126, Issue 4, pp. 1069-1082
- [329] J.C. Kaimal, "Horizontal Velocity Spectra in an Unstable Surface Layer" Journal of the Atmospheric Sciences, Vol. 35, Issue 1, pp. 18–24
- [330] Wind energy barometer 2008. EurObserv'ER Systèmes solaires Le journal des énergies renouvelables , n° 4, 2009.
- [331] Red Eléctrica de España, "The Spanish Power System. Wind power generation in real time", Available: http://www.ree.es/ingles/i-index_de.html
- [332] Order of Energy and Industry Ministry of date 5-9-1985, Published in BOE 12-9-1985, no. 219, pp. 28810.
- [333] J. Mur Amada, Ma Paz Comech Moreno, "Reactive Power Injection Strategies for Wind Energy Regarding its Statistical Nature", 6th International Workshop on Large-Scale Integration of Wind Power and Transmission Networks for Offshore Wind Farms. Delft, 2006.
- [334] G. George Yin, Qing Zhang, "Discrete-Time Markov Chains: two-time-scale methods and applications", Springer Mathematics, 2005.
- [335] Vidyadhar G. Kulkarni "Modeling, analysis, design, and control of stochastic system", Springer-Verlang New York 1999.
- [336] R. Billinton and R. N. Allan, Reliability Evaluation of Power Systems, 2nd ed. New York: Plenum Press, 1996.
- [337] A. D. Gordon, "Classification", CRC Press, 2nd Ed. 1999.
- [338] B. S. Everitt, S. Landau and M. Leese, "Cluster Analysis", Oxford University Press, 4th Ed. 2001.
- [339] IEC 61400-12-3, Wind turbine generator systems – Part 12-3: wind farm power performance testing, 2005. Working Group Draft.
- [340] Nikolai V. Shokhirev, "Hidden Markov Models", Available at www.shokhirev.com/nikolai/abc/alg/hmm/hmm.html
- [341] C. Luo and B. T. Ooi, "Frequency Deviation of Thermal Power Plants Due to Wind Farms", IEEE Trans. Energy Conversion, Sept. 2006, Vol. 21, N. 3, pp. 708-716.
- [342] Rodriguez, J.M.; Fernandez, J.L.; Beato, D.; Iturbe, R.; Usaola, J.; Ledesma, P.; Wilhelmi, J.R.; "Incidence on power system dynamics of high penetration of fixed speed and doubly fed wind energy systems: study of the Spanish case", IEEE Trans. Power Systems, Vol. 17, No 4, Nov. 2002, Pp.1089 - 1095
- [343] Cigré, Working Group C1.3, "Electric Power System Planning with the Uncertainty of Wind Generation" Technical Report 293, April 2006.
- [344] Wan, Y. "Wind Power Plant Behaviours: Analyses of Long-Term Wind Power Data". NREL/TP-500-36651, Aug. 2004. Available at www.osti.gov/bridge
- [345] S. M. Ross, "Introduction to Probability Models", Academic Press, 8th Edition, 2003.
- [346] G. Stefopoulos, A. P. Meliopoulos and G. J. Cokkinides, "Advanced probabilistic Power Flow Methodology", 15th PSCC, Liege, 2005
- [347] Chun-Lien Su, "Probabilistic Load-Flow Computation Using Point Estimate Method", IEEE Trans. Power Systems, Vol. 20, no. 4, Nov. 2005.
- [348] G. Verbic, C. A. Cañizares, "Probabilistic Optimal Power Flow in Electricity Markets Based on a Two Point Estimate Method", IEEE Trans. Power Systems, Vol. 21, No. 4, pp.1883 – 1893, Nov. 2006.
- [349] G. J. Anders, "Probability concepts in electric power systems", Ed. Wiley, 1991.
- [350] R. Billinton and R. N. Allan, Reliability Evaluation of Power Systems, 2nd ed. New York: Plenum Press, 1996.
- [351] D. Peña, "Análisis de datos multivariantes", McGraw-Hill, 2002.
- [352] P. Fernandes, B. Plateau and W. J. Stewart, "Efficient Descriptor-vector Multiplications in Stochastic Automata Networks", Journal of the ACM, Vol. 45, No. 3, May 1998, pp. 381-414.
- [353] J. Mur, J. Sallán, A.A. Bayod, "Statistical model of wind farms for power flow", ICREP 2003, Vigo.
- [354] J. Mur, M. P. Comech, "Reactive Power Injection Strategies for Wind Energy Regarding its Statistical Nature", Sixth International Workshop on Large-Scale Integration of Wind Power and Transmission Networks for Offshore Wind Farm. Delft, 2006.

- [355] UNE 206005 IN Determinación de la capacidad de regulación de potencia reactiva de parques eólicos. 2004 (Assesment of the reactive power ability of wind farms).
- [356] Ali Abur, Antonio Gómez Expósito, "Power System State Estimation: Theory and Implementation", CRC Press, 2004.
- [357] J. Mur, A. A. Bayod "Characterization of wind farm energy production in a zone by artificial neuronal networks", ICREP '03, Vigo 2003.
- [358] W. J. Stewart, "Introduction to the Numerical Solution of Markov Chains", Princeton University Press, 1994.
- [359] Schuhmacher, J., 1993. "INSEL – Interactive Simulation of Renewable Electrical Energy Supply Systems–, Reference Manual". University of Oldenburg, Renewable Energy Group, Dept. of Physics, PO Box 2503, D-26111 Oldenburg.
- [360] R. Dufo, "Dimensionamiento y control óptimos de sistemas híbridos aplicando algoritmos evolutivos", PhD., Zaragoza University, 2007.
- [361] B. Givan and R. Parr, "An Introduction to Markov Decision Processes", Purdue University, 2001.
- [362] E. A. Feinberg and A. Shwartz (editors), "Handbook of Markov Decision Processes. Methods and Applications", Kluwer 2002.
- [363] Raúl Vicastillo-Golvano, "Optimización de un banco de condensadores y reactancias en la subestación de un parque eólico", Graduation Project, Zaragoza University, June 2009.
- [364] Andrés E. Feijóo, José Cidrás "Modeling of Wind Farms in the Load Flow Analysis", IEEE Trans. Power Systems, Vol. 15, No. 2, Feb. 2000, pp. 110-115.
- [365] UNE-EN 50160 "Voltage characteristics supplied by general distribution networks" (in Spanish). 1999.
- [366] Royal Decree 436/2004, Boletín Oficial del Estado. Publishing date: 27th March 2004. Available at <http://www.boe.es/boe/dias/2004-03-27/pdfs/A13217-13238.pdf>
- [367] N. Jenkins, R. Allan, P. Crossley, D. Kirschen and G. Strbac "Embedded Generation", Ed. IEE 2000
- [368] Sveca, J., Soder, L., "Wind power integration in power systems with bottleneck problems", Power Tech Conference Proceedings, 2003 IEEE Bologna
- [369] V. Akhmatov, H. Knudsen, "An aggregate model of a grid-connected, large-scale, offshore wind farm for power stability investigations importance of windmill mechanical system", Electrical Power and Energy Systems 24 (2002) pp. 709-717
- [370] IEC 61400-12-1, Wind turbine generator systems – Part 12-1: Power performance measurements of electricity producing wind turbines, 2006. Committee Draft.
- [371] Suresh H. Jangamshetti, V. Guruprasada Rau "Normalized Power Curves as a Tool for Identification of Optimum Wind Turbine Generator Parameters", IEEE Trans, on Energy Conv., Vol. 16, No 3, Sept. 2001, pp 283-288.
- [372] G. J. Anders, "Probability concepts in electric power systems", Ed. Wiley, 1991.
- [373] C.L. Masters, J. Mutale, G. Strbac, S. Curcic and N. Jenkins "Statistical evaluation of voltages in distribution systems with embedded wind generation", IEE Proc.-Gener. Transm. Distrib. Vol. 147, N° 4, July 2000, pp. 207-212.
- [374] IEC 61400-12-3, Wind turbine generator systems – Part 12-3: wind farm power performance testing, 2005. Working Group Draft.
- [375] J.L. Rodríguez Amenedo, J.C. Burgos Díaz, S. Arnalte Gómez "Sistemas Eólicos de Producción de Energía Eléctrica. Editorial Rueda S.L., 2003.
- [376] Statistical Methods of Uncertainty Analysis for Metrology and Scientific Laboratories ISO 7C69/SC6/WG2 Draft 2. Available at <http://www.itl.nist.gov/div898/carroll/u1.htm>
- [377] J. Mur, J. Sallán, A.A. Bayod, "Statistical model of wind farms for power flow", ICREP 2003, Vigo.
- [378] UNE 206005 IN Determinación de la capacidad de regulación de potencia reactiva de parques eólicos. 2004 (Assesment of the reactive power ability of wind farms).
- [379] T. Ackerman, "Wind Power in Power Systems". Ed. Wiley 2005.
- [380] OM 12/1/1995, Boletín Oficial del Estado. Publishing date: 14th January 1995. Available at <http://www.boe.es/boe/dias/1995/01/14/pdfs/A01355-01377.pdf>
- [381] L. Bryans et Al., "Electric Power System Planning with the uncertainty of wind generation". CIGRÉ, Tecnical Brochure 293, W.G. C1.3.
- [382] ISO – Guide to the expression of uncertainty in measurement, 1995.
- [383] IEC 61400-12-2, Wind turbine generator systems – Part 12-2: Verification of power performance of individual wind turbines, 2005. Working Group Draft.
- [384] R. Allan, R. Billinton, "Probabilistic Assessment of Power Systems", Proceedings of the IEEE, Vol. 88, No 2, February 2000, pp 140-162.
- [385] C. Gherasim, "Signal Processing for Voltage and Current Measurements in Power Quality Assessment", PhD. Thesis, Katholieke Universiteit Leuven, May 2006
- [386] Klaus Heuk, Klaus-Dieter Dettmann, "Elektrische Energieversorgung", Vieweg, 3rd edition.
- [387] J. Mann, G.C. Larsen and T.J. Larsen, "Towards more realistic extreme load predictions", EWEC 2006, February 2006.
- [388] Igor Djuroic, Ljbisa Stankovic. "A Virtual Instrument for Time-Frequency Analysys". IEEE Trans. Instrumentation and Measurement, vol. 48, no. 6, December, 1999.
- [389] Tomasz P. Zielinski. "Joint Time-Frequency Resolution of Signal Analysis Using Gabor Transform" IEEE Trans. on Instr. Meas. Vol. 50, No. 5, pp. 1436-1444. 2001.
- [390] M. O. L. Hansen, "Aerodynamics of wind turbines", 2nd Ed., Earthscan 2008.
- [391] J. Peeters, "Simulation of dynamic drive train loads in a wind turbine", Ph. D. Dissertation, Katholieke Universiteit Leuven, 2006.

- [392] A. Ahlström, "Aeroelastic Simulation of Wind Turbine Dynamics", Ph.D., KTH, Stockholm, 2005
- [393] J.F. Manwell, J.G. McGowan and A.L. Rogers, "Wind Energy Explained. Theory, Design and Application.", 2002, Wiley
- [394] Eric Hau, "Wind Turbines. Fundamentals, Technologies, Application, Economics", 2nd Ed., Springer 2006.
- [395] R. Lanzafame, M. Messina, "Fluid dynamics wind turbine design: Critical analysis, optimization and application of BEM theory", *Renewable Energy* 32 (2007) 2291–2305
- [396] J. Jonkman, "Aeroelastic Simulation: FAST", Wind Turbine Design Codes Workshop, National Wind Technology Center, September 13-15, 2005.
- [397] "AeroDyn User's Guide", version 12.50, Dec. 2002.
- [398] F.M.White "Fluid Mechanics", 5th Ed., McGraw Hill International, (2003)
- [399] F. Kießling, "Modellierung des aeroelastischen Gesamtsystems einer Windturbine mit Hilfe symbolischer Programmierung", DFVLR report, DFVLR-FB 84-10, 1984
- [400] Snyder, M.H., "Wakes Produced by a Single Element and Multiple Element Wind Turbine Towers". *Wind Energy Conversion Devices*, Von-Kármán-Institut, 1981
- [401] L.J. Vermeer, J.N.Sørensen y A. Crespo (2003) "Wind Turbine Wake Aerodynamics" *Progress in Aerospace Sciences*. Vol. 39. Issues 6-7. Agosto-October 2003. pp. 467-510.
- [402] O. Rathmann, S. Frandsen, R. Barthelmie, "Wake modelling for intermediate and large wind farms", *EWEC* 2007.
- [403] Frandsen, S.; Barthelmie, R.J.; Rathmann, O.; Jørgensen, H.E.; Badger, J.; Hansen, K.; Ott, S.; Rethore, P.-E.; Larsen, S.E.; Jensen, L.E., Summary report: The shadow effect of large wind farms: measurements, data analysis and modelling. *Risø-R-1615(EN)* (2007) 35 p.
- [404] R.J. Barthelmie, S.T. Frandsen, K. Hansen, J.G. Schepers, K. Rados, W. Schlez, A. Neubert, L.E. Jensen, S. Neckelmann, "Modelling the impact of wakes on power output at Nysted and Horns Rev", *EWEC* 2008.
- [405] R.J. Barthelmie, S.T. Frandsen, O. Rathmann, K. Hansen, E.S. Politis, J. Prospathopoulos, D. Cabezón, K. Rados, S.P. van der Pijl, J.G. Schepers, W. Schlez, J. Phillips and A. Neubert, "Flow and wakes in large wind farms in complex terrain and offshore", *EWEC* 2008
- [406] A. Martins, P. C. Costa, A. S. Carvalho, "Coherence and wakes in wind models for electromechanical and power systems standard simulations", *EWEC* 2006.
- [407] A Jimenez, A Crespo, E Migoya and J Garcia "Large-eddy simulation of spectral coherence in a wind turbine wake", *Environ. Res. Lett.* 3 (January-March 2008).
- [408] A. Knauer, T.D. Hanson, B. Skaare, "Offshore Wind Turbine Loads in Deep-water Environment", *EWEC* 2006.
- [409] Vermeulen PEJ. "An experimental analysis of wind turbine wakes". *Proceedings of the International Symposium on Wind Energy Systems*, Lyngby, Denmark; 1980; 431-450.
- [410] WASP Manual, "Wake effect model", available at <http://www.wasp.dk>
- [411] R.J. Barthelmie, O. Rathmann, S.T. Frandsen, K. Hansen, E. Politis, J. Prospathopoulos, K. Rados, D. Cabezón, W. Schlez, J. Phillips, A. Neubert, J.G. Schepers and S.P. van der Pijl, "Modelling and measurements of wakes in large wind farms", *The Science of Making Torque from Wind*, IOP Publishing, 2007.
- [412] B. Lange, H.P. Waldl, R. Barthelmie, A. Gil-Guerrero, D. Heinemann, "Modelling of offshore wind turbine wakes with the wind farm program FLaP", *Wind Energy*, Vol. 6 Issue 1, Pp. 87 – 104.
- [413] R. Barthelmie, G. Larsen, S. Pryor, H. Bergström, M. Magnusson, W. Schlez, K. Rados, B. Lange, P. Vølund, S. Neckelmann, S. Mogensen, G. Schepers, T. Hegberg, L. Folkerts, "ENDOW: Efficient Development of Offshore Windfarms", *Wind Energy*, Vol. 7, Issue 3, Pp. 225 - 245
- [414] J. Mur, "Wind Power Variability in the Grid", Ph.D Thesis, Zaragoza University, October 2009.
- [415] Dennis C. Ghiglia, Mark D. Pritt, "Two-Dimensional Phase Unwrapping : Theory, Algorithms, and Software", June, 1998.
- [416] R. L. Smith, "Time Series", University of North Carolina, 1999. www.stat.unc.edu/faculty/rsmith.html (accessed on May 16, 2008).
- [417] W. A. Ardner, A. Napolitano, L. Paura, "Cyclostationarity: Half a century of research", *Signal Processing* 86 (2006) 639-697.
- [418] A. Papoulis, "Probability, Random Variables, and Stochastic Processes", McGraw-Hill, 4th ed., 2002.
- [419] O. Kallenberg, "Foundations of Modern Probability", Springer, 2nd Ed., 2002.
- [420] I. Fleischer, A. Kooharian, "On the Statistical Treatment of Stochastic Processes", *The Annals of Mathematical Statistics*, Vol. 29, No. 2 (Jun., 1958), pp. 544-549.

Bibliography on Wind Power Variability

The figures in the references correspond to the PhD. Thesis Dissertation "[Wind Power Variability in the Grid](#)", by J. Mur Amada, Zaragoza University, October 2009. The references greater than 421 have been added, since the Thesis may be getting a bit outdated.

1. [Directive 2009/28/EC of the European Parliament and of the Council of 23 April 2009 on the promotion of the use of energy from renewable sources and amending and subsequently repealing Directives 2001/77/EC and 2003/30/EC](#)
2. ["Report finds US is world's top wind producer". The Guardian. 2008-07-30. http://www.guardian.co.uk/ environment/2008/jul/30/windpower.energy. Retrieved 2008-08-24.](#)
3. [EnerNex Corporation, "Final Report - 2006 Minnesota Wind Integration Study, Volume 1," Nov. 30, 2006. Vol. 2](#)
4. [U.S. Department of Energy, "20% Wind Energy by 2030. Increasing Wind Energy's Contribution to U.S. Electricity Supply", July 2008](#)
5. [J. F. DeCarolus, D.W. Keith, "The Costs of Wind's Variability: Is There a Threshold?", The Electricity Journal, Volume 18, Issue 1, pp. 69-77, 2005](#)
6. [U.S. Department of Energy, "Wind Energy Myths", Wind Powering America Fact Sheet Series, May 2005](#)
7. [Stacy Feldman, "The Wind Power Variability Myth Gets Debunked, Again", SolveClimate, Jul 17th, 2009.](#)
8. [Pöyry PLC, "Impact of intermittency. How wind intermittency could shape the electricity markets?". Available at <http://www.ilexenergy.com/>](#)
9. [International Energy Agency, "Variability Of Wind Power And Other Renewables. Management options and strategies", 2005. Available: <http://www.iea.org / textbase/papers/2005/variability.pdf>](#)
10. [B. K. Sovacool, "The intermittency of wind, solar, and renewable electricity generators: Technical barrier or rhetorical excuse?", Utilities Policy 17 \(2009\), 288-296](#)
11. [R. Piwko, G. Boukarikm, K. Clark, G. Haringa, G. Jordan, N. Miller, Y. Zhou, J. Zimberlin, \(2004, Feb.\). The Effects of Integrating Wind Power on Transmission System Planning, Reliability, and Operations. GE Power Systems Energy Consulting. Schenectady, NY. Available: \[http://www.nyserda.org/publications/wind_integration_report.pdf\]\(http://www.nyserda.org/publications/wind_integration_report.pdf\)](#)
12. [C. Lindsay Anderson, Judith B. Cardell, "Reducing the Variability of Wind Power Generation for Participation in Day Ahead Electricity Markets", Proceedings of the 41st Hawaii International Conference on System Sciences, 2008.](#)
13. [G. Boyle "Renewable Electricity and the Grid. The Challenge of Variability", September 2007, Earthscan](#)

14. [E.M. Constantinescu, V.M. Zavala, M. Rocklin, S. Lee, M. Anitescu, "Unit Commitment with Wind Power Generation: Integrating Wind Forecast Uncertainty and Stochastic Programming", Argonne National Laboratory, September 2009](#)
15. [M.Milligan, "Modelling Utility-Scale Wind Power Plants. Part 2: Capacity Credit", Wind Energy, Volume 3, Issue 4, pp. 167-206, 2001](#)
16. [B. Parsons, Y. Wan, B. Kirby, "Wind Farm Power Fluctuations, Ancillary Services, and System Operating Impact Analysis Activities in the United States", National Renewable Energy Laboratory, 2001](#)
17. [B. Parson, M. Milligan, B. Zavadil, D. Brooks, B. Kirby, K. Dragoon, J. Caldwell, "Grid Impacts of Wind Power: A summary of recent studies in the United States" Wind Energy , vol. 7, Apr./Jun. 2004, pp 87-108.](#)
18. [Julija Matevosyan, "Wind power integration in power systems with transmission bottlenecks", KTH, Stockholm, 2006. Summary](#)
19. [H. Holttinen, B. Lemström, P. Meibom, H. Bindner, A. Orths, F. van Hulle, C. Ensslin, A. Tiedemann, L. Hofmann, W. Winter, A. Tuohy, M. O'Malley, P. Smith, J. Pierik, J. Olav Tande, A. Estanqueiro, J. Ricardo, E. Gomez, L. Söder, G. Strbac, A. Shakoor, J. C. Smith, B. Parsons, M. Milligan, Y. H. Wan, "Design and Operation of Power Systems with Large Amounts of Wind Power. State-of-the-art report", VTT Technical Research Centre of Finland, 2007.](#)
=> [Final report, Phase one 2006-08](#)
20. [I. Martí, G. Kariniotakis, P. Pinson, I. Sanchez, T. S. Nielsen, H. Madsen, G. Giebel, J. Usaola, A.M. Palomares, R. Brownsword, J. Tambke, U. Focken, M. Lange, G. Sideratos, G. Descombes, "Evaluation of Advanced Wind Power Forecasting Models - Results of the Anemos Project", EWEC 2006, Athens.](#)
=> [Presentation](#)
21. [Ignacio J Ramirez-Rosado, L. Alfredo Fernandez-Jimenez, Cláudio Monteiro, Joao Sousa, Ricardo Bessa, "Comparison of two new short-term wind-power forecasting systems", Renewable Energy \(2009\)](#)
22. [J. Juban, L. Fugon, G. Kariniotakis, "Uncertainty Estimation of Wind Power Forecasts", EWEC 2008, Brussels, Belgium.](#)
23. [Y. Wan, D. Bucaneg, "Short-term power fluctuations of large wind power plants", Journal of Solar Energy Engineering, Volume 124, pp. 427-431, 2002](#)
24. [J. Apt, "The spectrum of power from wind turbines", Journal of Power Sources 169 \(2007\) 369-374](#)
25. [P. Cappers, C. Goldman, D. Kathan "Demand response in U.S. electricity markets: Empirical evidence", Energy \(2009\).](#)
26. [K. Porter, D. Yen-Nakafuji and B. Morgenstern, "A Review of the International Experience with Integrating Wind Energy Generation", The Electricity Journal, Volume 20, Issue 8, October 2007, Pages 48-59.](#)
27. [A D. Lamont, "Assessing the long-term system value of intermittent electric generation technologies", Energy Economics 30 \(2008\) 1208-1231](#)
28. [M. A. Matos, R. Bessa, "Operating Reserve Adequacy Evaluation using Uncertainties of Wind Power Forecast", IEEE Bucharest PowerTech Conference, June 28th 2009.](#)
29. [H. Holttinen, "Estimating the impacts of wind power on power systems - summary of IEA Wind collaboration", Environ. Res. Lett. 3 \(2008\)](#)
30. [E. Hirst, J. Hild, "The Value of Wind Energy as a Function of Wind Capacity", The](#)

- [Electricity Journal, Volume 17, Issue 6, pp. 11-20, 2004.](#)
31. [D. Milborrow, "Managing Variability", A report to WWF-UK, RSPB, Greenpeace UK and Friends of the Earth EWNI, 24 June 2009.](#)
 32. [D. Snieckus, "Myth of wind variability problems debunked", Recharge News, July 9 2009.](#)
 33. [Operating the Electricity Transmission Networks in 2020. Initial Consultation. UK's National Grid, June 2009.](#)
 34. [IEA Wind Energy Annual Report 2006, July 2006](#)
 35. [M. Sanz A. Llombart A. A. Bayod J. Mur, "Power quality measurements and analysis for wind turbines", IEEE Instrumentation and Measurement Technical Conference 2000, pp. 1167-1172. May 2000, Baltimore.](#)
 36. [J. Mur Amada, A.A. Bayod Rújula, "Characterization of Spectral Density of Wind Farm Power Output", 9th Conference on Electrical Power Quality and Utilisation \(EPOU'2007\), Barcelona, 2007. ISBN 978-84-690-9441-9.](#)
 37. [W. Schlez, D. Infield, "Horizontal, two point coherence for separations greater than the measurement height", Boundary-Layer Meteor. 87 \(1998\), 459-480.](#)
 38. [Poul Sorensen, Nicolaos A. Cutululis, Antonio Viguera-Rodríguez, Henrik Madsen, Pierre Pinson, Leo E. Jensen, Jesper Hjerrild and Martin Donovan, "Modelling of Power Fluctuations from Large Offshore Wind Farms", WIND ENERGY, October 2007](#)
 39. [António P. Martins, Paulo C. Costa Adriano, S. Carvalho, "Coherence and wakes in wind models for electromechanical and power systems standard simulations", EWEC 2006, Athens.](#)
 40. [G. Papaefthymiou and Bernd Klöckl "MCMC for Wind Power Simulation", IEEE Trans. Energy Conv., 2008 \(to be published\).](#)
 41. [G. Papaefthymiou, "Integration of Stochastic Generation in Power Systems", Ph. D. Dissertation, Delf University, Neetherlands, 2007.](#)
 42. [Cristian Nichita, Dragos Luca, Brayima Dakyo, and Emil Ceanga, "Large Band Simulation of the Wind Speed for Real Time Wind Turbine Simulators", IEEE Transactions On Energy Conversion, Vol. 17, No. 4, December 2002.](#)
 43. [T. Petru and T. Thiringer, "Modeling of Wind Turbines for Power System Studies", IEEE Trans. On Power Systems, Vol. 17, No. 4, Nov. 2002, pp. 1132 - 1139](#)
 44. [P. Rosas, "Dynamic influences of wind power on the power system", Ph. D Thesis, Orsted-DTU, March 2003, ISBN: 87-91184-16-9.](#)
 45. [W. Schlez, D. Infield, "Horizontal, two point coherence for separations greater than the measurement height", Boundary-Layer Meteor. 87 \(1998\), 459-480.](#)
 46. [P. Sorensen, N. A. Cutululis, A. Viguera-Rodríguez, H. Madsen, P. Pinson, L. E. Jensen, J. Hjerrild, M. Donovan, "Modelling of Power Fluctuations from Large Offshore Wind Farms", Wind Energy, Oct 2007.](#)
 47. [E. Welfonder, R. Neifer and M. Spaimer, "Development And Experimental Identification Of Dynamic Models For Wind Turbines", Control Eng. Practice, Vol. 5, No. 1, pp. 63-73, 1997.](#)
 48. [J. Gordon Leishman "Challenges in Modeling the Unsteady Aerodynamics of Wind Turbines", 21st ASME Wind Energy Symposium, Reno, NV, Jan. 14-17, 2002.](#)
 49. [D. S. L. Dolan and P. W. Lehn "Real-Time Wind Turbine Emulator Suitable for Power Quality and Dynamic Control Studies" International Conference on Power Systems Transients \(IPST'05\) in Montreal, Canada on June 19-23,2005.](#)

50. [D. S. L. Dolan and P. W. Lehn, "Simulation Model of Wind Turbine 3p Torque Oscillations due to Wind Shear and Tower Shadow", IEEE Trans. Energy Conversion, Sept. 2006, Vol. 21, N. 3, pp. 717-724.](#)
51. [J. Cidrás, A.E. Feijóo, C. Carrillo González, "Synchronization of Asynchronous Wind Turbines" IEEE Trans, on Energy Conv., Vol. 17, No 4, Nov. 2002, pp 1162-1169](#)
52. [J. Mur, A.A. Bayod, S. Ortiz, R. Zapata, "Power Quality Analysis of Wind Turbines. Part II - Dynamic Analysis", ICREP 2003, Vigo.](#)
53. [M. Sanz, A. Llombart, Á. A. Bayod, J. Mur, "Power Quality Measurements and Analysis for Wind Turbines" IEEE Instrumentation and Measurement Technical Conference, IMTC 2000, pp. 1167-1172.](#)
54. [J. Mur, "WINDFREDOM, WIND variability in the FREquency DOMain", 2009. Program under the GNU General Program License, available freely at <http://www.windygrid.org/software>.](#)
55. [Benoit Cushman-Roisin, "Environmental Fluid Mechanics", John Wiley & Sons, 2007.](#)
56. [Simon Watson, "Introduction to the Atmospheric Boundary Layer", CREST MSc Flexible & Distance Learning Series. Wind Power Fundamentals. Crest, Loughborough University, 2003. \(not online\)](#)
57. [Kolmogorov, A. N., 1941. Dissipation of energy in locally isotropic turbulence. Dokl. Akad. Nauk SSSR, 32, 19-21.](#)
58. [Y. Tamura, A. Karrem, G. Solari, K. C. S.Kwok, J. D. Holmes. Report from IAWE Working Group WGE-Dynamic Response. 2003.](#)
59. [K. R Sreenivasan, A. J. Chambers, and R. A. Antonia, "Accuracy of moments of velocity and scalar fluctuations in the atmospheric surface layer." Boundary-Layer Meteorology, 14, 341-359, \(1978\).](#)
60. [Kaimal, J. and J. Finnigan, 1994: "Atmospheric Boundary Layer Flows; Their Structure and Measurements". Oxford University Press, New York, USA.](#)
61. [M. Metzger and H. Holmes "Time Scales in the Unstable Atmospheric Surface Layer", Boundary-Layer Meteorology, Vol. 126, No. 1, January 2008.](#)
62. [Stijn de Waele, A. van Dijk, P. Broersen, and P. G. Duynkerke, "Estimation of the integral time scale with time series models", 15th Conference on Boundary Layer and Turbulence, Wageningen, The Netherlands, 2002.](#)
63. [E. L. Petersen, N. G. Mortensen, L. Landberg, J. Hojstrup and H. P. Frank, "Wind Power Meteorology", Riso National Laboratory, Roskilde, Denmark, December 1997. Riso-I-1206\(EN\).](#)
64. [S. E. Larsen, H. R. Olesen and J. Hojstrup, "Parameterization of the low frequency part of spectra of horizontal velocity components in the stable surface boundary layer", Turbulence and Diffusion in Stable Environments, ed. J. C. R. Hunt, Clarendon Press, Oxford 1985, pp. 181-204.](#)
65. [J. Hojstrup, S. E. Larsen and P. H. Madsen, "Power spectra of horizontal wind components in the neutral atmospheric surface boundary layer", AMS 9th Symposium on Turbulence and Diffusion, Roskilde, Denmark 1990, pp. 305-308.](#)
66. [A. A. Townsend, "The structure of turbulent shear flows", 2nd ed., Cambridge University Press, 1976.](#)
67. [S. B. Pope , "Turbulent Flows", Cambridge University Press \(2000\)](#)
68. [S. Frandsen \(Ed.\), L. Chacon, A. Crespo, P. Enevoldsen, R. Gomez-Elvira, J. Hernandez, J. Hojstrup, F. Manuel, K. Thomsen, and P. Sorensen.,](#)

- "Measurements on and Modelling of Offshore Wind Farms", Riso National Laboratory, Roskilde, Denmark 1996.
69. Antebi, J., Zarghamee, M. S., & Kan, F. W. 1997, "Wind Characterization and Beam Pointing Error - Large Millimeter Telescope", SGH Report to LMT Project
 70. J. C. Kaimal, J. C. Wyngaard, Y. Izumi, and O. R. Cote, "Spectral Characteristics of Surface Layer Turbulence". Quarterly Journal of the Royal Meteorological Society, vol. 98, 1972.
 71. Davenport, A. G. 1961, Quart. J. Royal Meteorol. Soc., 87, 194
 72. T. von Karman, "Progress in the statistical theory of turbulence". Proceedings of the National Academy of Sciences of the United States of America. 1948; 34: 530-539.
 73. Morfiadakis EE, Glinou GL, Koulouvari MJ., "The Suitability of the von Karman Spectrum for the Structure of Turbulence in a Complex Terrain Wind Farm". Journal of Wind Engineering and Industrial Aerodynamics, vol. 62, 1996, 237-257.
 74. Shiau B-S, Chen Y-B. "Observation on Wind Turbulence Characteristics and Velocity Spectra near the Ground at the Coastal Region". Journal of Wind Engineering and Industrial Aerodynamics, vol. 90, 2002, 1671-1681.
 75. Frandsen S. "Turbulence and Turbulence-Generated Structural Loading in Wind Turbine Clusters". Riso-R-1188(EN), Roskilde, 2007.
 76. K. E. Kaasen, "Time Domain Model Representations of Standard Wind Gust Spectra", 9th Int. Offshore and Polar Engineering Conference, Brest, France, 1999.
 77. P. Teigen, A. Naess, "Extreme Response of Floating Structures in Combined Wind and Waves", Journal of Offshore Mechanics and Arctic Engineering, Vol. 125, pp. 87-93, May 2003
 78. Isaac Van der Hoven, "Power Spectrum Of Horizontal Wind Speed In The Frequency Range From 0.0007 To 900 Cycles Per Hour", Journal of the Atmospheric Sciences, Vol. 14, Issue 2, pp. 160-164
 79. F. Fiedler and H. A. Panofsky, "Atmospheric Scales and Spectral Gaps", Bulletin of the American Meteorological Society, Vol. 51, Issue 12 (Dec. 1970).
 80. T. Heggem, R. Lende and J. Lovseth, "Analysis of Long Time Series of Coastal Wind", Journal of the Atmospheric Sciences, Volume 55, Issue 18, pp. 2907-2917 (September 1998)
 81. P. Sorensen, N. A. Cutululis, J. Hjerrild, L. Jensen, M. Donovan, L. E. A. Christensen, H. Madsen, A. Viguera-Rodríguez, "Power Fluctuations from Large Offshore Wind Farms", Nordic Wind Power Conference, 22-23 May, 2006, Espoo, Finland.
=> Final Report
 82. K. Saranyasoontorn, L. Manuel, P. S. Veers, "A Comparison of Standard Coherence Models form Inflow Turbulence With Estimates from Field Measurements", Journal of Solar Energy Engineering, Vol. 126 (2004), Issue 4, pp. 1069-1082
 83. D. Baldocchi, E. Falgea and K. Wilsonc, "A spectral analysis of biosphere-atmosphere trace gas flux densities and meteorological variables across hour to multi-year time scales", Agricultural and Forest Meteorology, Vol. 107, Issue 1, 1 March 2001, Pages 1-27.

84. [M. Courtney, I. Troen. "Wind speed spectrum from one year of continuous 8 Hz measurements". In: 9. Symposium on turbulence and diffusion. 9. Symposium on turbulence and diffusion, Roskilde, 30 Apr - 3 May 1990. Jensen, N.O.; Kristensen, L.; Larsen, S.E. \(eds.\), \(American Meteorological Society, Boston, MA, 1990\) p. 301-304](#)
85. [P. Sorensen and N. Cutululis, A. Viguera-Rodríguez, H. Madsen, P. Pinson, L. E. Jensen, J. Hjerrild, M. Donovan, "Modelling of Power Fluctuations from Large Offshore Wind Farms", Wind Energy Vol. 11 \(2008\), pp. 29-43.](#)
86. [S. Frandsen, H.E. Jorgensen, J.D. Sorensen, "Relevant criteria for testing the quality of turbulence models", 2007 European Wind Energy Conference and Exhibition, Milan \(IT\), 7-10 May 2007. \(2007\) p. 128-132.](#)
87. [K. Saranyasontorn, L. Manuel, P. S. Veers, "On estimation of coherence in inflow turbulence based on field measurements", Proceedings of the 2004 ASME Wind Energy Symposium, pp. 424-434, Reno, Nevada, January 2004.](#)
88. [A. D. Hansen, C. Jauch, P. Sorensen, F. Iov, F. Blaabjerg "Dynamic wind turbine models in power system simulation tool DIgSILENT" Riso National Laboratory, Roskilde, December 2003, Riso-R-1400\(EN\).](#)
89. [A. D. Hansen, F. Iov, P. Sorensen, N. Cutululis, C. Jauch, F. Blaabjerg, "Dynamic wind turbine models in power system simulation tool DIgSILENT", Riso National Laboratory, Roskilde, Denmark August 2007, Riso-R-1400\(ed.2\)\(EN\).](#)
90. [Burton T, Sharpe D, Jenkins N, Bossanyi E., "Wind Energy Handbook". John Wiley & Sons Ltd, England, 2001.](#)
91. [Veers PS. "Three-Dimensional Wind Simulation". Sandia Report, SAND88-0152 I UC-261, 1988.](#)
92. [S.Heier "Grid Integration of Wind Energy Conversion Systems". John Wiley & Sons, New York 2006 \(2nd edition\).](#)
93. [T. F. Pedersen, J.-A. Dahlberg, A. Cuerva, F. Mouzakis, P. Busche, P. Eecen A. Sanz-Andres, S Franchini, S. M. Petersen, "ACCUWIND -Accurate Wind Speed Measurements in Wind Energy" Riso National Laboratory, Roskilde, Denmark, July 2006.](#)
94. [Mann J. "Wind Field Simulation". Probabilistic Engineering Mechanics, vol. 13, no 4, 1998, 269-282.](#)
95. [Ioannis Antoniou et al. "Influence of wind characteristics on turbine performance", EWEC, 2007](#)
96. [T.G. van Engelen, "Control design based on aero-hydro-servo-elastic linear models from TURBU \(ECN\)", EWEC 2007.](#)
97. [IEC 61400-1, "Wind Turbines - Part 1: Design Requirements, Int. Std.", 3rd Ed. 2005-2008.](#)
=> [Preview](#)
98. [P. Kristensen, "Power spectra and cross-spectra as seen from the moving blade of a wind turbine", J. Wind Eng. Ind. Aerodyn., 12, 245-250 \(1983\).](#)
99. [A. G. Davenport, "The spectrum of horizontal gustiness near the ground in high winds", Q. J. R. Meteorol. Soc., 87, 194-211 \(1961\).](#)
100. [J. Hojstrup, "Spectral coherence in wind turbine wakes", J. Wind. Eng. Ind. Aerodyn., 80, 137-146 \(1999\).](#)
101. [P. Kristensen and N. O. Jensen, "Lateral coherence in isotropic turbulence and in the natural wind", Boundary-Layer Meteorol., 17, 353-373 \(1979\).](#)

102. [P. J. Vermeer, J.N. Sorensen, A. Crespo, "Wind turbine wake aerodynamics", Progress in Aerospace Sciences 39 \(2003\) 467-510.](#)
103. [S. Frandsen, R. Barthelmie, O. Rathmann, H. E. Jorgensen, J. Badger, K. Hansen, S. Ott, P. E. Rethore, S. E. Larsen, L. E. Jensen, "Summary report: The shadow effect of large wind farms: measurements, data analysis and modelling", Riso National Laboratory, Roskilde, Denmark. October 2007, Riso-R- 1615 \(EN\)](#)
104. [S. Frandsen, H.E. Jorgensen, J.D. Sorensen, "Relevant criteria for testing the quality of turbulence models", EWEC 2007, p. 128-132.](#)
105. [P. Sorensen. "Frequency domain modelling of wind turbine structures". Riso-R-749. Roskilde 1994.](#)
106. [Wilkie J, Leithead WE, Anderson C, "Modelling of Wind Turbines by Simple Models". Wind Engineering, Vol. 14, no 4, 1990.](#)
107. [I. Troen and E. L. Petersen, "European Wind Atlas", Riso, 1989.](#)
108. [J. Tambke, J.A.T. Bye, B. Lange and J.-O. Wolff , "Wind Speed Profiles above the North Sea", Wind Energy - Proceedings of the Euromech Colloquium, Springer, Berlin 2007, p. 27 - 32](#)
109. [D. A. Spera, "Wind Turbine Technology", ASME Press, New York, 1994.](#)
110. [B. H. Bailey and S. L. McDonald, "Wind resource assessment handbook", AWS Scientific, Inc., www.awsscientific.com, April 1997](#)
111. [A. J. Eggers, Jr., R. Digumarthi, K. Chaney "Wind Shear and Turbulence Effects on Rotor Fatigue and Loads Control", Transactions of the ASME, Vol. 125, Nov. 2003.](#)
112. [Kelley, Neil, Shirazi, Mari, Hand, Maureen, and Jager, David, "Low-Level Jet Turbulence Field Test," NREL/NWTC, 2002 DOE Wind Program Review Meeting, May 7-9.](#)
113. [S. REHMAN; N. M. AL-ABBADI "Wind shear coefficients and their effect on energy production", Energy conversion and management, 2005, vol. 46, n 15-16, pp. 2578-2591](#)
114. [Engström S, Ganander H, Lindström R. "Short Term Power Variations in the Output of Wind Turbines". DEWI Magazin, no 19, 2001.](#)
115. [S. Hier, "Grid Integration of Wind Energy Conversion Systems", Wiley, 1998.](#)
116. [J. Sallán-Arasanz, "Estudio y desarrollo de nuevos sistemas de generación y conexión a red para máquinas asíncronas de rotor en cortocircuito impulsadas por turbinas eólicas para su funcionamiento a velocidad variable", Ph.D. Thesis, Universidad de Zaragoza, June 2002 \(in Spanish\).](#)
117. [J. F. Sanz Osorio, "Optimización de sistemas integrados de energías renovables para el abastecimiento de núcleos aislados.", Ph.D. Thesis, Universidad de Zaragoza, June 2007 \(in Spanish\).](#)
118. [Sorensen P., Hansen A.D., Janosi L., Bech J., Bak-Jensen B. "Simulation of interaction between wind farm and power system". Riso National Laboratory, 2001. Riso-R-1281](#)
119. [B. Stoevesandt, J. Peinke, A. Shishkin and C. Wagner, "Numerical simulation of dynamic stall using spectral/hp method", Wind Energy - Proceedings of the Euromech Colloquium, Springer, Berlin 2007, p. 241 - 244](#)
120. [M.P. Comech-Moreno, "Análisis y ensayo de sistemas eólicos ante huecos de tensión", Ph.D. Thesis, Universidad de Zaragoza, Octubre de 2007 \(in Spanish\).](#)
121. [V. Akhmatov, "Analysis of Dynamic Behaviour of Electrical Power Systems with Large Amount of Wind Power", Orsted-DTU, April 2003.](#)

122. [F. D. Bianchi, H. De Battista, and R. J. Mantz, "Wind Turbine Control Systems. Principles, Modelling and Gain Scheduling Design", Springer, 2006.](#)
123. [Chee-Mun Ong "Dynamic simulation of electric machinery using Matlab/Simulink", Prentice Hall, 1998.](#)
124. [B.C. Lesieutre, P.W. Sauer, M.A. Pai, "Development and comparative study of induction machine based dynamic P, Q load models", IEEE Transactions on Power Systems, Vol. 10, No. 1. February 1995.](#)
125. [G.K. Singh, "Self-excited induction generator research - a survey", Electric Power Systems Research 69 \(2004\) 107-114.](#)
126. [J.A.A. Melkebeek, D.W. Novotny, "Small signal dynamic analysis of regeneration and self-excitation in induction machines", Electric Machines Power Syst. 8 \(1983\) 259-280.](#)
127. [Y. Utug, M. Demirekler, "Modelling, analysis and control of a wind-turbine driven self-excited induction generator", IEE Proceedings, Vol. 135, Pt. C, No. 4, July 1988](#)
128. [F. Wu, X.P. Zhang, K. Godfrey and P. Ju, "Modeling and Control of Wind Turbine with Doubly Fed Induction Generator", PSCE 2006 conference.](#)
129. [D. Nagaria, G. N. Pillai, H. O. Gupta, "Small signal stability analysis of variable speed wind energy conversion system equipped with DFIG" International Journal of Distributed Energy Resources, Volume 4 Number 3 \(2008\) Pages 233 - 251](#)
130. [R. Erickson, S. Angkititrakul, and K. Almazeedi, "A New Family of Multilevel Matrix Converters for Wind Power Applications: Final Report". NREL Subcontract Report NREL/SR-500-40051, December 2006.](#)
131. [S. Masoud Barakati, "Modeling and Controller Design of a Wind Energy Conversion System Including a Matrix Converter", Ph. D. Thesis, University of Waterloo, Ontario, Canada, 2008.](#)
132. [V. Akhmatov, H. Knudsen, "An aggregate model of a grid-connected, large scale, offshore wind farm for power stability investigations-importance of windmill mechanical system", Electrical Power Systems 24 \(2002\) 709-717.](#)
133. [Kazachkov, S. Stapleton, "Modeling wind farms for power system stability studies", Power Technology Newsletter Issue 95, April 2004](#)
134. [P.M. Fernandez, J.R. Saenz, F. Jurado, "Dynamic models of wind farms with fixed speed wind turbines", Renewable Energy, 31 \(8\), pp.1203-1230, Jul 2006.](#)
135. [R. Arens, "Complex Processes for Envelopes of Normal Noise", IRE Transactions on Information Theory, September 1958, pp.204-207.](#)
136. [N. S. Pannu, A. J. McCoy and R. J. Read, "Application of the complex multivariate normal distribution to crystallographic methods with insights into multiple isomorphous replacement phasing", Acta Cryst. \(2003\), D59, 1801-1808.](#)
137. [M. Sanz, J. Mur, F. Gómez, R. Zapata, "Sistema de medida de calidad de red para parques eólicos", IX Jornadas Hispano-Lusas. Lisboa, 1998.](#)
138. [M. Sanz, A. Llombart, A. A. Bayod, J. Mur, R. Sierra "Análisis de la calidad de la energía generada en parques eólicos" X Reunión de Grupos de Investigación en Energía Eléctrica. Santander, 2000.](#)
139. [M. Sanz A. Llombart A. A. Bayod J. Mur, "Power quality measurements and analysis for wind turbines", IEEE Instrumentation and Measurement Technical Conference 2000, pp. 1167-1172. May 2000, Baltimore.](#)
140. [Joaquín Mur, Ángel A. Bayod, Jesús Sallán "An Experimental Study on Power](#)

Quality Wind Turbines" EWEC '03 (European Wind Energy Conference & Exhibition). Madrid, 2003.

141. Joaquín Mur, Ángel A. Bayod, Jesús Sallán "Profile of voltage in grids with wind farms" EWEC '03 (European Wind Energy Conference & Exhibition). Madrid, 2003.
142. M. Sanz, A. Llombart, J. Mur, R. Sierra, "Análisis de la calidad de la energía eléctrica entregada a la red de los parques eólicos de puntaza de Remolinos". Zaragoza University, April 1999.
143. M. Sanz, A. Llombart, J. Mur, I. Palacios, "Análisis de la calidad de la energía eléctrica entregada a la red de los parques eólicos de puntaza de Borja", Zaragoza University, September 1999.
144. M. Sanz, A. Llombart, J. Mur, F. Gómez, "Análisis de la calidad de la energía eléctrica entregada a la red de los parques eólicos de puntaza de Pola", Zaragoza University, December 1999.
145. M. Sanz, A. Llombart, J. Mur, R. Zapata, D. Romanos, S. Ortiz, "Análisis de la calidad de la energía eléctrica entregada a la red de los parques eólicos de Valdecuadros", Zaragoza University, August 2000.
146. "Manual de los programas realizados para los estudios en parques eólicos de Compañía Eólica Aragonesa S.A.", Zaragoza University, December 21st 1999.
147. J. Mur, "Parque eólico de VALDECUADROS. Manual de los programas realizados en VISUAL C++", Zaragoza University, March 9th 2000
148. Joaquín Mur, Ángel Antonio Bayod, Samuel Ortiz, Roberto Zapata "Power Quality Analysis of Wind Turbines. Part II - Dynamic Analysis", ICREP '03 (Internacional Conference on Renewable Energies and Power Quality), Vigo 2003.
149. CIRCE Foundation, "AIRE- Análisis Integral de Recursos Energéticos", web page teide.cps.unizar.es: 8080/pub/info.nsf/paginas/diveleaire accessed in October 13rd 2009.
150. Inycom T&M, "AIRE. Analizador Integral De Recursos Energéticos". Available at www.inycom.es. Accessed in October 13rd 2009.
151. Sami H. Karaki, Bassel A. Salim, and Riad B. Chedid, "Probabilistic Model of a Two-Site Wind Energy Conversion System", " , IEEE Transactions On Energy Conversion, Vol. 17, No. 4, December 2002
152. C. Vilar Moreno, "Voltage fluctuation due to constant speed wind generators" Ph. D. dissertation at Carlos III University, Leganés, Spain, 2003.
153. P. Sorensen, A. D. Hansen, P.A. Carvalho Rosas "Wind models for simulation of power fluctuations from wind farms", Journal of Wind Engineering and Ind. Aerodynamics 90 (2002), pp. 1381-1402
154. T. Thiringer, T. Petru, and S. Lundberg "Flicker Contribution From Wind Turbine Installations" IEEE Trans, on Energy Conv., Vol. 19, No 1, March 2004, pp 157-163
155. H. Amarís, J. Usaola. Evaluación en el dominio de la frecuencia de las fluctuaciones de tensión producidas por los generadores eólicos. V Jornadas Hispano-Lusas de Ingeniería Eléctrica. 1997.
156. W. Wangdee, R. Billinton "Considering Load-Carrying Capability and Wind Speed Correlation of WECS in Generation Adequacy Assessment", IEEE Trans, on Energy Conv., Vol. 21, No 3, Sept. 06, pp 734-741
157. I. Sánchez, "Short-term prediction of wind energy production," International Journal of Forecasting, 22, 43-56.
158. W. A. Gardner, "Cyclostationarity in Communications and Signal Processing", IEEE press, 1994.
159. J. Cidrás, A.E. Feijóo, C. Carrillo González, "Synchronization of Asynchronous Wind Turbines" IEEE Trans, on Energy Conv., Vol. 17, No 4, Nov. 2002, pp 1162-1169

160. J. Mur, M.P. Comech, "Reactive Power Injection Strategies for Wind Energy Regarding its Statistical Nature", Sixth International Workshop on Large-Scale Integration of Wind Power and Transmission Networks for Offshore Wind Farm. Delft, 2006.
161. P. (Prabha) Kundur, Neal J. Balu, Mark G. Lauby, "Power System Stability and Control", McGraw-Hill, 1994.
162. Chun-Lien Su, "Probabilistic Load-Flow Computation Using Point Estimate Method", IEEE Trans. Power Systems, Vol. 20, No. 4, November 2005, pp. 1843-1851.
163. G. Stefopoulos, A. P. Meliopoulos and G. J. Cokkinides, "Advanced Probabilistic Power Flow Methodology", 15th PSCC, Liege, 22-26 August 2005
164. H. Hurd, "Notes on the Periodogram", <http://www.stat.unc.edu/faculty/hurd.html> (accessed on May 16, 2008).
165. H. Bodén, "Signal Analysis", The Marcus Wallenberg Laboratory for Sound and Vibration Research. <http://www.ave.kth.se/education/msce/TSOVM/courses/SD2130/> (accessed on May 16, 2008).
166. D. M. Meko, "Applied Time Series Analysis", Ch. 6, University of Arizona, Spring 2007, <http://www.ltrr.arizona.edu/~dmeko/geos585a.html> (accessed on May 16, 2008).
167. H. Stark and J. Woods, "Probability and Random Processes with Applications to Signal Processing", Third Edition, Prentice Hall, 2002.
168. Oppenheim, A. V., R. W. Schaffer, and J. R. Buck. (Discrete-Time Signal Processing", 2nd ed. Upper Saddle River, NJ: Prentice Hall, 1999.
169. Timothy M. Hollis, "Power Spectral Density (PSD) Estimation", 2004, www.et.byu.edu/~tmh27/PSD.pdf (accessed January 14, 2008).
170. J.K. Cavers, Mobile Channel Characteristics, 2nd ed., Shady Island Press, 2003
171. J. K. Cavers, "Mobile Channel Characteristics", 2nd Ed., Shady Island Press, 2003..
172. A. Abdi, H. Hashemi, and S. Nader-Esfahani, "On the PDF of the Sum of Random Vectors", IEEE Trans. on Communications. Vol. 48, No.1, January 2000, pp 7-12.
173. Y. Baghzouz, R. F. Burch et al. "Time-Varying Harmonics: Part II Harmonic Summation and Propagation", IEEE Trans. On Power Systems, Vol. 17, No. 1, January 2002, pp. 279-285.
174. S. T. Tentzerakis and S. A. Papathanassiou, "An Investigation of the Harmonic Emissions of Wind Turbines", IEEE Trans, on Energy Conv., Vol. 22, No 1, March. 07, pp 150-158.
175. M.-S. Alouini, A. Abdi, M. Kaveh, "Sum of Gamma Variates and Performance of Wireless Communication Systems Over Nakagami-Fading Channels", IEEE Trans. On Vehicular Technology, Vol. 50, No. 6, pp. 1471-1480.
176. J.C. Kaimal, "Horizontal Velocity Spectra in an Unstable Surface Layer" Journal of the Atmospheric Sciences, Vol. 35, Issue 1, pp. 18-24
177. António Martins, Paulo C. Costa, Adriano S. Carvalho, "Coherence And Wakes In Wind Models For Electromechanical And Power Systems Standard Simulations", European Wind Energy Conferences EWEC 2006.
178. P. Li, H. Banakar, P. K. Keung, H.G. Far, and B.T. Ooi, "Macromodel of Spatial Smoothing in Wind Farms", IEEE Trans, on Energy Conv., Vol. 22, No 1, March. 07, pp 119-128.
179. M. Schwab, P. Noll, and T. Sikora, "Noise robust relative transfer function estimation", XIV European Signal Processing Conference, September 4 - 8, 2006, Florence, Italy.
180. P. Norgaard, H. Holttinen, "A Multi-turbine Power Curve Approach", in Proc. 2002 Nordic Wind Power Conference.
181. IEC 61400-4-15, Electromagnetic compatibility (EMC). Part 4: Testing and measurement techniques. Section 15: Flickermeter. Functional and design

specifications.

182. Kurt S. Hansen, Gunner Chr. Larsen, "De-trending of turbulence measurements", EWEC 2007, Milan
183. T. Thiringer, T. Petru, and C. Liljegren "Power Quality Impact of a Sea Located Hybrid Wind Park", IEEE Transactions On Energy Conversion, Vol. 16, No. 2, June 2001 pp. 123-127
184. T. Petru, T. Thiringer "Active flicker reduction from a sea-based 2.5 MW wind park connected to a weak grid", 2000 Nordic Workshop on Power and Industrial Electronics (NORpie 2000), Aalborg, Denmark, June 13-16, 2000.
185. T. Thiringer "Power Quality Measurements Performed on a Low-Voltage Grid Equipped with Two Wind Turbines", IEEE Trans. Energy Conversion, Vol. 11, No. 3, September 1996
186. T. Thiringer, J.-A. Dahlberg, "Periodic Pulsations from a Three-Bladed Wind Turbine", IEEE Trans Energy Conversion, Vol. 16, No. 2, June 2001
187. T. Thiringer, "Frequency Scanning for Power System Property Determination Applied to a Wind Power Grid" IEEE Trans. on Power Systems, Vol. 21, No. 2, MAY 2006
188. Nayeem Rahmat Ulla, "Topic 9.1: Power Quality Evaluation of a Sea Based Wind Farm", Nordic PhD course on Wind Power. Available at www.elkraft.ntnu.no/smola2005
189. S. A. Papathanassiou and Fritz Santjer, "Power Quality Measurements in an Autonomous Island Grid with High Wind Penetration", IEEE Transactions on Power Delivery, Vol 21, No 1, Jan. 2006, pp 218 - 224
190. T. Petru "Modeling of wind turbines for Power System Studies", Ph. Disertation, Chalmers University of Technology, Goteborg, Sweden 2003
191. P. Sorensen, A. D. Hansena and P. A. Carvalho Rosas, "Wind models for simulation of power fluctuations from wind farms", Journal of Wind Engineering and Industrial Aerodynamics, Vol. 90, No. 12-15, Dec. 2002, pp. 1381-1402.
192. P. Sorensen, A. Hansen, L. Janosi, J. Bech and B. Bak-Jensen, "Simulation of Interaction between Wind Farm and Power System", Riso National Laboratory, Roskilde, December 2001. Available at www.risoe.dk/rispubl/VEA/veapdf/ris-r-1281.pdf
193. A. D. Hansen, P. Sorensen, F. Blaabjerg and John Becho "Dynamic modelling of wind farm grid interaction", Wind Engineering Vol. 26, No. 4 , 2002, pp. 191-208
194. W. E. Leithead and S. Domínguez, "Coordinated Control Design for Wind Turbine Control Systems", EWEC 2006, Athens
195. H. Bindner, P. Norgard, "11kW Gaia Wind Turbine Connected to a Diesel Grid", Riso-I-nr2035(EN), Riso National Laboratory, Roskilde. Available at www.gaia-wind.com.
196. Stefan Marko, Ivan Darul'a, Stanislav Vlcek, "Development Of Wind Farm Models For Power System Studies", Journal of Electrical Engineering, VOL. 56, NO. 5-6, 2005, pp. 165-168.
197. K. Johnsen and B. Eliasson, "SIMULINK[®] Implementation of Wind Farm Model for use in Power System Studies", Nordic Wind Power Conference, 1-2 March, 2004, Chalmers University Of Technology.
198. J. Pierik, J. Morren, T. Engelen., S. Haan, Jan Bozelie "Development and validation of wind farm models for power system studies. Alsvik wind farm results", EWEC 2006, Athens.
199. J. Soens, J. Driesen, R. Belmans, "Equivalent Transfer Function for a Variable-speed Wind Turbine in Power System Dynamic Simulations", International Journal of Distributed Energy Resources, Volume 1 Number 2, April-June, 2005; pp. 111-133.
200. S. M. Ross, "Introduction to Probability Models", Academic Press (Elsevier), 2006.

201. ^p.N. Thibos, "Fourier Analysis for Beginners", Indiana University, <http://research.opt.indiana.edu/Library/FourierBook/toc.html> (accessed on May 16, 2008).
202. F. D. Neeser, J. L. Massey, "Proper Complex Random Processes with Applications to Information Theory", IEEE Transactions on Information Theory, Vol. 39, No. 4, July 1993, pp. 1293-1302.
203. B. Picinbono, "On Circularity", IEEE Trans. On Signal Processing, Vol. 42, No 12, Dec. 1994., pp. 3473-3482
204. J. Mur, J. Sallán, A.A. Bayod, "Statistical model of wind farms for power flow", ICREP 2003, Vigo. Available at : www.joaquinmur.eu
205. Wind Turbine Generator Systems-Part 21: Measurement and assessment of power quality characteristics of grid connected wind turbines, IEC61400-21.
206. N. Visboll, A. L. Pinegin, T. Fischer, J. Bugge. "Analysis of Advantages of the Double Supply Machine With Variable Rotation Speed Application in Wind Energy Converters". DEWI Magazin Nr. 11, August 1997.
207. A. Feijoo, J. Cidras. "Analysis of mechanical power fluctuations in asynchronous WECS". IEEE Transactions on Energy Conversion, Vol. 14, No. 3, pp. 284-291. Sept. 1999.
208. E. Bossanyi, Z. Saad-Saoud and N. Jenkins. Prediction of Flicker Produced by Wind Turbines. Wind Energy 1, pp 35-51. 1998.
209. IEC 61400-4-15, Electromagnetic compatibility (EMC). Part 4: Testing and measurement techniques. Section 15: Flickermeter. Functional and design specifications.
210. CEI IEC 1000-3-7, Electromagnetic compatibility (EMC). Part 3: Limits - Section 7: Assessment of emission limits for fluctuating loads in MV and HV power systems - Basic EMC publication.
211. Ministerio de Industria y Energía, "Orden de 5 de Septiembre de 1985", BOE número 219, ano 1985.
212. Joris Soens, "Impact Of Wind Energy In A Future Power Grid", Ph.D. Dissertation, Katholieke Universiteit Leuven, December 2005.
213. Z. Lubosny, "Wind Turbine Operation in Electric Power Systems", Ed. Springer 2003.
214. G. C. Larsen, W. Bierbooms and K. S. Hansen, "Mean Gust Shapes", Riso National Laboratory, Roskilde, Denmark.. December 2003, Riso-R-1133(EN)
215. W. Bierbooms, "Specific gust shapes leading to extreme response of pitch regulated wind turbines", The Science Of Making Torque From Wind, 28-31 August 2007, Technical University of Denmark
216. Bierbooms, WAAM (2005). Constrained stochastic simulation - generation of time series around some specific event in a normal process. Extremes, 8(3), 207-224.
217. P. S. Veers, Three dimensional wind simulation, Sandia National Laboratories, SAND88-0152, 1988.
218. J. Mur, "EQWIGUST, EQuivalent WInd GUST", 2009.
219. E. Bertin, M. Clusell, "Generalised extreme value statistics and sum of correlated variables", J. Phys. A: Math. Gen. 39, 7607 (2006)
220. G. C. Larsen, K. S. Hansen, "Statistical Model of Extreme Shear", Journal of Solar Energy Engineering, November 2005, Vol. 127, No. 4, pp. 444-455.
221. G. C. Larsen, "An asymptotic closed form solution for the distribution of combined wind speed and wind direction extremes", The Science of Making Torque, 2007. Technical University of Denmark
222. Z. Warhaft, "Passive scalars in turbulent flows", Annu. Rev. Fluid Mech. 2000. 32:203-240.
223. M. Nielsen, G. C. Larsen, J.Mann, S. Ott, K. S. Hansen, and B. J. Pedersen, "Wind Simulation for Extreme and Fatigue Loads", Riso National Laboratory, Roskilde, Denmark. January 2004, Riso-R- 1437 (EN).

224. J. Gottschall and J. Peinke, "Stochastic modelling of a wind turbine's power output with special respect to turbulent dynamics", *The Science Of Making Torque From Wind*, 28-31 August 2007, Technical University of Denmark.
225. M. Wächter, A. Rettenmeier, M. Kühn and J. Peinke, "Wind velocity measurements using a pulsed LIDAR system: first results", *IOP Conf. Series: Earth and Environmental Science* 1 (2008).
226. F. Böttcher, S. Barth and J. Peinke, "2007 Stoch Environ Res Ris Assess", 21 299-308
227. J.A. Molina, G.G. Farias, R.M. Dagnino, "A practical procedure to estimate the shape parameter in the generalized Gaussian distribution", *Technical Report, Centro de Investigación en Matemáticas, Guanajuato University, Mexico, 2001.*
228. B. Fox, D. Flynn, L. Bryans, N. Jenkins, D. Milborrow, M. O'Malley, R. Watson, O. Anaya-Lara, "Wind Power Integration: Connection and System Operational Aspects", *Wiley, 2007*
229. S. Rizzo and .A. Rapisarda, "Application of superstatistics to atmospheric turbulence", *International Conference Complexity, Metastability and Nonextensivity, Erice (Sicily) July 20-26 2004.*
230. S. Rizzo and .A. Rapisarda, "Environmental atmospheric turbulence at Florence airport", *8th Experimental Chaos Conference, 14-17 June 2004, Florence, ITALY, AIP Conference proceedings Vol. 742 , p.176.*
231. F. Böttcher, St. Barth, and J. Peinke, "Small and Large Scale Fluctuations in Atmospheric Wind Speeds", *Stochastic Environmental Research and Risk Assessment (SERRA) 21, 299 (2007)*
232. St. Barth, F. Böttcher and J. Peinke, "Superposition model for atmospheric turbulence", *Wind Energy - Proceedings of the Euromech Colloquium, Springer, Berlin 2007, p. 115 -118*
233. A. Wessel, J. Peinke and B. Lange, "Modelling turbulence intensities inside wind farms", *Wind Energy - Proceedings of the Euromech Colloquium, Springer, Berlin 2007, p. 253 - 256*
234. J. F. Price, "Lagrangian and Eulerian Representations of Fluid Flow: Kinematics and the Equations of Motion", 2006
235. P. Tabeling, "Two-dimensional turbulence: a physicist approach", *Physics Reports, Volume 362, Issue 1, May 2002, Pages 1-62,*
236. A.E. Gill, "Atmosphere-ocean Dynamics". *Academic Press, NY. 1982.*
237. M., Hossain, "Reduction of the dimensionality of turbulence due to a strong rotation". *Phys. Fluids 6 (4), 1077-1080. 1994.*
238. W.D. McComb, "The Physics of Fluid Turbulence". *Clarendon Press, Oxford. 1992.*
239. Y. Zhou, "A phenomenological treatment of rotating turbulence". *Phys. Fluids, 7 (8), 2092-2094. 1995.*
240. P. Constantin "Energy spectrum of quasigeostrophic turbulence". *Phys. Rev. Lett. 89 (18), 184501-184504. 2002.*
241. S. Rizzo and .A. Rapisarda, "Application of superstatistics to atmospheric turbulence", *International Conference Complexity, Metastability and Nonextensivity, Erice (Sicily) July 20-26 2004.*
242. S. Rizzo and .A. Rapisarda, "Environmental atmospheric turbulence at Florence airport", *8th Experimental Chaos Conference, 14-17 June 2004, Florence, ITALY, AIP Conference proceedings Vol. 742 , p.176.*
243. F. Böttcher, St. Barth, and J. Peinke, "Small and Large Scale Fluctuations in Atmospheric Wind Speeds", *Stochastic Environmental Research and Risk Assessment (SERRA) 21, 299 (2007)*
244. St. Barth, F. Böttcher and J. Peinke, "Superposition model for atmospheric turbulence", *Wind Energy - Proceedings of the Euromech Colloquium, Springer, Berlin 2007, p. 115 -118*
245. A. Wessel, J. Peinke and B. Lange, "Modelling turbulence intensities inside wind

- farms", Wind Energy - Proceedings of the Euromech Colloquium, Springer, Berlin 2007, p. 253 - 256
246. M. Wächter, A. Rettenmeier, M. Kühn and J. Peinke, "Wind velocity measurements using a pulsed LIDAR system: first results", IOP Conf. Series: Earth and Environmental Science 1 (2008).
 247. J. Peinke, E. Anahua, St. Barth, H. Gontier, A.P. Schaffarczyk, D. Kleinhaus , R. Friedrich, "Turbulence: a Challenging Issue for the Wind Energy Conversion", EWEC 2008 Proceedings.
 248. N. Barberis Negra, O. Holmstrom, B. Bak-Jensen, P. Sorensen, "Model of a synthetic wind speed time series generator", Wind Energy. 2008 ; vol. 11, nr. 2, September.
 249. M Nielsen, G C Larsen, K S Hansen, "Simulation of inhomogeneous, non-stationary and non-Gaussian turbulent winds", The Science of Making Torque from Wind, IOP Publishing, Journal of Physics: Conference Series 75 (2007)
 250. J. Eggers, Z. J. Wang, "Crossover behavior in turbulent velocity fluctuations", Physical Review E, Vol. 57, No. 4, April 1998
 251. K. Gurley, M. Tognarelli, and A. Kareem, "Analysis and Simulation Tools for Wind Engineering", Probabilistic Engineering Mechanics, 12(1), pp. 9-31, 1997.
 252. M. Grigoriu, "Non-Gaussian models for stochastic mechanics", Prob. Engr. Mech., 15, 15-23. (2000).
 253. [] St. Lück¹, Ch. Renner, J. Peinke and R. Friedrich, "The Markov- Einstein coherence length - a new meaning for the Taylor length in Turbulence", Physics letters. A, 2006, vol. 359, no5, pp. 335-338
 254. H.J. Kushner and G. Yin. "Stochastic Approximation Algorithms and Applications". Springer-Verlag, 1997. Revised second edition, 2003.
 255. Kushner, H. J. and P. G. Dupuis. "Numerical Methods for Stochastic Control Problems in Continuous Time", Springer; 2nd Rev. Edition (Jan 2001)
 256. S. O. Rice, "Mathematical analysis of random noise," Bell Syst. Tech. J., vol. 23, pp. 282-332, July 1944; vol. 24, pp. 46-156, Jan. 1945. Reprinted in N. Wax (ed.), Selected papers on noise and stochastic processes, Dover Publ.
 257. D.E. Cartwright, and M. S. Longuet-Higgins, "The statistical distribution of the maxima of a random function", Proc. Royal Soc. London Ser. A 237, 212-232. (1956).
 258. G. C. Larsen, W. Bierbooms, K. S. Larsen, "Statistics of Local Extremes", December 2003, Riso-R-1220(EN), Roskilde, Denmark.
 259. "Database on Wind Characteristics", Available at <http://www.winddata.com>
 260. P. Prandoni and M. Vetterli, "Signal Processing for Communications", EPFL press, 2008. Available at <http://www.sp4comm.org/webversion.html>
 261. M. Ebden, "Gaussian Processes for Regression: A Quick Introduction", Oxford University, August 2008. Available at <http://www.robots.ox.ac.uk/~mebden/reports/GPtutorial.pdf>
 262. /reports/GPtutorial.pdf
 263. C. E. Rasmussen, C. K. I. Williams, "Gaussian Processes for Machine Learning", MIT Press, 2006. Available at <http://www.gaussianprocess.org/gpml>
 264. O. Kallenberg, "Foundations on Modern Probability", Springer, 2nd Ed., 2002.
 265. W. Bierbooms, "Simulation of stochastic wind fields which encompass measured wind speed series", Proceedings of the EWEC 2004, (pp. 1-12). Brussel: EWEA.
 266. M. Shinozuka, C. M. Jan. "Digital simulation of random processes and its applications", Journal of Sound and Vibration, 25, No 1, 111-128, 1972.
 267. Shinozuka, M.: Simulation of multivariate and multidimensional random processess. J. Acoust. Soc. America. 357-368 (1971)
 268. W.Bierbooms, Po-Wen Cheng; G. Larsen, B. J. Pedersen, "Modelling of Extreme Gusts for Design Calculations - NewGust", The European commission, contract JOULE III JOR3-CT98-0239, Final Report. TU Delft, 2001, 25 p
 269. W.A.A.M Bierbooms, "Constrained Stochastic Simulation Of Wind Gusts For Wind

- Turbine Design", DUWIND Delft University Wind Energy Research Institute, March 2009.
270. G. Lindgren, "Some properties of a normal process near a local maximum", *Ann. Math. Stat.* 41, 1870-1883 (1970).
 271. C.R. Rao, "Linear Statistical Inference and its Applications", Wiley, 1965.
 272. R.E. Mortensen, "Random Signals and Systems", Wiley, New York, 1987.
 273. G. Moe, J. M. Niedzwecki, "Frequency of maxima of non-narrow banded stochastic processes", *Applied Ocean Research*, Vol. 27, Issue 6, Dec. 2005, pp. 265-272.
 274. S. L. Miller, D. G. Childers "Probability and Random Processes: With Applications to Signal Processing and Communications", 2nd Ed., Academic Press, 2004.
 275. S. Kotz, N. Lloyd Johnson, N. Balakrishnan, "Continuous Multivariate Distributions: Models and Applications", 2nd Ed., John Wiley and Sons, 2000.
 276. M. R. Milligan, "Modeling Utility-Scale Wind Power Plants. Part 2: Capacity Credit". NREL/TP-500-29701. March 2002.
 277. R. Billinton, W. Li, "Reliability Assessment of Electric Power Systems Using Monte Carlo Methods", Plenum Press, NY, pp. 351, 1994.
 278. Kushner, H. J. and P. G. Dupuis. "Numerical Methods for Stochastic Control Problems in Continuous Time", Springer; 2nd Rev. Edition (Jan 2001)
 279. Sato-Ilic, Mika, Jain, Lakhmi C., "Innovations in Fuzzy Clustering. Theory and Applications", Springer 2006.
 280. Scott Beaver and Ahmet Palazoglu, "Cluster Analysis of Hourly Wind Measurements to Reveal Synoptic Regimes Affecting Air Quality", *Journal of Applied Meteorology*, vol. 45 (2006), No 12, pp. 1710-1726.
 281. J. Filar, K. Vrieze, "Competitive Markov Decision Processes", 1997, Springer.
 282. M.L. Putterman, "Markov Decision Processes. Discrete Stochastic Dynamic Programming", John Willey, New York, 1994.
 283. J. R. Norris, "Markov Chains", Cambridge University Press, 1996
 284. Wai-Ki Ching, Michael K. Ng, "Markov Chains. Models, Algorithms and Applications", Springer 2006.
 285. V. G. Kulkarni, "Modeling, Analysis, Design, and Control of Stochastic Systems", Springer 1999.
 286. O. Cappé, E. Moulines, T. Rydén, "Inference in Hidden Markov Models", Springer, 2005.
 287. Munk, C. "Numerical Methods for Continuous-Time, Continuous-State Stochastic Control Problems". Publications from Department of Management 11, Odense University, 1997
 288. Avrachenkov, K., Sanchez, E. "Fuzzy chains and decision-making". *Fuzzy Optim. Decis. Making* 1 (2), 143-159, 2002.
 289. J.J. Buckley and E. Eslami, "Fuzzy Markov Chains: Uncertain Probabilities", *Mathware and Soft Computing*, 9(1):33-41, 2002.
 290. F. Salzenstein, C. Collet, S. Lecam and M. Hatt "Non-stationary fuzzy Markov chain", *Pattern Recognition Letters* 28 (2007) 2201-2208.
 291. J.J. Buckley, "Fuzzy Probabilities. New Approach and Applications", Springer, 2005.
 292. IEC 61400-12-1, Wind Turbines - Part 121: Power performance measurements of electricity producing wind turbines. 2007.
 293. IEC 61400-21, Wind Turbines - Part 21: Measurement and assessment of power quality characteristics of grid connected wind turbines. 1st Edition, 2001.
 294. Royal Degree 436/2004, Boletín Oficial del Estado. Publishing date: 27th March 2004. Available: <http://www.boe.es/boe/dias/2004-03-27/pdfs/A13217-13238.pdf>
 295. John H. Mathews and Kurtis Fink, "Numerical Methods using Matlab", 4th edition, 2004.

296. J. Mur Amada, A.A. Bayod Rújula, "Characterization of Spectral Density of Wind Farm Power Output", 9th Conference on Electrical Power Quality and Utilisation (EPQU'2007), Barcelona, 2007. ISBN 978-84-690-9441-9.
297. Janusz Marecki, Sven Koenig, Milind Tambe "A Fast Analytical Algorithm for Solving Markov Decision Processes with Continuous Resources" In Proceedings of the 20th International Joint Conference on Artificial Intelligence (IJCAI), 2007
298. Barry L. Nelson, "Stochastic Modeling (Analysis & Simulation)", Mac Graw-Hill, New York, 1995.
299. A.K. Jain, M.N. Murty, P.J. Flynn, "Data Clustering: A Review", ACM Computing Surveys, Vol. 31, No. 3, September 1999
300. J. Mur, A. A. Bayod "Characterization of wind farm energy production in a zone by artificial neuronal networks", ICREP '03 (Internacional Conference on Renewable Energies and Power Quality), Vigo 2003.
301. Sato-Ilic, Mika, Jain, Lakhmi C., "Innovations in Fuzzy Clustering. Theory and Applications", Springer 2006.
302. Shaning AD, Sen Z. "First-order Markov chain approach to wind speed modeling". J. Wind. Engineering Ind. Aerodynamics 2001, 89: 263-9.
303. A. Shamshad, M.A. Bawadi, W.M.A. Wand Hussing, T.A. Majid, S.A.M. Sanusi, "First and second order Markov chain models for synthetic generation of wind speed time series", Energy 30, 693-708, 2005.
304. Chistopher C. Tan, Norman C. Beaulieu, "On First-Order Markov Modeling for the Rayleigh Fading Channel", IEEE Trans. Communications, Vol. 48, No. 12, Dec 2000.
305. C.P. Robert, "Discretization and MCMC Convergence Assessment", Springer, 1998
306. M. K. Simon, S. M. Hinedi, and W. C. Lindsey, Digital Communication Techniques: Signal Design and Detection. Englewood Cliffs, NJ: Prentice-Hall, 1994.
307. R. C. Titsworth and L. R. Welch, "Power spectra of signal modulated by random and pseudorandom sequences," Jet Propulsion Lab., Pasadena, CA, Tech. Rep. 32-140, Oct. 1961.
308. D. F. Bishop, S. Million, T. M. Nguyen, and M. K. Simon, "Power Spectrum of Unbalanced NRZ and Biphasic Signals in the Presence of Data Asymmetry", IEEE Trans. Electromagnetic Compatibility, Vol. 40, No. 1, February 1998
309. Y. Yang, "General method for computing the power spectrum density of irreducible periodic Markov chains" IEEE GLOBECOM 98, Vol. 6, pp. 3320-3325, 8-12 Nov. 1998.
310. Papaefthymiou G, Klöckl B., "MCMC for Wind Power Simulation" IEEE Trans. Energy Conversion,
311. G. George Yin, Qing Zhang, "Discrete-Time Markov Chains. Two-Time-Scale Methods and Applications", Springer, 2005.
312. Alan S. WillSky, "Multiresolution Markov Models for Signal and Image Processing", Proceedings IEEE, Vol. 90, No. 8, August 2002.
313. Anne Benoit, L. Brenner, P. Fernandes, B. Plateau, "Aggregation of stochastic automata networks with replicas", Linear Algebra and its Applications 386 (2004) 111-136.
314. William J. Stewart, "Introduction to the Numerical Solution of Markov Chains", Princeton University Press, 1994.
315. Per Norgard, Gregor Giebel, Hannele Holttinen, Lennart Söder, Astrid Petterteig, "Fluctuations and predictability of wind and hydropower", Riso National Laboratory, Roskilde, Denmark, June 2004
316. Report of the Research Project "Análisis de la Energía entregada a la red de distribución eléctrica por las Centrales Eólicas - Compañía Eólica Aragonesa S. A.", Zaragoza University, January 1999.
317. Report of the Research Project "Análisis de la Energía entregada a la red de

- distribución eléctrica por las Centrales Eólicas - Neg-Micon Eólica S.A.", Zaragoza University, November 2000.
318. Hannele Holttinen, "Hourly Wind Power Variations in the Nordic Countries", *Wind Energy*, vol. 8 (2005), Issue 2, pp.173-195.
 319. K. Altaii, R.N. Farrugia, "Wind characteristics on the Caribbean island of Puerto Rico", *Renewable Energy* 28 (2003) pp. 1701-1710.
 320. Gilbert M. Masters, "Renewable and Efficient Electric Power Systems" , Wiley 2004.
 321. G. Papaefthymiou, "Integration of Stochastic Generation in Power Systems", Ph. D Thesis, Delft 2006
 322. Holttinen, H.; Lemström, B.; Meibom, P.; Bindner, H.; Orths, A. et al. "Design and operation of power systems with large amounts of wind power", 2007. VTT Working Papers : 82, Espoo. 119 p. + app. 25 p.
 323. B. Parsons, M. Milligan, B. Zavadil, D. Brooks, B. Kirby, K. Dragoon, J. Caldwell, "Grid Impacts of Wind Power: A Summary of Recent Studies in the United States", EWEC 2003.
 324. []B. Bidabad, B. Bidabad, "Complex Probability and Markov Stochastic Process". Proceeding of the 1st Iranian Statistics Conference, Isfahan University of Technology, 1992.
 325. Lawrence R. Rabiner, "A Tutorial on Hidden Markov Models and Selected Applications in Speech Recognition", *Proceedings of the IEEE*, Vol. 77, No. 2, February 1989
 326. Isaac Van der Hoven, "Power Spectrum Of Horizontal Wind Speed In The Frequency Range From 0.0007 To 900 Cycles Per Hour", *Journal of the Atmospheric Sciences*, Vol. 14, Issue 2, pp. 160-164
 327. Tore Heggem, Rune Lende, And Jorgen Lovseth, "Analysis of Long Time Series of Coastal Wind", *Journal of the Atmospheric Sciences*, Volume 55, Issue 18, pp. 2907-2917
 328. P. Sorensen, N. A. Cutululis, J. Hjerrild, L. Jensen, M. Donovan, L. E. A. Christensen, H. Madsen, A. Viguera-Rodríguez, "Power Fluctuations from Large Offshore Wind Farms", Nordic Wind Power Conference, 22-23 May, 2006, Espoo, Finland.
 329. K. Saranyasoontorn, L. Manuel, Paul S. Veers, "A Comparison of Standard Coherence Models form Inflow Turbulence With Estimates from Field Measurements", *Journal of Solar Energy Engineering*, Vol. 126, Issue 4, pp. 1069-1082
 330. J.C. Kaimal, "Horizontal Velocity Spectra in an Unstable Surface Layer" *Journal of the Atmospheric Sciences*, Vol. 35, Issue 1, pp. 18-24
 331. Wind energy barometer 2008. *EurObserv'ER Systemes solaires Le journal des énergies renouvelables* , n° 4, 2009.
 332. Red Eléctrica de Espana, "The Spanish Power System. Wind power generation in real time", Available: http://www.ree.es/ingles/i-index_de.html
 333. Order of Energy and Industry Ministry of date 5-9-1985, Published in BOE 12-9-1985, no. 219, pp. 28810.
 334. J. Mur Amada, Ma Paz Comech Moreno, "Reactive Power Injection Strategies for Wind Energy Regarding its Statistical Nature", 6th International Workshop on Large-Scale Integration of Wind Power and Transmission Networks for Offshore Wind Farms. Delft, 2006.
 335. G. George Yin, Qing Zhang, "Discrete-Time Markov Chains: two-time-scale methods and applications", Springer Mathematics, 2005.
 336. Vidyadhar G. Kulkarni "Modeling, analysis, design, and control of stochastic system", Springer-Verlang New York 1999.
 337. R. Billinton and R. N. Allan, *Reliability Evaluation of Power Systems*, 2nd ed. New York: Plenum Press, 1996.

338. A. D. Gordon, "Classification", CRC Press, 2nd Ed. 1999.
339. B. S. Everitt, S. Landau and M. Leese, "Cluster Analysis", Oxford University Press, 4th Ed. 2001.
340. IEC 61400-12-3, Wind turbine generator systems - Part 12-3: wind farm power performance testing, 2005. Working Group Draft.
341. Nikolai V. Shokhirev, "Hidden Markov Models", Available at www.shokhirev.com/nikolai/abc/alg/hmm/hmm.html
342. C. Luo and B. T. Ooi, "Frequency Deviation of Thermal Power Plants Due to Wind Farms", IEEE Trans. Energy Conversion, Sept. 2006, Vol. 21, N. 3, pp. 708-716.
343. Rodriguez, J.M.; Fernandez, J.L.; Beato, D.; Iturbe, R.; Usaola, J.; Ledesma, P.; Wilhelmi, J.R.; "Incidence on power system dynamics of high penetration of fixed speed and doubly fed wind energy systems: study of the Spanish case", IEEE Trans. Power Systems, Vol. 17, No 4, Nov. 2002, Pp.1089 - 1095
344. Cigré, Working Group C1.3, "Electric Power System Planning with the Uncertainty of Wind Generation" Technical Report 293, April 2006.
345. Wan, Y. "Wind Power Plant Behaviours: Analyses of Long-Term Wind Power Data". NREL/TP-500-36651, Aug. 2004. Available at www.osti.gov/bridge
346. S. M. Ross, "Introduction to Probability Models", Academic Press, 8th Edition, 2003.
347. G. Stefopoulos, A. P. Meliopoulos and G. J. Cokkinides, "Advanced probabilistic Power Flow Methodology", 15th PSCC, Liege, 2005
348. Chun-Lien Su, "Probabilistic Load-Flow Computation Using Point Estimate Method", IEEE Trans. Power Systems, Vol. 20, no. 4, Nov. 2005.
349. G. Verbic, C. A. Canizares, "Probabilistic Optimal Power Flow in Electricity Markets Based on a Two Point Estimate Method", IEEE Trans. Power Systems, Vol. 21, No. 4, pp.1883 - 1893, Nov. 2006.
350. G. J. Anders, "Probability concepts in electric power systems", Ed. Wiley, 1991.
351. R. Billinton and R. N. Allan, Reliability Evaluation of Power Systems, 2nd ed. New York: Plenum Press, 1996.
352. D. Pena, "Análisis de datos multivariantes", McGraw-Hill, 2002.
353. P. Fernandes, B. Plateau and W. J. Stewart, "Efficient Descriptor-vector Multiplications in Stochastic Automata Networks", Journal of the ACM, Vol. 45, No. 3, May 1998, pp. 381-414.
354. J. Mur, J. Sallán, A.A. Bayod, "Statistical model of wind farms for power flow", ICREP 2003, Vigo.
355. J. Mur, M. P. Comech, "Reactive Power Injection Strategies for Wind Energy Regarding its Statistical Nature", Sixth International Workshop on Large-Scale Integration of Wind Power and Transmission Networks for Offshore Wind Farm. Delft, 2006.
356. UNE 206005 IN Determinación de la capacidad de regulación de potencia reactiva de parques eólicos. 2004 (Assesment of the reactive power ability of wind farms).
357. Ali Abur, Antonio Gómez Expósito, "Power System State Estimation: Theory and Implementation", CRC Press, 2004.
358. J. Mur, A. A. Bayod "Characterization of wind farm energy production in a zone by artificial neuronal networks", ICREP '03, Vigo 2003.
359. W. J. Stewart, "Introduction to the Numerical Solution of Markov Chains", Princeton University Press, 1994.
360. Schuhmacher, J., 1993. "INSEL - Interactive Simulation of Renewable Electrical Energy Supply Systems-, Reference Manual". University of Oldenburg, Renewable Energy Group, Dept. of Physics, PO Box 2503, D-26111 Oldenburg.
361. R. Dufo, "Dimensionamiento y control óptimos de sistemas híbridos aplicando algoritmos evolutivos", PhD., Zaragoza University, 2007.
362. B. Givan and R. Parr, "An Introduction to Markov Decision Processes", Purdue

- University, 2001.
363. E. A. Feinberg and A. Schwartz (editors), "Handbook of Markov Decision Processes. Methods and Applications", Kluwer 2002.
 364. Raúl Vicastillo-Golvano, "Optimización de un banco de condensadores y reactancias en la subestación de un parque eólico", Graduation Project, Zaragoza University, June 2009.
 365. Andrés E. Feijóo, José Cidrás "Modeling of Wind Farms in the Load Flow Analysis", IEEE Trans. Power Systems, Vol. 15, No. 2, Feb. 2000, pp. 110-115.
 366. UNE-EN 50160 "Voltage characteristics supplied by general distribution networks" (in Spanish). 1999.
 367. Royal Decree 436/2004, Boletín Oficial del Estado. Publishing date: 27th March 2004. Available at <http://www.boe.es/boe/dias/2004-03-27/pdfs/A13217-13238.pdf>
 368. N. Jenkins, R. Allan, P. Crossley, D. Kirschen and G. Strbac "Embedded Generation", Ed. IEE 2000
 369. Sveca, J., Soder, L., "Wind power integration in power systems with bottleneck problems", Power Tech Conference Proceedings, 2003 IEEE Bologna
 370. V. Akhmatov, H. Knudsen, "An aggregate model of a grid-connected, large-scale, offshore wind farm for power stability investigations Z importance of windmill mechanical system", Electrical Power and Energy Systems 24 (2002) pp. 709-717
 371. IEC 61400-12-1, Wind turbine generator systems - Part 12-1: Power performance measurements of electricity producing wind turbines, 2006. Committee Draft.
 372. Suresh H. Jangamshetti, V. Guruprasada Rau "Normalized Power Curves as a Tool for Identification of Optimum Wind Turbine Generator Parameters", IEEE Trans, on Energy Conv., Vol. 16, No 3, Sept. 2001, pp 283-288.
 373. G. J. Anders, "Probability concepts in electric power systems", Ed. Wiley, 1991.
 374. C.L. Masters, J. Mutale, G. Strbac, S. Curcic and N. Jenkins "Statistical evaluation of voltages in distribution systems with embedded wind generation", IEE Proc.-Gener. Transm. Distrib. Vol. 147, No 4, July 2000, pp. 207-212.
 375. IEC 61400-12-3, Wind turbine generator systems - Part 12-3: wind farm power performance testing, 2005. Working Group Draft.
 376. J.L. Rodríguez Amenedo, J.C. Burgos Díaz, S. Arnalte Gómez "Sistemas Eólicos de Producción de Energía Eléctrica. Editorial Rueda S.L., 2003.
 377. Statistical Methods of Uncertainty Analysis for Metrology and Scientific Laboratories ISO 7C69/SC6/WG2 Draft 2. Available at <http://www.itl.nist.gov/div898/carroll/u1.htm>
 378. J. Mur, J. Sallán, A.A. Bayod, "Statistical model of wind farms for power flow", ICREP 2003, Vigo.
 379. UNE 206005 IN Determinación de la capacidad de regulación de potencia reactiva de parques eólicos. 2004 (Assesment of the reactive power ability of wind farms).
 380. T. Ackerman, "Wind Power in Power Systems". Ed. Wiley 2005.
 381. OM 12/1/1995, Boletín Oficial del Estado. Publishing date: 14th January 1995. Available at <http://www.boe.es/boe/dias/1995/01/14/pdfs/A01355-01377.pdf>
 382. ^p. Bryans et Al., "Electric Power System Planning with the uncertainty of wind generation". CIGRÉ, Tecnical Brochure 293, W.G. C1.3.
 383. ISO - Guide to the expression of uncertainty in measurement, 1995.
 384. IEC 61400-12-2, Wind turbine generator systems - Part 12-2: Verification of power performance of individual wind turbines, 2005. Working Group Draft.
 385. R. Allan, R. Billinton, "Probabilistic Assessment of Power Systems", Proceedings of the IEEE, Vol. 88, No 2, February 2000, pp 140-162.
 386. C. Gherasim, "Signal Processing for Voltage and Current Measurements in Power Quality Assessment", PhD. Thesis, Katholieke Universiteit Leuven, May 2006
 387. Klaus Heuk, Klaus-Dieter Dettmann, "Elektrische Energieversorgung", Vieweg,

3rd edition.

388. J. Mann, G.C. Larsen and T.J. Larsen, "Towards more realistic extreme load predictions", EWEC 2006, February 2006.
389. Igor Djuroic, Ljibisa Stankovic. "A Virtual Instrument for Time-Frequency Analysys". IEEE Trans. Instrumentation and Measurement, vol. 48, no. 6, December, 1999.
390. Tomasz P. Zielinski. "Joint Time-Frequency Resolution of Signal Analysis Using Gabor Transform" IEEE Trans. on Instr. Meas. Vol. 50, No. 5, pp. 1436-1444. 2001.
391. M. O. L. Hansen, "Aerodynamics of wind turbines", 2nd Ed., Earthscan 2008.
392. J. Peeters, "Simulation of dynamic drive train loads in a wind turbine", Ph. D. Dissertation, Katholieke Universiteit Leuven, 2006.
393. A. Ahlström, "Aeroelastic Simulation of Wind Turbine Dynamics", Ph.D., KTH, Stockholm, 2005
394. J.F. Manwell, J.G. McGowan and A.L. Rogers, "Wind Energy Explained. Theory, Design and Application.", 2002, Wiley
395. Eric Hau, "Wind Turbines. Fundamentals, Technologies, Application, Economics", 2nd Ed., Springer 2006.
396. R. Lanzafame, M. Messina, "Fluid dynamics wind turbine design: Critical analysis, optimization and application of BEM theory", Renewable Energy 32 (2007) 2291-2305
397. J. Jonkman, "Aeroelastic Simulation: FAST", Wind Turbine Design Codes Workshop, National Wind Technology Center, September 13-15, 2005.
398. "AeroDyn User's Guide", version 12.50, Dec. 2002.
399. F.M.White "Fluid Mechanics", 5th Ed., McGraw Hill International, (2003)
400. F. Kießling, "Modellierung des aeroelastischen Gesamtsystems einer Windturbine mit Hilfe symbolischer Programmierung", DFVLR report, DFVLR-FB 84-10, 1984
401. Snyder, M.H., "Wakes Produced by a Single Element and Multiple Element Wind Turbine Towers". Wind Energy Conversion Devices, Von-Kármán-Institut, 1981
402. ^p.J. Vermeer, J.N.Sorensen y A. Crespo (2003) "Wind Turbine Wake Aerodynamics" Progress in Aerospace Sciences. Vol. 39. Issues 6-7. Agosto- Octubre 2003. pp. 467-510.
403. O. Rathmann, S. Frandsen, R. Barthelmie, "Wake modelling for intermediate and large wind farms", EWEC 2007.
404. Frandsen, S.; Barthelmie, R.J.; Rathmann, O.; Jorgensen, H.E.; Badger, J.; Hansen, K.; Ott, S.; Rethore, P.-E.; Larsen, S.E.; Jensen, L.E., Summary report: The shadow effect of large wind farms: measurements, data analysis and modelling. Riso-R-1615(EN) (2007) 35 p.
405. R.J. Barthelmie, S.T. Frandsen, K. Hansen, J.G. Schepers, K. Rados, W. Schlez , A. Neubert, L.E. Jensen, S. Neckelmann, "Modelling the impact of wakes on power output at Nysted and Horns Rev", EWEC2008.
406. R.J. Barthelmie, S.T. Frandsen, O. Rathmann, K. Hansen, E.S. Politis, J. Prospathopoulos, D. Cabezón, K. Rados, S.P. van der Pijl, J.G. Schepers, W. Schlez, J. Phillips and A. Neubert, "Flow and wakes in large wind farms in complex terrain and offshore", EWEC 2008
407. A. Martins, P. C. Costa, A. S. Carvalho, "Coherence and wakes in wind models for electromechanical and power systems standard simulations", EWEC 2006.
408. A Jimenez, A Crespo, E Migoya and J Garcia "Large-eddy simulation of spectral coherence in a wind turbine wake", Environ. Res. Lett. 3 (January-March 2008).
409. A. Knauer, T.D. Hanson, B. Skaare, "Offshore Wind Turbine Loads in Deep-water Environment", EWEC 2006.
410. Vermeulen PEJ. "An experimental analysis of wind turbine wakes". Proceedings of the International Symposium on Wind Energy Systems, Lyngby, Denmark; 1980; 431-450.

411. WASP Manual, "Wake effect model", available at <http://www.wasp.dk>
412. R.J. Barthelmie, O. Rathmann, S.T. Frandsen, K. Hansen, E. Politis, J. Prospathopoulos, K. Rados, D. Cabezón, W. Schlez, J. Phillips, A. Neubert, J.G. Schepers and S.P. van der Pijl, "Modelling and measurements of wakes in large wind farms", *The Science of Making Torque from Wind*, IOP Publishing, 2007.
413. B. Lange, H.P. Waldl, R. Barthelmie, A. Gil-Guerrero, D. Heinemann, "Modelling of offshore wind turbine wakes with the wind farm program FLaP", *Wind Energy*, Vol. 6 Issue 1, Pp. 87 - 104.
414. R. Barthelmie, G. Larsen, S. Pryor, H. Bergström, M. Magnusson, W. Schlez, K. Rados, B. Lange, P. Volund, S. Neckelmann, S. Mogensen, G. Schepers, T. Hegberg, L. Folkerts, "ENDOW: Efficient Development of Offshore Windfarms", *Wind Energy*, Vol. 7, Issue 3, Pp. 225 - 245
415. J. Mur, "Wind Power Variability in the Grid", Ph.D Thesis, Zaragoza University, October 2009.
416. Dennis C. Ghiglia, Mark D. Pritt, "Two-Dimensional Phase Unwrapping : Theory, Algorithms, and Software", June, 1998.
417. R. L. Smith, "Time Series", University of North Carolina, 1999. www.stat.unc.edu/faculty/rsmith.html (accessed on May 16, 2008).
418. W. A. Ardner, A. Napolitano, L. Paura, "Cyclostationarity: Half a century of research", *Signal Processing* 86 (2006) 639-697.
419. A. Papoulis, "Probability, Random Variables, and Stochastic Processes", McGraw-Hill, 4th ed., 2002.
420. O. Kallenberg, "Foundations of Modern Probability", Springer, 2nd Ed., 2002.
421. I. Fleischer, A. Kooharian, "On the Statistical Treatment of Stochastic Processes", *The Annals of Mathematical Statistics*, Vol. 29, No. 2 (Jun., 1958), pp. 544-549.

422. [EWEA, "Wind Energy, the Facts - Wind Power Variability and Impacts on Power Systems"](#)
423. [W. Katzenstein, "Wind Power Variability, Its Cost, and Effect on Power Plant Emissions", PhD. Dissertation, July 2010.](#)
424. [Paul-Frederik Bach, "The Variability of Wind Power, Collected Papers 2009-2011", Renewable Energy Foundation, 2011.](#)
425. [Andre Shoucri and David R. Baker, "Montana Wind Power Variability Study", GENIVAR, September 2008.](#)
426. [Rui Wang and David R. Baker, "Alberta Wind Power Variability Study", Phoenix Engineering Inc., July 2005.](#)
427. [RenewableUK, "Wind Power and Variability", Renewable-UK Fact Sheet 02, June 2010.](#)
428. [Edvard Csanyi, "Wind Variability", Electrical Engineering Portal, November 2010.](#)

[American Wind Energy Association \(AWEA\)](#)

[Bonneville Power Administration Power Business Line Wind Power](#)

[Danish Wind Industry Association](#)

- [Wind Power Crash Course for Kids](#) By Danish Wind Energy Association
- [Guided Tour on Wind Energy](#) By Danish Wind Energy Association

[The Database of State Incentives for Renewable Energy \(DSIRE\)](#) .

[Wind and Hydropower Technologies Program](#)

[National Wind Coordinating Committee \(NWCC\)](#)

[National Wind Technology Center](#)

[Renewable Energy Policy Project: Wind Web Site](#)

[Sandia National Laboratory Wind Energy Technology](#)

- [Sandia National Laboratory Wind Energy Technolog links](#)

[Utility Wind Interest Group \(UWIG\)](#)

- [Utility Wind Interest Group \(UWIG\) Links](#) .

[Wind Energy in California](#)

[Wind Power Can Produce One Third of the World's Electricity by 2050 - By Greenpeace](#)

[Wind Powering America](#)

[WindPower Monthly](#)

[wind-works.org by Paul Gipe](#)

[www.windturbines.net](#)